
Version 23.0
December 2023

Space Telescope Imaging Spectrograph Instrument Handbook for Cycle 32



STScI | SPACE TELESCOPE
SCIENCE INSTITUTE

3700 San Martin Drive
Baltimore, MD 21218
<https://hsthelp.stsci.edu>

| | |
|--|-----|
| STIS Instrument Handbook | 5 |
| Acknowledgments | 7 |
| Chapter 1: Introduction | 8 |
| 1.1 Overview | 9 |
| 1.2 Introduction to the Handbook | 10 |
| 1.3 Handbook Layout | 13 |
| 1.4 Proposal Preparations and Observations with STIS | 19 |
| 1.5 The Help Desk at STScI | 20 |
| 1.6 The STIS Web Pages and Support Information | 21 |
| 1.7 Non-proprietary STIS Data | 23 |
| Chapter 2: Special Considerations for Cycle 32 | 24 |
| 2.1 STIS Repair and Return to Operations | 25 |
| 2.2 Summary of STIS Performance Changes Since 2004 | 26 |
| 2.3 New Capabilities for Cycle 32 | 27 |
| 2.4 Use of Available-but-Unsupported Capabilities | 28 |
| 2.5 Choosing Between COS and STIS | 30 |
| 2.6 Scheduling Efficiency and Visit Orbit Limits | 32 |
| 2.7 MAMA Scheduling Policies | 34 |
| 2.8 Prime and Parallel Observing: MAMA Bright-Object Constraints | 35 |
| 2.9 STIS Snapshot Program Policies | 37 |
| Chapter 3: STIS Capabilities, Design, Operations, and Observations | 38 |
| 3.1 Instrument Capabilities | 39 |
| 3.2 Instrument Design | 40 |
| 3.3 Basic Instrument Operations | 45 |
| 3.4 Designing STIS Observations | 49 |
| Chapter 4: Spectroscopy | 55 |
| 4.1 Overview | 56 |
| 4.2 First-Order Long-Slit Spectroscopy | 67 |
| 4.3 Echelle Spectroscopy in the Ultraviolet | 77 |
| 4.4 Objective Prism Spectroscopy | 80 |
| Chapter 5: Imaging | 84 |
| 5.1 Imaging Overview | 85 |
| 5.2 Optical CCD Imaging | 93 |
| 5.3 Ultraviolet Imaging with the MAMA Detectors | 98 |
| 5.4 Neutral Density Filters | 111 |
| Chapter 6: Exposure Time Calculations | 112 |
| 6.1 Overview | 113 |
| 6.2 Determining Count Rates from Sensitivities | 114 |
| 6.3 Throughput and Sensitivity | 121 |
| 6.4 Computing Exposure Times | 122 |
| 6.5 Detector and Sky Backgrounds | 125 |
| 6.6 Tabular Sky Backgrounds | 133 |
| 6.7 Extinction Correction | 136 |
| 6.8 Exposure Time Examples | 138 |
| Chapter 7: Feasibility and Detector Performance | 146 |
| 7.1 STIS Detectors | 147 |
| 7.2 The CCD | 148 |
| 7.3 CCD Operation and Feasibility Considerations | 165 |
| 7.4 The MAMA Detectors | 180 |
| 7.5 MAMA Operation and Feasibility Considerations | 189 |
| 7.6 MAMA Spectral and Spatial Offsetting | 202 |
| 7.7 MAMA Bright Object Limits | 203 |
| Chapter 8: Target Acquisition | 212 |

| | |
|--|-----|
| 8.1 Introduction | 213 |
| 8.2 STIS Onboard CCD Target Acquisitions - ACQ | 219 |
| 8.3 Onboard Target Acquisition Peakups - ACQ PEAK | 234 |
| 8.4 Determining Coordinates in the International Celestial Reference System (ICRS) Reference Frame | 240 |
| 8.5 Acquisition Examples | 241 |
| 8.6 STIS Post-Observation Target Acquisition Analysis | 250 |
| Chapter 9: Overheads and Orbit-Time Determination | 251 |
| 9.1 Overview | 252 |
| 9.2 STIS Exposure Overheads | 253 |
| 9.3 Orbit Use Determination Examples | 256 |
| Chapter 10: Summary and Checklist | 264 |
| 10.1 Phase I Proposing | 265 |
| 10.2 Phase II - Scheduling Approved Observations | 267 |
| Chapter 11: Data Taking | 269 |
| 11.1 Basic Operating Modes | 270 |
| 11.2 Exposure Sequences and Contemporaneous Calibrations | 282 |
| 11.3 Patterns and Dithering | 288 |
| 11.4 Fixing Orientation on the Sky | 296 |
| 11.5 Target Positioning | 301 |
| Chapter 12: Special Uses of STIS | 302 |
| 12.1 Slitless First-Order Spectroscopy | 303 |
| 12.2 Long-Slit Echelle Spectroscopy | 306 |
| 12.3 Time-Resolved Observations | 308 |
| 12.4 Observing Too-Bright Objects with STIS | 311 |
| 12.5 High Signal-to-Noise Ratio Observations | 312 |
| 12.6 Improving the Sampling of the Line Spread Function | 318 |
| 12.7 Considerations for Observing Planetary Targets | 319 |
| 12.8 Special Considerations for Extended Targets | 320 |
| 12.9 Parallel Observing with STIS | 321 |
| 12.10 Coronagraphic Spectroscopy | 323 |
| 12.11 Coronagraphic Imaging - 50CORON | 327 |
| 12.12 Spatial Scans with the STIS CCD | 332 |
| Chapter 13: Spectroscopic Reference Material | 338 |
| 13.1 Introduction | 340 |
| 13.2 Using the Information in this Chapter | 341 |
| 13.3 Gratings | 349 |
| First-Order Grating G750L | 350 |
| First-Order Grating G750M | 356 |
| First-Order Grating G430L | 362 |
| First-Order Grating G430M | 368 |
| First-Order Grating G230LB | 374 |
| Comparison of G230LB and G230L | 380 |
| First-Order Grating G230MB | 383 |
| Comparison of G230MB and G230M | 389 |
| First-Order Grating G230L | 392 |
| First-Order Grating G230M | 398 |
| First-Order Grating G140L | 404 |
| First-Order Grating G140M | 410 |
| Echelle Grating E230M | 416 |
| Echelle Grating E230H | 422 |
| Echelle Grating E140M | 428 |
| Echelle Grating E140H | 434 |

| | |
|--|-----|
| PRISM | 440 |
| PRISM Wavelength Relationship | 444 |
| 13.4 Apertures | 446 |
| 52X0.05 Aperture | 447 |
| 52X0.05E1 and 52X0.05D1 Pseudo-Apertures | 450 |
| 52X0.1 Aperture | 451 |
| 52X0.1E1 and 52X0.1D1 Pseudo-Apertures | 454 |
| 52X0.2 Aperture | 455 |
| 52X0.2E1, 52X0.2E2, and 52X0.2D1 Pseudo-Apertures | 457 |
| 52X0.5 Aperture | 458 |
| 52X0.5E1, 52X0.5E2, and 52X0.5D1 Pseudo-Apertures | 460 |
| 52X2 Aperture | 461 |
| 52X2E1, 52X2E2, and 52X2D1 Pseudo-Apertures | 463 |
| 52X0.2F1 Aperture | 464 |
| 0.2X0.06 Aperture | 467 |
| 0.2X0.2 Aperture | 469 |
| 0.2X0.09 Aperture | 471 |
| 6X0.2 Aperture | 473 |
| 0.1X0.03 Aperture | 475 |
| FP-SPLIT Slits 0.2X0.06FP(A-E) Apertures | 477 |
| FP-SPLIT Slits 0.2X0.2FP(A-E) Apertures | 480 |
| 31X0.05ND(A-C) Apertures | 484 |
| 0.2X0.05ND Aperture | 487 |
| 0.3X0.05ND Aperture | 489 |
| F25NDQ Aperture | 491 |
| 13.5 Spatial Profiles | 495 |
| First-Order Spatial Profiles | 496 |
| Echelle Spatial Profiles | 502 |
| 13.6 Line Spread Functions | 506 |
| First-Order Line Spread Functions | 507 |
| Echelle Line Spread Functions | 511 |
| 13.7 Spectral Purity, Order Confusion, and Peculiarities | 515 |
| 13.8 MAMA Spectroscopic Bright Object Limits | 528 |
| Chapter 14: Imaging Reference Material | 531 |
| 14.1 Introduction | 532 |
| 14.2 Using the Information in this Chapter | 533 |
| 14.3 CCD | 538 |
| CCD Clear Imaging - 50CCD | 539 |
| CCD Long-Pass Imaging F28X50LP | 547 |
| F28X50OIII - CCD | 554 |
| F28X50OII - CCD | 562 |
| 50CORON - Clear CCD | 569 |
| 14.4 NUV-MAMA | 570 |
| 25MAMA - NUV-MAMA, Clear | 571 |
| F25ND3 - NUV-MAMA | 579 |
| F25ND5 - NUV-MAMA | 584 |
| F25NDQ - NUV-MAMA | 589 |
| F25QTZ - NUV-MAMA, Longpass | 592 |
| F25SRF2 - NUV-MAMA, Longpass | 601 |
| F25MGII - NUV-MAMA | 606 |
| F25CN270 - NUV-MAMA | 615 |
| F25CIII - NUV-MAMA | 623 |
| F25CN182 - NUV-MAMA | 632 |

| | |
|--|-----|
| 14.5 FUV-MAMA | 640 |
| 25MAMA - FUV-MAMA, Clear | 641 |
| 25MAMAD1 - FUV-MAMA Pseudo-Aperture | 649 |
| F25ND3 - FUV-MAMA | 650 |
| F25ND5 - FUV-MAMA | 655 |
| F25NDQ - FUV-MAMA | 660 |
| F25QTZ - FUV-MAMA, Longpass | 663 |
| F25QTZD1 - FUV-MAMA, Longpass Pseudo-Aperture | 671 |
| F25SRF2 - FUV-MAMA, Longpass | 672 |
| F25SRF2D1 - FUV-MAMA, Longpass Pseudo-Aperture | 680 |
| F25LYA - FUV-MAMA, Lyman-alpha | 681 |
| 14.6 Image Mode Geometric Distortion | 690 |
| 14.7 Spatial Dependence of the STIS PSF | 692 |
| 14.8 MAMA Imaging Bright Object Limits | 697 |
| Chapter 15: Overview of Pipeline Calibration | 700 |
| 15.1 Pipeline Processing Overview | 701 |
| 15.2 How Phase II Parameter Choices Affect Calibration | 707 |
| 15.3 More Detailed Information | 708 |
| Chapter 16: Accuracies | 709 |
| 16.1 Summary of Accuracies | 710 |
| Chapter 17: Calibration Status and Plans | 715 |
| 17.1 Introduction | 716 |
| 17.2 Ground Testing and Calibration | 717 |
| 17.3 STIS Installation and Verification (SMOV2) | 718 |
| 17.4 Cycle 7 Calibration | 720 |
| 17.5 Cycle 8 Calibration | 722 |
| 17.6 Cycle 9 Calibration | 723 |
| 17.7 Cycle 10 Calibration | 724 |
| 17.8 Cycle 11 Calibration | 725 |
| 17.9 Cycle 12 Calibration | 726 |
| 17.10 SM4 and SMOV4 Calibration | 727 |
| 17.11 Cycle 17 Calibration Plan | 731 |
| 17.12 Cycle 18 Calibration Plan | 732 |
| 17.13 Cycle 19 Calibration Plan | 733 |
| 17.14 Cycle 20 Calibration Plan | 734 |
| 17.15 Cycle 21 Calibration Plan | 735 |
| 17.16 Cycle 22 Calibration Plan | 736 |
| 17.17 Cycle 23 Calibration Plan | 737 |
| 17.18 Cycle 24 Calibration Plan | 738 |
| 17.19 Cycle 25 Calibration Plan | 739 |
| 17.20 Cycle 26 Calibration Plan | 740 |
| 17.21 Cycle 27 Calibration Plan | 741 |
| 17.22 Cycle 28 Calibration Plan | 742 |
| 17.23 Cycle 29 Calibration Plan | 743 |
| 17.24 Cycle 30 Calibration Plan | 744 |
| 17.25 Cycle 31 Calibration Plan | 745 |
| Appendix A: Available-But-Unsupported Spectroscopic Capabilities | 746 |
| A.1 Introduction | 747 |
| A.2 Full Aperture Complement | 748 |
| A.3: Additional Available-but-Unsupported Options | 754 |
| Glossary | 755 |

STIS Instrument Handbook

Version 23.0 – December 2023

[PDF version](#)

Space Telescope Imaging Spectrograph Instrument Handbook for Cycle 32

User Support

Please contact the *HST* Help Desk for assistance. We encourage users to access the new web portal where you can submit your questions directly to the appropriate team of experts.

- Web: <http://hsthhelp.stsci.edu>
- E-mail: help@stsci.edu

Additional Resources

Information and other resources are available from the [STScI STIS website](#).

Revision History

| Version | Date | Editor |
|---------|---------------|--|
| 23.0 | December 2023 | Sophia Medallon, Emily Rickman, Jacqueline Brown |
| 22.0 | February 2023 | Sophia Medallon, Dan Welty |
| 21.0 | January 2022 | Laura Prichard, Dan Welty, Amy Jones |
| 20.0 | January 2021 | Doug Branton and Allyssa Riley |
| 19.0 | December 2019 | Allyssa Riley |
| 18.0 | January 2019 | Allyssa Riley |
| 17.0 | May 2018 | Allyssa Riley |
| 16.0 | January 2017 | Allyssa Riley |
| 15.0 | January 2016 | J. Biretta |
| 14.0 | January 2015 | J. Biretta |
| 13.0 | January 2014 | Svea Hernandez |
| 12.0 | December 2012 | Svea Hernandez |

| | | |
|------|---------------|--|
| 11.0 | December 2011 | Justin Ely |
| 10.0 | December 2010 | K. Azalee Bostroem |
| 9.0 | January 2010 | Charles Proffitt |
| 8.0 | December 2007 | Jessica Kim Quijano, Sherie Holfeltz, and Jesús Maíz-Apellániz |
| 7.0 | October 2003 | Jessica Kim Quijano and Bahram Mobasher |
| 6.0 | October 2002 | Charles Proffitt |
| 5.1 | July 2001 | Claus Leitherer |
| 5.0 | June 2001 | Claus Leitherer |
| 4.1 | July 2000 | Claus Leitherer |
| 4.0 | June 2000 | Claus Leitherer |
| 3.0 | June 1999 | Kailash Sahu |
| 2.0 | June 1998 | Nolan Walborn and Stefi Baum |
| 1.0 | June 1996 | Stefi Baum |

Citation

In publications, refer to this document as:

- Medallon, S., Rickman, E., and Brown, J. et al. 2023 "STIS Instrument Handbook," Version 23.0, (Baltimore: STScI)

Acknowledgments

This document is written and maintained by the STIS Team in the Instruments Division of STScI with the assistance of colleagues in the Operations and Engineering Division. Contributions to the current edition were made by J. Brown, J. Carlberg, M. Dallas, S. Dieterich, A. Fullerton, A. Jones, S. Lockwood, S. Medallon, T. Monroe, E. Rickman, M. Siebert, D. Stapleton, and D. Welty. We thank the STScI HDox Coordinators, Dan Coe (former) and Jenna Ryon, for their support in editing and publishing this *Handbook*.

We also thank the many people who have contributed to past versions of this *Handbook* including members of the Space Telescope European Coordinating Facility (ST-ECF, ceased operations on 31 December 2010), in particular Michael Rosa and Jeremy Walsh, and the STIS Instrument Definition Team (IDT) at Goddard Space Flight Center (GSFC), particularly Bruce Woodgate¹ (PI), Randy Kimble, Chuck Bowers, and Ted Gull. We also thank Don Lindler (Sigma Space Corporation) for his technical contributions and Susan Rose (former STScI Senior Technical Editor) for supporting previous edits of this *Handbook*.

¹ Deceased.

Chapter 1: Introduction

Chapter Contents

- [1.1 Overview](#)
- [1.2 Introduction to the Handbook](#)
- [1.3 Handbook Layout](#)
- [1.4 Proposal Preparations and Observations with STIS](#)
- [1.5 The Help Desk at STScI](#)
- [1.6 The STIS Web Pages and Support Information](#)
- [1.7 Non-proprietary STIS Data](#)

1.1 Overview

The Space Telescope Imaging Spectrograph (STIS) is a versatile imaging spectrograph, originally installed in 1997 during *HST* servicing mission 2. STIS provides spatially resolved spectroscopy from 1150 to 10,300 Å at low to medium spectral resolution, high spatial resolution echelle spectroscopy in the ultraviolet (UV), solar-blind imaging in the UV, time tagging of photons in the UV for high time resolution, direct and coronagraphic imaging in the optical, and very high signal-to-noise ratio spectra in the NUV/optical/NIR. Its capabilities are thus complementary to those of the Cosmic Origins Spectrograph (COS).

After several years of successful operation, observations with STIS were suspended in August 2004, when a power supply in the Side-2 electronics failed. Nearly five years later, STIS was successfully repaired during the fourth *HST* servicing mission (SM4) in May 2009 and resumed science operations with all channels. Following the repair, most aspects of instrument operations and performance were very similar to what they had been prior to the 2004 failure. There were, however, some important changes at that point, and the behavior of the instrument has continued to evolve. Some of those changes will be outlined in [Chapter 2](#), and additional details will be given elsewhere in this *Handbook* as appropriate.

This *Handbook* provides instrument-specific information needed to propose for STIS observations (Phase I), design accepted programs (Phase II), and understand STIS in detail.

This chapter explains the layout of the *Handbook* and describes how to use the [Help Desk](#) at STScI and the STScI [STIS website](#) to get help and further information. Instrument and operating updates will be posted on the [STIS website](#).

1.2 Introduction to the Handbook

[1.2.1 Document Conventions](#)

[1.2.2 Examples Used in this Handbook](#)

The *STIS Instrument Handbook* is the basic reference manual for the Space Telescope Imaging Spectrograph (STIS); it describes the instrument's properties, performance, operations, and calibration. The *Handbook* is maintained by the STIS team at STScI. Wherever possible, the most recent operational data have been incorporated into this revised edition.

We have designed the document to serve three purposes:

- To provide instrument-specific information for preparing Phase I STIS observing proposals.
- To provide instrument-specific information to support the design of Phase II proposals for accepted STIS programs.
- To provide technical information about the performance and operation of the instrument that can help in the understanding of problems and in the interpretation of data acquired with STIS.

This *Handbook* is not meant to serve as a manual for the reduction and analysis of data taken with STIS. The *STIS Data Handbook* (also available from the [STIS website](#) or the [HST Documentation website](#)) describes how to work with STIS data.

1.2.1 Document Conventions

This document follows the usual STScI convention in which terms, words, and phrases which are to be entered by the user in a literal way on an *HST* proposal are shown in a typewriter font (e.g., STIS/CCD , SHADOW). Names of software packages or commands (e.g., **calstis**) are given in boldface.

Wavelengths in this *Handbook* and in STIS data products are always measured in vacuum conditions. Wavelength units in this *Handbook* are in Angstroms (Å).

1.2.2 Examples Used in this Handbook

The *Handbook* uses six observational examples to illustrate various scenarios such as calculation of exposure times, estimation of overheads, etc. throughout the text. The examples are:

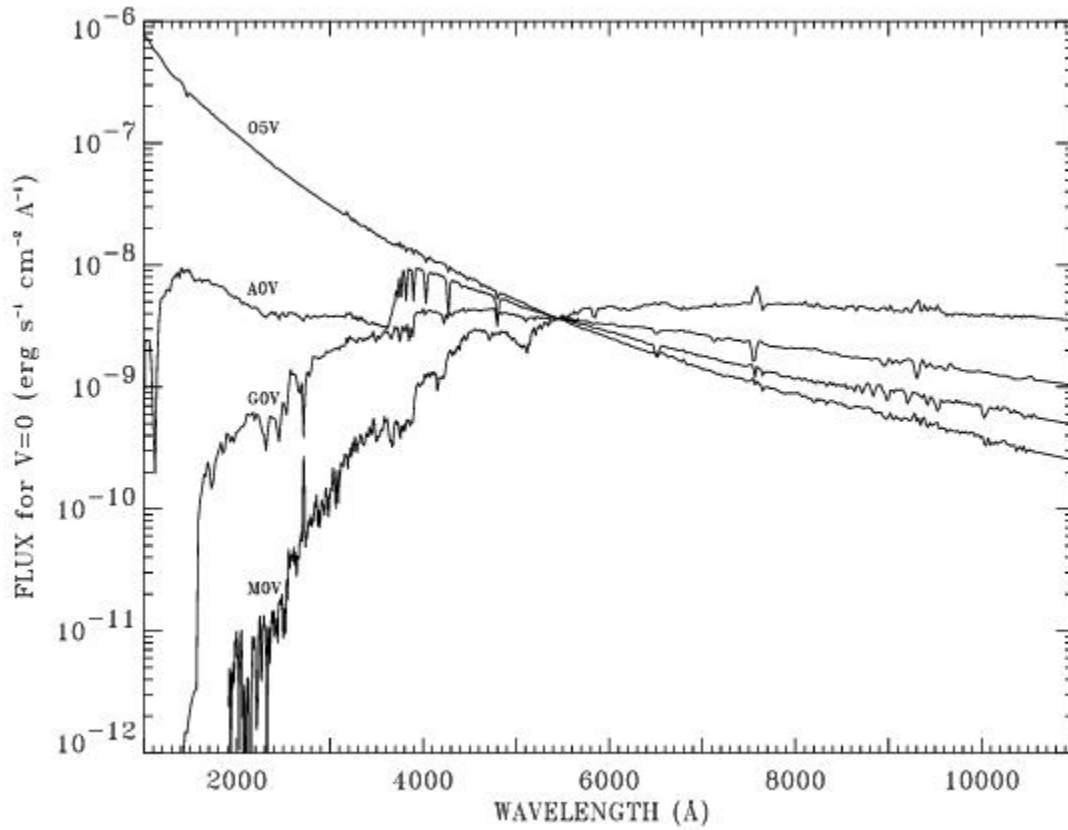
- Long-slit optical spectroscopy of the nearby galaxy NGC 4406 (M86).
- Long-slit optical and UV spectroscopy and optical imaging of NGC 6543, the Cat's Eye planetary nebula.
- First-order low-resolution spectroscopy covering STIS' full wavelength range from 1150 Å in the UV to 10,300 Å in the near-infrared (NIR) of the solar analog star P041-C, in the continuous viewing zone (CVZ).
- Echelle spectroscopy of the O-type star Sk-69°215 in the Large Magellanic Cloud (LMC), a target in the CVZ.
- Deep optical imaging of a random field.
- Time-resolved UV spectroscopy of the flare star AU Mic.

In addition, we use stellar spectra throughout the *Handbook* to illustrate signal-to-noise ratio calculations and derive limiting magnitudes. [Figure 1.1](#) shows the normalized spectra of O, A, G, and M stars from an observed catalog of stars (for details, see Buser, 1978, A&A, 62, 411) which are used in the *Handbook* examples.

Many of the performance characteristics of STIS change over time. These changes include gradual decreases in optical throughput, increases in detector dark currents, and decreasing charge transfer efficiencies. Most of the figures and tables illustrating throughputs, signal-to-noise calculations, bright object limits, and limiting magnitudes had been recalculated for the Cycle 17 version of this *Handbook* based on the best available performance estimates for Cycle 17. Except where otherwise noted these tables and figures have *not* been updated for the additional changes expected for Cycle 32. In most cases the differences will be modest. For more up-to-date performance estimates, it is suggested that users consult the [Performance](#) section of the STIS web pages and the STIS **ETCs** (Exposure Time Calculators; available at <http://etc.stsci.edu/>). The sensitivities and other instrument parameters adopted for use with the Cycle 32 **ETCs** are our best estimates for April 2024 (i.e., mid-Cycle 31).

The software tools used to process, inspect, and analyze STIS data have also evolved over time. In particular, the **IRAF/STSDAS** routines originally used for analyses of STIS (and other *HST*) data are no longer supported by STScI, and they have been largely replaced by python-based tools performing the same (or very similar) functions (see, e.g., the [stistools](#) package). While most of the software references in this *Handbook* now are to the newer python-based tools/routines, a few references still remain to some of the **IRAF/STSDAS** routines, particularly where no exact replacement has been established.

Figure 1.1: Spectra of O5V, A0V, G0V, and M0V Stars.



These spectra are used throughout the handbook and are normalized at 5550 \AA . Note the dramatic differences in the UV properties.

1.3 Handbook Layout

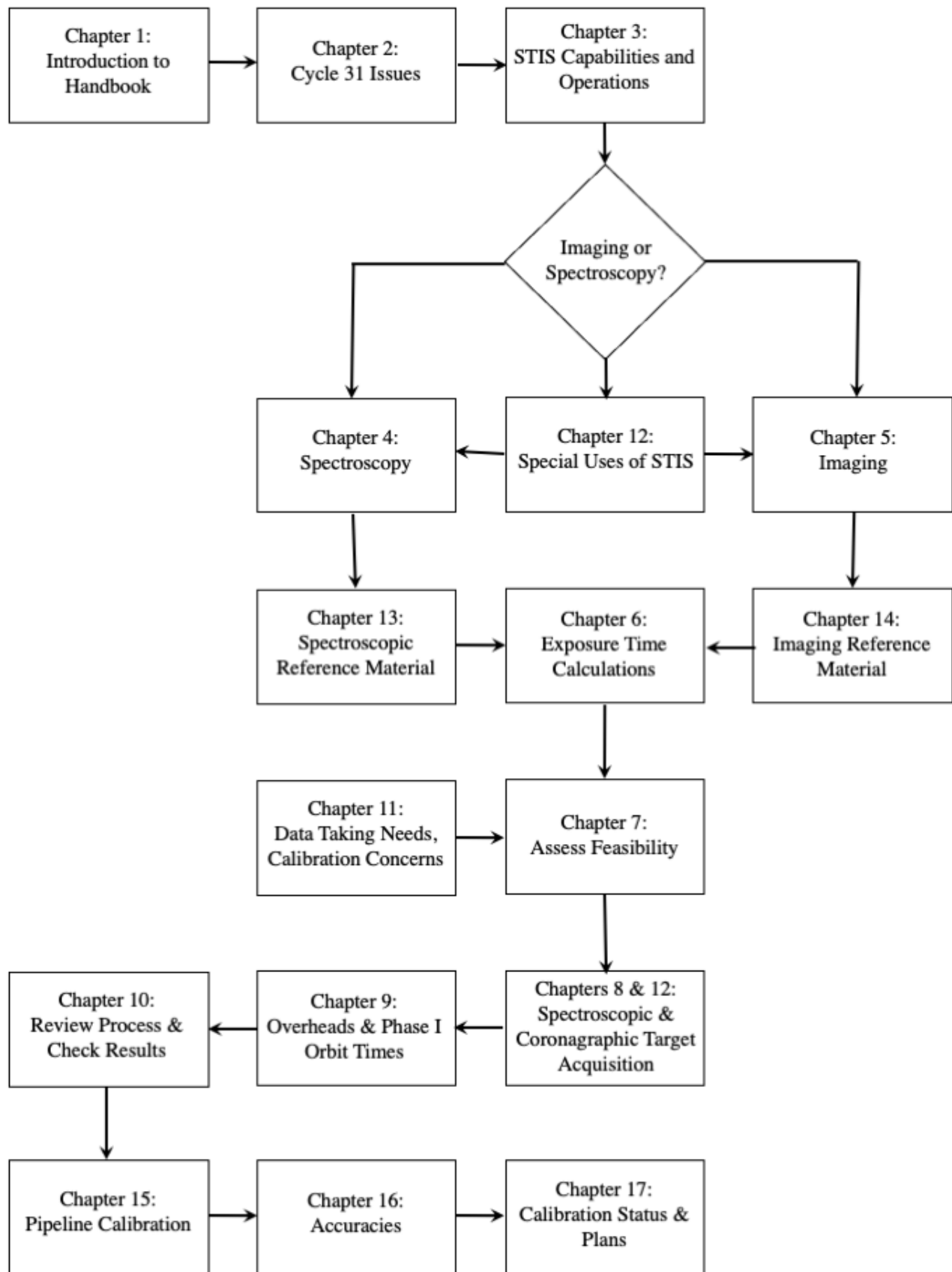
To guide you through STIS' capabilities and help optimize your scientific use of the instrument we have divided this *Handbook* into four parts:

- Part I - Introduction
- Part II - User's Guide
- Part III - Supporting Material
- Part IV - Calibration

Figure 1.2 provides a road map of this *Handbook*.

The Supporting Material and Calibration sections contain technical information which supports the material found in the *User's Guide*; readers are referred to the information at appropriate points in the *User's Guide*.

Figure 1.2: Handbook Roadmap.



The chapters in this Handbook are as follows:

- Part I: Introduction
 - [Chapter 1](#), *Introduction*, includes information about getting help and where to find additional information about STIS.
 - [Chapter 2](#), *Special Considerations for Cycle 32*, describes special policy considerations for using STIS during Cycle 32. A comparison is provided between STIS and COS capabilities.
- Part II: User's Guide
 - [Chapter 3](#), *STIS Capabilities, Design, Operations, and Observations*, provides an overview of STIS' full capabilities. Discussion is provided to help guide you through the technical details you need to consider in choosing the optimum STIS configuration and in determining the number of orbits to request.
 - [Chapter 4](#), *Spectroscopy*, provides a detailed, grating-by-grating description of STIS' spectroscopic capabilities, including spectral resolutions, throughputs, and descriptions of the slits and apertures.
 - [Chapter 5](#), *Imaging*, provides a detailed, filter-by-filter description of STIS' imaging capabilities.
 - [Chapter 6](#), *Exposure Time Calculations*, describes how to perform signal-to-noise and exposure time calculations, either by using pencil and paper, or by using the software tools provided on the [STIS website](#).
 - [Chapter 7](#), *Feasibility and Detector Performance*, provides a description of the three detectors and their physical characteristics, capabilities, and limitations, including saturation, linearity, and bright object limits.
 - [Chapter 8](#), *Target Acquisition*, helps you select the optimum target acquisition sequence needed to place the target in the desired science aperture.
 - [Chapter 9](#), *Overheads and Orbit-Time Determination*, provides information needed to convert a series of planned science exposures to an estimated number of orbits, including spacecraft and STIS overheads. This chapter applies principally to the planning of Phase I proposals.
 - [Chapter 10](#), *Summary and Checklist*, presents a summary and a checklist you should use to assure that there are no major omissions in your Phase I and Phase II proposals.
- Part III: Supporting Material
 - [Chapter 11](#), *Data Taking*, describes data-taking with STIS, including the instrument operating modes (ACCUM, TIME-TAG), the use of subarrays and binning, and the various types of "associated" observations and contemporaneous calibrations (WAVECALs, CCDFLATS, CR-SPLIT, PATTERNS). This chapter also discusses dithering and how to orient the long slits.
 - [Chapter 12](#), *Special Uses of STIS*, provides information on special science uses of STIS, including slitless spectroscopy, long-slit echelle spectroscopy, time-resolved spectroscopy and imaging, observations of very bright targets, techniques for obtaining higher signal-to-noise and spectral sampling, observations of planetary objects, parallel observing, coronagraphic spectroscopy and imaging, and spatial scanning with the CCD.
 - [Chapter 13](#), *Spectroscopic Reference Material*, contains the detailed plots of sensitivities, line spread functions, aperture throughputs, and the tables of bright object limits referred to in [Chapter 4](#).
 - [Chapter 14](#), *Imaging Reference Material*, contains the detailed plots of sensitivities, point spread functions, aperture throughputs, and the tables of bright object limits referred to in [Chapter 5](#).
- Part IV: Calibration

- [Chapter 15](#), *Overview of Pipeline Calibration*, briefly describes the processing of STIS data by the STScI pipeline and the products that are sent to observers.
- [Chapter 16](#), *Accuracies*, summarizes the accuracies for STIS data calibrated by the STScI pipeline.
- [Chapter 17](#), *Calibration Status and Plans*, provides an overview of the current state of STIS calibration and development plans for the immediate future.

1.4 Proposal Preparations and Observations with STIS

1.4.1 The STIS Team at STScI

Use the *STIS Instrument Handbook* together with the Cycle 32 *HST Call for Proposals* (CfP) and *HST Primer* when assembling your STIS Phase I proposal. The CfP provides policy and instructions for proposing. The *HST Primer* provides a basic introduction to the technical aspects of *HST* and its instruments, and explains how to calculate the appropriate number of orbits for your Phase I observing time requests. The *STIS Instrument Handbook* contains technical information about STIS, describing its expected performance and presenting suggestions for use. [Chapter 2](#) of the *Handbook* describes special considerations for Cycle 32.

If your Phase I proposal is accepted, you will be asked to submit a Phase II proposal in which you specify the exact configurations, exposure times, and sequences of observations that STIS and the telescope should perform. To assemble your Phase II proposal, use the *STIS Instrument Handbook* in conjunction with the [Phase II Proposal Instructions](#). These instructions describe the exact rules and syntax that apply to the planning and scheduling of STIS observations and provide relevant observatory information. You should also check the [STIS website](#) for any updates relevant to the current proposal Cycle. Many other useful *HST* documents are also available on-line at: <https://www.stsci.edu/hst/documentation>.

1.4.1 The STIS Team at STScI

STScI has a team of Instrument Scientists, Scientific Programmers, and Staff Scientists who support the development, operation, and calibration of the STIS Instrument. This team is also responsible for supporting STIS users and (in addition) provides archival support for the heritage instrument, [Goddard High Resolution Spectrograph \(GHRS\)](#).

1.5 The Help Desk at STScI

STScI has a [Help Desk](#) whose staff, together with affiliated responders from the various instrument teams, can quickly provide answers on any HST-related topic, including questions regarding STIS and the proposal process.

If you have questions about the phase II implementation of your approved STIS program, usually it is best to reach out to your Contact Scientist (CS). If you do not have a CS, you may send a request to the Help Desk asking for one to be assigned to your program. If your program has already executed, if you are working with archival data, or if you are unsure about whether or not you have a CS, you should direct all inquiries to the Help Desk, at <https://hsthhelp.stsci.edu>.

The Help Desk staff have access to all of the resources available at the Institute, and they maintain a database of previous inquiries so that frequently asked questions can be quickly answered. (The answers to many frequently asked questions can also be found in the knowledge base on the [help desk website](#).) The Help Desk staff can also provide hard copies of STScI documentation, including *Instrument Science Reports* and *Instrument Handbooks* (though this service may be unavailable during the pandemic). In any case, electronic copies of documents are available via the Web.

Questions sent to the Help Desk will receive at least a preliminary response within two working days. The Help Desk staff will do their best to fully answer the question, but if the staff on duty cannot provide an answer, they will contact the appropriate expert(s) at STScI to obtain and deliver the answer. By sending your request to the Help Desk, you are guaranteed that you will obtain a timely and appropriate response.

To contact the HST Help Desk at STScI, we encourage users to access the new web portal, where one can both access the knowledge base and submit questions directly to the appropriate team of experts.

- Website: <https://hsthhelp.stsci.edu>
- E-mail: help@stsci.edu

1.6 The STIS Web Pages and Support Information

The STIS team at STScI maintains webpages (see [Figure 1.3](#)) as part of STScI's Web service. The URL for the top level STScI STIS website is <https://www.stsci.edu/hst/instrumentation/stis>.

The STIS webpages include up-to-date information about STIS operations and performance. The section *STIS Instrument Resources* has links to this information (which can be found below the green-blue box with STIS Handbooks and Documentation on the STIS top level website), organized into the main navigational categories listed below:

- *Instrument Design*: A high-level summary of the basic design and operation of STIS, including summary information on the [detectors](#), [gratings](#), [apertures](#), and [filters](#) available for use.
- *Performance*: More detailed information on actual on-orbit performance of STIS. Sub-categories are [image quality](#), [sensitivity](#), [spectral resolution](#), [throughput](#), [background](#), [accuracy](#), [monitoring](#), [calibration monitors](#), and [anomalies](#).
- *Proposing*: Things you need to know in order to successfully construct and submit [Phase I](#) and [Phase II](#) proposals for STIS observations, and how to monitor the status of your observing program.
- *Observing Strategies*: Discussions of [target acquisitions](#), [pushing the limits](#), and other aspects of the design of [imaging](#) and [spectroscopic](#) observations with STIS.
- *Data Analysis & Software Tools*: Resources describing STIS data characteristics and analysis, including the [STIS Data Handbook](#). [Software tools](#) for planning STIS observations and calibrating data (e.g., the [Exposure Time Calculators \(ETC\)](#), [stistools](#), and the [Target Acquisition Simulator \(TAS\)](#)).
- *Calibration*: Information on STIS calibration plans and close-out reports for all Cycles.
- *Documentation*: Electronic versions of the *Instrument* and *Data Handbooks* as well as detailed technical information concerning the development, performance, testing, operation, and calibration of STIS as documented in a series of [STIS Instrument Science Reports \(ISRs\)](#) and [STScI Analysis Newsletters \(STANs\)](#). These reports can be downloaded directly from the website.
- *Flux Recalibration*: Some information regarding the re-calibration of STIS fluxes, in response to new stellar atmospheric models for the primary calibration standard stars.

Note: the menu tabs in the purple box near the top of the page (e.g. HST Home, About, Proposing) are for the main HST webpages and are not STIS-specific links.

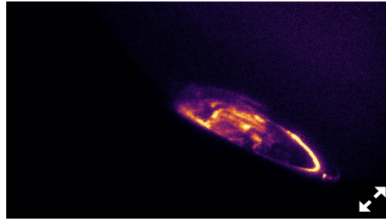
Additional information about getting help with STIS questions or data is available via the [Help Desk](#).

Figure 1.3: STIS Top Level Web Page.

About STIS

The **Space Telescope Imaging Spectrograph** (STIS) was installed on the Hubble Space Telescope (HST) during the second servicing mission (SM2) in 1997. STIS is a versatile imaging spectrograph, providing spatially resolved spectroscopy from 1150 to 10300 Å at low to medium spectral resolution, high spatial resolution echelle spectroscopy in the UV, solar-blind imaging in the UV, time-tagging of photons for high time resolution in the UV, and direct and coronagraphic imaging in the optical.

STIS operated on Side-1 electronics until 2001, when it experienced an electronic failure. It then switched to the redundant set of electronics, Side-2, where it operated as normal until 2004, when a power supply on Side-2 failed. STIS remained inoperable until it was repaired successfully in 2009 during Servicing Mission 4 (SM4). STIS has since been operating on Side-2 electronics with all ultraviolet and optical channels.



Over the course of Cycle 24 and 151 orbits, STIS was used to observe Jupiter's moons and aurorae in program 14634 (PI: Grodent). The data used to produce this GIF was taken with the STIS FUV-MAMA in TIMETAG mode.

STIS Handbooks and Documentation:

[STIS Instrument Handbook](#) ↗

[STIS Data Handbook](#) ↗

Current Status

STIS is Operational.

Web Tools and Helpful Links

[HST Exposure Time Calculator \(ETC\)](#) ↗

[HST Spectroscopic Legacy Archive \(HSLA\)](#) ↗

Program Information

Proposal ID #

STIS Instrument Resources

| | | |
|--------------------------------------|--|-----------------------------|
| Instrument Design | Performance | Proposing |
| Observing Strategies | Data Analysis & Software Tools | Calibration |
| Documentation | Flux Recalibration | |

1.7 Non-proprietary STIS Data

During regular STIS operations, the majority of existing STIS data is non-proprietary and available for retrieval from the *HST* Data Archive. The data include, but are not limited to, data taken under the [Treasury GO Programs](#) and Long-term GO Programs. Observations taken as part of our calibration programs are nominally non-proprietary as soon as they are in the archive. Additionally, GTO and GO observations normally become available when their proprietary periods expire. For most programs this occurs six months after the data are archived, although for selected programs a shorter period may apply. You can use [the MAST portal](#) or the [HST Archive Web interface](#) to search for such data directly. Any such data may be freely acquired, as described in the [STIS Data Handbook](#), for technical or scientific use. Examples of non-proprietary STIS science data are shown as illustrative examples throughout this *Handbook*.

All STIS data collected prior to the Side-2 failure have been reprocessed in the same way that all other data are processed. Formerly, those data were reprocessed using a modified version of the ingest pipeline and stored in the On-The-Fly Reprocessing system (OTFR), which has since been replaced by the *HST* Online Cache. All STIS data collected prior to the Side-2 failure are available to the community on the *HST* Online Cache, alongside all other data. For general information regarding obtaining *HST* data, see the overview in the [HST Data Handbook](#). Note that the files in the archive will be reprocessed automatically when the software or reference files are updated. For information on the appropriate reference files, see https://archive.stsci.edu/hst/help/bestref_help.html.

As part of the original STIS re-calibration and re-ingest for the OTFR, science exposures that lacked associated auto-wavecalcs but that did have GO wavecalcs were identified. For those cases, the science data and GO lamp exposures were combined into associations that treat the GO wavecalcs in the same way as auto-wavecalcs. As a side effect of the association of GO wavecalcs, the science exposures involved have new dataset names, and the lamp exposures now used as wavecalcs will no longer appear in the archive catalog as independent datasets.

STIS data taken after the 2009 repair are processed through the pipeline soon after the observations are completed, using the most up-to-date versions of the software and reference files. GO wavecalcs are associated with the corresponding science exposures in the same manner as auto-wavecal exposures were prior to the Side-2 failure, and do not appear in the archive catalog as independent datasets.

Chapter 2: Special Considerations for Cycle 32

Chapter Contents

- 2.1 STIS Repair and Return to Operations
- 2.2 Summary of STIS Performance Changes Since 2004
- 2.3 New Capabilities for Cycle 32
- 2.4 Use of Available-but-Unsupported Capabilities
- 2.5 Choosing Between COS and STIS
- 2.6 Scheduling Efficiency and Visit Orbit Limits
- 2.7 MAMA Scheduling Policies
- 2.8 Prime and Parallel Observing: MAMA Bright-Object Constraints
- 2.9 STIS Snapshot Program Policies

2.1 STIS Repair and Return to Operations

In May 2001, the Space Telescope Imaging Spectrograph (STIS) switched over from using Side-1 to Side-2 electronics when a short circuit blew a fuse, knocking out the Side-1 electronics. STIS operated on Side-2 electronics until it ceased science operations on 03 August 2004, due to the failure of a power supply within the Side-2 electronics.

In May 2009, during the fourth spacewalk of the *HST* Servicing Mission 4, (SM4), the STIS Side-2 circuit board containing the failed low-voltage power supply was replaced. This repair fully restored the STIS instrument to operation with capabilities similar to those it had before the Side-2 failure. In the appropriate sections of this *Handbook*, the performance changes since 2004 in detector dark currents, throughputs, and charge transfer efficiency (CTE) will be discussed.

Many figures and tables were originally updated for the Cycle 17 (first post-SM4) version of this handbook, using our best estimates of instrument performance for Cycle 17. In many cases, those figures and tables have not been revised to take into account the modest changes expected between those projected values and the estimated Cycle 32 performance. For more up-to-date performance values, users should consult the [Performance](#) section of the STIS web pages and the [STIS ETCs](#).

The sensitivities and other instrument parameters adopted for use with the Cycle 32 **ETCs** have been updated with our best estimates for April 2025.

STIS will be among the instruments available for inclusion in Cycle 32 Phase I proposals. Please consult the [Cycle 32 Call for Proposals](#) and the Cycle 32 Proposal Announcement webpages (available through the [Proposing Overview](#) web page) for any updates on instrument status.

2.2 Summary of STIS Performance Changes Since 2004

The performance of STIS after its repair during SM4 is similar in most respects to its performance prior to the 2004 failure, but there are some important differences. While most of the changes in performance represent the continuation of previous trends (and were anticipated), some of the changes (e.g., in the behavior of the *NUV-MAMA* dark current) were not expected. All of these changes need to be taken into account when planning new STIS observations. Detailed descriptions of the differences are given in the appropriate sections of this *Handbook*, but for the convenience of users familiar with the previous performance of STIS we list the most important of the changes below, linked to the appropriate sections of the *Handbook*:

- [Changes in CCD Read Noise](#) (7.2.3)
- [CCD Dark Current](#) (7.3.1)
- [Charge Transfer Efficiency](#) (7.3.7)
- [Figure 7.1: Relative Sensitivity vs. Time for First-Order CCD L-Modes G230LB, G430L, and G750L](#) (7.2.5)
- [NUV-MAMA Dark Current after SM4](#) (7.5.2; see Figure 7.20)

For the most up-to-date values of some of the more frequently monitored quantities, users should consult the [Performance](#) section of the STIS web pages. The [STIS ETCs](#) are regularly updated to reflect the current/anticipated detector characteristics.

2.3 New Capabilities for Cycle 32

Spatial Scanning

Although spatial scanning with the STIS CCD is not a new capability in Cycle 32 (the first actual use of this available-but-unsupported mode was in Cycle 24), our understanding of its capabilities is evolving. For relatively bright targets, spatial scanning can allow many more photons to be collected in a single exposure (without saturating the CCD), better flat fielding, better removal of the fringing in near-IR spectra, and more robust removal of hot pixels and cosmic rays. Signal-to-noise ratios of 600–800 (in the 1D extracted spectra) have been achieved in several programs using this mode. To further explore the capabilities of spatial scanning with STIS, the STIS team conducted special calibration programs in Cycles 25 and 28 aimed at characterizing the reproducibility of the fluxes in time series observations (e.g., as commonly used for studies of transiting exoplanets). Some results from the initial analyses of those data can be found in the [STIS September 2020 STAN](#); a paper containing a more complete discussion is in preparation. For more information about using spatial scanning with STIS, see [Section 12.12](#).

Disabling Monthly MAMA Offsets

As discussed in [Section 7.6.2](#), the position of first-order MAMA spectra on the detectors is offset slightly, on a monthly basis, in order to guard against possible uneven charge depletion in the detectors. Because the detector sensitivity varies slightly with offset from the nominal position, STIS flux calibration programs routinely disable the usual monthly offsets with use of the `MSMOFF` mode. Because the MAMA detectors have not shown any evidence of uneven charge depletion (see [ISR 2021-02](#)), beginning in Cycle 30 this previously restricted capability will become available-but-unsupported for those GO programs requiring very high photometric accuracy or reproducibility. Scientific justification for the use of the `MSMOFF` mode is required for it to be approved. Please include this justification in your Phase I proposal (reach out to the [Help Desk](#) for help with the Phase I implementation) and speak with your STIS Contact/Instrument Scientist should you like to implement this in Phase II.

2.4 Use of Available-but-Unsupported Capabilities

The set of core instrumental modes/capabilities of STIS described in this *Handbook* that will be supported for Cycle 32 enables an enormous range of scientific applications.

There are, however, additional "Available-but-Unsupported" capabilities (e.g., additional slits and data-taking formats) that are not described in this *Handbook* and that are not supported for Cycle 32. If you find that your science cannot be performed with the supported modes and parameters described in this *Handbook*, you may wish to consider use of an unsupported mode, which may be approved for use upon consultation with a STIS Instrument Scientist. A general description of STIS available-but-unsupported echelle, first-order grating, and `NUV_PRISM` capabilities is given in [Appendix A](#). Complete lists of the supported and available-but-unsupported combinations of aperture, optical element, wavelength, and detector, for each type of observation (`ACQ`, `ACQ/PEAK`, `ACCUM`, `TIME-TAG`) are given in the various subsections of [section 8](#) in the [Phase II Proposal Instructions](#).

The use of unsupported modes comes at a price, and they should be used only if the technical requirement and scientific justification are particularly compelling. Proposers should be aware of the following caveats regarding unsupported modes:

- STScI adopts a policy of shared risk with the observer for the use of unsupported capabilities. Requests to repeat failed observations taken with unsupported capabilities will not be honored if the failure is related to the use of the unsupported capability.
- User support from STScI for observation planning, as well as data reduction and analysis, for unsupported capabilities will be limited and provided at a low priority. Users taking data with unsupported capabilities should be prepared to shoulder the increased burden of the planning, calibration, reduction, and analysis.
- While enabling "available-but-unsupported" modes in the Phase II APT makes all of these options available in APT, observers must remember that they are allowed to use only those particular "available-but-unsupported" capabilities for which they have been specifically granted permission.
- Some of the options that are accessible as "available" in the APT software may nonetheless be prohibited for a variety of technical or policy reasons, and their presence in APT does not necessarily mean that permission will be granted to use them, regardless of any scientific justification that may be supplied. Observers should specifically note any restrictions on allowed observational modes that are listed in the [Cycle 32 Call for Proposals](#).
- Calibrations for unsupported capabilities will not be provided by STScI. Either users must determine that they can create calibration files from data in the *HST* Archive or they must obtain calibrations as part of their observations. The STScI pipeline will not calibrate data taken in unsupported modes but will deliver uncalibrated FITS files (or in some cases partially calibrated FITS files) to the observer and the *HST* Archive.

Cycle 32 Phase I proposals that include use of unsupported STIS capabilities must include the following:

1. Justification of why the science cannot be done with a supported configuration;
2. A request for any observing time needed to perform calibrations;
3. Justification for the added risk of using an unsupported mode in terms of the scientific payback;
4. Demonstration that the observers are able to bear the increased burden of calibration, reduction, and analysis of their data.

During the Phase II proposal submission process, STScI must also formally approve the use of an available-but-unsupported mode. This allows STScI to evaluate the request and ensures that no problems associated with the request have come to light since the submission of the Phase I proposal. We require the PI to summarize the above four points in a brief email message requesting approval for use of an available-but-unsupported mode.

The increased burden of calibrating data taken using available-but-unsupported modes also makes the use of such data for archival research significantly more difficult. As a result, requests for use of unsupported modes which do not adequately address the above four points, or which will result in only marginal improvements in the quality of the data obtained, may be denied by STScI, even if the request was properly included in the Phase I proposal.

2.5 Choosing Between COS and STIS

With the installation of COS and the repair of STIS, *HST* has two spectrographs with significant overlap in spectral range and resolving power. Each has unique capabilities, and the decision of which to use will be driven by the science goals of the program and the nature of the target to be observed.

The [primary design goal of COS](#) was to improve the sensitivity of *HST* to point sources in the far-ultraviolet (FUV; from about 1100 to 1800 Å). In this wavelength range, the throughput of the COS FUV channel exceeds that of the STIS `FUV-MAMA` by factors of 10 to 30, and the combination of the spectroscopic resolving power ($\sim 20,000$) and wavelength coverage (300 to 370 Å per setting) of the medium-resolution COS FUV modes results in a discovery space (throughput times wavelength coverage) for observations of faint FUV point sources that is at least 10 times greater for most targets than that of STIS modes with comparable resolution, and is as much as 70 times greater for faint, background-limited point sources. COS also has the unique capability to observe down to wavelengths as short as 900 Å.

In the NUV (approximately 1700–3200 Å), COS and STIS have complementary capabilities. To accommodate the NUV detector format, the COS NUV spectrum is split into three non-contiguous stripes, each of which covers a relatively small range in wavelength. Obtaining a full NUV spectrum of an object requires several set-ups and exposures (6 or more for the medium-resolution gratings and 4 for G230L). When broad NUV wavelength coverage is needed, there will be circumstances in which obtaining a single STIS spectrum is more efficient than taking separate COS spectra.

Because the dark rate of the COS NUV detector is substantially lower than that of STIS, COS will often be superior for faint sources, even when more exposures are required to achieve full wavelength coverage. The mean dark rate of the STIS `NUV-MAMA` reached a minimum near ~ 0.0015 counts/pixel/s around 2016, but has since increased to ~ 0.0013 , where we expect it to remain during Cycle 32. The COS NUV dark rate has been increasing with time, but even if current trends continue, the projected mean value of ~ 0.00125 counts/s/pixel will still be much smaller than the rate for STIS. Observers are advised to perform detailed calculations using both the COS and STIS **ETCs** and to consider carefully the relative instrument overheads to determine which combination of instruments and modes is best for their science.

For observations of extended sources, the spatial resolution offered by STIS must be weighed against the superior sensitivity of COS. One of the primary design goals of STIS was to provide spatially resolved spectra in the ultraviolet (UV), optical, and NIR. The STIS long slits, when used with the first-order gratings, allow spatially resolved observations that exploit the intrinsically high resolution of *HST* over the full width of the detectors (approximately 0.05 arcseconds per 2-pixel spatial-resolution element over a length of 25 arcseconds with the `NUV-` and `FUV-MAMAs`, and ~ 0.1 arcseconds per 2-pixel spatial-resolution element over a length of 52 arcseconds with the CCD).

COS was optimized for point-source observations. While COS has relatively large entrance apertures (2.5 arcseconds diameter), flux from regions more than 0.5 arcseconds from the aperture center is significantly vignetted. These large apertures also mean that objects extended in the dispersion direction will yield spectra with lower spectral resolution. In addition, the optical design of the FUV channel limits the achievable spatial resolution, showing FWHM in the spatial direction that vary between ~ 0.25 arcseconds and ~ 1.5 arcseconds depending on grating and wavelength. The COS NUV channel uses a different optical design and has a spatial resolution comparable to that of the STIS first-order NUV modes (~ 0.05 arcseconds), with somewhat better sampling; however, for sources extending more than 1 arcsecond in the spatial direction, the various NUV spectral segments will begin to overlap.

The line-spread functions (LSFs) of both instruments exhibit non-Gaussian wings due to mid-frequency zonal (polishing) errors in the Optical Telescope Assembly (OTA). Using STIS, one can minimize their effects through the use of narrow apertures. On COS, narrow apertures are not available. The broad wings of the COS LSF, especially in the short wavelengths of FUV band, can affect the detectability of faint, narrow features and blend closely spaced lines. Studies that require accurate knowledge of the line profile will require full consideration of the COS LSF. The non-Gaussian wings of the COS LSF should have only modest impact on science programs targeting broad lines and continuum sources.

Both COS detectors and the STIS MAMA detectors are prohibited from observing objects that exceed specific brightness levels (see Sections 7.7, 13.8, and 14.8 in this handbook, and Chapter 10 in the COS IHB). Some brightness limits have been established for the health and safety of the instrument, while others are practical limits that are set to ensure good data quality. Because STIS is less sensitive than COS, the brightness limits for STIS tend to be significantly less stringent. In the NUV range, the STIS G230LB and G230MB gratings can also be used with the STIS CCD, which has no bright-object limitations. STIS also has a number of small and neutral-density apertures that can be used with the MAMA detectors to attenuate the light of a too-bright object. COS has only a single neutral-density filter that attenuates by a factor of about 200 but also degrades the spectral resolution by a factor of 3 to 5. In most cases, some combination of STIS gratings and apertures will be a better choice for observing a UV-bright object than COS with its neutral-density aperture. Users are advised to compare results from the COS and STIS ETCs to decide on an appropriate strategy for their target.

The STIS high-dispersion echelle modes E140H and E230H have resolving powers of $\sim 114,000$ (or even $R \sim 200,000$ with the 0.1×0.03 aperture and specialized data reduction; see Section 12.6), significantly higher than the best COS resolution. Also, STIS can obtain spectra in the optical and NIR at wavelengths up to $10,200 \text{ \AA}$, while the maximum wavelength observable by COS is about 3200 \AA .

Both STIS and COS can perform observations in TIME-TAG mode, whereby the time of each photon's arrival is recorded. STIS is capable of a much finer time resolution (125 microseconds vs. 32 milliseconds for COS), although few programs require such a high sampling rate. Due to its lower sensitivity, STIS may be able to observe a target in TIME-TAG mode that is too bright for TIME-TAG observations with COS. On the other hand, TIME-TAG data acquired with the COS FUV detector includes information on the pulse-height distribution, while TIME-TAG data obtained with the STIS MAMAs and the COS NUV-MAMA do not. Pulse-height information can be valuable in identifying and rejecting background counts in the spectra of faint sources.

Observers should also note that many COS NUV modes are only sparsely used, and the corresponding STIS NUV modes are likely to have more extensive calibration.

2.6 Scheduling Efficiency and Visit Orbit Limits

Calendar time for the scheduling and execution of long visits has become severely oversubscribed. To assure a greater degree of scheduling efficiency and avoid such heavy oversubscription, a 5-contiguous-orbit limit was imposed for Cycle 8 and beyond for both CCD and MAMA visits.

For the MAMA detectors, this limit is due to the number of South Atlantic Anomaly (SAA) free contiguous orbits. It is possible to have 6 of these orbits, however they are rare. Anything longer will never be schedulable. If a 6-orbit constraint is combined with any phase, timing and/or orient constraint restrictions then the visit will likely be unschedulable. STIS MAMA visits with 6 orbits require a compelling science justification and proposers must take into account the additional limitations that these longer visits place on observations and schedulability.

STIS CCD observations are possible to schedule in SAA impacted orbits. Therefore, there is slightly more flexibility with those observations being longer than 5 orbits with proper science justification. Scheduling longer orbit visits can be challenging, particularly when coupled with phase, time and/or orient constraints. Visits with 7 or more contiguous orbits can have very few scheduling opportunities per cycle (between zero and three).

Observers with programs using more than 5 orbits per target should take note of the following advice when splitting their observations into multiple visits:

- Target acquisition sequences will need to be repeated at the start of each visit when using small entrance apertures with STIS. Imaging and slitless spectroscopy do not normally require a target acquisition.
- There exists the potential for some image rotation between visits unless the `SAME ORIENT AS <first visits #>` special requirement is used. When `SAME ORIENT AS` is used, the accuracy is a few milliarcseconds.
- Users are strongly encouraged to structure observations of 2-3 orbits duration each, unless longer visits are explicitly required to reach the stated science goals.
- **Moving targets and spatial scanning:** As of Cycle 28, limitations due to the gyro configuration of *HST* and its pointing control system restrict visits on moving targets to no more than two contiguous orbits. For similar reasons, for spatial scanning programs, each visibility period must have at least 6 minutes of time under FGS control (i.e., 6 minutes without scanning).

In structuring their programs, observers should carefully consider the positional accuracies that will be required. Acquisitions of point-source targets are generally accurate to ~10 milliarcseconds (see [Section 8.2](#)), and somewhat greater accuracy can be achieved by using a peakup in a small aperture ([Section 8.3](#); see also the summary in [Table 16.5](#)). Within a given visit, *HST* pointing is generally very stable (~5 milliarcseconds rms), and small angle maneuvers can be similarly accurate ([Section 8.2.3](#)). For most single, non-variable point-source targets, a long series of exposures could, in principle, be obtained either in a single long (but difficult to schedule) visit or in two or more shorter visits, with somewhat shorter total exposure time but greater schedulability. If there are several different, closely-spaced targets to be observed (requiring slight movements of the telescope but using the same guide stars), and if very precise offsets (few milliarcsecond accuracy) between the different targets are required, then it might be desirable to observe all the targets in a single long visit. If such precise offsets are not required; however, then the observations could be obtained in separate shorter visits (e.g., with one target per visit). In cases where a target acquisition is performed for slit spectroscopy, one should follow the same procedure for the target acquisition in the subsequent visits as in the first.

Visits can be scheduled close in time by specifying the GROUP WITHIN visit requirement. Timing constraints of this type, however, should be used only if required by the science, since overconstraining visits affects the ability to schedule efficiently.

2.7 MAMA Scheduling Policies

Since the MAMA (see [Section 3.2.1](#)) control electronics were found on orbit to be subject to resets due to cosmic ray impacts, the MAMAs are operated only during the contiguous orbits of each day that are free of the South Atlantic Anomaly (SAA). We therefore limit the duration of any single MAMA visit (i.e., a single continuous observation series) to five orbits. Additionally, to facilitate scheduling and maximize the orbits available for MAMA observations, in certain circumstances we require observers to split their CCD and MAMA exposures into separate visits. Specifically, for STIS programs containing both CCD and MAMA scientific (not target acquisition) exposures, in which there are more than 30 minutes of observing time using the CCD in a single visit (inclusive of overheads), and for which that visit requires more than a single orbit, the exposures *must* be split into visits that separate the CCD from the MAMA exposures. Hence, this policy allows multi-orbit mixed visits with 30 minutes or less of total CCD scientific time, or single-orbit mixed visits regardless of the CCD/MAMA ratio. For programs that *require* CCD and MAMA scientific exposures in the same visit (e.g., variability monitoring programs), exceptions can be made if a well-justified explanation is given in the Special Requirements section of the Phase I proposal.

2.8 Prime and Parallel Observing: MAMA Bright-Object Constraints

The STIS MAMA detectors are subject to damage at high-illumination rates, as explained in greater detail in [Section 7.7](#). To protect the instrument, we have established limits on the maximum count rate at which the detectors may be illuminated. These count-rate limits translate into a set of configuration-dependent, bright-object screening magnitudes. The spectroscopic bright-object screening magnitudes are summarized in [Table 13.45](#), and the imaging counterparts in [Table 14.40](#).

STScI will perform screening of all MAMA exposures prior to scheduling. Targets not established as safe for the configuration in which they are being observed will not be scheduled. Observations that pass screening but are lost on orbit due to a bright-object violation will not be rescheduled. Observers are responsible for assuring that their observations do not violate the MAMA count-rate limits. A detailed description of the MAMA bright-object limits and the observers' responsibility is presented in [Section 7.7](#) and in [STIS ISR 2000-01](#).

Observers should note that the **ETC** global count-rate calculations for STIS echelle modes include a correction factor that takes into account the substantial amount of scattered light that falls outside the spectral extraction region but which still falls on the detector. In Cycle 25, this factor was updated in the **ETC** based on new measurements, and for many central wavelength settings this resulted in a substantial increase in the predicted global count rate. Observers are advised to redo all calculations with the most recent version of the **ETC** to verify that the proposed observation is feasible. Additional details may be made available on the [STIS website](#) or via [Space Telescope Analysis Newsletters \(STANs\)](#).

To assure that STScI can adequately screen observations, special constraints are imposed on parallel observing with the MAMAs:

- No pure parallels are allowed using STIS.
- Coordinated parallels are not allowed with MAMA imaging modes or with the NUV/MAMA-PRISM.
- Coordinated parallels are allowed for other (non-PRISM) spectroscopic modes used with the MAMA detectors only if an exact spacecraft orientation (**ORIENT**) is requested and the RA and Dec of the parallel field determined. Note that the specification of an exact orient usually limits the scheduling of observations to a ~4–8 week period each year. The observer is responsible for assuring that observations do not violate the MAMA count-rate limits both for coordinated parallel MAMA observations and for primes.
- Coordinated parallels with STIS CCD modes may be performed without any required restrictions on the allowed range of orientations.

Targets that are one magnitude or more fainter than the magnitude limits in the screening tables generally pass screening. For a target that may exceed a screening limit after correction for extinction and slit losses, observers must provide UV or optical data adequate to establish safety according to the guidelines detailed in [Section 7.7](#). If such data are not available, they must be obtained in a safe *HST* configuration (see [Section 7.7](#) for more details) or from another source; if obtained with *HST*, the required orbits must be requested in Phase I.

Normal MAMA bright object limits apply to all objects that may be within 5 arcseconds of the entrance aperture. In addition, there are special limits that apply to any extremely bright object that may be within 13.5 arcseconds of the aperture. Full details are given in [Section 7.7.4](#).

Please also note that those proposing MAMA target-of-opportunity observations should provide an explanation in the Phase I proposal of how the safety of the proposed observations of the target will be ensured.

2.9 STIS Snapshot Program Policies

For Cycle 32, STIS MAMA imaging modes and the STIS NUV-MAMA PRISM will not be allowed in snapshot programs. Other spectroscopic STIS MAMA snapshots are allowed, but the combined total of STIS MAMA and COS snapshot targets accepted in Cycle 32 will be restricted. See the [Cycle 32 Call for Proposals](#) for further details. The prohibition on MAMA imaging and PRISM snapshot targets was instituted because the labor-intensive field bright-object checking requirements, when combined with the low-execution probability for STIS MAMA snapshots, results in a very inefficient use of resources. Likewise, moving targets are not permitted for STIS MAMA snapshot visits. Variable STIS MAMA snapshot targets must have well-defined maximum UV fluxes, which will be used for the bright-object checking. There are no restrictions on the numbers or variability of proposed STIS CCD snapshot targets, as they do not require bright-object checking and have a significantly higher expected completion rate. Thus, use of the STIS CCD G230LB or G230MB gratings is encouraged as an alternative to the NUV-MAMA for snapshot programs.

In addition, STIS MAMA snapshot proposals should be limited to one or a few straightforward configurations. Specifically, use of the F25NDQ filters will not be allowed in MAMA snapshot proposals. Use of the 0.2x0.2 echelle aperture is recommended (and now supported) for first-order programs that have no scientific need for a long slit, in order to expedite the field bright-object screening process. Because of the limited resources available for bright-object checking, combined with the relatively low expected completion rate, excessively complex STIS MAMA snapshot targets, fields, or instrumental configurations may not be implemented in Phase II. If in doubt on this issue, please consult with a member of the STIS Team via the [Help Desk](#).

Chapter 3: STIS Capabilities, Design, Operations, and Observations

Chapter Contents

- [3.1 Instrument Capabilities](#)
- [3.2 Instrument Design](#)
- [3.3 Basic Instrument Operations](#)
- [3.4 Designing STIS Observations](#)

3.1 Instrument Capabilities

STIS uses two-dimensional detectors operating from the ultraviolet (UV) to the near-infrared (NIR). First-order gratings cover the full spectral range and are designed for spatially resolved spectroscopy using a long slit. The echelle gratings, available only in the UV, are designed to maximize the spectral coverage in single observations of point sources. The STIS Flight Software supports onboard target acquisitions and pickups to place targets on slits. The STIS optics and detectors have been designed to exploit *HST*'s high spatial resolution.

STIS can be used to obtain:

- Echelle spectroscopy at medium to high spectral resolution ($R \sim 30,000\text{--}114,000$ ¹), covering a broad simultaneous spectral range ($\Delta\lambda \sim 800$ or 200 \AA , respectively) between $1150\text{--}3100 \text{ \AA}$.
- Spatially resolved, long-slit (or slitless) spectroscopy from the UV to the NIR ($1150\text{--}10,300 \text{ \AA}$) at low to medium spectral resolution ($R \sim 500\text{--}17,000$) in first order.

In addition to these two prime capabilities, STIS also provides:

- Imaging capability using the solar-blind FUV-MAMA detector ($1150\text{--}1700 \text{ \AA}$), the solar-insensitive NUV-MAMA detector ($1150\text{--}3100 \text{ \AA}$), and the optical CCD ($2000\text{--}10,300 \text{ \AA}$), through a small complement of narrow-band and broad-band filters.
- Slitless spectroscopy ($R \sim 10\text{--}500$) between $1150\text{--}3100 \text{ \AA}$.
- High time-resolution ($\Delta\tau = 125$ microseconds) imaging and spectroscopy between $1150\text{--}3100 \text{ \AA}$ and moderate-time-resolution ($\Delta\tau \sim 20$ seconds) CCD imaging and spectroscopy between $2000\text{--}10,300 \text{ \AA}$.
- Coronagraphic imaging between $2000\text{--}10,300 \text{ \AA}$ and bar-occulted spectroscopy over the entire spectral range ($1150\text{--}10,300 \text{ \AA}$).
- Spatially scanned spectra with the STIS CCD ($2000\text{--}10,300 \text{ \AA}$).

[Table 4.1](#) and [Table 5.1](#) provide a full list of gratings for spectroscopy and filters for imaging.

STIS is a versatile instrument that can be used for a broad range of scientific programs. The 50-arcsecond long slit and high quantum efficiency in the optical, provided by the CCD, enables spatially resolved spectroscopy of extended and/or diffuse astronomical sources. This is particularly important for studies of the dynamics of galactic nuclei, the kinematics of active galaxies, and the properties of diffuse galactic nebulae. The wide wavelength coverage of STIS facilitates line-ratio studies; for instance, the low-resolution first-order gratings span the range $1150\text{--}10,300 \text{ \AA}$ in just four exposures. Slitless spectroscopy provides emission-line images of astronomical objects, and coronagraphic imaging and spectroscopy can reveal the nature of extended gaseous regions surrounding bright continuum sources. Spatial scanning can yield very high-S/N ratio spectra and very reproducible fluxes (in broad or narrow bands) for time series studies (e.g., of exoplanets and their atmospheres).

¹ In the past, it was possible to achieve $R \sim 200,000$ with the 0.1×0.03 aperture; however, recently we have seen that the smallest apertures are negatively impacted by degrading focus. The maximum resolution achievable by these small apertures could be affected (see [STIS ISR 2017-01](#) for more information about the degrading focus and [Section 12.6](#) for more information about improving the sampling of the line-spread function).

3.2 Instrument Design

[3.2.1 Detectors](#)

[3.2.2 STIS Physical Configuration](#)

In this section, we provide a high-level summary of the basic design of STIS, concentrating on the information most relevant to your *HST* observing proposal. Subsequent chapters provide more detailed information.

3.2.1 Detectors

STIS uses three large-format (1024 × 1024 pixel) detectors (see [Chapter 7](#) for more details), as follows:

- A Scientific Image Technologies (SITe) CCD, called the *STIS/CCD*, with ~0.05 arcsecond square pixels, covering a nominal 52 × 52 arcsecond square field of view (FOV), operating from 1640 to 10,300 Å.
- A Cs₂Te Multi-Anode Microchannel Array (MAMA) detector, called the *STIS/NUV-MAMA*, with ~0.025 arcsecond square pixels, and a nominal 25 × 25 arcsecond square field of view (FOV), operating in the NUV from 1600 to 3100 Å.
- A solar-blind CsI MAMA, the *STIS/FUV-MAMA*, with ~0.025 arcsecond square pixels, and a nominal 25 × 25 arcsecond square FOV, operating in the FUV from 1150 to 1700 Å.

The CCD

The CCD provides high quantum efficiency and good dynamic range in the NUV through NIR. The CCD produces a time-integrated image in the *ACCUM* data-taking mode. As with all CCDs, there is noise (*read noise*) and time (*read time*) associated with reading out the detector. Time-resolved work with this detector is done by taking a series of short exposures. The minimum exposure time is 0.1 second, and the minimum time between successive identical exposures is 45 seconds for full-frame, but can be reduced to 20 seconds for subarray readouts. CCD detectors are capable of high dynamic range observations. The dynamic range for a single exposure ultimately is limited by the depth of the CCD full well (144,000 electrons), which determines the total amount of charge (or counts) that can accumulate in any one pixel during any one exposure without causing saturation. For *GAIN=1*, it is further limited (to 33,000 electrons) by saturation in the gain amplifier. For more information about the CCD saturation, see [Section 5.1.4](#) or [STIS ISR 2015-06: CCD Saturation Effects](#). Cosmic rays will also affect all CCD exposures. CCD observations should be broken into multiple exposures (called *CR-SPLITS*) of no more than 1000 seconds each, whenever possible, to allow for the removal of cosmic rays in post-observation data processing; during Phase II you can specify the *CR-SPLIT* optional parameter to do this (see [Chapter 11](#)).

The MAMAs

The two MAMAs are *photon-counting* detectors which provide two-dimensional UV capability. They can be operated either in `ACCUM` mode, to produce a time-integrated image, or in `TIME-TAG` mode to produce an event stream with high (125 microseconds) time resolution. In `ACCUM` mode, photons are accumulated into a 2048×2048 , 16-bit-per-element oversampled array. The data can be left in that over-sampled (or `highres`) format, which is the default for scientific exposures, or they can be binned to produce a 1024×1024 native-format image. Doppler correction for the spacecraft motion is applied automatically onboard for data taken in the higher spectral resolution `ACCUM` modes.

Because the STIS MAMA detectors can be damaged by high levels of illumination, their use is subject to both local (individual pixel) and global (total illumination on the detector) brightness limits. Due to the characteristics of the detectors and the associated electronics, the global count rate also exhibits a slight (but correctable) non-linearity. At very high global illumination rates ($\geq 285,000$ counts/s), however, the counting becomes incomplete in a way that is not correctable. At somewhat higher illumination rates, the MAMA detectors are subject to damage. We have therefore defined conservative absolute local and global count-rate limits, which translate to a set of configuration-dependent bright-object screening limits for observations with the STIS MAMA detectors. Sources which violate the absolute count-rate limits in a given configuration *cannot be observed in that configuration*, as discussed in [Section 7.7](#); see also STIS ISRs [1996-28](#), [1996-31](#), and [1998-08](#). Note that additional screening limits have been adopted for M dwarfs, as this class of objects can exhibit large and unpredictable flares. Details regarding those screening limits and the procedure to follow for clearing observations of M dwarfs can be found in [STIS ISR 2017-02](#).

Early concerns about the signal-to-noise attainable with the MAMAs have been alleviated by experience in orbit. Values of 50:1 per spectral resolution element in extracted spectra are routinely obtained for point sources with sufficient counting statistics when integrated over the extraction aperture. Higher signal-to-noise values of 100–300 can be obtained by stepping the target along the slit in the first-order modes, or by use of special multiple slits with the echelles (see [Chapter 12](#)). Current information indicates that the flat fields are stable to $\pm 1\text{--}2\%$. See also [Section 16.1](#).

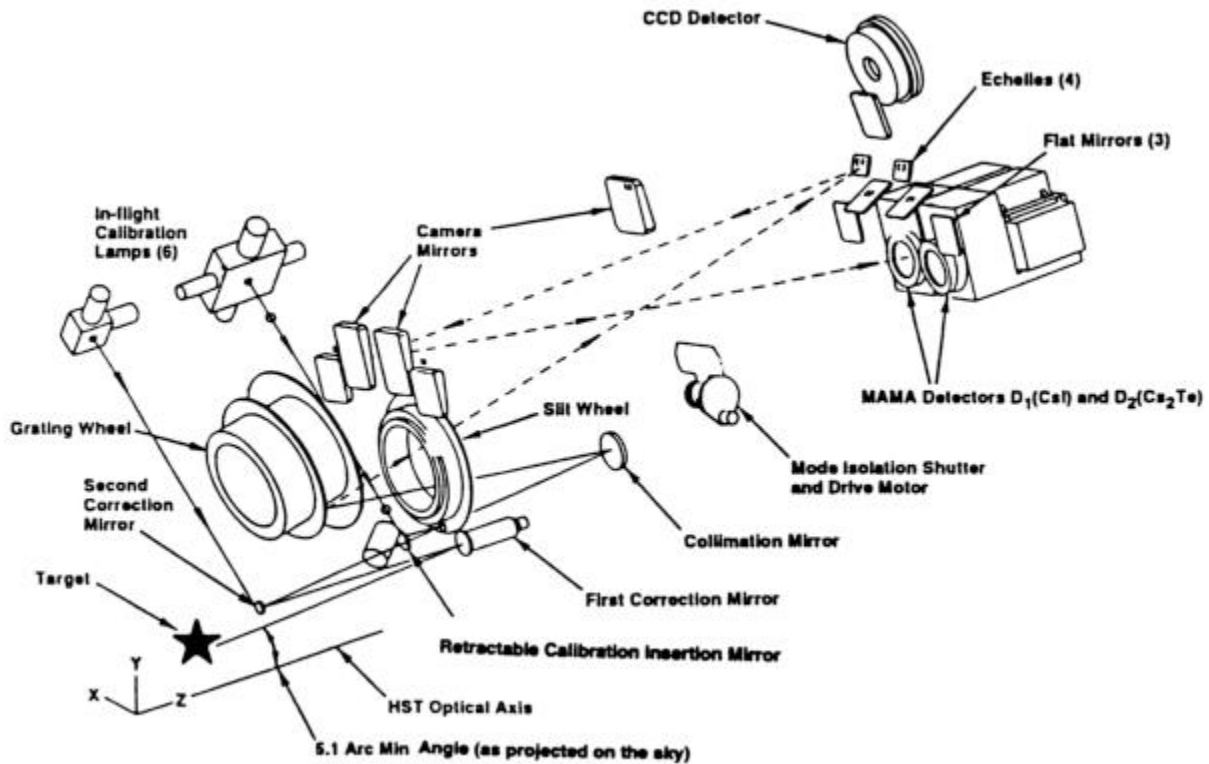
Highres

The MAMA detectors have 1024×1024 physical or so-called native-format pixels. However, each count is detected by multiple electrodes, so the charge distribution among the electrodes can be used to centroid the incident charge cloud to subpixel resolution. The gain of the `highres` 2048×2048 mode is a $\sim 10\text{--}30\%$ increase in resolution at the price of the increased fixed-pattern noise due to poorly characterized charge partition among the electrodes. The `highres` flat fields have much more structure than the 1024×1024 flats, with adjacent columns and rows differing by $\sim 30\%$ in an off/on pattern whose variability is appreciably higher than for 1024×1024 format images. This effect and the inherently lower signal-to-noise ratio in the full resolution flat-field images (nominally ~ 20 to 1 per `highres` pixel) suggest that it may be difficult to routinely realize the benefit in resolution. However, we note that data taken in `highres` mode can always be binned to 1024×1024 on the ground in post-observation data processing, and since the extra overheads in `highres` mode are typically quite small, `highres` is the default data-taking mode for the MAMA. The pipeline bins the data to 1024×1024 format during calibration, so that the pipeline output calibrated images are native format (see the [STIS Data Handbook](#) for more details). We note, however, that a method of correcting the increased fixed-pattern noise in `highres` mode has been devised (see [Jenkins & Tripp 2001, ApJS, 137, 297](#)).

3.2.2 STIS Physical Configuration

The STIS optical design includes corrective optics to compensate for *HST*'s spherical aberration, a telescope focal plane slit-wheel assembly, collimating optics, a grating selection mechanism, fixed optics, and camera focal plane detectors. An independent calibration lamp assembly illuminates the focal plane with a range of continuum and emission line lamps. A simplified schematic showing major mechanisms and detectors, and a medium-resolution echelle mode light path is shown in [Figure 3.1](#).

Figure 3.1: Simplified STIS Optical Design.



Slit and Grating Wheels

The *slit wheel* contains apertures and slits for spectroscopy and the clear, filtered, and coronagraphic apertures for imaging. Slit-wheel positioning is repeatable to very high precision: ± 7.5 and ± 2.5 milliarcseconds in the spatial and spectral directions, respectively.

The *grating wheel*, or so-called Mode Selection Mechanism (MSM), contains the first-order gratings, the cross-disperser gratings used with the echelles, the prism, and the mirrors used for imaging. The MSM is a nutating wheel which can orient optical elements in three dimensions. It permits the selection of one of its 21 optical elements as well as adjustment of the tip and tilt angles of the selected grating or mirror. As described in [Routine Wavecals](#) below, the grating wheel exhibits non-repeatability which is corrected for in post-observation data processing using contemporaneously obtained comparison-lamp exposures.

For some gratings, only a portion of the spectral range of the grating falls on the detector in any one exposure. These gratings can be scanned (tilted by the MSM) so that different segments of the spectral format are moved onto the detector for different exposures. For these gratings a set of pre-specified central wavelengths, corresponding to specific MSM positions, i.e., grating tilts, has been defined (see [Chapter 4](#)).

Calibration Lamp Systems

STIS has two independent calibration subsystems, the Hole in the Mirror (HITM) system and the Insert Mechanism (IM) system. The HITM system contains two Pt-Cr/Ne line lamps used to obtain wavelength calibration exposures and to illuminate the slit during target acquisitions. Light from the HITM lamps is projected through a hole in the second correction mirror (CM2). In some very early STIS data, the STIS external shutter was left open during the HITM wavecal exposure and the spectra of the lamp and the sky were recorded simultaneously. However, this is no longer an available option. Now the external shutter is always closed during the HITM lamp exposures. The IM system contains flat-fielding lamps (a tungsten lamp for CCD flats, a deuterium lamp for *NUV-MAMA* flats, and a krypton lamp for *FUV-MAMA* flats) and a single Pt-Cr/Ne line comparison lamp. When the IM lamps are used, the Calibration Insert Mechanism (CIM) is inserted into the light path and all external light is blocked. Observers will be relieved to know that the ground system will *automatically* choose the right subsystem (see [Section 3.3](#)) and provide the necessary wavelength calibration exposures.

3.3 Basic Instrument Operations

3.3.1 Typical STIS Observing Sequence

Target Acquisitions and Peakups

Once the telescope acquires its guide stars, your target will normally be within $\sim 1\text{--}2$ arcseconds of the aperture center. For science observations taken through slits which are smaller than 3 arcseconds in either dimension, and for use of the coronagraphic bars, you will need to specify a target acquisition exposure to center the target in the science aperture. The nominal accuracy of STIS point source ($V < 21$) target acquisitions is 0.01 arcsecond. If either dimension of the aperture is less than or equal to 0.1 arcsecond, the acquisition exposure should be followed by one or more peakup exposures to refine the centering of point or point-like sources. Peakup accuracy is 5% of the slit width used. Acquisition exposures always use the CCD, one of the filtered or unfiltered apertures for CCD imaging, and a mirror as the optical element in the grating wheel. Peakup exposures use a science slit and the CCD, with either a mirror or a spectroscopic element in the grating wheel. Target acquisitions and acquisition peakups are described in detail in [Chapter 8](#).

Routine Wavecal

Each time the MSM is moved to select a new optical element or to tilt a grating, the resulting spectrum is projected onto the detector with a positional error (lack of repeatability) of $\leq \pm 3$ low-resolution (MAMA) pixels. Additionally, thermal effects can cause small drifts over multi-orbit observations. An internal calibration lamp observation (WAVECAL) will automatically be taken following each use of a new grating element or new tilt position, and after ~ 1 orbit in any one setting. This allows for the calibration of the zero point of the wavelength (dispersion) and spatial (perpendicular to dispersion) axes in the spectroscopic science data during post-observation data processing. These routine, automatically occurring, wavecal observations are expected to provide sufficient wavelength zero-point accuracy for the vast majority of GO science. Only if your science requires particularly accurate tracking of the wavelength zero points do you need to insert additional wavecal observations in your exposure sequence (see also [Chapter 11](#)).

Data Storage and Transfer

At the conclusion of each `ACCUM` exposure, the science data are read out from the detector in use and placed in STIS' internal memory buffer, where they are stored until they can be transferred to the *HST* data recorder (and thereafter to the ground). This design makes for more efficient use of the instrument, as up to 7 CCD or 1024×1024 MAMA, or two 2048×2048 MAMA full-frame images (see [Section 3.2 Highres](#)) can be stored in the internal buffer at any time. A frame can be transferred from the internal buffer to the data recorder during subsequent exposures, as long as those exposures are longer than 3 minutes in duration.

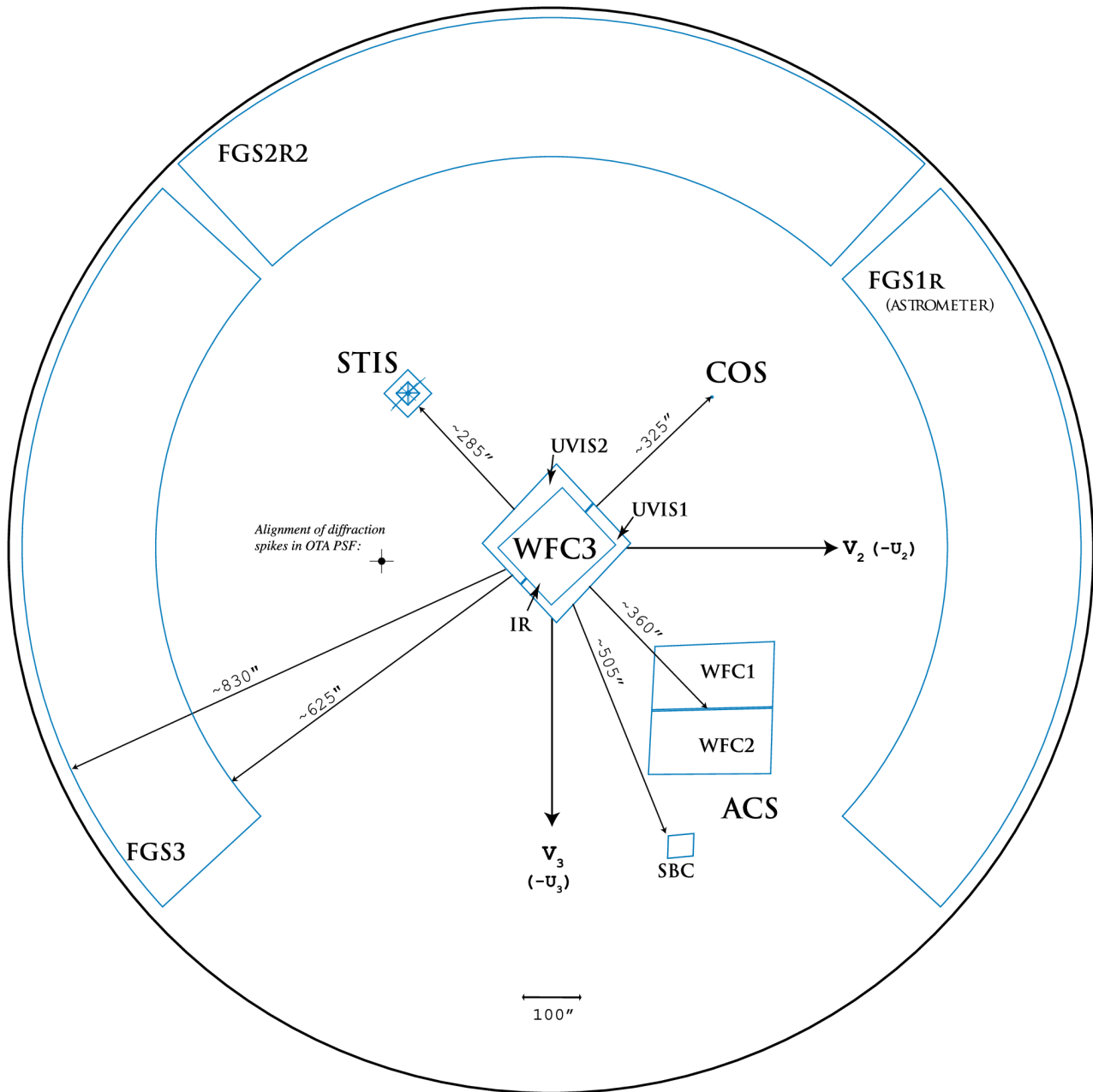
STIS' internal buffer stores the data in a 16 bit-per-pixel format. This structure imposes a maximum of 65,536 data numbers per pixel. For the MAMA detectors this maximum is equivalent to a limit on the total number of photons per pixel which can be accumulated in a single exposure. For the CCD, the full well (and not the 16 bit buffer format) limits the photons per pixel which can be accumulated without saturating in a single exposure. See [Chapter 7](#) and [Chapter 11](#) for a detailed description of detectors and data taking with STIS.

Parallel Operations

STIS' three detectors do not operate in parallel with one another—only one detector can be used at any one time. Exposures with different STIS detectors can, however, be freely interleaved in an observing sequence, and there is no extra setup time or overhead in moving from one detector to another. The three detectors, sharing the bulk of their optical paths, also share a common field of view of the sky.

STIS can be used in parallel with any of the other science instruments on *HST*. [Figure 3.2](#) shows the *HST* field of view after SM4. Dimensions in this figure are approximate; accurate aperture positions can be found on STScI's Observatory webpage on [FOV geometry](#). The STIS dispersion is along AXIS1 (roughly 135 degrees clockwise from U_3) and the slits are parallel to AXIS2 (roughly 45 degrees clockwise from U_3); see also [Figure 11.1](#). The policy for applying for parallel observing is described in the *Call for Proposals*. We provide suggestions for designing parallel observations with STIS in [Section 12.9](#). While the STIS CCD can always be used in parallel with another instrument, there are some restrictions on the use of the MAMA detectors in parallel, as described in [Section 2.8](#).

Figure 3.2: Post-SM4 *HST* Field of View.



3.3.1 Typical STIS Observing Sequence

In the optical, STIS is often used to observe extremely faint objects, so long observations are common. The combination of high spatial resolution, spectral resolution, and low read noise from the CCD will encourage the taking of multiple (~ 1000 s) exposures to allow cosmic ray rejection. Observations with the MAMA detectors do not suffer from cosmic rays or read noise, but long integration times will often be needed to obtain sufficient signal-to-noise in the photon-starved UV.

A typical STIS observing sequence consists of an initial target acquisition and possibly an acquisition peakup to center the target in a slit, followed by a series of long (~10–40 minute) exposures with a single optical element at a given wavelength setting. It may also include a series of multiple long exposures taken with different gratings or with a single grating at a number of tilts. Observers will generally not take their own wavecal exposures; routine automatic wavecal will allow wavelength and spatial zero points to be determined in post-observation data processing, requiring no input from the user. Observations that include wavelengths longer than 7000 Å should be accompanied by fringe-flat exposures (discussed in [Chapter 11](#)).

3.4 Designing STIS Observations

- 3.4.1 Identify Science Requirements and Define STIS Configuration
- 3.4.2 Determine Exposure Time and Check Feasibility
- 3.4.3 Identify Need for Non-Science Exposures and Constraints
- 3.4.4 Determine Total Orbit Request

In this section, we describe the sequence of steps you will need to take when designing your STIS observing proposal. The process is an iterative one, as you trade off between maximum spatial and spectral resolution, signal-to-noise, and the limitations of the instrument itself. The basic sequence of steps in defining a STIS observation (see [Figure 3.3](#)) is:

- Identify science requirements and select basic STIS configuration to support those requirements.
- Estimate exposure time to achieve required signal-to-noise ratio and check feasibility, including saturation and bright object limits.
- Identify any additional non-science (target acquisition, pickup and calibration) exposures needed.
- Calculate total number of orbits required, taking into account the overhead. Use APT to obtain accurate estimates of orbit length.

3.4.1 Identify Science Requirements and Define STIS Configuration

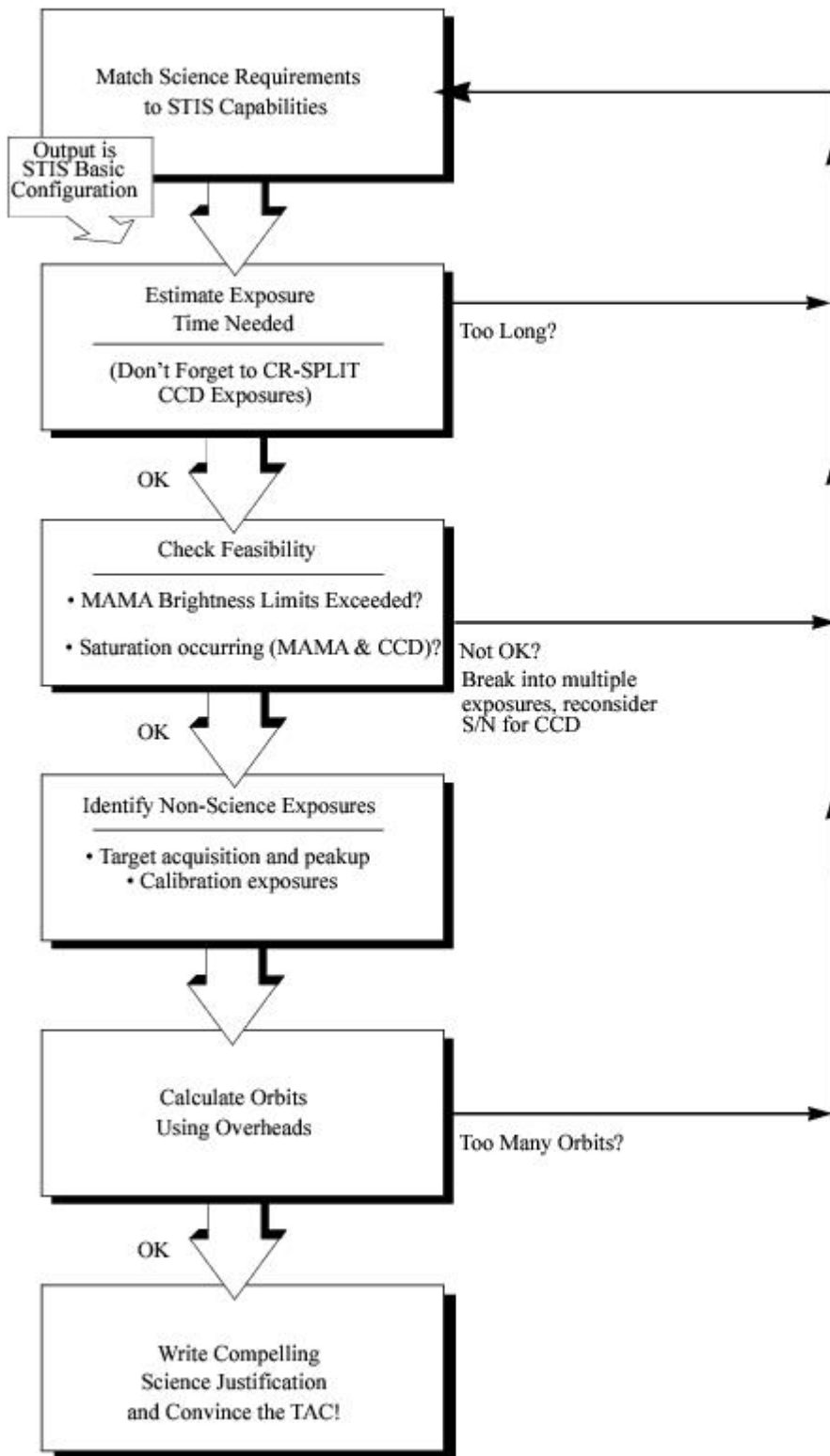
First and foremost, you must identify the science you wish to achieve with STIS. Some basic decisions you will need to make are:

- Spectroscopy or imaging?
- Wavelength region(s) of interest?
- Spectral resolution and spectral coverage required?
- Nature of target—extended source (long slit or full aperture) or point source?

In addition you will need to establish whether you require:

- High signal-to-noise ratio
- Time resolution
- Coronagraphy
- High photometric accuracy

Figure 3.3: Defining a STIS Observation.



As you choose your science requirements and work to match them to the instrument's capabilities, keep in mind that those capabilities differ greatly depending on whether you are observing in the NUV

/optical/NIR with the CCD or in the FUV/NUV with the MAMA detectors. Tradeoffs are described in [Table 3.1](#).

Table 3.1: Science Decision Guide.

| Decision | Affects | Tradeoffs |
|--------------------------|------------------------------|---|
| Wavelength regime | Detector and gratings | 1640-10,300 Å — CCD 1600-3100 Å — NUV-MAMA 1150-1700 Å — FUV-MAMA |
| Spectral resolution | Detector, gratings, aperture | $R < 20,000$ (first order) with CCD, NUV or FUV-MAMA, or $R \geq 30,000$ (echelle) with NUV or FUV-MAMA only. Wider apertures generally yield slightly poorer resolution, with more prominent low-level broad wings in the PSF |
| Spectral range | Gratings | Spectral range covered in a single exposure differs radically for different gratings. |
| Extended or point source | Gratings | First-order gratings designed for spatially resolved and point source observations. Echelle gratings designed for point source observations (long-slit echelle spectroscopy will suffer order overlap for extended sources, but can be done for sources with weak continua). |
| Time resolution | Detector | If time resolution < 20 seconds required, must use NUV or FUV-MAMA. |
| Coronagraphy | Detector and aperture | <i>Bright-object</i> ¹ coronagraphy available with CCD only. Coronagraphic imaging available with CCD only. Barred coronagraphic spectroscopy available with all detectors. |

¹ The bright object limits for MAMA observations apply to coronagraphic observations as well, i.e., coronagraphic observations of targets which are too bright for the MAMA detectors are not allowed.

Spectroscopy

For spectroscopic observations, the configuration is: detector (CONFIGURATION), operating mode (MODE=ACCUM or TIME-TAG), slit (APERTURE), grating (SPECTRAL ELEMENT), and central wavelength (CENWAVE). In [Chapter 4](#) we provide detailed information about each of the spectroscopic grating modes of STIS.

Imaging

For imaging observations, the configuration is detector (CONFIGURATION), operating mode (MODE=ACCUM or TIME-TAG), and filter (APERTURE); the mirror will be used as the spectral element for imaging observations. [Chapter 5](#) presents detailed information about each of STIS' imaging modes.

Special Uses

We refer you to [Chapter 12](#) if you are interested in any of the following special uses of STIS: slitless spectroscopy or extended-source echelle observations, time-resolved work, bright object or high signal-to-noise observations, planetary studies, parallel observations, coronagraphy, spatially scanned spectra.

3.4.2 Determine Exposure Time and Check Feasibility

Once you have selected your basic STIS configuration, the next steps are:

- Estimate the exposure time needed to achieve your required signal-to-noise ratio, given your source brightness. (You can use the STIS [Exposure Time Calculator \(ETC\)](#) for this: see [Chapter 6](#) and the plots in [Chapter 13](#) and [Chapter 14](#).)
- For observations using the MAMA detectors, assure that your observations do not exceed brightness (count rate) limits (see [Section 7.7](#)). (You can use the STIS [ETC](#) for this.)
- For observations using the MAMA detectors, assure that for pixels of interest your observations do not exceed the limit of 65,536 accumulated counts/pix per exposure imposed by the STIS 16 bit buffer (see [Section 7.5.1](#)).
- For observations using the CCD detector, assure that for pixels of interest, you do not exceed the per pixel saturation count limit of the CCD. (You can use the STIS [ETC](#) for this.)
- For MAMA `TIME-TAG` exposures check that your observations are feasible and do not violate any `TIME-TAG` specific count rate or data volume constraints (see [Chapter 11](#)).

To determine your exposure time requirements, consult [Chapter 6](#) where an explanation of how to calculate signal-to-noise and a description of the sky backgrounds are provided. To assess whether you are close to the brightness, signal-to-noise, and dynamic range limitations of the detectors, refer to [Chapter 7](#). For a consideration of data-taking strategies and calibration exposures, consult [Chapter 11](#).

If you find that the exposure time needed to meet your signal-to-noise requirements is too great, or that you are constrained by the detector's brightness or dynamic range limitations, you will need to adjust your base STIS configuration. [Table 3.2](#) summarizes the options available to you and steps you may wish to take as you iterate to select a STIS configuration which is both suited to your science and technically feasible.

Table 3.2: Feasibility Guide.

| Action | Outcome | Recourse |
|---|---|--|
| Estimate exposure time | If too long, then re-evaluate instrument configuration. | Reduce resolving power, or use wider slit, or change detectors and wavelength regime, or use larger binning. |
| Check saturation limit for CCD observations | If you wish to avoid saturation, then reduce time per exposure. | Divide total exposure time into multiple, short exposures. ¹ |

| | | |
|--|---|--|
| Check bright object limits for MAMA observations | If source is too bright, then re-evaluate instrument configuration. | Increase spectral resolution, or choose narrower slit, or use neutral-density filter, or change detectors and wavelength regime. |
| Check 65,536 counts/pix limit for MAMA observations ² | If limit exceeded, then reduce time per exposure. | Divide total exposure time into multiple, short exposures. ³ |

¹ Splitting CCD exposures increases the exposure time needed to achieve a given signal-to-noise ratio because of the read noise. Splitting an exposure into multiple exposures also increases the overheads, slightly reducing on-source time.

² See [Section 7.5.1](#).

³ Splitting MAMA exposures has no effect on signal-to-noise ratio since there is no read noise with the MAMAs. Splitting an exposure into multiple exposures does increase the overheads, slightly reducing on-source time. See [Chapter 9](#) for more information.

3.4.3 Identify Need for Non-Science Exposures and Constraints

Having identified your desired sequence of *science* exposures, you need to determine what *non-science* exposures you may require to achieve your scientific goals. Specifically, you need to:

- Determine which (if any) target acquisition and acquisition pickup exposures will be needed to center your target in your aperture to the accuracy required for your scientific aims (e.g., you may wish to center the nucleus of a galaxy in the 52×0.1 arcsecond slit and orient the long axis of the slit along the major axis of the galaxy to some accuracy). To assess your acquisition needs, refer to [Chapter 8](#). To determine a specific orientation for the STIS long slit, refer to [Chapter 11](#).
- If you require more accurate wavelength zero points than the routine calibrations provide, you can insert additional comparison lamp exposures (`TARGET_NAME=WAVE`) at shorter intervals or of longer duration than the routine, automatic wavecal observations. To determine your wavelength calibration exposure needs, refer to [Chapter 11](#).
- CCD observations longward of 7000 Å are subject to severe fringing, which can be well corrected only by flat-field exposures obtained contemporaneously with the science exposures. Hence, you should include such flat-field exposures if observing near 7000 Å or longward. Fringing is discussed in [Chapter 7](#) and the specification of corrective flat fields (CCDFLATS) is discussed in [Chapter 11](#).

3.4.4 Determine Total Orbit Request

In this, the final step, you place all your exposures (science and non-science, alike) into visits, including tabulated overheads, and determine the total number of orbits you require. Refer to [Chapter 9](#) when performing this step. If you are observing a point source and find your total time request is significantly affected by data transfer overheads (which will be the case only if you are taking many separate exposures under 3 minutes), you can consider the use of CCD subarrays to lessen the data volume. Subarrays are described in [Section 11.1 CCD Subarrays](#).

Due to the sensitivity of certain STIS electronic components to charged particles, there are some special constraints on the duration and structure of MAMA visits which preclude operating the MAMAs at all during orbits which cross the South Atlantic Anomaly (SAA). Since there are a limited number of SAA-free orbits per day, MAMA visits are limited to a maximum of five orbits. Longer programs must be broken into shorter visits. Moreover, in order to conserve orbits available for MAMA observations, programs which combine CCD and MAMA observations must be divided into separate visits for each detector type, unless the CCD portion consumes less than 30 minutes including overheads or the visit is only one orbit long (see [Chapter 2](#)).

At this point, if you are happy with the total number of orbits required, you're done! If you are unhappy with the total number of orbits required, you can re-iterate by adjusting your instrument configuration, lessening your acquisition requirements, changing your signal-to-noise or wavelength requirements, until you find a scenario which allows you to achieve (and convince the Telescope Allocation Committee [TAC] of the merits of) your scientific goals with STIS.

Chapter 4: Spectroscopy

Chapter Contents

- [4.1 Overview](#)
- [4.2 First-Order Long-Slit Spectroscopy](#)
- [4.3 Echelle Spectroscopy in the Ultraviolet](#)
- [4.4 Objective Prism Spectroscopy](#)

4.1 Overview

- 4.1.1 Throughputs
- 4.1.2 Limiting Magnitudes
- 4.1.3 Saturation
- 4.1.4 MAMA Bright Object Limits
- 4.1.5 Scanned Gratings: Prime and Secondary (Tilt) Positions
- 4.1.6 Cross-Over Regions
- 4.1.7 Neutral Density Slits for Spectroscopy

There are 15 spectroscopic modes which are summarized in [Table 4.1](#) below. They comprise low- and intermediate-resolution first-order modes designed to be used with a complement of long slits over the entire wavelength range, and intermediate- and high-resolution echelle modes that have been optimized for point-source observations through short echelle slits and are available only in the ultraviolet (UV; see [Figure 4.1](#)).

Table 4.1: STIS Spectroscopic Capabilities.

| Grating | Spectral Range (Å) | | Spectral Resolution | | No. Prime Tilts ² | Detector | Recommended Slits (apertures) ^{3,4,5,6,7,8,9,10} |
|--------------------------------------|--------------------|----------|-------------------------------------|---|------------------------------|----------|--|
| | Complete | Per Tilt | Scale $\Delta\lambda$ (Å per pixel) | Resolving Power ¹ ($\lambda/2\Delta\lambda$) | | | |
| <i>MAMA First-Order Spectroscopy</i> | | | | | | | |
| G140L | 1150-1730 | 590 | 0.60 | 960-1440 | 1 | FUV-MAMA | 52X0.05D1, 52X0.1D1 |
| G140M | 1140-1740 | 55 | 0.05 | 11,400-17,400 | 12 | FUV-MAMA | 52X0.2D1, 52X0.5D1 52X2D1, 25MAMAD1 F25SRF2D1, F25QTZD1 |
| G230L | 1570-3180 | 1616 | 1.58 | 500-1010 | 1 | NUV-MAMA | |
| G230M | 1640-3100 | 90 | 0.09 | 9110-17,220 | 18 | NUV-MAMA | |
| <i>CCD First-Order Spectroscopy</i> | | | | | | | |
| G230LB | 1680-3060 | 1380 | 1.35 | 620-1130 | 1 | CCD | 52X0.05E1 |
| G230MB | 1640-3190 | 156 | 0.15 | 5470-10,630 | 11 | CCD | 52X0.1E1 52X0.2E1 52X0.5E1 |
| G430L | 2900-5700 | 2800 | 2.73 | 530-1040 | 1 | CCD | 52X2E1 |

| | | | | | | | |
|----------------------------------|-------------|------|-------------------|---------------|----|----------|---|
| G430M | 3020-5610 | 286 | 0.28 | 5390-10,020 | 10 | CCD | |
| G750L | 5240-10,270 | 5030 | 4.92 | 530-1040 | 1 | CCD | 52X0.2 E2 52X0.5 E2 |
| G750M | 5450-10,140 | 572 | 0.56 | 4870-9050 | 9 | CCD | 52X2E2 |
| <i>MAMA Echelle Spectroscopy</i> | | | | | | | |
| E140M | 1144-1710 | 567 | $\lambda/91,700$ | 45,800 | 1 | FUV-MAMA | 0.2X0.2, 0.2X0.06 |
| E140H | 1140-1700 | 210 | $\lambda/228,000$ | 114,000 11 | 3 | FUV-MAMA | 0.2X0.2, 0.2X0.09 |
| E230M | 1605-3110 | 800 | $\lambda/60,000$ | 30,000 | 2 | NUV-MAMA | 0.2X0.2, 0.2X0.06 |
| E230H | 1620-3150 | 267 | $\lambda/228,000$ | 114,000 11 | 6 | NUV-MAMA | 0.2X0.2, 0.2X0.09 |
| <i>MAMA Prism Spectroscopy</i> | | | | | | | |
| PRISM | 1150-3620 | 2470 | 0.2-72 | 10-2500 | 1 | NUV-MAMA | 25MAMA, 52X0.05, 52X0.1, 52X0.2, 52X0.5, 52X2 |

¹ See [Section 13.6](#) for detailed estimates.

² Number of exposures at distinct tilts needed to cover spectral range of grating with 10% wavelength overlap between adjacent settings.

³ For a complete list of supported and available-but-unsupported apertures for each grating, see [Table A.1](#).

⁴ Naming convention gives dimensions of slit in arcseconds. E.g., 52x0.1 indicates the slit is 52 arcsec long perpendicular to the dispersion direction and 0.1 arcsec wide in the dispersion direction. The F (e.g., in 52x0.2F1) indicates a fiducial bar to be used for coronagraphic spectroscopy.

⁵ For MAMA first-order modes, only ~25 arcsec of a long slit's length projects on the detector. (See also [Section 4.2.2](#)).

⁶ Full-aperture clear (50CCD or 25MAMA), longpass-filtered (F25QTZ or F25SRF2 in UV), and neutral-density-filtered slitless spectroscopy are also supported with the appropriate first-order and echelle gratings, as well as the PRISM.

⁷ The following slits are also supported for all echelle gratings. The 6x0.2 and 52x0.05 long slits are intended for use with extended emission line objects; order overlap must be considered when using these slits. Also the high S/N multi-slits 0.2x0.2FP(A-E) and 0.2x0.06FP(A-E) (see [Chapter 12](#)), the very narrow 0.1x0.03 slit for maximum spectral resolution, and the 0.2x0.05ND, 0.3x0.05ND, and 31x0.05ND(A-C) neutral density slits.

⁸ The 0.1x0.09 and 0.1x0.2 slits are supported with E230H only. F25MGII is supported with all NUV-MAMA gratings and the PRISM.

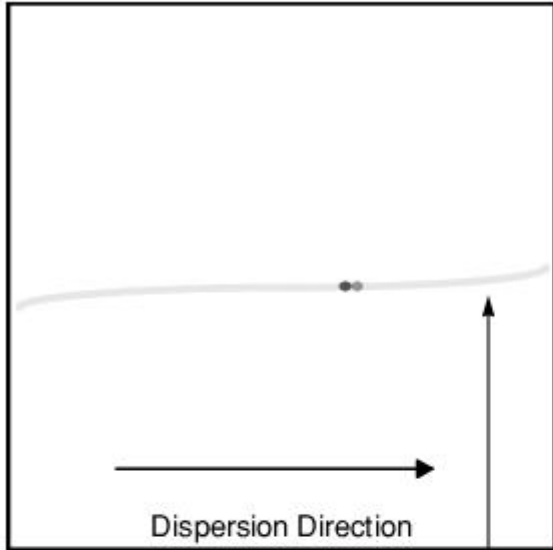
⁹ The 0.2x0.2 aperture is also supported with all first-order gratings. It is available-but-unsupported with the PRISM.

¹⁰ The F25SRF2 aperture can be used with the PRISM to filter out (geocoronal) Lyman- α emission.

¹¹ Resolution of 200,000 or greater is possible when used with the 0.1x0.03 slit and special observing and data reduction techniques.

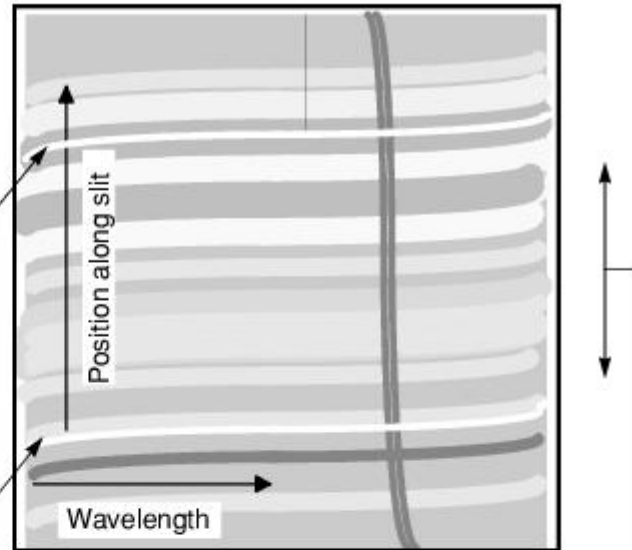
Figure 4.1: Sample Uncalibrated Spectral Images (distortion is exaggerated).

a.) Uncalibrated Long-Slit Spectrum of Point Source



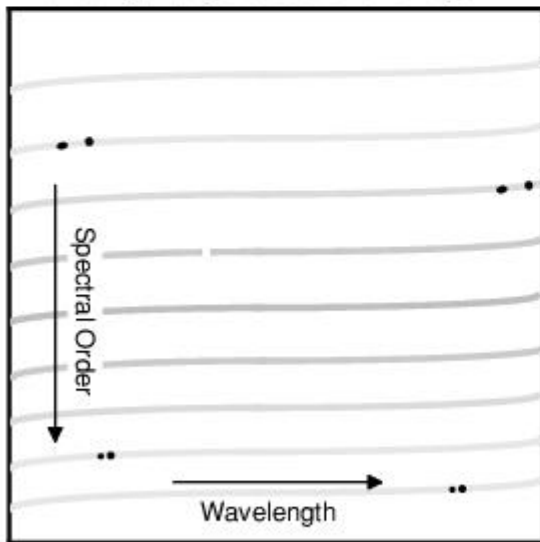
Point source showing continuum and two strong emission lines

b.) Uncalibrated Long-Slit Spectrum of Diffuse Source



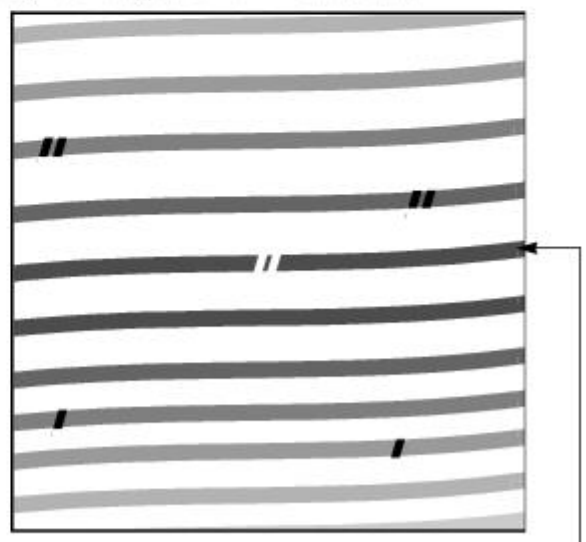
Strong doublet emission line
Bars on long slit
Spatially varying continuum

c.) Echelle Spectrum of Point Source Showing Multiple Orders on One Image



Two strong emission lines. Adjacent orders have ~10% overlap in wavelength so lines appearing at the start of one order will also appear at the end of the next.

d.) Echelle Spectrum of Diffuse Source



Absorption lines at wavelength near center of order. Continuum from extended object fills short slit.

4.1.1 Throughputs

To illustrate the broad wavelength coverage provided by STIS and the relative throughputs achievable across STIS' wavelength regime, we show in [Figure 4.2](#) the system throughput of the four low-resolution, first-order modes on a single plot (where the throughput is defined as the end-to-end effective area divided by the geometric area of a filled, unobstructed, 2.4 meter aperture). To allow you to judge the relative throughputs of different spectroscopic configurations, we plot in [Figure 4.3](#) the efficiency of all grating modes for each of the four primary wavelength regimes on a common plot. These plots allow you to gauge the relative efficiencies of STIS in different configurations. Note, however, that these curves give the throughput at the time that STIS was initially calibrated (approximately 1997.7). Throughput changes, determined from monitoring observations since STIS was installed, are discussed in [Sections 7.2.5](#) and [7.4.3](#). The throughput curves shown for the echelle modes trace the peak of the echelle blaze function for each order; throughputs near the ends of each order are lower by ~20 to 40%.

Figure 4.2: System Throughput of STIS' Low-Resolution, First-Order Grating Modes.

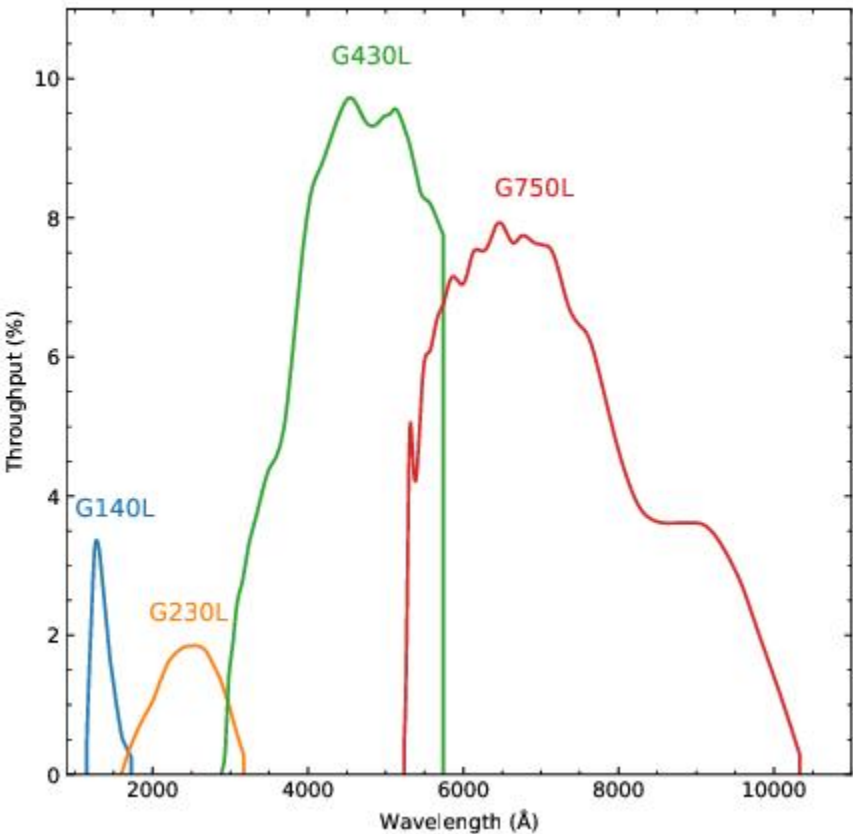
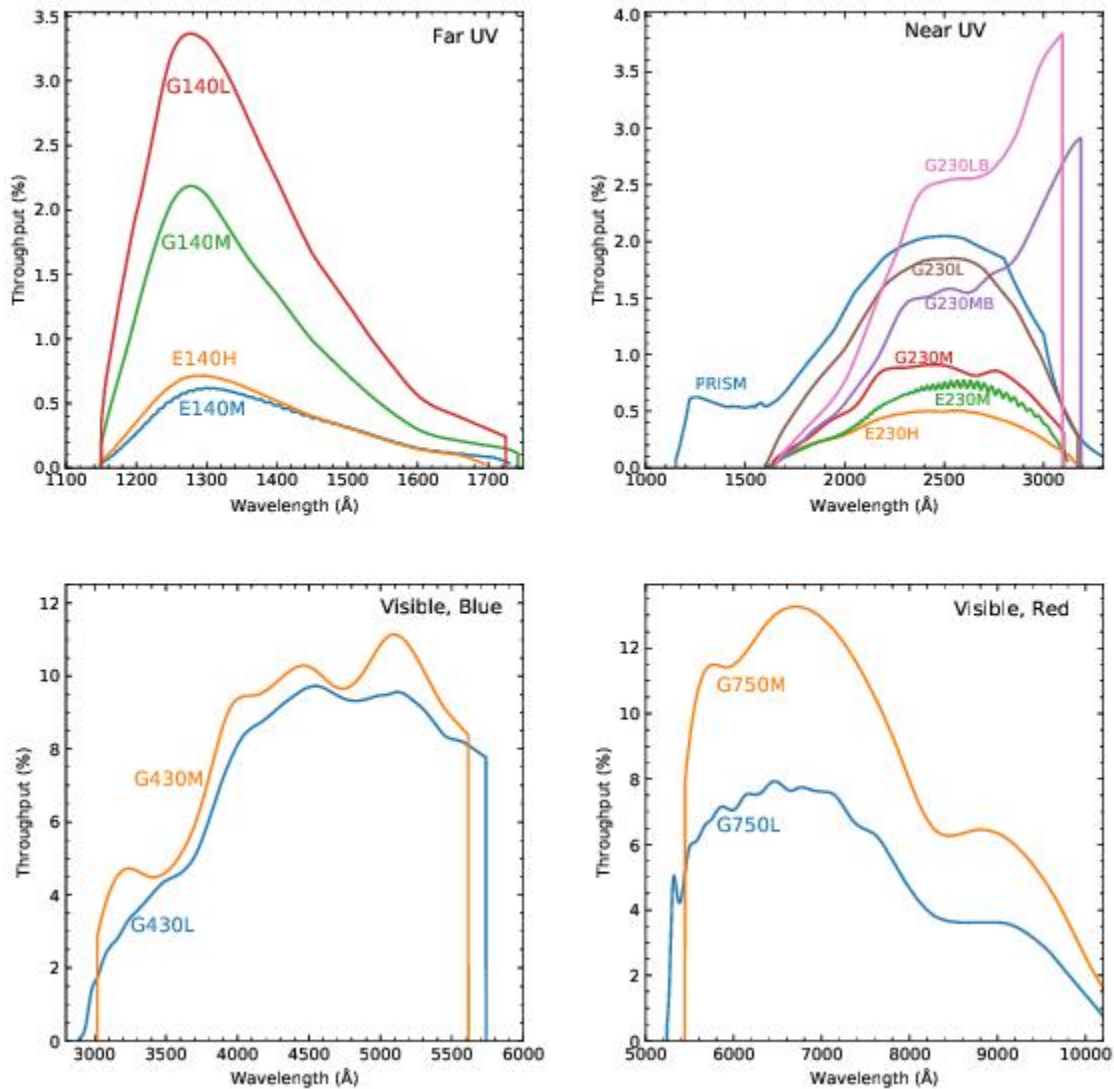


Figure 4.3: System Throughput of STIS' Grating Modes.



4.1.2 Limiting Magnitudes

In Table 4.2 below, we give the V magnitude for an A0V star that gives a signal-to-noise ratio of 10 in the continuum (per spectral resolution element around the peak of the grating response), in a 1 hour exposure, where we have integrated over the PSF in the direction perpendicular to the dispersion, and assumed the 52x0.2 slit for the first-order gratings and the 0.2x0.2 slit for the echelles. The adopted sensitivities are those estimated for August 2008.

Table 4.2: Limiting A0 V Star V Magnitudes.

| Grating | Wavelength (Å) | Magnitude |
|---------|-----------------|-----------|
| G750L | 7000 | 20.8 |
| G750M | 7000 | 19.0 |
| G430L | 5500 | 20.8 |
| G430M | 5500 | 18.4 |
| G230LB | 3000 | 18.3 |
| G230MB | 3000 | 15.4 |
| G230L | 2600 | 18.4 |
| G230M | 2600 | 14.4 |
| G140L | 1350 | 16.7 |
| G140M | 1350 | 13.4 |
| E230M | 2700 | 13.2 |
| E230H | 2600 | 11.6 |
| E140M | 1400 | 10.7 |
| E140H | 1350 | 9.8 |
| PRISM | 2300 (slitless) | 20.6 |

4.1.3 Saturation

Both CCD and MAMA observations are subject to saturation at high total accumulated counts/pix. The CCD can be saturated due to the saturation of the detector itself or of the gain amplifier for CCDGAIN=1. MAMA saturation can occur due to the 16-bit format of its memory buffer. The nature of the saturation for CCD and MAMA spectroscopic observations is described in [Section 7.3.2](#) and [Section 7.5.1](#), respectively.

4.1.4 MAMA Bright Object Limits

The MAMA detectors are subject to absolute bright object limits, above which targets cannot be observed.

We direct MAMA observers to the discussion presented in [Section 7.7](#). For summary tables of bright object screening magnitudes for all spectroscopic modes, see [Section 13.8](#). It is the observer's responsibility to be sure that proposed observations do not exceed the MAMA bright object limits.

4.1.5 Scanned Gratings: Prime and Secondary (Tilt) Positions

For the intermediate-resolution gratings and echelles (except E140M), only a portion of the full spectral range of the grating falls on the detector in any one exposure, and the gratings must be scanned (tilted) with a separate exposure taken at each tilt position, in order to cover the full spectral range (see [Figure 4.4](#) and [Figure 4.5](#) below). Accordingly, for these scanned gratings, the user may select a single exposure at a given wavelength, or a series of exposures at different wavelengths to cover a larger wavelength range. The user must choose either prime or secondary settings. The prime settings cover the full spectral range with 10% wavelength overlap between observations taken at adjacent settings. The secondary settings cover selected absorption or emission lines and may be more convenient to use in some applications. For the intermediate-resolution gratings, we expect the photometric and wavelength calibration accuracies to be higher for the prime settings than for most of the secondary settings, as calibrations for the latter are inferred from those taken at prime settings. Early in the operation of STIS, the photometric accuracies of the primary echelle settings were higher; however, for post-SM4 observations the photometric accuracies of the primary and secondary settings are comparable. The central wavelengths, and corresponding minimum and maximum wavelengths, are presented in the individual grating sections in [Chapter 13](#).

Figure 4.4: Scanned First-Order Gratings.

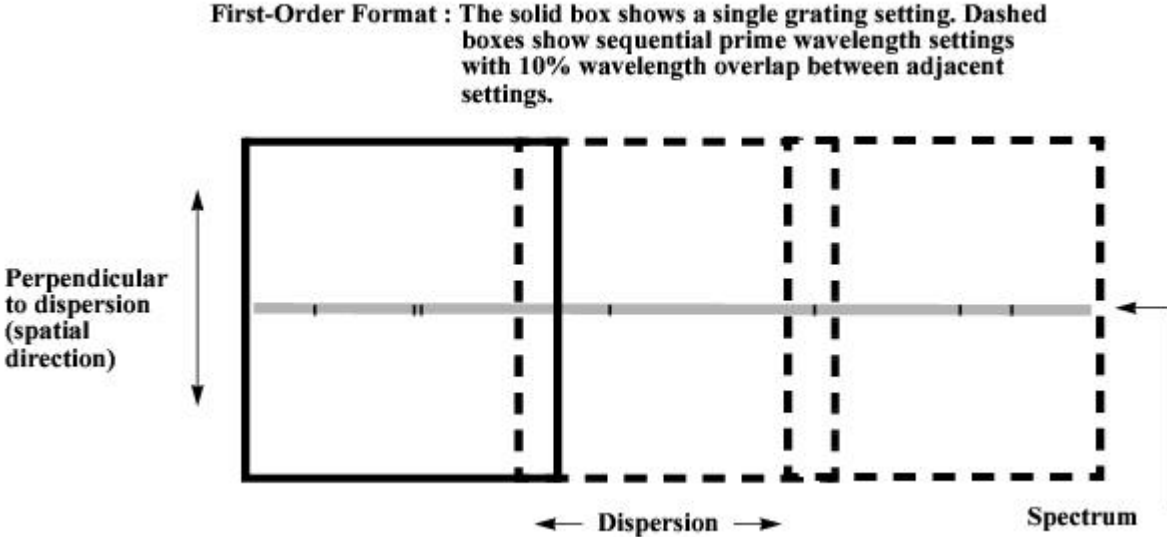
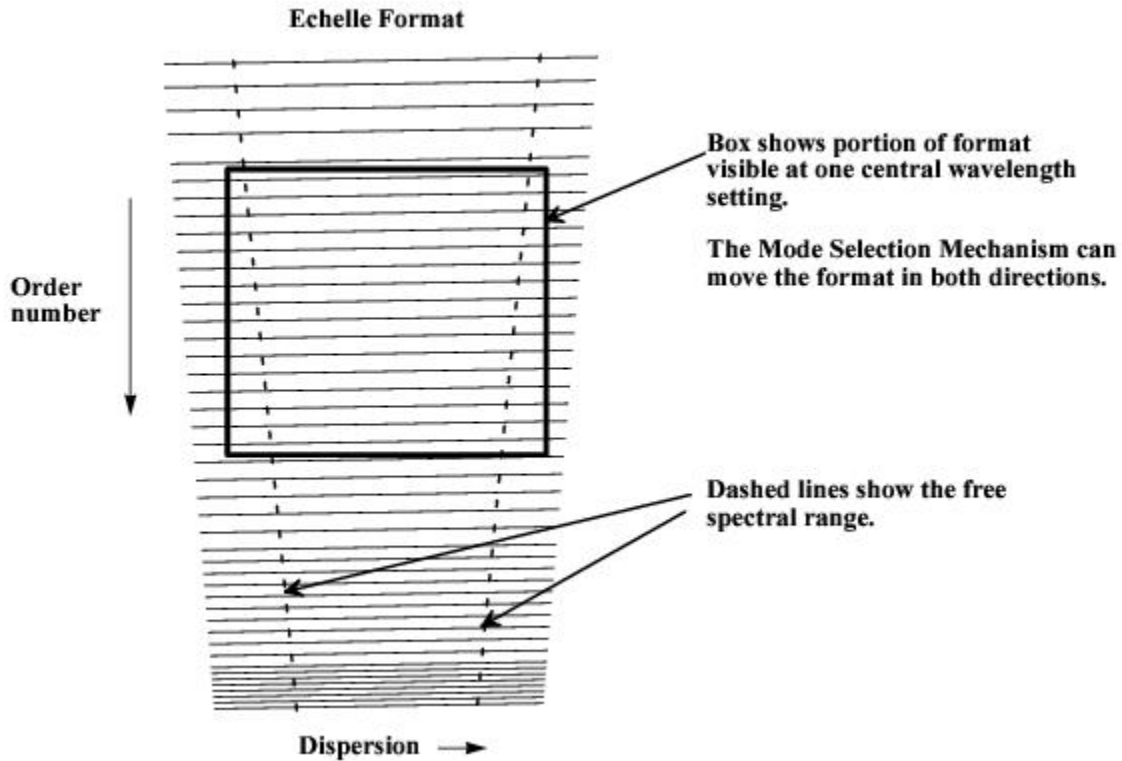


Figure 4.5: Scanned Echelle Gratings.



4.1.6 Cross-Over Regions

In the near-ultraviolet (NUV), where the CCD has comparable sensitivity to the NUV-MAMA, you may want to consider using the G230LB or G230MB gratings with the CCD instead of the G230L and G230M gratings with the MAMA. You will get improved throughput down to at least 2500 Å, a larger slit length, and use of the CCD rather than the MAMA (see [Figure 4.3](#) and [Chapter 13](#)). On the other hand, the CCD has read noise, cosmic ray sensitivity, hot pixels, and charge transfer efficiency losses. Also, for *red* objects, scattered light can be more of a problem with the red-sensitive CCD than with the solar-insensitive NUV-MAMA (see [STIS ISR 2022-05](#)). For a solar-type spectrum, CCD data at wavelengths shorter than 2100 Å are dominated by scattered light.

4.1.7 Neutral Density Slits for Spectroscopy

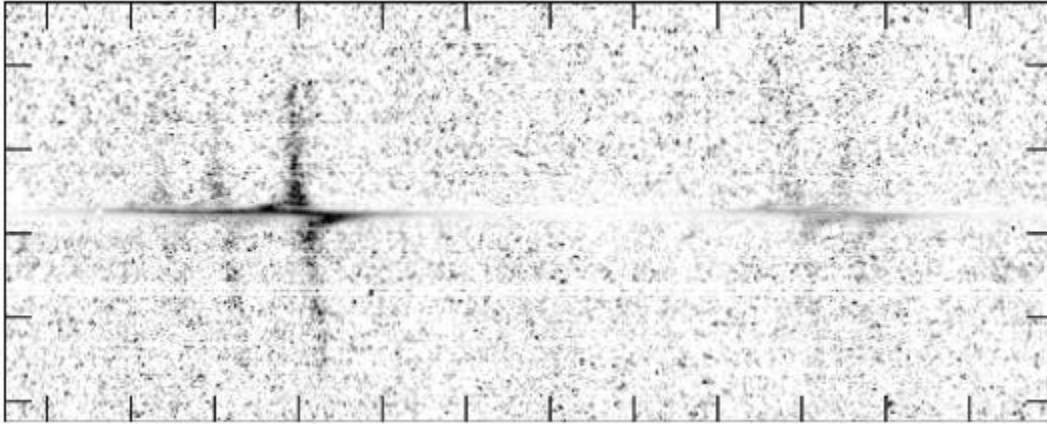
The use of the 31X0.05NDA, 31X0.05NDB, and 31X0.05NDC neutral density slits are supported with both the MAMA first order and echelle gratings. These slits are nominally 31 × 0.05 arcseconds in size, and have throughput reduction factors of roughly 6, 14, and 33, respectively, and are implemented in both APT and the STIS ETC. At this time their use with the PRISM remains "available-but-unsupported." Additional information can be found in [31X0.05ND\(A-C\) Apertures](#).

4.2 First-Order Long-Slit Spectroscopy

- [4.2.1 Gratings for First-Order Spectroscopy](#)
- [4.2.2 Slits for First-Order Spectroscopy](#)
- [4.2.3 STIS Pseudo-Aperture Positions](#)
- [4.2.4 Detailed First-Order Spectroscopic Information](#)

STIS first-order mode long-slit spectroscopy has a wide observing range from the near-infrared (NIR) through the optical and into the UV. [Figure 4.6](#) shows an early STIS result measuring the black hole mass in the nucleus of a nearby galaxy.

Figure 4.6: Greyscale Representation of STIS G750M 52X0.2 Long-Slit Spectrum of the Nuclear Region of M84.



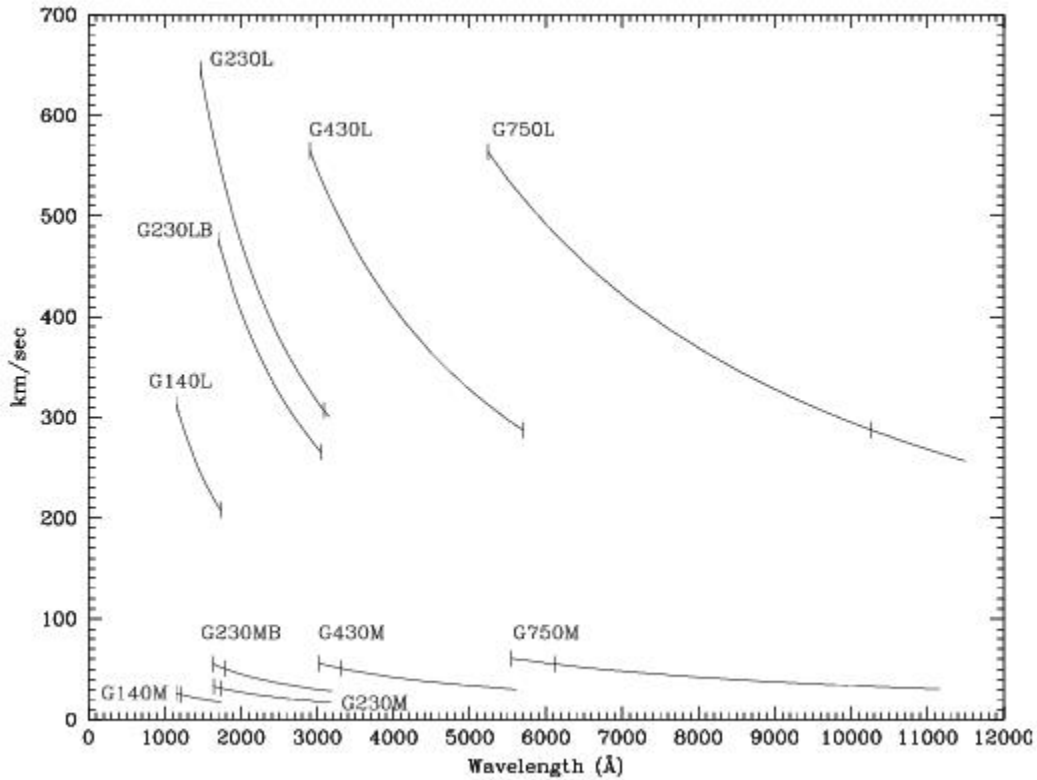
This figure shows the velocity structure of the H α , [N II], and [S II] emission lines in the inner gaseous disk. The continuum has been subtracted from the data and they have been renormalized. (Figure courtesy of Gary Bower and Richard Green, see also Bower et al. 1998, ApJ, 492, L111).

4.2.1 Gratings for First-Order Spectroscopy

There are 10 first-order gratings available for long-slit spectroscopy, providing resolving powers of ~ 500 – $17,000$ from the UV at 1150 \AA through the NIR at $\sim 10,000 \text{ \AA}$. The wavelength coverage and kinematic resolution of the first-order gratings are summarized in [Figure 4.7](#). Briefly:

- For resolutions of $\sim 500 \text{ km/s}$ use:
 - G140L at 1150 – 1700 \AA .
 - G230L (MAMA) or G230LB (CCD) at 1600 – 3100 \AA .
 - G430L at 2900 – 5700 \AA .
 - G750L at 5250 – $10,300 \text{ \AA}$.
- For resolutions of $\sim 50 \text{ km/s}$ use:
 - G140M at 1150 – 1700 \AA .
 - G230M (MAMA) or G230MB (CCD) at 1650 – 3100 \AA .
 - G430M at 3050 – 5600 \AA .
 - G750M at 5450 – $10,100 \text{ \AA}$.

Figure 4.7: Wavelength Coverage Versus Kinematic Resolution of First-Order Modes.



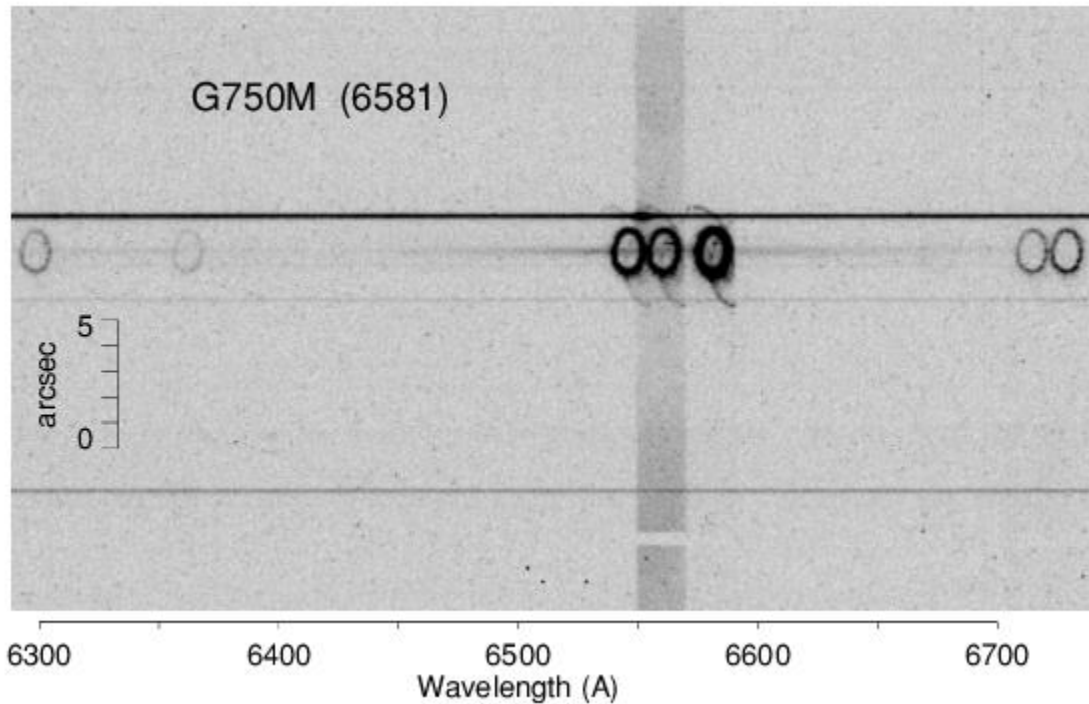
The hatches indicate the wavelength coverage at a single scan setting.

4.2.2 Slits for First-Order Spectroscopy

Supported for use with the first-order gratings are long slits of widths 0.05, 0.1, 0.2, 0.5 and 2.0 arcseconds (in the dispersion direction), and lengths of 52 arcseconds (as projected on the CCD detector) or 25 arcseconds (as projected on the MAMA detectors) for the MAMA low-resolution, first-order gratings (G230L and G140L) and 28 arcseconds for the MAMA intermediate-resolution, first-order gratings (G230M and G140M).¹ Note that the 0.1 arcsecond width matches the 2 pixel resolution of the CCD, while the 0.05 arcsecond width does so for the MAMAs, providing maximum spectral resolution. The 0.2 arcsecond-wide slit is the general utility slit used most often; it provides a good compromise between resolution and throughput. Programs requiring accurate absorption line measurements in continuum sources should always use slits of widths ≤ 0.2 arcsecond, since for larger apertures the spectral purity is significantly degraded by the telescope plus instrumental point spread function (PSF); see [Section 13.7](#). Finally, we expect the wider 0.5 and 2.0 arcsecond slits to be used predominantly in photon-starved UV observations of extended sources, but provide them for use in the optical as well to assure that line-ratio studies with coverage from the UV to the optical can sample the same physical region on the sky. Additionally, they are the most photometric slits as their throughput is least affected by centering and telescope breathing. Of course, observations of *extended* sources with wide slits will have correspondingly degraded spectral resolutions (see [Table 13.41](#) and [Table 13.42](#)).

The first-order gratings can also be used "slitless" to obtain two-dimensional spectra of targets, or pseudo "images." Slitless spectroscopic data will not be fully calibrated by the STScI pipeline, and it will require directed post-observation data processing by the user, as ambiguous overlap of wavelengths from different parts of sources can occur in the image (see [Section 12.1](#)). [Figure 4.8](#) shows an example of the use of the 52x2 slit with the G750M grating to obtain such a series of emission line images of SN1987A.

Figure 4.8: STIS G750M 6581 Å 52X2 Spectral Image of SN1987A.



This shows the images of the inner circumstellar ring in [O I], H α , [N II], and [S II]. Diffuse H α emission from the LMC fills the 52 \times 2 slit, and broad H α emission from the SN is also visible. The continua of stars produce the horizontal bands. The image shown is a 950 \times 450 subsection of the 1024 \times 1024 image. (Figure courtesy of Jason Pun and George Sonneborn, see also Sonneborn et al. 1998, *ApJ*, 492, L139).

Note that for the FUV-MAMA first-order modes, the projection of the slit image on the detector has deliberately been shifted by \sim 110-130 low-resolution pixels (or \sim 3.25 arcseconds) below center (versus the above center offset used prior to March 15, 1999), to avoid having the spectrum fall on the shadow of the repeller wire (see also [Section 7.6](#) and [Section 11.1.2](#)). This shift applies to all data taken with the G140L and G140M gratings, regardless of the aperture used.

Note also that the monthly offsetting of MAMA first-order spectral modes can additionally shift the projection of the spectrum on the detector by up to \sim \pm 40 low-resolution AXIS2 pixels (about 1 arcsecond). See [Section 7.6](#) for further discussion. Beginning in Cycle 30, users can request disabling the monthly offsets as an available-but-unsupported mode for those programs requiring the strictest control of instrument systematics.

The 0.2X0.2 aperture is now supported for use with all first-order gratings. This is intended to be used for observations where a long slit might allow light from another target into the aperture, thereby creating either contamination problems or bright object concerns. Note, however, that the use of such a short slit will make background subtraction more difficult, especially at wavelengths where airglow lines are important.

4.2.3 STIS Pseudo-Aperture Positions

A number of "pseudo-aperture" positions have been defined for STIS spectroscopy, which allow a target to be placed at positions other than the geometrical center of the aperture without the need to specify a `POS TARG`. These include the E1 and E2 positions, which place the target closer to the CCD readout to minimize losses due to charge transfer inefficiency (CTI), and the D1 aperture positions, which can be used to place a faint target near the bottom of the FUV-MAMA detector, where the dark current is significantly reduced. Note that the E1 positions may be used with any first-order STIS CCD grating. The E2 positions may only be used with G750M and G750L. The D1 positions may only be used with the G140L and G140M gratings, except for the 52X0.1D1 and 52X0.05D1 positions, which are also supported for CCD ACQ/PEAK observations.

Here we describe these pseudo-aperture locations and their intended purposes. Note that all of these pseudo-apertures define new positions within existing apertures. As a result, the `APERTURE` keyword in the headers of the archived data will contain the name of the parent aperture, while the `PROPAPER` keyword will contain the aperture name specified in the Phase II proposal. For example, if the Phase II proposal requests the 52X0.1D1 position, the `APERTURE` keyword will be set to 52X0.1, while the `PROPAPER` keyword will be 52X0.1D1.

E1 Aperture Positions to Decrease CTE Loss

As the STIS CCD detector has accumulated radiation damage over time, the Charge Transfer Efficiency (CTE) has decreased (see [Section 7.3.7](#)). For faint sources observed near the center of the CCD detector, this can result in the loss of 18% or more of the detected signal during the readout. Since the amount of these CTE losses depends on both the observed signal and background counts, there is no simple way to correct for these losses, and they can significantly affect the shape of a measured spectrum. Noticeable effects can be seen even in well exposed spectra. In addition to its effects on the counts from the observed astronomical source, CTE effects re-distribute some of the electrons in hot pixels and cosmic rays into "tails" that lag behind during the readout. These tails add significant background noise to long exposures that is not taken into account by the [STIS Exposure Time Calculator \(ETC\)](#), and which can be difficult to remove. CTE effects also result in a value for the effective dark current that is about 60% larger at the center of the detector than it is near the E1 positions (see [Figure 7.8](#)). However, the STIS team has created a software package to apply CTE loss corrections to CCD data. More information can be found in STIS ISRs [2015-04](#) and [2015-05](#) as well as in [Section 7.3.9](#). Also see the [CTE correction webpage](#) for information about the software used to correct for this. At present, these corrections are not automatically applied in the STScI STIS data pipeline.

All of these effects can also be significantly ameliorated by moving the location of the source image on the detector closer to the amplifier, thereby reducing the number of parallel transfers that occur during the readout. To this end, so-called E1 aperture positions (52X0.05E1, 52X0.1E1, 52X0.2E1, 52X0.5E1, and 52X2E1) have been defined near row 900 on the STIS CCD detector for use with the STIS first-order gratings. The use of these aperture positions is strongly recommended for the observation of faint sources. For high signal-to-noise observations of bright targets we recommend continuing to use the regular aperture positions near the center of the detector. Extensive calibration observations were performed during Cycles 11 and 12 to ensure that the calibration at the E1 aperture positions is of the same quality as it is for sources observed at the usual location on the STIS CCD. Further information regarding the use of the E1 aperture positions can be found in [Section 7.3.8](#).

E2 Aperture Positions for Better Fringe Flats

In 1999, the E1 aperture positions were introduced to allow first-order CCD spectra to be positioned at row 900 near the CCD readout amplifier, where the Charge Transfer Efficiency (CTE) is higher than at the standard positions. This works well; however, for G750L and G750M spectra taken near row 900, the fringe flats have to be done using the 52X0.1 aperture rather than the 0.3X0.09 aperture, which is usually used for fringe flats near the center of the detector (see [Section 11.2.3](#) for a more detailed discussion of infrared [IR] fringe flats). Unfortunately, the 52X0.1 slit is shifted by about one pixel in the dispersion direction from the centers of the wider long slits. This misalignment reduces the accuracy of fringe correction.

To address this, we have defined three E2 aperture locations: 52X0.2E2, 52X0.5E2, and 52X2E2. When these apertures are specified, the target is placed off-center in the slit, at a position coincident with the 52X0.1E1 aperture. This improves the match between the fringes in the target and lamp spectra. Be aware, however, that the 52X0.2E2 aperture position is offset sufficiently from the physical center of the aperture that there will be noticeable changes in the aperture throughput and line-spread function.

These E2 aperture positions should only be used for ACCUM exposures with the G750L or G750M gratings when fringe flats with the 52X0.1 aperture are also being done. If a peakup is desired before using the E2 apertures, the peakup should be done using the 52X0.1E1 aperture.

D1 Aperture Positions for Low FUV Dark Current

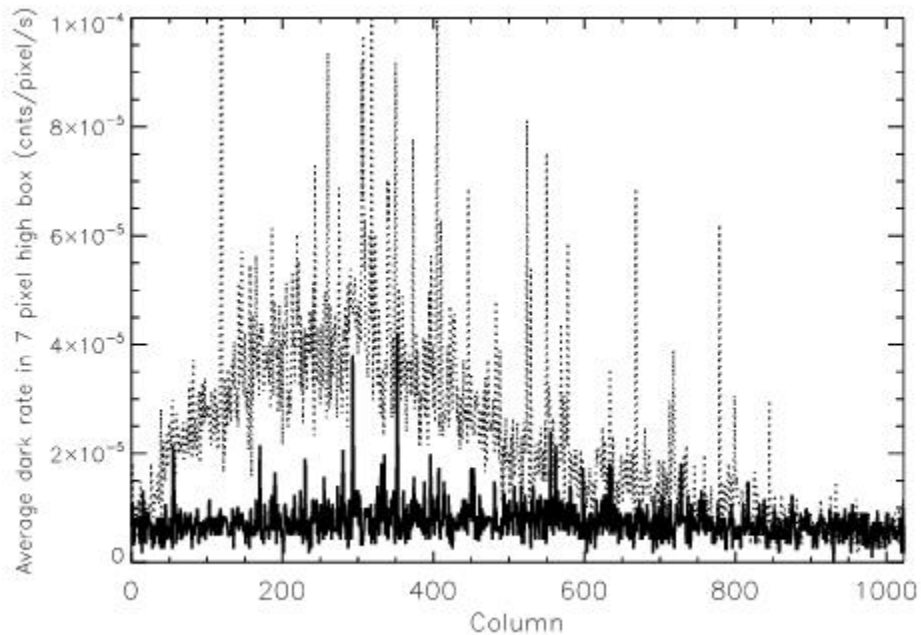
The FUV-MAMA suffers from an irregular dark glow that varies unpredictably in intensity. When this glow is absent, the typical dark rate of the FUV-MAMA detector is about 6×10^{-6} counts/pix/s. When the glow is strong, it can enhance the dark current to as much as 1×10^{-4} counts/pix/s over a large fraction of the detector. For first-order spectra, the best way to minimize this extra dark current is to put the target at a location on the detector where the extra dark current is small.

For first-order spectra of faint sources less than about 1 arcsecond in angular extent, we recommend that this be done by placing the target about 2 arcseconds above the bottom edge of the FUV-MAMA detector. Since for the G140L and G140M the regular aperture positions are projected about 3 arcseconds below the center (in order to avoid the shadow of the FUV-MAMA repeller wire), an additional displacement of about -6.8 arcseconds is required in the cross-dispersion, or y, direction. This can reduce the extra dark current by up to a factor of 6 (see [Figure 4.9](#)). For G140L observations, the default D1 position will place the spectrum about 2 arcseconds above the bottom edge of the detector. The monthly offsetting of the spectral location (see [Section 7.6](#)) will shift this by as much as ± 1 arcsecond. Because of the larger cross dispersion plate scale of the G140M, variations of the default spectral position for different G140M CENWAVE values, and the monthly spectral offsetting, G140M spectra taken at the D1 aperture positions will be located 3 to 5 arcseconds above the bottom edge of the FUV-MAMA detector.

Note that the background subtraction might be more difficult due to the proximity to the edge of the detector, depending on the extent of the target. Therefore, use of this position is recommended only for objects sufficiently faint that the FUV-MAMA dark current is the major limitation on the achievable accuracy.

The D1 apertures listed in the [Table 4.3](#) are supported for first-order spectroscopic ACCUM or TIME-TAG observations with the G140L and G140M. The 52X0.1D1 and 52X0.05D1 apertures are also supported for CCD ACQ/PEAK observations. Note that the 25MAMAD1, F25QTZD1, and F25SRF2D1 aperture locations are intended only for first-order FUV-MAMA slitless spectroscopy. Users who wish to offset faint imaging targets to avoid the worst of the FUV dark current should look at [Figure 7.21](#) or consult with a STIS Instrument Scientist via the [Help Desk](#).

Figure 4.9: The FUV-MAMA Mean Dark Current.



The **FUV-MAMA** mean dark current (dotted line) as a function of the detector column number (in a seven pixel high extraction box near the standard extraction position located 3 arcseconds below the detector center) is compared with that in a box near the D1 pseudo-aperture position 6.8 arcseconds further down (solid line). The data used are an average of 125 dark monitor exposures, each of 1380 seconds, taken between May 2003 and August 2004. This illustrates the typical reduction in the dark current affecting first-order spectra that will result from putting the target 2 arcseconds above the bottom of the detector.

Sensitivity Differences at the Pseudo-Aperture Positions

The throughputs at the **E1** and **D1** pseudo-apertures, as functions of wavelength, are generally similar to those at the corresponding nominal (central) positions. However, there is some vignetting of the gratings that changes the overall system throughput slightly with varying position along the long slits. At the **E1** positions, the overall low-dispersion throughputs are decreased by 2-3%, while at the **D1** position the **G140L** throughput is increased by 2-7%. For the medium-resolution grating **G140M** at the **D1** position, the throughput changes are $\sim 3\%$ at 1272\AA and $\sim \pm 10\%$ at 1567\AA (see [ISR 2022-06](#)). Other **G140M** CENWAVE values are expected to have throughput differences comparable to the 3-10% range measured for those two settings. Since these throughput changes do not depend on the wavelength alone, but also on the grating and the position on the detector, they are handled in the pipeline calibration by the use of low-order flat fields (LFLT files) rather than by a change in the aperture throughput curve. Note, however, that only **G140L** has this throughput variation corrected by its LFLT file. The LFLT files for **G140M** modes are currently single valued (value = 1.0) everywhere.

The throughput of the **52X2E2** and **52X0.5E2** positions are similar to that of the corresponding **E1** positions. For the **52X0.2E2** aperture, the throughput is about 20% lower than for the **52X0.2E1** position.

Table 4.3: Gratings Supported with STIS Pseudo-aperture Positions.

| Pseudo-aperture | Science Gratings | Supported Peak-up Elements |
|-----------------|------------------|-----------------------------|
| 52X0.05E1 | CCD first-order | CCD first-order, CCD Mirror |
| 52X0.1E1 | CCD first-order | CCD first-order, CCD Mirror |
| 52X0.2E1 | CCD first-order | none (52X0.1E1 recommended) |
| 52X0.5E1 | CCD first-order | none |
| 52X2E1 | CCD first-order | none |
| 52X0.2E2 | G750L, G750M | none (52X0.1E1 recommended) |
| 52X0.5E2 | G750L, G750M | none |
| 52X2E2 | G750L, G750M | none |
| 52X0.05D1 | G140L, G140M | CCD first-order, CCD Mirror |
| 52X0.1D1 | G140L, G140M | CCD first-order, CCD Mirror |
| 52X0.2D1 | G140L, G140M | none |
| 52X0.5D1 | G140L, G140M | none |
| 52X2D1 | G140L, G140M | none |
| 25MAMAD1 | G140L, G140M | none |
| F25SRF2D1 | G140L, G140M | none |
| F25QTZD1 | G140L, G140M | none |

4.2.4 Detailed First-Order Spectroscopic Information

The properties of each of the first-order gratings are described in detail, grating by grating, in [Chapter 13](#); see the first column of [Table 4.1](#) for links to the appropriate page for each grating.

The detailed properties of the long slits (e.g., throughputs and line spread as functions of wavelength), plate scales, and encircled energies for the first-order gratings are presented under [Section 13.4](#), [Section 13.5](#), and [Section 13.6](#).

¹ The MAMA first-order modes have varying spatial plate scales; see [Chapter 13](#).

4.3 Echelle Spectroscopy in the Ultraviolet

- [4.3.1 Echelle Gratings](#)
- [4.3.2 Slits for Echelle Spectroscopy](#)
- [4.3.3 Detailed Echelle Information](#)

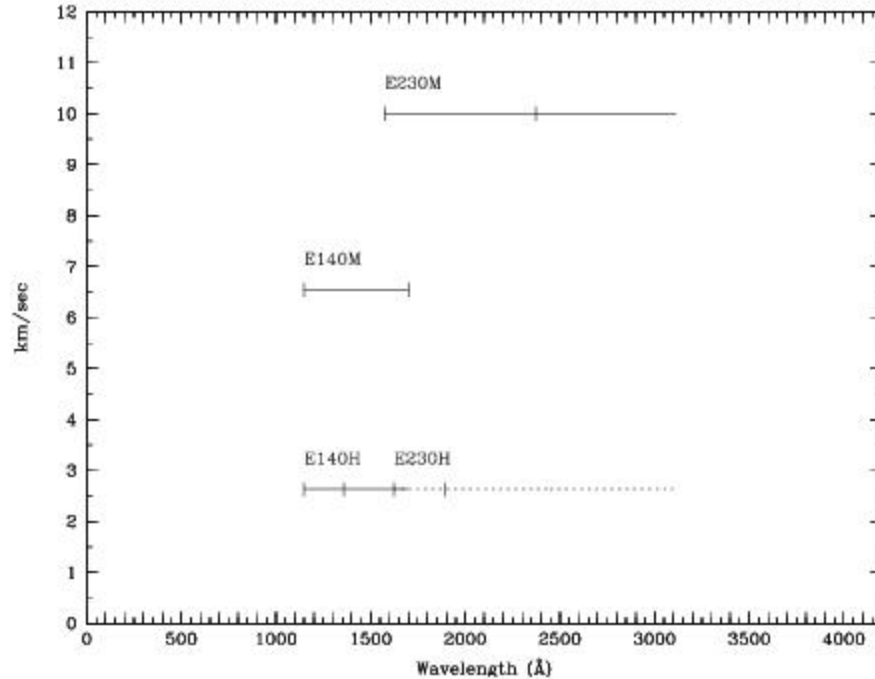
An example of STIS E230H echelle spectroscopy (both the echelle spectrum and a few sample extracted orders) of star CPD-59D2603 showing the interstellar absorption from the Carina Nebula is given in [Figure 15.3](#). (See also Walborn et al. 1998, ApJ, 492, L169.)

4.3.1 Echelle Gratings

There are four echelle grating modes that provide spectroscopic coverage from $\sim 1145 \text{ \AA}$ to 3100 \AA at resolving powers from $R \sim 30,000$ to $R \sim 114,000$ (or even $R \sim 200,000$ with the 0.1×0.03 aperture and specialized data reduction; see [Section 12.6](#)). Through simultaneous observation of multiple orders, they are designed to maximize the spectral coverage achieved in a single exposure of a point source. [Figure 4.10](#) below summarizes the wavelength coverage and kinematic resolutions of the echelle gratings. In short:

- For $\sim 10 \text{ km/s}$ resolution use:
 - E140M at $1144\text{--}1730 \text{ \AA}$.
 - E230M at $1600\text{--}3100 \text{ \AA}$.
- For $\sim 2.5 \text{ km/s}$ resolution use:
 - E140H at $1140\text{--}1700 \text{ \AA}$.
 - E230H at $1600\text{--}3100 \text{ \AA}$.

Figure 4.10: Echelle Wavelength Coverage vs. Kinematic Resolution.



Hatches indicate wavelength coverage at a single scan setting. The dashed line shows the E230H coverage. See [Table 4.1](#) and [Chapter 13](#) for more details.

4.3.2 Slits for Echelle Spectroscopy

Short echelle slits, which ensure order separation, are available for use with the echelle gratings. For each mode a short slit of width 0.2 arcsecond is provided, along with a slit whose width matches a two pixel projection in the dispersion direction; either 0.09 arcsecond for the H modes, or 0.06 arcsecond for the M modes. In addition, an ultra-narrow slit of width 0.025 arcsecond (0.1x0.03 in the *Proposal Instructions*) is supported with all of the echelles, for the highest spectral resolution of bright objects. Also, two multi-slits with different widths (called the FP-SPLIT slits) are supported for use with the echelles to provide optimally placed multiple exposures which maximize S/N. Their use is discussed in [Chapter 12](#).

Although we do not recommend routine use, the echelle gratings can be used with a long slit (the 6x0.2 slit) to obtain echelle spectroscopy of extended objects with weak continua. Long-slit echelle data, however, will not be calibrated by the STScI pipeline, and they will require more extensive post-observation processing by the user since ambiguous overlap of wavelengths from different parts of sources will occur in the image (see [Section 12.2](#) if you are considering such observations). In addition to the spectral purity considerations in the dispersion direction mentioned above for the first-order gratings, echelle observations are subject to contamination in the cross-dispersion direction by scattered light. This effect is aggravated toward shorter wavelengths as the orders become more crowded. Continuum sources should not normally be observed with slit lengths greater than 0.2 arcsecond, and even then special data analysis may be required to optimize the accuracy of the results. See [Section 13.7](#).

4.3.3 Detailed Echelle Information

The properties of each of the echelle gratings are described in detail, grating by grating, in [Chapter 13](#) ; see the first column of [Table 4.1](#) for links to the appropriate page for each grating.

The detailed properties of the echelle slits (e.g., throughputs and line spreads as functions of wavelength), the plate scales, and the encircled energies for the echelle modes are presented under [Section 13.4](#), [Section 13.5](#), and [Section 13.6](#).

4.4 Objective Prism Spectroscopy

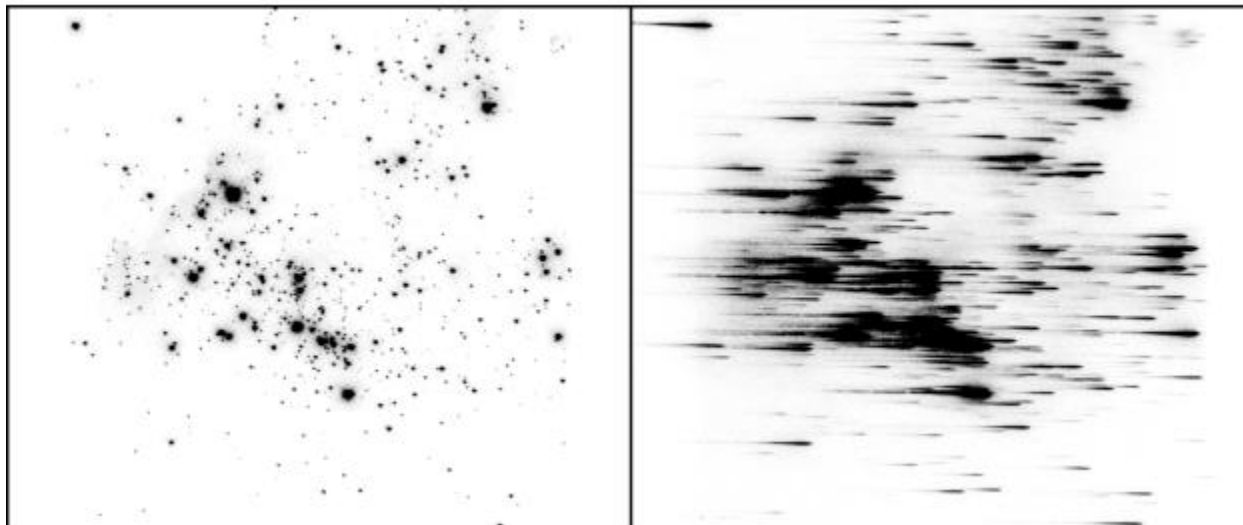
✔ *Beginning in Cycle 30, the use of the STIS PRISM will be an available-but-unsupported mode due to the growing uncertainty of its absolute flux calibration (see [Section 13.3/PRISM](#)). Observers interested in using this optical element who require absolute flux calibration will need to plan to observe their own flux standard star.*

The STIS PRISM is used with the STIS NUV-MAMA and provides spectra from 1150 to 3620 Å at resolving powers of up to ~2500 in the FUV declining to ~10 at optical wavelengths. In [Figure 4.11](#) we compare a direct NUV-MAMA image of the star cluster NGC 604 with a PRISM exposure of the same field. This example illustrates the power of the prism mode to simultaneously provide spectra covering a wide wavelength range of many objects in a single field of view. Note that the ACS also has the capability of performing slitless UV spectroscopy.

As can be seen in [Figure 4.11](#), an NUV objective-prism spectrum does not cover the full range of the detector in the dispersion direction. In many cases, there will be a significant number of counts only over an extent of ~200 pixels due to the large dispersion and low sensitivity at short wavelengths. This characteristic can be an advantage over a grating such as the G230L in crowded fields, since it reduces the possibility of overlap between different sources.

The PRISM can be used at two wavelength settings, 1200 and 2125 Å. These are approximately the wavelengths that will lie at the center of AXIS1 on the detector for the two settings. The relationship between wavelength and pixel number along the central spectral trace is shown in [Figure 4.12](#) for each setting. The dispersion as a function of wavelength is shown in [Figure 4.13](#) for each setting.

Figure 4.11: $NUV-MAMA$ image (left) and objective-prism exposure (right) of NGC 604.



These images of NGC 604, a Scaled OB Association, were obtained under GO program 9096. The dispersion direction is nearly parallel to the x-axis.

Figure 4.12: Wavelength vs. Pixel Number along the Central Spectral Trace for the PRISM at Wavelength Settings 1200 and 2125 Å.

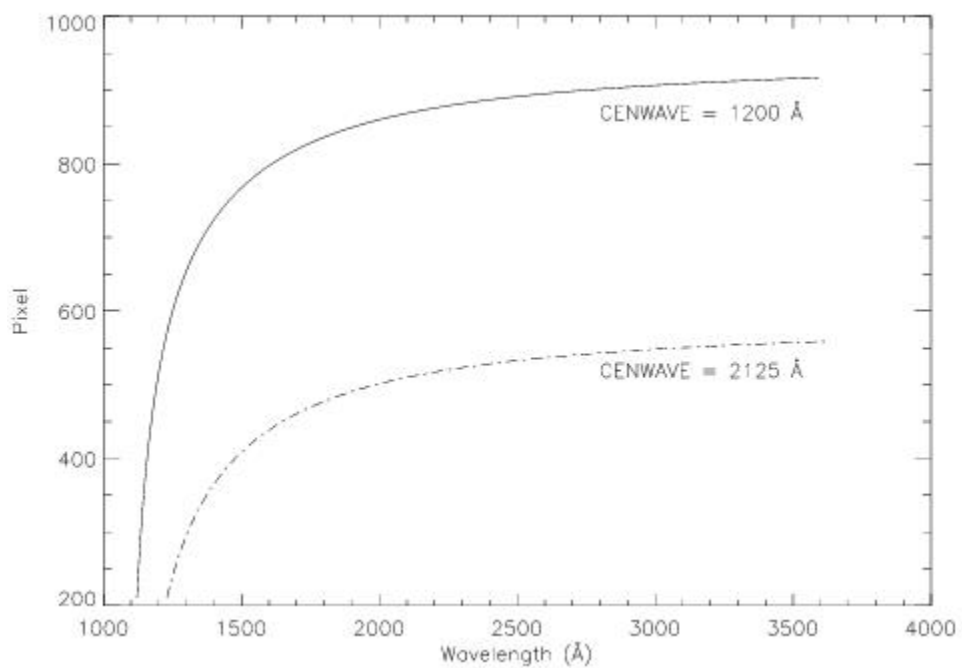
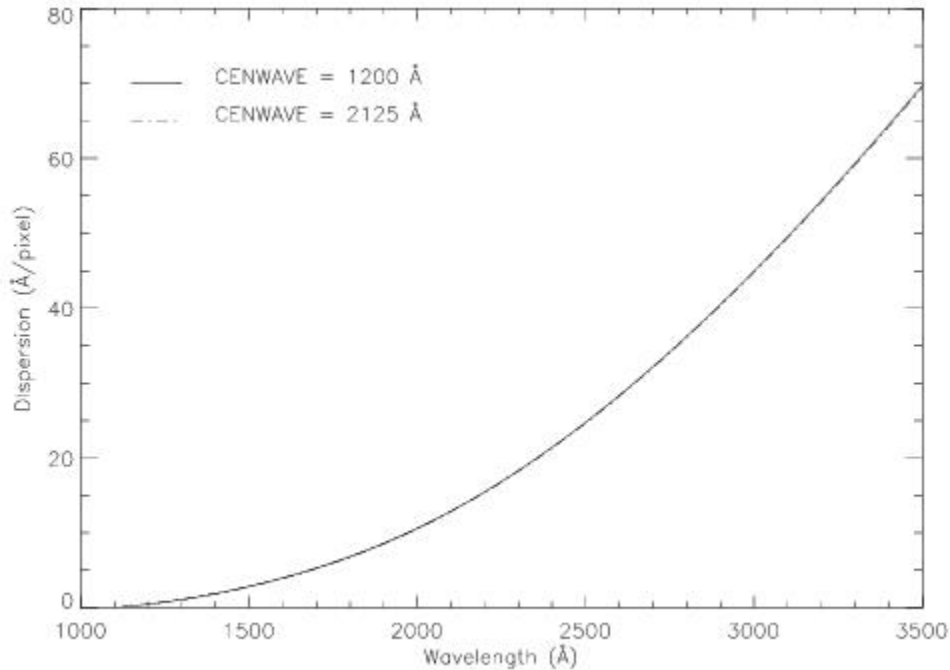


Figure 4.13: Dispersion as a Function of Wavelength for the PRISM at Wavelength Settings 1200 Å (solid) and 2125 Å (dot-dash).



The PRISM can be used with the clear MAMA aperture (25MAMA) or with either longpass UV filtered aperture (F25SRF2 or F25QTZ) to provide a 25×25 arcsecond field of view (see also F25SRF2 and F25QTZ). The longpass filter F25SRF2 blocks geocoronal Lyman- α 1216 Å and the F25QTZ longpass filter blocks both geocoronal Lyman- α and geocoronal O I 1302 Å triplet, significantly reducing the background from these lines (which is otherwise spread throughout the image) at the price of losing the short-wavelength range of the spectrum. In addition, the neutral-density filters (Table 5.1) are supported for PRISM spectroscopy, as are the 52X0.05, 52X0.1, 52X0.2, 52X0.5, and 52X2 long slits.

Observers will generally want to also obtain a *direct image* of the field when taking an objective prism spectrum, so they can later determine the centering of the objects in their prism data. Because the PRISM and the mirrors used for imaging are both in the Mode Selection Mechanism, zero-point shifts will occur between the PRISM and imaging data (see Section 3.2.2, [Slit and Grating Wheels](#)). For a discussion of the observations needed to measure these shifts, see [Section 12.1](#).

✔ **Note that slitless PRISM spectroscopy produces images in which, a priori, the wavelength at a given pixel is not known, and source-dependent overlap of spectra can occur. For these reasons, slitless PRISM spectroscopic data will not be calibrated automatically by the STScI pipeline. Instead, users will have to reduce and analyze their data off-line.**

Chapter 5: Imaging

Chapter Contents

- [5.1 Imaging Overview](#)
- [5.2 Optical CCD Imaging](#)
- [5.3 Ultraviolet Imaging with the MAMA Detectors](#)
- [5.4 Neutral Density Filters](#)

5.1 Imaging Overview

- [5.1.1 Caveats for STIS Imaging](#)
- [5.1.2 Throughputs and Limiting Magnitudes](#)
- [5.1.3 Signal-To-Noise Ratios](#)
- [5.1.4 Saturation](#)
- [5.1.5 Full-field Sensitivity](#)

STIS can be used to obtain images of undispersed light in the optical and ultraviolet (UV). When STIS is used in imaging mode, the appropriate clear or filtered aperture on the slit wheel is rotated into position, and a mirror on the Mode Selection Mechanism (MSM) is moved into position (see [Figure 3.1](#)).

[Table 5.1](#) provides a complete summary of the clear and filtered apertures available for imaging with each detector. In [Figure 5.5](#) through [Figure 5.13](#) we show the integrated system throughputs.

Table 5.1: STIS Imaging Capabilities

| Aperture Name | Filter | Pivot Wavelength ¹ (λ_c in Å) | FWHM ² ($\Delta\lambda$ in Å) | Field of View (arcsec ²) | Detector |
|---|-------------------------------|--|--|---|--------------------------------|
| <i>Visible - plate scale ~ 0.05078 arcseconds per pixel³</i> | | | | | |
| 50CCD | Clear | 5852 | 4410 | 52 × 52 | STIS/CCD |
| F28X50LP | Optical longpass | 7229 | 2722 | 28 × 52 ⁴ | STIS/CCD |
| F28X50OIII | [O III] | 5006 ⁵ | 6 | 28 × 52 ⁶ | STIS/CCD |
| F28X50OII | [O II] | 3737 | 62 | 28 × 52 ⁷ | STIS/CCD |
| 50CORON | Clear + coronagraphic fingers | 5852 | 4410 | 52 × 52 | STIS/CCD |
| <i>Ultraviolet - plate scale ~0.0246 arcseconds per pixel⁸</i> | | | | | |
| 25MAMA (NUV , FUV) | Clear | 2250 1374 | 1202 324 | 25 × 25 | STIS/NUV-MAMA STIS/FUV-MAMA |
| F25QTZ (NUV , FUV) | UV near longpass | 2365 1595 | 995 228 | 25 × 25 | STIS/NUV-MAMA STIS/FUV-MAMA |

| | | | | | |
|---|--|---------------|-------------|--|--------------------------------|
| F25SRF2 (NUV, FUV) | UV far longpass | 2299 1457 | 1128 284 | 25 × 25 | STIS/NUV-MAMA STIS/FUV-MAMA |
| F25MGII | Mg II | 2802 | 45 | 25 × 25 | STIS/NUV-MAMA |
| F25CN270 | Continuum ~2700 Å | 2709 | 155 | 25 × 25 | STIS/NUV-MAMA |
| F25CIII | C III] | 1989 | 173 | 25 × 25 | STIS/NUV-MAMA |
| F25CN182 | Continuum ~1800 Å | 1981 | 514 | 25 × 25 | STIS/NUV-MAMA |
| F25LYA | Lyman-α | 1221 | 72 | 25 × 25 | STIS/FUV-MAMA |
| <i>Neutral-Density-Filtered Imaging</i> ⁹ | | | | | |
| F25NDQ1 F25NDQ2 F25NDQ3 F25NDQ4 (Aperture , NUV, FUV) | ND=10 ⁻¹ ND=10 ⁻² ND=10 ⁻³ ND=10 ⁻⁴ | 1150-10,300 Å | | 13.4 × 9.7 13.8 × 15.1 11.4 × 15.3 11.8 × 9.5 | STIS/ALL |
| F25ND3 (NUV, FUV) | ND=10 ⁻³ | 1150-10,300 Å | | 25 × 25 | STIS/ALL |
| F25ND5 (NUV, FUV) | ND=10 ⁻⁵ | 1150-10,300 Å | | 25 × 25 | STIS/ALL |

¹ See [Section 14.2.1](#) for definition of pivot wavelength.

² See [Section 14.2.1](#) for definition of FWHM.

³ The CCD plate scales differ by ~1% in the *AXIS1* and *AXIS2* directions. See [Section 14.6](#).

⁴ *AXIS2=Y* is 28 arcsec; *AXIS1=X* is 52 arcsec. See [Figure 3.2](#) and [Figure 11.1](#).

⁵ Values given for the F28X50OIII filter exclude the effects of this filter's red leak.

⁶ *AXIS2=Y* is 28 arcsec; *AXIS1=X* is 52 arcsec. See [Figure 3.2](#) and [Figure 11.1](#).

⁷ *AXIS2=Y* is 28 arcsec; *AXIS1=X* is 52 arcsec. See [Figure 3.2](#) and [Figure 11.1](#).

⁸ The MAMA plate scales differ by ~1% in *AXIS1* and *AXIS2* directions. FUV-MAMA uses different mirrors in filtered vs. unfiltered modes; the filtered mode plate scale has 0.3% more arcsec/pixel. See [Section 14.6](#).

⁹ The neutral density filters with the CCD detector can only be used as available-but-unsupported apertures.

5.1.1 Caveats for STIS Imaging

There are several important points about imaging with STIS which should be kept in mind:

- The filters are housed in the slit wheel, and while they are displaced from the focal plane, they are not far out of focus. This location means that imperfections (e.g., scratches, pinholes, etc.) in the filters can cause artifacts in the images. These features do not directly flat-field out because the projection of the focal plane on the detector shifts from image to image due to the nonrepeatability of the MSM's placement of the mirror (careful post-processing may be able to account for registration errors).
- The quality of the low-order flat fields for the MAMA imaging modes limits the photometric accuracy obtained over the full field of view (see [Section 16.1](#)).
- The focus varies across the field of view for imaging modes, with the optical performance degrading by ~40% at the edges of the field of view for the MAMA detectors and by ~30% for the CCD (see [Section 14.7](#)).
- STIS CCD imaging slightly undersamples the intrinsic PSF. The use of dithering (see [Section 11.3](#)) to fully sample the intrinsic spatial resolution and to cope with flat-field variations and other detector nonuniformities may be useful for many programs.
- Two of the STIS narrow-band filters (F28X500III and F25MGII) have substantial red leaks (see [Figure 5.5](#) and [Figure 5.11](#), respectively).
- The STIS CCD will have far more "hot" pixels and a much higher dark current than the newer CCDs.
- Programs requiring high photometric precision at low count levels with the CCD should use GAIN=1; programs at high count levels should use GAIN=4. At GAIN=4 the CCD exhibits a modest read noise pattern that is correlated on scales of tens of pixels. (See [Section 7.2.10](#).)
- At wavelengths longward of ~9000 Å, internal scattering in the STIS CCD produces an extended PSF halo (see [Section 7.2.8](#)). Note that the ACS WFC CCDs have a front-side metallization that mitigates a similar problem in that camera, while the WFC3 CCD does not exhibit this problem.
- The dark current in the MAMA detectors varies with time and temperature, and in the FUV-MAMA it also varies strongly with position, although it is far lower overall than in the NUV-MAMA (see the discussion of [Section 7.5.2](#)).
- The repeller wire in the FUV-MAMA detector (see [Section 7.4](#)) leaves a 5-pixel-wide shadow that runs from approximately pixel (0, 543) to (1024, 563) in a slightly curved line. The exact position of the wire varies with the optical element used.
- The Charge Transfer Efficiency (CTE) of the STIS CCD is decreasing with time. The effects of the CTE decline are most serious for the lower rows of the detector and for faint sources with low background levels. For further details see [Section 7.3.7](#).

5.1.2 Throughputs and Limiting Magnitudes

In [Figure 5.1](#), [Figure 5.2](#), and [Figure 5.3](#), we show the throughputs (where the throughput is defined as the end-to-end effective area divided by the geometric area of a filled, unobstructed, 2.4 meter aperture) of the full set of available filters for the CCD, the NUV-MAMA, and the FUV-MAMA, respectively.

Figure 5.1: STIS CCD Clear and Filtered Imaging Mode Throughputs.

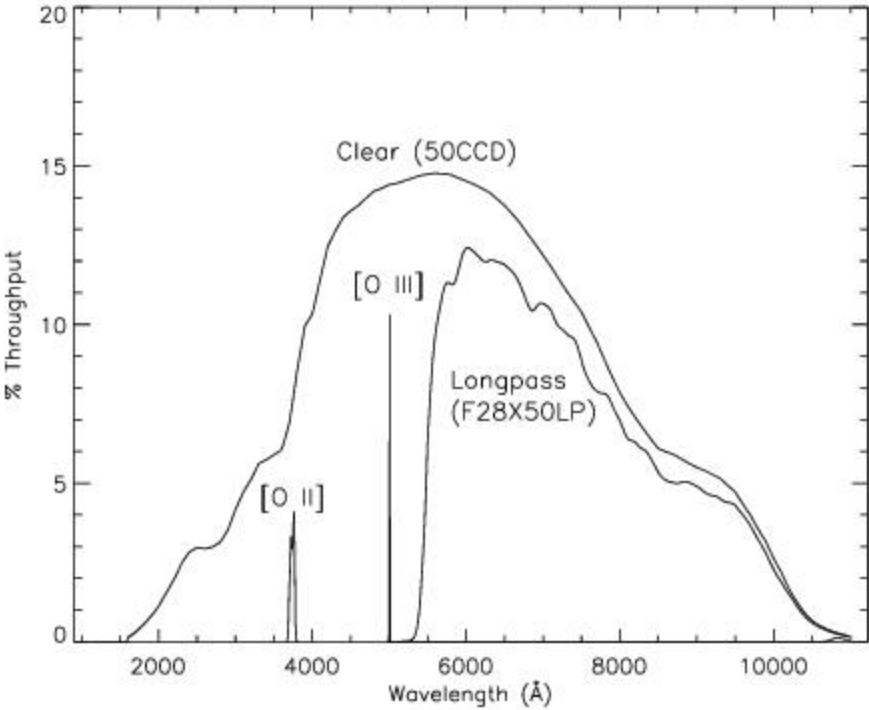


Figure 5.2: STIS NUV-MAMA Clear and Filtered Imaging Mode Throughputs.

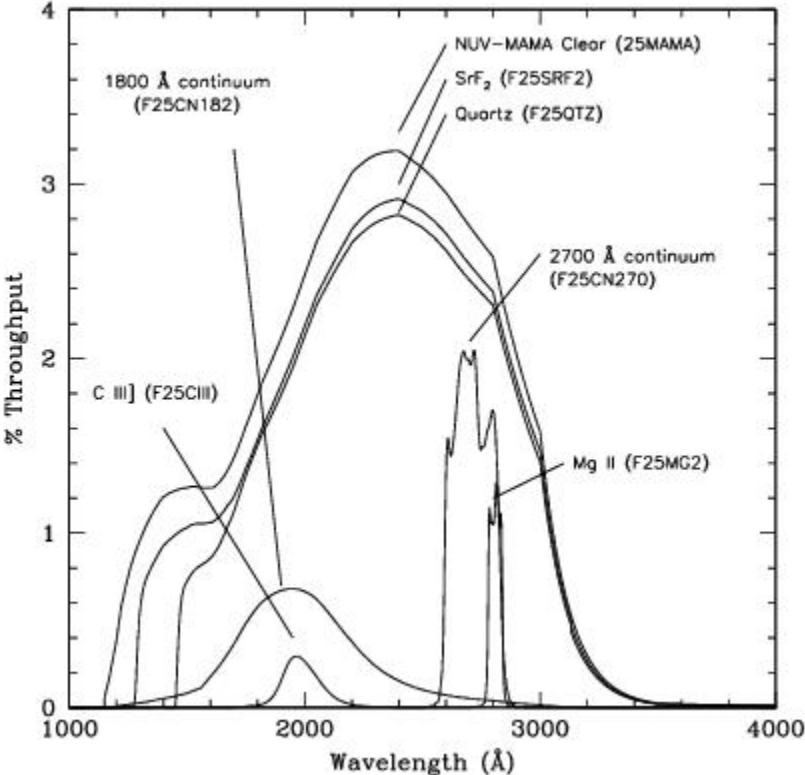
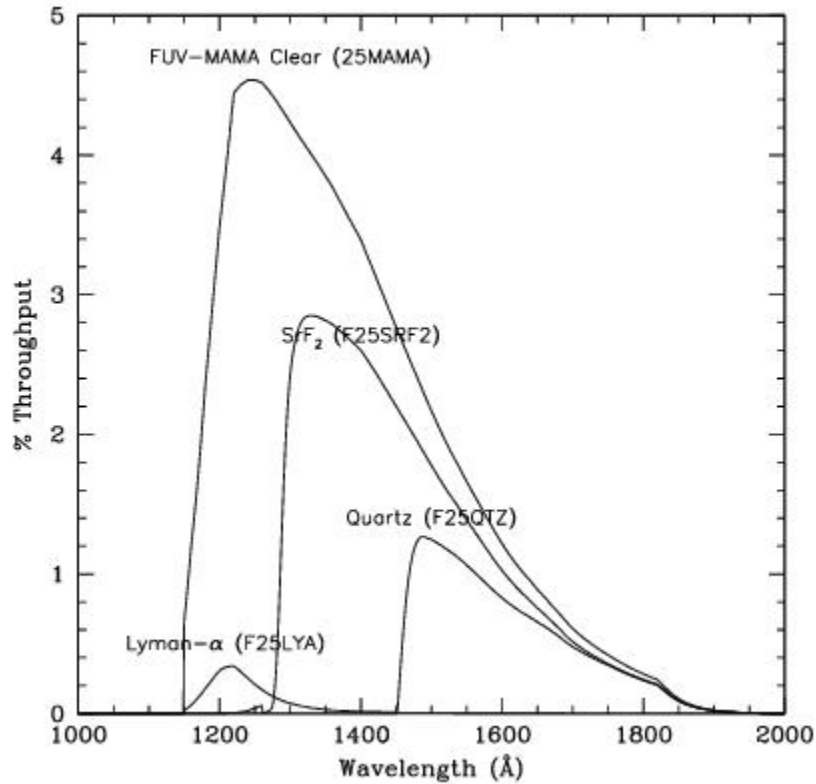


Figure 5.3: STIS FUV-MAMA Clear and Filtered Imaging Mode Throughputs.



Limiting Magnitudes

In [Table 5.2](#) below, we give the A0V star V magnitude reached during a one-hour integration which produces a signal-to-noise ratio of 10 integrated over the number of pixels needed to encircle 80% of the PSF flux. The sensitivities adopted here are our best estimate for August 2008. The observations are assumed to take place under average zodiacal background and low earth-shine conditions. These examples are for illustrative purposes only and the reader should be aware that for dim objects, the exposure times can be highly dependent on the specific background conditions. For instance, if a 26.7 magnitude A star were observed under high zodiacal light and high earth shine, the exposure time required to reach signal-to-noise of 10 with CCD clear would be twice as long as the one stated in [Table 5.2](#).

Table 5.2: Limiting A Star V Magnitudes

| Detector | Filter | Magnitude | Filter | Magnitude |
|----------|----------|-----------|----------------------|-----------|
| CCD | Clear | 26.7 | [O II] | 21.3 |
| CCD | Longpass | 25.8 | [O III] ¹ | 20.5 |
| NUV-MAMA | Clear | 23.9 | | |

| | | | | |
|----------|--------------------|------|-------------------------------|------|
| NUV-MAMA | Longpass quartz | 24.1 | Longpass SrF ₂ | 24.1 |
| NUV-MAMA | C III] | 19.4 | 1800 Å continuum | 21.5 |
| NUV-MAMA | Mg II ² | 20.5 | 2700 Å continuum ³ | 22.2 |
| FUV-MAMA | Clear | 20.5 | Lyman-α | 16.0 |
| FUV-MAMA | Longpass quartz | 21.8 | Longpass SrF ₂ | 21.6 |

¹ This filter has substantial red leaks see [Section 5.2.4](#).

² This filter has substantial red leaks see [Mg II: F25MGII](#).

³ This filter has substantial red leaks see [2700 Å Continuum: F25CN270](#).

5.1.3 Signal-To-Noise Ratios

In [Chapter 14](#) we present, for each imaging mode, plots of exposure time versus magnitude to achieve a desired signal-to-noise ratio. These plots, which are referenced in the individual imaging mode sections that follow, are useful for getting an idea of the exposure time you need to accomplish your scientific objectives. More detailed estimates can be made either by using the sensitivities given in [Chapter 14](#) or by using the [STIS Imaging Exposure Time Calculator](#) (ETC).

5.1.4 Saturation

Both CCD and MAMA imaging observations are subject to saturation at high total accumulated counts per pixel: the CCD due to the depth of the full well and the saturation limit of the gain amplifier for CCDGAIN=1; and the MAMAs due to the 16-bit format of the buffer memory (see [Section 7.3.2](#) and [Section 7.5.1](#)). In [Chapter 14](#), saturation levels as functions of source magnitude and exposure time are presented in the S/N plots for each imaging mode. [STIS ISR 2015-06: STIS CCD Saturation Effects](#) provides an in-depth analysis of the CCD saturation, in which it is found that the center of the detector has a full-well depth of 128,000 e⁻ but drops off towards the sides. The top of the detector has a substantially higher full-well depth at ~160,000 e⁻, which can cause serial transfer artifacts.

5.1.5 Full-field Sensitivity

[STIS ISR 2022-02](#) analyzes imaging from all three STIS detectors spanning 25 years to measure its full-field sensitivity (updating analysis presented in [STIS ISR 2013-02](#)). Residual magnitude trends of stars in standard stellar fields were derived and averaged to track if there were any residual time changes in photometry following an initial time-dependent sensitivity correction in the **CALSTIS** pipeline. Results from STIS ISR 2022-02 are roughly consistent with those from STIS ISR 2013-02 measured over the same time period (1997 to 2012), and show magnitude trends are within the target $\sim 1\%$ STIS flux calibration accuracy (e.g., [Bohlin et al. 2019](#)). We observe stronger negative magnitude trends (i.e., sources appearing brighter with time) when including more recent data. This implies that the TDS models are over correcting the data which could mean that the loss of imaging sensitivity is slowing at a more rapid rate than the spectroscopic TDS models predict, as determined independently for all three STIS detectors. However we note that these trends are still within the quoted 5% photometry errors for STIS (see [Section 16.1](#)). We also measure point spread functions for each image and find no significant trends in their full-width-half-max values with time for any detector.

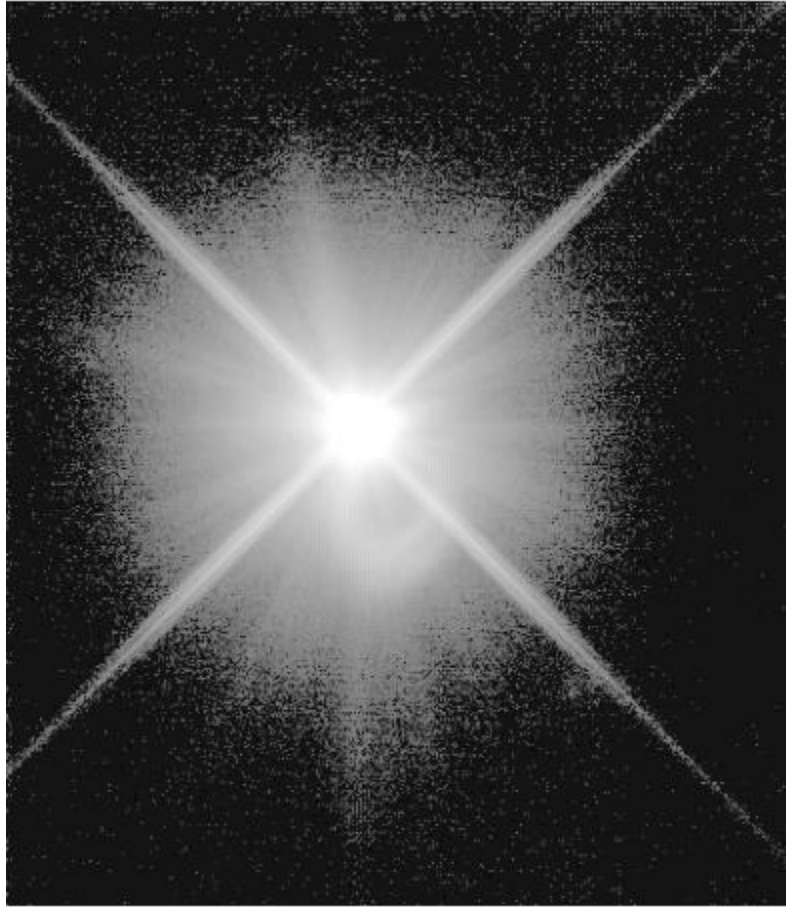
5.2 Optical CCD Imaging

- [5.2.1 Effect of the Optical Baffles on STIS CCD Imaging](#)
- [5.2.2 Unfiltered \(Clear\) CCD Imaging: 50CCD and 50CORON](#)
- [5.2.3 Optical Longpass: F28X50LP](#)
- [5.2.4 \[OIII\]: F28X50OIII](#)
- [5.2.5 \[O II\]: F28X50OII](#)

The CCD imaging capability of STIS was designed primarily for target acquisitions, and therefore, only a small number of filters are available. Nevertheless, STIS CCD imaging has scientific utility of its own due to the high throughput and relatively low read noise of the CCD detector. STIS CCD imaging can be obtained as prime pointings or in parallel with other instruments.

The optical performance of the CCD in imaging mode is good, and the plate scale of the CCD is 0.05078 arcseconds per pixel, providing a good compromise between sampling of the PSF and field of view. There is some degradation of the image quality towards the edge of the field. Observers can assume that 15-20% of the light from a point source falls in a single STIS CCD pixel and that ~80% of the light from a point source is contained within a 5 × 5 pixel region. An image of a typical point source is shown in [Figure 5.4](#). See [Chapter 14](#) for encircled energies at the field center for the different imaging modes and information on the field dependence of the PSF. For a discussion of the coronagraphic mask, see [Section 12.11](#).

Figure 5.4: A Co-added Image of SAO 255271 Taken Using 50CCD.



This figure is plotted with a logarithmic intensity scale and is about 10" across. It shows the structure in the STIS PSF. The ring seen below the center of the PSF is a ghost image. The position angle of this ghost varies as a function of location on the CCD (see [Section 7.2.8](#) and [Figure 7.6](#)). The throughputs used for the CCD imaging modes are for the most part based on measurements of on-orbit calibration data and are accurate to within 5%.

5.2.1 Effect of the Optical Baffles on STIS CCD Imaging

Calibration observations were taken to investigate whether the baffle structures around the CCD detector scatter light from the stars outside the CCD detector into its field of view, and if so, by how much. Images were taken with a bright star placed at 12 different positions, 10 arcseconds and 37 arcseconds away from the edge of the detector. The analysis of the images showed that there are no measurable scattering components by the baffle structures around the detector. Placing the bright star beyond the edge of the detector thus acts as an effective coronagraph for the STIS CCD detector (see [Proffitt et al. 2004, ApJ, 612, 481](#) for more details).

5.2.2 Unfiltered (Clear) CCD Imaging: 50CCD and 50CORON

The 50CCD aperture is a clear, unvignetted aperture which provides maximum sensitivity over the full 52×52 arcsecond field of view. The shape of the bandpass is governed by the detector, which has sensitivity from ~ 2000 to $10,300 \text{ \AA}$. [Figure 5.1](#) shows the throughput as a function of wavelength for this imaging mode (see also [Chapter 14](#) for sensitivities, signal-to-noise plots, and saturation plots).

The coronagraphic aperture 50CORON contains two wedges and a bar which can be used to occult a bright object. The unocculted parts of the aperture are clear, and so the throughput as a function of wavelength is the same as for the 50CCD aperture. Further details about this aperture as well as advice for conducting STIS coronagraphic observations are given in [Section 12.11](#).

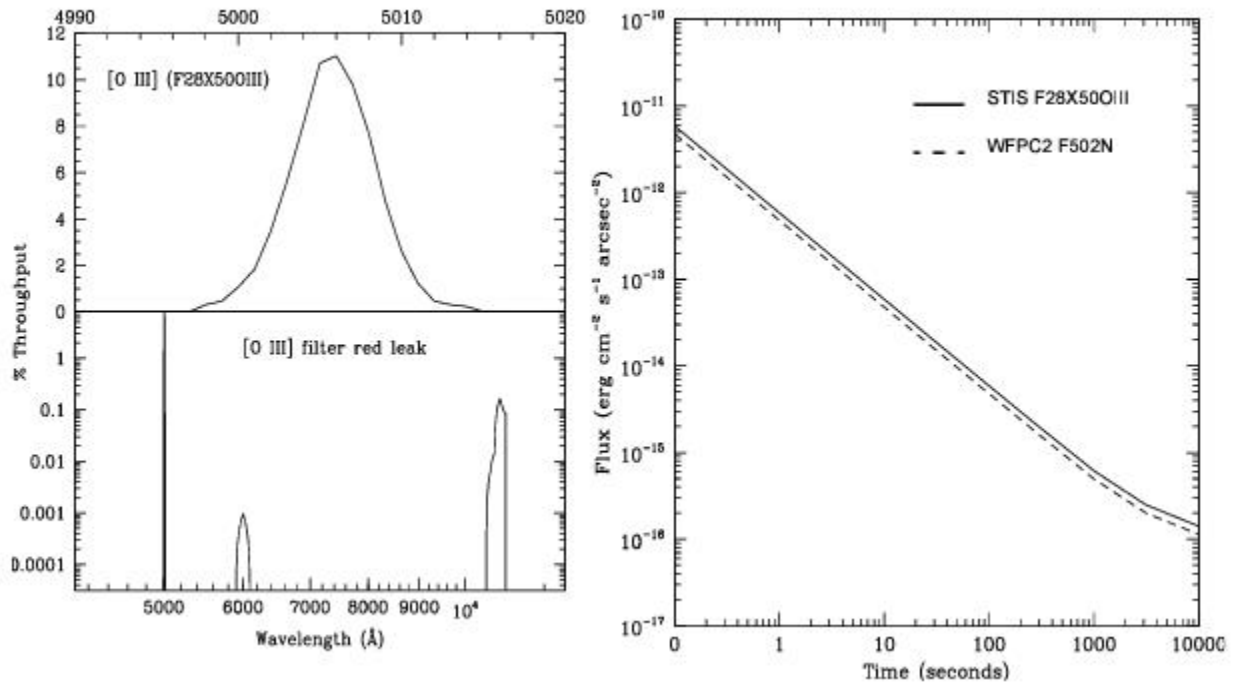
5.2.3 Optical Longpass: F28X50LP

The STIS longpass filter cuts off at $\lambda < 5500 \text{ \AA}$. It images a 28×52 arcsecond field of view. The F28X50LP filter is the principal target acquisition aperture (see [Selecting the Imaging Aperture](#)). The integrated system throughput for this filter is given in [Figure 5.1](#) (see also [CCD Long-Pass Imaging F28X50LP](#) for sensitivities, signal-to-noise plots, and saturation plots).

5.2.4 [OIII]: F28X50OIII

This filter images a 28×50 arcsecond field of view and can be used in target acquisitions or for direct imaging in the light of [O III]. The [O III] filter integrated system throughput and a signal-to-noise comparison with the WFPC2 [O III] filter are shown in [Figure 5.5](#) (see also [F28X50OIII - CCD](#) for sensitivities, signal-to-noise plots, and saturation plots). The STIS [O III] filter is very narrow: only 6.2 \AA wide, compared to the WFC3 [O III] filter which is roughly 65 \AA wide. The STIS [O III] filter has a substantial red leak that begins at $10,600 \text{ \AA}$ and continues to at least $12,000 \text{ \AA}$. In the case of a very red star (K0 spectral type), the red leak will contribute approximately one-third of the detected counts. The red leak for this filter is included in the passbands used by the [STIS ETC](#) and [synphot](#). Observers are encouraged to use these tools to predict source and background count rates carefully.

Figure 5.5: F28X500III Throughput and Flux vs. Exposure Time.

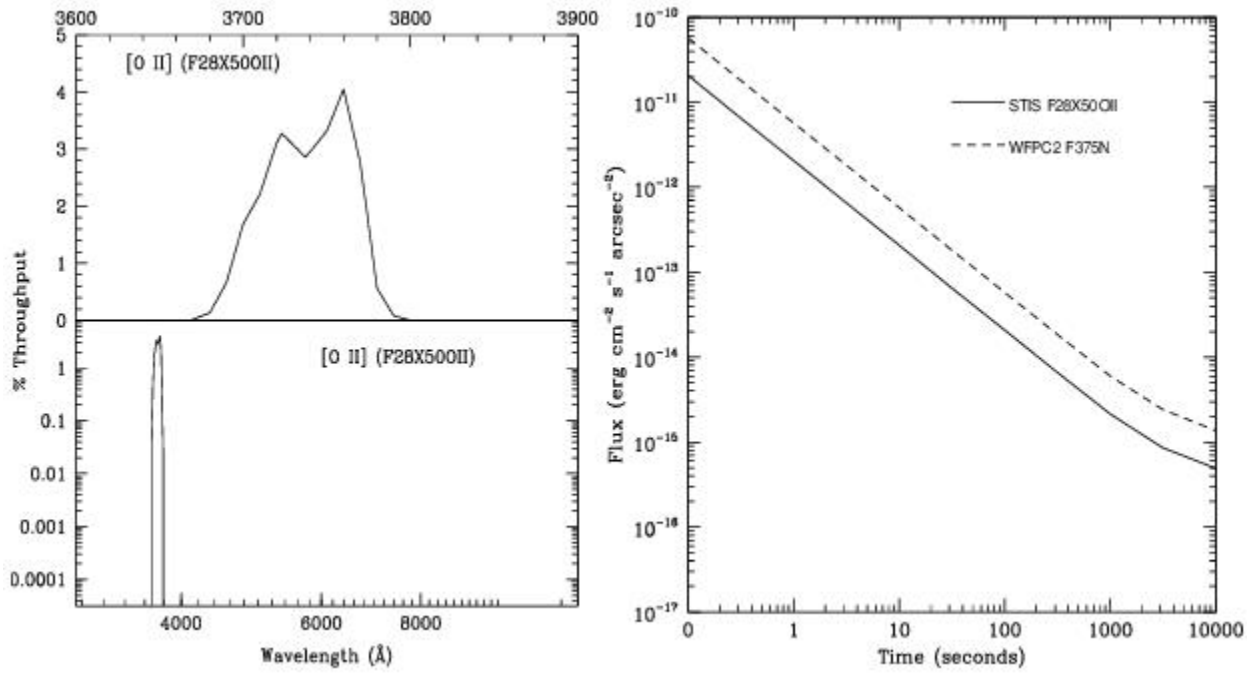


(Left) Integrated System Throughput and (right) Flux vs. Exposure Time to achieve a signal-to-noise=5 compared to WFPC2 for a FWHM=1 Å line, integrated over an area of one square arcsecond.

5.2.5 [O II]: F28X500II

The [O II] filter images a 28 × 52 arcsecond field of view and can be used in target acquisitions or for direct imaging in the light of [O II]. The [O II] filter integrated system throughput and a signal-to-noise ratio comparison with WFPC2's [O II] filter are shown in Figure 5.6. See F28X500II - CCD for sensitivities, signal-to-noise and saturation plots.

Figure 5.6: F28X500II: Throughput and Flux vs. Exposure Time.



(Left) Integrated System Throughput and (right) Flux vs. Exposure Time to achieve a signal-to-noise=5 compared to WFPC2 for a FWHM=1 Å line, integrated over an area of one square arcsecond. There is no substantial red leak in this filter.

5.3 Ultraviolet Imaging with the MAMA Detectors

- [5.3.1 Bright Object Limits](#)
- [5.3.2 Optical Performance](#)
- [5.3.3 Unfiltered \(Clear\) MAMA Imaging: 25MAMA](#)
- [5.3.4 FUV Red Leak](#)
- [5.3.5 Longpass-Filtered MAMA Imaging: F25SRF2 and F25QTZ](#)
- [5.3.6 MAMA Narrow-Band-Filtered Imaging](#)

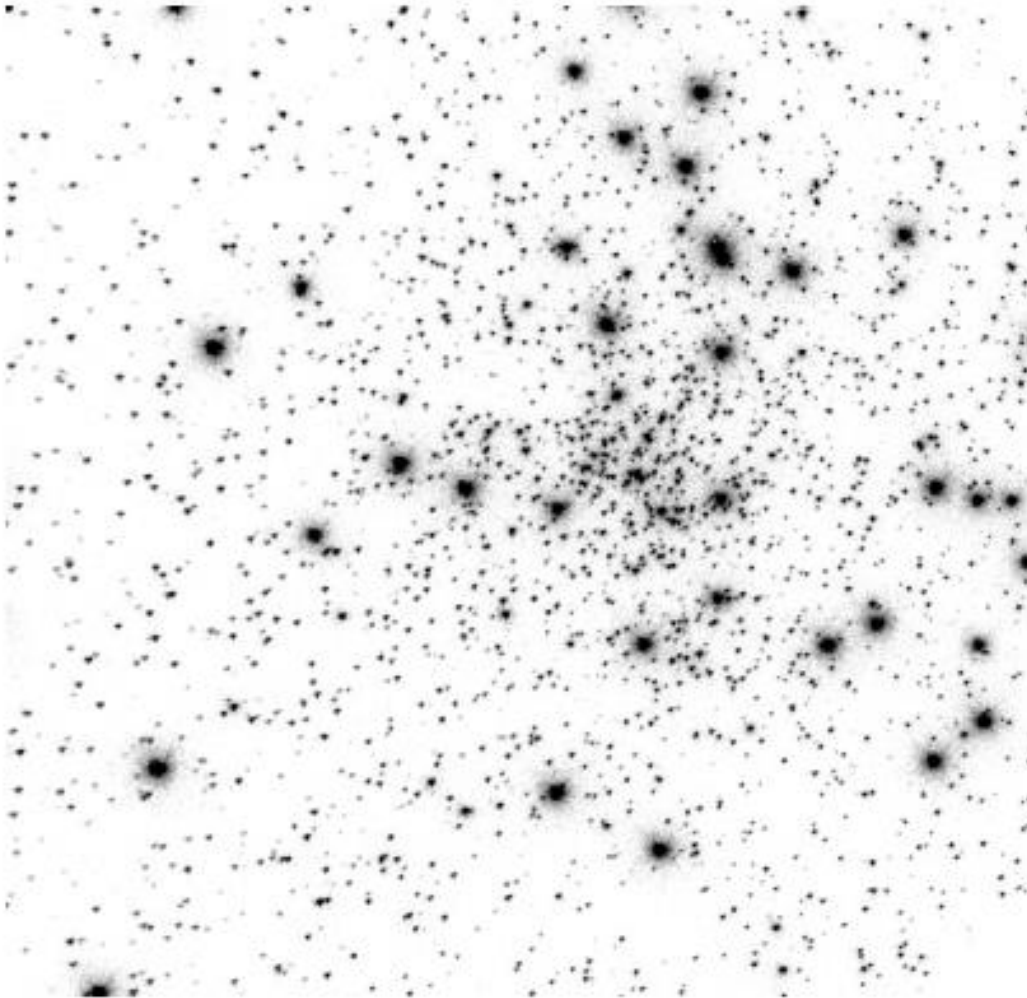
The filtered and clear apertures available for UV imaging are summarized in [Table 5.1](#). Although there are only a small number of filters available, the solar-blind and solar-insensitive properties of the FUV-MAMA and NUV-MAMA detectors, respectively, coupled with their 25×25 arcsecond field of view, good spatial sampling, and ability to detect rapid variability, give STIS UV imaging capabilities that are complementary to those of ACS. The throughputs of the STIS MAMA imaging modes assumed for this *Handbook* are mostly based on on-orbit calibration observations.

Most figures and tables were updated for the Cycle 17 version of this *Handbook* using our best estimates of instrument performance for Cycle 17. Except where otherwise noted, we have not redone these figures and tables to take into account the modest changes expected between those projected values and the estimates for the current cycle. These throughputs are good to within 5% in the FUV and NUV.

The throughputs in the [STIS ETC](#), the calibration reference files, as well as those used by [Astropy's synphot](#) package will continue to be updated as further analysis of the calibration data continues. As of the publication of this *Handbook*, the sensitivities used in those software packages are our best estimates for April 2025 (i.e., mid-Cycle 32).

[Figure 5.7](#) shows an example of MAMA imaging data of a globular cluster taken as part of the Cycle 7 calibration of STIS using the quartz filter and the NUV-MAMA.

Figure 5.7: 320 Second NUV-MAMA Image of NGC 6681 Taken with the F250TZ Filter.



This image was part of the Cycle 7 Calibration Monitoring Program 7720. All the points are stars.

5.3.1 Bright Object Limits

The MAMA detectors are subject to absolute bright object limits, above which targets cannot be observed. They are particularly stringent for the MAMA imaging modes (being as faint as $V=20.3$ for the clear modes), and apply to all sources illuminating the field of view.

We direct MAMA observers to [Section 7.7](#). For summary tables of absolute bright object screening magnitudes for the imaging modes, see [Section 14.8](#).

It is the observers' responsibility to ensure that their observations do not exceed the MAMA bright object limits.

5.3.2 Optical Performance

The MAMA plate scale is ~ 0.0246 arcsec/pix in imaging mode, providing a good compromise between the sampling of the PSF in the UV and field of view. [Chapter 14](#) shows encircled energies as a function of wavelength for MAMA imaging, and provides information on the geometric distortions of the images. The MAMA detector PSFs exhibit broad wings, which are substantially higher in the NUV-MAMA than the FUV-MAMA. [Figure 7.16](#) shows sample detector PSFs for the MAMAs.

5.3.3 Unfiltered (Clear) MAMA Imaging: 25MAMA

Each MAMA can be used with the 25MAMA clear aperture to image a 25×25 arcsecond field of view of the sky, providing the maximum throughput and wavelength coverage in the NUV and FUV as shown in [Figure 5.2](#) and [Figure 5.3](#). However, NUV-MAMA clear direct images will be slightly out of focus because the corresponding mirror on the MSM optimally focuses for use of a filter. It is recommended that the F25SRF2 longpass filter (see [Section 5.3.5](#)) be used instead of 25MAMA (clear) for direct imaging with the NUV-MAMA. The same does not apply to the FUV-MAMA, which has separate MSM mirrors for clear and filtered imaging.

The sky background can be significant for unfiltered FUV-MAMA observations. The strongest contributor is the geocoronal Lyman- α line. Global count rates of several 10^4 counts/s over the whole detector are not unusual during daytime observations. The same applies to slitless FUV spectroscopy. For observations of large, UV-faint targets, where background subtraction becomes critical, unfiltered imaging may introduce significant noise. In addition, the background may be variable during long exposures. Longpass filtered imaging may be profitable in this case.

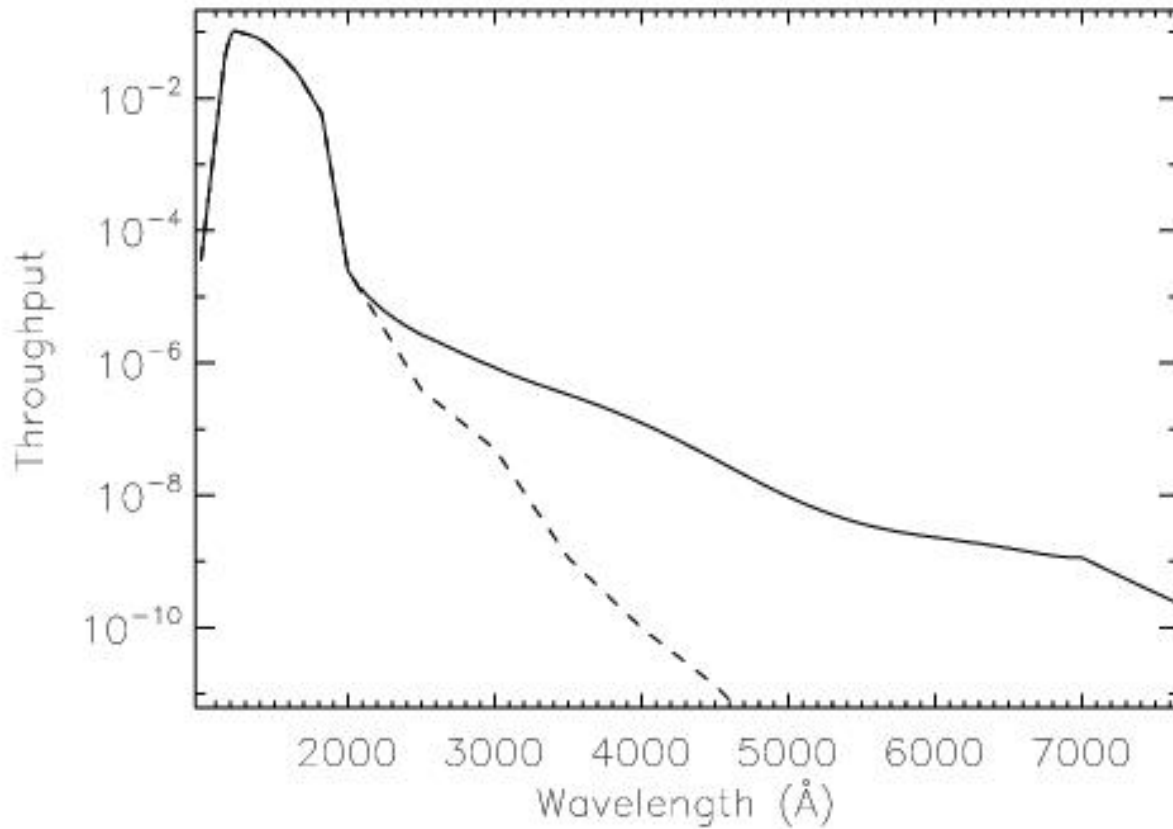
5.3.4 FUV Red Leak

Ground measurements of the FUV-MAMA quantum efficiency indicated that it dropped dramatically longward of ~ 2000 Å, which would have made it effectively solar blind, while the NUV-MAMA also showed a reduced response toward the red, longward of ~ 3500 Å (see [Figure 5.9](#)).

The ACS SBC (solar blind channel) has been known to have a significantly larger sensitivity to optical photons than pre-launch testing had indicated. Since the STIS FUV-MAMA is very similar in design to the ACS SBC, available data were scrutinized to determine whether a similar red leak existed for the STIS detector.

A good test case was a set of observations of Saturn where G140L, G230L, and FUV-MAMA SFR2 imaging observations were taken in the same visit. Comparison of the flux levels measured in these observations suggest that the optical throughput of the STIS FUV-MAMA detector, although still quite low, is indeed substantially higher than the pre-launch measurement. Based upon these observations and the estimated wavelength dependence of the optical throughput for the SBC, a preliminary revision to the FUV-MAMA imaging throughput curve has been devised (see [Figure 5.8](#)), and has been incorporated into the FUV-MAMA imaging throughput curves shown in [Chapter 14](#). Note that this revision results in only trivial changes to the formal calculation of bandpass parameters, and should only affect FUV-MAMA imaging observations of very red objects.

Figure 5.8: A Preliminary Revision of the FUV-MAMA Throughput Curve (solid line) is Compared to the Previous Estimate of the Throughput (dashed line).



There is little STIS data available suitable for confirming the wavelength or time dependence of this extra optical throughput.

[Table 5.3](#) and [Table 5.4](#) give the percentages of detected photons arising in the UV versus optical for observations of different stellar types with the clear MAMA imaging modes. The data for the FUV-MAMA include the effects of the estimated red leak.

Figure 5.9: Out-of-Band Spectral Responses of FUV and NUV-MAMA Clear Imaging Modes.

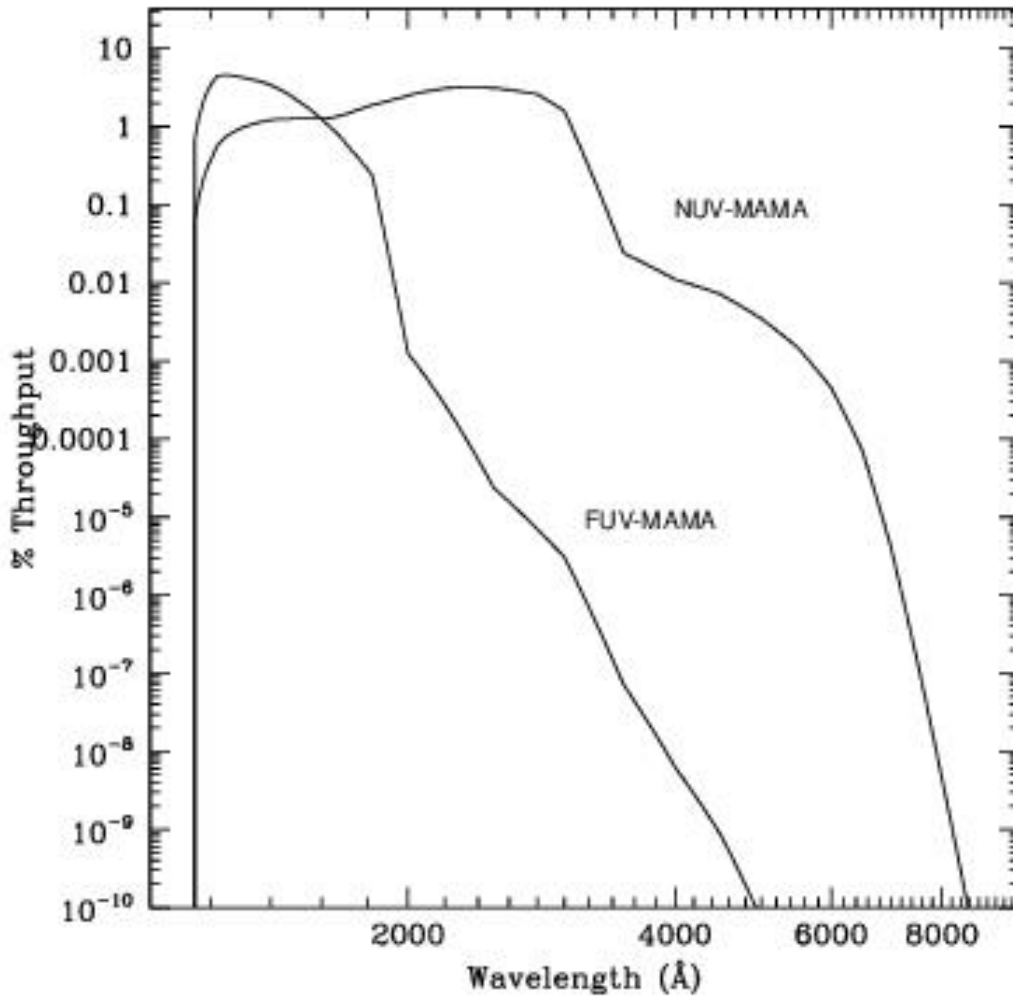


Table 5.3: Visible-Light Rejection of the FUV-MAMA Clear Imaging Mode.

| Stellar Type | T_{eff} (K) | Log g | Percentage of All Detected Photons which Have $\lambda < 1800 \text{ \AA}$ | Percentage of All Detected Photons which Have $\lambda < 3000 \text{ \AA}$ |
|--------------|----------------------|-------|--|--|
| O3 | 45,000 | 4.5 | 99.5 | 100.0 |
| B0 | 30,000 | 4.0 | 99.4 | 100.0 |
| A0 | 9,500 | 4.0 | 97.2 | 100.0 |
| A5 | 8,250 | 4.0 | 82.6 | 99.9 |
| F0 | 7,250 | 4.0 | 68.3 | 99.5 |
| G0 | 6,000 | 4.5 | 31.2 | 72.7 |
| K0 | 5,250 | 4.5 | 5.1 | 27.6 |

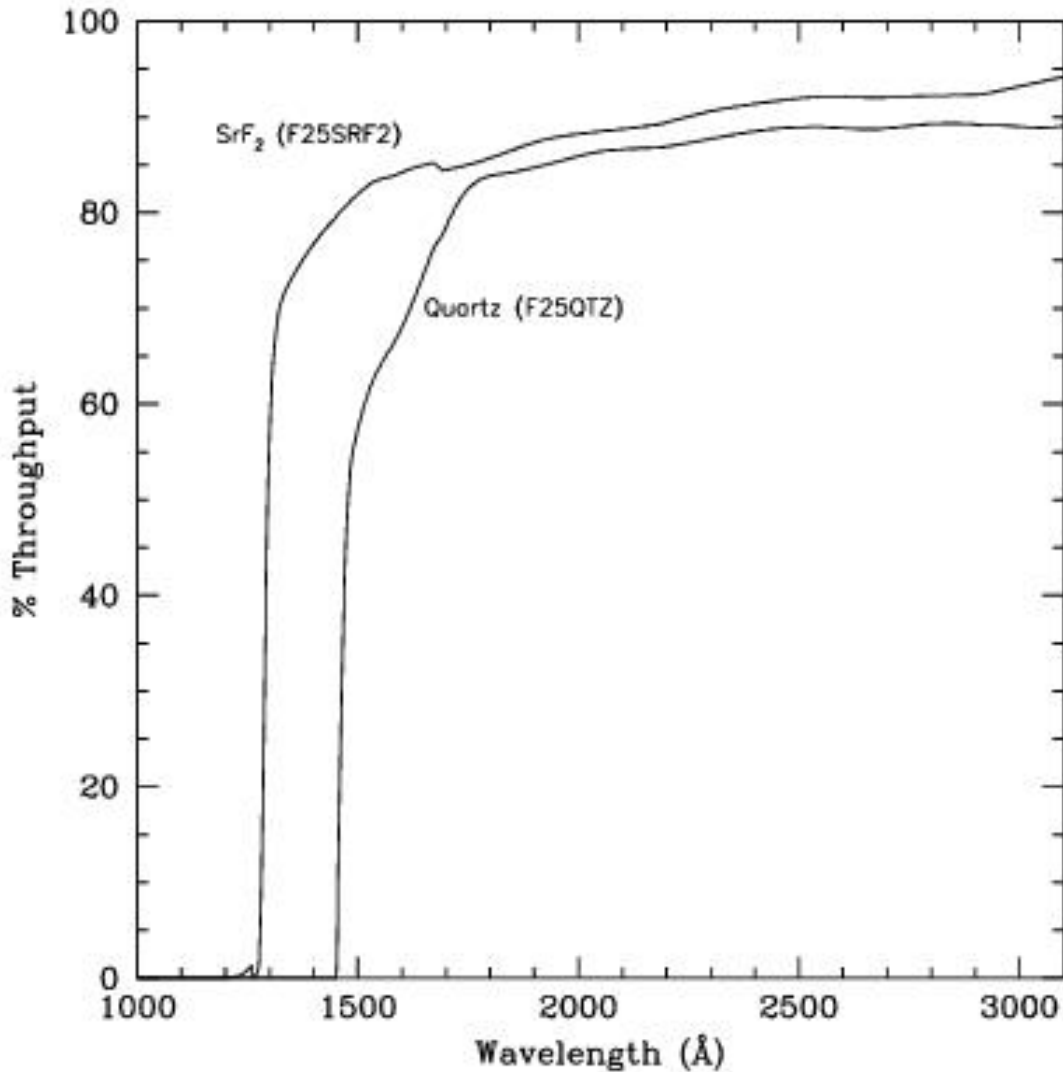
Table 5.4: Visible-Light Rejection of the **NUV-MAMA** Clear Imaging Mode.

| Stellar Type | T_{eff} (K) | Log g | Percentage of all Detected Photons which have $\lambda < 3000 \text{ \AA}$ | Percentage of all Detected Photons which have $\lambda < 5000 \text{ \AA}$ |
|--------------|----------------------|-------|--|--|
| O3 | 45,000 | 4.5 | 97.9 | 100.0 |
| B0 | 30,000 | 4.0 | 97.6 | 100.0 |
| A0 | 9,500 | 4.0 | 93.0 | 99.9 |
| A5 | 8,250 | 4.0 | 90.0 | 99.8 |
| F0 | 7,250 | 4.0 | 85.0 | 99.7 |
| G0 | 6,000 | 4.5 | 71.3 | 99.2 |
| K0 | 5,250 | 4.5 | 56.9 | 97.7 |

5.3.5 Longpass-Filtered MAMA Imaging: **F25SRF2** and **F25QTZ**

The integrated system throughputs of the two UV longpass filters when used with the **NUV-MAMA** and **FUV-MAMA** are shown in [Figure 5.2](#) and [Figure 5.3](#) (for sensitivities, signal-to-noise plots, and saturation plots of **F25SRF2** see [F25SRF2 - NUV-MAMA, Longpass](#) and [F25SRF2 - FUV-MAMA, Longpass](#) and of **F25QTZ** see [F25QTZ - NUV-MAMA, Longpass](#) and [F25QTZ - FUV-MAMA, Longpass](#)). The filter (only) throughputs of these two filters are shown in [Figure 5.10](#). These filters image a 25×25 arcsecond field of view. The cutoff wavelengths of **F25SRF2** and **F25QTZ** were chosen to exclude a) geocoronal Lyman- α 1216 \AA and b) O I 1302 \AA triplet and O I] 1356 \AA , respectively; use of these filters significantly reduces the total sky background in the UV. These filters can be used by themselves in imaging mode, or with the prism or any first-order UV grating in slitless spectroscopic observations, to reduce the background due to geocoronal emission (see [Section 4.4](#) and [Section 12.1](#)). **F25SRF2** images, combined with images taken in series with the **FUV-MAMA/25MAMA** clear, can also be used to obtain Lyman- α images (see [Lyman Alpha: F25LYA](#) and Clear-Minus-SRF2).

Figure 5.10: F25SRF2 and F25QTZ Filter-Only Transmissions.



5.3.6 MAMA Narrow-Band-Filtered Imaging

The filters for MAMA imaging include:

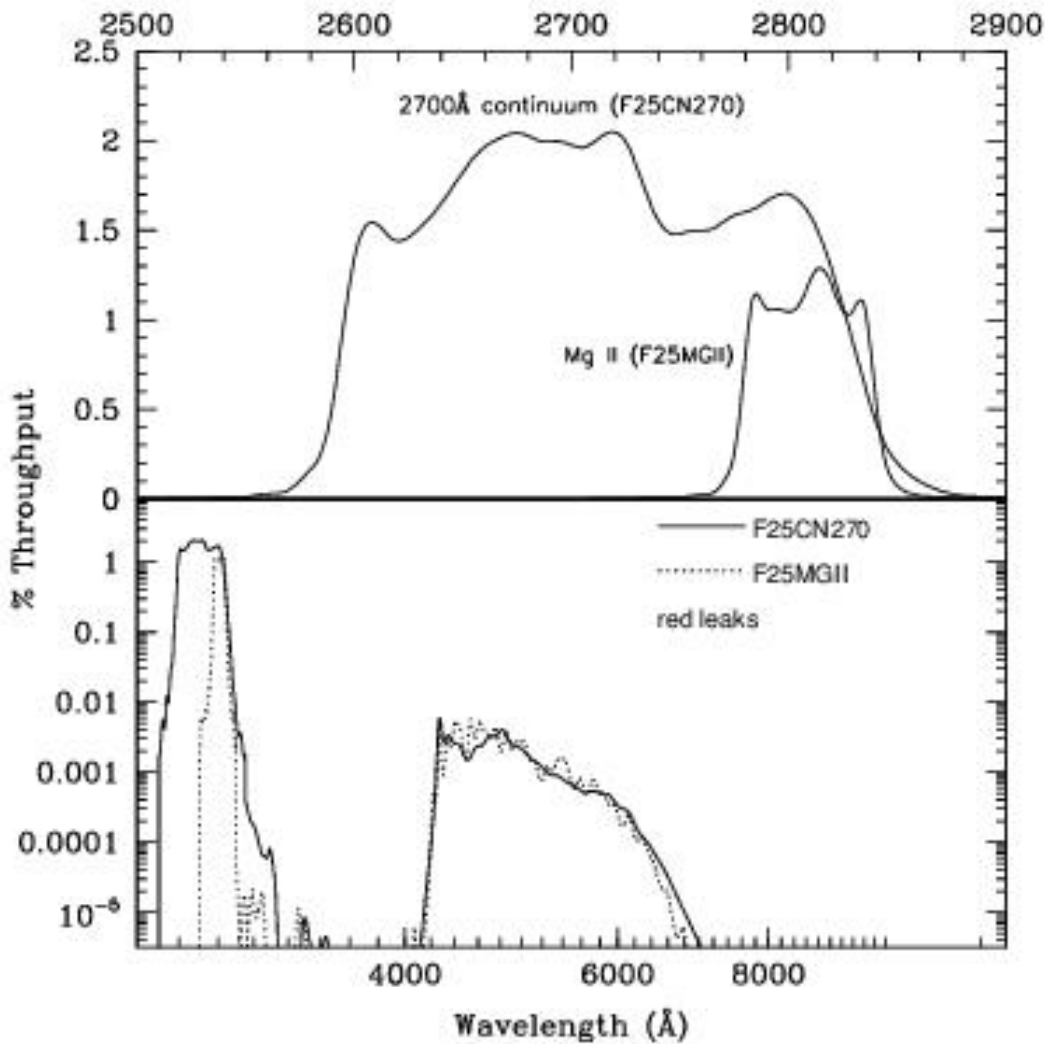
- A narrow-band filter (F25MGII) which images the magnesium doublet at 2796–2803 Å, and a matched medium-band continuum filter (F25CN270) centered at 2700 Å (for sensitivities, signal-to-noise plots, and saturation plots, see pages [F25MGII - NUV-MAMA](#) and [F25CN270 - NUV-MAMA](#)).
- A narrow-band filter (F25CIII) which images the semi-forbidden C III] lines at 1907–1909 Å, among the strongest nebular (low-density) lines in the UV, and a matched medium-band continuum filter (F25CN182) centered at 1800 Å (for sensitivities, signal-to-noise plots, and saturation plots, see [F25CIII - NUV-MAMA](#) for F25CIII and [F25CN182 - NUV-MAMA](#) for F25CN182).
- A narrow-band filter (F25LYA) which images Lyman- α ; this filter has a relatively low throughput, and we recommend that you consider, instead, obtaining two FUV-MAMA images, one through the 25MAMA unfiltered aperture and a second with the SrF₂ longpass filter. The difference of

these two images will isolate Lyman- α with much higher throughput than the F25LYA filter. Alternatively, the ACS SBC can be used with the F122M filter (for sensitivities, signal-to-noise plots, and saturation plots of F25LYA, see [F25LYA - FUV-MAMA, Lyman- \$\alpha\$](#)).

Mg II: F25MGII

The F25MGII filter images a 25×25 arcsecond field of view in the light of the doublet lines of Mg II (2796 and 2803 Å). [Figure 5.11](#) shows the integrated system throughput (see also [F25MGII - NUV-MAMA](#) for sensitivities, signal-to-noise plots, and saturation plots). There is a substantial red leak in this filter starting at approximately 4200 Å and extending to at least 13,000 Å. For stellar spectral types O and B, less than 2% of the detected counts will be due to red leak. This percentage rises to 7% for an A0 star. For a K0 star, 75% of the counts will be due to red leak. The red leak for this filter is included in the passbands used by the [STIS ETC](#) and **synphot**. Observers are encouraged to use these tools to predict source and background count rates carefully.

Figure 5.11: F25MGII and F25CN270 Integrated System Throughputs.



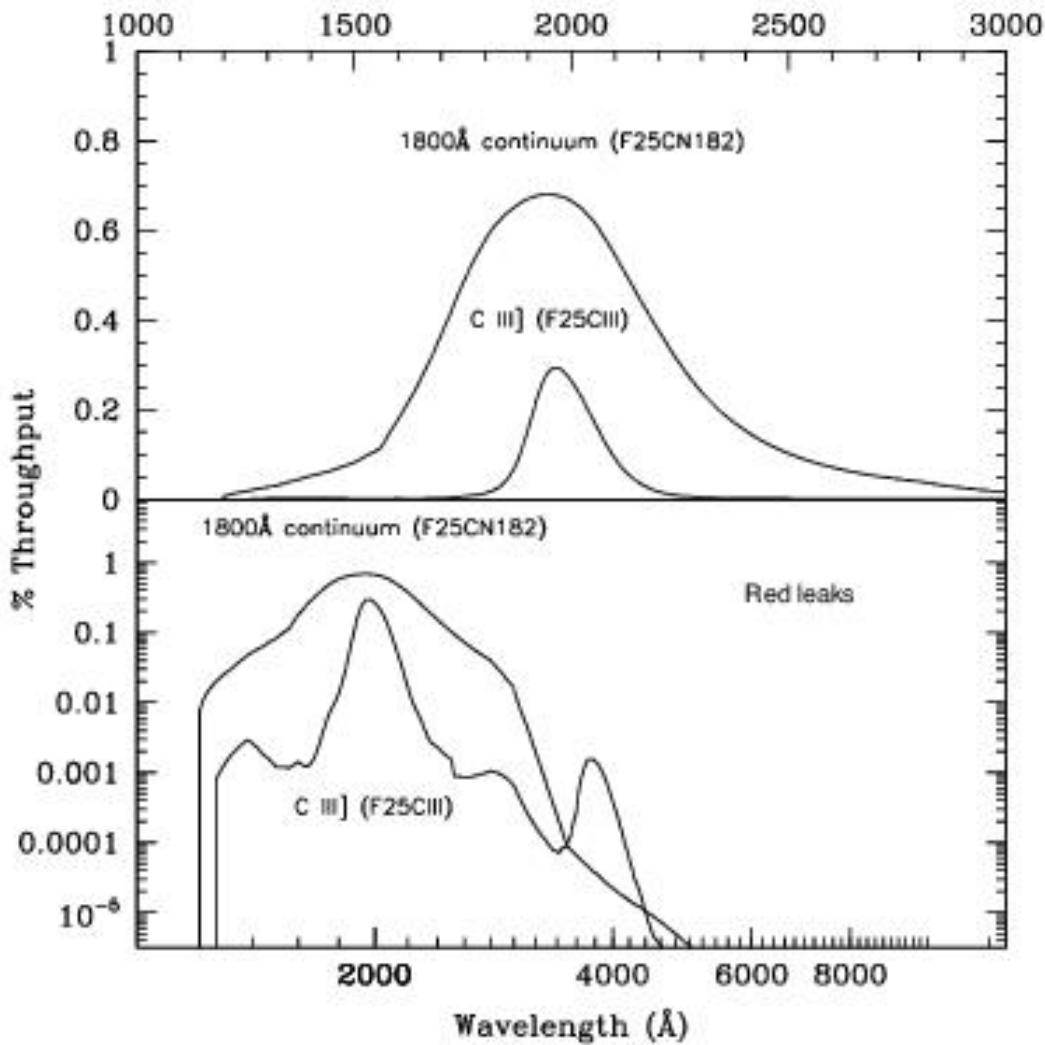
2700 Å Continuum: F25CN270

The 2700 Å continuum filter images a 25 × 25 arcsecond field of view and can be used to measure the continuum for Mg II emission line images. The F25CN270 filter integrated system throughput is shown in Figure 5.11 (see also F25CN270 - NUV-MAMA for sensitivities, signal-to-noise plots, and saturation plots). There is a substantial red leak in this filter starting at approximately 4200 Å and extending to at least 12,000 Å. For a K0 star, roughly 40% of the detected counts will be due to red leak. The red leak for this filter is included in the passbands used by the STIS ETC and synphot. Observers are encouraged to use these tools to predict source and background count rates carefully.

C III]: F25CIII

The F25CIII filter images a 25×25 arcsecond field of view in the light of C III] at 1907–1909 Å. The F25CIII integrated system throughput is shown in [Figure 5.12](#) (see also [F25CIII - NUV-MAMA](#) for sensitivities, signal-to-noise plots, and saturation plots). The out-of-band suppression for this filter is fairly good.

Figure 5.12: F25C III and F25CN182 Integrated System Throughputs.



1800 Å Continuum: F25CN182

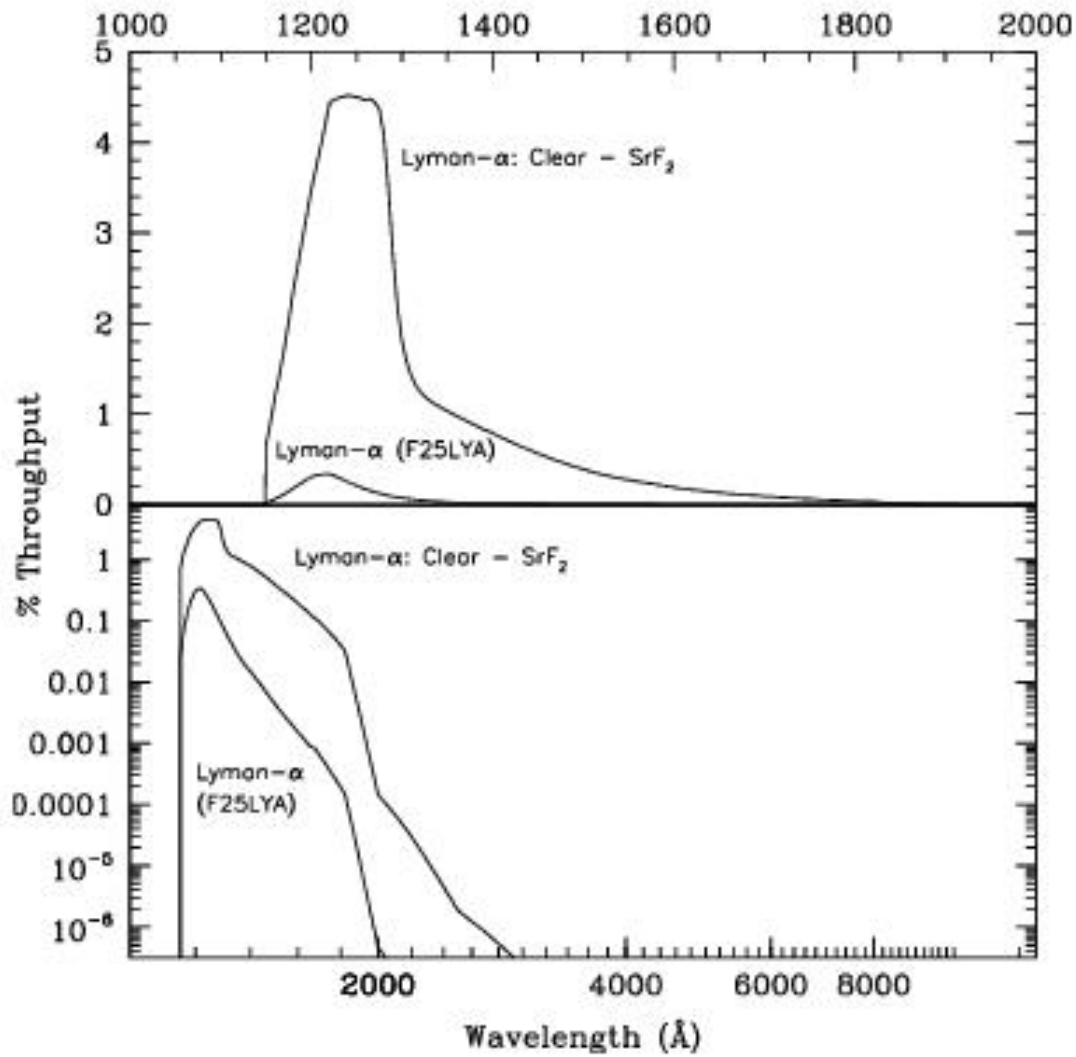
The 1800 Å continuum filter images a 25 × 25 arcsecond field of view, and can be used to measure the continuum for C III] emission line images. The F25CN182 filter integrated system throughput is shown in [Figure 5.12](#) (see also [F25CN182 - NUV-MAMA](#) for sensitivities, signal-to-noise plots, and saturation plots).

Lyman Alpha: F25LYA and Clear-Minus-SRF2

The F25LYA filter images a 25×25 arcsecond field of view and can be used to obtain emission line images in the light of Lyman- α . The F25LYA filter integrated system throughput is shown in [Figure 5.13](#) (see also [F25LYA - FUV-MAMA](#), [Lyman- \$\alpha\$](#) for sensitivities, signal-to-noise plots, and saturation plots).

At the price of a slightly wider bandpass, and the need to take two exposures, Lyman- α can be isolated by taking one image with the clear (25MAMA) aperture and a second with the longpass (F25SRF2) filter and differencing the two. The integrated system throughput for this imaging sequence is appreciably higher than for the narrowband F25LYA filter, as shown in [Figure 5.13](#).

Figure 5.13: Lyman- α Imaging Integrated System Throughputs.



5.4 Neutral Density Filters

STIS has a complement of neutral-density (ND) filters, which can be used with the CCD, the *NUV-MAMA*, and the *FUV-MAMA* spanning from ND1 (attenuation of 10^{-1}) to ND5. The ND5 filter appears to have a UV throughput of at most 10^{-6} , substantially smaller than prelaunch estimates.

F25NDQ1, F25NDQ2, F25NDQ3, and F25NDQ4 are physically four separate quadrants of a single 25×25 arcsecond filter occupying a single position on the slit wheel. Each quadrant having a different neutral density factor and the number appended to each name is the approximate dex ND factor. The target is put into the appropriate quadrant when one of these apertures is requested. However, it should be noted that all four quadrants project onto the detector, and each quadrant plus a 5 arcsecond surrounding perimeter must be considered for bright object limits. Thus, although one may request placement of a bright object centered in F25NDQ4, no other objects in the surrounding region may violate the bright-object limits for the other quadrants. This includes a 5 arcsecond restrictive border around the interior of the selected quadrant, effectively reducing its size. In practice, for safety reasons any object that would produce a global count rate exceeding 1.5×10^6 counts/s or a local count rate above 500 counts/s/pix in F25NDQ1, may not be observed using any of the other quadrants, since pointing problems could cause this bright source to end up in F25NDQ1. To ensure accurate placement of a bright object in the selected quadrant, a CCD target acquisition must also be specified. Also note that the boundaries between the four quadrants are not well centered, and as a result the sizes of the quadrants vary. [Figure 13.83](#) shows a lamp image of this aperture, and [Table 13.34](#) gives the approximate dimensions of each quadrant and the default locations where targets are placed.

F25ND3 and F25ND5 are each individual 25×25 arcsecond filtered apertures, occupying unique locations on the slit wheel. Detailed information for F25ND3 and F25ND5 can be found in [F25ND3 - NUV-MAMA](#), [F25ND3 - FUV-MAMA](#), [F25ND5 - NUV-MAMA](#), and [F25ND5 - FUV-MAMA](#).

Chapter 6: Exposure Time Calculations

Chapter Contents

- [6.1 Overview](#)
- [6.2 Determining Count Rates from Sensitivities](#)
- [6.3 Throughput and Sensitivity](#)
- [6.4 Computing Exposure Times](#)
- [6.5 Detector and Sky Backgrounds](#)
- [6.6 Tabular Sky Backgrounds](#)
- [6.7 Extinction Correction](#)
- [6.8 Exposure Time Examples](#)

6.1 Overview

6.1.1 The STIS Exposure Time Calculators

In this chapter we explain how to use the sensitivities and throughputs provided in [Chapter 13](#) and [Chapter 14](#) to determine the expected count rate from your source and how to calculate exposure times to achieve a given signal-to-noise ratio for your STIS observations taking various background contributions into account. At the end of the chapter, in [Section 6.8](#), you will find examples to guide you through specific cases.

6.1.1 The STIS Exposure Time Calculators

Three [STIS Exposure Time Calculators \(ETCs\)](#) are available to help you with your proposal preparation. The three [ETCs](#), available via the [STIS web pages](#), are the **Imaging ETC**, the **Spectroscopic ETC**, and the **Target Acquisition ETC (TA ETC)**. These calculators provide count rates for given source and background parameters and calculate signal-to-noise ratio for a given exposure time, or exposure time for a given signal-to-noise ratio. If you have a calibrated spectrum of your source, you can upload it directly from your machine using the [ETC](#) website. The [ETC](#) also determines peak per-pixel count rates and total (integrated over the detector) count rates to aid you in your feasibility assessment. The [ETC](#) also warns you if your observations exceed the local or global brightness limits for MAMA observations (see [Chapter 7](#)). Lastly, in the case of the **Spectroscopic ETC**, the task produces a simulated one-dimensional spectrum for a given STIS configuration and source. Plots of output spectra are rendered directly in the [ETC](#). Users may also download ASCII or CSV formatted data tables of the source and noise counts per pixel per wavelength bin. The input and output parameters in the **TA ETC** are specifically designed to facilitate exposure time estimates for target acquisition purposes (see [Chapter 8](#) for more details on acquisitions). The [ETCs](#) have extensive [online help](#) which explains how to use them and gives the details of the performed calculations.

6.2 Determining Count Rates from Sensitivities

6.2.1 Spectroscopy

6.2.2 Imaging

In the simplest terms, the instrumental sensitivity (S) times the flux from your object of interest gives the counts/s (C) expected from your source times the gain (G) (i.e., it gives counts for the MAMA and electrons for the CCD):

$$C \times G = S \times Flux .$$

Later in this chapter we provide specific formulae appropriate for imaging and spectroscopic modes, which can be used to calculate the expected count rates from your source and the signal-to-noise ratio. The formulae are given in terms of sensitivities, but we also provide transformation equations between the throughput (T) and sensitivity (S) for imaging and spectroscopic modes.

Sensitivities and throughputs are presented in graphical and tabular form as a function of wavelength for the spectroscopic modes in [Chapter 13](#), and for the imaging modes in [Chapter 14](#). Given the source characteristics and the sensitivity of the STIS configuration, calculating the expected count rate over a given number of pixels is straightforward. The additional information you will need for spectroscopic observations is the aperture transmission (T_A), the encircled energy fraction (ϵ_r) in the direction perpendicular to the dispersion, the number of pixels per spectral resolution element (or line spread function $FWHM$) and the plate scale, which are provided in [Chapter 13](#). For imaging observations you need only the encircled energies and plate scales. Below, we describe how to determine two quantities:

1. The counts/s (C) from your source over some selected area of N_{pix} pixels.
2. The peak per-pixel count rate (P_{cr}) from your source—useful for avoiding saturated exposures and for assuring that MAMA observations do not exceed the local bright object limits.

We consider the cases of point sources and diffuse sources separately below.

6.2.1 Spectroscopy

Sensitivity Units and Conversions

The spectroscopic point source sensitivity, S_{λ}^p , has the following units, depending on the detector:

CCD: $(e^-/s/pix_{\lambda})/(incident\ erg/cm^2/s/\text{\AA})$

MAMA: $(counts/s/pix_{\lambda})/(incident\ erg/cm^2/s/\text{\AA})$

where:

- pix_λ = a pixel in the dispersion direction;
- counts and electrons refer to the total received from the point source integrated over the PSF in the direction perpendicular to the dispersion (along the slit);
- S_λ^p is corrected for time dependent and temperature dependent variations, aperture losses, and CTE losses by pipeline calibration.

The spectroscopic diffuse source sensitivity, S_λ^d , has the following units, depending on the detector:

CCD: (electrons/s/ pix_λ / pix_s)/(incident erg/s/cm²/Å/arcsec²)

MAMA: (counts/s/ pix_λ / pix_s)/(incident erg/s/cm²/Å/arcsec²)

where:

- pix_λ = a pixel in the dispersion direction;
- pix_s = a pixel in the spatial direction.

S_λ^p and S_λ^d are related through the relation:

$$S_\lambda^d \cong \left(S_\lambda^p \times m_s \times W \right),$$

where:

- m_s is the plate scale in arcsec/pix in the spatial direction (i.e., in the direction perpendicular to the dispersion);
- W is the slit width in arcseconds;
- S_λ^d is corrected for time dependent and temperature dependent variations by pipeline calibration.

In general, we have assumed that the diffuse source has a uniform brightness over the area of interest and that the spectrum can be approximated as a continuum source (i.e., any emission or absorption lines are broader than the resolution after taking the effect of the slit into account).

Point Source

For a point source, the count rate, C , from the source integrated over an area of $N_{pix} = N_{\lambda pix} \times N_{spix}$ pixels can be expressed as:

$$C = \frac{F_{\lambda} \times S_{\lambda}^p \times T_A \times \epsilon_f \times N_{\lambda pix}}{G},$$

where:

- G is the gain (always 1 for the MAMA, and 1 or 4 depending on the choice of CCDGAIN for the CCD);
- F_{λ} = the continuum flux from the astronomical source, in erg/s/cm²/Å;
- T_A = the aperture transmission (a fractional number less than 1);
- ϵ_f = the fraction of the point source energy contained within N_{spix} pixels in the spatial direction;
- $N_{\lambda pix}$ = the number of wavelength pixels integrated over. For an unresolved emission line, $N_{\lambda pix}$ is just the number of pixels per spectral resolution element and F_{λ} is simply the total flux in the line in erg/s/cm² divided by the product of the dispersion in Å/pix and $N_{\lambda pix}$ (i.e., divided by the *FWHM* of a resolution element in Å);
- N_{spix} = the number of pixels integrated over in the spatial direction.

The peak counts/s/pix from the point source is given by:

$$P_{cr} = \frac{\epsilon_f(1) \times F_{\lambda} \times S_{\lambda}^p \times T_A}{G},$$

where:

- $\epsilon_f(1)$ is the fraction of energy contained within the peak pixel;
- F_{λ} , S_{λ}^p , and T_A are as above.

Diffuse Source

For a diffuse continuum source over $N_{pix} = N_{\lambda pix} \times N_{spix}$, the count rate, C , can be expressed as:

$$C = \frac{I_{\lambda} \times S_{\lambda}^d \times N_{\lambda pix} \times N_{spix}}{G},$$

where:

- I_λ = the surface brightness of the astronomical source, in $\text{erg/s/cm}^2/\text{\AA}/\text{arcsec}^2$;
- $N_{\lambda\text{pix}}$ = the number of wavelength pixels integrated over in the dispersion direction. For an unresolved emission line, $N_{\lambda\text{pix}}$ is just the number of pixels per spectral resolution element, and I_λ is simply the total flux in the line in $\text{ergs/s/cm}^2/\text{arcsec}^2$ divided by the product of the dispersion in $\text{\AA}/\text{pix}$ and $N_{\lambda\text{pix}}$ (i.e., divided by the *FWHM* of the resolution element in \AA);
- N_{spix} = the number of pixels integrated over in the spatial direction.

For a diffuse continuum source the peak counts/s/pix, P_{cr} is given by:

$$P_{cr} = \frac{I_\lambda \times S_\lambda^d}{G} .$$

For a diffuse, *spectrally unresolved emission-line source* the peak counts/s/pix, P_{cr} is essentially independent of slit size and is given by:

$$P_{cr} = \frac{I_{line} \times S_\lambda^d \times w}{G \times W \times FWHM} ,$$

where:

- I_{line} is the intensity in $\text{erg/s/cm}^2/\text{arcsec}^2$ in the line;
- *FWHM* is the full width half max of the instrumental profile in \AA , which for STIS is nearly always $2 \text{ pixels} \times d$, where d is the dispersion in $\text{\AA}/\text{pix}$;
- w is the slit width in arcseconds which projects to n pixels in the detector plane, where n is the width of the resolution element in pixels. Note that w is numerically equal or close to twice the plate scale in the dispersion direction for all modes;
- W is the actual slit width in arcseconds.

Thus, for STIS in particular, this expression reduces to:

$$P_{cr} \sim \frac{I_{line} \times S_\lambda^d \times m_\lambda}{W \times d \times G} ,$$

where:

- d is the dispersion in $\text{\AA}/\text{pix}$;
- m_λ is the plate scale in the dispersion direction;
- All else is as above.

The counts from the emission line will be spread over $N_{\lambda\text{pix}}$ pixels where $N_{\lambda\text{pix}}$ is the slit width per plate scale in the dispersion direction ($N_{\lambda\text{pix}} = W/m_\lambda$).

6.2.2 Imaging

Sensitivity Units and Conversions

The imaging point source sensitivity, S_{λ}^p , has the following units, depending on the detector:

$$\text{CCD: } (e^{-}/s/\text{\AA})/(\text{incident erg/s/cm}^2/\text{\AA})$$

$$\text{MAMA: } (\text{counts/s/\AA})/(\text{incident erg/s/cm}^2/\text{\AA}).$$

where:

- counts and electrons refer to the total number received from the point source integrated over the PSF.

The imaging diffuse-source sensitivity, S_{λ}^d , has the following units, depending on detector:

$$\text{CCD: } (e^{-}/s/\text{\AA}/\text{pix})/(\text{incident erg/s/cm}^2/\text{\AA}/\text{arcsec}^2)$$

$$\text{MAMA: } (\text{counts/s/\AA}/\text{pix})/(\text{incident erg/s/cm}^2/\text{\AA}/\text{arcsec}^2).$$

Thus S_{λ}^p and S_{λ}^d are related through the relation:

$$S_{\lambda}^d \cong \left(S_{\lambda}^p \times m_s^2 \right),$$

where:

- m_s is the plate scale in arcsec/pix.

Point Source

For a point source, the count rate, C , over an area of N_{pix} pixels can be expressed as:

$$C = \frac{\int F_{\lambda} \times S_{\lambda}^p \times \epsilon_f d\lambda}{G},$$

where:

- F_{λ} = the flux from the astronomical source, in ergs/s/cm²/Å;
- ϵ_f = the fraction of the point source energy encircled within N_{pix} pixels;
- the integral is over the bandpass.

The peak counts/s/pix from the point source are given by:

$$P_{cr} = \frac{\int F_{\lambda} \times S_{\lambda}^p \times \epsilon_f(1) d\lambda}{G},$$

where:

- $\epsilon_f(1)$ is the fraction of energy encircled within the peak pixel;
- F_{λ} and S_{λ}^p are as above;
- the integral is over the bandpass.

If the flux from your source can be approximated by a flat continuum, then:

$$C = \frac{F_{\lambda} \epsilon_f \int S_{\lambda}^p d\lambda}{G}.$$

We can now define an equivalent bandpass of the filter (B_{λ}) such that:

$$\int S_{\lambda}^p d\lambda = S_{peak}^p B_{\lambda},$$

where:

- S_{peak}^p is the peak sensitivity;
- B_{λ} is the effective bandpass of the filter.

The count rate from the source can now be written as:

$$C = \frac{F_{\lambda} \epsilon_f S_{peak}^p B_{\lambda}}{G}.$$

In [Chapter 14](#), we give the value of B_λ and S_{peak}^p for various filters.

Diffuse Source

For a diffuse source, the count rate, C , can be expressed as:

$$C = \frac{\int I_\lambda \times S_\lambda^d \times N_{pix} d\lambda}{G} = \frac{\int I_\lambda \times S_\lambda^p \times m_s^2 \times N_{pix} d\lambda}{G},$$

where:

- I_λ = the surface brightness of the astronomical source, in $\text{erg/s/cm}^2/\text{\AA}/\text{arcsec}^2$;
- N_{pix} = the number of pixels integrated over;
- the integral is over the bandpass.

For a diffuse source the peak counts/s/pix, P_{cr} , is given trivially by:

$$P_{cr} = \frac{\int I_\lambda \times S_\lambda^d d\lambda}{G},$$

where we have assumed the source to be uniformly bright.

6.3 Throughput and Sensitivity

So far, we have given the formulae for count rates in terms of the sensitivity (S). If you would like to use the throughput (T) rather than the sensitivity, you can use the following conversion equations.

For *imaging modes*, the transformation between T and S is given by:

$$S_{\lambda} = \frac{T_{\lambda} A \lambda}{hc} = \frac{A_{\text{eff}} \lambda}{hc}$$

where:

- S_{λ} is the sensitivity at wavelength λ ;
- T_{λ} is the system throughput at λ ;
- A is the area of an unobstructed 2.4 meter telescope (i.e., 45,239 cm²);
- h is Planck's constant;
- c is the velocity of light;
- A_{eff} is the effective area given by $A_{\text{eff}} = T_{\lambda} A$.

For *spectroscopic modes*, the transformation equation can be written as:

$$S_{\lambda} = \frac{T_{\lambda} A \lambda d}{hc} = \frac{A_{\text{eff}} \lambda d}{hc}$$

where:

- d is the dispersion in Å/pix.

In the first two examples given at the end of this chapter, we specifically show how the calculations can be done both in terms of the sensitivity and the throughput.

6.4 Computing Exposure Times

6.4.1 Calculating Exposure Times for a Given Signal-to-Noise

To derive the exposure time to achieve a given signal-to-noise ratio, or to derive the signal-to-noise ratio you will achieve in a given exposure time for your source, there are four principal ingredients:

- Expected count rate from your source over some area (C);
- The area (in pixels) over which those counts are received (N_{pix}).
- Sky background (B_{sky}) in counts/pix/s;
- The detector background, or dark current, (B_{det}) in counts/s/pix, and the read noise (RN) in counts, if using the CCD.

As of Cycle 25, the **ETC** has a trio of Dark Rate choices for the CCD. These choices; low (top), medium (default) and high (bottom), correspond to location on the detector and allow a more precise estimate of the dark current for a particular CCD configuration. We would like to emphasize that, while the **ETC** can only reflect an average of the dark current rate, the STIS FUV dark current rate in particular exhibits tremendous variations with position on the detector (due to the infamous glow region) and with the time during which the HV has been on. These effects are described in detail in [Section 7.5.2](#), in particular in [Figure 7.21](#) and [Figure 7.22](#). STIS FUV MAMA users whose observations are sensitive to dark current (e.g., faint targets) are strongly encouraged to read the corresponding documentation to assess the feasibility of their observations and better constrain the exposure time needed to achieve the required accuracy.

Section 6.5 provides the information you need to determine the sky-plus-detector background for your observation.

6.4.1 Calculating Exposure Times for a Given Signal-to-Noise

The signal-to-noise ratio, $StoN$ is given by:

$$StoN = \frac{CtG}{\sqrt{CtG + N_{pix}(B_{sky} + B_{det})Gt + (N_{pix}/N_{bin})(N_{read}RN^2)}}$$

where:

- C = the signal from the astronomical source in counts/s;
- t = the integration time in seconds;
- G = the gain (always 1 for the MAMAs and 1 or 4 for the CCD, depending on your choice of CCDGAIN);
- N_{pix} = the total number of detector pixels integrated over to achieve C ;
- B_{sky} = the sky background in counts/s/ pix;
- B_{det} = the detector dark current in counts/s/ pix;
- N_{bin} = the total number of on-chip binned pixels for the CCD = BINAXIS1×BINAXIS2 (see ["Binning"](#));

- N_{read} = the number of CCD readouts (Note for the [ETC](#), the number of CCD readouts is equal to the number of CR-SPLITS);
- RN = the read noise in electrons; = 0 for MAMA observations.

Observers using the CCD normally take sufficiently long integrations so that the CCD read noise is not important. This condition is met when:

$$CtG + N_{pix} (B_{sky} + B_{det}) Gt \gg 2 (N_{pix} / N_{bin}) N_{read} RN^2 .$$

For all MAMA observations, and for CCD observations in the regime where read noise is not important, the integration time to reach a signal-to-noise ratio, $StoN$, is given by:

$$t = \frac{(StoN)^2 (CG + N_{pix} G [B_{sky} + B_{det}])}{C^2 G^2} .$$

If your source count rate is much higher than the sky plus detector backgrounds, then this expression reduces further to:

$$t = \frac{(StoN)^2}{CG} .$$

More generally, the required integration time to reach a signal to noise ratio, $StoN$, is given by:

$$t = \frac{(StoN)^2 (CG + N_{pix} G [B_{sky} + B_{det}])}{2C^2 G^2} + \frac{\sqrt{(StoN)^4 (CG + N_{pix} G [B_{sky} + B_{det}])^2 + 4(StoN)^2 C^2 G^2 ((N_{pix} / N_{bin}) N_{read} RN^2)}}{2C^2 G^2} .$$

Special Case: Spectroscopic CCD Observations at $\lambda < 2500 \text{ \AA}$

In the optical, each photon generates a single electron (i.e., counts \times the gain correspond to the total number of electrons). However, in the NUV, shortward of $\sim 3200 \text{ \AA}$, there is a finite probability of creating more than one electron per ultraviolet (UV) photon (see Christensen, O., 1976, J. App. Phys., 47, 689). Theoretically, the quantum yield (Q , or the mean number of electrons generated per photon) is given by the energy of the photon divided by 3.65 eV, and ranges from $Q = 1.06$ electrons for every UV photon at 3200 \AA , to $Q = 1.89$ electrons for every photon at 1800 \AA . The actual electron yield of the STIS CCD has not been measured in the NUV.

The sensitivity plots correctly predict the number of electrons generated per UV photon. However, since multiple electrons are generated from a single photon, the signal to noise achieved in a given integration time is affected. The explicit expression is given by:

$$StoN = \frac{Q^{-1} CtG}{\sqrt{Q^{-1} (C + N_{pix} B_{sky}) Gt + N_{pix} B_{det} Gt + (N_{pix} / N_{bin}) N_{read} RN^2}} .$$

For observations which are not in the read noise or dark current limited regime, the effective signal to noise you should expect to achieve is then $\sim 1/\sqrt{Q}$ times the signal-to-noise ratio calculated directly from the sensitivities given in [Chapter 13](#) ignoring this effect. This effect is negligible at 3000 Å but amounts to 40% at 1800 Å.

6.5 Detector and Sky Backgrounds

6.5.1 Detector Backgrounds
6.5.2 Sky Background

When calculating expected signal-to-noise ratios or exposure times, the background from the sky and the background from the detector must be taken into account.

6.5.1 Detector Backgrounds

Table 6.1 shows the read noise and dark current characteristics of the detectors, taken from [Chapter 7](#). Note that the FUV MAMA detector background is highly variable and this should be taken into account when observing faint sources. See the discussion in sections [4.2.3](#) and [7.5.2](#) for additional details.

Table 6.1: Detector Backgrounds.

| Background | CCD | NUV-MAMA | FUV-MAMA |
|--------------|---|--------------------------------------|---|
| Read noise | 6.4 (for CCDGAIN=1) 8.8 (for CCDGAIN=4) ¹ e ⁻ /pix | 0 | 0 |
| Dark current | ~3.2 × 10 ⁻² e ⁻ /s/pix | ~1.8 × 10 ⁻³ counts/s/pix | (0.07-6.0) × 10 ⁻⁴ , ² counts/s/pix |

¹ To convert to counts/s/pix for CCDGAIN=4, divide by 4.016.

² Varies widely with position on detector and time since high-voltage turn-on.

6.5.2 Sky Background

The sources of sky background which will affect STIS observations include:

- Earthshine (ES)
- Zodiacal light (ZL)
- Geocoronal emission (GC)

The continuum background in counts/s/pix for *spectroscopic observations* can be computed as:

$$B_{sky}^{\lambda} = \frac{I_{\lambda} \times S_{\lambda}^d}{G},$$

where:

- I_{λ} is the surface brightness of the sky background, in ergs/s/cm²/Å/arcsec²;

- S_{λ}^d is the diffuse-source sensitivity for the grating mode.

The background in counts/s/pix for *imaging observations* can be computed as:

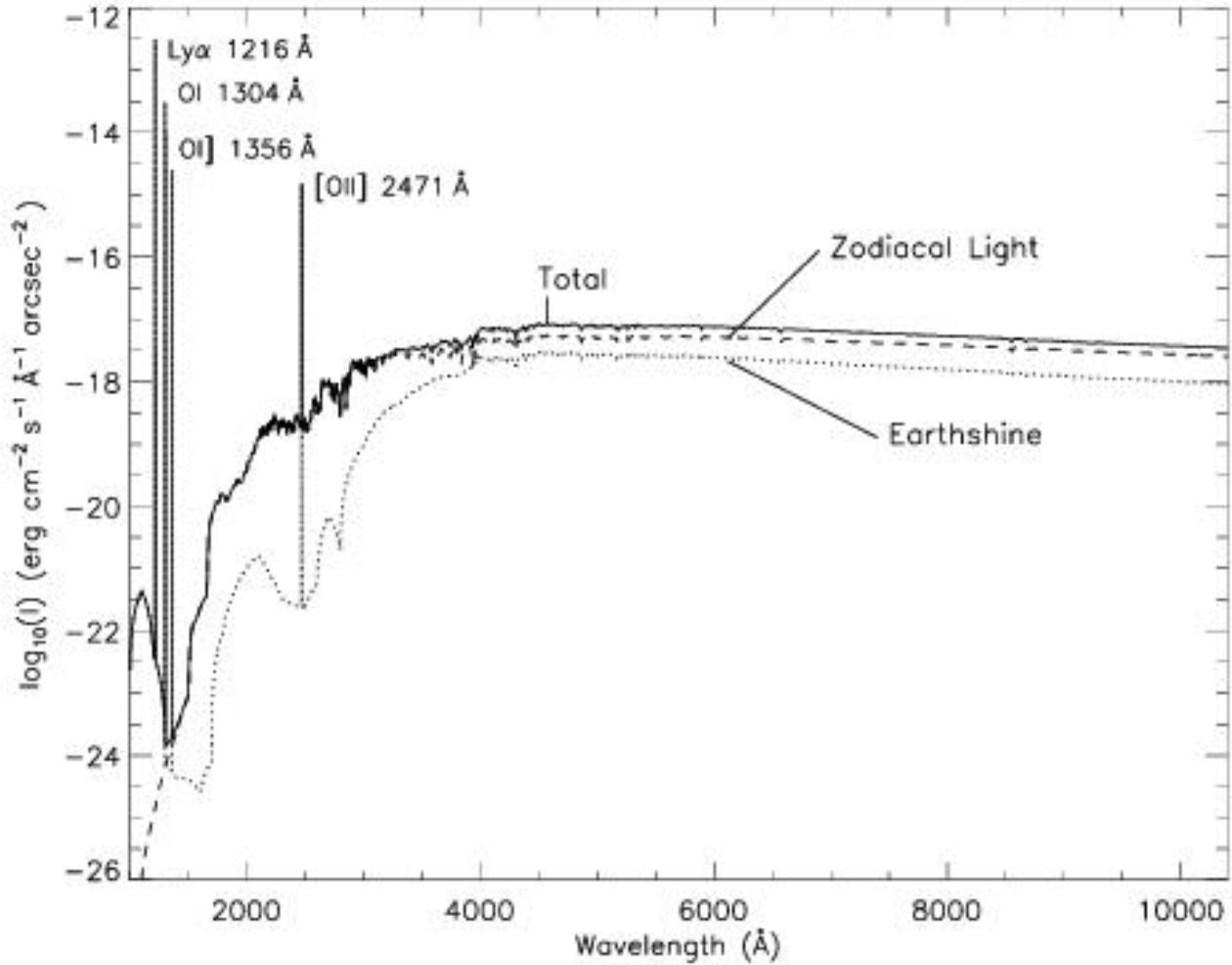
$$B_{sky}^{\lambda} = \frac{\int I_{\lambda} \times S_{\lambda}^d d\lambda}{G},$$

where:

- I_{λ} is the surface brightness of the sky background, in ergs/s/cm²/Å/arcsec²;
- S_{λ}^d is the diffuse-source sensitivity for the imaging mode.
- The integral is over the bandpass.

In [Figure 6.1](#) we plot the "high" zodiacal light and earthshine background intensity as a function of wavelength, identifying the separate components which contribute to the background. The information in this figure is presented in tabular form in [Table 6.4](#). In the [ETCs](#) and in this *Handbook*, the choices for earthshine of "shadow," "average," and "extremely high" correspond to 0%, 50% of, and twice the "high" values in [Table 6.4](#). For the zodiacal sky background, the values in [Table 6.4](#) correspond to a high value of $m_V = 22.1$ arcsec⁻² from [Table 6.2](#), while the low and average zodiacal light are scaled to $m_V = 23.3$ arcsec⁻² and 22.7 arcsec⁻², respectively. The strength of the geocoronal (airglow) line emissions are as shown in [Table 6.5](#); the "average" values of these are plotted in [Figure 6.1](#).

Figure 6.1: Sky Background Intensity as a Function of Wavelength.



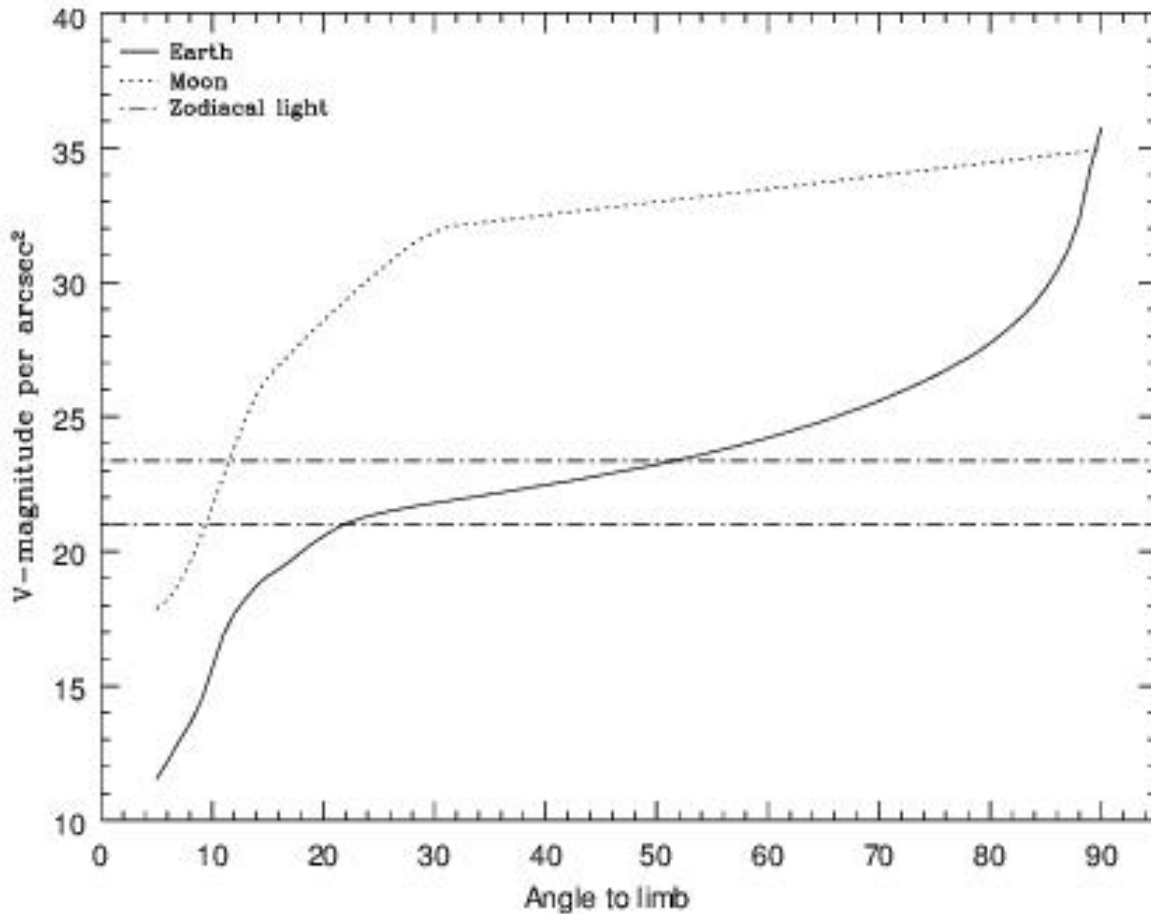
The zodiacal contribution corresponds to $m_v = 22.1 \text{ arcsec}^{-2}$. The earthshine is for a target which is 38° from the limb of the sunlit Earth. Use Figure 6.2 to estimate background contributions at other angles. The geocoronal airglow line intensities are plotted at "average" intensities and are in $\text{ergs/cm}^2 / \text{s/arcsec}^2$.

Background Variations and LOW-SKY

In the UV the background contains important contributions from airglow lines. These vary from day to night and as a function of *HST* orbital position. The airglow lines are an important consideration for imaging mode observations and can be for spectroscopic observations as well. Away from the airglow lines, at wavelengths shortward of $\sim 3000 \text{ \AA}$, the background is dominated by zodiacal light and is generally much lower than the intrinsic detector background. The contribution of zodiacal light does not vary dramatically with time and varies by only a factor of about three throughout most of the sky. Table 6.2 gives the variation of the zodiacal background as a function of helio ecliptic latitude and longitude. For a target near ecliptic coordinates of (50,0) or (-50,0), the zodiacal light is relatively bright at $m_v = 20.9 \text{ arcsec}^{-2}$, i.e., about 9 times the polar value of $m_v = 23.3 \text{ arcsec}^{-2}$.

Earthshine, on the other hand, varies strongly depending on the angle between the target and the bright Earth limb. The variation of the earthshine as a function of limb angle from the sunlit Earth is shown in [Figure 6.2](#). The figure also shows the contribution of the Moon which is typically much smaller, and the full range of the zodiacal contribution. For reference, the limb angle is approximately 24° when the *HST* is aligned toward its orbit pole (i.e., the center of the CVZ).

Figure 6.2: Background Contributions from the Moon, Earth, and Zodiacal Light.



The values are V magnitude per square arcsecond due to the moon and the sunlit Earth as a function of angle between the target and the limb of the bright Earth or moon. Zodiacal light levels range between $m_v = 22.1$ and $23.3 \text{ mag arcsec}^{-2}$.

For observations longward of 3500 \AA , the earthshine always dominates the background at small ($<22^\circ$) limb angles. In fact, the background increases exponentially for limb angles $<22^\circ$. The background near the bright Earth limb can also vary by a factor of ~ 2 on time scales as short as two minutes, which suggests that the background from earthshine also depends upon the reflectivity of the terrain over which *HST* passes during the course of an exposure. The total background at limb angles greater than the bright-Earth avoidance angle of 20° appears to show no significant dependence on position within the small *HST* fields of view. Details of the sky background as it affects STIS are discussed by Shaw et al. (STIS ISR 1998-21) and Giavalisco et al. (WFC3 ISR 2002-12).

Table 6.2: Approximate Zodiacal Sky Background in V magnitude arcsec⁻² as a Function of Heliocentric Coordinates, sourced from Leinert et al. (1998). See the [ETC documentation](#) for finer sampling.

| Heliocentric Longitude (deg) | Heliocentric Latitude (deg) | | | | | | |
|------------------------------|-----------------------------|------|------|------|------|------|------|
| | 0° | 15° | 30° | 45° | 60° | 75° | 90° |
| 180° | 22.0 | 22.3 | 22.6 | 22.9 | 23.1 | 23.3 | 23.2 |
| 165° | 22.2 | 22.4 | 22.7 | 22.9 | 23.2 | 23.3 | 23.2 |
| 150° | 22.3 | 22.5 | 22.8 | 23.0 | 23.2 | 23.3 | 23.2 |
| 135° | 22.4 | 22.5 | 22.8 | 23.1 | 23.2 | 23.3 | 23.2 |
| 120° | 22.3 | 22.5 | 22.8 | 23.1 | 23.2 | 23.3 | 23.2 |
| 105° | 22.1 | 22.4 | 22.8 | 23.0 | 23.2 | 23.2 | 23.2 |
| 90° | 21.9 | 22.2 | 22.6 | 22.9 | 23.1 | 23.2 | 23.2 |
| 75° | 21.6 | 22.1 | 22.5 | 22.8 | 23.0 | 23.2 | 23.2 |
| 60° | 21.2 | 21.8 | 22.3 | 22.6 | 23.0 | 23.1 | 23.2 |
| 45° | SA | 21.3 | 22.0 | 22.4 | 22.8 | 23.1 | 23.2 |
| 30° | SA | SA | SA | 22.2 | 22.7 | 23.0 | 23.2 |
| 15° | SA | SA | SA | SA | 22.5 | 23.0 | 23.2 |
| 0° | SA | SA | SA | SA | 22.5 | 23.0 | 23.2 |

Note: A value of “SA” denotes positions in the solar avoidance zone.

Table 6.3 contains the expected count rates from different sky backgrounds in various STIS modes, which you can use to determine whether your observations would be background limited.

Observations of the faintest objects may need the special requirement `LOW-SKY` in the Phase II observing program. `LOW-SKY` observations are scheduled during the part of the year when the zodiacal background is no more than 30% greater than the minimum possible value for the given sky position. `LOW-SKY` also invokes the restriction that exposures will be obtained at angles greater than 40° from the bright Earth limb to minimize earthshine and the UV airglow lines. The `LOW-SKY` special requirement limits the times at which targets within 60° of the ecliptic plane will schedule and limits visibility to about 48 minutes per orbit.

The **ETC** provides the user with the flexibility to separately adjust both the zodiacal (none, low, average, high) and earthshine (none, average, high, extremely high) sky background components in order to determine if **LOW-SKY** is advisable for a given program. However, the absolute sky levels that can be specified in the **ETC** may not be achievable for a given target. As shown in [Table 6.2](#), the minimum zodiacal background level for an ecliptic target is $m_v = 22.4$, which is brighter than both the low and average options with the **ETC**. By contrast, a target near the ecliptic pole would always have a **zodiacal=low** background in the **ETC**. The user is cautioned to carefully consider sky levels as the backgrounds obtained in *HST* observations can cover significant ranges.

Table 6.3: Count Rates by Sky Background and STIS Mode.

| Mode | Count Rates (counts/s/pix) | | | | |
|---------------------------|----------------------------|--|--|--|---|
| | Zodiacal ¹ | Earthshine + Geocoronal Lines | | | |
| | | Ex. High Earth ² High Air Glow | High Earth ³ High Air Glow | Avg. Earth ⁴ Avg. Air Glow | Shadow Earth ⁵ Low Air Glow |
| CCD Clear | 1.0×10^{-1} | 9.1×10^{-2} | 4.6×10^{-2} | 2.3×10^{-2} | 3.9×10^{-6} |
| CCD Longpass | 6.1×10^{-2} | 5.1×10^{-2} | 2.6×10^{-2} | 1.3×10^{-2} | 1.7×10^{-10} |
| NUV-MAMA Clear | 6.2×10^{-5} | 4.5×10^{-3} | 4.5×10^{-3} | 2.3×10^{-3} | 3.6×10^{-4} |
| NUV-MAMA SrF ₂ | 5.7×10^{-5} | 7.1×10^{-4} | 7.0×10^{-4} | 3.5×10^{-4} | 4.5×10^{-6} |
| NUV-MAMA Qtz | 5.5×10^{-5} | 2.5×10^{-4} | 2.5×10^{-4} | 1.3×10^{-4} | 1.2×10^{-6} |
| FUV-MAMA Clear | 2.1×10^{-8} | 4.3×10^{-2} | 4.3×10^{-2} | 2.1×10^{-2} | 3.9×10^{-3} |
| FUV-MAMA SrF ₂ | 1.9×10^{-8} | 2.6×10^{-3} | 2.5×10^{-3} | 1.3×10^{-3} | 2.0×10^{-5} |
| FUV-MAMA Qtz | 1.8×10^{-8} | 1.5×10^{-8} | 1.4×10^{-8} | 6.8×10^{-9} | 6.3×10^{-11} |
| FUV-MAMA Lyman- α | 1.4×10^{-11} | 3.2×10^{-3} | 3.2×10^{-3} | 1.6×10^{-3} | 3.1×10^{-4} |

¹ Zodiacal contribution is the same as in [Figure 6.1](#) and [Table 6.4](#) ($m_v=22.1$ -arcsec⁻²).

² Corresponds to *HST* pointing 24° from the limb of the sunlit Earth.

³ Corresponds to *HST* pointing around 38° from the limb of the sunlit Earth, where the earthshine is 50% of the "extremely high" value.

⁴ Corresponds to *HST* pointing around 50° from the limb of the sunlit Earth, where the earthshine is 25% of the "extremely high" value.

⁵ Earthshine for shadow is 0 in the continuum, while the UV geocoronal emission lines are reduced from the high to the low values in [Table 6.5](#).

Geocoronal Emission and Shadow

Background due to geocoronal emission originates mainly from hydrogen and oxygen atoms in the exosphere of the Earth. The emission is concentrated in a very few lines. The brightest line is Lyman- α at 1216 Å. The strength of the Lyman- α line varies between about 2 and 20 kilo-Rayleighs (i.e., between 6.1×10^{-14} and 6.0×10^{-13} ergs/s/cm²/arcsec² where 1 Rayleigh = 10^6 photons/s/cm²/[4 π steradians]) depending on the time of the observation and the position of the target relative to the Sun. The next strongest contribution is from the triplet O I 1302, 1304, 1306 Å, which rarely exceeds 10% of Lyman- α . The typical strength of the O I 1302 Å triplet is about 2 kilo-Rayleighs (which corresponds to about 5.7×10^{-14} ergs/s/cm²/s/arcsec²) at the daylight side and about 150 times fainter on the night side of the *HST* orbit. O I] 1356 Å and [O II] 2471 Å lines may appear in observations on the daylight side of the orbit, but these lines are at least 10 times weaker than the O I 1302 Å lines. The widths of the lines also vary. The line widths given in [Table 6.5](#) are representative values assuming a temperature of 2000 K.

The geocoronal emission lines are unresolved at the first-order resolutions of STIS but the emission fills the slit in the spatial dimension. A wider slit or slitless observing does not increase the background counts per pixel from geocoronal emission but does increase the area (range of wavelengths or pixels in the dispersion direction) over which that background is received. Observations with a slit which is n pixels wide in dispersion will be affected by geocoronal emission in a roughly n pixel region centered on the relevant geocoronal emission line wavelength. For slitless spectroscopy in the UV, the effects of geocoronal emission must be taken into account at all pixels, unless a longpass filter is employed to block off the short wavelength emission (see also [Section 5.3.5](#) and [Section 12.1](#)).

It is possible to request that exposures be taken when *HST* is in the umbral shadow of the earth to minimize geocoronal emission (e.g., if you are observing weak lines at ~1216 or ~1304 Å) using the special requirement SHADOW. Exposures using this special requirement are limited to roughly 25 minutes per orbit, exclusive of the guide-star acquisition (or reacquisition) and can be scheduled only during a small percentage of the year. SHADOW reduces the contribution from the geocoronal emission lines by roughly a factor of ten, while the continuum earthshine is set to 0. If you require SHADOW, you should request it in your Phase I proposal (see the [Call for Proposals](#)).

An alternate strategy for reducing the effects of geocoronal emissions is to use time resolved observations, so that any data badly affected by geocoronal emission can simply be excluded from the final co-addition. This can be done either by doing the observations in TIME-TAG mode or by just taking a series of short (~5 min) ACCUM mode exposures over the course of each orbit.

Observers should also remember that geocoronal lines will also produce weak absorption features in the spectra of extended targets.

6.6 Tabular Sky Backgrounds

We provide a table of the “high” sky background numbers as plotted in [Figure 6.1](#), for easy reference. See the text and the caption in [Figure 6.1](#) for more details. The high sky values are defined as the earthshine at 38° from the limb and by the high zodiacal light of $m_V = 22.1 \text{ arcsec}^{-2}$. The contributions of the geocoronal emission lines are tabulated separately in [Table 6.5](#).

Table 6.4: High Sky Background (excluding geocoronal emission lines).

| Wavelength \AA | High Earthshine $\text{erg/s/cm}^2/$ \AA/arcsec^2 | High Zodiacal Light $\text{erg/s/cm}^2/$ \AA/arcsec^2 | Total Background $\text{erg/s/cm}^2/$ \AA/arcsec^2 |
|----------------------------|--|--|---|
| 1,000 | 2.41e-23 | 9.69e-29 | 2.41e-23 |
| 1,100 | 4.38e-22 | 1.04e-26 | 4.38e-22 |
| 1,200 | 4.01e-23 | 1.08e-25 | 4.03e-23 |
| 1,300 | 7.41e-25 | 6.59e-25 | 1.40e-24 |
| 1,400 | 4.29e-25 | 2.55e-24 | 2.98e-24 |
| 1,500 | 4.16e-25 | 9.73e-24 | 1.01e-23 |
| 1,600 | 2.55e-25 | 2.35e-22 | 2.35e-22 |
| 1,700 | 7.89e-25 | 7.21e-21 | 7.21e-21 |
| 1,800 | 9.33e-23 | 1.53e-20 | 1.54e-20 |
| 1,900 | 4.39e-22 | 2.25e-20 | 2.29e-20 |
| 2,000 | 1.01e-21 | 3.58e-20 | 3.68e-20 |
| 2,100 | 1.60e-21 | 1.23e-19 | 1.25e-19 |
| 2,200 | 7.49e-22 | 2.21e-19 | 2.22e-19 |
| 2,300 | 3.32e-22 | 1.81e-19 | 1.81e-19 |
| 2,400 | 2.50e-22 | 1.83e-19 | 1.83e-19 |
| 2,500 | 2.39e-22 | 2.53e-19 | 2.53e-19 |
| 2,600 | 5.62e-22 | 3.06e-19 | 3.06e-19 |
| 2,700 | 6.77e-21 | 1.01e-18 | 1.02e-18 |
| 2,800 | 2.03e-21 | 2.88e-19 | 2.90e-19 |
| 2,900 | 4.32e-20 | 2.08e-18 | 2.12e-18 |
| 3,000 | 9.34e-20 | 1.25e-18 | 1.35e-18 |

| | | | |
|-------|----------|----------|----------|
| 3,100 | 2.07e-19 | 1.50e-18 | 1.70e-18 |
| 3,200 | 3.60e-19 | 2.30e-18 | 2.66e-18 |
| 3,300 | 4.27e-19 | 2.95e-18 | 3.38e-18 |
| 3,400 | 6.40e-19 | 2.86e-18 | 3.50e-18 |
| 3,500 | 8.20e-19 | 2.79e-18 | 3.61e-18 |
| 3,600 | 1.06e-18 | 2.74e-18 | 3.80e-18 |
| 3,700 | 1.22e-18 | 3.32e-18 | 4.54e-18 |
| 3,800 | 1.23e-18 | 3.12e-18 | 4.35e-18 |
| 3,900 | 1.52e-18 | 3.34e-18 | 4.86e-18 |
| 4,000 | 2.38e-18 | 4.64e-18 | 7.01e-18 |
| 4,250 | 2.38e-18 | 4.65e-18 | 7.03e-18 |
| 4,500 | 2.86e-18 | 5.58e-18 | 8.44e-18 |
| 4,750 | 2.79e-18 | 5.46e-18 | 8.25e-18 |
| 5,000 | 2.63e-18 | 5.15e-18 | 7.77e-18 |
| 5,250 | 2.67e-18 | 5.37e-18 | 8.04e-18 |
| 5,500 | 2.58e-18 | 5.34e-18 | 7.92e-18 |
| 5,750 | 2.54e-18 | 5.40e-18 | 7.94e-18 |
| 6,000 | 2.42e-18 | 5.25e-18 | 7.67e-18 |
| 6,250 | 2.26e-18 | 5.02e-18 | 7.28e-18 |
| 6,500 | 2.17e-18 | 4.92e-18 | 7.09e-18 |
| 6,750 | 2.07e-18 | 4.79e-18 | 6.87e-18 |
| 7,000 | 1.93e-18 | 4.55e-18 | 6.48e-18 |
| 7,250 | 1.85e-18 | 4.43e-18 | 6.29e-18 |
| 7,500 | 1.74e-18 | 4.23e-18 | 5.97e-18 |
| 7,750 | 1.63e-18 | 4.04e-18 | 5.67e-18 |
| 8,000 | 1.56e-18 | 3.92e-18 | 5.49e-18 |
| 8,250 | 1.48e-18 | 3.76e-18 | 5.23e-18 |
| 8,500 | 1.35e-18 | 3.50e-18 | 4.85e-18 |
| 8,750 | 1.31e-18 | 3.43e-18 | 4.74e-18 |
| 9,000 | 1.22e-18 | 3.23e-18 | 4.44e-18 |

| | | | |
|--------|----------|----------|----------|
| 9,250 | 1.15e-18 | 3.07e-18 | 4.21e-18 |
| 9,500 | 1.10e-18 | 2.98e-18 | 4.08e-18 |
| 9,750 | 1.04e-18 | 2.86e-18 | 3.91e-18 |
| 10,000 | 1.00e-18 | 2.78e-18 | 3.78e-18 |
| 10,250 | 9.54e-19 | 2.67e-18 | 3.63e-18 |
| 10,500 | 9.04e-19 | 2.56e-18 | 3.46e-18 |
| 10,750 | 8.41e-19 | 2.41e-18 | 3.25e-18 |
| 11,000 | 8.03e-19 | 2.31e-18 | 3.11e-18 |

Table 6.5: Geocoronal (Airglow) Emission Lines.

| Wavelength (Å) | ID | Line Width (Å) | Intensity | | | | | |
|-------------------|--------|----------------|----------------|--|----------------|--|----------------|--|
| | | | High | | Average | | Low | |
| | | | kilo-Rayleighs | erg/s/cm ² /arcsec ² | kilo-Rayleighs | erg/s/cm ² /arcsec ² | kilo-Rayleighs | erg/s/cm ² /arcsec ² |
| 1215.67 | Lyα | 0.04 | ~20 | 6.1e-13 | ~10 | 3.05e-13 | 2 | 6.1e-14 |
| 1302 ¹ | O I | 0.013 | ~2 | 5.7e-14 | ~1 | 2.85e-14 | 0.013 | 3.8e-16 |
| 1356 | O I] | 0.013 | ~0.2 | 5.0e-15 | ~0.1 | 2.5e-15 | ~0.001 | 3.0e-17 |
| 2471 | [O II] | 0.023 | <0.2 | 3.0e-15 | <0.1 | 1.50e-15 | <0.001 | 1.5e-17 |

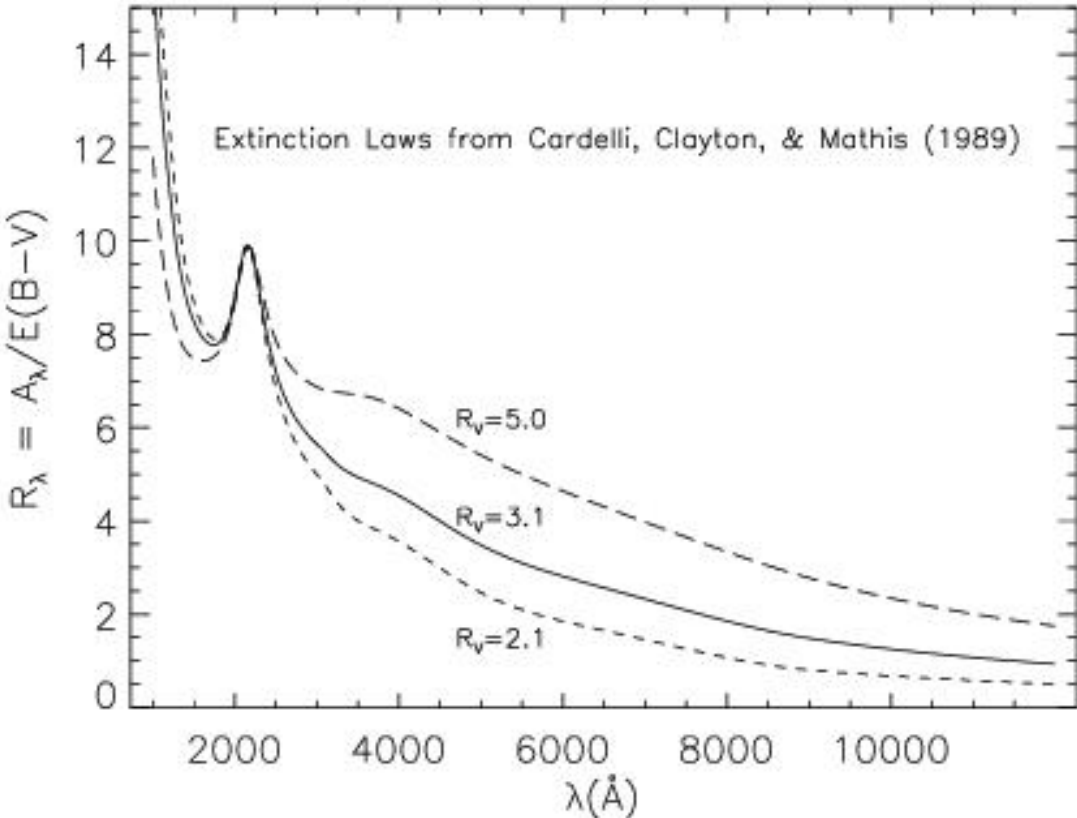
¹ Blend of 1302.2, 1304.9, and 1306.0 with intensity ratio 3:2:1.

6.7 Extinction Correction

Extinction can dramatically alter the counts expected from your source, particularly in the UV. Extinction curves, however, have a strong metallicity and environment dependence, and this variation is largest at UV wavelengths. Sample extinction curves can be seen in [Koornneef and Code, Apj, 247, 860, 1981 \(LMC\)](#); [Bouchet et al., A&A, 149, 330, 1985 \(SMC\)](#); and [Calzetti, Kinney, and Storchi-Bergmann, Apj, 429, 582, 1994](#), and references therein. At lower metallicities, the 2200 Å bump, which is so prominent in the galactic extinction curve, disappears and $A_\lambda/E(B-V)$ increases at UV wavelengths. However, as discussed by [Gordon et al. 2003 \(Apj, 594, 279\)](#), the extinction curve for any sight line depends on the local environment, and even within the Magellenic clouds, many examples can be found that are closer to the typical Galactic extinction law than to the Koornneef & Code curve.

The **ETC** now offers four Galactic extinction curves from [Cardelli, Clayton, & Mathis 1989 \(Apj, 345, 245\)](#), with R_V values ranging from 2.1 to 5.0. Examples of these curves are shown in [Figure 6.3](#). Of these, the "Milky Way Diffuse" curve with $R_V = 3.1$ is the default setting and a good choice for an average Galactic extinction curve. Also available are curves for the LMC Average, the LMC Supershell, and the SMC bar extinction from [Gordon \(2003\)](#), as well as the extragalactic Starburst attenuation law of Calzetti. Further details of the extinction curves implemented in the **ETC** can be found [here](#).

Figure 6.3: Galactic Extinction versus Wavelength from Cardelli, Clayton, & Mathis (1989) for a variety of RV values.



6.8 Exposure Time Examples

- [6.8.1 Spectroscopy of Diffuse Source \(M86\)](#)
- [6.8.2 Spectroscopy of Solar-Analog Star P041-C](#)
- [6.8.3 Extended Source with Flux in cgs Units \(NGC 6543\): Imaging and Spectroscopy](#)
- [6.8.4 Echelle Spectroscopy of a Bright Star, Reddened LMC Star](#)
- [6.8.5 Imaging a Faint Stellar Source](#)
- [6.8.6 Time-Tag Observations of a Flare Star \(AU Mic\)](#)

Here are a few simple examples to illustrate how an integration time may be computed for point sources and diffuse sources. The flux values given here are for illustrative purposes only; you need to check the flux values if you are planning your own observations of one of these targets. Also note that the examples in this section have not been updated to take into account the latest revised values for throughputs and other detector parameters, and so the numerical results presented here will differ from the more up-to-date **ETC** calculations.

6.8.1 Spectroscopy of Diffuse Source (M86)

We want to observe M86, an elliptical galaxy in Virgo, using the G750M grating at a central wavelength setting of $\lambda_c = 6768 \text{ \AA}$, the CCD detector and the 52x0.2 arcsec slit. Our aim is to calculate the H α count rate in the central region of M86 and the expected signal-to-noise ratio per resolution element for an exposure time of 1 hour. M86 has an inhomogeneous surface brightness distribution in H α , and the line is well resolved with this grating. Let us consider a region with an H α surface brightness of $I_\lambda = 1.16 \times 10^{-15} \text{ erg/s/cm}^2/\text{\AA}/\text{arcsec}^2$ (note the unit—it is not the entire H α flux but the flux per unit wavelength interval) and a continuum surface brightness $I_\lambda = 2.32 \times 10^{-16} \text{ erg/s/cm}^2/\text{\AA}/\text{arcsec}^2$. To derive the H α and continuum count rates from the source we use the formula from [Chapter 13](#):

- $S_\lambda^d = 1.14 \times 10^{13} \text{ counts/s/pix}_\lambda/\text{pix}_s$ per incident $\text{erg/s/cm}^2/\text{\AA}/\text{arcsec}^2$.
- $N_{\lambda\text{pix}} = 4$ and $N_{\text{spix}} = 2$ (1 resolution element).

Using the equation given by the [Diffuse Source](#) calculation, we get the count rate $C = 0.106 \text{ counts/s}$ in H α and $C = 0.021 \text{ counts/s}$ in the continuum. Since we are interested in the properties of the H α line, the H α counts constitute the signal, while both the H α counts and the continuum counts contribute to the noise.

The sky background is negligible in comparison to the source, but the dark current ($4.5 \times 10^{-3} \text{ count/s/pix} \times 8 \text{ pixels} = 0.020 \text{ count/s}$) and the read noise squared ($29 \text{ e-/pix} \times 8 \text{ pixels} \times 3 \text{ reads} = 465 \text{ counts}$, for CR-SPLIT=3) are important here. Substituting the numbers into the equation for signal-to-noise, we get:

$$StoN = 10.7 = \frac{0.106 \times 3600}{\sqrt{(0.127 \times 3600) + (8 \times 0.0045 \times 3600) + (8 \times 3 \times 29)}} .$$

To increase our signal-to-noise or decrease our exposure time, we can consider using on-chip binning. Let us bin 2 pixels in the spatial direction so that $N_{bin} = 2$. To allow adequate sampling of our new binned pixels, we leave $N_{\lambda pix} = 4$, but set $N_{spix} = 4$, so $N_{pix} = 16$ and then $C = 0.212$ for H α and $C = 0.254$ for the sum of H α and continuum. To compute the time to achieve a signal-to-noise of 12 using this configuration, we use the full expression for the exposure time given in [Section 6.4.1](#), generalized to treat the line counts (for signal) and total counts (for noise) separately, and determine that roughly 35 minutes are needed in this configuration:

$$t = 2104 = \frac{144 \times (0.254 + 16 \times 0.0045)}{2 \times 0.212^2} + \frac{\sqrt{20736 \times (0.254 + 16 \times 0.0045)^2 + 4 \times 144 \times 0.212^2 \times 8 \times 3 \times 29}}{2 \times 0.212^2}$$

6.8.2 Spectroscopy of Solar-Analog Star P041-C

We wish to study the shape of the continuum spectrum of the solar-analog star P041-C from the near-infrared (NIR) to the NUV. We wish to obtain spectroscopy with the CCD detector covering the entire useful spectral range from 2000 Å to 10,300 Å with gratings G230LB, G430L, and G750L. Since we require accurate photometry, we use the wide 52x0.5 slit. The goal is to reach a signal-to-noise ratio of 25 in the NUV (at 2300 Å), 100 in the blue, and 280 in the red. P041-C has $V = 12.0$.

The fluxes of P041-C at the desired wavelengths obtained from a spectrum of the Sun scaled from $V = -26.75$ to $V = 12.0$, are available [here](#).

G230LB

We illustrate the calculation of the exposure time for the G230LB grating. P041-C is found to have a flux of 1.7×10^{-15} erg/s/cm²/Å at 2300 Å.

We get the following values for G230LB from [Chapter 13](#):

- $S_{2300}^p = 1.7 \times 10^{14}$ counts/s/pix $_{\lambda}$ per incident erg/s/cm²/Å;
- $T_A = 0.86$ for the aperture throughput, taken from [Chapter 13](#);
- $\epsilon_f = \sim 0.8$;
- $N_{spix} = 3$, since $\sim 80\%$ of the point source light is encircled within 3 pixels;
- $N_{\lambda pix} = 2$, since two pixels resolve the LSF.

Using the equation in [Section 6.2.1](#), we calculate a point source count rate of $C = 0.34$ counts/s over $N_{pix} = 6$ pixels for GAIN=1.

The source count rates can be compared with the background and detector dark current rates. We'll make the approximation that the background and detector rates are negligibly small for this setting; therefore we can neglect their contributions. Since we are aiming for a signal-to-noise ratio of 25, we can estimate that we must obtain 625 counts minimum. The read noise squared (~ 350 over 6 pixels for 2 readouts) must therefore be taken into account. Finally, since we are observing with the CCD in the NUV, we must correct for the effect of the multiple-electron process (see [Section 6.4](#)). This will cause the exposure time to be scaled approximately by Q , where Q is ~ 1.5 at 2300 Å. Using the [STIS ETC](#), we estimate the required time for $S/N = 25$ is ~ 3560 seconds. To check that we indeed get $S/N = 25$, we use the [formula](#), in [Section 6.4](#).

$$S/N \approx 25 \approx \frac{(0.34/1.5)3560}{\sqrt{(0.34/1.5)3560 + 350}} .$$

G750L and G430L

Exposure times for the two remaining wavelength settings can be calculated directly as $time = signal-to-noise^2/C$ since the read noise, detector background, and sky background are negligible. As above, 3 pixels are taken to contain 80% of the flux. The results are summarized in [Table 6.6](#).

Table 6.6: Low Resolution Spectroscopy of Solar Analog Star.

| Grating | G230LB | G430L | G750L $\lambda_c = 7751$ |
|--|-----------------------|-----------------------|-----------------------------|
| Wavelength (Å) | 2300 | 5000 | 7800 |
| Flux (ergs/s/cm ² /Å) | 1.7×10^{-15} | 5.9×10^{-14} | 3.5×10^{-14} |
| Point Source Sensitivity (counts/s/pix _{λ} per ergs/s/cm ² /Å) | 1.7×10^{14} | 3.1×10^{15} | 5.0×10^{15} |
| Aperture throughput (T_A) | 86% | 90% | 89% |
| $N_{\lambda pix}$ | 2 | 2 | 2 |
| N_{spix} to encircle 80% of PSF | 3 | 3 | 3 |
| C (counts/s from source over $N_{\lambda pix} = 2$) | 0.34 | 240 | 240 |
| Signal-to-noise ratio desired | 25 | 100 | 280 |
| Total exposure time | 3560 seconds | 41 seconds | 330 seconds |

6.8.3 Extended Source with Flux in cgs Units (NGC 6543): Imaging and Spectroscopy

Let us consider NGC 6543, the Cat's Eye planetary nebula, where the aim is to use the CCD to image using the [O II] filter, and to do spectroscopy both in the visible and in the UV.

Imaging

The aim is to get a signal-to-noise ratio of 30 using the [O II] filter. We know that NGC 6543 is about 6 times fainter in [O II] than in H β , and its total flux at [O II] 3727 Å is $\sim 4.4 \times 10^{-11}$ erg/s/cm² contained within 1 Å. Since the radius of the object is about 10 arcseconds, the average [O II] surface brightness is about 1.4×10^{-13} erg/s/cm²/arcsec²/Å.

We take:

- $S_{\lambda}^d = 6.7 \times 10^{11}$ counts/s/pix/Å per incident erg/s/cm²/Å/arcsec² as given in [Chapter 14](#).
- We take $N_{pix} = 4 \times 4 = 16$, since a resolution element has radius of two pixels (see [Chapter 14](#)).

To calculate the count rate we use the equation in [Section 6.2.1](#) for diffuse sources and determine a per-pixel count rate of 0.094 counts/s/pix or a count rate $C = 1.5$ counts/s over 16 pixels. The background and the dark current can be neglected. To get a signal-to-noise of 30 we need $\sim 10^3$ counts, so the read noise can also be neglected and we can use the simplified expression to calculate exposure time (see [Section 6.4.1](#)). We obtain 10^3 counts in ~ 667 seconds. To allow post-observation removal of cosmic rays we use CR-SPLIT=2. We note that in each ~ 330 second exposure we predict a mean of ~ 31 counts/pix, and thus we are safely within the limits of the CCD full well.

Diffuse Source Spectroscopy in the Visible and Ultraviolet Regions

In the visible, the aim is to get a signal-to-noise of about 100 at $\lambda = 4861$ Å, with the G430M grating at a central wavelength setting of $\lambda_c = 4961$ Å, the CCD detector, and the 52x0.1 arcsecond slit. In the UV, the aim is to get a signal-to-noise ratio of about 20 at the C IV ~ 1550 Å line with the G140M grating at a central wavelength setting of $\lambda_c = 1550$ and the FUV-MAMA detector. To increase our signal-to-noise ratio in the UV, we use the 52x0.2 arcsecond slit for the G140M spectroscopic observations.

Visible Region

NGC 6543 has an average H β surface brightness of $S(\text{H}\beta) \sim 8.37 \times 10^{-13}$ erg/s/cm²/Å/arcsec² at 4861 Å and has a radius of about 10 arcseconds.

We take from [Chapter 13](#):

- $S_{\lambda}^d = 1.62 \times 10^{12}$ counts/s/pix_λ/pix_s per incident erg/s/cm²/Å/arcsec² for G430M;
- $N_{\lambda pix} = N_{spix} = 2$ since 2 pixels resolves the LSF and PSF;

Using the equation for diffuse sources in [Section 6.2](#), we derive a per-pixel count rate of 1.4 counts/s/pix and a count rate integrated over the four pixels of $C = 5.4$ counts/s at 4861 Å from the astronomical source. The sky background and the detector background are much lower. To allow cosmic ray removal in post-observation data processing, we use CR-SPLIT=3. To achieve a signal-to-noise of 100, we require a total of roughly 10,000 counts, so read noise should be negligible, even over 4 pixels and with NREAD=3. We calculate the time required to achieve signal-to-noise of 100, using the simplified equation [Section 6.4.1](#), and determine that we require roughly 30 minutes:

$$t = 1850 = \frac{10000}{5.4} .$$

At a count rate of ~1 counts/s/pix for 600 seconds per CR-SPLIT exposure, we are in no danger of hitting the CCD full-well limit.

Ultraviolet Region

The C IV flux of NGC 6543 is $\sim 2.5 \times 10^{-12}$ erg/s/cm²/arcsec² spread over ~1 Å. The line, with a FWHM ~ 0.4 Å, will be well resolved in the G140M configuration using the 52x0.2 slit.

We take from [Chapter 13](#):

- $S_{\lambda}^d = 5.15 \times 10^9$ counts/s/pix_λ/pix_s per incident erg/s/cm²/Å/arcsec² for G140M at $\lambda = 1550$ Å using the 0.2 arcsecond wide slit.
- We take $N_{\lambda pix} = N_{spix} = 8$, since the line emission is spread over the ~8 pixels of the slit width in dispersion, and we are willing to integrate flux along the slit to improve the signal-to-noise ratio.

Using the equation for diffuse sources in [Section 6.2.1](#), we determine a per-pixel peak count rate of ~0.013 counts/s/pix and a count rate over the 64 pixels of $C = 0.82$ counts/s at 1550 Å from the astronomical source. The sky and detector backgrounds are still negligible, and the read noise is zero for the MAMA detector so we can use the simplified equation for exposure time, see [Section 6.4.1](#). We determine that we require ~7 minutes:

$$t = 490 = \frac{400}{0.82} .$$

We are well below the MAMA local linearity limit of 50 counts/s/pix. Even assuming the nebula evenly illuminates the full 28 arcseconds of the long slit, we are well below the global absolute and linearity limits, since the flux from the nebula is concentrated in the C IV emission line. Then the global count rate, if the source fully fills the slit in the spatial direction, is given roughly by $(0.015 \times 8 \times 1024)$

\lll 200,000 counts/s. Finally, we are well below the MAMA 16 bit buffer limit of a maximum of 65,536 counts/pix integrated over the exposure duration.

6.8.4 Echelle Spectroscopy of a Bright Star, Reddened LMC Star

The aim here is to do high-resolution echelle spectroscopy of an O5 star in the LMC at 2500 Å, using the E230H grating at a central wavelength of $\lambda_c = 2513$ Å and using the 0.2x0.09 arcsecond slit. The aim is to get a signal-to-noise ratio of about 50 from photon statistics. We will assume that the exact UV flux of the star is unknown and we need to estimate it from the optical data. This calculation of the stellar flux at 2500 Å involves 2 steps:

1. Calculation of the dereddened flux at 5500 Å.
2. Calculation of predicted flux at 2500 Å taking reddening with standard extinction and stellar models into account.

Dereddened Magnitude and Prediction of 2500 Å Flux

We assume that it is an O5 V star with $V = 11.6$ and $B - V$ is -0.09 . The expected $B - V$ value from such a star is -0.35 , so that $E(B - V) = 0.26$ mag.

We assume all the extinction to be due to the LMC, and use the appropriate extinction law (Koornneef and Code, ApJ, 247, 860, 1981). The total visual extinction is then $R \times E(B - V) = 3.1 \times 0.26 = 0.82$, leading to an unreddened magnitude of $V_0 = 10.78$. The corresponding flux at 5500 Å (using the standard zero point where $V = 0$ corresponds to $F(5500 \text{ Å}) = 3.55 \times 10^{-9} \text{ erg/s/cm}^2$) is $F(5500 \text{ Å}) = 1.73 \times 10^{-13} \text{ erg/s/cm}^2/\text{Å}$.

The model atmosphere of Kurucz predicts $F(2500 \text{ Å})/F(5500 \text{ Å}) = 17.2$ for an O5 star, which leads to a flux of $F(2500 \text{ Å}) = 2.98 \times 10^{-12} \text{ erg/s/cm}^2/\text{Å}$ at 2500 Å for the unreddened star. Reddening will diminish this flux by a factor of $10^{-0.4 \times A(2500 \text{ Å})}$, where the absorption at 2500 Å can be determined from the extinction curve; the result in this case is ~ 0.3 . Thus the predicted flux of this star at 2500 Å is $9.0 \times 10^{-13} \text{ erg/s/cm}^2/\text{Å}$.

Exposure Time Calculation

We take from [Chapter 13](#):

- $S_\lambda^d = 2.9 \times 10^{11} \text{ counts/s/pix}_\lambda$ per incident $\text{erg/s/cm}^2/\text{Å}$ for E230H;

- $T_A = 0.659$ for the aperture throughput;
- $\epsilon_f = 0.8$ for the encircled energy;
- $N_{\lambda pix} = 2$, since two pixels resolve the LSF;
- $N_{spix} = 3$, since 80% of the point source light is encircled by 3 pixels.

Using the equation for point sources in [Section 6.2](#), we determine a total count rate from the star of $C = 0.3$ counts/s over 6 pixels. From [Chapter 13](#) we see that ~ 22 percent of the point source flux will be contained within the peak pixel. Thus the peak per pixel count rate will be approximately $0.3 \times 0.22 / (0.8 \times 2) = 0.045$ counts/s/pix and well within the local linear counting regime. We can use the information that we register ~ 0.3 counts/s for every two pixels in the dispersion direction to estimate the global count rate (over the entire detector) as follows. Each order contains ~ 1024 pixels, and the E230H grating at the central wavelength setting of 2513 \AA covers 33 orders (see [Chapter 13](#)). A rough estimate of the global count rate is thus $\sim 33 \times 512 \times 0.3 / 0.8 \sim 6400$ counts/s and we are well within the linear range.

To calculate the integration time, we can ignore both the sky background and the detector dark current which are several orders of magnitude fainter than the source. To achieve a signal-to-noise ratio of 50, we then require ~ 2500 counts which would take a total of ~ 2.3 hours. Fortunately, this is a CVZ target!

6.8.5 Imaging a Faint Stellar Source

Consider a case where the aim is to image a faint ($V = 28$), A-type star with the clear filter and the CCD detector. We want to calculate the integration time required to achieve a signal-to-noise ratio of 5. The count rate from the source is 0.113 counts/s distributed over about 25 pixels using the information in [Chapter 14](#). If we assume the background to be “typical high” ([Table 6.3](#)), the count rate due to the background integrated over the bandpass is ~ 0.15 counts/s/pix or 3.8 counts/s in 25 pixels (and the detector dark rate is 35 times lower). We will need to be able to robustly distinguish cosmic rays if we are looking for faint sources, so we will use `CR-SPLIT=4`. We use the [STIS ETC](#) to estimate the required exposure time to be 8548 seconds. To reproduce the numbers given by the [ETC](#), we use the equation in [Section 6.4.1](#):

$$SN = 5 = \frac{0.113 \times 8548}{\sqrt{0.113 \times 8548 + 0.15 \times 25 \times 8548 + 0.0045 \times 25 \times 8548 + 25 \times 29 \times 4}}.$$

Alternately, we could have requested `LOW-SKY` (see [Section 6.5.2](#)), since these observations are sky-background limited. In that case the sky background integrated over the bandpass produces ~ 0.035 counts/s/pix to which we add the detector dark current to get a total background of 0.039 counts/s/pix. Using the full equation for exposure time again, we then determine that we require only ~ 60 minutes. This option is preferable to perform this experiment. To check the S/N, we use the equation in [Section 6.4.1](#):

$$SN = 5 = \frac{0.113 \times 3645}{\sqrt{(0.113 \times 3645) + (0.035 \times 25 \times 3645) + (0.0045 \times 25 \times 3645) + (25 \times 29 \times 4)}}.$$

6.8.6 Time-Tag Observations of a Flare Star (AU Mic)

Suppose the aim is to do `TIME-TAG` observations of a flare star such as AU Mic, in the hydrogen Lyman- α 1216 Å line (see [Section 11.1.3](#)). We wish to observe it with the G140M grating, the MAMA detector and a 0.2 arcsecond slit. AU Mic has $V = 8.75$, the intensity of its Ly- α line is about $6 (\pm 3) \times 10^{-12}$ erg/s/cm²/Å, and the width (FWHM) of the line is about $0.7 (\pm 0.2)$ Å. We will assume that during bursts, the flux might vary by a factor of 10, so that the line flux may be up to 60×10^{-12} erg/cm²/s/Å.

AU Mic is an M star and its UV continuum is weak and can be neglected.

We use from [Chapter 13](#):

- $S_{\lambda}^d = 2.30 \times 10^{12}$ counts/s/pix _{λ} per incident erg/s/cm²/Å;
- Aperture throughput $T_A = 0.6$;
- Encircled energy $\epsilon_f = 0.8$;
- $N_{spix} = 10$;
- Derive $N_{\lambda pix} = 14$ since the line FWHM is ~ 0.7 Å and the dispersive plate scale for G140M is 0.05 Å/pix;

Plugging these values into the point source equation in [Section 6.2.1](#), we get $C = 927$ counts/s over 10×14 pixels, or ~ 1160 counts/s from the source during a burst (taking $\epsilon_f = 1.0$). This is well below the MAMA `TIME-TAG` global linearity limit of 30,000 counts/s and the continuous observing limit of 26,000 count/s. The line is spread over 14 pixels in dispersion and roughly only 10% of the flux in the dispersion direction falls in the peak pixel; thus the peak per-pixel count rate, P_{cr} , is roughly $927/(14 \times 10) = 7$ counts/s/pix, and we are not near the MAMA local linearity limit.

For a `TIME-TAG` exposure, we need to determine our maximum allowed total observation time, which is given by $6.0 \times 10^7/C$ seconds or roughly 1079 minutes = 18 hours. For Phase II only, we will also need to compute the value of the `BUFFER-TIME` parameter, which is the time in seconds to reach 2×10^6 counts, in this case 2157 seconds (= $2 \times 10^6/927$).

Chapter 7: Feasibility and Detector Performance

Chapter Contents

- [7.1 STIS Detectors](#)
- [7.2 The CCD](#)
- [7.3 CCD Operation and Feasibility Considerations](#)
- [7.4 The MAMA Detectors](#)
- [7.5 MAMA Operation and Feasibility Considerations](#)
- [7.6 MAMA Spectral and Spatial Offsetting](#)
- [7.7 MAMA Bright Object Limits](#)

7.1 STIS Detectors

STIS employs two fundamentally different types of detectors: an ultraviolet (UV)-optimized CCD for use from the near-UV (NUV) to the near-infrared (NIR), and Multi-Anode Microchannel Array detectors, known as MAMAs, for use in the UV. The CCD and the MAMA detectors are used in different ways and impose their own unique limitations on the feasibility of observations performed with them. Below, we present the properties of the STIS detectors, describe how to use them to optimize scientific programs, and list the steps you should take to ensure the feasibility of your observations.

7.2 The CCD

- 7.2.1 Detector Properties
- 7.2.2 Effects of the Change to STIS Side-2 Electronics on CCD Performance
- 7.2.3 STIS CCD Performance After Repair During SM4
- 7.2.4 CCD Spectral Response
- 7.2.5 CCD Sensitivity
- 7.2.6 CCD Long Wavelength Fringing
- 7.2.7 Fringing Due to the Order Sorter Filters
- 7.2.8 Optical Performance
- 7.2.9 Readout Format
- 7.2.10 Analog-to-Digital Conversion: Selecting the CCDGAIN
- 7.2.11 Long-term Rotational Drift

7.2.1 Detector Properties

The STIS CCD is a low-noise device capable of high sensitivity in the visible and the NUV. It is a thinned, backside-illuminated device manufactured by Scientific Imaging Technologies (SITe). In order to provide NUV imaging performance, the CCD was backside-treated and coated with a wide-band anti-reflectance coating. The process produces acceptable NUV quantum efficiency (QE) without compromising the high QE of the visible bandpass. The CCD camera design incorporates a warm dewar window, designed to prevent buildup of contaminants on the window, which were found to cause a loss of UV throughput for the WFPC2 CCDs. A summary of the STIS CCD performance is given in [Table 7.1](#). Read noise and dark current values are based on data taken in Cycle 30. See the [STIS website](#) for further updates.

Table 7.1: CCD Detector Performance Characteristics.

| Characteristic | CCD Performance |
|--------------------|--|
| Architecture | Thinned, backside illuminated |
| Wavelength range | 1640–10,300 Å |
| Pixel format | 1024 × 1024 illuminated pixels |
| Field of view | 52 × 52 arcseconds ² |
| Pixel size | 21 × 21 micrometers ² |
| Pixel plate scale | 0.05078 arcseconds |
| Quantum efficiency | ~20% @ 3000 Å ~67% @ 6000 Å ~29% @ 9000 Å |
| Dark count rate | 0.029 e ⁻ /s/ pix (but varies with detector temperature and Y-position) |

| | |
|--|--|
| Read noise (Amp D) (effective values) | 6.2 e ⁻ rms at GAIN=1 (1 e ⁻ of which is pattern noise) 8.7 e ⁻ rms at GAIN=4 (0.2 e ⁻ of which is pattern noise) |
| Full well | 128,000 e ⁻ over the inner portion of the detector 108,000 e ⁻ over the outer portion of the detector |
| Saturation limit | 33,000 e ⁻ at GAIN=1 130,000 e ⁻ at GAIN=4 (varies slightly over detector) |

7.2.2 Effects of the Change to STIS Side-2 Electronics on CCD Performance

In May 2001, the primary Side-1 electronics on STIS failed. Operations were subsequently resumed using the backup Side-2 electronics. CCD observations have been affected in two ways.

First, the Side-2 electronics do not have a working CCD temperature controller, and the detector can no longer be held at a fixed temperature. As a result, the CCD dark current now fluctuates with the detector temperature. Fortunately, the dark current variation correlates with the CCD housing temperature. The dark current scales with housing temperature at a rate between 5% and 10%/°C, depending upon the individual pixel and when the exposure was taken in the lifetime of STIS. This is approximated by a 7%/°C correction. Further details are given in [STIS ISR 2001-03](#), [STIS ISR 2018-05](#), and references therein. All reference file dark images prepared for use with STIS/CCD data taken during Side-2 operations are now scaled to a standard housing temperature of 18°C before being delivered. Before subtraction of the appropriate dark file from Side-2 CCD data, the `calstis` package rescales the dark using the CCD housing temperature value in the `OCCDHTAV` keyword which is found in the extension header of each sub-exposure.

The second change is an increase in the read noise by about 1 electron when `CCDGAIN=1` and by 0.2 electrons when `CCDGAIN=4`. This extra read noise appears in the form of coherent pattern noise, and under some circumstances it may be possible to reduce this noise by using Fourier filtering techniques. A discussion of this can be found in [STIS ISR 2001-05](#) and the astronomical community has produced other methods of subtracting out this noise (see the conference proceeding from the *HST* Calibration Workshop on [Autofilet.pro](#) as well as the [original Autofilet code](#)).

7.2.3 STIS CCD Performance After Repair During SM4

The repair made during SM4 restored the Side-2 electronics to operation; the failure that had affected Side-1 electronics was not accessible, and the Side-1 electronics remain inoperative. As a result, the changes to CCD operations introduced by the switch to the Side-2 electronics, including both the inability to actively control the CCD chip temperature and the extra coherent pattern noise discussed above, continue to affect STIS operations after the repair. For additional information please see [STIS ISR 2009-02](#).

Changes in CCD Read Noise

The coherent pattern noise appears to be unchanged in its amplitude and behavior, however, the overall read noise of the STIS CCD has increased after the repair. During the period of Side-2 operations, the mean read noise measured using the default readout amplifier with `CCDGAIN=1` was 5.44 electrons; in the months after SM4 and during Cycle 17 calibrations the mean was 5.62 electrons. For `CCDGAIN=4`, the read noise increased from 7.6 electrons to 8.0 electrons. Similar increases in read noise were seen in the three other STIS CCD amplifiers.

A further increase in the Amp D read noise was seen on May 15, 2014. After this date the `CCDGAIN=1` read noise was 6.2 electrons, and that for `CCDGAIN=4` was 8.5 electrons. (Amps A and C appear to have been unaffected at this time.) This increase is thought to have been caused by radiation damage early in the Amp D signal chain electronics. In September of 2016, Amp C showed an increase by ~7% and has remained steady at this new readnoise value. Additional increases of this type are possible, and the read noise is monitored on a regular basis. Amp D continues to show the lowest read noise among the four amplifiers; it remains the default amplifier and is used for all GO science exposures.

Increasing Effects of Radiation Damage

During the period that it was inoperative, the STIS CCD continued to accumulate radiation damage. This resulted in increasing dark current ([Section 7.3.1](#)), a larger number of hot pixels ([Section 7.3.5](#)), and decreasing charge-transfer efficiency ([Section 7.3.7](#)). Such degradation affects all CCDs in a space environment and was expected.

7.2.4 CCD Spectral Response

The spectral response of the unfiltered CCD is shown in [Figure 5.1](#) (labeled as 50CCD). This figure illustrates the extremely wide bandpass over which this CCD can operate. The wide wavelength coverage is an advantage for deep optical imaging (although the Advanced Camera for Surveys and the Wide Field Camera 3 are better suited to most optical imaging programs). The NUV sensitivity of the CCD makes it a good alternative to the `NUV-MAMA` for low- and intermediate-resolution spectroscopy from ~1700 to 3100 Å using the `G230LB` and `G230MB` grating modes ([Table 4.1](#)).

Based on data to date, the STIS CCD does not suffer from Quantum Efficiency Hysteresis (QEH)—that is, the CCD responds in the same way to light levels over its whole dynamic range, irrespective of the previous illumination level.

7.2.5 CCD Sensitivity

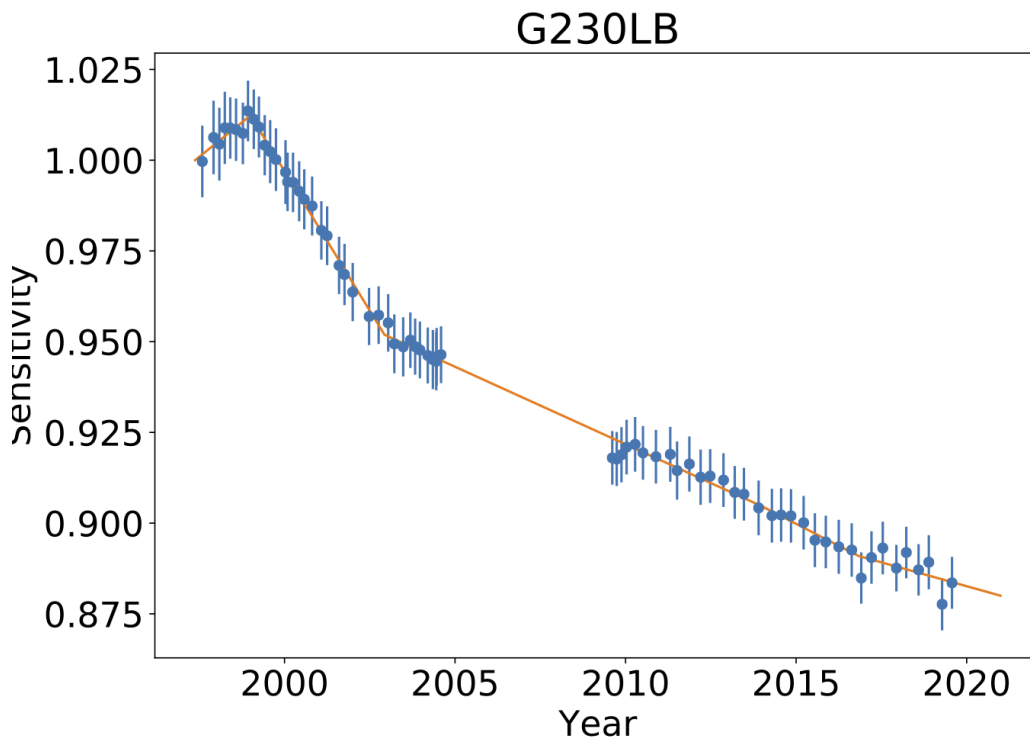
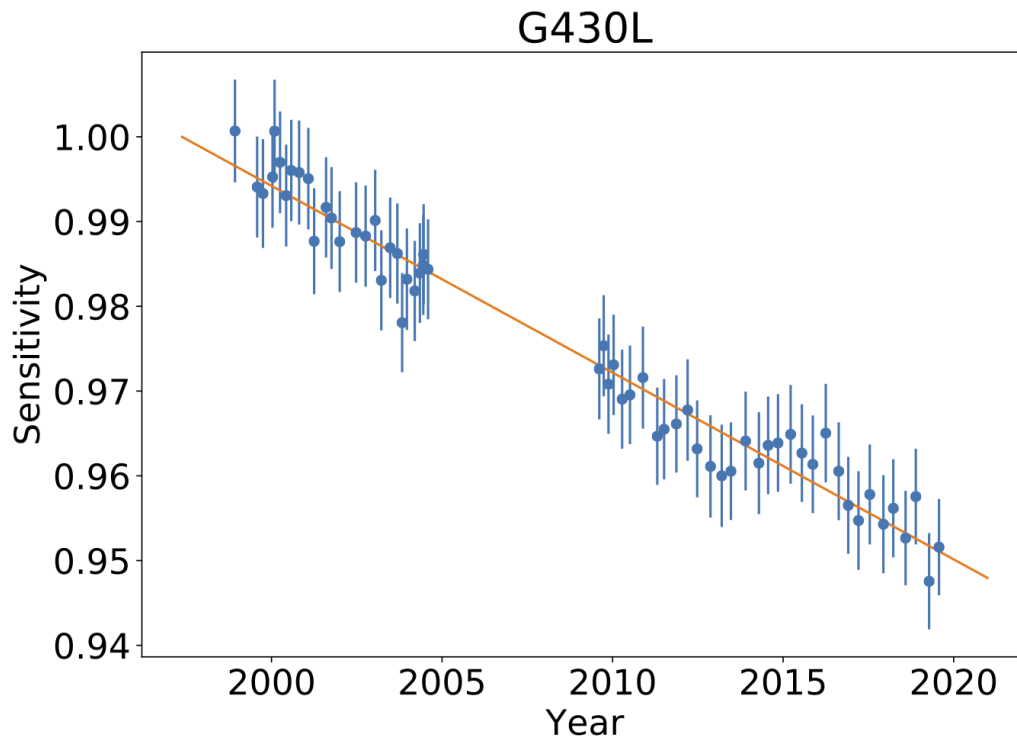
Sensitivity variations in CCD spectroscopic configurations are due primarily to increasing charge-transfer efficiency (CTE) losses (see [Section 7.3.7](#)), temperature fluctuations since the switch to the Side-2 electronics (see [Section 7.2.2](#)), and actual time-dependent changes in sensitivity. For a more detailed analysis of the STIS Sensitivity Monitor observations from 1997 through March 2004 please refer to [STIS ISR 2004-04](#). Sensitivity monitor measurements collected between March 2004 and STIS failure in August 2004 are consistent with the trends reported in this ISR.

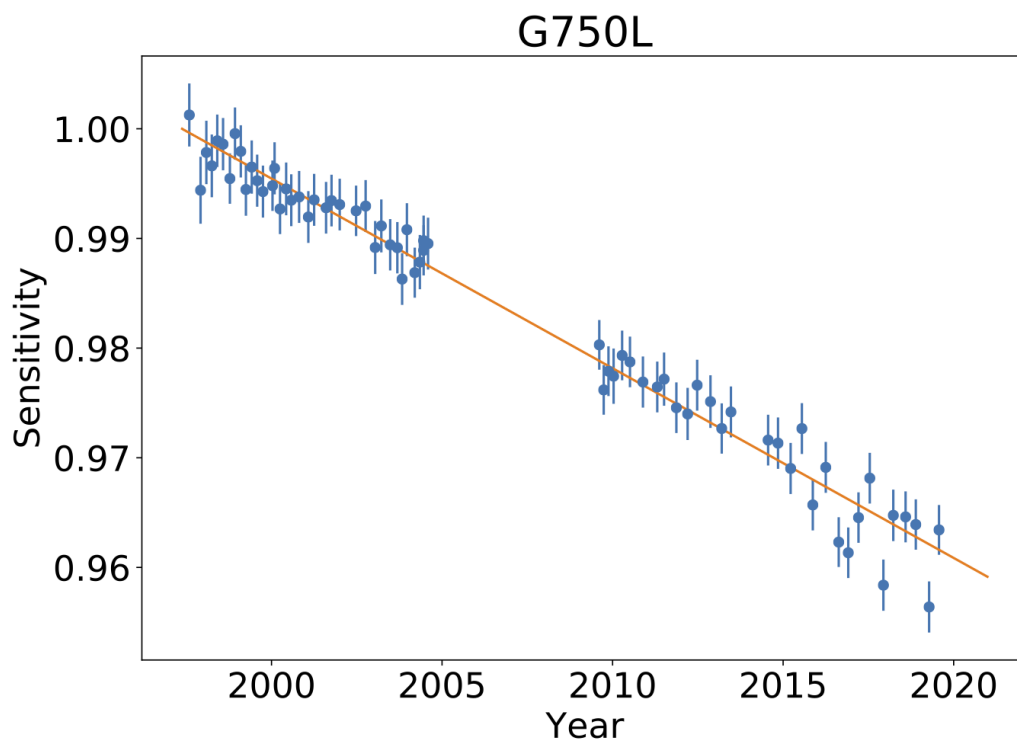
Since the switch to Side-2 operations, a linear trend of the sensitivity with temperature has been found for all first-order modes. The Side-2 dependencies pre-SM4 are +0.33, +0.20, and +0.05%/°C for G230LB, G430L, and G750L, respectively (see [STIS ISR 2009-02](#)). Note that, on Side-2, the CCD detector temperature cannot be measured directly, and so the CCD housing temperature is used as a surrogate.

Trends for time-dependent sensitivity (TDS) for the CCD low-resolution (L) modes are shown in [Figure 7.1](#). Sensitivities measured after SM4 are consistent with an extrapolation of the trends seen before the 2004 failure. Consistent with pre-failure trends, the sensitivity demonstrates a temperature dependence of +0.32, +0.21, and +0.06%/°C for G230LB, G430L, and G750L, respectively (see [STIS ISR 2014-02](#)). Selected wavelength settings of the medium-resolution (M) gratings G230MB, G430M, and G750M have also been monitored. Sensitivity trends measured for the limited M-mode wavelength coverage are similar to those observed in the L-modes at corresponding wavelengths. The G230LB and G230MB CCD configurations exhibit behavior similar to that found for the NUV-MAMA G230L mode (see [Section 7.4.3](#)), featuring an increase in sensitivity during the first 1.5 years of STIS operations, followed by decreasing sensitivity, with a slow-down in the decline beginning in early 2002 (see [Figure 7.15](#)).

TDS corrections for all CCD modes have been implemented into the STIS pipeline as new TDSTAB reference files (see [Section 15.1](#)) and will correct fluxes of extracted spectra for sensitivity changes to a typical accuracy of 1% or better. CTE corrections have also been implemented (see [Section 7.3.7](#)). These new TDS trends have also been incorporated into reference files used by [Astropy's synphot](#) and the [STIS ETCs](#). This enables count rate predictions to take the sensitivity changes into account. The default TDS throughputs for [synphot](#), and [STIS ETC](#) calculations are extrapolated to their values for a date of April 2023.

Figure 7.1: Relative Sensitivity vs. Time for First-Order CCD L-Modes G230LB, G430L, and G750L.





7.2.6 CCD Long Wavelength Fringing

Like most CCDs, the STIS CCD exhibits fringing in the red, longward of $\sim 7500 \text{ \AA}$. This fringing limits the signal-to-noise routinely achievable in the red and NIR unless contemporaneous fringe flats are obtained (see below). In principle, fringing can also affect imaging observations if the source's emission over the 50CCD or F28X50LP bandpass is dominated by emission lines redward of 7500 \AA . However, if the bulk of the emission comes from blueward of 7500 \AA , then emission from multiple wavelengths will smooth over the fringe pattern so that imaging will not be affected by fringing.

The amplitude of the fringes is a strong function of wavelength and spectral resolution. [Table 7.2](#) lists the observed percentile peak-to-peak and rms amplitudes of the fringes as a function of central wavelength for the G750M and G750L gratings. The listed "peak-to-peak" amplitudes are the best measure of the impact of the fringing on your data. The rms values at wavelengths $< 7000 \text{ \AA}$ give a good indication of the counting statistics in the flat-field images used for this analysis.

Table 7.2: Fringing Amplitude in Percent as a Function of Wavelength.

| Wavelength (\AA) | G750M peak-to-peak | G750M rms | G750L peak-to-peak | G750L rms |
|-----------------------------|--------------------|-----------|--------------------|-----------|
| 6,100 | — | 1.21 | — | — |
| 6,250 | — | 1.23 | — | — |

| | | | | |
|--------|-------|-------|-------|------|
| 6,600 | — | 1.23 | — | — |
| 6,750 | — | 1.29 | — | — |
| 7,250 | 4.62 | 1.52 | 3.18 | 2.13 |
| 7,750 | 9.61 | 3.10 | 8.58 | 3.08 |
| 8,250 | 10.53 | 3.26 | 6.76 | 2.80 |
| 8,750 | 14.83 | 3.85 | 10.81 | 3.98 |
| 9,250 | 27.16 | 9.00 | 23.42 | 7.92 |
| 9,750 | 32.09 | 10.78 | 25.35 | 8.96 |
| 10,250 | 18.23 | 6.04 | 17.30 | 5.89 |

The fringe pattern can be corrected by rectification with an appropriate flat field. The fringe pattern is a convolution of the contours of constant distance between the front and back surfaces of the CCD and the wavelength of the light on a particular part of the CCD. The fringe pattern has been shown to be very stable, as long as the wavelength of light on a particular part of the CCD stays constant. However, due to the grating wheel positioning uncertainty ([Section Slit and Grating Wheels](#)) and the effect of temperature drifts in orbit, the wavelength on a particular part of the CCD will vary from observation to observation. Thus, the best de-fringing results are obtained by using a contemporaneous flat ("fringe flat"), i.e., a tungsten lamp flat taken at the same grating wheel setting and during the same orbit as your scientific exposures.

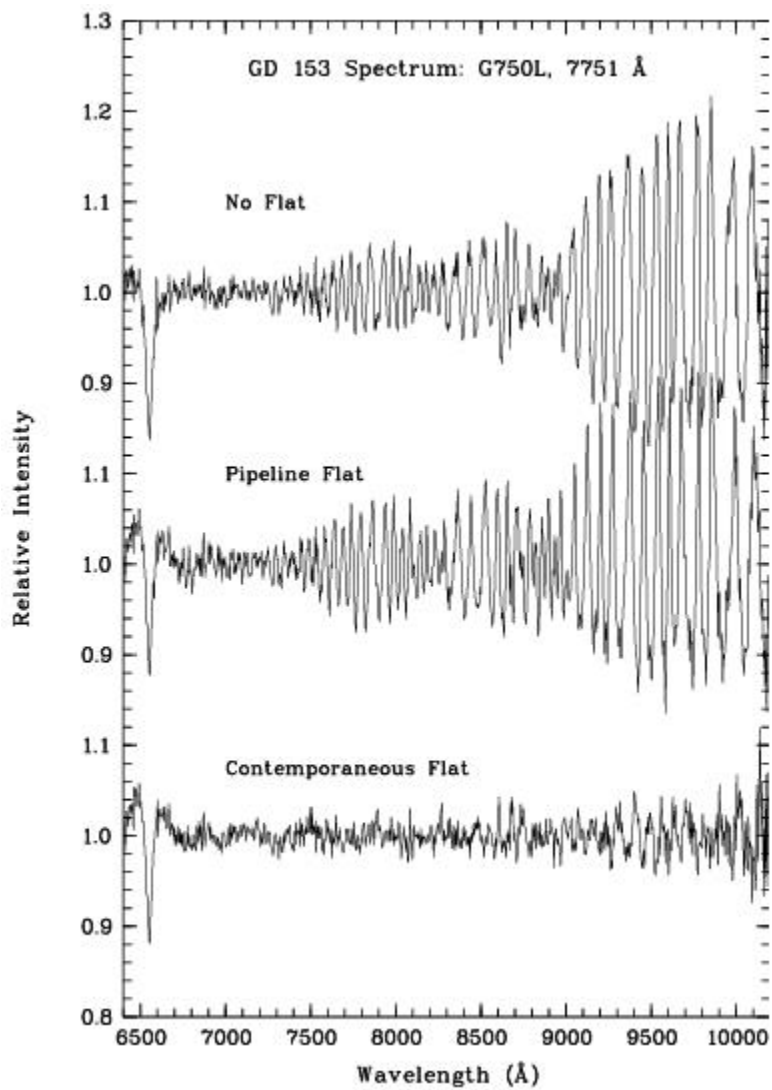
[Table 7.3](#) compares the estimated peak-to-peak fringe amplitudes *after* flat-fielding by the library flat and those after flat fielding with an appropriately processed contemporaneous flat. These estimates are based upon actual measurements of spectra of both point sources and extended sources made during Cycle 7 (the results for point sources and extended sources were essentially the same). [Figure 7.2](#) shows such a comparison for a G750L spectrum of a white dwarf; in this figure, the top panel shows white dwarf GD153 (central wavelength 7751 Å) with no flat-field correction, the second spectrum shows the result of de-fringing with the standard pipeline flat field, and the third spectrum shows the result of de-fringing with a contemporaneous flat (all spectra were divided by a smooth spline fit to the stellar continuum). It is clear that a contemporaneous flat provides a great improvement over the use of a library flat. Therefore, if you are observing in the far red (>7500 Å) and using grating G750L or G750M, you should take a contemporaneous flat field along with your scientific observations. More detailed information and analysis on fringe correction for STIS long-wavelength spectra can be found in [STIS ISR 1998-19](#) and [STIS ISR 1998-29](#). Tips for defringing spectra can be found in the [July 2021 STAN](#) and includes references and examples for using the new STIS Python package [defringe](#)."

Table 7.3: Residual Fringe Amplitude (rms, in percent) after Flat-Fielding with Library Pipeline Flat and a Contemporaneous Flat.

| Wavelength (Å) | G750M, library flat: residual | G750M, contemp. flat: residual ¹ | G750L, library flat: residual | G750L, contemp. flat: residual |
|----------------|-------------------------------|---|-------------------------------|--------------------------------|
| 7,500 | 3.0 | 1.2 | 4.0 | 0.9 |
| 7,750 | 2.5 | 1.3 | 5.3 | 0.8 |
| 8,000 | 4.2 | 1.3 | 7.5 | 1.0 |
| 8,250 | 4 | 1.0 | 5.3 | 0.9 |
| 8,500 | 5 | 0.9 | 8.3 | 1.0 |
| 8,750 | 6 | 0.9 | 6.5 | 0.9 |
| 9,000 | 8 | — | 8.3 | 1.0 |
| 9,250 | 10 | — | 17.5 | 1.4 |
| 9,500 | 11 | — | 18.7 | 2.0 |
| 9,750 | 12 | — | 19.7 | 2.4 |
| 10,000 | 10 | — | 11.7 | 2.4 |

¹ Measurements of the fringe amplitude have not been made yet for G750M wavelength settings redward of 8561 Å. However, from our experience with fringe corrections we expect the residual fringe amplitudes to be of order 1% when contemporaneous fringe flats are used.

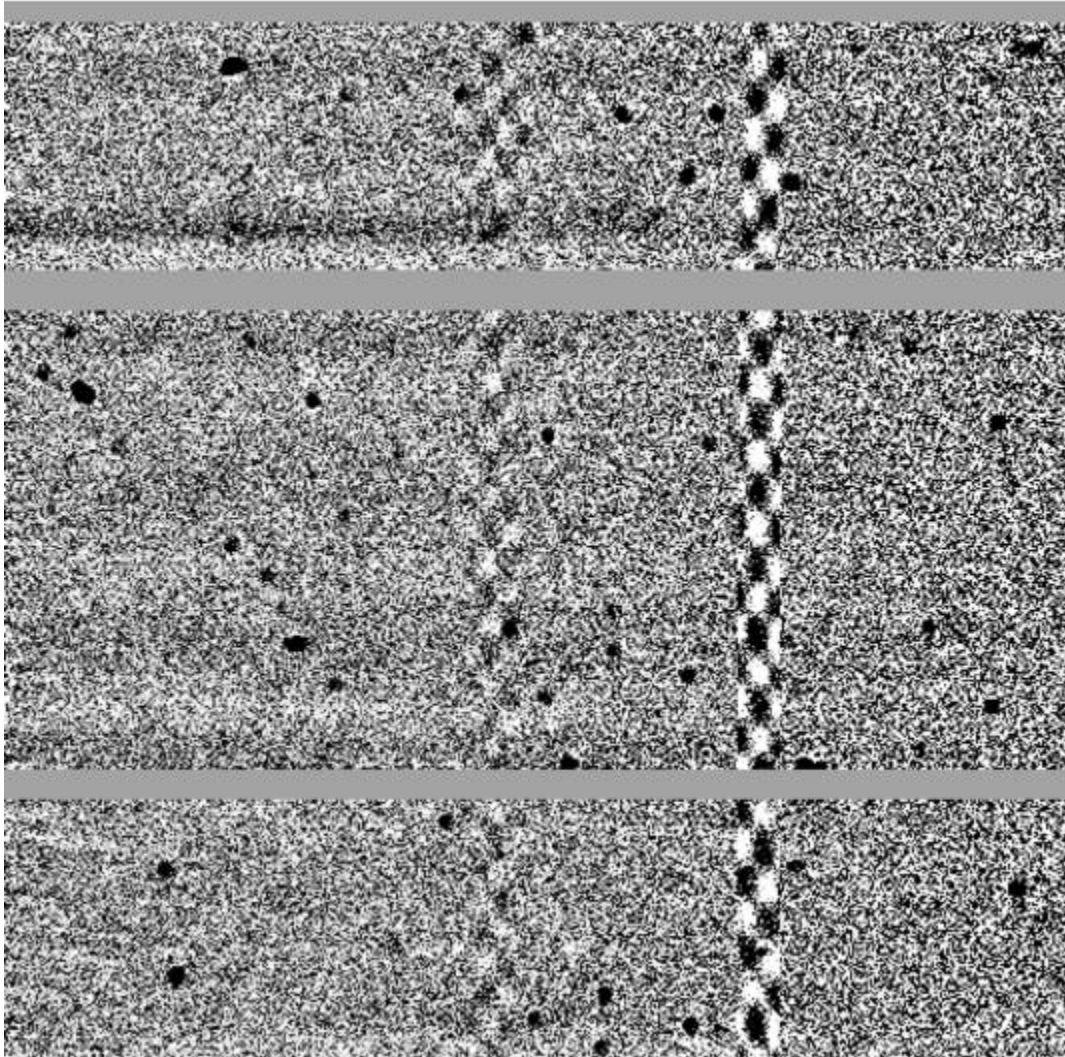
Figure 7.2: Comparison of De-fringing Capabilities of Reference File Flats and Those of Contemporaneous Flats.



7.2.7 Fringing Due to the Order Sorter Filters

Examination of long slit observations in the CCD spectroscopic modes has revealed periodic variations of intensity along the slit when highly monochromatic, calibration lamp sources are used. An example of such "chevron-pattern" variations is shown in [Figure 7.3](#) and [Figure 7.4](#). These variations are thought to be the result of transmission variations through the highly parallel faces of the order sorting filters that are situated next to the gratings in the optical path. In the cross dispersion direction, the modulation amplitude depends on the line width with a maximum of 13% for a monochromatic source in G430L and G430M modes, and 4.5% in G750L and G750M modes. Periods range from 40–80 pix/cycle. In the dispersion direction, there is a small, residual, high-frequency modulation with a peak amplitude of about 1.5% in G430M at the 5471 Å setting and with smaller amplitudes in all other modes and settings. No such modulation has been observed in any of the MAMA modes. Some modulation is also apparent in the CCD G230LB and G230MB modes, however the amplitudes of these modulations are much smaller.

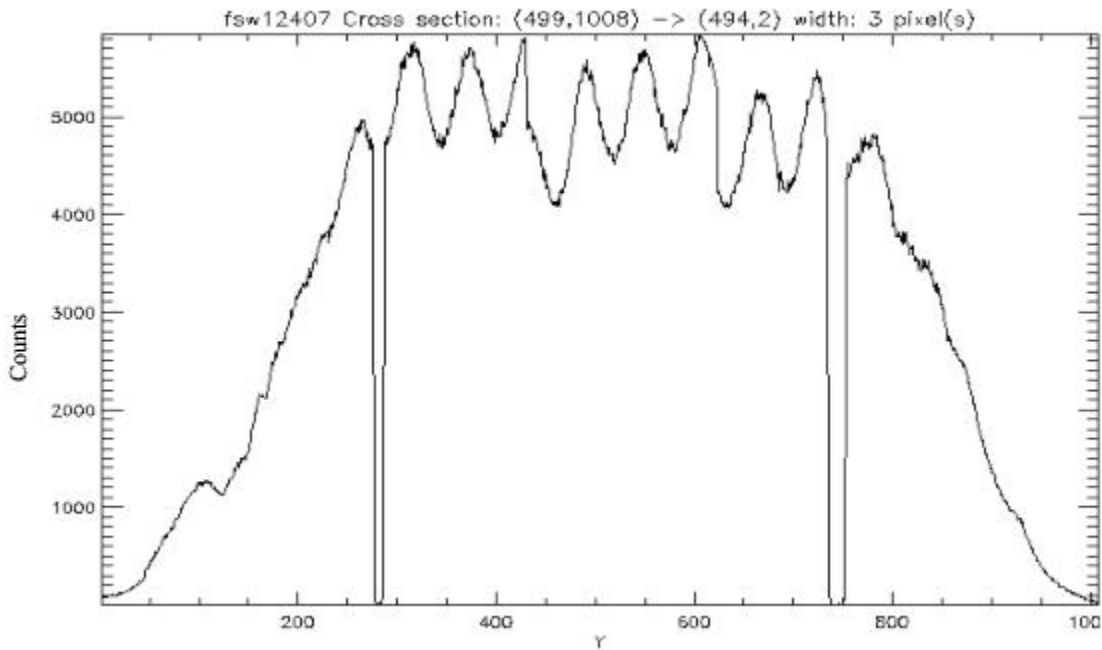
Figure 7.3: An Example of the "Chevron Pattern" Variations.



CCD image of a calibration lamp exposure which shows the chevron-pattern variations. The image is taken with the G430L grating and a 2 arcsecond slit. The chevron patterns are seen at the position of the emission lines.

It should be noted that this effect is pronounced only for monochromatic sources; the modulation is negligible for continuum sources. So far, such modulation has not been observed in any astronomical observations. A calibration program would be necessary to investigate this effect further.

Figure 7.4: The 52X0.2 Slit Illumination Near 4269Å in Mode G430L Obtained with the Pt-Cr /Ne Calibration Lamp.



7.2.8 Optical Performance

Verification testing has shown that STIS meets its image-quality specifications. While the optics provide fine images at the focal plane, the detected point-spread functions (PSFs) are degraded somewhat more than expected by the CCD at wavelengths longward of about 7500 Å, where a broad halo appears, surrounding the PSF core. This halo is believed to be due to scatter within the CCD mounting substrate, which becomes more pronounced as the silicon transparency increases at long wavelengths. The effects of the red halo (see Figure 7.5), which extend to radii greater than 100 pixels (5 arcseconds), are not included in the encircled energies as a function of observing wavelength that are described for the CCD spectroscopic and imaging modes in Chapter 13 and 14, respectively. However, estimates of the encircled energy vs. radius that include the halo are shown in Table 7.4. The integrated energy in the halo amounts to approximately 20% of the total at 8050 Å and 30% at 9050 Å (see also STIS ISR 1997-13 for the implication for long-slit spectroscopic observations at long wavelengths). Note that the ACS WFC CCDs have a front-side metallization that reduces the large angle long wavelength halo problem in those detectors. This problem has been eliminated from the WFC3 CCD.

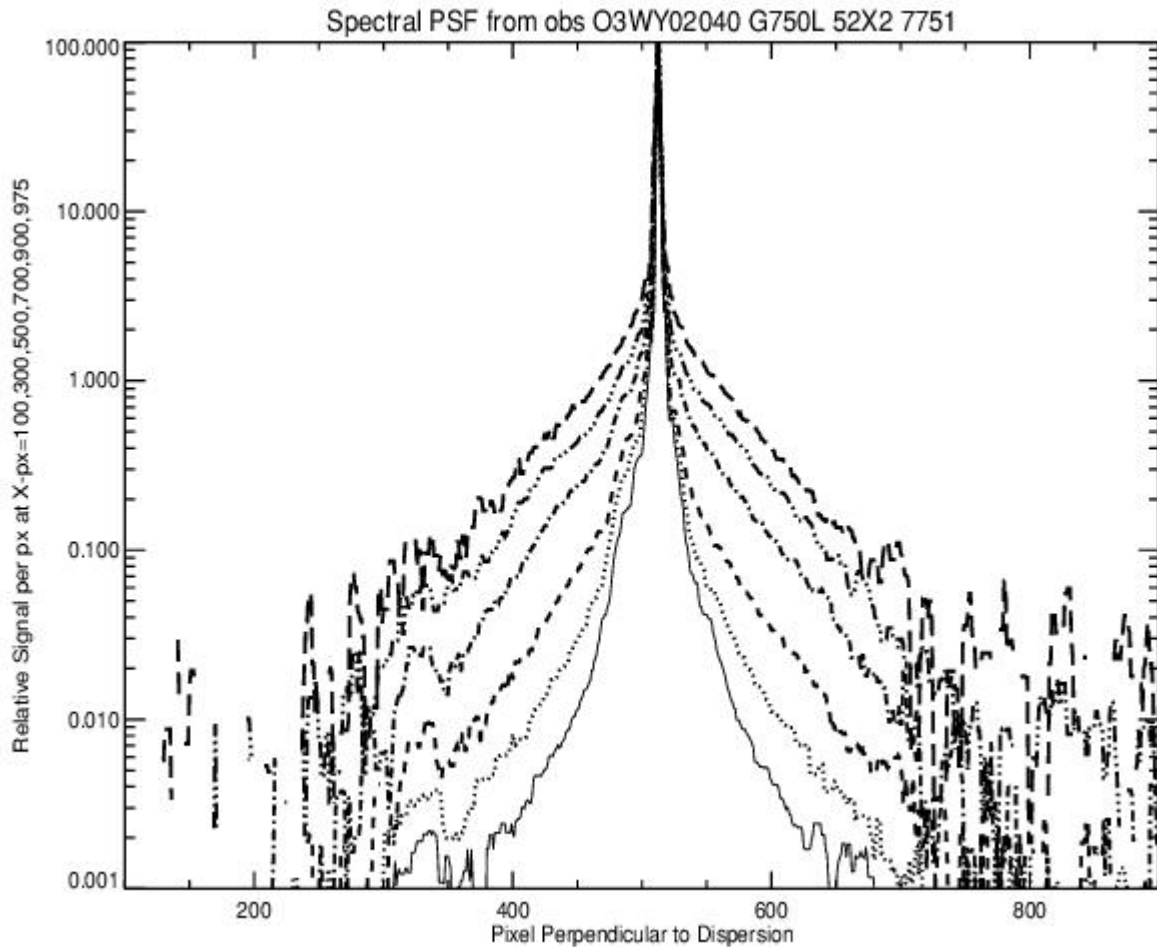
Table 7.4: Model of Encircled Energy Fraction as a Function of Wavelength for STIS CCD Imaging.

| λ (Å) | Fraction in Central Pixel | Aperture Radius in Pixels | | | | | | | |
|------------------|------------------------------|---------------------------|-------|-------|-------|-------|-------|-------|-------|
| | | 2 | 5 | 10 | 15 | 19.7 | 39.4 | 59 | 118 |
| 1,750 | 0.246 | 0.667 | 0.873 | 0.949 | 0.979 | 0.990 | 0.998 | 1.000 | 1.000 |
| 3,740 | 0.283 | 0.704 | 0.857 | 0.920 | 0.945 | 0.960 | 0.994 | 0.999 | 1.000 |

| | | | | | | | | | |
|--------|-------|-------|-------|-------|-------|-------|-------|-------|-------|
| 5,007 | 0.253 | 0.679 | 0.857 | 0.916 | 0.934 | 0.948 | 0.985 | 0.997 | 1.000 |
| 6,500 | 0.214 | 0.597 | 0.865 | 0.902 | 0.927 | 0.942 | 0.966 | 0.975 | 0.992 |
| 7,500 | 0.178 | 0.536 | 0.825 | 0.866 | 0.892 | 0.909 | 0.942 | 0.957 | 0.986 |
| 8,500 | 0.141 | 0.463 | 0.748 | 0.799 | 0.827 | 0.848 | 0.897 | 0.924 | 0.973 |
| 9,500 | 0.100 | 0.342 | 0.607 | 0.672 | 0.705 | 0.733 | 0.809 | 0.857 | 0.946 |
| 10,000 | 0.080 | 0.275 | 0.518 | 0.589 | 0.624 | 0.655 | 0.748 | 0.810 | 0.926 |
| 10,500 | 0.064 | 0.238 | 0.447 | 0.517 | 0.553 | 0.585 | 0.690 | 0.764 | 0.907 |

The CCD plate scale is 0.05072 arcsec/pix for imaging observations (see [STIS ISR 2001-02](#)), and in the spatial (across the dispersion) direction for spectroscopic observations. Due to the effect of anamorphic magnification, for spectroscopic observations the plate scale in the dispersion direction is slightly different and it depends on the grating used and its tilt. The plate scale in the dispersion direction ranges from 0.0512 to 0.0581 arcsec/pix (see [STIS ISR 1998-23](#)).

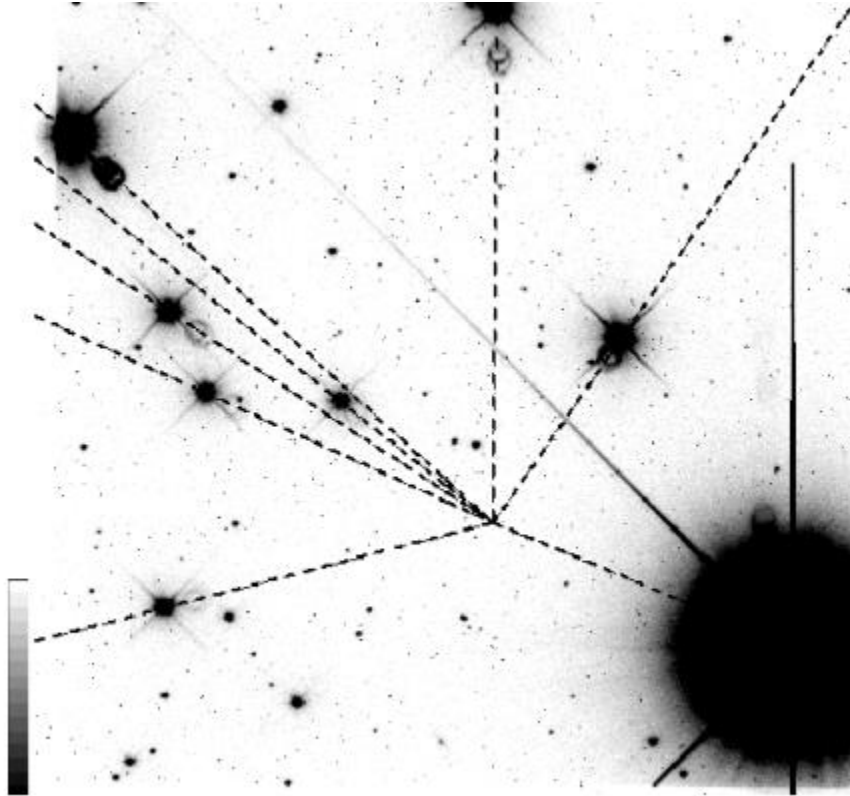
Figure 7.5: The Red Halo.



Cross-sections of the signal distribution perpendicular to the dispersion direction for G750L, at six wavelengths from 5752 Å to 10020 Å. Each PSF is normalized to a peak value of 100. The strong wavelength dependence of the PSF provides a clean separation of the curves.

The CCD detector produces a relatively faint, out-of-focus, ring-shaped "ghost" image, due to specular reflection from the CCD surface and window. The ring contains about 1% of the total energy in the image and is very stable. Additional rings of similar size can be seen at other locations in the field in grossly saturated images, but these contain only of order 10^{-5} of the total energy and are thus not likely to be detected in normal scientific images. Lines drawn from stars in images through their respective ghosts are found to converge at a "radiant point" located to the lower right of the image center. This effect is illustrated in Figure 7.6 where the line segments are drawn from pixel coordinates (528, 342) (in 1024×1024 user coordinates) through the centroids of the brightest stars in the image. Note that these line segments intercept the centers of the ring-like ghosts very well. Observers who wish to avoid placing very faint objects within the range of the ghosts may want to take this geometry into account when writing Phase II submissions.

Figure 7.6: Ring-Shaped Ghost Images Near Bright Point Sources (50CCD Image).



7.2.9 Readout Format

A full detector readout is 1062×1044 pixels including physical and virtual overscans. Scientific data are obtained on 1024×1024 pixels, each projecting to $\sim 0.05 \times 0.05$ arcseconds on the sky. For spectroscopic observations, the dispersion axis runs along `AXIS1` (image X or along a row of the CCD), and the spatial axis of the slits runs along `AXIS2` (image Y or along a column of the CCD). The CCD supports the use of subarrays to read out only a portion of the detector, and on-chip binning. For more details see [Section 11.1.1](#).

7.2.10 Analog-to-Digital Conversion: Selecting the `CCDGAIN`

Electrons that accumulate in the CCD wells are read out and converted to data numbers (DN, the format of the output image) by the analog-to-digital converter at a default `CCDGAIN` of $1 \text{ e}^-/\text{DN}$ (i.e., every electron registers 1 DN). The CCD is also capable of operating at a gain of $4 \text{ e}^-/\text{DN}$ ¹. The analog-to-digital converter operates at 16 bits, producing a maximum of 65,536 DN/pix. This is not a limitation at either gain setting, because other factors set the maximum observable DN to lower levels in each case (see [Section 7.3.2](#)).

The CCDGAIN=1 setting has the lower read noise ([Table 7.1](#)) and digitization noise. Although the read noise has increased since the switch to the Side-2 electronics in July 2001 (see [Section 7.2.2](#)), CCDGAIN=1 is still the most appropriate setting for observations of faint sources. However, saturation occurs at about 33,000 e⁻ at the CCDGAIN=1 setting (as described in [Section 7.3.2](#)).

The CCDGAIN=4 setting allows use of the entire CCD full well of 130,000 e⁻, and use of the CCDGAIN=4 setting is therefore recommended for imaging photometry of objects whenever more than 33,000 e⁻ might be obtained in a single pixel of an individual sub-exposure. However, short exposures taken in CCDGAIN=4 show a large-scale pattern noise ("ripple") that is not removed by the standard bias images. This pattern noise is in addition to the usual coherent noise visible since STIS switched to using the backup Side-2 electronics. [Figure 7.7](#) (a 0.2 second exposure of a lamp-illuminated small slit) shows an example of the CCDGAIN=4 ripple. The peak-to-peak intensities of these ripples vary from near zero to about 1 DN, and there is a large amount of coherence in the noise pattern. This coherence makes background determination difficult and limits the precision of photometry of faint objects in shallow exposures taken using CCDGAIN=4.

The CCD response when using CCDGAIN=4 remains linear even beyond the 130,000 e⁻ full-well limit if one integrates over the pixels bled into ([Section 7.3.2](#)), and for specialized observations needing extremely high S/N, this property may be useful.

Figure 7.7: Ripple Effect in Short Exposures with CCDGAIN=4.



7.2.11 Long-term Rotational Drift

The CCD was shown to have a long-term rotational drift rate of 0.0031 ± 0.0001 degrees/year in a recent study ([STIS ISR 2022-01](#)). This analysis measured rotation of dust motes in 50CCD flat fields spanning 20 years. The results are supported by two more independent studies ([Nguyen et al. 2021](#); [Dressel et al. 2007](#)). At present, no corrections are made to CCD data to account for the long-term rotational evolution of the CCD flat fields.

¹ Measurement of the CCDGAIN=4 to CCDGAIN=1 ratio after SM4 finds that CCDGAIN=4 actually corresponds to $4.087 \pm 0.007 e^-/DN$. See [STIS ISR 2017-05](#).

7.3 CCD Operation and Feasibility Considerations

- 7.3.1 CCD Dark Current
- 7.3.2 CCD Saturation
- 7.3.3 CCD Shutter Effects
- 7.3.4 Cosmic Rays
- 7.3.5 Hot Pixels
- 7.3.6 CCD Bias Subtraction and Amplifier Non-Linearity
- 7.3.7 Charge Transfer Efficiency
- 7.3.8 Mitigation of CTE Loss for Long-Slit Spectroscopy
- 7.3.9 Pixel-Based CTI Corrections for the STIS CCD
- 7.3.10 Ultraviolet Light and the STIS CCD

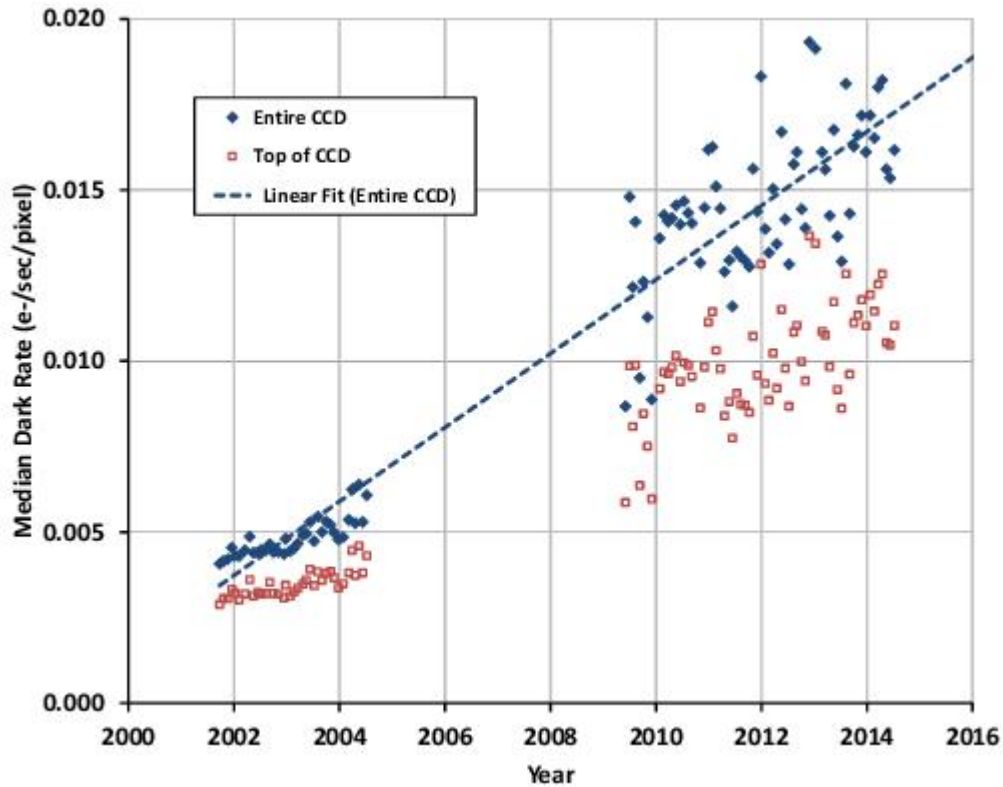
7.3.1 CCD Dark Current

At launch in 1997, the median dark rate (excluding hot pixels) for the STIS CCD was about $0.0015 \text{ e}^-/\text{s}$. The on-orbit environment causes radiation damage which, over time, increases both the dark current and the number of hot pixels. The CCD is annealed once every four weeks by turning off the thermo-electric cooler (TEC) which allows the CCD to warm from its usual operating temperature near -83° C to approximately $+5^\circ \text{ C}$. While this slows the effects of radiation damage it does not eliminate it. By the time that the STIS Side-1 electronics failed in May 2001, the median dark rate had increased to about $0.004 \text{ e}^-/\text{s}$.

As the Side-2 electronics lack a working temperature sensor at the detector itself, the CCD can no longer be maintained at a fixed temperature, and this causes both the temperature of the CCD chip and the dark current to vary as the temperature of the *HST* aft-shroud environment into which the STIS CCD TEC radiates heat changes. This leads to fluctuations of the CCD dark current on short time scales as *HST* changes its orientation with respect to the Sun and Earth and moves in and out of the Earth's shadow, as well as on longer time scales where the heat input can vary due to the annual changes of the Earth's distance from the Sun, the degradation of *HST*'s thermal insulation, and the heat inputs from other *HST* instruments. While the CCD detector temperature can no longer be directly measured, it has been shown that the temperature of the CCD housing (available in the telemetry value OCCDHTAV) can be used as a surrogate for the detector temperature. The dark current scales are observed to increase by between 5% and 10% for each degree increase in housing temperature, depending upon the individual pixel and when the exposure was taken in the lifetime of STIS. This is approximated by a $7\%/^\circ \text{ C}$ correction, (see [STIS ISR 2001-03](#) for additional details).

The combination of radiation damage and the resulting loss of charge transfer efficiency ([Section 7.3.7](#)), also results in a dark current that is no longer distributed uniformly over the detector. The effective dark current is much lower near the top of the detector, close to the readout register. This provides another reason to utilize the E1 aperture positions when observing faint objects (see [Section 7.3.8](#)). The trend for the dark current both at the center of the detector and near the top of the chip at the E1 aperture positions is shown in [Figure 7.8](#). In this figure, all measured dark values have been scaled to a CCD housing temperature of 18° C, which is typical of values observed during September 2009. We expect that the CCD dark current will continue to increase with time and note that the scatter in the dark current values has increased when compared to the scatter in dark current values for darks taken prior to SM4. See [STIS ISR 2012-02](#) for detailed information on the behavior of the CCD dark current after SM4. For use in the [STIS ETC](#) for Cycle 31, we have adopted dark current values of 0.025, 0.030, and 0.036 e⁻/s; these values are the expected values at the detector bottom, middle, and top (near the E1 position) during April 2024.

Figure 7.8: STIS CCD Dark Current History.



The median values (after iterative rejection of hot pixels) of the STIS CCD dark current since the switch to Side-2 electronics are shown for the entire chip and the top of the detector (row 900 near the E1 aperture positions). For this figure, all measurements have been scaled to a CCD housing temperature of 18° C, which is representative of temperatures seen in the Fall of 2009. The dashed line shows a linear fit to data for the entire CCD.

7.3.2 CCD Saturation

There are no hard bright object limits to worry about for CCD observations, because the CCD cannot be damaged by observations of bright sources. However, the CCD pixels do saturate at high accumulated count levels, due to the finite depth of the CCD full well. The level at which the behavior of individual pixels deviates from linearity varies over the surface of the chip. Near the center of the detector, (row 515), this may occur after collecting about 130,000 e-/pixel, while some regions saturate at levels as low as 120,000 e-/pixel. The variation of the CCD full well over the chip occurs because of nonuniformity in the process of boron implantation, which creates the potential wells in this type of CCD. Accumulations up to the full well limit can be observed only in the CCDGAIN=4 setting, as the gain amplifier already saturates at ~33,000 e-/pix in the CCDGAIN=1 setting (see [Section 7.2.10](#)).

Saturation imposes a limit on the product of the count rate and the integration time. Keep the total counts in the *pixels of interest* below the saturation level, either by keeping the exposure time short enough that the limit is not violated in any single integration or by choosing a more appropriate configuration. You can allow saturation to occur in regions of the image over which you do not wish to extract information (e.g., you can allow a star or single emission line to saturate if you are interested in other features). Remember, however, that once the CCD well is over full, charge will bleed along the columns of the CCD so that neighboring pixels (along the slit for spectroscopic observations) will also be affected. Saturation *cannot* be corrected in post-observation data processing.

An interesting workaround for this is described in [Gilliland, Goudfrooij & Kimble, 1999, PASP 111, 1009](#). For $CCDGAIN=4$ the response remains linear up to, and even far beyond saturation if one integrates over the pixels receiving the charge bleed. Because the bleeding is perpendicular to the dispersion direction, for point sources such saturation does not compromise spectral purity. Signal to noise values of $\sim 10,000$ have been demonstrated for saturated data (see [STIS ISR 1999-05](#) for a time series application and [Bohlin & Gilliland, 2004, AJ 127, 3508](#) for a measurement of Vega's absolute flux). This technique is, however, best applied near the center of the detector. Near the top of the detector, (e.g., at the E1 aperture position near row 900), the full well depth of the detector is larger, and this can lead to serial transfer artifacts when too many electrons are read out of a single pixel. For more information see [STIS ISR 2015-06](#).

In [Section 6.2](#), we explained how to determine the peak counts/s/pix expected for your observation. In [Chapter 13](#) for each spectroscopic mode and in [Chapter 14](#) for each imaging mode, we provide plots of exposure time to fill the CCD well versus source flux for each STIS configuration. Lastly, [STIS ETCs](#) are available to ensure that your observations will not saturate sources of interest.

The minimum CCD exposure time is 0.1 seconds, providing a true limit to the brightest source that can be observed *without saturating*.

i For standard applications keep the accumulated e^-/pix per exposure below 120,000 at $CCDGAIN=4$ (determined by the CCD full well), and below 30,000 at $CCDGAIN=1$ (determined by gain amplifier saturation).

7.3.3 CCD Shutter Effects

The STIS CCD camera features a high-speed shutter that eliminates the need for a shutter illumination correction, even at the shortest commandable exposure time of 0.1 seconds. The only two minor drawbacks of using this shortest exposure time are the following: (i) a non-reproducible large-scale variation in intensity of a very low amplitude ($\sim 0.2\%$) which is due to a slight non-uniformity of the shutter speed, and (ii) a mean count rate which is $\sim 3\%$ lower than those of longer exposures, which is due to an inaccuracy of the shutter timing at this setting. These minor effects occur only for the shortest exposure times, and disappear completely for exposure times of 0.3 seconds and longer.

7.3.4 Cosmic Rays

All CCD exposures are affected by cosmic rays. The rate of cosmic ray hits in orbit is very high compared to ground-based observations. The current rate at which pixels are affected by cosmic ray hits is 30.0 (± 3.7) pixels per second for the STIS CCD. To allow removal of cosmic rays in post-observation data processing we recommend that whenever possible, given signal-to-noise constraints, you take two or more exposures in any given CCD configuration (see also [Section 11.2.2](#)). The greater the number of independent exposures, the more robust is the removal of cosmic rays and for very long integrations it is convenient to split the exposure into more than two separate images to avoid coincident cosmic ray hits. As an example, for two 1200 second exposures, about 1250 CCD pixels will be hit in both images and will therefore be unrecoverable. Moreover, since cosmic ray hits typically affect ~ 5 pixels per event, these pixels will not be independently placed, but rather will frequently be adjacent to other unrecoverable pixels. In general, we recommend that individual exposures should not exceed ~ 1000 seconds duration to avoid excessive amounts of uncorrectable cosmic rays in the images. However, observers must balance the benefit of removing cosmic rays against the loss in signal-to-noise that results from the splitting of exposures when in the read noise-limited regime.

In observations of faint sources, particularly for dispersed light exposures, the intrinsic count rates can be very low. The exposure time needed to reach a break-even between the read-out noise and the Poisson noise per pixel associated with the minimal sky background is ~ 15 minutes for imaging in 50CCD mode, and ~ 36 minutes for slitless spectroscopy with G750L. With a dark current of $0.009 \text{ e}^-/\text{s}$ it takes 35 minutes of integration for the Poisson statistics on the detector background to equal the read noise. Therefore, repeated short exposures of faint sources can significantly increase the total noise from added readouts. Selecting the correct number and length of repeated integrations requires a consideration of the trade-off between increased read noise and more robust cosmic ray elimination. The [STIS ETC](#), or the S/N plots in [Chapter 13](#) and [Chapter 14](#), can help you determine whether your observations are in the read noise dominated regime.

i *Be sure to take at least two identical CCD exposures in each configuration to allow removal of cosmic rays in post-observation data processing.*

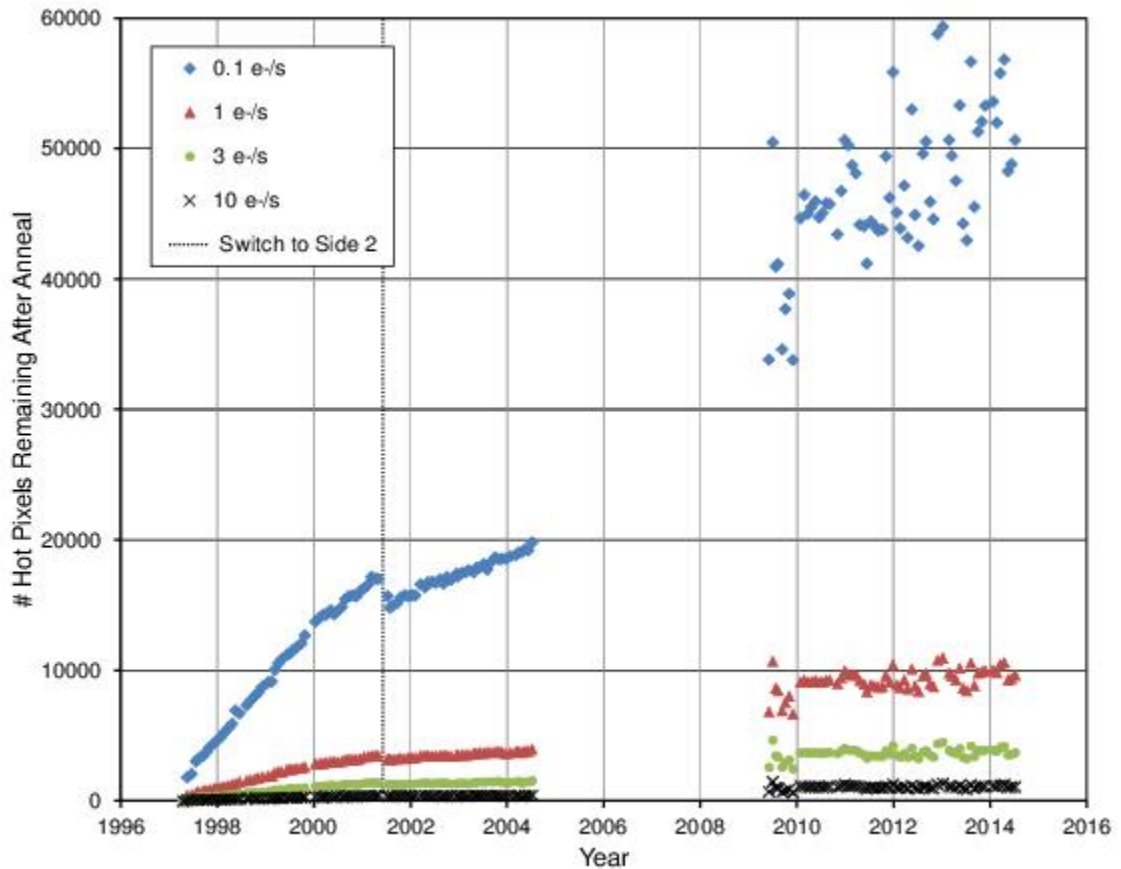
7.3.5 Hot Pixels

Hot pixels, caused by radiation damage, occur in the STIS CCD. Dark frames are routinely obtained twice a day in order to maintain a master list of hot pixels and to update the pipeline superdark reference files on a weekly basis. On a monthly time scale, the CCD is raised to ambient temperature, from its normal operating temperature of $\sim -83^\circ \text{C}$, in order to permit annealing of hot pixels.

Analysis of on-orbit data has shown that the annealing process is successful in slowing the growth rate of transient hot pixels (hotter than $0.1 \text{ e}^-/\text{s}/\text{pix}$) each month. Apart from the transient hot pixels, there is a substantial number of hot pixels that stay persistently hot after anneals. In early 2014, $\sim 5\%$ of the pixels of the STIS CCD were persistently hot, and the total number of hot ($>0.1 \text{ e}^-/\text{s}/\text{pix}$) pixels immediately after an anneal was $\sim 53,000$.

[Figure 7.9](#) illustrates the long-term increase in hot pixel numbers with time. The different symbols indicate numbers of pixels with dark current above each listed threshold immediately after an anneal. The break in the trend near year 2001 reflects the switch to the STIS Side-2 electronics. In this figure, Side-2 darks were scaled to a housing temperature of 18° C, which corresponds to a detector temperature lower than the -83° C set point that was used when the Side-1 electronics were functional. The large scatter seen in data points just before the start of 2010 is due to the fact that STIS had been turned off and on several times during SMOV4. A detailed description of the variation in hot pixel numbers since launch and the differences between the anneal rates while running under Sides 1 and 2 can be found in [STIS ISR 2009-01](#).

Figure 7.9: Hot Pixels Remaining After Each Anneal.



Note that both binned and spectral data will increasingly suffer from the effects of hot pixels as the percentage of non-annealed pixels increases. Just prior to an anneal, up to 4.88% of all CCD pixels are hot, i.e., both persistent and "annealable" hot pixels. In the case of spectral data, with a normal extraction box height of 7 pixels, this means that 34.1% of the extracted pixels will be affected by a hot pixel. For imaging data involving rectification, the rectification process interpolates unrecovered hot pixels into the four adjacent pixels. For the case of $M \times N$ binning, therefore, $4 \times M \times N$ pixels will be affected by a combination of the binning and rectification process.

While post-pipeline calibration using appropriate STIS reference superdarks allows one to subtract most hot pixels correctly (to within the accuracy set by Poisson statistics), the best way to eliminate all hot pixels is by dithering (making pixel-scale positional offsets between individual exposures). Dithering as a method of data taking is described in detail in [Section 11.3](#). A guide on dither strategies and advantages, together with example data is available in the [HST Dither Handbook](#).

7.3.6 CCD Bias Subtraction and Amplifier Non-Linearity

Analysis of CCD images taken during ground calibration and in Cycle 7 has revealed low-level changes in the bias pattern (at the tenths of a DN level) and a low-level amplifier nonlinearity. This non-linearity ("amplifier ringing") was uncovered during the analysis of the overscan region on flat-field images (reported in [STIS ISR 1997-09](#)). The bias value of a given row in the serial overscan region of flat-field images is *depressed* with respect to the nominal bias value by an amount proportional to the mean signal in that row. However, the small proportionality factors and low DN levels at which the nonlinearity occurs render the problem negligible for most STIS scientific applications. Instances of data that may be slightly affected by this problem (at the <1% level) are aperture photometry of faint sources (in imaging mode), especially in the case of a crowded region with nearby bright sources that would cause a local depression of the bias value, and photometry of diffuse extended objects that cover a large number of pixels. The brightest hot pixels (see [Section 7.3.5](#)) also cause a measurable local depression in the bias value, but their effect is corrected by using the appropriate superdark reference file (or daily dark file) during CCD calibration.

Observers taking full-frame CCD images obtain both physical overscan (i.e., actual CCD pixels; columns 1-19 and 1016-1062 on the raw image) and virtual overscan (i.e., added electronically to the image; rows 1-20 on the raw image) on their frames; the virtual overscan is not subject to the amplifier nonlinearity problem and can be used to estimate the importance of this effect in the images. Observers using subarrays (e.g., to reduce the time interval between reads and limit the data volume when performing variability observations in the optical; see also [Chapter 11](#)) will obtain only the physical overscan.

7.3.7 Charge Transfer Efficiency

Radiation damage at the altitude of the *HST* orbit causes the charge transfer efficiency (CTE) of the STIS CCD to degrade with time. The effect of imperfect CTE is the loss of signal when charge is transferred through the CCD chip during the readout process. As the nominal read-out amplifier (Amp D) is situated at the top right corner of the STIS CCD, the CTE problem has two possible observational consequences: (1) making objects at lower row numbers (more pixel-to-pixel charge transfers) appear fainter than they would if they were at high row numbers (since this loss is suffered along the *parallel* clocking direction, it is referred to as *parallel CTE loss*); and (2) making objects on the left side of the chip appear fainter than on the right side (referred to as *serial CTE loss*). In the case of the STIS CCD, the serial CTE loss has been found to be negligible for practical purposes. Hence we will only address *parallel CTE loss* for the STIS CCD in this *Handbook*.

The current lack of a comprehensive theoretical understanding of CTE effects introduces an uncertainty for STIS photometry. The CTE problems are caused by electron traps in the CCD that are filled as charge passes through the pixels. However, not all traps are accessible to all electrons passing through. Some traps are only accessible if there is significant charge involved. This model suggests that there will not be significant CTE losses in the presence of background, particularly for faint stars, because background electrons fill the traps before the charge associated with such stars passes through. There will still be some loss for brighter stars with background, because their charge may access traps that are unaffected by the background that previously clocked through. Faint stars in areas with little background may suffer from larger losses.

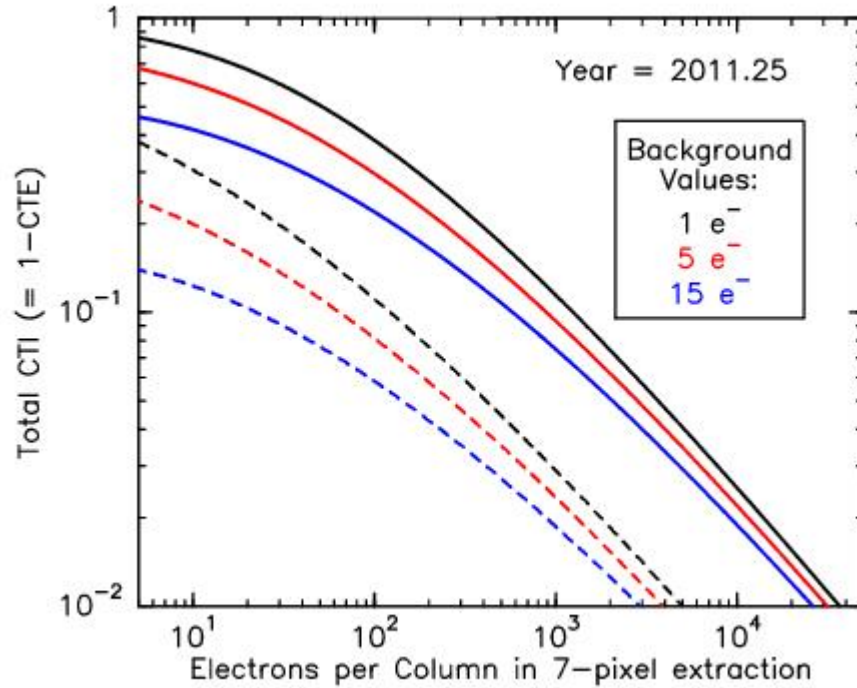
In general, the amount of (parallel) CTE loss depends on the elapsed time on orbit, the distance (i.e., the number of CCD rows) from the source location on the CCD chip to the readout amplifier, the source signal, and the background level.

It should be noted at the outset that the effect of CTE loss has not, as yet, been incorporated into the [STIS ETCs](#). Thus, should you believe the CTE losses described herein may impact your spectroscopic or imaging observing program, you will need to provide longer exposure times in your Phase II proposal to compensate for the anticipated losses. In particular, observers using the STIS CCD to observe faint targets (especially in spectroscopic mode) producing less than a few hundred electrons above a low background, are advised to adjust their exposure times appropriately (within the restrictions of their allocated number of *HST* orbits).

Analysis of a comprehensive calibration program has allowed us to derive a formula to correct spectroscopic observations of point sources for the parallel-register Charge Transfer Inefficiency ($CTI = 1 - CTE$). This correction has been implemented in the standard calibration pipeline. For spectra at the standard reference position at the CCD center, CTE losses as big as 20% are corrected to within 1% at high signal levels, and to within $\sim 1.5\%$ at low signal levels of ~ 100 electrons. Further information on CTE loss in spectroscopic mode, including the CTI correction formula, can be found in [STIS ISR 2006-03](#). The correlation of fractional signal loss and the shift of the centroid of the spectrum is demonstrated in [STIS ISR 2006-01](#). For the CCD imaging mode, no correction is available at present in the pipeline, and we refer the reader to [Goudfrooij and Kimble's 2002 HST Calibration Workshop article](#) for the parametrization of the CTE loss, and [Goudfrooij et al. 2006](#) (PASP, 118, 1455, 2006).

[Figure 7.10](#) depicts the amount of CTE loss suffered as a function of source signal and background level, for spectra taken at epoch 2011.25 with the target at the center of the detector (solid lines) and at the E1 aperture position (dashed lines). Note that the CTE loss can be significant. A typical spectrum with a signal of about $150 \text{ e}^-/\text{pix}$ along the dispersion direction (extracted over the spatial extent of the PSF) and a background level of $5 \text{ e}^-/\text{pix}$ (appropriate for a 1000 second exposure in G430L mode) is expected to experience a CTE loss of $\sim 34\%$ at epoch 2011.25 when located in the center of the CCD, and a loss of $\sim 10\%$ when placed at the E1 aperture position (discussed below), which is much closer to the readout amplifier. For a background of $1 \text{ e}^-/\text{pix}$ (e.g., a 200 second exposure), a spectrum with the same source signal level would suffer a CTE loss of $\sim 36\%$ if placed at the center of the detector, and $\sim 11\%$ at the E1 aperture position. This emphasizes the need to take CTE losses into account when estimating exposure times needed to accomplish your science goals.

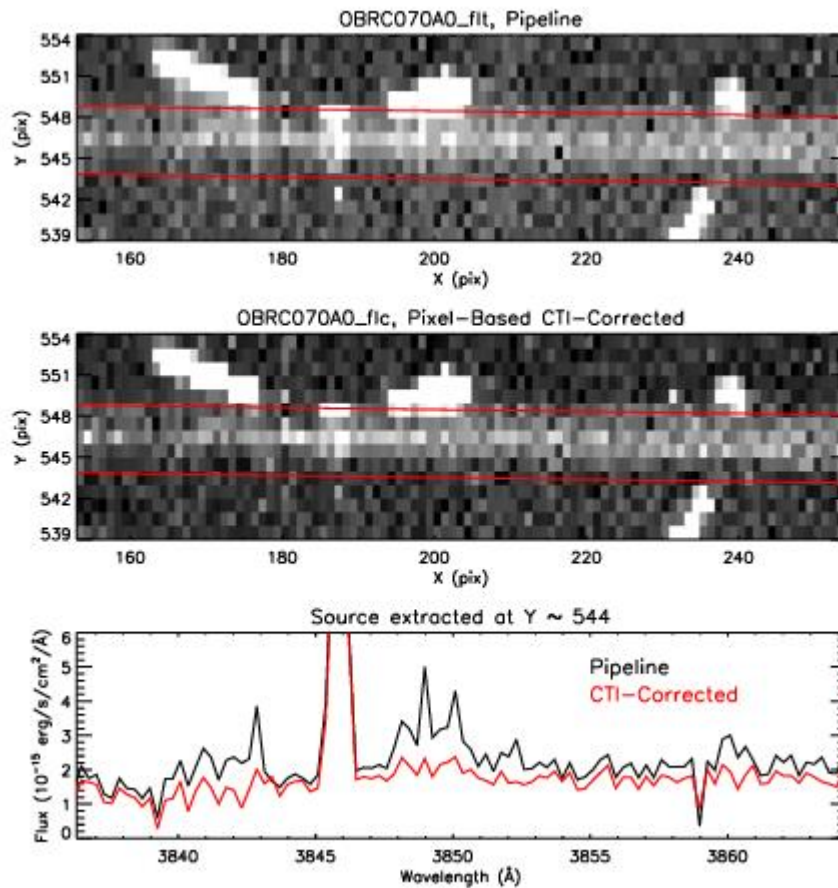
Figure 7.10: Estimated Charge Transfer Inefficiency (CTI = 1-CTE) as a Function of Signal Level (per column) for Spectroscopy of a Point Source Observed in Calendar Year 2011.25.



The solid lines are for targets placed at the center of the detector, and the dashed lines are for targets placed at the E1 aperture position. The colors black, red, and blue indicate a background of 1, 5, and 15 electrons per pixel, respectively. The CTI is expressed as the fraction of charge lost outside the default signal extraction box of 7 pixels perpendicular to the dispersion. Note the CTI-decreasing effect of added background, which argues for an observing strategy involving long exposure times.

Our discussion thus far has focused on the loss of flux due to charge transfer inefficiencies, but another effect is also important: trails from cosmic rays and hot pixels that lie between the target and the read-out amplifier (downstream trails) add noise to the target's spectrum or image. To explore the effects of CTE trails on faint spectra, consider the spectrum plotted in [Figure 7.11](#). It was observed in late 2012 with grating G430M for a total of 540 seconds using CR-SPLIT=1. The cosmic rays just above the extraction region produce downstream CTE trails that get included in the 1D extracted spectrum. For comparison, the same data are processed with the [STIS pixel-based CTE-correction](#) and extracted, showing a reduction in the trail contamination. These faint CTE trails represent an important source of noise that is not included in the ETC. For more information on this effect, see [STIS ISR 2011-02](#).

Figure 7.11: Spectroscopic observation with and without the pixel-based CTI correction.



The top two images show 2D data obtained from a multi-source observation through the 52x0.2 long slit near $Y = 544$, with a 5 pixel extraction region marked in red. The top image shows the pipeline FLT data, while the middle image has been processed through the STIS pixel-based CTI correction, thus reducing downstream cosmic ray trails. The bottom plot shows the corresponding 1D extracted spectra. To mitigate the downstream CTE effects of cosmic rays and hot pixels, users should move observations to the E1 position ($Y \sim 900$), take multiple reads, or observe with multiple dither positions.

For the observer, a few strategies for minimizing the effect of CTE loss should be noted. First of all, one should maximize the exposure time whenever possible in order to increase the object counts and the sky background per exposure, both of which reduce CTE loss. Users who are thinking about dithering and shortening their exposure times (e.g., to allow for more dither positions) may want to take this into account. Furthermore, to reduce the number of charge transfers and the consequent loss of signal as illustrated above, observers using the CCD for long-slit spectroscopy of sources having a spatial extent of less than about 3 arcseconds are urged to use the pseudo-apertures located near row 900 of the CCD (the 52x*E1 apertures; see [Section 7.3.8](#)).

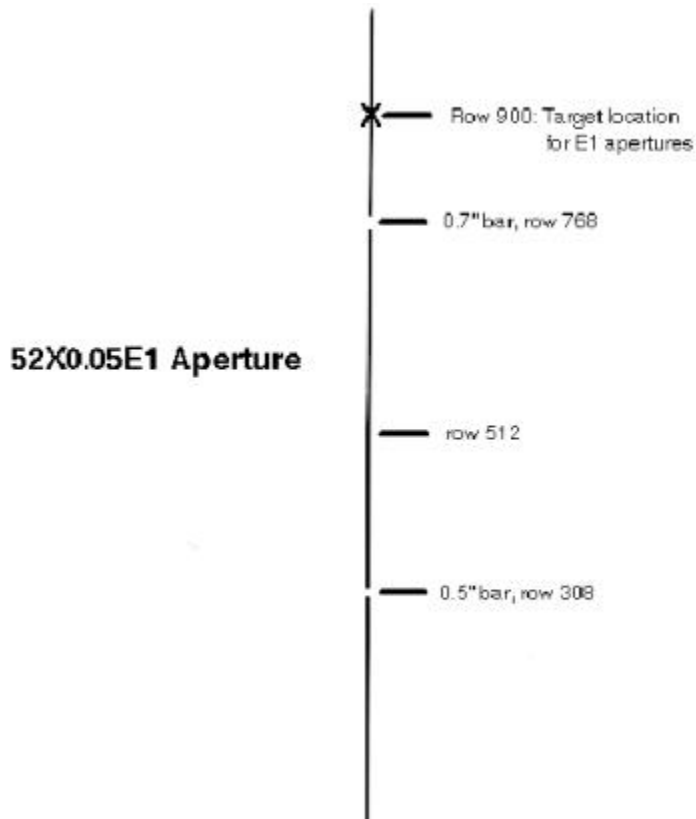
The STIS team created a stand-alone pixel-based CTI correction script. As of right now, it can only process non-binned, full-frame data read out with amplifier D and from after SM4. More information and links to installing the script may be found at the [Pixel Based CTI page](#).

7.3.8 Mitigation of CTE Loss for Long-Slit Spectroscopy

Decreasing charge transfer efficiency in the STIS CCD has a detrimental effect on faint spectra acquired at the default location at the center of the chip. For sources with fluxes less than $\sim 1 \times 10^{-16}$ erg/cm²/s/Å, less than ~ 100 electrons are accumulated per pixel in exposure times of 1000 seconds or less. (This is the longest integration time we recommend due to the deleterious impact of multiple cosmic rays in a CR-SPLIT at longer integration times.) At signal levels of 50–100 electrons, 25% or more of the charge can be lost during readout due to charge transfer inefficiencies. Many STIS science programs have fluxes in this range. For spectra of point sources and compact objects such as galactic nuclei, the full length of the slit is not needed. A target location closer to the read-out amplifier near the end of the slit can decrease the charge lost during parallel transfers by a factor of ~ 4 . One could achieve this offset through the use of offset targets or appropriate POS-TARG entries on the Phase II proposal, but these methods are a bit cumbersome and can be prone to error.

Therefore, for first-order spectra we have defined a set of E1 pseudo-apertures that use the same physical long slits available for STIS CCD observations, but have their default target placement near row 900, ~ 5 arcseconds from the top of the STIS CCD. This is schematically illustrated in [Figure 7.12](#). Observers can use these aperture names to place their targets at this location in a rather transparent fashion.

Figure 7.12: Location of the E1 Aperture Positions.



The E1 aperture names and the approximate Y location of the resulting spectra are given in [Table 7.5](#). Use of the E1 aperture name eliminates the need to specify an offset for the ACQ/PEAK and a POSTARG. These apertures are also recognized by the calibration pipeline software, so spectra are extracted from the correct location using appropriate wavelength solutions, spectral traces, and background regions. For optimum throughput when using these apertures, we recommend using an ACQ/PEAK exposure to center the target in the aperture when using aperture 52X0.1E1 and 52X0.05E1. While use of these apertures will reduce CTE losses, we caution observers to carefully assess the potential impact on their science programs due to the decreased spatial coverage and the relative locations of the bars on the slit.

Table 7.5: E1 Aperture Names and Approximate Y Location of the Resulting Spectra.

| Aperture | Y Location | ACQ/PEAK |
|-----------|------------|----------|
| 52X2E1 | 894 | no |
| 52X0.5E1 | 893 | no |
| 52X0.2E1 | 893 | no |
| 52X0.1E1 | 898 | yes |
| 52X0.05E1 | 898 | yes |

7.3.9 Pixel-Based CTI Corrections for the STIS CCD

The STIS team at STScI has created stand-alone automated software to apply Charge Transfer Inefficiency (CTI) corrections to STIS CCD data. This software will remove trails and other artifacts caused by CTI effects in the CCD detector, and will help correct target fluxes and positions to their proper values. The software script, called `stis_cti`, uses a pixel-based correction algorithm, and will correct both images and spectra. The script automatically generates CTI corrected dark reference files, applies CTI corrections to the science data, and outputs the usual `calstis` products with CTI corrections applied. Currently only the most common observation modes are supported—full-frame, non-binned data, taken with the default CCD amplifier D and after SM4. The script will not correct the signal-to-noise ratio degradation which results from CTI, and hence it is still important for observers to mitigate CTI effects as much as possible during observation. It is available to the community for download and use. Further information can be found at the [STIS website](#) under [Software Tools](#).

[STIS ISR 2022-03](#) details a study comparing the effects of the older empirical CTI correction and the new pixel-based CTI correction on photometry. Post-SM4 data analyzed span from 2010 to 2022 and the study explores the absolute differences between the CTI corrected magnitudes, and their spatial, time and magnitude dependence. The magnitude offsets for the two CTI methods are smallest for the brightest stars and deviate further from zero with increasing magnitude (<18 mag: 0.020 mag, 0.12%; 18–19 mag: 0.037 mag, 0.20%; 19–22 mag: –0.084 mag, –0.35%). Stars brighter than 19 mag are marginally over-corrected with both CTI methods. Stars fainter than 19 mag are slightly under-corrected by the pixel-based CTI method and slightly over-corrected with the empirical flux CTI method. Generally, the magnitude offsets between the codes are small (< 1%), consistent with past results, and well within the quoted ~ 5% STIS photometric errors (See [Section 16.1](#)). Previous ISRs comparing the two CTI correction methods focused on the photometric performance ([STIS ISR 2015-04](#), updated in [STIS ISR 2022-03](#)), astrometric performance ([STIS ISR 2015-05](#)), and detector spatial and temperature CTI dependence ([STIS ISR 2015-03](#)).

7.3.10 Ultraviolet Light and the STIS CCD

In the optical, each photon generates a single electron. However, in the NUV, shortward of ~3200 Å there is a finite probability of creating more than one electron per UV photon (see [Christensen, O., J. 1976](#), *App. Phys.* 47, 689). Users will need to take this into account when calculating signal-to-noise ratios and exposure times for the G230LB and G230MB gratings, as described in [Section Special Case: Spectroscopic CCD Observations at \$\lambda < 2500\$ Å](#).

Initial laboratory testing of STIS CCDs showed that excessive illumination by UV light can cause an elevation in residual dark current, due to a surface chemistry effect. However, the actual STIS flight CCD was tested for this effect during ground calibration by the STIS IDT and the effect was found to be much less than previously suspected; this effect is now a concern *only* for clear (50CCD) imaging of *extremely UV-bright targets*. Observations of fields with UV-bright objects should be dithered (i.e., positional offsets applied between readouts) to ensure that the UV tail from bright sources does not cause a residual elevation of the dark current for subsequent science observations. It is also recommended to use the longpass-filtered aperture, F28X50LP, rather than the 50CCD clear aperture, during target acquisitions (see also [Section 8.2.3](#)) when possible. The specific results of the ground testing on the effect of UV overillumination are summarized in [Table 7.6](#). Note that at launch in 1997 the median STIS CCD dark current was about 0.0015 counts/pix/s.

Table 7.6: Effect of CCD UV Overillumination on Elevation of Dark Current.

| Overillumination Rate (e ⁻ /pix) | Initial Dark Current Elevation (e ⁻ /pix/s) | Time to Return to Nominal |
|--|---|---------------------------|
| 500,000 | 0.0075 | 30 min |
| 5,000,000 | 0.00225 | 40 min |

7.4 The MAMA Detectors

- [7.4.1 MAMA Properties](#)
- [7.4.2 MAMA Spectral Response](#)
- [7.4.3 MAMA Sensitivity](#)
- [7.4.4 Optical Performance](#)

7.4.1 MAMA Properties

There are two MAMA detectors: the *STIS/FUV-MAMA* provides coverage from 1150 to 1700 Å and the *STIS/NUV-MAMA* provides coverage from 1600 to 3100 Å (with some additional, but lower response below 1600 Å). The STIS MAMA detectors are photon-counting devices that process events serially. They can be used to take data in either an accumulate (*ACCUM*) mode in which a time-integrated image is produced, or in a time series (*TIME-TAG*) mode in which the detector location and time of arrival of each photon event are recorded as an event stream (see [Section 11.1.2](#) and [Section 11.1.3](#), respectively). The primary benefits afforded by the STIS MAMAs, in comparison with previous *HST* UV spectroscopic detectors such as those of the GHRs and FOS, are high spatial resolution, two-dimensional imaging over a relatively large field of view, and low background for point sources. The MAMA detector was developed by J. Timothy and R. Bybee for X-ray and UV imaging applications. The properties of the STIS MAMA detectors are summarized in [Table 7.7](#) and described in detail in [Timothy \(2016\)](#).

Table 7.7: STIS MAMA Detector Characteristics.

| Characteristic | FUV-MAMA | NUV-MAMA |
|---|---|-----------------------------|
| Photocathode | CsI | Cs ₂ Te |
| Wavelength range | 1150–1700 Å | 1600–3100 Å |
| Pixel format | 1024 × 1024 | 1024 × 1024 |
| Pixel size | 25 × 25 μm ² | 25 × 25 μm ² |
| Image mode pixel plate scale | 0.0245" × 0.0247" (clear) 0.0246" × 0.0247" (filtered) | 0.0245" × 0.0248" |
| Field of view | 25.1" × 25.3" (clear) 25.2" × 25.3" (filtered) | 25.1" × 25.4" |
| Quantum efficiency | 24% @ 1216 Å | 9% @ 2537 Å |
| Dark count | 5 × 10 ⁻⁶ to 6 × 10 ⁻⁴ counts/s/pix | 0.001 to 0.002 counts/s/pix |
| Global count rate linearity limit ¹ | 285,000 counts/s | 285,000 counts/s |

| | | |
|--|-------------------|-------------------|
| Local count rate linearity limit ^{1 2} | ~220 counts/s/pix | ~340 counts/s/pix |
|--|-------------------|-------------------|

¹ Rate at which counting shows 10% deviation from linearity. These count rates are well above the bright object screening limits (see [Section 7.7.2](#)).

² The MAMA Linearity reference file was changed to use the 1% deviation from linearity values of ~22 counts/s/pix (FUV-MAMA) and ~34 counts/s/pix (NUV-MAMA) in September 1999 to better handle saturated pixels with high count rates that were not being flagged using the 10% deviation from linearity values.

[Figure 7.13](#) and [Figure 7.14](#) illustrate the design of the FUV- and NUV-MAMA, respectively. A photocathode material is deposited on the front surface. The FUV-MAMA has an opaque CsI photocathode deposited directly on the face of the curved microchannel plate (MCP); the NUV-MAMA has a semi-transparent Cs₂Te photocathode deposited on the back side of the detector's entrance window.

Target photons strike the photocathode, liberating single photoelectrons that pass into the microchannel plate (MCP). There they are multiplied to a pulse of $\sim 4 \times 10^5$ electrons. The pulse is recorded by an anode array behind the photocathode and detected by the MAMA electronics which process it, rejecting false pulses and determining the origin of the photon event on the detector.

The FUV-MAMA has a field electrode (*repeller wire*) which is used to repel electrons emitted away from the microchannel plate back into the channels. This provides an increase in quantum efficiency of the detector at the price of a small increase in the detector PSF halo. The repeller wire is normally on for FUV-MAMA observations (but see [Section 7.4.4](#)).

Figure 7.13: Design of the FUV-MAMA.

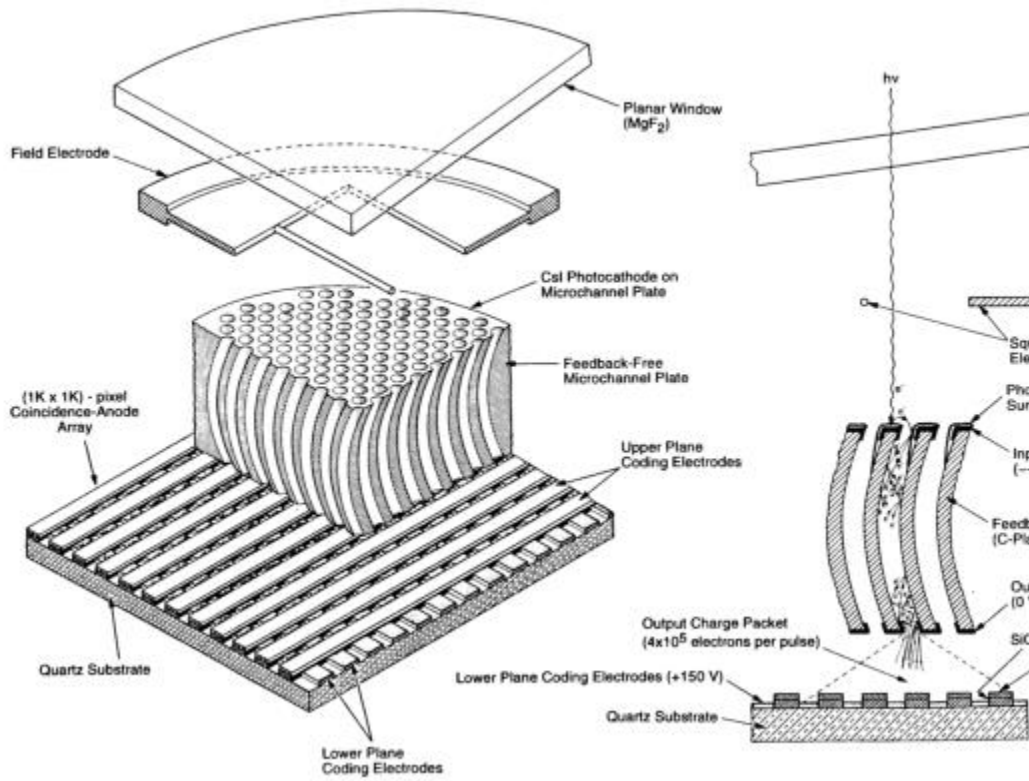
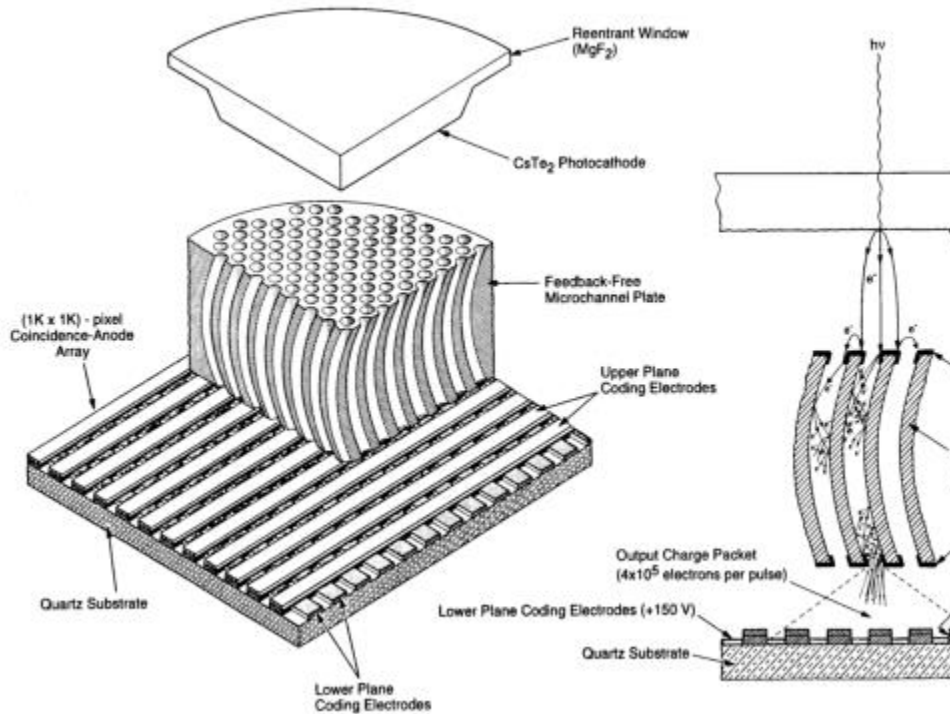


Figure 7.14: Design of the NUV-MAMA.



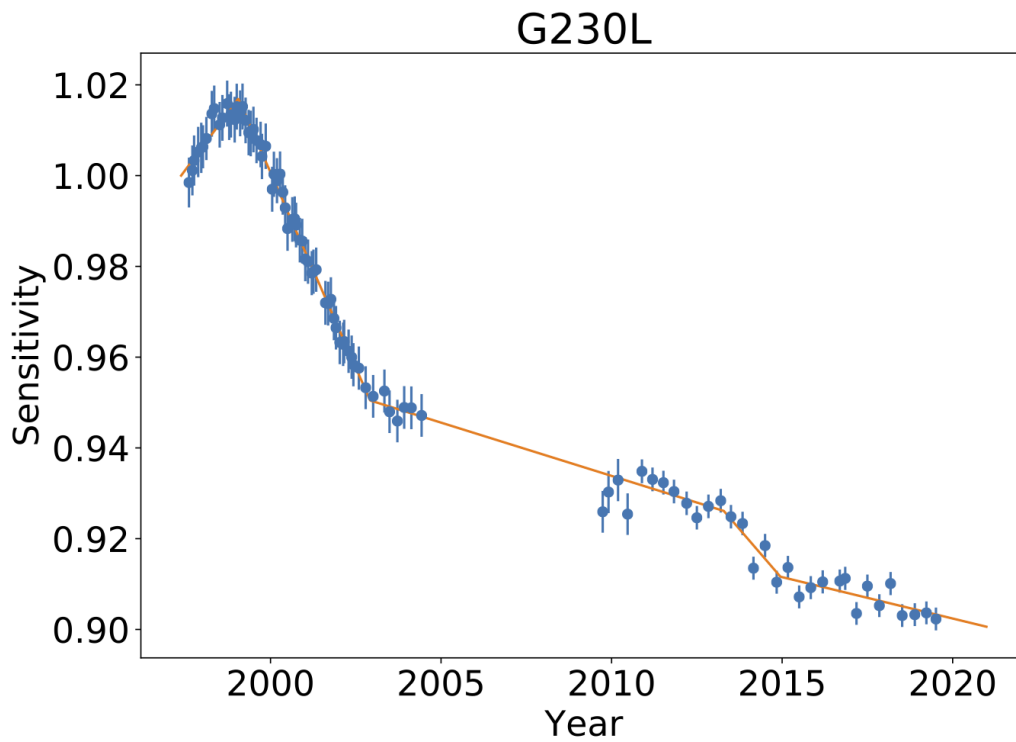
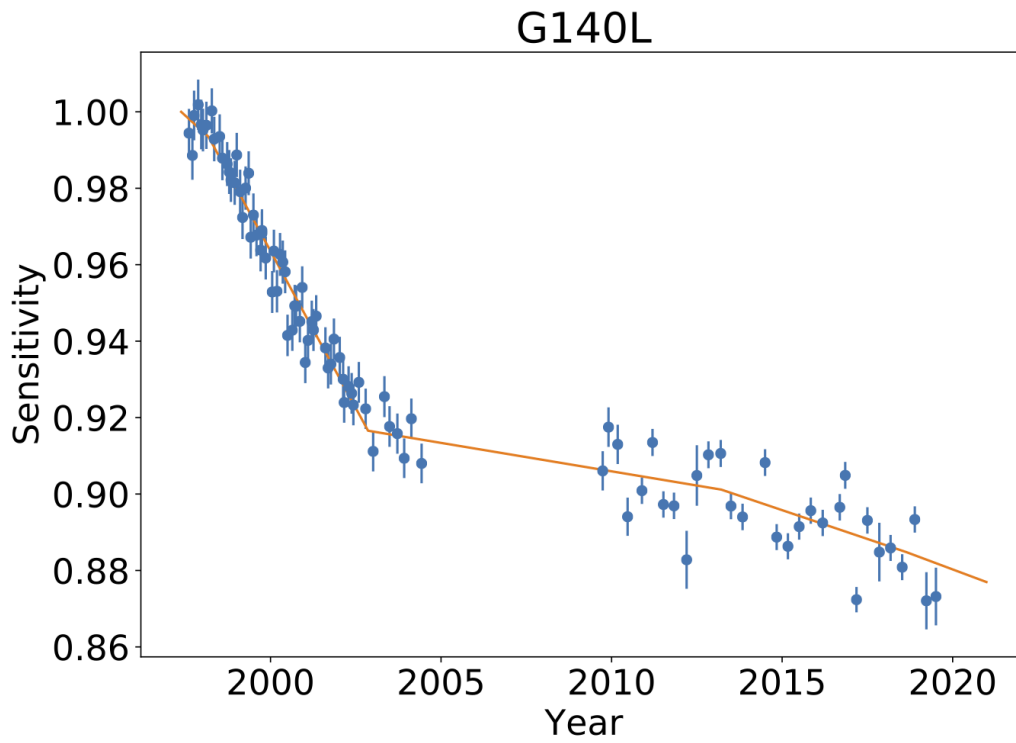
7.4.2 MAMA Spectral Response

The spectral responses of the unfiltered FUV- and NUV-MAMAs are illustrated in Figure 5.9. The peak photocathode response of the FUV-MAMA occurs at Lyman- α (1215.7 Å). Its spectral response is defined by the cutoff of the MgF₂ window at 1150 Å at short wavelengths, and by the relatively steep decline of the CsI photocathode at long wavelengths. Out-of-band QE at longer wavelengths (>2000 Å) is $<10^{-6}$ yielding excellent solar-blind performance. The NUV-MAMA spectral response has a relatively flat maximum (~10%) that encompasses 1800-2600 Å. The photocathode QE declines to ~4% at 3150 Å, while at longer wavelengths the out-of-band QE is $\sim 10^{-4}$. (See also Section 5.3.3.)

7.4.3 MAMA Sensitivity

The STIS MAMA detector modes, similarly to those of the STIS CCD, suffer from changes in sensitivity that depend on both temperature and time. A STIS Sensitivity Monitoring program similar to that aimed at characterizing the CCD behavior has been used to characterize the MAMAs (see [Section 7.2](#) about the CCD program). The well-known sensitivity of the FUV-MAMA to temperature for the first-order mode G140L has been confirmed to be $-0.32\%/^{\circ}\text{C}$. No significant change with temperature for the NUV-MAMA first-order G230L mode has been registered. Following a correction for the temperature dependence, the sensitivities of the FUV first-order modes decrease linearly with time by wavelength-dependent amounts ranging up to a few percent per year. For the NUV first-order configurations, the sensitivities increased during the first 1.5 years of STIS operations and then began to drop, by wavelength-dependent amounts comparable to those in the FUV. There was a significant slow-down in the decline of the time-dependent sensitivity (TDS) of all STIS observational modes beginning in 2002. All detectors continued to decline during the years STIS was inoperative. For the STIS Echelle modes, the TDS corrections adopted are taken to be the same as for the corresponding low-order modes. Note that new photometric throughput tables were created based on Cycle 17 data, and then were updated again in 2023 ([July 2023 STAN](#)). TDS corrections for all STIS spectra are implemented in the data reduction pipeline (see [Section 15.1](#)). [Figure 7.15](#) shows the sensitivity trends for the STIS NUV and FUV MAMAs. **Synphot** and the **ETC** also include TDS corrections for STIS data. For Cycle 32, these default to the estimated throughputs for April, 2025.

Figure 7.15: Relative Wavelength-Averaged Sensitivity of STIS MAMA First-Order Low-Resolution Modes G140L and G230L as a Function of Time.



7.4.4 Optical Performance

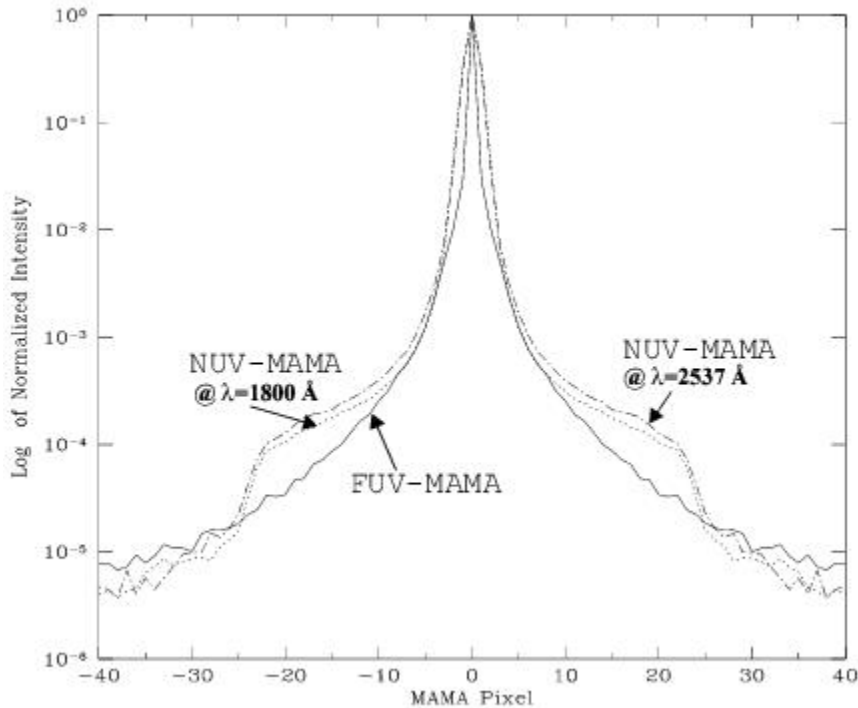
Both MAMAs exhibit low-level extended wings in their detector point spread functions (PSFs), with the NUV-MAMA PSF being considerably worse. Sample MAMA detector PSFs are shown in [Figure 7.16](#). For those wishing to model their effect on absorption or emission line equivalent-width measurements or coronagraphic observations, the LSFs and detector PSFs are maintained on the STScI [STIS website](#). Data for spectral modes can be found at:

<http://www.stsci.edu/hst/instrumentation/stis/performance/spectral-resolution>

Links to the plots of the imaging mode PSFs can be found in the table at:

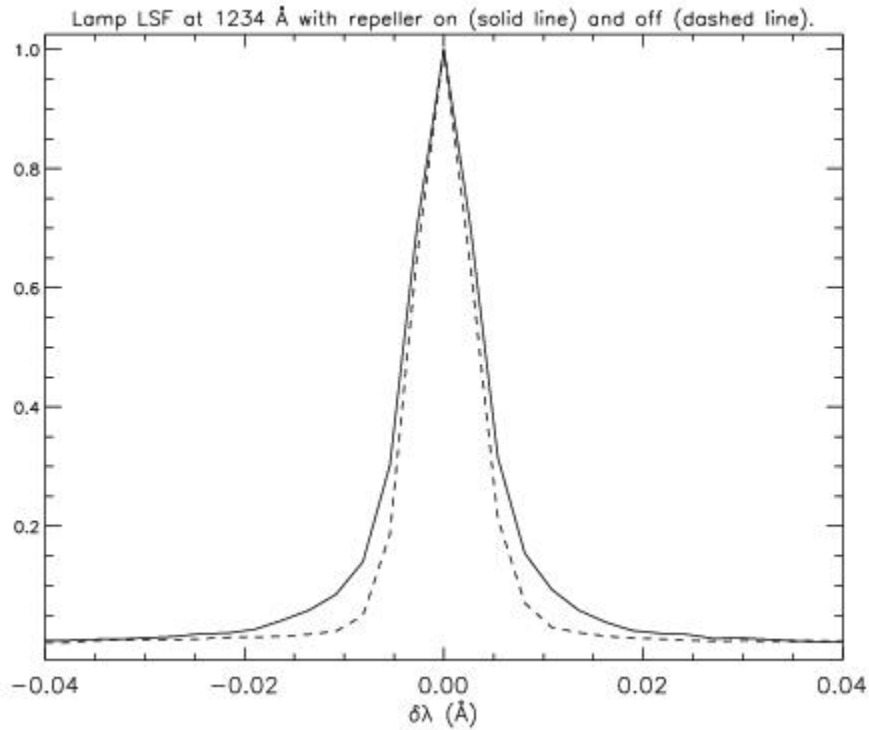
<http://www.stsci.edu/hst/instrumentation/stis/performance/image-quality>.

Figure 7.16: MAMA Detector PSFs.



The FUV-MAMA includes a repeller wire that establishes an electric field above the microchannel plate, to deflect forward-ejected photoelectrons back into the microchannel pores. The repeller wire is normally on for FUV-MAMA observations, but an improvement to the FUV-MAMA PSF (at the expense of a 35% decrease in sensitivity) can be made by disabling the high voltage to this wire. This procedure is only recommended for observations that use the E140H, and perhaps also the E140M, gratings when used with the 0.1x0.03 aperture (sometimes called the "Jenkins slit") for observations shortward of 1400 Å (see Section 3.1 on the smallest STIS apertures, caveat detailed in the footnote). In pre-launch testing, resolutions as high as $R \sim 220,000$ were obtained in observations of a mono-isotopic emission line lamp in *highres mode*, and $R \sim 200,000$ has been achieved on-orbit (e.g., Jenkins & Tripp 2001, *ApJS*, 137, 297). Figure 7.17 shows the effect of disabling the repeller voltage for the case of an observation of a line lamp with the E140H CENWAVE=1234 Å setting. Note that the main difference is not the FWHM of the central core, but a decrease in the intensity of the line wings.

Figure 7.17: Average Profile of Calibration Lamp Line at 1234 Å with the Repeller Wire On and Off.



Only a small number of proposals per Cycle requesting the repeller off mode will be accepted. Note that repeller off observations will require special treatment, so a scientific case will need to be made for why these observations are necessary.

Also note that, due to the large PSF of *HST* in imaging mode (currently 3.5 low-resolution pixels), there is no advantage in performing *FUV-MAMA* imaging observations with the repeller wire voltage turned off.

7.5 MAMA Operation and Feasibility Considerations

- [7.5.1 MAMA Saturation—Overflowing the 16 Bit Buffer](#)
- [7.5.2 MAMA Darks](#)
- [7.5.3 MAMA Signal-to-Noise Ratio Limitations](#)
- [7.5.4 MAMA Nonlinearity](#)

7.5.1 MAMA Saturation—Overflowing the 16 Bit Buffer

The MAMA is a photon-counting detector: as each event is recorded, the buffer memory for the corresponding pixel is incremented by one integer. The buffer memory stores values as 16 bit integers; hence the maximum number it can accommodate is 65,536 counts per pixel in a given `ACCUM` mode observation. When accumulated counts per pixel exceed this number, the values will wrap, i.e., the memory resets to 0. As an example, if you are counting at 25 counts/s/pix, you will reach the MAMA "accumulation" limit in ~44 minutes.

Keep accumulated counts/pix below this value by breaking individual exposures into multiple identical exposures (see also [Section 11.2.4](#)), each of which is short enough that fewer than 65,536 counts are accumulated per pixel. There is no read noise for MAMA observations, so no penalty is paid in lost signal-to-noise ratio when exposures are split. There is only a small overhead for each MAMA exposure ([Chapter 9](#)).

i *Keep the accumulated counts per pixel below 65,536, by breaking single exposures into multiple exposures, as needed.*

7.5.2 MAMA Darks

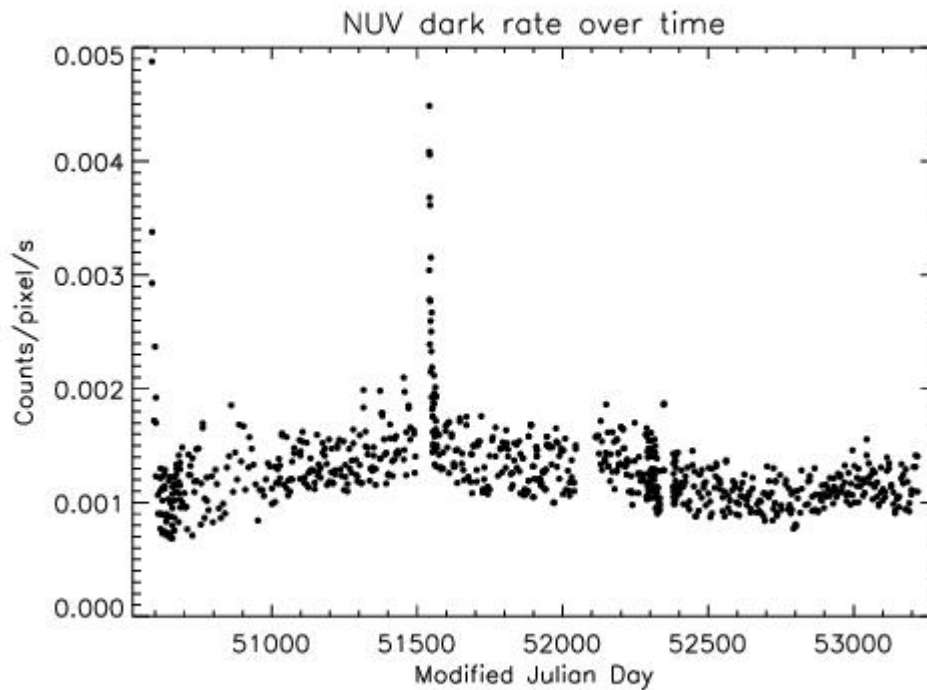
The STIS MAMA detectors have intrinsically very low dark currents. Dark currents measured during ground testing were less than 10 counts/s for the `FUV-MAMA` and less than 30 counts/s for the `NUV-MAMA` over the whole detector. For the `FUV-MAMA`, this exceptionally low dark current was initially achieved on orbit. For the `NUV-MAMA`, charged particle impacts on the MgF_2 faceplate cause a higher background that resulted in a dark current of 800–2000 counts/s, varying both with temperature and the thermal history of the detector. This particular phenomenon is not present for the `FUV-MAMA`, but the dark current for that detector now also varies with time, temperature and position. The different dark current behaviors of the detectors are discussed in more detail below, and up-to-date information can be found on the [Monitoring page](#) of the STIS website. We split the discussion of the NUV dark current into before and after servicing mission 4 (SM4) where the electronics were switched and STIS become operational again.

NUV-MAMA Dark Current Before SM4

Most of the dark current in the NUV-MAMA comes from phosphorescence of impurities in the MgF_2 detector faceplate. A simple model of the phenomenon was developed by Jenkins and Kimble that envisions a population of impurity sites each having three levels: (1) a ground state, (2) an excited energy level which can decay immediately to the ground state, and (3) a meta-stable level that is at an energy slightly below the one that can emit radiation. The meta-stable states are initially populated by charged particle impacts that mostly occur during passages through the South Atlantic Anomaly (SAA). Hours or days later, the electrons trapped in these meta-stable states are thermally excited to an unstable upper level and then emit a photon as they decay to the ground state. This thermal excitation rate is proportional to $\exp(-\Delta E/kT)$, where ΔE is the energy difference between the levels, T is temperature of the detector and k is the Boltzmann's constant. The behavior of the count rate vs. temperature leads to an estimate of 1.1 eV for ΔE .

While this temperature dependent function does a good job of predicting the short term response of the NUV dark current to temperature changes, the longer term response is more complex. In equilibrium, the number of decays will match the number of excitation events. A sudden temperature increase would then result in an initial rapid increase in the dark rate, as the meta-stable states are more easily depopulated at higher temperatures. However, after several days, the population of meta-stable states would reach a new equilibrium, resulting in a dark rate that, while higher than the equilibrium rate was at the cooler temperature, is significantly lower than the short term response to the same temperature increase. The predicted large temporary increases in the dark rate were observed after the initial STIS installation, and also after Servicing Mission 3a (see [Figure 7.18](#)).

Figure 7.18: The NUV-MAMA Dark Rate as Measured from Dark Monitor Exposures Between 1997 and 2004.

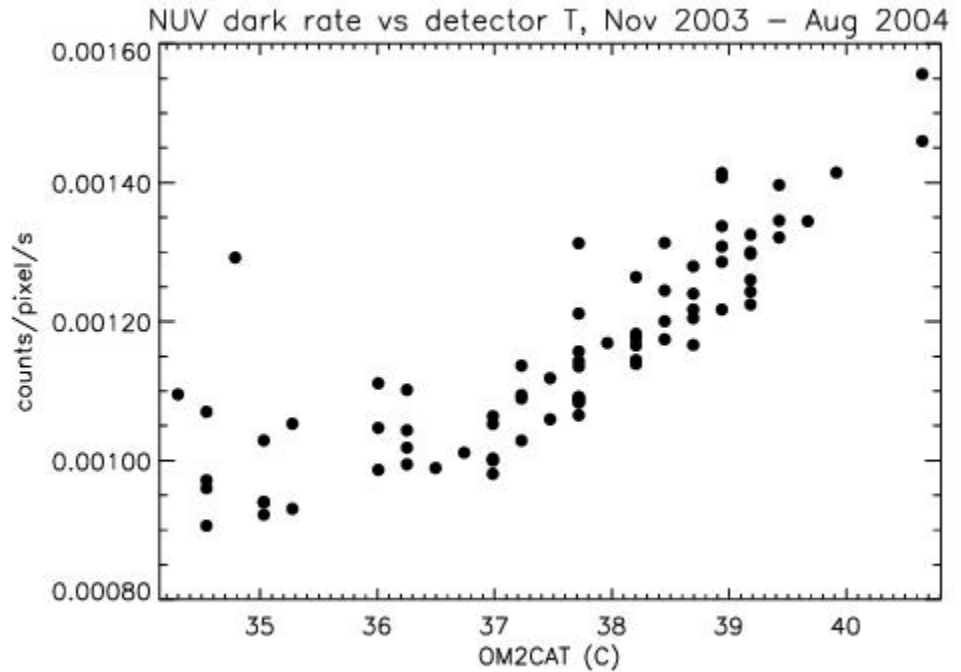


Note the large, but temporary, increases in the dark rate after initial installation of STIS and after SM3a (near MJD 51500), when the detector was turned back on after being cold for several weeks. Also note the long term fluctuations in the mean dark current.

At a fixed detector temperature of 30° C, the time-constant for the dark current to reach an equilibrium value is about 8 days. In practice because the MAMA high-voltage power supplies have to be shut down during SAA impacted orbits, the detector temperature varies from about 27° C to 40° C on a roughly daily time scale, and the dark current never reaches equilibrium. In addition, the real rate of excitations caused by charged particle impacts is not directly measurable and is expected to vary unpredictably on all time scales. Even the time averaged excitation rate may differ considerably from year to year, depending on the low earth orbit radiation environment.

During the last nine months of STIS operations prior to the failure in August 2004, the typical NUV-MAMA dark current ranged between 8×10^{-4} and 1.6×10^{-3} counts/pix/s (Figure 7.19). Changes in the low earth orbit radiation environment affect the rate at which the meta-stable impurity states are populated. For Cycle 17 planning purposes we had guessed that the equilibrium STIS NUV-MAMA dark current would be 10% higher than it was during 2003-2004; which implied a range of dark count rate values between 8.5×10^{-4} and 1.7×10^{-3} counts/pix/s. However, as we will see in the next section (NUV-MAMA Dark Current after SM4), this drastically underestimated the actual dark rate seen after SM4.

Figure 7.19: NUV Dark Current vs. OM2CAT Temperature Between November 2003 and August 2004.



To predict the NUV dark current and subtract it as part of standard processing, the **calstis** pipeline uses a simple temperature dependent relation:

$$darkrate = norm \cdot 1.805 \times 10^{20} \cdot \exp(-12211.8/\max(T, Tmin))$$

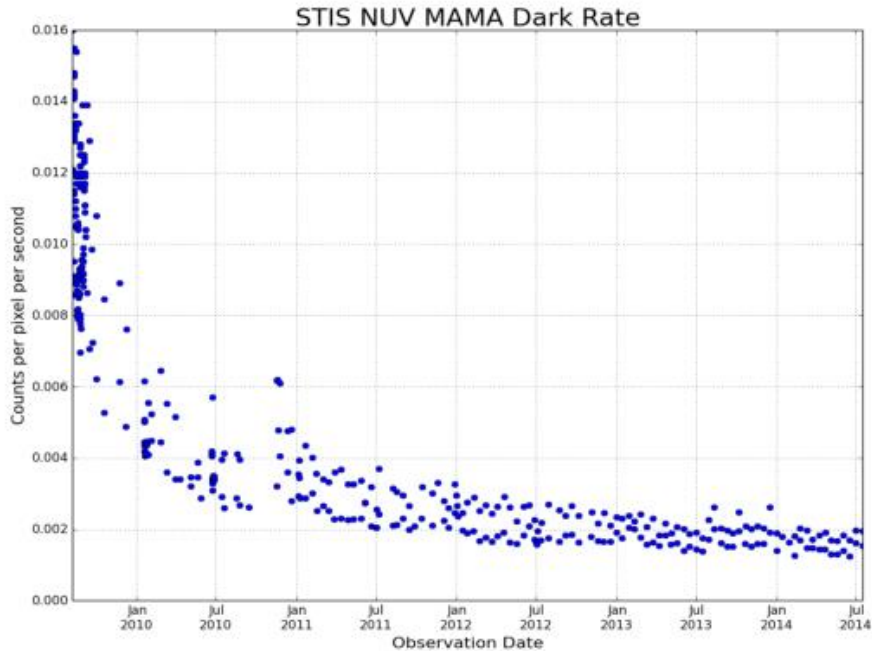
Both *norm* and *Tmin* are slowly varying functions of time that are empirically adjusted to give a good match to the observed dark rate, and which are tabulated in the temperature dependent dark correction table (TDCTAB) reference file. The temperature for a given observation is taken from the OM2CAT telemetry value, which is included in the extension header of each MAMA observation. This approach usually predicts the dark rate with 5 to 10% accuracy, although the error in individual cases may be substantially larger.

Because 99% of the NUV-MAMA dark current is due to photons hitting the detector, it is appropriate to apply the flat field prior to subtracting the dark current. The dark current varies slowly across the face of the detector, being about 1.25 times higher near the lower left corner (AXIS1, AXIS2 < 300) than at the center. This shape varies with time and temperature enough that subtraction of the scaled dark reference may leave a residual, spatially varying dark current. This is easiest to remove by fitting a low-order two-dimensional function to the background vs. pixel position.

NUV-MAMA Dark Current after SM4

After the Side-2 failure in 2004, STIS was in safe mode with only the survival heaters powered. During this period, the MAMA tubes were at an average temperature of 3.8° C, much lower than the normal operational temperature range of about 29° C to 34° C. We therefore expected to see a temporary increase in the dark current after the post-SM4 recovery of the MAMA tubes due to the increased population of meta-stable states at the colder safe-mode temperature. Detailed modeling led us to expect that the peak dark count rate would not be too much bigger than that seen after SM3a where the MAMAs had been off for about three months. We also expected that any excess would decline with a e-folding time of a week or so, as had been seen previously. This would have allowed the NUV-MAMA dark rate to return to the previous operational range of between 0.0009 and 0.0017 counts/pix /s within about a month of the STIS recovery after SM4.

Figure 7.20: NUV-MAMA Dark Current after SM4.



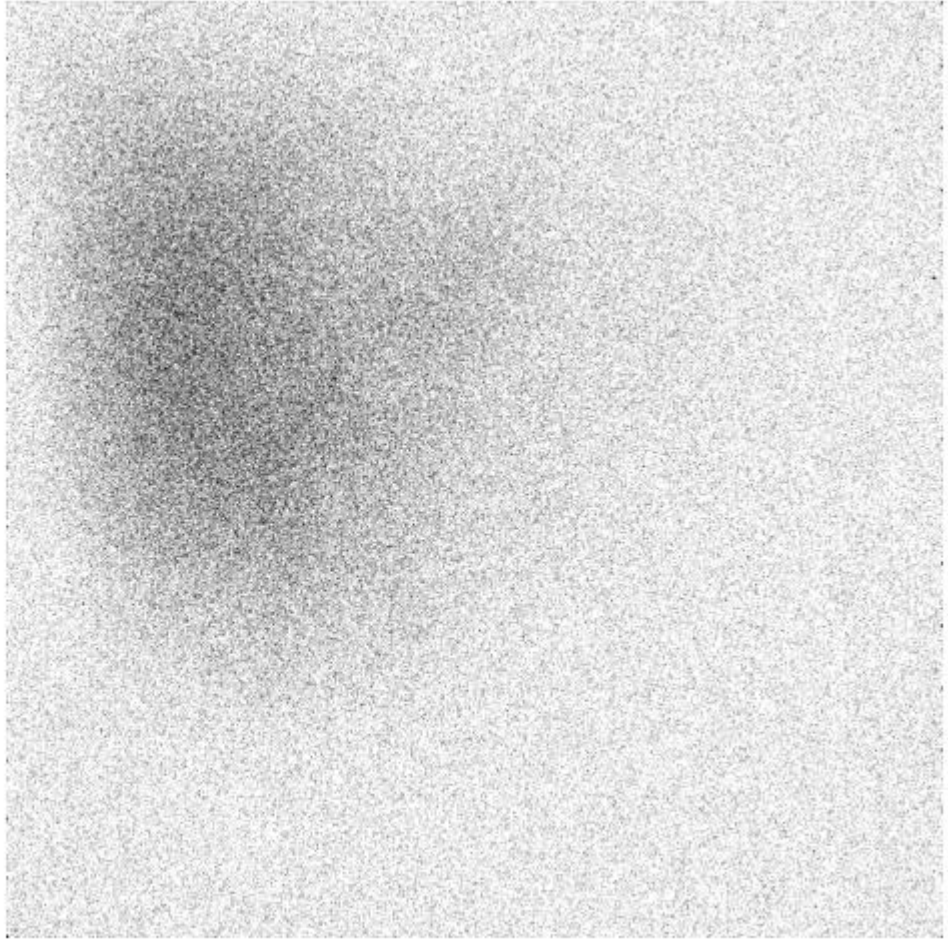
Instead we found initial dark count rates for the NUV-MAMA as high as 0.016 counts/pix/s (Figure 7.20). As was the case before SM4, the dark current shows short time scale variations that depend exponentially on the detector temperature, with the overall level also varying on longer time scales. However, for the new component of the dark current, the decay time-scale appears to be much longer than the one to two weeks previously seen. Initially the excess dark current appeared to be declining with an e-folding time of about 100 days; however over subsequent months, the rate of decline has continued to slow. By mid-2010 the dark rate was fluctuating between about 0.0025 and 0.0042 counts/pix/s, and it appears that additional significant declines will take years rather than months. For planning purposes and the STIS ETCs, we will adopt a mean NUV-MAMA dark current of 0.0013 counts/pix/s for mid-Cycle 32 (April 2025). Updates on the current state of the dark current are posted on the [STIS MAMA dark monitor pages](#).

FUV-MAMA Dark Current

The FUV-MAMA dark current is substantially lower than that of the NUV-MAMA . Initially, values as low as 7 counts/s across the face of the detector (7×10^{-6} counts/pix/s) could be routinely expected. However, there is also an intermittent glow that covers a large fraction of the detector (see Figure 7.21). The source of the dark current is not phosphorescence, but is intrinsic to the micro-channel plate array (it was seen in ground testing). This glow can substantially increase the dark current over a large fraction of the detector, and this leads to count rates of up to 300 counts/s integrated across the face of the detector.

An example of the dark current variation across the detector can be seen in Figure 7.21, which is the sum of a number of 1380-second dark frames taken during periods of high dark current. The dark current in the lower right quadrant appears to be stable to within 10% over time. The dark current in the upper left quadrant varies with time and temperature. The total dark current can be approximated by the sum of a constant dark current plus a "glow" image, scaled to the net rate in the upper left quadrant.

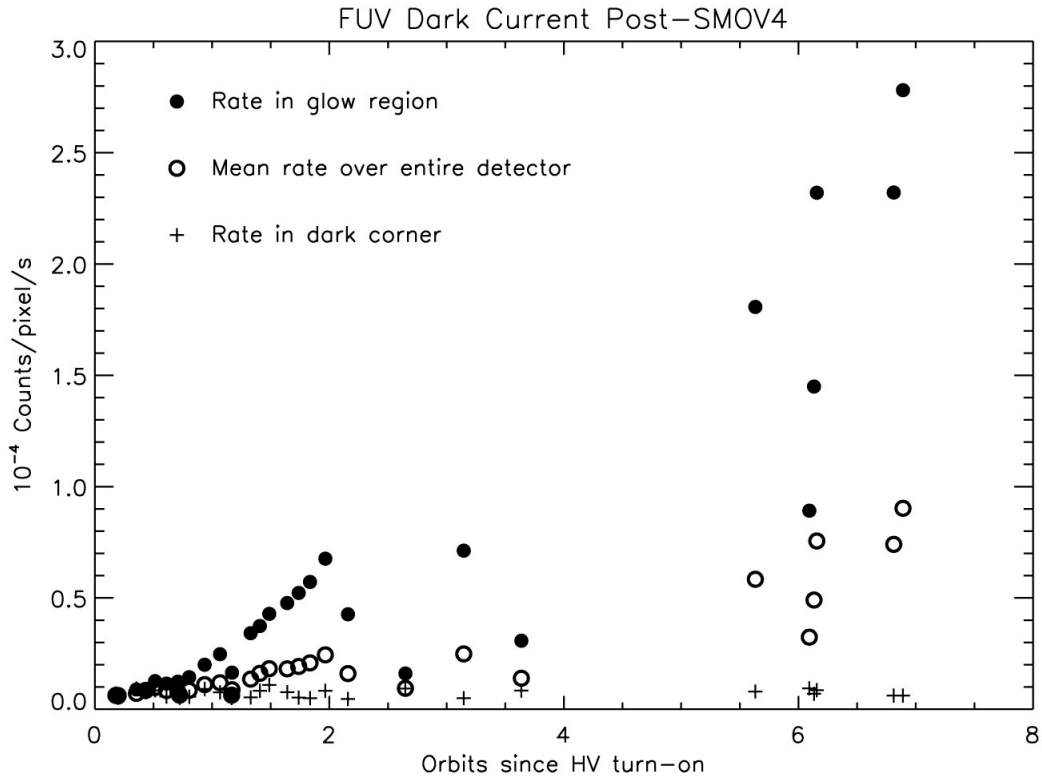
Figure 7.21: Dark Current Variation Across FUV-MAMA Detector.



The region in the upper left quadrant has the higher dark current.

During the first two years of STIS operations, this glow was only present intermittently, but since mid-1999 it has been present more often than not. The glow increases with the amount of time the detector high-voltage has been on since the last SAA passage. The rate of increase is greater when the detector is warmer, and it has also been increasing from year to year, even under otherwise comparable conditions. The dark monitor measurements for the first few months of STIS operations after the repair during SM4 are shown in [Figure 7.22](#), while long-term monitor measurements are shown in [Figure 7.23](#).

Figure 7.22: Post SM-4 FUV-MAMA Dark Monitor Measurements obtained between Jun. 9 and Oct. 1, 2009.



The average count rate for a region in the upper left of the FUV detector that is centered on the bright glow, (pixels [200:400,600:800]), is plotted as a function of the time since the detector high voltage was turned on (filled circles). Also shown is the mean rate for the whole detector (open circles), and the mean rate in the dark corner (pluses), delimited by the subarray [900:1000,10:110]. In Figure 7.22, the FUV-MAMA dark current is shown for 35 dark monitor observations taken between 2009-Jun-09 and 2009-Oct-01. On days that the FUV-MAMA is used, the MAMA high voltage is turned on for the block of *HST* orbits that is unaffected by SAA passages, and as the detector warms up, the glow increases. Filled circles show the count rate in a region centered on the peak of the dark glow (pixels [200:400,600:800]), while the open circles show the average rate for the entire detector. Note that the lower right corner of the detector (pixels [900:1000,10:110]), denoted by plus signs, shows little or no increase over the initial low dark current values.

Figure 7.23: FUV-MAMA Long-Term Dark Current after SM4.

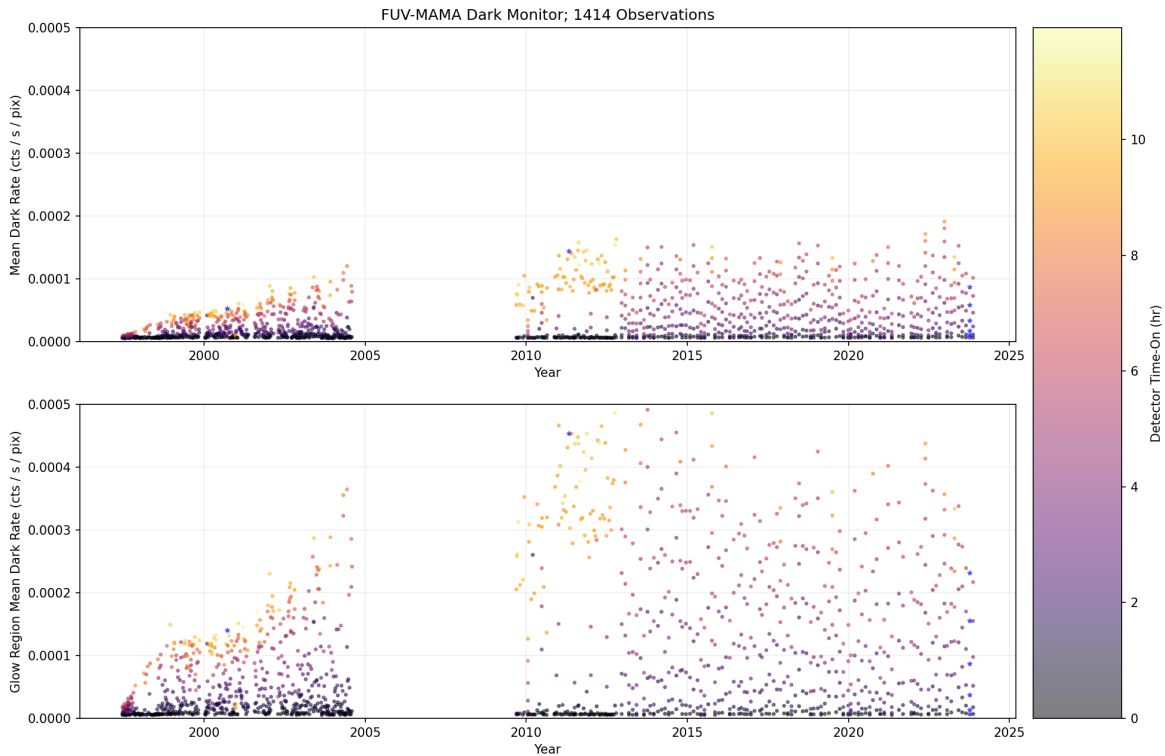


Figure 7.23 shows the long-term FUV dark current before and after SM4. The top plot shows the average dark rate over time for the full detector, while the bottom plot is restricted to the glow region. The different colors show how the dark rate trends vary with high voltage on-time. The dark current varies depending upon the detector region, detector temperature, high voltage on-time, as well as a long-term increase. The vertical distribution of points on the graph changes in 2013, but this is merely due to a change in scheduling of calibration observations relative to the high-voltage turn-on. After SM4, the overall level of the glow appears to be similar to what had been seen in 2004, but because the physical origin of the FUV detector glow is poorly understood, it is difficult to predict what the future behavior will be. Past experience would indicate that the overall level of the glow will continue to increase.

For Cycle 32 planning purposes, we recommend assuming that in the center of the glow region the mean dark current will start with a value near 3.0×10^{-5} counts/pix/s at the beginning of each SAA-free block of orbits, but will then increase at a rate of about 6×10^{-5} counts/pix/s/*HST*-orbit, reaching peak values as high as 5×10^{-4} counts/pix/s. In the dark corner of the detector, the count rate will remain very low, with a rate near 3.0×10^{-5} counts/pix/s. The STIS **ETC** currently defaults to 7.5×10^{-5} counts/pix/s, as representative of the expected mean rate averaged over the whole detector in the first 2-3 orbits. While the **ETC** can only reflect the average of the dark current rate, the STIS FUV dark current rate in particular exhibits tremendous variations with the position on the detector. STIS FUV-MAMA users whose observations are sensitive to dark current (e.g., faint targets) are strongly encouraged to [read the corresponding documentation](#) to assess the feasibility of their observations and better constrain the exposure time needed to achieve the required accuracy.

The count rates discussed above refer to the native MAMA detector pixels. When comparing to **ETC** results these values need to be scaled by the number of pixels included in an extracted spectral "pixel" or resolution element. For observers of bright targets, even the highest FUV-MAMA dark rates will have a negligible impact on data quality. For observers of very faint targets, there are a number of possible mitigation strategies. For spectra of faint point sources, the observer should consider whether one of the COS FUV channels might be a better choice, as these have both much higher overall throughput and much lower detector background than comparable STIS modes. If STIS spectral observations are needed (e.g., to provide higher spatial resolution in the cross dispersion direction), the dark rate can also be minimized by putting the source near the bottom of the FUV-MAMA detector below the worst of the extra detector glow. The "D1" aperture positions are intended for this purpose (see [Section 4.2.3](#)). If neither of these strategies is adequate, the proposers should contact the [HST Help Desk](#) to discuss whether it may be practical to schedule their observations immediately after the detector high voltage has been ramped up, when the intrinsic detector background is lowest.

Because of the need to schedule STIS MAMA operations around the South Atlantic Anomaly (SAA), in practice, the FUV-MAMA detector is usually turned on only one time per day, and there is usually only about one orbit per day available where a detector background close to 1×10^{-5} c/s/pixel can be expected, so it may not be possible to satisfy all such requests. *Justification for this scheduling constraint must be provided under the Special Requirements section of the the Phase I proposal.*

Time-varying dark current for the FUV-MAMA is not currently subtracted by the pipeline. Some "average glow" images are available for off-line reduction to reduce the effects of the glow region. Users should contact the [HST Help Desk](#) to obtain access to these images.

Because the dark current is so low in the MAMA detectors, a typical STIS FUV-MAMA observation will have less than one count/pix from the dark. It is good to keep this in mind when reducing the data, as various standard measures of background (the median for example) are not good estimates when the data are quantized into just a few values. The best way to estimate the background is to identify hot pixels using the standard reference files, then use an unclipped mean for the remaining pixels in a source-free region of the image.

7.5.3 MAMA Signal-to-Noise Ratio Limitations

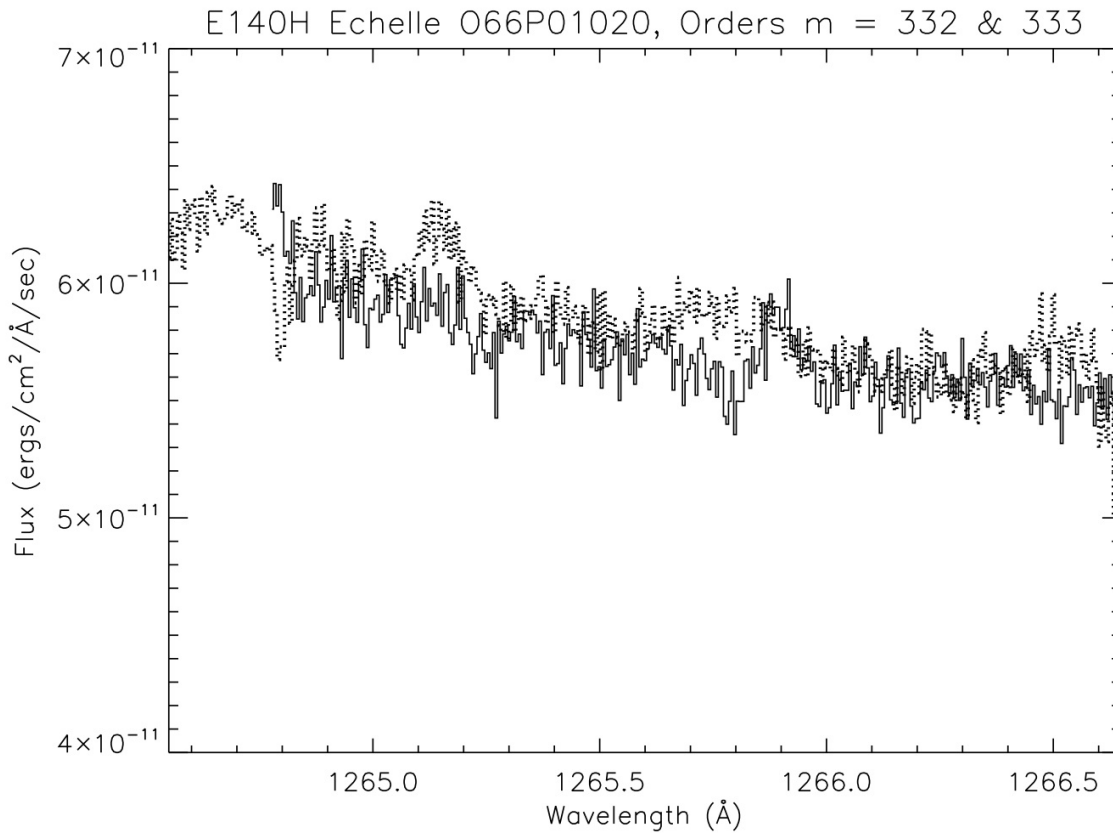
MAMA detectors are capable of delivering signal-to-noise ratios (S/N) of the order of 100:1 per spectral resolution element or even higher. Tests in orbit have demonstrated that such high S/N is possible with STIS ([Kaiser et al., 1998, Proc. SPIE, 3356, 415](#); [Gilliland, STIS ISR 1998-16.](#))

High S/N observations of several standard stars were obtained during STIS commissioning, and they were reduced with flats obtained during preflight testing of the detectors. Signal-to-noise ratios of 125 and 150 per spectral resolution element (for an 11 pixel extraction height in the cross dispersion direction) were achieved for the FUV- and NUV-MAMA observations, respectively; see [Chapter 12](#) for a more detailed discussion.

For targets observed at a fixed position on the detector, the signal-to-noise ratio is limited by systematic uncertainties in the small-scale spatial and spectral response of the detector. The MAMA flats show a fixed pattern that is a combination of several effects including beating between the MCP array and the anode pixel array, variations in the charge-cloud structure at the anode, and low-level capacitive cross-coupling between the fine anode elements. Intrinsic pixel-to-pixel variations are 3.9% and 2.8% rms for the FUV- and NUV-MAMA, respectively, in 1024 × 1024 pixel format. In the highres 2048 × 2048 format ([Section 3.2.1](#)) the intrinsic variations are much larger. This fixed pattern appears to be stable at the 1-2% level.

The structure of the flat may vary slightly for different modes due to different incidence angles of the incoming photons on the microchannel-plate pores. A possible example of this is shown in [Figure 7.24](#), where for an echelle E140H observation, the measured fluxes in the overlapping spectral range of two adjacent orders are displayed. The individual orders show broad features with widths of 10 to 30 pixels and amplitudes of 2 to 4% that are not reproduced in the other order at the same wavelengths. No corresponding features appear in the flat fields at these locations. These features also appear to be very sensitive to the exact placement of the spectrum on the detector, as other high signal-to-noise observations at the same CENWAVE setting do not show them. At wavelengths that are not covered by multiple spectral orders, the only way to distinguish this kind of detector artifact from a weak feature in the target spectrum is to use some kind of dithering to place the feature at multiple locations on the detector (see [Section 12.5.1](#)).

Figure 7.24: Flat-Field Features in a MAMA Spectrum.



The STIS echelle E140H spectrum O66P01020 of HD 24534 is shown for the wavelength range covering the overlap between spectral orders $m = 332$ (solid line) and $m = 333$ (dotted line). A number of weak features appear in only one of the two spectral orders, indicating that these are detector artifacts rather than real features in the stellar spectrum.

Observing strategies for achieving spectral S/N higher than $\sim 100:1$ are discussed in [Chapter 12](#). For echelle mode spectra, observers may want to consider the use of the FP-SPLIT slits, or use multiple CENWAVE settings with overlapping wavelength ranges; for first-order mode observations, they may wish to dither the target along the slit.

Since MAMA observations can be binned in post-observation data processing with no additional signal-to-noise price, the option to obtain MAMA observations with unequal binning (e.g., BINAXIS1=1, BINAXIS2=2) was disabled starting in Cycle 8.

7.5.4 MAMA Nonlinearity

Global

The MAMA detectors exhibit nonlinearity (photon incidence rate not equal to photon count rate) greater than 5% at global (across the entire detector) count rates of order 200,000 counts/s. The nonlinearity can be approximately corrected in post-observation data processing for rates up to ~285,000 counts/s. The MAMA detectors (plus processing software) are not able to count reliably at rates exceeding 285,000 count/s. For this reason and to protect the detectors from damage, observations at such high rates are not allowed (see [Section 7.7](#)).

Local

The MAMA detectors remain linear to better than 1% in their counting up to ~220 counts/s/pix for the FUV-MAMA and 340 counts/s/pix for the NUV-MAMA. At higher rates, they experience local (at a given pixel) nonlinearity. The nonlinearity effect is image dependent—that is, the nonlinearity observed at a given pixel depends on the photon rate affecting neighboring pixels. This property makes it impossible to correct reliably for the local nonlinearity in post-observation data processing. In addition, the MAMA detectors are subject to damage at high local count rates (see [Section 7.7](#)).

7.6 MAMA Spectral and Spatial Offsetting

[7.6.1 FUV First-Order Spatial Offset to Avoid Repeller Wire](#)

[7.6.2 Monthly Spatial and Spectral Offsetting of MAMA Modes](#)

7.6.1 FUV First-Order Spatial Offset to Avoid Repeller Wire

For the FUV-MAMA, the repeller wire produces a small shadow on the detector (with a depth of ~10%) which is apparent on FUV-MAMA flat-field images (see [Section 7.4.1](#)). To avoid first-order mode spectra falling on the repeller wire shadow, all data taken with the G140L and G140M gratings are projected to fall ~3.25 arcseconds (or ~110-130 low-resolution pixels, depending on the exact setting) below the detector center (see also [Section 11.1.2](#)). This offsetting is done using the Mode Select Mechanism to tilt the grating. For these modes the projected field of view is therefore asymmetric with respect to the specified target coordinates. Note that in Cycle 7, prior to March 15, 1999, the offset from the detector center was done in the opposite direction (to near `AXIS2=632`). However, as this caused G140L and G140M point source spectra to fall onto the region of the FUV-MAMA with the highest dark current (see [FUV-MAMA Dark Current](#)), this was changed to the current setting. Observers who wish to match the fields of view of Cycle 7 observations will need to take this difference into account.

7.6.2 Monthly Spatial and Spectral Offsetting of MAMA Modes

Beginning in January 1998 the projections of the spectra on the detector for *all* NUV- and FUV-MAMA spectroscopic modes were shifted slightly each month. This procedure was instituted in order to minimize uneven charge depletion in the microchannel plates that would increase the non-uniformity of the flat fields. These monthly charge-offsetting shifts, recorded in header keywords `MOFFSET1` and `MOFFSET2`, can shift the spectrum by up to ± 15 low-resolution pixels in `AXIS1` (dispersion) and up to ± 40 low-resolution pixels in `AXIS2` (cross-dispersion). Observers are advised to select settings that keep wavelength ranges and targets of interest away from the extreme ends of the long slits, lest they be inadvertently shifted off the edge of the detector.

Since August 2002, however, this monthly offsetting has been disabled for the MAMA echelle modes, though it continues to be done for 1st order MAMA spectroscopic modes. It was realized that moving the echelle spectrum in the `AXIS1` direction shifts the echelle blaze function by a different amount than it shifts the wavelength scale. This misalignment of the blaze function with the wavelength scale makes proper flux calibration of the extracted spectrum significantly more difficult. In addition, the larger shifts in the spatial direction could change the set of echelle orders included on the detector.

STIS flux calibration programs routinely disable the usual monthly offsets with use of the `MSMOFF` mode. Because the MAMA detectors have not shown any evidence of uneven charge depletion (see [ISR 2021-02](#)), beginning in Cycle 30 this previously restricted capability was made available-but-unsupported for those GO programs requiring very high photometric accuracy or reproducibility. Scientific justification for the use of the `MSMOFF` mode is required in the Phase I for it to be approved (contact the [Help Desk](#) for help implementing this mode). See [Section A.3](#) for more information.

7.7 MAMA Bright Object Limits

[7.7.1 Overview](#)

[7.7.2 Observational Limits](#)

[7.7.3 How Do You Determine if You Violate a Bright Object Limit?](#)

[7.7.4 Policy and Observers' Responsibilities in Phase I and Phase II](#)

[7.7.5 Policy on Observations that Fail Because They Exceed Bright Object Limits](#)

[7.7.6 What To Do If Your Source is Too Bright for Your Chosen Configuration?](#)

[7.7.7 Bright Object Protection for Solar System Observations](#)

STScI has responsibility to ensure that the MAMA detectors are not damaged through over-illumination. Consequently, we have developed procedures and rules to protect the MAMAs. We ask all potential users to share in this responsibility by reading and taking note of the information in this section and designing observing programs that operate in the safe regime for these detectors.

7.7.1 Overview

The MAMA detectors are subject to catastrophic damage at high global and/or local count rates and therefore cannot be used to observe sources that exceed the defined safety limits. Specifically, charge is extracted from the microchannel plate during UV observations, and overillumination can cause a decrease of quantum efficiency in the overexposed region, or even catastrophic failure if excess gas generation from the microchannel plates causes arcing in the sealed tube.

To safeguard the detectors, checks of the global (over the whole detector) and local (per pixel) illumination rates are automatically performed in flight for all MAMA exposures. The *global illumination rate* is monitored continuously. If the global rate approaches the level where the detector can be damaged, the high voltage on the detector is automatically turned off. This event can result in the loss of all observations scheduled to be taken with that detector for the remainder of the current observing calendar (~1 week). The *peak local illumination rate* is measured over the MAMA field at the start of each new exposure. If the local rate approaches the damage level, the STIS shutter will close, and that exposure will be lost. Details of these procedures may be found in STIS ISRs [1996-28](#), [1996-31](#), and [1998-08](#).

i *Sources that would over-illuminate the MAMA detectors cannot be observed. It is the responsibility of the observer to avoid specifying observations that exceed the limits described below.*

7.7.2 Observational Limits

To ensure both the safety of the MAMA detectors and the robustness of the observing timeline, we have established observational limits on the incident count rates. Observations that exceed the allowed limits will not be scheduled.

The definitive guidelines for bright object limits are given in [STIS ISR 2000-01](#), but the following brief discussion is included here for convenience. The allowed limits are given in [Table 7.8](#), which includes separate limits for non-variable and irregularly-variable sources. The global limits for irregularly variable sources are a factor 2.5 more conservative than for sources with predictable fluxes. Predictable variable sources are treated as non-variable for this purpose. Examples of sources whose variability is predictable are Cepheids or eclipsing binaries. Irregularly variable sources are, for instance, cataclysmic variables or AGN. Here and in general, "pixel" refers to the 1024 × 1024 format (low-res pixels).

Table 7.8: Absolute MAMA Count Rate Limits

| Target | Limit Type | Mode | Channel | Screening Limit |
|----------------------|------------|---|-----------|-------------------------------|
| Non-variable | Global | All modes other than 1st-order spectroscopy | FUV & NUV | 200,000 counts/s |
| Non-variable | Global | 1st-order spectroscopy | FUV & NUV | 30,000 counts/s |
| Non-variable | Local | Imaging | FUV & NUV | 100 counts/s/pix |
| Non-variable | Local | Spectroscopy | FUV & NUV | 75 counts/s/pix |
| Irregularly Variable | Global | All modes other than 1st-order spectroscopy | FUV & NUV | 80,000 counts/s ¹ |
| Irregularly Variable | Global | 1st-order spectroscopy | FUV & NUV | 12,000 counts/s ¹ |
| Irregularly Variable | Local | Imaging | FUV & NUV | 100 counts/s/pix ¹ |
| Irregularly Variable | Local | Spectroscopy | FUV & NUV | 75 counts/s/pix ¹ |

¹ Applies to the phase when the target is brightest.

7.7.3 How Do You Determine if You Violate a Bright Object Limit?

As a first step, you can check your source *V* magnitude and peak flux against the bright object screening magnitudes in [Table 13.45](#) or [Table 14.40](#) for your chosen observing configuration. In many cases, your source properties will be much fainter than these limits.

However, if you are near these limits, then you need to carefully consider whether your source will be observable in that configuration. Note that the limits in these tables assume zero extinction, and for spectroscopic observations do not include slit losses. Thus you will want to correct the limits appropriately for your source's reddening and the aperture throughput.

You can use the information presented in [Section 6.2](#) to calculate your peak and global count rates or (more conveniently) you can use the STIS [ETCs](#) to calculate the expected count rates from your source. The [ETCs](#) have a host of template stellar spectra available. If you have a UV spectrum of the source, you can also input it directly into the calculators. The calculators will evaluate both the global and per pixel count rates and will warn you if the exposure exceeds the absolute bright object limits.

You should also be aware that the local rate monitor does not perform a measurement of the actual flux per pixel. Instead, the check image is binned into "superpixels," each one with a size of 8×8 (imaging) or 4×8 (spectroscopy) regular (low-res) pixels, and the resulting measured flux for each superpixel is transformed into a peak flux per pixel, assuming that a single isolated point source contributes to the flux in that bin. Therefore, you should be extra careful when observing a crowded field or a slightly resolved source in imaging mode, since it is possible for the exposure to be aborted even when no single source violates the local rate limit (e.g., two or more stars fall inside the same bin or a source with a non-point source radial profile is present in the field). See [STIS ISR 1996-31](#) for more details.

7.7.4 Policy and Observers' Responsibilities in Phase I and Phase II

i *It is the observers' responsibility to ensure that their observations do not exceed the bright object count limits stated in [Table 7.8](#).*

It is your responsibility to ensure that you have checked your planned observations against the brightness limits prior to proposing for Phase I. If your proposal is accepted and we (or you) subsequently determine in Phase II that a source violates the absolute limits, then you will either have to: a) choose a different configuration, if possible, b) change the target, if allowed, or c) lose the granted observing time. We encourage you to include a justification in your Phase I proposal if a target is within 1 magnitude of the bright object limits for your observing configuration. For MAMA target-of-opportunity proposals, please provide an explanation or strategy of how you will ensure that your target can be safely observed in your Phase I proposal. The observing strategy might include additional observations, obtained over a time-scale appropriate to the particular type of object, with either *HST* or ground-based telescopes. Proposers should be aware that this type of observation requires extra resources. STScI reserves the right to limit the number of visits requiring quiescence verification observations within 20 days or less of an *HST* observation to no more than 12 such visits per Cycle including all *HST* instruments.

Following their Phase I approval, proposers of MAMA observations are required to check both their targets and the fields surrounding those targets (as defined below) in detail for excessively bright sources, by the Phase II deadline. The relevant policies and procedures are described here.

STScI has developed bright object tools (**BOT**) to conduct detailed field checking prior to MAMA program implementation. These tools are based on an automated analysis of the fields by means of data from the Second Guide Star Catalogue (GSC2) and displays of the Digital Sky Survey (DSS). GSC2 provides two magnitudes (photographic *J* and *F*), hence one color, for most fields down to about 22nd mag, which, combined with conservative spectral type vs. color relationships, supports determinations of safety (or otherwise) for individual objects. In the best cases, these procedures allow expeditious safety clearing, but in some cases the GSC2 is inadequate (e.g., due to crowding or to the absence of data for one of the filters). In such cases, supplementary information must be provided by the proposers to support the bright object protection (BOP) process. The target should always be checked directly in the **ETC** with the more detailed information generally available for it, rather than relying on its **BOT** field report data.

Subsequently, automated *GALEX* screening was added as a selectable option in the **BOT**. The AIS (all-sky) sources are screened as unreddened O5 stars and reported as either safe or unsafe. This is a powerful tool, because it is based directly on UV fluxes; e.g., previously unknown hot companions to late-type stars will be revealed. The target should still be checked with the **ETC**, but if the field passes it can be cleared, subject to verification with the *GALEX* image or catalogue display that there is complete coverage of the macro-aperture field. Unsafe objects require further investigation. The *GALEX* fluxes are upper limits in crowded regions because of the relatively low spatial resolution, and the source may clear with more specific parameter information. Please note that the fluxes and magnitudes given in the current version of the *GALEX* catalog do not include any correction for the local count rate non-linearity that affects high count rate sources. This can lead to serious underestimates of the flux for the brightest stars in the *GALEX* catalog. An estimate of the possible size of this effect is detailed in section 4.4 of [Morrissey et al. 2007 \(ApJS, 173, 682\)](#). The *GALEX* screening done by the **BOT** now includes this estimated correction. This will sometimes result in the **BOT** reporting *GALEX* magnitudes that are brighter than those given in the *GALEX* catalog itself.

While STScI will check all targets and fields before any MAMA observations are cleared, by policy observers must provide screened, safe targets for MAMA programs, as well as supplementary data (as needed) to verify target and field safety. The **APT/BOT**, including an **Aladin** interface, makes the BOP procedures accessible for GO use. Extensive help files and training movies are available. While the procedures may appear complex at first, their convenience and straightforward application rapidly become apparent. All MAMA proposers must conduct BOP reviews of their targets and fields in conjunction with their Phase II preparations. By doing so, they will more quickly become aware of any problems, such as the need for supplementary data, which might otherwise entail lengthy implementation delays following the Phase II deadline. (One exception is for moving target fields, which must be cleared after the scheduling windows have been established.) To assist with these procedures, a Contact Scientist (CS) who is a MAMA/BOP specialist will be assigned to each MAMA program. The CS will interact with the GO as necessary and requested, both during the Phase II preparations and through program execution, and will perform independent checks on the safety of the observations.

For a single default MAMA pointing with unconstrained orientation, a circular field including a buffer around the rotated aperture must be cleared. The **APT/BOT** automatically reports on all GSC2 stars or *GALEX* sources within that field. If any displacements from the default pointing (e.g., **POSTARGS**, patterns, or mosaics) are specified, the field to be cleared increases commensurately. **POSTARG** vectors and the enlarged, rotated field circles are conveniently displayed in **APT/Aladin**. No unsafe star or star with unknown properties may lie within 5 arcseconds of the detector edge at any orientation (or 13.5 arcseconds for very bright sources, see below). **POSTARGS** and/or orientation restrictions may be introduced to avoid bright objects in the fields, however.

A GO proposing MAMA observations must send to the designated CS, by the Phase II deadline, the [ETC](#) calculations for each discrete target, as well as reports on any unsafe or unknown stars from [APT/BOT](#) for each field, either showing that the observations are in fact safe or documenting any unresolved issues. In the latter case, including inadequacy of [BOT/GSC2/GALEX](#) to clear the observations, other photometric or spectroscopic data sources must be sought by the GO to clear the fields. Although automatic BOP calculations are currently available only for GSC2 and *GALEX*, many additional data sources are available directly through the [APT/Aladin](#) interface, including the STScI Mikulski Archive (MAST), which contains data from *IUE* as well as from *HST*. An existing UV spectrogram of the target (or of a similar object) may be imported directly into the [ETC](#). *IUE* spectral data used for BOP calculations must be low resolution, taken through the large *IUE* aperture. If model spectra are used in the [ETC](#), the [original Kurucz models](#), which were used to define bright object limitations, should be used for early-type stars, rather than the more recent [Castelli & Kurucz models](#). For stars later than the Sun, none of the provided models is adequate, since they lack the chromospheric emission lines that dominate the actual FUV flux. In such cases, actual UV data, either for the target or for a very similar object, must be used. In the worst cases, new *HST* observations in safe configurations or ground based data may be required to clear the fields for BOP. In general, any such supporting *HST* observations must be obtained within the existing Phase I time allocation.

If a given star has only a *V* magnitude, it must be treated as an unreddened O5 star. (The older Kurucz O5 model with higher T_{eff} in the [ETC](#) should be used for BOP purposes.) If one color is available, it may be processed as a reddened O5 (which will always have a greater UV flux than an unreddened star of the same color). If two colors are available, then the actual spectral type and reddening can be estimated separately. The [APT/BOT](#) now automatically clears stars with only a single GSC2 magnitude, if they are safe when assumed to be unreddened O5 stars. Any other "unknowns" must be cleared explicitly. See also the special considerations for M dwarfs (below).

It is not expected that all such issues will be resolved by the Phase II deadline, but they should at least be identified and have planned resolutions by then. Another possible resolution is a change to a less sensitive MAMA or to a CCD configuration. Any MAMA targets or fields that cannot be demonstrated to be safe to a reasonable level of certainty in the judgement of the CS will not be observed. It is possible that equivalent alternative targets may be approved upon request in that case; but any observations that trigger the onboard safety mechanisms will not be replaced.

A related issue is MAMA pointing or configuration changes after the targets and fields have been cleared by the STScI BOP review. Any such changes must be approved by the STIS Team on the basis of a specific scientific justification and a new BOP review by the GO, which may be submitted via the CS if absolutely necessary. However, in general such requests should be avoided by ensuring that submitted MAMA specifications are final, to prevent a need for multiple BOP reviews.

GOs planning MAMA observations of unpredictably variable targets, such as cataclysmic variables, are reminded of the special BOP procedures in effect for them, which are detailed in [ACS ISR 2006-04](#). Observers should contact the [HST Help Desk](#) for more information about implementing these procedures.

Special Considerations for M Dwarfs

Because M dwarfs can exhibit strong (and unpredictable) flaring, special procedures have been developed ([STIS ISR 2017-02](#)) to check any known or potential such objects within the clearance regions. For programs targeting known M dwarfs, the CS will provide a spreadsheet based on those procedures for the GO to use to assess the safety of the proposed observations. Somewhat cruder assessments, based on available photometry, may be used to (conservatively) evaluate any possible additional M dwarfs in the clearance regions around the designated targets, if the information required for the full spreadsheet analysis is not available.

In some cases, the 2MASS JHK magnitudes may be the only photometry available for an otherwise "unknown" star. It is possible to estimate V and $E(B-V)$ from those data on the assumption of a reddened O5 star, and thus determine its count rates in the **ETC**. [F. Martins & B. Plez, A&A, 457, 637 \(2006\)](#), derive $(J-H)_0 = -0.11$ for all O stars; and $(V-J)_0 = -0.67$, $(V-H)_0 = -0.79$ for early O types (The K band should be avoided for BOP because of various instrumental and astrophysical complications). [M. S. Bessell & J. M. Brett, PASP, 100, 1134 \(1988\)](#), Appendix B, give relationships between the NIR reddenings and $E(B-V)$. These data determine the necessary parameters. Note that the **ETC** also supports direct entry of observed magnitudes along with any specified value for $E(B-V)$. Magnitudes, colors, and parallaxes from Gaia, together with the intrinsic values tabulated by E. Mamajek [here](#), may also be of use, particularly for later-type stars (though these are not currently supported in the **ETC**).

Pointings Close To Objects Violating Safety Limits

Pointings close to objects violating safety limits must be screened since (i) the possibility of *HST* pointing errors exists, and (ii) the light of a bright point source may pose a safety threat even if observed at a distance of several arcseconds.

Any field object within 5 arcseconds of the edge of an aperture used for a MAMA observation is subject to the same bright object limits as targets that are in the aperture. Targets or field objects falling in an annular region extending from 5 to 13.5 arcseconds from the edge of the aperture are also subject to some restrictions. Any object in this zone producing either a global count rate in excess of 1.5×10^6 counts/s or a local count rate greater than 500 counts/s/pix is not permitted. See [STIS ISR 2000-01](#) for a discussion of the current screening procedures.

7.7.5 Policy on Observations that Fail Because They Exceed Bright Object Limits

If your source passes screening, but causes the automatic flight checking to shutter your exposures or shut down the detector voltage causing the loss of your observing time, *then that lost time will not be returned to you*; it is the observer's responsibility to ensure that observations do not exceed the bright object limits.

7.7.6 What To Do If Your Source is Too Bright for Your Chosen Configuration?

If your source is too bright for one configuration, it may be observable in another configuration e.g., in a higher-dispersion configuration. The options open to you if your source count rate is too high in a given configuration include:

- Select a narrower slit that passes only a fraction of the source flux, for spectroscopic observations.
- Select a higher dispersion grating.
- For NUV low-resolution and medium-resolution spectroscopy, consider using the CCD G230LB and G230MB modes (see [Section 4.1.6](#)).
- Employ a neutral-density filter.
- Change configurations to observe a different portion of the spectrum of your target (e.g., change the central wavelength).

It may be possible to avoid bright field objects by specifying `ORIENT` restrictions to the visit and/or `POS TARGS` for the exposures.

For further advice, see [Section 12.4](#).

7.7.7 Bright Object Protection for Solar System Observations

Observations of planets with STIS require particularly careful planning due to the very stringent overlight limits of the MAMAs. In principle, [Table 13.45](#) and [Table 14.40](#) can be used to determine if a particular observation of a solar system target exceeds the safety limit. In practice, the simplest and most straightforward method of checking the bright object limits for a particular observation is to use the STIS `ETC`. With a user-supplied input spectrum, or with assumptions about the spectral energy distribution of the target, the `ETC` will determine whether a specified observation violates any bright object limits.

Generally speaking, for small ($< \sim 0.5$ – 1 arcsecond) solar system objects the local count rate limit is the more restrictive constraint, while for large objects ($> \sim 1$ – 2 arcseconds) the global limit is much more restrictive.

As a first approximation, small solar system targets can be regarded as point sources with a solar (G2 V) spectrum, and if the V magnitude is known, [Table 13.45](#) and [Table 14.40](#) can be used to estimate whether an observation with a particular STIS grating or filter is near the bright object limits. V magnitudes for the most common solar system targets (all planets and satellites, and the principal minor planets) can be found in the *Astronomical Almanac*. This approximation should provide a conservative estimate, particularly for the local limit, because it is equivalent to assuming that all the flux from the target falls on a single pixel, which is an overestimate, and because the albedos of solar system objects are almost always < 1 (meaning that the flux of the object will be less than that of the assumed solar spectrum at UV wavelengths where the bright object limits apply). A very conservative estimate of the global count rate can be obtained by estimating the peak (local) count rate assuming all the flux falls on one pixel, and then multiplying by the number of pixels subtended by the target. If these simple estimates produce numbers near the bright object limits, more sophisticated estimates may be required to provide assurance that the object is not too bright to observe in a particular configuration.

For large solar system targets, checking of the bright object limits is most conveniently done by converting the integrated V magnitude (V_o , which can be found in the *Astronomical Almanac*) to V magnitude/arcsec² as follows:

$$V/\text{arcsec}^2 = V_o - 2.5 \log(1/\text{area}),$$

where area is the area of the target in arcsec². This V/arcsec^2 and the diameter of the target in arcsec can then be input into the [ETC](#) (use the Solar Spectrum template in the *HST* Standard Star menu for the spectral energy distribution) to test whether the bright object limits can be satisfied.

Alternatively, an observed spectrum obtained with a known slit size can be used as input to the [ETC](#). Most calibration techniques produce units of flux (e.g., ergs/s/cm²/Å), even for extended targets. Such a calibration implicitly assumes a flux per solid angle (i.e., the angle subtended by the observing slit or object, whichever is smaller), and it is more appropriate to convert to units of surface brightness (ergs/s/cm²/Å/arcsec²) by dividing the calibrated flux by the appropriate area (slit size or object size, whichever is *smaller*). If such a spectrum is available, it can be immediately examined and compared with the local limit in units of surface brightness given in [Table 13.45](#) and [Table 14.40](#), or passed to the [ETC](#) as a user-supplied spectrum. It can also be easily converted to counts/s/pix by using the diffuse-source sensitivities for the appropriate grating or filter provided in this *Handbook*. Note that the sensitivities in this *Handbook* assume a specific slit *width*, so they need to be scaled by the desired slit width. The [ETC](#) provides another check of the local limit: if the peak count rate per pixel exceeds the local limit of 75 (for spectroscopic observations) or 100 (for imaging observations) counts/s/pix, such an observation would not be allowed. The global limit can be checked by summing the count rate per pixel over wavelength, and multiplying by the desired slit length (in arcseconds) divided by the pixel size (0.0247 arcsecond) to produce total counts per second for the observation. If this number is larger than the appropriate global limit, the observation should not be performed because it will cause the instrument to enter safe mode. For such cases, a smaller slit size or higher-resolution grating could then be considered.

Jupiter and Saturn

Detailed calculations and observational experience show that for Jupiter and Saturn, all FUV-MAMA imaging and spectroscopic modes are safe. Most NUV spectroscopic modes can also be used, but in many cases it will be necessary to use a very small or neutral density aperture to avoid excessive count rates. Of course the STIS CCD G230LB and G230MB gratings can be used without any bright object limitations, but for a red planetary object these CCD spectra will suffer substantial contamination from scattered light at shorter wavelengths.

Note that the global rate limit of 30,000 counts/s for first order spectroscopy was imposed because of the STIS Bright Scene Detection Monitor (see [STIS ISR 96-028](#)), which samples the output of every 32nd row. It could be triggered if a bright point source spectrum fell directly on one of the monitored rows. For extended sources observed with a long slit, the larger global limit of 200,000 counts/s is the relevant one for both echelle and first order spectroscopic observations.

Jupiter and Saturn are much too bright to be observed with most STIS NUV-MAMA imaging modes. However, the UVIS channel of the Wide Field Camera 3 (WFC3) has a number of UV filters that provide a better alternative for most NUV imaging science, as they have a larger field of view and no safety related bright object limits.

Field Safety Checks for Moving Targets

Multiple stellar fields along their paths must also be cleared for safety of moving target observations. Of course, this cannot be accomplished until scheduling windows are assigned, and it may have to be iterated if the windows change. An automated capability to do that has been added to the **APT/BOT**. Your Contact Scientist will advise and assist with this procedure.

Chapter 8: Target Acquisition

Chapter Contents

- [8.1 Introduction](#)
- [8.2 STIS Onboard CCD Target Acquisitions - ACQ](#)
- [8.3 Onboard Target Acquisition Peakups - ACQ PEAK](#)
- [8.4 Determining Coordinates in the International Celestial Reference System \(ICRS\) Reference Frame](#)
- [8.5 Acquisition Examples](#)
- [8.6 STIS Post-Observation Target Acquisition Analysis](#)

8.1 Introduction

- [8.1.1 Initial Pointing](#)
- [8.1.2 Acquisitions](#)
- [8.1.3 Peakups](#)
- [8.1.4 Drift Rates](#)

All STIS spectroscopy using apertures less than 3 arcseconds in size and all coronagraphic observations will require an onboard STIS target acquisition (ACQ) and possibly an acquisition/peakup (ACQ/PEAK) exposure to center the target in the scientific aperture at each new visit to a target. In this Chapter, we provide the basic information you need to choose an acquisition strategy for your program.

STIS target acquisitions employ the CCD camera to image the target's field directly and onboard flight software processes the image to locate the position of the target. STIS acquisitions are very reliable, accurate (typically ± 0.01 arcsecond for $V < 21$ point sources), and quick (~ 6 minutes). For the narrow slits (≤ 0.1 arcsecond), an ACQ/PEAK is required, which is accurate to $\sim 5\%$ of the slit width used in the peakup, and takes typically ~ 6 minutes. For particularly faint targets ($V > 21$) or complex diffuse sources, overheads will be somewhat more and accuracies somewhat reduced (see details below).

For Phase I proposals, you do not need to determine the details of your acquisition, but need only to determine if an ACQ, and possibly an ACQ/PEAK, is required, include the necessary orbital time (which is normally dominated by the associated overheads), and assure yourself that your program can be accomplished.

For Phase II, you will need to work out the details of your acquisition procedure, and we provide two tools to assist in this task, as well as examples of different target acquisition (TA) scenarios (see [Section 8.5](#)). To determine the correct exposure time, we provide (via the STIS webpage) a [Target Acquisition Exposure Time Calculator \(TA ETC\)](#). The input and output parameters in the **TA ETC** (as compared with the **Imaging ETC**) are specifically designed to facilitate exposure time estimates for target acquisition purposes. For example, the **TA ETC** input and output parameters take into account the following:

- The target acquisition can be done only with the CCD detector.
- The CHECKBOX (see below) size is always 3×3 pixels for a point source, and $n \times n$, where n is an odd number between 3 and 105, for diffuse sources.
- The CCDGAIN is always 4.
- The default S/N is 40 for the calculation of exposure time.

To determine the correct CHECKBOX size for DIFFUSE targets, we provide a [Target Acquisition Simulator \(TAS\)](#), which implements the same algorithms as the flight software, and so should give results in good agreement with what will happen in orbit. The TAS takes as input an image, extracts a subarray centered on the coordinates provided, and searches for the brightest location by passing a CHECKBOX over the subarray.

Below we describe acquisition and peakup exposures for spectroscopy. More details on centering of targets behind the coronagraphic bars and wedges are described in [Section 12.11](#), but examples are provided at the end of this chapter.

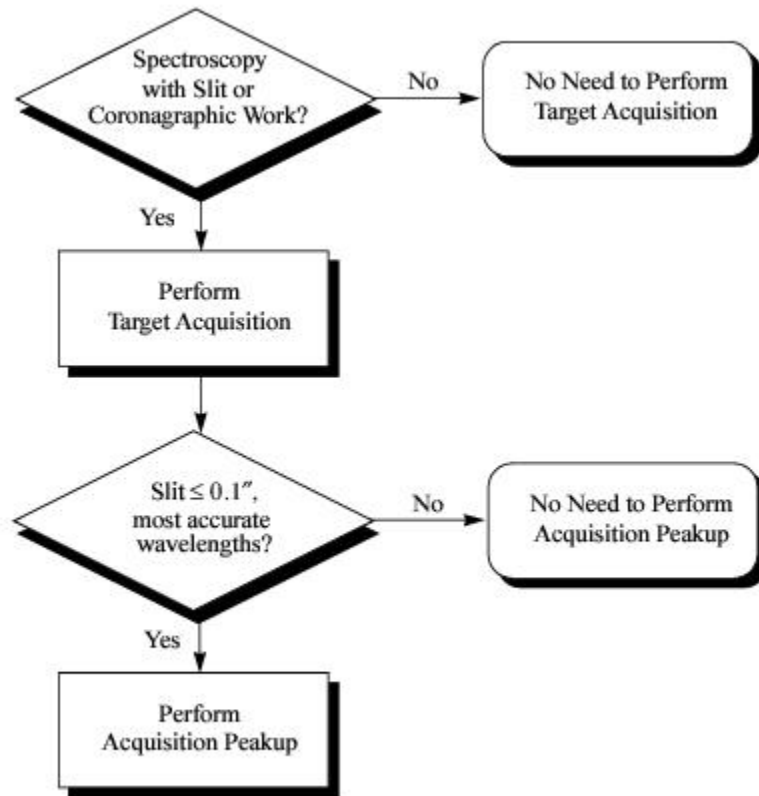
8.1.1 Initial Pointing

The error in initial placement of the target on the detector is due to error in the guide star catalog positions, error in the alignment of the science instrument (SI) to the fine guidance sensors (FGSs), and error in the target position itself. Guide star positions in the Guide Star Catalog 1 (GSC1), still in use when STIS operations were suspended during Cycle 13 in August 2004, had errors $\sim 1\text{--}2$ arcseconds. With the introduction of GSC2 coordinates in Cycle 15, those errors were reduced to ~ 0.25 arcseconds. The recent incorporation of coordinates from Gaia DR1 has further reduced the positional errors of the guide stars to ~ 0.2 arcseconds, with relative errors of order a few mas.

FGS-to-SI alignment tends to drift, especially in the first year following the installation of an FGS. Up until STIS operations were suspended, alignment errors were typically less than 1 arcsecond, but as great as 1.5 arcseconds for one FGS. Following Servicing Mission 4, the STIS-to-FGS alignment was found to be within 0.3 arcseconds of its expected position. In March 2012 the STIS position was re-measured using a new FGS calibration performed in January of the same year. The previously mentioned 0.3 arcsecond offset was corrected and the accuracy of the STIS-to-FGS alignment was improved to ~ 0.013 arcsecond. However, new data obtained in 2013–2014 indicate the STIS-to-FGS alignment drifted again in early 2013. As of Sept. 2014, the error was (again) around 0.3 arcseconds. At the present time the FGS-to-SI alignment error is similar in size to the GSC2 catalog error. Any future updates will be posted to the STIS web pages.

For scientific observations taken through spectroscopic slits and for imaging observations with one of the coronagraphic apertures, you will need to use an onboard STIS target acquisition and possibly an acquisition pickup to center your target. [Figure 8.1](#) shows a decision flow for determining whether you require an acquisition or both an acquisition and a pickup to center your target. Remember that accurate target placement is necessary to ensure accurate wavelength calibration of spectra as well as good throughput and accurate flux calibration of targets viewed through small apertures. (See Section 4.3 in the [STIS Data Handbook](#) for a more comprehensive discussion of the accuracy of flux and wavelength calibration.)

Figure 8.1: Determining Acquisition Requirements.



8.1.2 Acquisitions

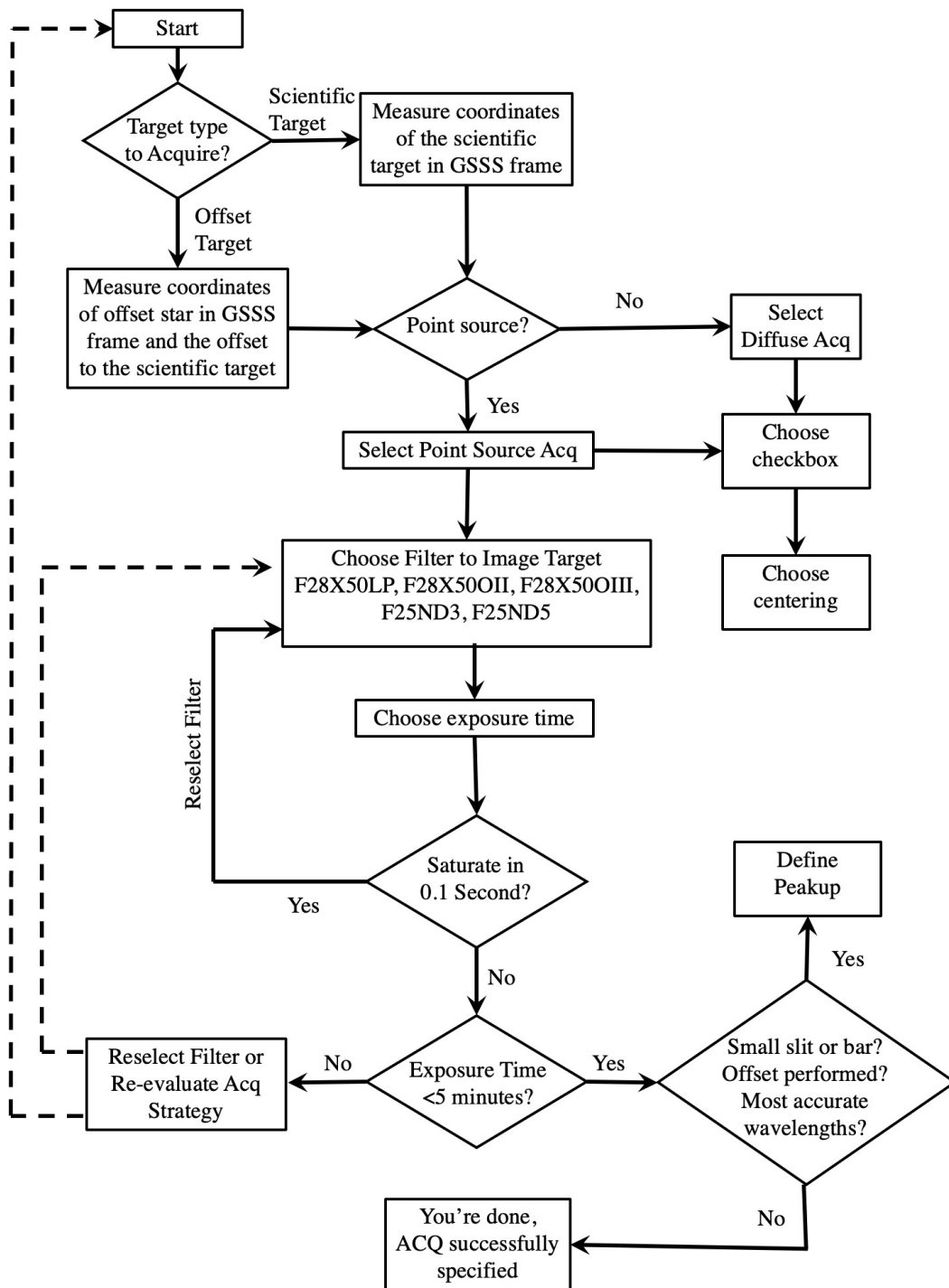
STIS target acquisition exposures (`MODE=ACQ`) always use the CCD, one of the filtered or unfiltered apertures for CCD imaging, and a mirror as the optical element in the grating wheel. Acquisition exposures center your target in the slit or behind a coronagraphic bar to an accuracy (2σ) of ~ 0.01 arcsecond for a point source, and 0.01 to 0.1 arcsecond for a diffuse object (larger targets have larger errors). A typical STIS point source target acquisition takes ~ 6 minutes.

8.1.3 Peakups

An acquisition peakup exposure (`MODE=ACQ/PEAKUP`) must be taken following the target acquisition exposure to refine the centering of point or point-like sources in slits less than or equal to 0.1 arcsecond wide (or tall). Peakup exposures use a slit, are taken with the CCD as the detector, and with either a mirror or a spectroscopic element in position on the grating wheel. Typical target acquisition centering accuracies following a peakup sequence are 0.05 times the dimension of the slit or bar. Typical STIS imaging point source peakups take ~5–10 minutes; see [Table 8.5](#) for the formulae needed to determine the duration of a peakup acquisition. Any uncertainty in the target's position along the dispersion direction translates directly into an uncertainty in the zero point of the wavelength scale. So observers who need the best possible absolute wavelength accuracy will need to perform an `ACQ/PEAKUP` even if their science observations will be performed using a wide aperture. However, the `ACQ/PEAKUP` exposure itself should never use an aperture wider than 0.1 arcsecond in the dispersion direction. A peakup on the target may also be warranted if the initial acquisition was of an offset star.

[Figure 8.2](#) shows the complete decision tree for STIS target acquisitions.

Figure 8.2: Process of Defining a Target Acquisition Scheme.



8.1.4 Drift Rates

For most exposures, two guide stars will be used to support the observation, enabling correction of drift. In some cases, however, it may not be possible to find a guide star pair to support the observation, or the observation may drop to single guide star mode because one of the guide stars cannot be acquired. In that case, the roll of the telescope is under GYRO control, which will allow a slow drift of the target on a circular arc centered on the single guide star. If you are informed that only single guide stars can be found for your observation, you can try to get a guide star pair by relaxing the scheduling requirements (e.g., expand the `ORIENT` range). If you must use a single guide star for a multiple-orbit visit, or if your observation is especially time-critical and would be significantly degraded by failure to single guide star mode, you should consider including a re-centering `ACQ/PEAK` during the visit.

Table 8.1 gives what is generally the worst case object motion of the target on the detector for a single guide star observation. For example, if a science observation in an 0.2 arcsecond slit is 3 orbits in duration, then the target would move to the edge of the aperture; a 2 orbit visit would leave the target halfway toward the edge. Thus, only single orbit visits should be done on a single guide star. However, for science in a 2 arcsecond slit, the motion over 4 orbits only takes the target 13% of the way to the edge of the slit. Thus, if high photometric accuracy is not required, a single guide star should be sufficient for the larger slits.

Table 8.1: Single Guide Star Target Position Shift in Arcseconds vs. Time and Orbits.

| Drift (arcseconds) | | | | | | | | | |
|--------------------|------|------|------|------|------|--------|------|------|------|
| Seconds (x1000) | | | | | | Orbits | | | |
| 1 | 2 | 5 | 10 | 15 | 20 | 1 | 2 | 3 | 4 |
| 0.005 | 0.01 | 0.03 | 0.06 | 0.08 | 0.10 | 0.03 | 0.06 | 0.10 | 0.13 |

For a completed observation, you can use information in the headers of the archived files to make a better estimate of the drift of the target for a single guide star observation. The rate of the drift of the radiant (radius) of the circle traced by the target about the guide star is unknown for any particular observation, but typically is expected to be in the range of 1.0 to 1.5 milliarcsec/s. To calculate the approximate magnitude of the drift of the target on the detector, you will need to find the distance of the target from the acquired guide star. The header of the observation log file `jif.fits` identifies the acquired guide star (`GSD_ID`) and gives its right ascension (`GSD_RA`) and declination (`GSD_DEC`) in degrees. For example, for a target 10 arcmin from the guide star, a drift of the guide-star-to-target radiant of 1 milliarcsec/s during a 1000 second exposure would cause the target to move 0.0029 arcsecond on the detector. The direction of the motion on the detector can be deduced from header keywords in the science data describing the position angle of the detector (e.g., `PA_APER`), in combination with the direction perpendicular to the radiant.

8.2 STIS Onboard CCD Target Acquisitions - ACQ

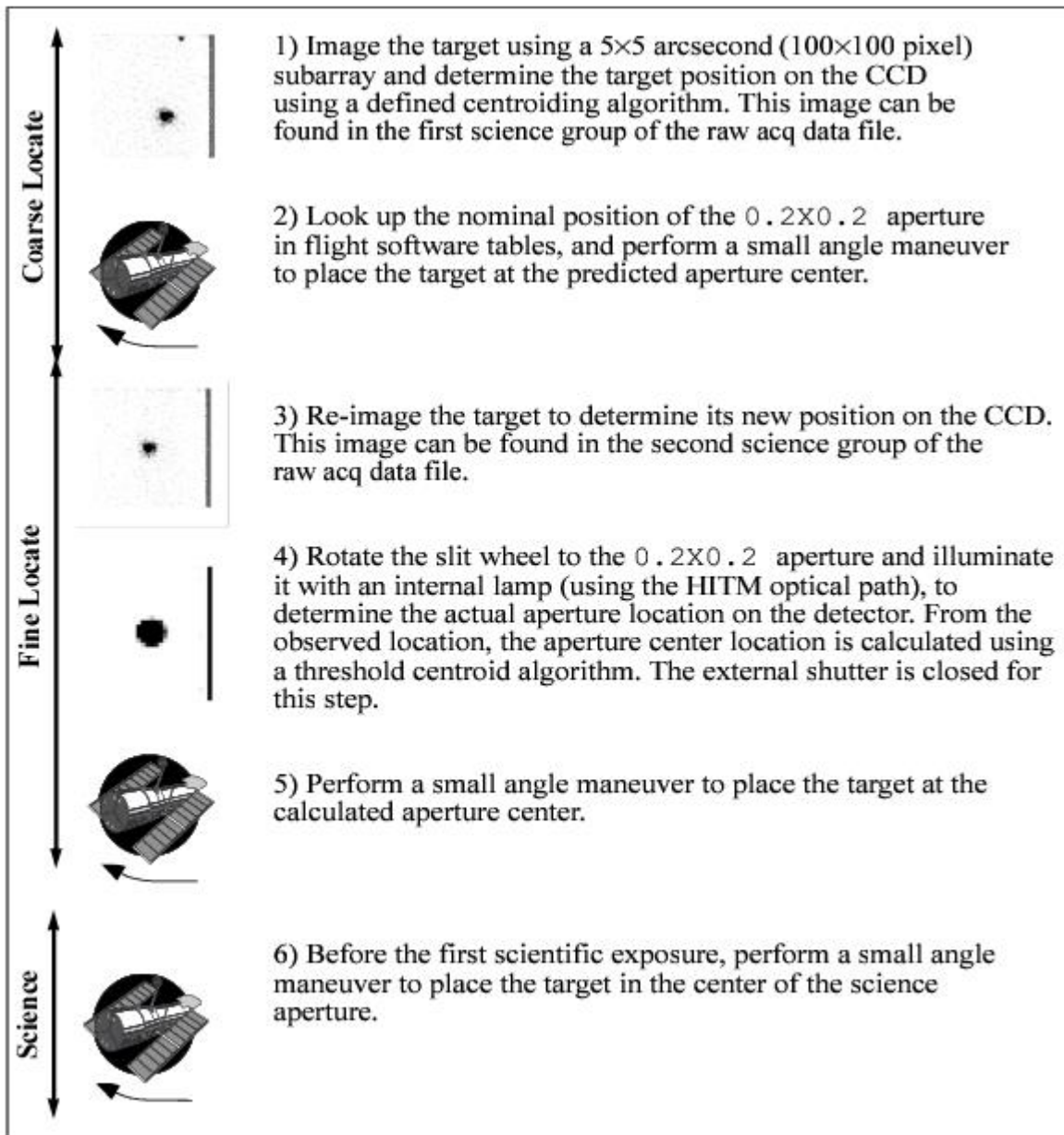
- [8.2.1 How It Works](#)
- [8.2.2 Target Location Algorithms](#)
- [8.2.3 Selecting Target Acquisition Parameters](#)
- [8.2.4 Specifying Acquisitions in Phase II](#)
- [8.2.5 Solar System Acquisitions](#)

8.2.1 How It Works

A target acquisition is performed at the beginning of a visit, and acquisition exposures are controlled by the Flight Software (FSW). [Figure 8.3](#) highlights the basic steps in the acquisition process. The sequence comprises two discrete stages: the coarse-locate phase (steps 1-2) and the fine-locate phase (steps 3-5); a sixth step centers the target in the science aperture. The coarse-locate phase is performed to place the target as close as possible to the aperture center prior to the final telescope move. This step ensures that the final slew needed to move the target into the aperture is a small one, and it minimizes uncertainties in the calculation of the required slew caused by detector or optical distortions. The target acquisition steps are discussed in detail below.

1. The target is located. A pair of 5×5 arcsecond (100×100 pixel) CCD images is taken of the sky using a user-selected filtered or unfiltered imaging aperture; for diffuse acquisitions, the field will be larger (see [Section 8.2.2](#)). The images are offset by 3 pixels in both X and Y to allow for removal of hot pixels via dithering. The flight software processes the images as needed (to realign the images, remove the bias level, flag bad pixels, and remove cosmic rays)¹ and applies one of two possible finding algorithms to determine the coordinates of the target. The "bright" column at the edge of the acquisition field is an artifact of the subarray readout and is ignored by the flight software.
2. The spacecraft is then moved to place the target at the nominal center of the 0.2×0.2 slit.
3. The target is re-imaged and the target coordinates are redetermined. This second target location is performed to minimize the final slew in step 5, and to reduce the error associated with that slew.
4. The location of the 0.2×0.2 slit is determined relative to the target. The external shutter is closed (to prevent a possible overlight condition), the 0.2×0.2 slit is rotated into position by the slit wheel, and an image is obtained with the slit illuminated by a HITM line lamp (see [Section 3.2.2](#) for a description of the HITM optical path). The slit image is processed and a finding algorithm is then used to determine the coordinates of the center of the slit.
5. The flight software calculates the offset between the target location and the 0.2×0.2 slit, and performs a small angle maneuver of *HST* to place the target in the center of the aperture.
6. The object is placed in the science aperture (by a small angle maneuver using the known offset between the two slits) just prior to the execution of the scientific exposure. If another science exposure is made with a different aperture, the pointing is automatically adjusted to account for any difference in the locations of the science apertures.

Figure 8.3: Target Acquisition Schematic.



An acquisition exposure produces data, which include the images of the target produced in steps 1 and 3, and the image of the 0.2×0.2 slit produced in step 4. These data will be returned to you with your scientific data as part of the pipeline products, and they can be analyzed with the [tastis tool](#) in [stistools](#).

8.2.2 Target Location Algorithms

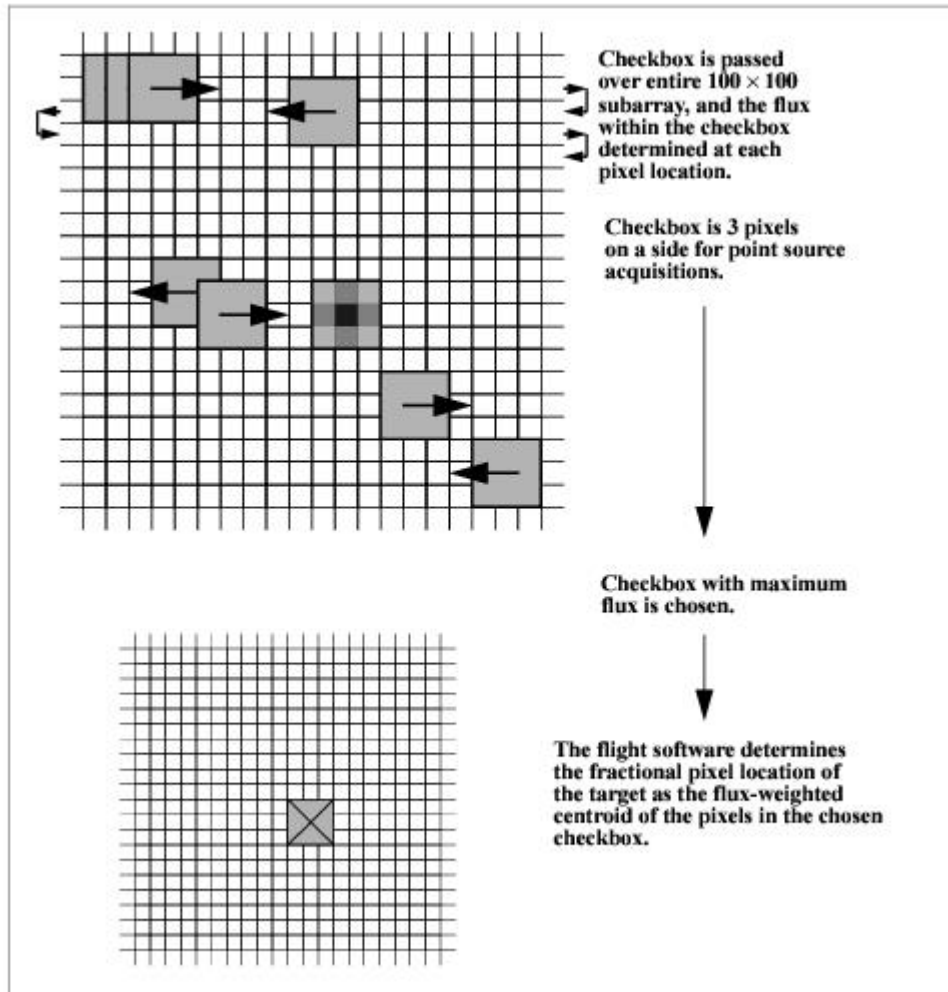
STIS supports two basic types of acquisitions: point source acquisitions (`ACQTYPE=POINT`) and diffuse source acquisitions (`ACQTYPE=DIFFUSE`). Diffuse source acquisitions are appropriate for sources that exhibit smooth or peaked surface brightness *on some size scale*, such as centers of galaxies, some planets and planetary satellites (see [Section 8.2.5](#)), or nebulae.

To locate the target, the flight software first passes a square *checkbox* over the image and determines the flux contained within the checkbox at each pixel in the subarray. The flight software then selects the checkbox with the maximum flux and determines the target center within that checkbox according to the type of acquisition specified.

Point Source Acquisition

For point source acquisitions (`ACQTYPE=POINT`), the checkbox size is fixed at 3×3 pixels (0.15×0.15 arcsecond) and the flight software determines the target location by finding the flux-weighted centroid of the pixels in the brightest checkbox (see [Figure 8.4](#)).

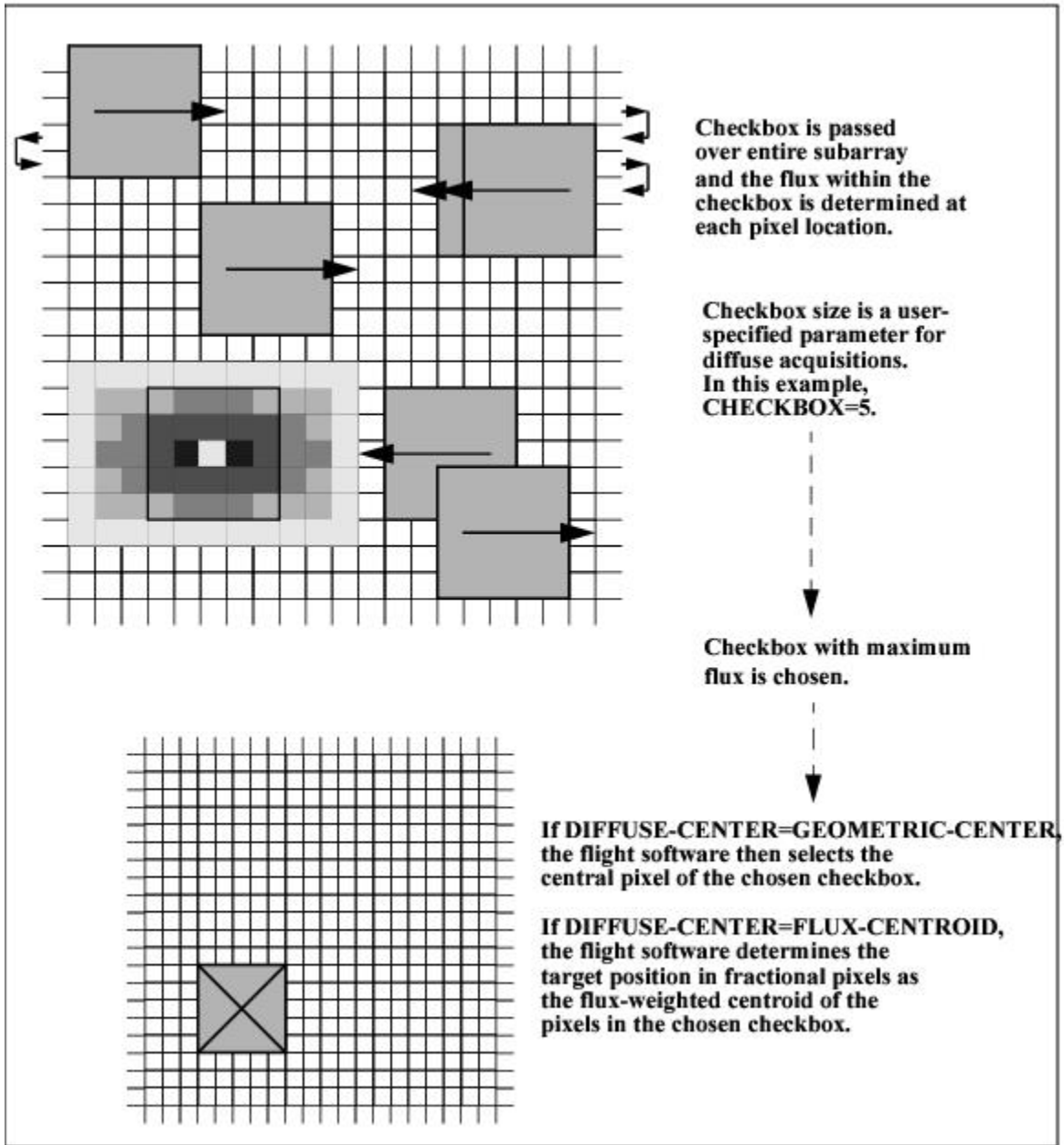
Figure 8.4: How the Checkbox Works for Point Source Acquisitions.



Diffuse Acquisition

For diffuse acquisitions ($ACQTYPE=DIFFUSE$), the flight software determines the target location either by finding the flux-weighted centroid of the pixels in the brightest checkbox or by determining the geometric center of the brightest checkbox (see [Figure 8.5](#)).

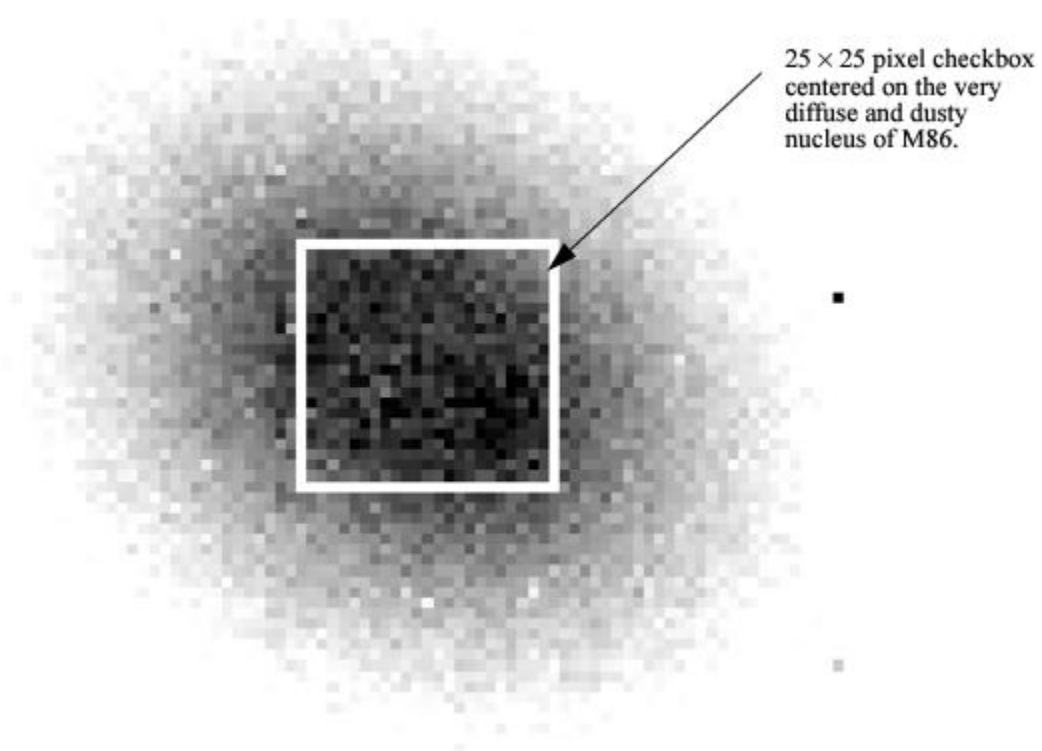
Figure 8.5: How the Checkbox Works for Diffuse Acquisitions.



For diffuse acquisitions, the user must specify both the target acquisition centering method (DIFFUSE-CENTER= GEOMETRIC-CENTER or FLUX-CENTROID) and the checkbox size. The user sets CHECKBOX= n , where n must be an odd number between 3 and 105: the checkbox will then have dimension $n \times n$ pixels. CHECKBOX should be set to the minimum size which ensures that the brightest checkbox will be the one centered on the region of interest (i.e., if your object is peaked within a region of 1 arcsecond, set CHECKBOX=21 [= (1arcsecond)/(0.05 arcsec/pix) + 1]). The maximum checkbox is 105 pixels on each side, or $\sim 5 \times 5$ arcseconds. The subarray used for a diffuse-source acquisition target image is CHECKBOX+101 pixels on each side. The [STIS Target Acquisition Simulator](#) can be used to determine the optimal CHECKBOX size. For more information about determining the optimal checkbox size, please see the [November 2018 STIS STAN](#).

Figure 8.6 shows a simulated example of a diffuse source, the nucleus of the galaxy M86, acquired using a diffuse-source acquisition.

Figure 8.6: Simulated Diffuse Acquisition of Elliptical Galaxy M86.



Created by running the flight-software algorithm on a STIS image. `ЧЕКБВОХ=25` produced good centering. Smaller values caused checkbox to center on local brightness enhancements offset from galaxy center.

8.2.3 Selecting Target Acquisition Parameters

To plan your acquisition, you must select:

- The target you are going to acquire (scientific target or offset object).
- The type of acquisition, point or diffuse, and if you are performing a diffuse acquisition, the target acquisition centering algorithm and checkbox size.
- The filtered `APERTURE` to be used for target imaging during the acquisition.
- The exposure time for the image used to determine the location of the -target.
- The program aperture, which determines if you need a pickup acquisition.

[Figure 8.2](#) shows the flow of specifying a target acquisition scheme.

Selecting the Acquisition Object

The first step is to determine what object you are going to use for your target acquisition. Note that the STIS software will always acquire the brightest object in the 5×5 arcsecond search area. If your target is isolated, or if there are no brighter objects in the STIS bandpass you have selected (see below) within 5 arcseconds of your target, then you can acquire your target directly. If there are brighter targets nearby, then you will need to acquire an offset target (generally the brightest nearby star), and then perform a slew to the scientific target. The offset technique is also recommended for precise pointing to specific surface or atmospheric features for large ($> \sim 4$ arcseconds) planetary targets such as Mars, Jupiter, and Saturn, with the offset target being a planetary satellite (see [Section 8.2.5](#) for further details). Note that *HST* performs small angle maneuvers (SAM) quite accurately, with a 3 arcsecond maneuver having an error of 0.003 arcsecond, while a 2 arcminute maneuver (the maximum to ensure that a single set of guide stars can be used for both targets) yields a 0.02 arcsecond error. The offset should not significantly affect target acquisition centering accuracy even in the smallest echelle slits, and your target acquisition centering uncertainty will generally be dominated by your knowledge of the absolute offset between the acquisition star and your target. If you are uncertain whether a nearby object is brighter than your target in the STIS bandpass, it is safest to select an isolated object and perform your acquisition on it.

If you are observing a diffuse source, you should first check to see if there is a suitable star which you can use as an acquisition target; an offset can then be used to move to the desired position, as needed. If you wish to acquire a diffuse object directly, then it is important to know your source structure as seen at ~ 0.1 arcsecond resolution to properly plan your acquisition strategy if you need accurate (a few tenths of an arcsecond) centering. We recommend that you first check the *HST* archive to determine if your target has been observed by *HST* with WFPC1, WFPC2, WFC3, FOC, STIS or ACS. If it has, that exposure can be used to determine the optimal acquisition strategy using the [Target Acquisition Simulator](#). If it has not yet been observed with *HST*, we suggest you take an early acquisition image, either with the STIS or with WFC3, which you can use to determine your optimal acquisition strategy. This is particularly important if your program requires placement of a narrow slit accurately on a diffuse object.

Once you have selected your acquisition object, you need to measure its coordinates (when possible, i.e., not for moving targets) in the Guide Star reference frame; information on measuring coordinates can be found [here](#).

To derive absolute coordinates, you can use **TweakReg** from the **drizzlepac** package to align your data to the GAIA catalog. This procedure is demonstrated in [this notebook](#).

i *Note that the initial acquisition subarray is 5 arcseconds on each side; your target coordinates must be supplied accurately in the ICRS frame during Phase 1I to assure your target will be in the initial acq image, given that the initial guide star pointing accuracy is usually ~ 0.2 – 0.3 arcseconds but occasionally as large as 1 arcsecond.*

Selecting the Acquisition Type

If you are acquiring a point-like object, you should select the optional parameter for a point source acquisition (ACQTYPE=POINT). This selection will find the flux-weighted centroid of the object using a 3 × 3 checkbox. If you are acquiring a diffuse object, you should select the diffuse source acquisition (ACQTYPE=DIFFUSE). A diffuse acquisition will also require selecting the target acquisition centering algorithm (DIFFUSE-CENTER= FLUX-CENTROID or GEOMETRIC-CENTER) and a checkbox size (CHECKBOX=3-105). Note that selecting a DIFFUSE acquisition with CHECKBOX=3 and DIFFUSE-CENTER=FLUX-CENTROID is equivalent to selecting the POINT source algorithm. A [Target Acquisition Simulator](#) is available to assist you in selecting the best checkbox size if you have an image at a similar resolution to that of STIS and in a similar bandpass.

Selecting the Imaging Aperture

The apertures available for target acquisitions are the same set that can be used for CCD imaging and are listed in [Table 8.2](#) below. They include the visible longpass filter, the clear unfiltered aperture, the [O III] narrowband filter, the [O II] narrowband filter, and the neutral-density filters which provide attenuations for bright sources of 10^{-3} and 10^{-5} . F28X50LP is the preferred target acquisition aperture. The longpass filter is preferred (compared to the clear 50CCD aperture) because it blocks the UV photons, which can otherwise elevate the detector dark count in the subsequent scientific exposures (see [Section 7.3.10](#)). For bright sources which saturate the CCD in 0.1 second with the longpass filter (see [Table 8.3](#)), you can use either the narrowband [O III] (F28X50OIII) or [O II] (F28X50OII) filters as the acquisition aperture, or one of the neutral density filters. The [O II] and [O III] filters can also be used to locate the target in the light of an emission line. Note that the [O III] filter has a large red leak at $\lambda > 10,000 \text{ \AA}$ (see [Chapter 14](#)), so it should be used with caution; the [O II] filter has no measurable red leak.

Table 8.2: Apertures for Target Acquisitions.

| Aperture Name | Filter Type | Comment |
|---------------|--------------------------------|--|
| F28X50LP | Optical longpass | Preferred target acquisition aperture |
| F28X50OII | [O II] | Use for bright sources or to center on emission line structure |
| F28X50OIII | [O III] (has severe red leak) | Use for bright sources or to center on emission line structure |
| F25ND3 | Neutral density, ND= 10^{-3} | Use only for targets too bright for other filters |
| F25ND5 | Neutral density, ND= 10^{-5} | Use only for targets too bright for other filters |
| 50CCD | Clear | Use for acquisitions of faintest sources only |

i We recommend the longpass F28X50LP filter for all target acquisitions of sources with V magnitudes between 10 and 23.

Determining Exposure Time for the ACQ Exposure

To achieve robust target location:

- A *minimum* signal-to-noise ratio of at least 40 (over the checkbox) or 1700 electrons (425 DN) must be obtained on each target image obtained during the ACQ exposure. Higher signal-to-noise ratios should be considered if practical (see below).
- For DIFFUSE acquisitions with large checkbox sizes (i.e., CHECKBOX > 9), a contrast relative to surrounding regions of *at least* 40 e⁻/pix (or equivalently 10 DN/pix) must be obtained for the region of the source being "found."
- The target image cannot be allowed to saturate the CCD full well (144,000 electrons).
- The exposure time must be less than 5 minutes for point source acquisitions and less than the maximum allowed (see below) for diffuse acquisitions.
- A CCDGAIN of 4 is used for all acquisition images.

It should be considered that the count rates recommended above are the *minimum* count rates needed for the acquisition to have a high chance of success. However, obtaining ACQ images with significantly higher signal-to-noise ratios than these minima do provide an additional degree of protection against failures caused by a poor estimate of the source count rate or by a bad initial pointing that puts the target just outside the acquisition subarray (in the latter case, the diffraction spikes or the wings of the PSF may well be detected in the initial image and moved to the detector center, allowing the ACQ to succeed during the fine-locate phase). Such deeper exposures are therefore recommended if the additional overheads are small compared to the overhead time for ACQ exposures (typically 6 minutes), and if there is no chance of saturating the CCD. For a point source, the full well limit of 144,000 electrons in the central pixel corresponds to an ETC S/N estimate of about 400:1.

The maximum possible exposure time for a point source acquisition (ACQTYPE=POINT) exposure is 5 minutes; this limit restricts acquisitions to sources brighter than 24.5 mag in V. This limit is imposed because, for longer exposure times, the target acquisitions become compromised by coincident cosmic ray impacts, which will lead to acquisition failures. The maximum possible exposure time for a diffuse acquisition depends on the checkbox and is given by:

$$t_{max} = [5 \times 100 / (101 + CHECKBOX)] \text{ minutes .}$$

The minimum exposure time allowed for an acquisition is 0.1 second. Table 8.3 gives the limiting magnitudes at which the CCD will saturate in a 0.1 second exposure; sources brighter than these limits cannot be acquired with the CCD using these filters. Remember that the ND filters can also be used to acquire targets; these filters provide attenuations of 10⁻³ (7.5 magnitudes) and 10⁻⁵ (12.5 magnitudes) relative to the clear (50CCD) filter. Note that the ND filters are contained in the slit wheel with other slits and apertures, and so cannot be used in conjunction with other filters. The table illustrates that it is possible to image any star using a filter from the suite, including the neutral-density filters, available for STIS.

Table 8.3: V Magnitude Limits for Saturation of a 0.1 Second CCD Exposure Time as a Function of Aperture.

| Spectral Type | Limiting Magnitude | | | | |
|---------------|--------------------|----------|-----------|------------|----------|
| | 50CCD | F28X50LP | F28X500II | F28X500III | F25ND3/5 |
| | | | | | |

| | | | | | |
|---------------------|------|-----|-----|-----|----------|
| O5 V | 10.0 | 8.0 | 4.7 | 2.3 | 2.9/-3.5 |
| B1 V | 9.8 | 8.0 | 4.5 | 2.3 | 2.8/-3.5 |
| B5 V | 9.7 | 8.0 | 4.1 | 2.3 | 2.6/-3.6 |
| B8 V | 9.5 | 8.0 | 3.7 | 2.3 | 2.5/-3.7 |
| A1 V | 9.4 | 8.0 | 3.2 | 2.2 | 2.5/-3.7 |
| A3 V | 9.4 | 8.0 | 3.1 | 2.2 | 2.4/-3.7 |
| A5 V | 9.3 | 8.0 | 3.1 | 2.2 | 2.4/-3.7 |
| F0 V | 9.3 | 8.1 | 3.1 | 2.0 | 2.4/-3.6 |
| F5 V | 9.3 | 8.2 | 3.0 | 2.0 | 2.4/-3.5 |
| F8 V | 9.3 | 8.2 | 2.9 | 1.9 | 2.4/-3.5 |
| ¹ G2 V | 9.3 | 8.3 | 2.7 | 1.9 | 2.4/-3.5 |
| ² G8 V | 9.3 | 8.4 | 2.1 | 1.7 | 2.4/-3.4 |
| ³ K2 V | 9.3 | 8.4 | 2.0 | 1.7 | 2.4/-3.3 |
| ⁴ KM III | 9.4 | 9.0 | 1.6 | 1.7 | 2.8/-2.7 |
| Power Law | 9.4 | 8.6 | 3.4 | 1.7 | 2.7/-3.3 |

¹ Calculations performed using the Solar template available in the STIS **ETC**.

² Calculations performed using *IUE* data for the star Tau Ceti.

³ Calculations performed using *IUE* data for the star Epsilon Eri.

⁴ Calculations performed using *IUE* data for nine *IUE* stars of these types.

Figure 8.7 and Figure 8.8 can help you estimate exposure times—they plot exposure time versus *V* magnitude to achieve a signal-to-noise ratio of 40 for stars having a range of spectral types, for the clear, longpass, [O III], and [O II] filters. To determine the exact exposure time for your target, you should use the **STIS TA ETC** (see Section 8.5). Note that the overheads in target acquisitions are substantially longer than most exposure times, so as long as you do not approach saturation (i.e., come within 30% of the full well) you should increase your exposure time by a factor of at least a few above the minimum required (e.g., if the exposure time to obtain a S/N of 40 is 0.3 second, then you should lengthen it to 1 second if no saturation occurs). Also consider whether a shorter exposure in a higher throughput filter might give better S/N (see Table 8.3 for the brightest magnitude as a function of filter and target spectral type which can be observed without saturating the acquisition exposure). The exposure time entered into your Phase II template is the time for each of the two exposures in the ACQ sequence, unlike the case of CR-SPLIT observations where it is the total time.

Figure 8.7: Time to Achieve a Signal-to-Noise Ratio of 40 for CCD Acquisitions.

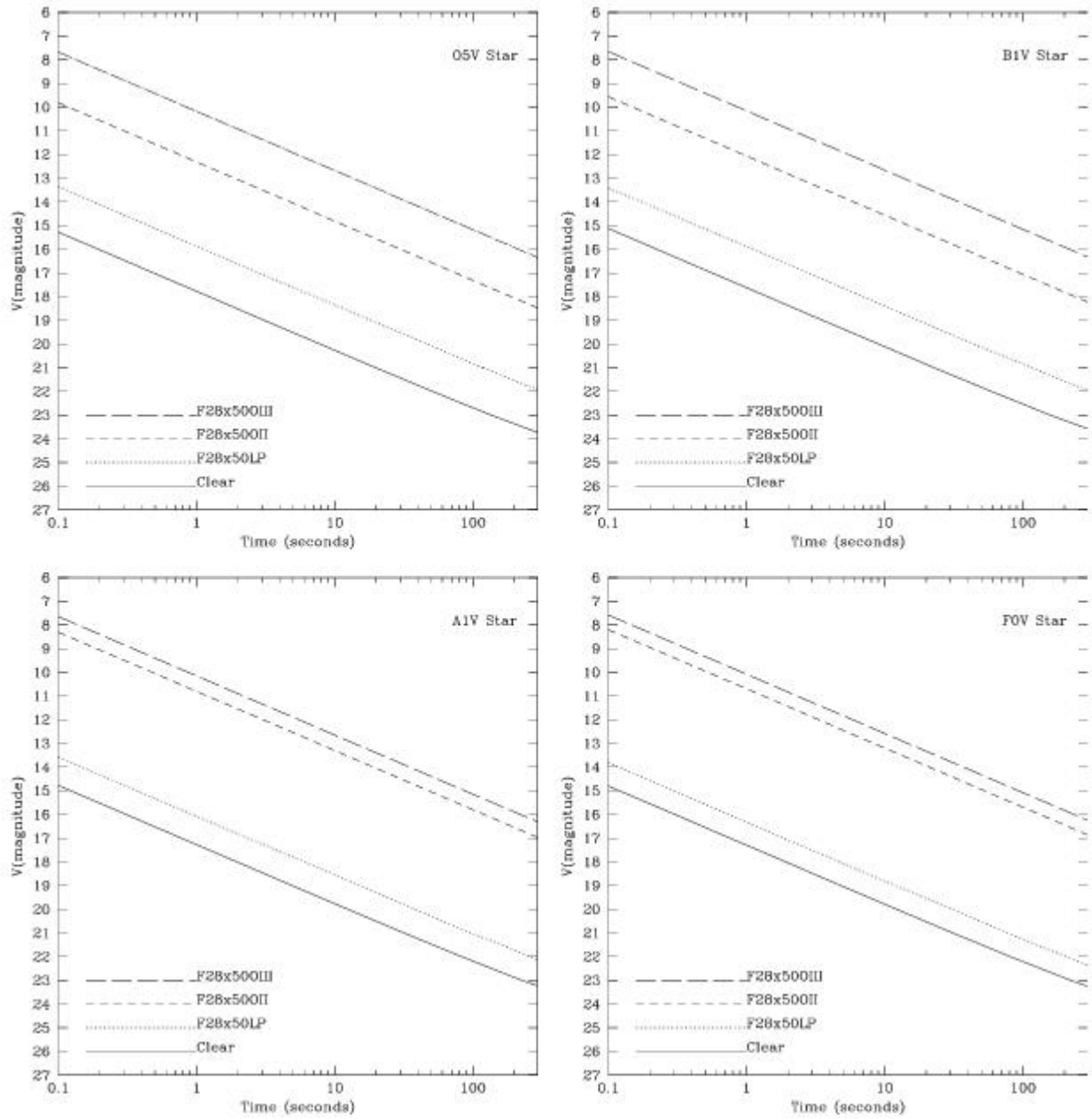
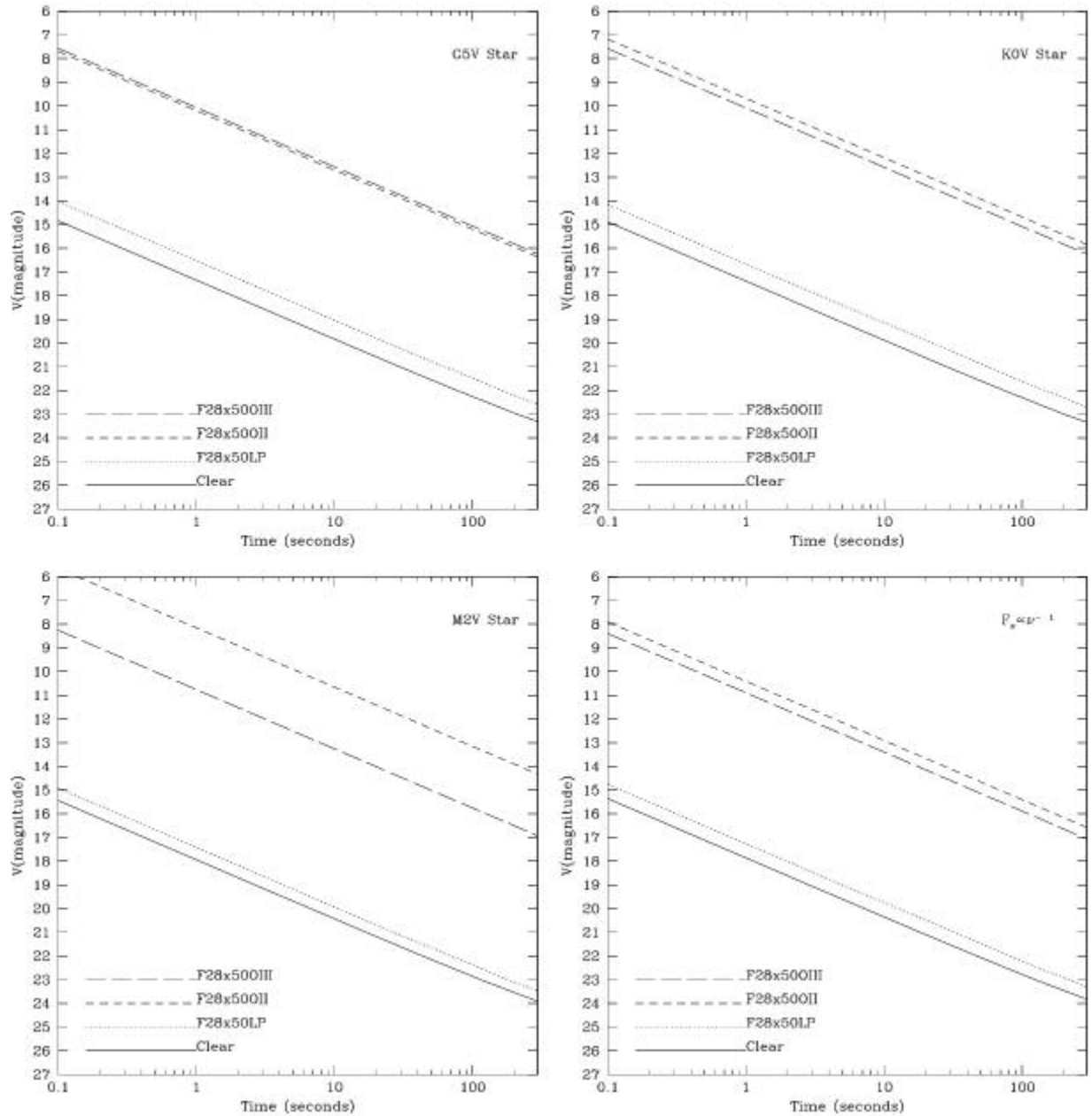


Figure 8.8: Time to Achieve a Signal-to-Noise Ratio of 40 for CCD Acquisitions.



8.2.4 Specifying Acquisitions in Phase II

Acquisition exposures must be specified during Phase II before the scientific exposures for which they are intended. The user requests a target acquisition exposure by specifying `MODE=ACQ` on the APT Phase II exposure parameters page and setting `ACQTYPE`. The default is `ACQTYPE=POINT`, but `ACQTYPE=DIFFUSE` is also an option. If `ACQTYPE=DIFFUSE` is selected, the observer must also specify `DIFFUSE-CENTER` and `CHECKBOX`.

ETC and Phase II examples are provided in [Section 8.5](#).

8.2.5 Solar System Acquisitions

The ACQ procedure can be used for solar system targets as well as fixed targets. The difference is in the specification of the target position, which is outlined in Chapter 4 of the [HST Phase II Proposal Instructions](#). For satellites less than 0.1 arcsecond in diameter, a point source ACQ is sufficient. For satellites of greater diameter, ACQTYPE=DIFFUSE with DIFFUSE-CENTER=GEOMETRIC and a CHECKBOX size chosen to match the satellite diameter are recommended. To acquire a planetary feature or a satellite transiting the planet, another satellite in the system can generally be used as an offset target. If precise pointing to a specific feature is not required, then blind pointing (which is generally accurate to ~0.2–1.0 arcseconds) can be used for larger targets such as Mars, Jupiter, and Saturn. The types of acquisitions recommended for the most common solar system targets is summarized in [Table 8.4](#).

Table 8.4: Solar System Acquisitions.

| Target | Type of Acquisition | Offset Target |
|--|---------------------|--------------------|
| Venus | Offset target | Star |
| Mars | Offset target | Deimos |
| Jupiter | Offset target | Galilean satellite |
| Saturn | Offset target | Satellite |
| Uranus | Diffuse source | |
| Neptune | Diffuse source | |
| Satellite or asteroid <~0.1 arcseconds | Point source | |
| Satellite or asteroid >~0.1 arcseconds | Diffuse source | |
| Transiting satellite | Offset target | Another satellite |
| Comet | Diffuse source | |

The coordinates of the planets and their satellites are derived from ephemerides obtained by STScI from JPL. The accuracies of the ephemerides are maintained by JPL on their [Planetary Satellite Ephemerides](#) page; see also the JPL [Horizons](#) service for computing ephemerides.

Your Program Coordinator can provide detailed information on ephemerides and tracking for your observations.

Special care must be taken when tracking satellites with rapidly changing direction or velocity. Observers should be aware that moving targets are tracked by *HST* with the assumption that the object is moving on a linear track with constant velocity. Depending on the visit structure, the same linear track may continue through several exposures. The scheduling software sets a generally appropriate limit on the duration of a linear track which depends on the target being tracked, but not on details of the target motion at the time. In some situations (for example, near the inflection point of an orbit), the approximation could result in inadequate tracking when using a narrow slit. If this may be a problem, the observer can consult the proposal's designated Program Coordinator to find out how long the same track will be used for a series of exposures, and whether it is possible to break the visit into shorter tracks. Alternatively, one can plan to observe during a more linear part of the orbit.

Acquisition exposure times can be accurately estimated using the [STIS Target Acquisition ETC](#): use the Kurucz model G2 V (solar spectrum), and normalize it using the *V* magnitude for point-like (≤ 0.1 arcsecond) objects or the *V* magnitude per arcsecond² and the appropriate target size in arcseconds for more extended targets.

¹ The processing done by the FSW is rudimentary: a single, pre-determined, bias number is subtracted, bad pixels are set to the average of the 4 adjacent pixels, negative-valued pixels are set to zero, and each pixel is assigned the minimum from the two images (as a form of cosmic ray and hot pixel rejection). Hence, ACQ exposures are not suited for accurate photometry.

8.3 Onboard Target Acquisition Peakups - ACQ PEAK

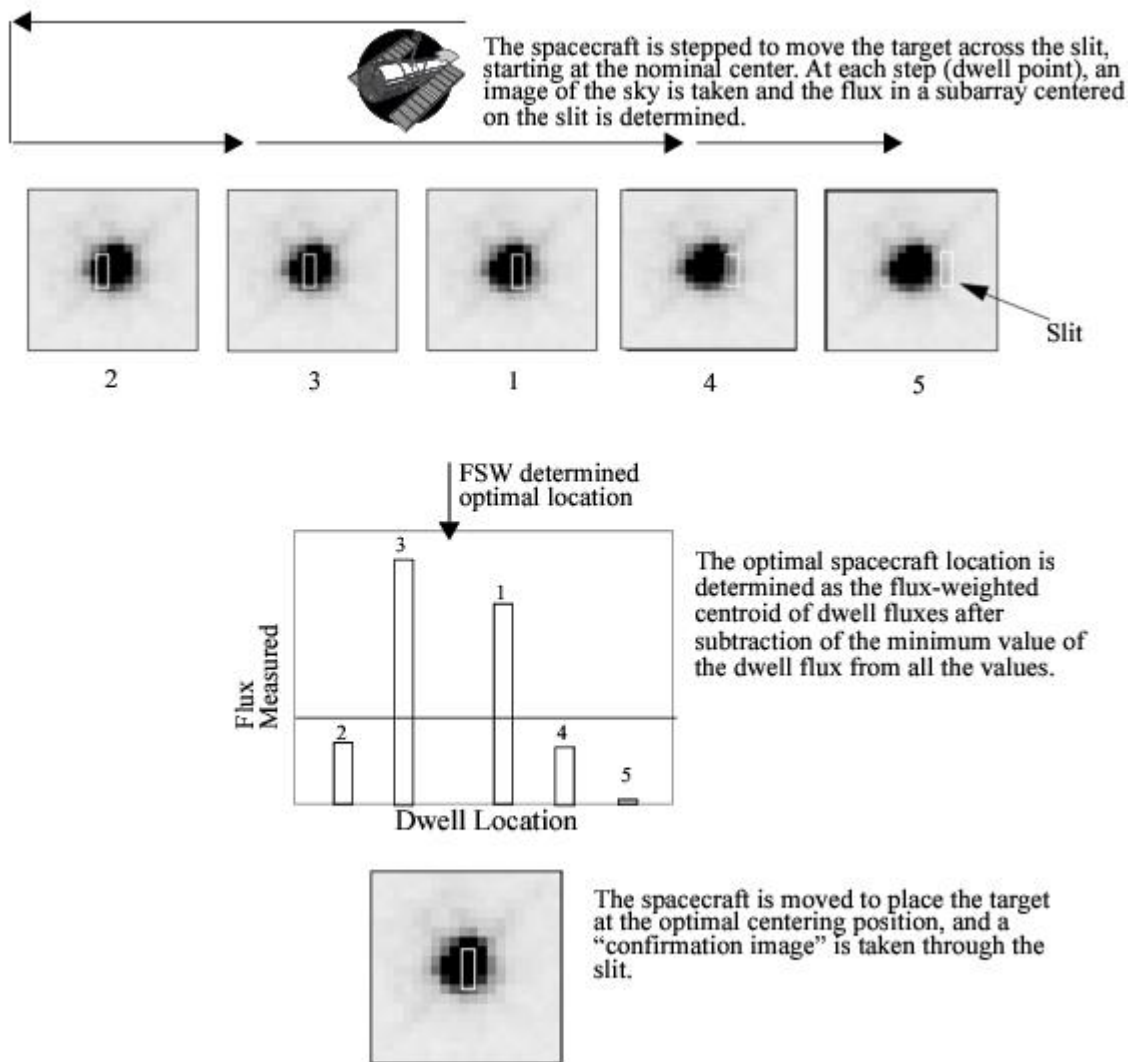
8.3.1 Selecting Peakup Parameters

8.3.2 Specifying Acquisition Peakups in Phase II

When slits of width less than or equal to 0.1 arcsecond are used, an acquisition-peakup exposure should be performed (following the acquisition exposure) to center the target in the slit. You should also consider performing a peakup on the target if you have initially acquired an offset star (rather than your target), to compensate for any additional uncertainties in your knowledge of the offsets. We also recommend that for a long series of exposures taken through slits which are less than or equal to 0.1 arcsecond in either dimension, a peakup be performed at least every 4-5 orbits. This will ensure that drifts (see [Section 8.1.4](#)) do not cause the target to move out of the slit. Programs with more stringent requirements on position or wavelength stability will need more frequent peakups.

[Figure 8.9](#) illustrates the basic peakup sequence. When a peakup exposure is performed, the telescope is moved to step the target across the slit. At each step (or dwell point), an image¹ of the sky is taken and the total flux in a specified subarray is determined. To allow for a more accurate calculation, the minimum flux value in the peakup (the PEDESTAL) is subtracted from each step. The flight software then selects the position of maximum flux, using a flux-weighted centroiding technique to determine the optimum position to a fraction of a dwell step. At the conclusion of the ACQ/PEAK exposure, the FSW moves the telescope to position the target at the derived optimal position within the aperture. A "confirmation image" is then taken through the aperture on the subarray and is included in the ACQ/PEAK data set.

Figure 8.9: Schematic of Peakup Sequence.



Peakup exposures can be taken with either a mirror (to peak up in undispersed white light) or a grating (to peak up in dispersed light), and with the CCD detector only. Subarrays can be specified to limit the region of the detector (sky) over which the flux is determined at each dwell point. The default subarray sizes, 32×32 for white-light (mirror) peakups and 32 (perpendicular to the dispersion) $\times 1022$ (in the dispersion direction) for dispersed-light peakups, are appropriate for peakups on point sources. They should be changed only if you are performing diffuse-source peakups or if you wish to isolate a single line in dispersed-light peakups, and only upon consultation with an Instrument Scientist.

i We recommend performing all CCD peakups using the mirror unless your target is too bright.

You do not specify the parameters of the stepping sequence employed during the peakup; it is predetermined, based on the aperture you have chosen. [Table 8.5](#) below shows the scan sequence employed for all of the long and echelle slits. The scan sequence for a peakup may include a linear scan in the dispersion direction (`SEARCH=LINEARAXIS1`), a linear scan perpendicular to the dispersion axis (`SEARCH=LINEARAXIS2`), or a spiral search pattern (`SEARCH=SPIRAL`). Additional parameters are the number of steps (`NUMSTEPS`) and the step intervals between each dwell point (`STEPSIZE`). Note that all `ACQ/PEAKS` are single-stage peakups, except for the smallest slit (`0.1X0.03`). When using the `0.1X0.03` slit, users are advised to add two `ACQ/PEAKS` as shown in [Table 8.5](#).

Table 8.5: Peakup Scan Sequences and Parameters for Supported Spectroscopic Slits.

| Slit | AXIS2 Spatial (arcseconds) | AXIS1 Dispersion (arcseconds) | Step Size (arcsec) | | Scan Type | NSTEPS | | |
|--|----------------------------------|-------------------------------------|-----------------------|-------|--|--------|-------|-------|
| | | | AXIS2 | AXIS1 | | AXIS2 | AXIS1 | Total |
| Long Slits | | | | | | | | |
| 52X0.05 , 52X0. 05E1, 52X0. 05D1 | 52 | 0.05 | | 0.036 | LINEARAXIS1 | | 7 | 7 |
| 52X0.1, 52X0. 1E1, 52X0. 1D1 | 52 | 0.1 | | 0.075 | LINEARAXIS1 | | 5 | 5 |
| 52X0. 2F1-R ¹ | 52 | 0.2 | | 0.150 | LINEARAXIS1 | | 3 | 3 |
| Echelle Slits for E230M and E140M | | | | | | | | |
| 0.2X0. 06 | 0.2 | 0.063 | 0.150 | 0.048 | 1) LINEARAXIS1 2) LINEARAXIS2 | 3 | 5 | 8 |
| Echelle Slits for E230H and E140H | | | | | | | | |
| 0.2X0. 09 | 0.2 | 0.09 | 0.150 | 0.069 | 1) LINEARAXIS2 2) LINEARAXIS1 | 3 | 5 | 8 |
| Specialty Slits | | | | | | | | |

| | | | | | | | | |
|--|-----|-------|-------|-------|--|---|---|----|
| 31X0.05ND(A-C) | 31 | 0.05 | | 0.039 | 1) LINEARAXIS1 | | 7 | 7 |
| 0.2X0.05ND | 0.2 | 0.05 | 0.150 | 0.039 | 1) LINEARAXIS1 2) LINEARAXIS2 | 3 | 7 | 10 |
| 0.3X0.05ND | 0.3 | 0.05 | 0.250 | 0.039 | 1) LINEARAXIS1 2) LINEARAXIS2 | 3 | 7 | 10 |
| 0.2X0.06FP(A-E) | 0.2 | 0.06 | 0.150 | 0.048 | 1) LINEARAXIS1 2) LINEARAXIS2 | 3 | 7 | 10 |
| 0.1X0.03 (peakup in 0.2x0.09 ² followed by spiral in 0.1X0.03) | 0.2 | 0.09 | 0.150 | 0.069 | 1) LINEARAXIS2 | 3 | 5 | 8 |
| | 0.1 | 0.025 | 0.018 | 0.01 | 2) LINEARAXIS1 3) SPIRAL | 3 | 3 | 9 |

¹ Peakup acquisitions are not recommended for apertures wider than 0.1 arcsec.

² The 0.2X0.05ND or the 0.3X0.05ND slits can be used in place of the 0.2X0.09 slit.

8.3.1 Selecting Peakup Parameters

To plan your acquisition peakup, you must specify:

- The optical element.
- The APERTURE (program slit) upon which to peak up.
- The exposure time for the peakup image.

Selecting the Optical Element

Peakups can be performed by using the STIS CCD either with a dispersive element in a spectroscopic configuration with any of the allowed grating combinations, or in undispersed white light in an imaging configuration. Most peakup exposures should be performed in imaging mode (white light).

If your target is otherwise too bright to perform a pickup with the CCD camera mirror in place, you can use the echelle slit $0.2 \times 0.05 \text{ND}$ (which has an ND filter with a factor of 100 attenuation) or the $0.3 \times 0.05 \text{ND}$ (with attenuation by a factor of 1000), or use a dispersed-light pickup. Also note that if you wish to peak up in a particular line for which there is no imaging filter, a dispersed light pickup using a grating should be used. Observers should generally perform dispersed light pickups with the same gratings and apertures they intend to use for their scientific observations. If a dispersed light pickup will be performed with a grating other than that used for the scientific observation, an additional overhead of ~ 3 min should be included to account for movement of the grating wheel.

Selecting the Aperture

A pickup can be done using any of the long or echelle slits listed in [Table 8.5](#) as the `APERTURE`. You will (typically) want to specify the pickup aperture as the aperture used for the subsequent scientific observations, although it is possible to specify a smaller aperture than your program aperture if you require higher target acquisition centering accuracy in wider slits (which normally do not require peak-ups). The slit-to-slit positioning accuracy is 0.005 arcsecond. Instances in which you may wish to utilize a smaller aperture for the acquisition are observations requiring accurate photometry (where the source should be properly centered in a wide slit) and bright-source acquisitions. Note that pickups using the `NX0.2` apertures (those with widths of 0.2 arcseconds in the dispersion direction) are no longer recommended as they provide no refinement in pointing over that routinely achieved in a normal `ACQ`. If an `ACQ/PEAK` is needed for an `NX0.2` science exposure (e.g., after an `ACQ` on an offset target or to re-center after a few orbits), better positioning accuracy can be achieved with a narrower aperture, such as `NX0.1`.

The suffix `E1` on an aperture name (e.g., `52X0.2E1`) indicates that the target will be positioned high on the CCD detector, at about row 900, in that aperture. This is useful for greatly reducing CTE effects, since that location is close to the default readout amplifier. If an `E1` aperture is used for the science exposure, it is best to use an `E1` aperture for the pickup, to eliminate small errors in slewing and possible small errors in the definitions of the `E1` positions.

For coronagraphic imaging, the bar and wedge positions on the `50CORON` aperture are all large enough that a pickup is not required. However, if you require especially accurate target acquisition centering (for example, to place a calibration star at the same position under the bar or wedge to measure the scattered-light profile), then a pickup may be useful. Note that a peakdown acquisition is not recommended (see [Section 12.10](#)).

Determining the Pickup Exposure Time

The *minimum* required exposure time for CCD imaging (mirror) pickups is the time to obtain a minimum of 5000 electrons (1250 DN) from a point source, or equivalently, 5000 electrons from the peak of a diffuse source which is contained in a 4×4 pixel region. For CCD dispersive (grating) pickups, the *minimum* exposure time is the time to obtain a minimum of 80,000 electrons (20,000 DN) integrated across the spectrum from a point source, or equivalently, 80,000 electrons from the peak of a diffuse source integrated over 4 pixels perpendicular to the dispersion axis. For CCD dispersive pickups on a single emission line, the exposure time is the time to obtain a minimum of 5000 electrons in the chosen line; a small subarray is selected to isolate the line.

To determine the exact exposure time, you should use the [STIS TA ETC](#) (for acquisitions and imaging peakups) or the [Spectroscopic ETC](#) (for dispersive peakups). For acquisitions and peakups *you must be sure not to saturate* the CCD during your exposure. [Table 8.3](#) lists, for a range of spectral types, the brightest magnitude at which a CCD peakup exposure can be performed in white light, assuming zero slit losses. Note that the overheads in target acquisition are substantially longer than most exposure times, so as long as you do not approach saturation (within 30% of the full well) your target, you should increase your exposure time by a factor of 2-5 above the minimum required (e.g., if the exposure time to obtain the requisite number of electrons is 0.3 second, then you can lengthen it to 1 second if no saturation occurs). This is especially important for peakups, where low signal-to-noise is the leading cause of poor centering.

There is a limit on the maximum exposure time allowed for CCD peakups, which is imposed to ensure that multiple coincident cosmic rays do not affect the target acquisition centering accuracy. [Table 8.6](#) lists the maximum CCD exposure time for point source white-light and dispersed-light peakups for each aperture. More generally, the maximum allowed exposure time for CCD ACQ/PEAKS in minutes is:

$$t_{max} = 17 \times 1 / \sqrt{NUMSTEPS \times SIZEAXIS1 \times SIZEAXIS2 / (32 \times 32)}$$

Table 8.6: Maximum Allowed Exposure Times for CCD Peakups.

| Slit (APERTURE) | Maximum Exposure Time for Dwell (minutes) | |
|----------------------------|---|---------------|
| | Imaging | Spectroscopic |
| 52X0.1, 52X0.1E1, 52X0.1D1 | 7.6 | 1.3 |
| 0.2X0.06 | 7.6 | 1.3 |
| 0.2X0.09 | 7.6 | 1.3 |
| 0.2X0.05ND | 6.4 | 1.1 |

8.3.2 Specifying Acquisition Peakups in Phase II

The user requests a peakup acquisition exposure during Phase II by specifying `MODE=ACQ/PEAK` on the APT Phase II exposure parameters page. The default settings for the scan (`SEARCH`, `NUMSTEPS`, `STEPSIZE`) for your chosen `APERTURE` are then automatically selected from the lookup table.

¹ For CCD ACQ/PEAKS the same type of processing is applied as in acquisitions by the FSW to remove the bias and cosmic rays, with the only difference being that there is no offset performed between the two images taken at each pointing, for obvious reasons.

8.4 Determining Coordinates in the International Celestial Reference System (ICRS) Reference Frame

The *HST* reference frame is effectively defined by the positions of the Guide Stars that are selected for each pointing. The initial Guide Star Catalog (GSC1) was an all-sky catalog of stars down to 15th magnitude built from Schmidt Sky Survey plates. In March 2006, an updated catalog (GSC2) was introduced. GSC2 was derived from more recent epoch plates and was calibrated to be on the International Celestial Reference System (ICRS), which had been adopted by the IAU as the new fundamental reference frame. This simplified the procedure for providing *HST* coordinates since it removed the necessity to tie the object coordinates back to the GSC1 and the plates used to construct it. More recently, coordinates from *Gaia* have been incorporated - further reducing the relative positional errors between guide stars. Guidelines for obtaining the coordinates of your target in the ICRS are given in the [HST Phase II Proposal Instructions](#).

8.5 Acquisition Examples

- 8.5.1 Point Source Acquisition of an Isolated Object
- 8.5.2 Point Source Acquisition of Bright, Isolated Object with CCD Dispersed Light Pickup
- 8.5.3 Diffuse Source Acquisition of a Spiral Galaxy
- 8.5.4 Point Source Acquisition in a Crowded Field
- 8.5.5 Point Source Acquisition of a QSO with Fuzz Behind the Fiducial Bar
- 8.5.6 Point Source Acquisition of a Bright, Isolated Star into the Wedge

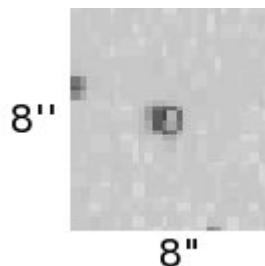
The following are examples of how to determine the acquisition scenario, and how to derive the correct exposure times. Each example shows an image of the target, the input parameters for the **ETC**, and the parameters that you will need to provide in your Phase II proposal.

⚠ Note that the final numbers in the examples in this section are from a previous version of the **ETC** and will not match up exactly if rerunning these calculations with the current **ETC**.

Note also that the **APT** preview format used throughout this section may not be the one in use at the time you are crafting your proposal.

8.5.1 Point Source Acquisition of an Isolated Object

In this first example an isolated $V = 19$ mag QSO ($z = 1.5$) is to be acquired, with the scientific exposures to be obtained in the 52×0.5 slit.



The target is isolated, so it will be acquired with a point source acquisition. The object is faint, so we can use the preferred $F28 \times 50LP$ filter. The **TA ETC** is then used to determine an exposure time of 11.4 seconds. Note that the $GAIN=4$ and $CR-SPLIT=1$ *must be used* for the **ETC** to ensure that you have a S/N of at least 40 in each of the two images obtained during the **ACQ** process. The object does not saturate the CCD, and the exposure time is less than 5 minutes, so we have devised a valid target acquisition. Given that the exposure time is so short, we can lengthen the time to 15.0 seconds (which yields a peak value of 1600 electrons, well below saturation) to make certain we have enough signal for a good acquisition. Since the data are being obtained in a wide slit, we do not need to perform an **ACQ/PEAKUP**, and our acquisition is complete.

Target Acquisition ETC Parameters - ACQ

- Detector - CCD;
- Filter - LongPass;
- Gain = $4 e^-/ADU$;
- Check Box - 3×3 ;

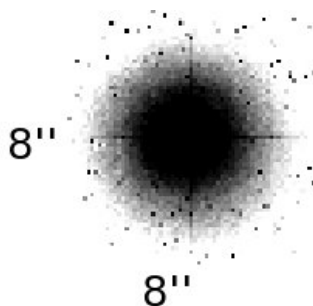
- Target was a point source;
- Spectrum: QSO with $z = 1.5$;
- Source Flux: $V = 19$;
- Average Galactic Extinction of $E(B-V) = 0.0$;
- The Zodiacal Light is average;
- The earthshine is average;

Phase II Parameters for ACQ Exposure:

| Exp | Label | Target Name | Config | OpMode | Aperture | SpElement | Wavlen | Iter | ExpTime (secs) |
|---|----------------|-------------|----------|-----------|-------------|-----------|--------|------|----------------|
| 1 | | QSO | STIS/CCD | ACQ | F28X50LP | MIRROR | | 1 | 15.0 |
| Special Requirements: Comments: Optional Parameters: ACQTYPE=POINT, | | | | | | | | | |
| | Sub-exposures: | Copy | Split | Orbit Num | Actual Time | | | | |
| | | | | | | | | | |

8.5.2 Point Source Acquisition of Bright, Isolated Object with CCD Dispersed Light Peakup

In this example—point source acquisition of a bright, isolated object with a CCD dispersed light peakup—an isolated $V = 3.5$ mag M2 I star is to be acquired, with the scientific exposures to be obtained in the 0.2×0.06 echelle slit.



The scientific target will be acquired with a point source acquisition, but because the object is so bright, we cannot use the preferred F28X50LP filter. Instead, we will use the F28X500II filter, and the TA ETC yields an exposure time of 0.06 second, which is less than the minimum allowed time of 0.1 second. Note that the GAIN=4 and CR-SPLIT=1 *must be used* for the ETC to assure that you have a S/N of at least 40 in each of the two images obtained during the ACQ process. We will increase the exposure time to 1.0 second. The object does not saturate the CCD, and the exposure time is less than 5 minutes, so we have devised a valid target acquisition.

The data are being obtained in a narrow slit, so we need to perform an ACQ/PEAK acquisition. The target is far too bright to perform the pickup with the MIRROR, so we will do a dispersed light pickup. Since we cannot perform a CCD pickup with an echelle grating, we will use the G430M grating with the CCD and the program slit (0.2x0.06); note that for an ACQ/PEAK, this combination is allowed. For a 1 second exposure with 1 x 1 binning, the ETC gives a peak count of 4279 electrons (well below saturation) and a total count of 5.8×10^4 electrons.

Target Acquisition ETC Parameters - ACQ:

- Detector = CCD;
- Filter = O II;
- Gain = 4 e⁻/ADU;
- Check Box = 3 x 3;
- Target was a point source;
- Spectrum: M2I (Model Spectrum);
- Source Flux: V = 3.5;
- Average Galactic Extinction of E(B-V) = 0.0;
- The Zodiacal Light is average;
- The earthshine is average;

Spectroscopic ETC Parameters - ACQ/PEAK:

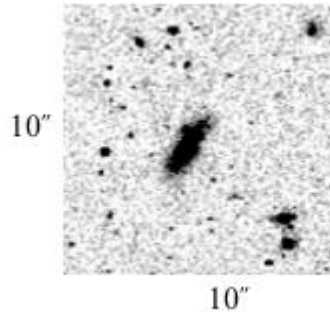
- Grating = g430m;
- Central Wavelength = 4194;
- Slit = 0.2x0.06;
- Specified Wavelength = 4194.1 angstroms;
- Gain = 4 e⁻/ADU;
- CR-SPLIT (Total number of images) = 1;
- Target was a point source;
- Spectrum: M2 I (Model Spectrum);
- Source Flux: V = 3.5;
- Average Galactic Extinction of E(B-V) = 0.0;
- The Zodiacal Light is average;
- The earthshine is average;

Phase II Parameters for ACQ and ACQ/PEAK Exposures:

| Exp | Label | Target Name | Config | OpMode | Aperture | SpElement | Wavlen | Iter | Exp Time (secs) |
|---|-------|-------------|----------|----------|-----------|-------------|--------|------|-----------------|
| 1 | | BRIGHT-STAR | STIS/CCD | ACQ | F28X50OII | MIRROR | | 1 | 1.0 |
| Special Requirements: Comments: Optional Parameters: ACQTYPE=POINT, | | | | | | | | | |
| Sub-exposures: | | | Copy | Split | Orbit Num | Actual Time | | | |
| | | | | | | | | | |
| 2 | | BRIGHT-STAR | STIS/CCD | ACQ/PEAK | 0.2X0.06 | G430M | 4194 | 1 | 1.0 |
| Special Requirements: Comments: Optional Parameters: | | | | | | | | | |
| Sub-exposures: | | | Copy | Split | Orbit Num | Actual Time | | | |
| | | | | | | | | | |

8.5.3 Diffuse Source Acquisition of a Spiral Galaxy

In this example an isolated galaxy with a flux of 1.5×10^{-14} erg/cm²/s /Å/arcsec² at 8000 Å is to be acquired, with the scientific exposures to be obtained in the 52x0.2 slit.



The target is isolated, so it will be acquired using a diffuse-source acquisition. After trying various checkbox sizes in the **TAS** (the image is from WFPC2), we determine that the appropriate **CHECKBOX** size is 9, and that we will use the **FLUX-CENTROID** algorithm. The object is faint, so we can use the preferred **F28X50LP** filter. The **TA ETC** is then used to determine an exposure time of 0.21 second. Note that the **GAIN=4** and **CR-SPLIT=1** *must be used* for the **ETC** to ensure that you have a S/N of at least 40 in each of the two images obtained during the **ACQ** process. The object does not saturate the CCD, and the exposure time is less than 5 minutes, so we have devised a valid target acquisition. Given that the exposure time is so short, we can lengthen it to 2.0 seconds to make certain we have enough signal for a good acquisition. Since the data are being obtained in a wide slit, we do not need to perform an **ACQ/PEAKUP**, and our acquisition is complete.

Target Acquisition ETC Parameters - ACQ:

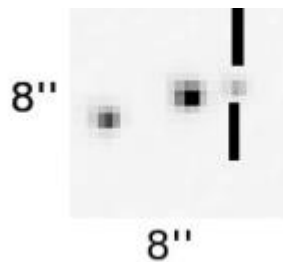
- Detector - CCD;
- Filter = LongPass;
- Gain = $4 \text{ e}^-/\text{ADU}$;
- Check Box = 9×9 ;
- Target was an extended source with a diameter of 3 arcseconds;
- Spectrum: Spiral Spectrum;
- Source Flux: $1.5 \text{ e}^{-14} \text{ erg/cm}^{-2}/\text{s}/\text{\AA}$ at 8000 Å;
- Average Galactic Extinction of $E(B-V) = 0.0$;
- The Zodiacal Light is average;
- The earthshine is average;

Phase II Parameters for ACQ Exposure:

| Exp | Label | Target Name | Config | OpMode | Aperture | SpElement | Wavlen | Iter | Exp Time (secs) |
|--|----------------|-------------|----------|--------|-----------|-------------|--------|------|-----------------|
| 1 | | GALAXY | STIS/CCD | ACQ | F28X50LP | MIRROR | | 1 | 2.0 |
| Special Requirements: Comments: Optional Parameters: ACQTYPE=DIFFUSE, DIFFUSE-CENTER=FLUX-CENTROID, CHECKBOX=9, | | | | | | | | | |
| | Sub-exposures: | | Copy | Split | Orbit Num | Actual Time | | | |
| | | | | | | | | | |

8.5.4 Point Source Acquisition in a Crowded Field

In this example a $V = 19$ mag nova in a field with a brighter companion is to be acquired, with the scientific exposures to be obtained in the 52x0.1 slit. We have a spectrum of the nova that we will use to perform the exposure time calculations, according to the [ETC](#) instructions.



The target is in a crowded field and the on-board acquisition procedure will acquire the brightest object in the field, not our target. If a ground-based image were the only image of this field available and the spectral types of the neighboring stars were unknown, then an isolated offset star outside of the immediate field of the nova would need to be acquired. However, the above image was obtained with WFPC2 and the F555W filter, which has a similar bandpass to the STIS F28X50LP filter. We therefore know that the object to the southeast of the nova is clearly the brightest object in the field ($V = 16.5$), and it will be our acquisition object. The object is faint enough that we can use the preferred F28X50LP filter. Since we do not know the spectral type of the acquisition star, we will make a worst-case (i.e., fewest counts) assumption that the star is of spectral type O5 and unreddened. The [TA ETC](#) is then used to determine an exposure time of 2.0 seconds. Note that the GAIN=4 and CR-SPLIT=1 must be used for the [ETC](#) to ensure that you have a S/N of at least 40 in each of the two images obtained during the ACQ process. The object does not saturate the CCD, and the exposure time is less than 5 minutes, so we have devised a valid target acquisition. Note that since we do not know the spectral type of the object, we need to confirm that if the star had a spectral type of M6 V (which gives the most counts in the F28X50LP bandpass), it would still not saturate. Given that the exposure time is so short, we can lengthen it to 3.0 seconds to make certain we have enough signal for a good acquisition.

After acquiring the offset star, we need to slew the telescope to the nova, and since the data will be taken with a narrow slit, we need to perform an ACQ/PEAK acquisition. The peakup will be performed in the program slit (52X0.1), and we will use the CCD and the MIRROR. A 1 second exposure with 1 × 1 binning yields 655 electrons in the central 25 pixels of the target, so an exposure time of 8 seconds yields 5240 electrons, which meets the minimum requirement of 5000 electrons. We then need to lengthen the exposure time to 20 seconds to ensure we get more than the minimum required. The object does not saturate the CCD, and the exposure time is less than 7.6 minutes (the maximum time for a peakup with the 52X0.1 slit), so we have devised a valid peakup target acquisition.

Target Acquisition ETC Parameters - ACQ:

- Detector = CCD;
- Filter = LongPass;
- Gain = 4 e⁻/ADU;
- Check Box = 3 x 3;
- Target was a point source;
- Spectrum: O5V (Model Spectrum);
- Source Flux: V = 16.5;
- Average Galactic Extinction of E(B-V) = 0.0;
- The Zodiacal Light is average;
- The earthshine is average;

Imaging ETC Parameters - ACQ/PEAK:

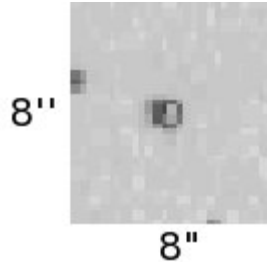
- Detector = CCD;
- Filter = Clear;
- Gain = 4 e⁻/ADU;
- CR-SPLIT (Total number of images) = 1;
- Target was a point source;
- Spectrum: nova (User's);
- Source Flux: V = 19;
- Average Galactic Extinction of E(B-V) = 0.0;
- The Zodiacal Light is average;
- the earthshine is average;

Phase II Parameters for ACQ and ACQ/PEAK Exposures:

| Exp | Label | Target Name | Config | OpMode | Aperture | SpElement | Wavlen | Iter | Exp Time (secs) |
|---|-------|-------------|----------|----------|-----------|-------------|--------|------|-----------------|
| 1 | | OFFSET-STAR | STIS/CCD | ACQ | F28X50LP | MIRROR | | 1 | 3.0 |
| Special Requirements: Comments: Optional Parameters: ACQTYPE=POINT, | | | | | | | | | |
| Sub-exposures: | | | Copy | Split | Orbit Num | Actual Time | | | |
| | | | | | | | | | |
| 2 | | NOVA | STIS/CCD | ACQ/PEAK | 52X0.1 | MIRROR | | 1 | 20.0 |
| Special Requirements: Comments: Optional Parameters: | | | | | | | | | |
| Sub-exposures: | | | Copy | Split | Orbit Num | Actual Time | | | |
| | | | | | | | | | |

8.5.5 Point Source Acquisition of a QSO with Fuzz Behind the Fiducial Bar

In this example an isolated $V = 16.5$ mag QSO ($z = 0.2$) is to be acquired, with the scientific exposures to be obtained with the QSO behind the 52X0.2F1 fiducial bar.



The target is isolated, so it will be acquired using a point source acquisition. The object is faint, so we can use the preferred F28X50LP filter. The **TA ETC** is then used to determine an exposure time of 2.2 seconds. Note that the **GAIN=4** and **CR-SPLIT=1** must be used for the **ETC** to ensure that you have a **S/N** of at least 40 in each of the two images obtained during the **ACQ** process. The object does not saturate the CCD, and the exposure time is less than 5 minutes, so we have devised a valid target acquisition. Given that the exposure time is so short, we can lengthen it to 3.0 seconds to make certain we have enough signal for a good acquisition.

The 52X0.2F1 aperture is wide enough that a pickup is not needed. The occulting bar is even wider (0.5 arcsecond), so the **ACQ** exposure should place the target behind the occulting bar.

Target Acquisition ETC Parameters - ACQ:

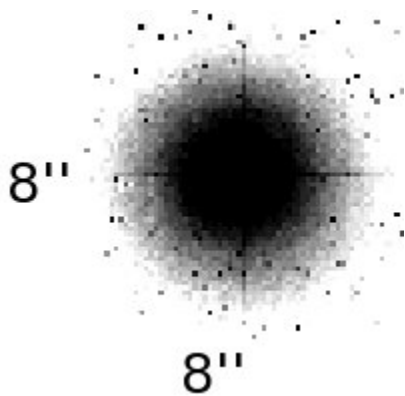
- Detector = CCD
- Filter = LongPass
- Gain = $4 e^-/ADU$
- Check Box = 3×3
- Target was a point source
- Spectrum: QSO with $z = 0.2$
- Source Flux: $V = 16.5$
- Average Galactic Extinction of $E(B-V) = 0.0$
- The Zodiacal Light is average
- The earthshine is average

Phase II Parameters for ACQ Exposure:

| Exp | Label | Target Name | Config | OpMode | Aperture | SpElement | Wavlen | Iter | Exp Time (secs) |
|---|----------------|-------------|----------|-----------|-------------|-----------|--------|------|-----------------|
| 1 | | G-STAR | STIS/CCD | ACQ | F25ND3 | MIRROR | | 1 | 0.5 |
| Special Requirements: Comments: Optional Parameters: ACQTYPE=POINT, | | | | | | | | | |
| | Sub-exposures: | Copy | Split | Orbit Num | Actual Time | | | | |
| | | | | | | | | | |

8.5.6 Point Source Acquisition of a Bright, Isolated Star into the Wedge

In this example an isolated $V = 6.0$ mag G2 V star is to be acquired, with the scientific exposures to be obtained with the star behind the WEDGEA1.8 mask.



The target will be acquired with a point source acquisition, but because the object is so bright, we cannot use the preferred F28X50LP filter. Instead, we will use the F25ND3 neutral-density filter, and the TA ETC yields an exposure time of 0.02 second, which is less than the minimum allowed time of 0.1 second. Note that the GAIN=4 and CR-SPLIT=1 *must be used* for the ETC to assure that you have a S/N of at least 40 in each of the two images obtained during the ACQ process. We will therefore increase the exposure time to 0.5 second. The object does not saturate the CCD, and the exposure time is less than 5 minutes, so we have devised a valid target acquisition.

The star is to be accurately placed behind the WEDGE which is 1.8 arcseconds in size and in this example, we will perform an ACQ/PEAK acquisition. The peakup will be performed in the 0.3X0.05ND slit (peakdown acquisitions are not recommended, see Section 12.10), and we will use the CCD and the MIRROR.¹ A 1 second exposure yields 47,000 electrons in the target *after* you correct it for the aperture throughput [both the neutral-density (10^{-3}) and the slit throughput (55%)]. We have more than the minimum requirement of 5000 electrons in the target, the object does not saturate the CCD, and the exposure time is less than 6.4 minutes (the maximum time for a peakup with the 0.3X0.05ND slit), so we have devised a valid peakup target acquisition.

Target Acquisition ETC Parameters - ACQ:

- Detector = CCD;
- Filter = ND3;
- Gain = 4 e⁻/ADU;
- Check Box = 3 x 3;
- Target was a point source;
- Spectrum: G2V (Model Spectrum);
- Source Flux: V = 6.0;
- Average Galactic Extinction of $E(B-V) = 0.0$;
- The Zodiacal Light is average;
- The earthshine is average;

Imaging ETC Parameters - ACQ/PEAK:

- Detector = CCD;
- Filter = Clear;
- Gain = 4 e⁻/ADU;
- CR-SPLIT (Total number of images) = 1;
- Target was a point source;
- Spectrum:G2V (Model Spectrum);
- Source Flux: V = 6.0;
- Average Galactic Extinction of $E(B-V) = 0.0$;
- The Zodiacal Light is average;
- The earthshine is average;

Phase II Parameters for ACQ and ACQ/PEAK Exposures:

| Exp | Label | Target Name | Config | OpMode | Aperture | SpElement | Wavlen | Iter | Exp Time (secs) |
|---|----------------|-------------|----------|-----------|-------------|-----------|--------|------|-----------------|
| 1 | | G-STAR | STIS/CCD | ACQ | F25ND3 | MIRROR | | 1 | 0.5 |
| Special Requirements: Comments: Optional Parameters: ACQTYPE=POINT, | | | | | | | | | |
| | Sub-exposures: | Copy | Split | Orbit Num | Actual Time | | | | |
| | | | | | | | | | |

¹ Note that peak-ups are only really needed if the PI wants a pointing accuracy better than ~13 mas.

8.6 STIS Post-Observation Target Acquisition Analysis

8.6.1 Did the Acquisition Succeed?

Unlike with earlier *HST* spectrographs, it is now possible to determine what the instrument acquired during an observation. The methods described below can be used to make either a coarse (eyeball estimate) or a fine (exact pixel) determination.

8.6.1 Did the Acquisition Succeed?

[Section 5.2](#) of the *STIS Data Handbook* describes in detail how to determine if an acquisition succeeded. We recommend the use of the **tastis** tool in **stistools** as a quick way to determine how well an acquisition worked. For `ACQ` exposures, this tool will report where the target was found at the beginning of the coarse and fine locate stages, where the reference aperture projected onto the detector, and will also give the individual and total slews in units of both CCD pixels and arcseconds. For `ACQ/PEAK` exposures, the tool will report the relative flux at each pointing of the pickup, the slew made, and the flux in the confirmation image. For both kinds of acquisition exposures the **tastis** task will issue a warning message if the fluxes or slews reported appear to fall outside the normal range of values expected for a successful acquisition.

Contents of `ACQ` and `ACQ/PEAK` image files

It can also be useful to directly examine the images provided in the acquisition data files. The STScI calibration pipeline will produce raw data files that contain images taken during the acquisition sequence as well as information about the measurements done at each stage of the acquisition.

For `ACQ` exposures, each raw file will contain three images, each in a separate fits image extension. The first science image extension shows the image taken at the beginning of the coarse locate phase and shows where the target was initially found. The second science image extension shows the image recorded after the coarse locate slew has been done. The third science extension shows where the image of the standard reference aperture, as illuminated by a tungsten lamp, projects onto the detector. The `ACQ/PEAK` raw fits file contains the final "confirmation" image of the target viewed through the aperture in the first image extension and the fluxes measured in the stepping pattern in the fourth extension. Further details of these files and their contents are discussed in [Section 5.2](#) of the *STIS Data Handbook*.

Target Acquisition Simulator

While the **tastis** tool in **stistools** is normally adequate to determine whether or not your acquisition succeeded, sometimes, especially for complex extended objects, a more complete simulation of the acquisition sequence may be useful. Once you have your data, you can use the [Target Acquisition Simulator](#) to determine the exact position of the source that was acquired. The **TAS** will take the STIS image of the initial pointing and, using the same algorithm as the flight software, tell you the location of the target, in pixel coordinates.

Chapter 9: Overheads and Orbit-Time Determination

Chapter Contents

- [9.1 Overview](#)
- [9.2 STIS Exposure Overheads](#)
- [9.3 Orbit Use Determination Examples](#)

9.1 Overview

After you establish the set of scientific exposures and any additional target acquisition or calibration exposures that you require for your program, you are ready to determine the total number of orbits to request. Generally, this is a straightforward exercise involving compilation of the overheads on the individual exposures, packing the exposure plus overhead time into individual orbits, and tallying up the results to determine your total orbit request. In some cases, it may be an iterative process as you refine your exposure requests to more fully exploit the orbits.

The *HST Call for Proposals* and the *HST Primer* provide information on the Observatory policies and practices with respect to orbit-time requests. In the following sections, we provide a summary of the STIS-specific overheads and give several examples that illustrate how to calculate your orbit requirements for Phase I Proposals. Note that the *HST Primer* provides a more limited summary of overheads that are intended to be conservative. In the unlikely case that an overhead calculation using the *HST Primer* requires less time than one calculated using the information in this chapter, you should use the result from this chapter to ensure that you do not end up with a time allocation that is insufficient to carry out your program in Phase II.

Alternatively, you could also use the **APT** to create a simple program. **APT** automatically takes the appropriate overheads into account and provides a statistically estimated orbit length to assist in constructing the observation program.

9.2 STIS Exposure Overheads

Our current estimates of the overheads on STIS exposures are summarized in [Table 9.1](#) and [Table 9.2](#). All numbers given are approximate and rounded up to the nearest half minute; they do not differentiate in detail the overheads for different STIS modes and configurations. These overhead times are to be used (in conjunction with the actual exposure times and the *HST Primer*) to estimate the total number of orbits for your proposal. After your *HST* proposal is accepted, you will be asked to submit a Phase II proposal to support scheduling of your approved observations. At that time you will be presented with actual, up-to-date overheads by the scheduling software. *Allowing sufficient time for overheads in your Phase I proposal is important; additional time to cover unplanned overheads will not be granted later.*

The following list presents important points for each type of overhead:

- **Generic (Observatory Level) Overheads:**
 - The first time you acquire an object you must include the overhead for the guide-star acquisition (6 minutes).
 - In subsequent contiguous orbits you must include the overhead for the guide-star reacquisition (4 minutes). If you are observing in the Continuous Viewing Zone (see the *HST Primer*), no guide-star reacquisitions are required.
 - Time needs to be allowed for each deliberate movement of the telescope; e.g., if you are performing a target acquisition exposure on a nearby star and then offsetting to your target, or if you are taking a series of exposures in which you move the target relative to the slit, you must allow time for the moves (20 seconds to 60 seconds depending on length of slew, see [Table 9.1](#) and [Table 9.2](#)).
 - Remember the policy with regard to MAMA and CCD observations in the same visit (see [Chapter 2](#)).
- **Scientific Exposures:**
 - The overhead times are dominated by the time to move the grating wheel (MSM), which is ~3.0 minutes per move, worst case, and the readout time (CCD). Again, we stress that in Phase II the overheads will frequently be less, but it is important to plan Phase I using the conservative overheads given in [Table 9.2](#) to ensure that you will have adequate time for your scientific goals.
- **CCD and MAMA Spectroscopic Exposures and Wavecals:**
 - The quoted overheads on the first spectroscopic exposure in a visit, or a spectroscopic exposure within a visit containing a change of grating or grating tilt, allow for the taking of a single automatic wavecal exposure to permit post-observation determination of the zero point of the wavelength (and spatial) scales. If you plan a series of exposures at a given grating setting which extends over 40 minutes in exposure time, then you need to include time for an additional automatic wavecal for each 40-minute period. However for certain types of observing programs, careful crafting of the Phase II proposal can force the additional automatic wavecals associated with long observations (greater than ~40 minutes) into occultation (see [Section 11.2.1](#)).
- **Moving Targets:**
 - Additional overheads will be incurred for observations of solar system targets. The moving target overheads (~1 minute in duration) are dependent upon current slew rates and are updated as necessary.

Table 9.1: Scientific Exposure Overheads: General, Acquisition, and Pickup

| Action | Overhead |
|---|---|
| Generic (Observatory Level) | |
| Guide-Star acquisition | Initial acquisition overhead = 6 minutes. Reacquisitions on subsequent orbits = 4 minutes per orbit. |
| Spacecraft POS-TARG moves | 1 minute for offsets <1 arcminute and >10 arcseconds. 0.5 minute for offsets between 1-10 arcseconds. 10 seconds for offsets <1 arcsecond in size. |
| Acquisitions and Peakups | |
| Target acquisition (to place target in STIS aperture); see also Chapter 8 . | For $V \leq 21$ point sources, 6 minutes. For diffuse acqs, add $0.2 \times$ checkbox 2 seconds to the nominal 6 minutes. |
| Acquisition peakups; see also Chapter 8 . | For $V \leq 21$, 6 minutes for one peakup; note that a second peakup is required for the 0.1×0.03 aperture; dispersed light peakups may require an additional 3 minutes overhead for change in optical element. More generally, see Table 8.5 . |
| End of CVZ Visit | |
| End of CVZ visit | Final STIS buffer dump = 3 minutes. Return mechanisms to normal = 4.5 minutes. For non-CVZ observations, these activities occur during the final occultation period, with no impact on target visibility. |

Table 9.2: STIS Scientific Exposure Overheads: Imaging and Spectroscopy

| Action | Overhead | | | |
|--|------------------|----------------|------------------|------------------|
| | Imaging | | Spectroscopy | |
| | CCD (minutes) | MAMA (minutes) | CCD (minutes) | MAMA (minutes) |
| First scientific exposure | 4.5 | 5.0 | 5.0 ¹ | 8.0 ¹ |
| Identical exposure in series (within an orbit) | 1.0 ² | 0.5 | 1.0 | 0.5 |
| Exposure in series with grating move only | 3.0 | 3.0 | 5.0 ¹ | 8.0 ¹ |
| Move of aperture wheel: change of slit or aperture, change of filter | 1.0 | 1.0 | 1.0 | 1.0 |
| Additional automatic wavecal for series of identical exposures extending more than ~40 minutes | n/a | n/a | 1.5 | 4.0 |

| | | | | |
|--|-----------------------------|--------------------------|-----------------------------|--------------------------|
| Overhead for data management for exposures >3 minutes in duration | 0 | 0 | 0 | 0 |
| Overhead for data management, for a series of full-frame exposures, each SHORTER than 3 minutes in duration (see CCD Subarrays for subarray rules) | 3 minutes every 7 exposures | 2 minutes every exposure | 3 minutes every 7 exposures | 2 minutes every exposure |
| Additional Calibration Exposures: Extra GO Wavecals ³ and Fringe Flats | | | | |
| MAMA wavecal exposure | 4.0 minutes | | | |
| CCD wavecal exposure | 1.5 minutes | | | |
| CCD fringe flat exposure | 2 minutes | | | |
| Slitless Spectroscopy (image of field, image of slit, wavecal) | 9 minutes | | | |

¹ Includes auto wavecal. At Phase II, wavecals occurring at the beginning or end of an orbit will be pushed into occultation, providing increased time for scientific observing.

² For $CR-SPLIT = n$, each exposure has a 1 minute overhead, so there will be $(n - 1)$ minutes of *extra* overhead. If small CCD subarrays are used, the overhead per exposure decreases to 20 seconds.

³ Use these only for additional wavecal exposures beyond those taken automatically.

9.3 Orbit Use Determination Examples

[9.3.1 Sample Orbit Calculation 1: Long-Slit Spectroscopy of the Galaxy M86](#)

[9.3.2 Sample Orbit Calculation 2: Low Dispersion Spectroscopy of Solar Analog Star P041-C](#)

[9.3.3 Sample Orbit Calculation 3: Imaging and Spectroscopy of the Cat's Eye Planetary Nebula, NGC 6543](#)

[9.3.4 Sample Orbit Calculation 4: MAMA Echelle Spectroscopic Exposures in the CVZ](#)

[9.3.5 Sample Orbit Calculation 5: Faint CCD Imaging](#)

The easiest way to learn to compute total orbit time requests is to work through a few examples. The five examples provided below have been calculated using **APT 20.2**, which will be somewhat out-of-date. The results for the latest version of **APT**, which should be used by proposers, will be similar but slight differences might appear. All times are rounded to the nearest tenth of a minute. Also note the slight differences in the target acquisitions.

- Example 1 is a pattern-stepped series of long-slit CCD spectroscopic exposures mapping out the H α nebula in the center of the galaxy M86. This uses a diffuse-source acquisition and no peakup.
- Example 2 is a series of spectroscopic observations of the solar-analog, CVZ star P041-C, using all of the first-order, low-resolution CCD gratings. This example uses a point source acquisition and no peakup on the target.
- Example 3 is an imaging and spectroscopic program observing NGC 6543, the Cat's Eye Nebula. This uses a point source acquisition.
- Example 4 is a set of long MAMA spectroscopic exposures of Sk -69° 215 using the E230H grating through a narrow echelle slit, taken in the CVZ. This uses a point source acquisition and peakup on the target, and includes re-peakups during the course of the long observations.
- Example 5 is a faint CCD imaging program of point sources around the star GGH202 EIS J033259.26-273810.5. This uses no acquisition.

9.3.1 Sample Orbit Calculation 1: Long-Slit Spectroscopy of the Galaxy M86

This example is for an observation of the H α nebula in the center of the Virgo elliptical M86, using the CCD, the 52x0.2 slit and the G750M grating. A series of exposures is taken, each stepped relative to the next by 0.2 arcsecond, in the direction perpendicular to the slit, in order to cover the inner 0.6 arcseconds of the galaxy completely. Based on the signal-to-noise ratio calculation presented in [Section 6.8.1](#), we require an integration time of ~30 minutes per position to obtain a signal-to-noise ratio of ~10. The scientific exposures for this proposal, therefore, comprise all of the following:

- A CR-SPLIT=2, ~30 minute spectroscopic exposure¹ with G750M at a central wavelength of $\lambda = 6768 \text{ \AA}$ at location 1.
- A CR-SPLIT=2, ~30 minute spectroscopic exposure with G750M at a central wavelength of $\lambda = 6768 \text{ \AA}$ at location 2.
- A CR-SPLIT=2, ~30 minute spectroscopic exposure with G750M at a central wavelength of $\lambda = 6768 \text{ \AA}$ at location 3.

We need to include time for the guide-star acquisition at the start of the first orbit, followed by an acquisition exposure. No pickup will be done, since we are covering the nebula by stepping the slit and the slit is wider than 0.1 arcsecond. In this example, we assume a diffuse source acquisition, with a checkbox size of 25 pixels (roughly 1.25 arcseconds). The checkbox needs to be large as this galaxy has a very flat and dusty profile; see [Figure 8.5](#).

The mean surface brightness of the galaxy within this region is $\sim 2 \times 10^{-15}$ ergs/s/cm²/Å/arcsec², based on WFPC2 V-band images in the *HST* archive. Using the information in [Section 6.4](#) or the [STIS TA ETC](#) we determine that, using the CCD longpass filter, F28X50LP, for $t_{\text{exp}} = 1$ second, we achieve more than the required signal-to-noise ratio needed over the checkbox for the target acquisition. We use the formula in [Table 9.1](#), plug in CHECKBOX=25 and exptime=1.0, and determine that the acquisition will take roughly 8 minutes.

This is not a CVZ observation, so because more than 1 orbit is required we need to include time for the guide-star reacquisition at the beginning of each orbit. The individual exposures in this example are long enough that we do not need to include extra overhead for data management. We are satisfied with the automatic wavecal exposures which are taken for each spectroscopic observation at a new MSM position. We do not require fringe flats as we are observing at wavelengths shortward of 7500 Å.

We assume a visibility period of 54 minutes per orbit, appropriate for a target at M86's declination of +13° (see the [HST Primer](#)). Based on the reasoning presented in [Table 9.3](#), below, we conclude that the observations can be squeezed into ~2 orbits with some loss of sensitivity. Alternately, one could choose to increase the signal-to-noise, and ask for 3 orbits.

APT provides the capability to select preset patterns with user-supplied options to facilitate planning. For this example, a mosaic of the inner 0.6 arcseconds of M86 can be obtained by specifying Pattern Type="STIS-PERP-TO-SLIT", Purpose="Mosaic" (which will step the aperture on the target), Number of Points="3", Point Spacing="0.2", Coordinate Frame="POS-TARG" (which specifies pattern execution in the spacecraft frame) and click Center Pattern.

Table 9.3: Orbit Calculation for Example 1.

| Action | Time (minutes) | Explanation |
|--|----------------|--|
| <i>Orbit 1</i> | | |
| Initial Guide-Star acquisition | 5.6 | Needed at start of observation of new target |
| Target acquisition | 6.0 | Diffuse acquisition with checkbox=25, $t_{\text{exp}} = 1.0$ s |
| Offset target 0.2 arcseconds to initial position | 0.3 | Move to position 1 in pattern |
| Auto-wavecal | 3.8 | Auto-wavecal before first science exposure |
| Scientific exposure, G750M, $\lambda_c = 6768$ Å, position 1 | 31.6 | 30.0 minutes exposure time 1.6 minutes for exposure overhead for CR-SPLIT |

| | | |
|---|------|--|
| Offset target 0.2 arcseconds to position 2 | 0.3 | Move to position 2 in pattern |
| Orbit 2 | | |
| Guide-Star Reacquisition | 3.7 | Start of new orbit |
| Additional wavecal | 1.2 | New orbit |
| Scientific exposure, G750M, $\lambda_c = 6768 \text{ \AA}$, position 2 | 22.6 | 21.0 minutes exposure time 1.6 minutes for exposure overhead for CR-SPLIT |
| Step target 0.2 arcseconds \perp to slit | 0.3 | Move to position 3 in pattern |
| Scientific exposure, G750M, $\lambda_c = 6768 \text{ \AA}$, position 3 | 22.6 | 21.0 minutes exposure time 1.6 minutes for exposure overhead for CR-SPLIT |

9.3.2 Sample Orbit Calculation 2: Low Dispersion Spectroscopy of Solar Analog Star P041-C

In this example the scientific objective is to observe the solar-analog CVZ star P041-C from the near-infrared (NIR) to the near-ultraviolet (NUV) with STIS' low-resolution, first-order gratings and the 52x0.5 arcsecond slit. The series of exposures includes:

- CR-SPLIT=2, ~7 minute spectroscopic exposure with G430L at the central wavelength of $\lambda = 4300 \text{ \AA}$.
- CR-SPLIT=3, ~43 minute spectroscopic exposure with G230LB at the central wavelength of $\lambda = 2375 \text{ \AA}$.
- CR-SPLIT=2, ~5 minute spectroscopic exposure with G750L at the central wavelength of $\lambda = 7751 \text{ \AA}$.

We need to include time for the guide-star acquisition at the start of the first orbit, followed by an acquisition exposure. This target is a bright point source. We will use the longpass filter F28X50LP for the target acquisition. Using the [STIS TA ETC](#) we find that an exposure time of 0.1 seconds gives a SNR >100 without saturating the CCD. No peakup is needed as we are using the 0.5 arcsecond wide slit. This is a CVZ observation so each orbit is ~96 minutes. We need to include time for the CCD long-wavelength fringe flats (see [Section 11.2.3](#)), and since this is a CVZ observation the fringe flat will not move into the occultation. As shown in [Table 9.4](#), we can easily perform this observation in a single orbit.

Table 9.4: Orbit Calculation for Example 2.

| Action | Time (minutes) | Explanation |
|--------------------------------|----------------|--|
| Orbit 1 | | |
| Initial Guide-Star acquisition | 5.6 | Needed at start of observation of new target |
| Target acquisition | 6.0 | Point source acquisition on target |

| | | |
|--|------|---|
| Auto-wavecal | 2.4 | 2.4 minutes for auto-wavecal for G430L |
| Scientific exposure, G430L, $\lambda = 4300 \text{ \AA}$ | 9.4 | 7.0 minutes exposure time 2.4 minutes for CR-SPLIT=2 exposure overhead |
| Auto-wavecal | 4.0 | 4.0 minutes for auto-wavecal after for G230LB |
| Scientific exposure, G230LB, $\lambda = 2375 \text{ \AA}$ | 46.1 | 43 minutes exposure time 3.1 minutes for CR-SPLIT=3 exposure overhead |
| Auto-wavecal | 2.0 | 2.0 minutes for auto-wavecal after 40 minutes |
| Auto-wavecal | 3.2 | 3.2 minutes for auto-wavecal for G750L |
| Scientific exposure, G750L, $\lambda = 7751 \text{ \AA}$ | 7.4 | 5.0 minutes exposure time 2.4 minutes for CR-SPLIT=2 exposure overhead |
| CCD fringe flat G750L | 4.5 | 0.8 minutes Fringe flat exposure time 3.7 minute Fringe flat overhead |

9.3.3 Sample Orbit Calculation 3: Imaging and Spectroscopy of the Cat's Eye Planetary Nebula, NGC 6543

In this example the scientific objectives are to obtain [O II] images of planetary nebula NGC 6543, as well as an optical spectrum at H β and an ultraviolet (UV) spectrum at C IV. The exposure time calculations for these observations are presented in [Section 6.8.3](#). The specific exposures in this series include:

- A CR-SPLIT=2, ~5 minute exposure with the F28X500II filter.
- A CR-SPLIT=2, ~30 minute exposure with G430M at a central wavelength of $\lambda = 4961 \text{ \AA}$ using the 52X0.1 long slit.
- A ~30 minute exposure with G140L at C IV and the 52X0.1 long slit.

We need to include time for the guide-star acquisition at the start of the first orbit, followed by an acquisition exposure. The central star of the Cat's Eye Nebula is used as the acquisition target. It has a V magnitude ~11.5. Checking [Table 8.3](#), we conclude that the star is faint enough to not saturate the CCD in imaging mode with the longpass aperture F28X50LP and an exposure time of 0.1 seconds. We therefore use it for the target acquisition. We wish to perform a pickup exposure as well, to center the star in the 0.1 arcsecond wide slit. We consult [Table 8.3](#) and conclude that the source is not bright enough to saturate the CCD if we perform an undispersed (white-light) pickup with the mirror and an exposure time of 0.1 seconds.

This is not a CVZ observation, so because more than 1 orbit is required we need to include time for the guide-star reacquisition at the beginning of each orbit. The individual exposures in this example are long enough that we do not need to include extra overhead for data management. We are satisfied with the automatic wavecal exposures that are taken for each spectroscopic observation at a new MSM position.

We assume a visibility period of 59 minutes per orbit, appropriate for a target at our source's declination of 66° (see the *HST Primer*). Based on the reasoning presented in Table 9.5 below, we conclude that a total of 2 orbits is required to perform these observations. Note that the MAMA and CCD observations have been split into separate visits in accordance with the stated policy (See Section 2.7).

Table 9.5: Orbit Calculation for Example 3.

| Action | Time (minutes) | Explanation |
|---|----------------|--|
| <i>Orbit 1</i> | | |
| Initial Guide-Star acquisition | 5.6 | Needed at start of observation of new target |
| Target acquisition | 6.0 | Performed on central star |
| Pointing Maneuver | 0.3 | |
| Peakup acquisition | 6.6 | White light peakup performed on central star |
| Auto-wavecal | 3.7 | 3.7 second auto-wavecal for the G140L science exposure |
| G140L scientific exposure | 31.5 | 31 minutes total scientific exposures time 0.5 second overhead |
| <i>Orbit 2 (A whole new visit to keep MAMA and CCD exposures separate)</i> | | |
| Guide-Star reacquisition | 3.7 | Needed at start of observation of new target |
| Target acquisition | 6.0 | Performed on central star |
| Pointing Maneuver | 0.3 | |
| Peakup acquisition | 6.5 | White light peakup performed on central star |
| Auto-wavecal | 3.1 | 3.1 second auto-wavecal for G430M science exposure |
| CR-SPLIT=2 scientific exposure with G430M at $\lambda = 4961 \text{ \AA}$ | 31.4 | 29.7 minutes total scientific exposure time 1.6 minutes for exposure overhead for CR-SPLIT |
| Pointing Maneuver | 0.3 | |
| CR-SPLIT=2 [O II] imaging using F28X500II | 8.4 | 5.0 minutes total scientific exposure time 3.4 minutes overhead for imaging exposure and CR-SPLIT |

9.3.4 Sample Orbit Calculation 4: MAMA Echelle Spectroscopic Exposures in the CVZ

In this example we wish to obtain a long total integration (~400 minutes) in the CVZ using E230H and the 0.2x0.09 slit. The exposure time calculations for this example are presented in [Section 6.8.4](#).

We choose to break the observation up into roughly identical 40 minute exposures. We acquire the target using a CCD point source acquisition and then pickup in dispersed light using the CCD and the same slit as intended for the scientific observations. The star is Sk -69° 215, an O5 star with a V magnitude of 11.6. Checking [Table 8.3](#), we conclude that the source will not saturate the CCD if observed for 0.1 seconds in the longpass filter F28X50LP, and we choose to perform the acquisition then on Sk -69° 215 with this filter as the aperture.

We then perform a dispersed-light pickup using the G230LB grating with the CCD detector. We can estimate the exposure time required by determining with the **Spectroscopic ETC** the total counts over the detector in 1 second for the clear filter and scaling by 65% for the slit throughput for 0.2x0.09 (see [0.2X0.09 Aperture](#)). Since we must attain 80,000 counts over the detector, we require less than 1 second per dwell point of the pickup. We choose a 1 second exposure time. The pickup overhead for this slit is $360 + 20 \times t_{exp}$. We thus conclude that the pickup will require $360 + 20 \times 1 = 380$ seconds or ~6.3 minutes. In practice, using **APT 20.2**, the peak-ups ran between 7.5 and 8.3 minutes.

Since this is a CVZ observation, we do not need to include time for reacquisitions. However, since it is a long observation and a narrow slit, we decide we will re-perform a pickup midway through the observation.

Additionally, since this is a long observation taken at a given grating position, we need to include time for the automatic wavecal which will be taken every 40 minutes of elapsed pointed time. Since the auto-wavecal exposures are short for this configuration, time must be allocated for a buffer dump prior to each auto-wavecal.

For CVZ targets, an orbit is 96 minutes. We conclude we require a total of 5 CVZ orbits to perform this program, as summarized in [Table 9.6](#).

Table 9.6: Orbit Calculation for Example 4.

| Action | Time (minutes) | Explanation |
|--|----------------|---|
| <i>CVZ Observations: 5 orbits @ 96 minutes/orbit</i> | | |
| Initial Guide-Star acquisition | 5.6 | Needed at start of observation of new target |
| Target acquisition | 6.0 | Point source acquisition on target |
| Pointing | 0.3 | |
| Pickup exposure in 0.2x0.09 slit | 7.5 | Echelle slit dispersed-light pickup |
| Automatic wavecal | 3.5 | Automatic wavecal for first science exposure |
| First scientific exposure E230H | 42.5 | 40.0 minutes exposure time 0.5 minutes overhead 2.0 minutes buffer dump |

| | | |
|------------------------------------|------|---|
| Automatic wavecal after 40 minutes | 1.4 | 1.4 minutes including overhead |
| Second scientific exposure E230H | 42.5 | 40.0 minutes exposure time 0.5 minutes overhead 2.0 minutes buffer dump |
| Automatic wavecal after 40 minutes | 1.4 | 1.4 minutes |
| Third scientific exposure | 42.5 | 40.0 minutes exposure time 0.5 minutes overhead 2.0 minutes buffer dump |
| Automatic wavecal after 40 minutes | 1.4 | 1.4 minutes including overhead |
| Fourth scientific exposure | 42.5 | 40.0 minutes exposure time 0.5 minutes overhead 2.0 minutes buffer dump |
| Automatic wavecal after 40 minutes | 1.4 | 1.4 minutes including overhead |
| Fifth scientific exposure | 42.5 | 40.0 minutes exposure time 0.5 minutes overhead 2.0 minutes buffer dump |
| Automatic wavecal after 40 minutes | 1.4 | 1.4 minutes including overhead |
| Peakup to recenter target | 8.3 | Echelle slit peakup |
| Automatic wavecal | 3.4 | For science exposure after peakup |
| Sixth scientific exposure | 42.5 | 40.0 minutes exposure time 0.5 minutes overhead 2.0 minutes buffer dump |
| Automatic wavecal after 40 minutes | 1.4 | 1.4 minutes including overhead |
| Seventh scientific exposure | 42.5 | 40.0 minutes exposure time 0.5 minutes overhead 2.0 minutes buffer dump |
| Automatic wavecal after 40 minutes | 1.4 | 1.4 minutes including overhead |
| Eighth scientific exposure | 42.5 | 40.0 minutes exposure time 0.5 minutes overhead 2.0 minutes buffer dump |
| Automatic wavecal after 40 minutes | 1.4 | 1.4 minutes including overhead |
| Ninth scientific exposure | 42.5 | 40.0 minutes exposure time 0.5 minutes overhead 2.0 minutes buffer dump |
| Automatic wavecal after 40 minutes | 1.4 | 1.4 minutes including overhead |

| | | |
|------------------------------------|------|---|
| Tenth scientific exposure | 42.5 | 40.0 minutes exposure time 0.5 minutes overhead 2.0 minutes buffer dump |
| Automatic wavecal after 40 minutes | 1.4 | 1.4 minutes including overhead |

9.3.5 Sample Orbit Calculation 5: Faint CCD Imaging

In this program we wish to take deep images of a field to look for faint point sources, as described in [Section 6.8.5](#). We look at the field around GGH2002 EIS J033259.26-273810.5, a K0V star with a V magnitude of 22.18. We request `LOW-SKY` as this observation is background limited. At our declination, we find from the [HST Primer](#) that there are 45 minutes of visibility per orbit. The observations consist of:

- A single `CR-SPLIT=4`, ~28 minute exposure using the 50CCD clear aperture with the CCD.

We determine that we can execute this program in 1 orbit, as summarized in [Table 9.7](#).

Table 9.7: Orbit Calculation for Example 5.

| Action | Time (minutes) | Explanation |
|--|----------------|---|
| <i>Orbit 1</i> | | |
| Initial Guide-Star acquisition | 6.5 | Needed at start of observation of new target |
| <code>CR-SPLIT=4</code> exposure, using 50CCD in imaging mode. | 33.4 | 28.0 minutes exposure time 3.4 minutes overhead for <code>CR-SPLIT</code> exposures 2.0 minutes buffer dump |

¹ Here and below, `CR-SPLIT= n` , m minute exposure implies there will be n exposures with a total of m minutes across the exposures. In this example there will be 2 exposures each of 15 minutes for a total of 30 minutes.

Chapter 10: Summary and Checklist

Chapter Contents

- [10.1 Phase I Proposing](#)
- [10.2 Phase II - Scheduling Approved Observations](#)

10.1 Phase I Proposing

10.1.1 Phase I Orbit Allocation Examples

At this point you should have assembled all the information you need to submit your Phase I *HST* observing proposal. During the course of this process you should review the items listed below.

For All Proposals:

- Check the catalog of previously executed and accepted programs to search for any duplications, and if present, provide a justification for duplicate observations.
- Justify any special requirements (e.g., *SHADOW*, interactive acquisition, CVZ, target-of-opportunity, time critical scheduling, or the re-use target capability).
- Consider any special calibrations (e.g., unusually accurate wavelength determination requiring additional non-automatic wavecal exposures, fringe flats, or slitless spectroscopy), and account for their time in your request.
- Check your exposure times and configurations to ensure they are sufficient to provide the desired signal-to-noise ratios and accuracies, without saturation.
- Check that no visit is longer than 3 orbits.
- Allocate time for a target acquisition with appropriate centering accuracy. In exceptional cases, analysis of a previous *HST* image is necessary for setting up the acquisition parameters (see [Chapter 8.2.3](#)). The orbit request for taking these pre-acquisition images must be included in the Phase I proposal.
- Include all applicable overheads so that in Phase II you will have enough orbits available to successfully implement your observations.
- Make sure that all configurations used in your proposal are included in the summary table.
- If applicable, justify the use of any available-but-unsupported modes, and explain how you plan to deal with calibration issues.

For CCD Observations:

- Check that you are not exceeding the CCD full well counts/pix limit for pixels (emission lines or objects) of interest.
- Allow time for *CR-SPLIT* observations and dithering, as needed.

For MAMA Observations:

- Check that your source does not exceed the absolute bright object count rate limits for MAMA exposures. For target-of-opportunity programs, explain how you plan to show that the target does not exceed the bright object limits.
- Check that you are not exceeding the MAMA 65,536 counts/pix buffer imposed limit over pixels (emission lines or objects) of interest.
- Check that your proposal does not violate the policy that restricts the mixing of CCD and MAMA observations in the same visit, (see [Section 2.7](#)). Be sure that you are requesting sufficient orbits to allow the MAMA and CCD observations to be done in separate visits. Provide a justification if the scientific needs of your program require violating this policy.
- If early acquisition images in support of MAMA bright object checking are necessary, they must be included in the Phase I orbit request.
- Remember that MAMA pure parallels are not allowed (see [Section 2.8](#)).
- Be aware of the limits on the number of targets for STIS/MAMA and COS snapshot and survey programs (see [Section 2.9](#)).

If you have visits with both CCD and MAMA observations, check that there is less than 30 minutes of science observing time (including overheads) with the CCD, or that the target is observed for only one orbit (See [Section 2.7](#)).

10.1.1 Phase I Orbit Allocation Examples

Phase I orbit allocation examples are presented in the *HST Primer*. Additional examples of Phase I orbit estimations are worked through in this Handbook (see [Section 1.2.2](#), [Section 6.8](#), and [Section 9.3](#)).

10.2 Phase II - Scheduling Approved Observations

Below, we provide a checklist for observers filling out Phase II proposals. You should do the following prior to submitting your program.

For All Proposals:

- Update the text in the Phase II template "Observing Description" and "Special Requirements"—they were copied from your Phase I proposal and may need modification based on TAC comments and definition of the observation details.
- Specify your coordinates (especially for spectroscopic observations) in the Guide Star reference frame. Be sure to specify the coordinate source used. If your target has significant proper motion, be sure to also include this information in the appropriate fields in the Phase II proposal file. Check that the units of the proper motion are correct, and that the epoch specified is consistent with the coordinates supplied.
- Specify accurate *V* magnitude, fluxes, spectral type, and colors for your target. This is *required* for MAMA targets to allow for bright object checking and screening. If you are using the MAMAs and have UV photometry (e.g., from *GALEX*) for your target, provide it.
- Properly specify your exposures.
- Include target acquisitions and pickups as needed.
- Specify any needed orientation and/or timing requirements. To facilitate scheduling, please provide the broadest possible ranges for these requirements that are consistent with your scientific needs. If multiple ORIENTS are possible, please include the alternatives.
- Specify any allocated coordinated parallel exposures.
- Include any additional wavecal exposures if needed.
- Verify the correct usage (i.e., direction) of your PATTERN optional requirement or POS-TARGs (if used).
- For slitless spectroscopy or prism observations, remember to take an image and the proper calibration sequence if needed (see Chapters 12.1 and 4.4).
- Check the [Phase II](#) webpage for any updates. You can also find there instructions for requesting changes to your program and observing policies.

For CCD Observations:

- CR-SPLIT CCD exposures, as appropriate. Keep individual exposure times <1000 s if possible to avoid excessive cosmic ray events.
- Add fringe-flat exposures for G750L and G750M observations at $\lambda > 7500 \text{ \AA}$.
- Consider the use of dithering for imaging observations, or stepping along the slit for spectroscopic observations.
- Consider whether moving the target closer to the CCD readout by using the E1 pseudo-aperture positions to reduce charge transfer efficiency (CTE) effects would benefit your program. If observing in the far red, consider the E2 pseudo-apertures to improve fringe removal.

For MAMA Observations:

- Re-verify that your target falls below the bright object limits.
- For TIME-TAG observations, verify the value for BUFFER-TIME.
- Consider the use of dithering for imaging observations.
- Consider the use of stepping along the slit for first-order modes or the use of FP-SPLIT slits for echelle modes, when high signal-to-noise is required.

- For faint objects, consider using the D1 pseudo-apertures to mitigate the FUV-MAMA dark current.

Chapter 11: Data Taking

Chapter Contents

- [11.1 Basic Operating Modes](#)
- [11.2 Exposure Sequences and Contemporaneous Calibrations](#)
- [11.3 Patterns and Dithering](#)
- [11.4 Fixing Orientation on the Sky](#)
- [11.5 Target Positioning](#)

11.1 Basic Operating Modes

- [11.1.1 CCD ACCUM Mode](#)
- [11.1.2 MAMA ACCUM Mode](#)
- [11.1.3 MAMA TIME-TAG Mode](#)

STIS currently supports four basic operating modes:

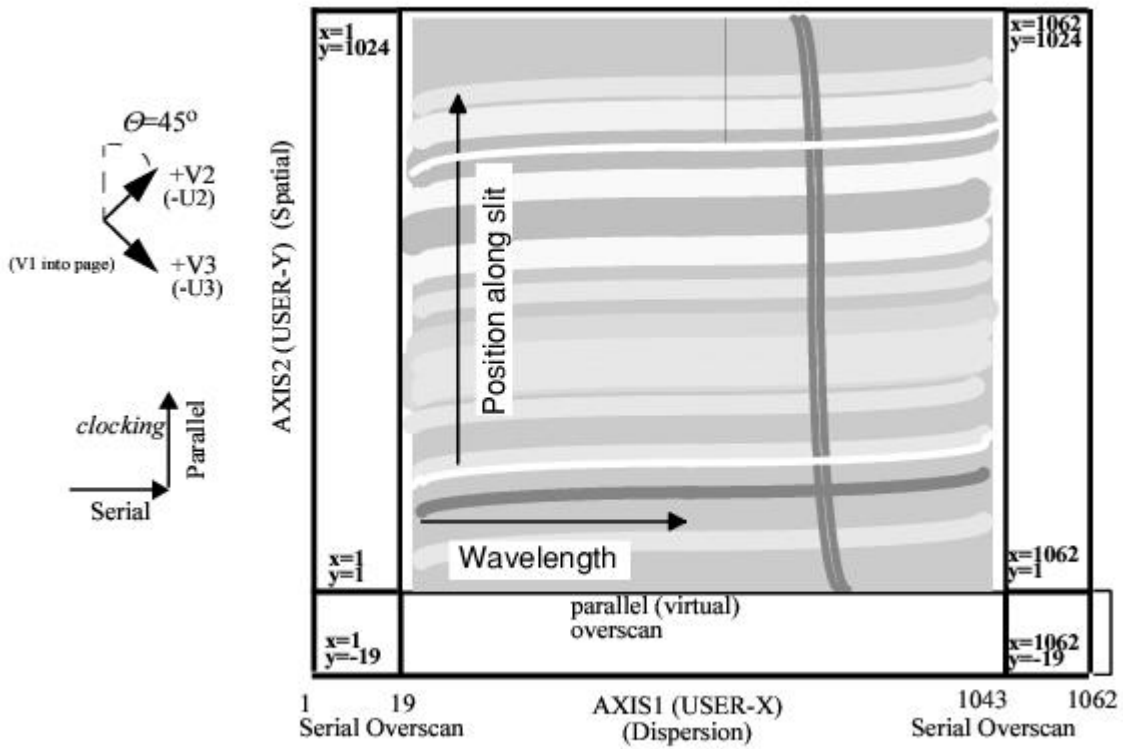
- **ACCUM** operating modes for the CCD and MAMAs, which produce a time-integrated accumulated image. These have been the most commonly used modes.
- **TIME-TAG** operating mode for the MAMA detectors, which outputs an event stream of high-time-resolution observations in the ultraviolet (UV). When feasible, observers are encouraged to use TIME-TAG mode, as it offers several advantages and increases the legacy value of the observations.
- **ACQ** (acquisition) and **ACQ/PEAKUP** operating modes for the CCD and MAMAs, which are used to acquire targets in the spectroscopic slits and behind coronagraphic bars and masks. Target acquisitions are described in [Chapter 8](#).

11.1.1 CCD ACCUM Mode

The STIS CCD has only a single operating mode, **ACCUM**, for science data. The CCD pixels accumulate charge during the exposure in response to photons. The charge is read out at the end of the exposure at a selectable gain (number of e^- /DN) and converted to 16 bit data numbers (DN) by the A-to-D converter. The DN are stored as 16-bit words (with a range 0 to 65,535) in the STIS data buffer memory array. At the default **CCDGAIN=1**, the gain amplifier saturation level (33,000 electrons), and not the 16-bit format, limits the total counts that can be sustained in a single exposure without saturating (see also [Section 7.2.10](#), [Section 7.3.2](#), and [STIS ISR 2016-01](#)). At the other supported gain, **CCDGAIN=4**, the CCD full well (which can be as low as 120,000 e^- or 30000 DN in some regions of the detector) determines the saturation limit.

A full detector readout is actually 1062×1044 pixels, with physical and virtual overscans. Scientific data are obtained on 1024×1024 pixels, each projecting to $\sim 0.05 \times 0.05$ arcsecond on the sky. The dispersion axis runs along **AXIS1** (image X or along a row of the CCD), and the spatial dimension of the slit runs along **AXIS2** (image Y or along a column of the CCD). [Figure 11.1](#) illustrates the full CCD format and its orientation with respect to the spacecraft (U2 and U3 or V2 and V3) axes. Arrows indicate the orientation of the parallel and serial clocking. The readout directions depend on the amplifier used. For the default amplifier D, the readout is at the upper right corner. It includes 19 columns of leading and 19 columns of trailing physical overscan in **AXIS1**, and 20 trailing rows of virtual overscan in **AXIS2**. The trailing serial overscan as well as the parallel overscan pixels are used to determine the bias level in post-observation data processing. The parallel overscan can also be used in the diagnosis of charge-transfer problems (see [STIS ISR 2022-07](#) for more information on charge-transfer efficiency).

Figure 11.1: CCD ACCUM Mode Format for a Long-Slit Spectrum.



The minimum CCD exposure time is 0.1 second and the maximum possible exposure time is 4.7 hours (though we cannot imagine wanting a single exposure longer than 60 minutes, and cosmic rays often become increasingly troublesome for exposures longer than about 1000 seconds). The minimum time between identical exposures for CCD full-frame (1062 × 1044) images is ~45 seconds.

¹ This time is dominated by the time it takes to read out the CCD (29 seconds for the full frame) and can be reduced to ~19 seconds if you use a subarray (see [CCD Subarrays](#)).

Binning

The CCD supports on-chip binning. When on-chip binning is used, the specified numbers of pixels in the serial and parallel directions are read out as a single pixel. The advantage of CCD binning is that the read noise per binned pixel is comparable to the read noise per unbinned pixel. If your signal-to-noise per pixel is dominated by read noise when no binning is used, you can thus increase the signal-to-noise by binning. The disadvantages of using on-chip binning are (a) it reduces the resolution of your spectrogram or image, (b) the relative number of pixels affected by cosmic rays increases, and (c) the relative number of 'hot' pixels (which was ~5% of all unbinned CCD pixels as of 2014; see [Chapter 7.3.5](#)), increases by a factor proportional to the binning factor. On-chip binning of 1, 2, or 4 pixels in both the `AXIS1` and `AXIS2` directions is supported. Note that on-chip binning is not allowed when subarrays are used.

The number of hot pixels has been increasing steadily with time due to accumulated radiation damage on the STIS CCD (see the discussion of hot pixels in [Chapter 7.3.5](#)). The impact of hot pixels on binned data has thus become significantly larger. Also note that when spectral data are spatially rectified, a single pixel in the original data will be interpolated into four pixels in the rectified image. For data binned $N \times M$ on board the spacecraft, a single bad pixel will, after rectification, affect the equivalent of $4 \times N \times M$ pixels in an unbinned image.

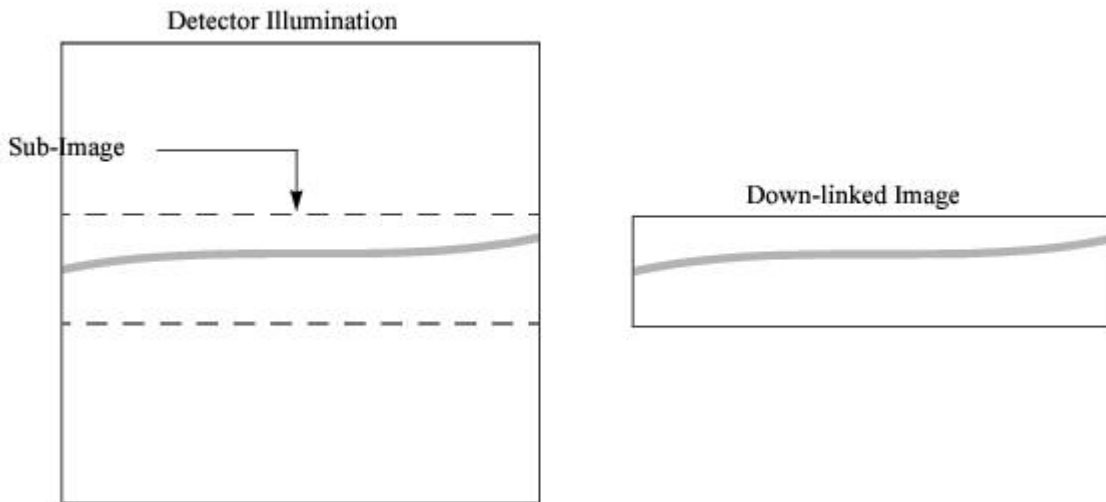
When using the [ETC](#) to estimate the effects of on-board binning on the S/N of CCD observations, be aware that increasing the binning in the dispersion direction may cause the [ETC](#) to use a larger resolution element for its S/N calculation. Be sure to understand how much of any increase in the S/N number output by the [ETC](#) is due to an actual decrease in the read noise and how much is simply due to a change in the size of the resolution element assumed for the calculation.

During Phase II, you specify the binning for your CCD observations using the `BINAXIS1` and `BINAXIS2` optional parameters. The default values are 1.

CCD Subarrays

Subarrays can be used when the CCD detector is read out. Generally, there is no need to use a subarray for STIS data. The main scientific use of CCD subarrays is for time-resolved optical spectroscopy, where subarrays can be used to reduce the CCD read time and to keep the data volume at a manageable level. CCD subarrays can also be specified for CCD `ACQ/PEAK` observations to limit the region in a diffuse object (e.g., a galaxy) over which the flux is summed for the pickup. When a subarray is used, only the portion of the detector which is within the specified subarray is read out and transmitted to the ground (see [Figure 11.2](#)—note that the spectrogram curvature is exaggerated in this figure).

Figure 11.2: Using Subarrays.



As described in [Section 11.1.1](#), full-frame CCD readouts are composed of 1062×1044 pixels: 1024×1024 data pixels, 19 leading and 19 trailing serial overscan pixels, and 20 trailing parallel overscan pixels. Dispersion runs along `AXIS1` and the long dimension of the slit runs along `AXIS2`. Subarrays are required to span the full width of the CCD detector in the serial (dispersion) direction in order to ensure they contain the serial overscan needed to determine the bias level; however, you can control the height of the subarray in the parallel direction (i.e., along the slit for long-slit spectroscopic observations). Note that no parallel overscan is returned for subarrays (see [Section 7.3.6](#)). Subarray size is specified in Phase II by the parameter `SIZEAXIS2`, the size in pixels of the subarray in the `AXIS2` direction.

The minimum allowed value of `SIZEAXIS2` for `ACCUM` mode observations is 30 pixels (corresponding to 1.5 arcseconds), and `SIZEAXIS2` must be an even number of pixels. By default the target is placed within a few pixels of the center of the subarray. For a few central wavelength settings, however, the target may be systematically offset by up to 30 pixels in the spatial direction. Observers should consult with the [Help Desk](#) prior to using `SIZEAXIS2` with a value of less than 64 pixels.

Use of Subarrays to Reduce the CCD Read Time

The minimum time between identical CCD exposures is the readtime + 16 seconds. The time to read out a CCD subarray is:

$$\text{readtime} = 2.0 + \text{SIZEAXIS2} \times 0.026 \text{ seconds}$$

Using the smallest available subarray, which is 30 pixels high, you can thus reduce the minimum time between identical exposures to ~19 seconds (16 seconds overhead plus 3 seconds read time). The minimum time between full-frame CCD exposures is $16 + 29 = 45$ seconds.

Use of Subarrays to Reduce Data Volume

The format of the data you receive when you use a CCD subarray will have dimensions $1062 \times \text{SIZEAXIS2}$, will cover the full range in the dispersion direction, and will include the serial overscan. The STIS buffer can hold seven full-frame CCD exposures at one time, or $7 \times (1024/\text{SIZEAXIS2})$ exposures at any one time. Full-frame CCD data acquired in one exposure can be transferred to the *HST* data recorder during the subsequent exposure(s) as long as the integration time of the subsequent exposure is longer than 3.0 minutes. If you are taking a series of exposures which are shorter than that, the buffer cannot be emptied during an exposure, and once the STIS buffer fills up, there will be a pause in the exposure sequence of roughly 3 minutes as the buffer is emptied (see [Chapter 9.2](#)). This problem can sometimes be avoided with the judicious use of subarrays.

11.1.2 MAMA ACCUM Mode

In MAMA `ACCUM` mode exposures, photons are accumulated into a 2048×2048 , 16-bit-per-element oversampled array in the STIS data buffer memory as they are received. At the end of the exposure, the data can be left in the over-sampled (or [highres](#)) format, which is the default for scientific exposures, or they can be binned along `AXIS1` and `AXIS2` to produce a 1024×1024 native-format image. Dispersion runs along `AXIS1` and the spatial dimension of the slit runs along `AXIS2`. [Figure 11.3](#) and [Figure 11.4](#) illustrate the format and coordinate system for MAMA images, showing how first-order and echelle `ACCUM` mode spectrograms appear. `PRISM` images have dispersion along `AXIS1`. Note that for `FUV-MAMA G140L` and `G140M` the target is placed of order 110-130 pixels below the detector center, to ensure that it will not fall on the shadow of the repeller wire (see [Section 7.6](#)). The slit center is thus projected ~ 3.25 arcseconds below the detector center along `AXIS2`, and there will be ~ 3.25 arcseconds less spatial sky coverage to decreasing `AXIS2` and ~ 3.25 arcseconds more spatial sky coverage to increasing `AXIS2` (along the slit) for observations with those gratings. Data taken prior to March 15, 1999 had the slit center offset above the detector center, for the same reason. Note also the effects of the monthly offsetting, which applies to all first-order MAMA modes, as well as to the echelle modes prior to August 2002 (see [Section 7.6](#)).

Figure 11.3: MAMA Mode Format for First-Order, Long-Slit -Spectroscopy.

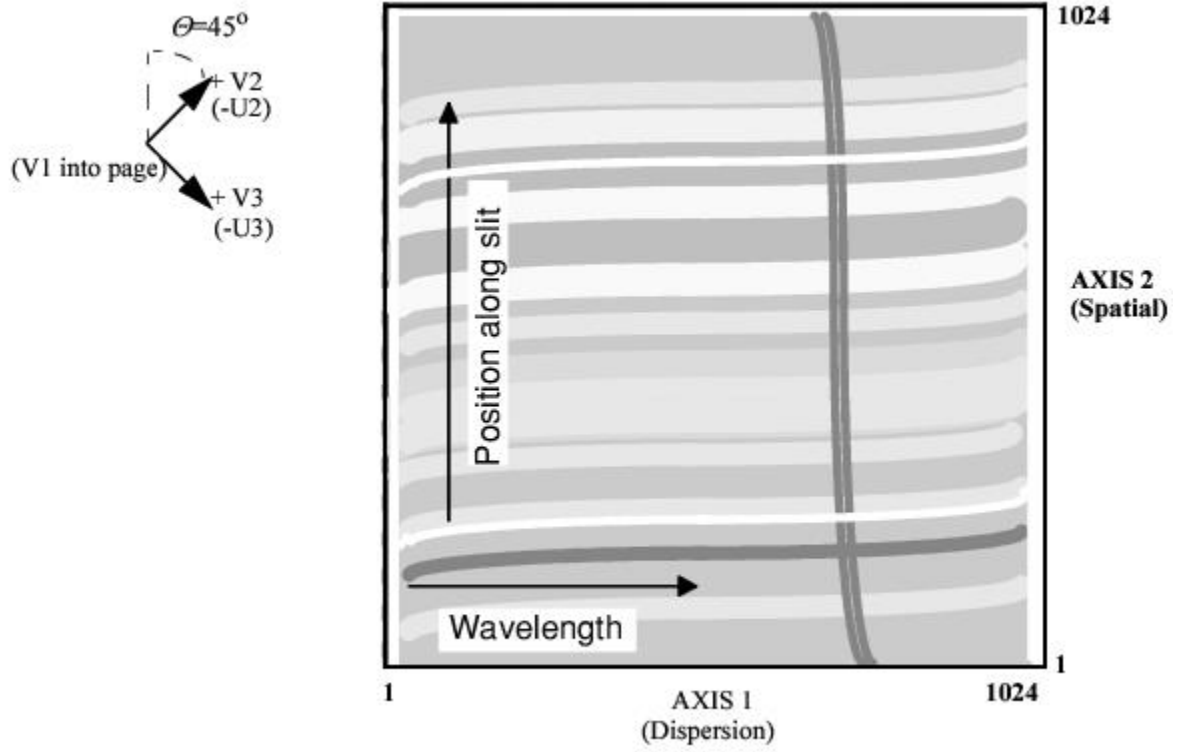
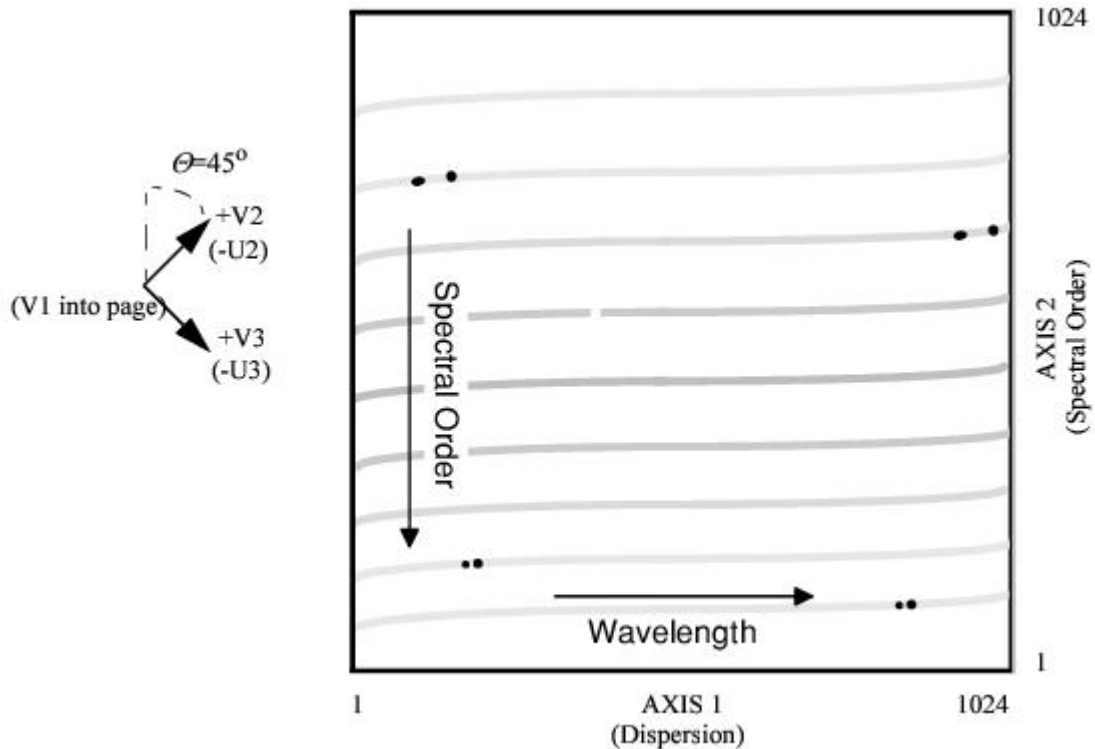


Figure 11.4: MAMA Mode Format for Echelle Spectroscopy.



The minimum MAMA `ACCUM` mode exposure time is 0.1 second and the maximum exposure time is 1.8 hours. For a series of identical MAMA `ACCUM` science exposures, there is a minimum overhead between exposures of ~ 30 seconds if the exposure time is longer than 2 minutes. Exposures shorter than 2 minutes incur larger overheads of ~ 2.5 minutes. This difference arises because in the former case the buffer can be dumped to the *HST* recorder during the subsequent exposure (i.e., in parallel), but in the latter case there is insufficient time to dump the buffer during the subsequent exposure and the buffer must be dumped serially (i.e, using observing time). However, other factors may influence the timing of buffer dumps, causing them to occur serially after the first science exposure even when it exceeds 2 minutes.

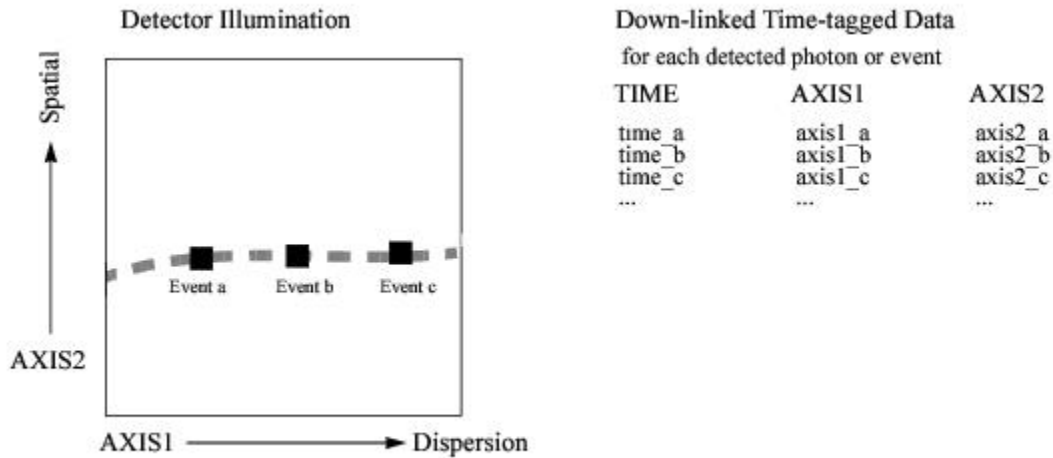
For the MAMA medium-resolution first-order modes and medium and high-resolution echelle modes (i. e., gratings G140M, G230M, E230M, E230H, E140M, and E140H), a correction for Doppler shifting of the photon energies due to *HST* spacecraft motion is applied as the photons are counted, prior to their addressing in STIS data buffer memory. The leading and trailing pixels in the dispersion direction (`AXIS1`) for Doppler-corrected exposures therefore receive less effective integration time, since source photons at the corresponding wavelengths have been Doppler-shifted off the edge of the detector for some fraction of the total exposure time. This effect is strongest in the high-resolution echelle modes, where for a maximum *HST* spacecraft velocity of 7.5 km/s, the leading and trailing ~ 20 `AXIS1` pixels will have reduced effective exposure times.

11.1.3 MAMA TIME-TAG Mode

TIME-TAG mode is used for high-time-resolution spectroscopy and imaging in the UV. When used in TIME-TAG mode, the MAMA produces an event stream of `AXIS1`, `AXIS2`, and `TIME` data points, with a time resolution of 125 microseconds. The volume of data produced in TIME-TAG mode can be very large, and the data therefore must be continuously transferred from the STIS internal buffer to the data recorders to sustain TIME-TAG exposures of any significant duration. Beginning in Cycle 22, however, the use of TIME-TAG mode (rather than ACCUM mode) has been encouraged for MAMA observations with count rates below 20,000 cts/s. TIME-TAG opens-up the time domain window and increases the legacy value of the observations. It also offers enhanced capability to remove time intervals of data which are impacted by geocoronal emission. Count rate restrictions do apply in TIME-TAG mode, however — see [Buffer Management in TIME-TAG Mode](#).

The axis orientation in TIME-TAG is the same as in ACCUM mode (see [Figure 11.3](#)). The spacecraft time (absolute zero point of the time) is routinely known to 10 millisecond accuracy. No Doppler correction is applied by the flight software for TIME-TAG mode, but the correction can be applied during the post-processing of the data. The recorded times are the spacecraft times, which can be converted to heliocentric times using the ephemeris of the Earth and the spacecraft. TIME-TAG mode is illustrated in [Figure 11.5](#). Processing of TIME-TAG data by the STScI pipeline is described in [Section 15.1](#).

Figure 11.5: TIME-TAG Mode.



Event Processing in TIME-TAG Mode

In **TIME-TAG** mode, events detected on the anode wires are queued in a 4096-event first-in first-out (FIFO) prior to time assignment and subsequent storage in a STIS memory buffer. When the FIFO is less than half full, 4 events can be processed during each 125 microsecond tick of the STIS clock, corresponding to a maximum stable count rate of 32,000 counts/s. Times are assigned shortly after detection, when the event is extracted from the FIFO. This is the desired operating state in **TIME-TAG** mode. Higher count rate situations (described below) should be avoided because they result in less accurate times, lost events, and buffer management problems.

For global count rates up to 50,000 counts/s, the FIFO will gradually fill until more than 2048 events are queued. At this point 2048 events are processed in a tight loop requiring only 41 milliseconds, instead of the usual 64 milliseconds. Processing then reverts to the slower rate until the FIFO is again more than half full. In this mode, the times associated with each event have 125 microsecond resolution, but suffer from significantly larger systematic delays. Also, the observing sequence will be frequently interrupted to handle STIS buffer dumps (described below).

For count rates above 50,000 counts/s, the FIFO will fill faster than events can be processed, even in fast mode. When the FIFO fills, all events in the FIFO are discarded and the empty FIFO begins filling with new events. In this mode event times are essentially uniform, providing essentially no information about source variability.

Buffer Management in TIME-TAG Mode

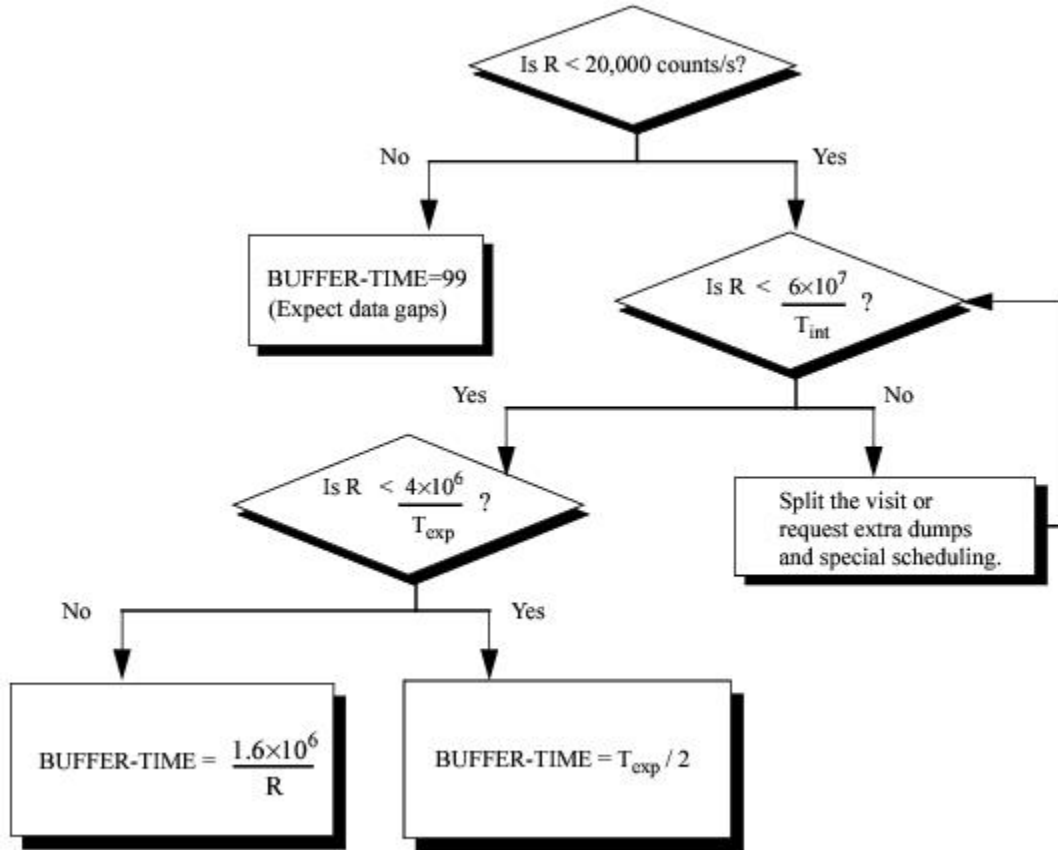
For **TIME-TAG** observations, STIS memory is divided into two 8 megabyte buffers, each of which can hold up to 2×10^6 events. If the cadence between scheduled buffer dumps is at least 99 seconds, then one buffer can be actively recording new events, while previously recorded events in the other buffer are being dumped to an *HST* data recorder. Thus, events can be dumped to STIS memory without gaps only if the global count rate is below 20,000 counts/s.

During Phase II proposal preparation, observers must specify in advance the time between dumps using the `BUFFER-TIME` parameter. The following constraints should be considered when selecting a `BUFFER-TIME`:

- To prevent loss of data, `BUFFER-TIME` should be short enough that fewer than 2×10^6 events are expected in the interval between dumps. If R is the expected count rate (predicted by the [STIS ETC](#), for example), then `BUFFER-TIME` should be smaller than $2 \times 10^6/R$. A bit of margin protects against source variability or inaccurate count rate predictions. Be sure to include sky and detector backgrounds when estimating count rates.
- On the other hand, the nominal STIS allocation on the *HST* data recorders allows at most 30 total buffer dumps in any one visit, and fewer is desirable. For the minimum continuously sustainable `BUFFER-TIME` of 99 seconds, this limit on dumps corresponds to a total exposure time of only 50 minutes. It is sometimes possible to schedule downlinks from the *HST* data recorders to the ground during a specific `TIME-TAG` visit. Thus, with a strong scientific justification, it may be possible to accommodate visits that require more than 30 dumps. Such requests should be justified quantitatively in the Phase I proposal.
- Finally, `BUFFER-TIME` should be at least 99 seconds when more than 2 dumps are expected. Otherwise, the observing sequence will be interrupted whenever both buffers are in the process of being dumped. In such cases it is probably better to choose a `BUFFER-TIME` of 99 seconds. This guarantees that photons will be recorded whenever the active buffer has remaining space. If the active buffer fills in less than the selected `BUFFER-TIME`, additional photons will be discarded until the next dump begins. Reliable flux calibration is not possible in such cases.

In summary, `BUFFER-TIME` should be less than $2 \times 10^6/R$, but longer than 1/30 the total exposure time and longer than 99 seconds. As an added precaution against data loss, it is recommended to use a `BUFFER-TIME` of $1.6 \times 10^6/R$, which adds a 20% safety margin. In some cases it will not be possible to satisfy all of these criteria, in which case multiple short `ACCUM` exposures should be considered as an alternative. [Figure 11.6](#) illustrates the process of estimating `BUFFER-TIME`

Figure 11.6: Estimation of **BUFFER-TIME**.



T_{int} refers to the total integration time (in seconds) of all the exposures in the visit, and T_{exp} refers to the integration time (in seconds) of the particular exposure under consideration.

i Remember to include contributions from all the sources expected to fall on the detector, the sky, geocoronal line emissions and detector backgrounds along with your source counts when computing R . It is important that you include a safety margin of at least 20% in your estimation of **BUFFER-TIME**. Specifying too small a **BUFFER-TIME** (< 99 seconds) can lead to loss of data after the first dump of 2 million events.

Differences in COS and STIS **TIME-TAG** Handling

Users familiar with the **TIME-TAG** mode of the STIS instrument should be aware that COS buffer management differs in some details from that of STIS. At the end of a STIS exposure, the entire buffer is read out, regardless of the buffer time set or the number of counts expected. Setting the STIS buffer time to any value greater than or equal to half the total exposure time will result in having only this single dump at the end of the exposure. Setting the buffer time to less than half the exposure time will cause one or more intermediate dumps to also occur during the exposure, but the time required for the dump after the exposure will not change.

COS, on the other hand, reads out only the fraction of the buffer that is expected to contain recorded events. This fraction is based on the specified buffer time (t_{buf}) and exposure time (t_{exp}). If $t_{\text{buf}} > t_{\text{exp}}$, only a fraction $t_{\text{exp}}/t_{\text{buf}}$ of the buffer will be read out. Similarly, at the end of a multi-dump exposure with $t_{\text{buf}} < t_{\text{exp}}$, sufficient time will be allocated for COS to read only the fraction of the buffer expected to contain data. This approach increases observing efficiency by avoiding the allocation of more time than necessary for the buffer dump at the end of the exposure. It also requires more caution in the setting of buffer times: If the actual count rate is greater than expected, some events that were recorded in the buffer memory will never be read out. The guidelines in this section are designed to help COS users to maximize observing efficiency and avoid data loss. Users requiring additional assistance should contact the [HST Help Desk](#).

¹ This constraint implies that there will be 45 seconds of overhead per full-frame CR-SPLIT, i.e., if CR-SPLIT=3, there will be 3×45 seconds of overhead on the set of 3 exposures due to CCD setup and readout.

11.2 Exposure Sequences and Contemporaneous Calibrations

- [11.2.1 Auto-Wavecal](#)
- [11.2.2 CR-SPLIT](#)
- [11.2.3 Fringe Flat Fields](#)
- [11.2.4 Repeat Exposures](#)

There are several instances when a series of associated STIS exposures (rather than a single exposure) will be taken. The data from these exposure sequences are generally processed as a single unit through the STIS calibration pipeline, with the scientific data from the multiple *associated* exposures appearing in a single file (for a high-level overview of the STIS calibration pipeline and the data product format see [Chapter 15](#)). While you do not have to specify that you plan a series of associated exposures in your Phase I proposal, it is helpful to know about these sequences when planning your proposal. In Phase II, once your proposal has been accepted and you are working on scheduling your observations, you will be able to see and use these sequences. All are generated from a single exposure logsheet line in your Phase II proposal.

We discuss several types of associated exposures below:

- Automatic wavecal exposures taken with scientific data to allow calibration of the spectroscopic and spatial zero points.
- CCD `CR-SPLIT` exposures taken to allow removal of cosmic rays in the scientific data during post-observation data processing.
- Multiple identical repeat exposures, which can be taken to provide time resolutions of tens of seconds (CCD) or minutes (MAMA).
- Pattern sequences, in which the target is stepped, for example along the slit to mitigate the impact of hot pixels or perpendicular to the slit to map a two-dimensional region for spectroscopic observations, or in a dither pattern for imaging observations.

In addition, there are two types of contemporaneous calibration observations that observers may take with their scientific observations in special circumstances:

- GO wavecal, taken if exceptional wavelength accuracy is required, or for slitless spectroscopy.
- CCD fringe flats (`CCDFLAT`) which need to be taken for near-infrared (NIR; $\lambda > 7500 \text{ \AA}$) observations in the grating modes if high -signal-to-noise is required.

11.2.1 Auto-Wavecal

The STIS optical path from source to detector passes through the aperture (slit) wheel (where the filters for imaging also are housed) and then reflects from one of the elements mounted on the Mode Selection Mechanism (MSM) which houses the first-order gratings, the prism, the cross-dispersers for use with the echelles, and the mirrors for imaging work (see [Figure 3.1](#)). Lack of exact repeatability in the MSM causes the center of the spectrogram (as defined by the aperture and wavelength centers) to fall on a slightly different detector location each time there is a movement of the MSM (the MSM-induced offsets in dispersion and the spatial direction have been measured to be ± 3 pixels or less). In addition, for MAMA first order spectrographic observations, the aperture location on the detector is deliberately shifted each month to ensure equalization of extracted charge across the detector.

To allow calibration of the zero point of the aperture location and the zero point of the wavelength scale for spectroscopic observations, a line lamp observation (so-called *wavecal*) is taken *automatically* each time the MSM is moved. In addition, if a series of exposures or a single long exposure is taken at a single MSM setting, then an additional wavecal will automatically be taken when there is a pause in data taking *if* 40 minutes of exposure time has passed since the previous wavecal. Here, 40 minutes is the time constant for thermal changes which might affect the wavelength accuracy. Testing in orbit has shown that in extreme conditions (when there is a swing from hot to cold), worst-case thermal shifts of roughly 0.3 pix/hr can be seen; however, monitoring shows that under typical observing conditions, thermal drifts are of the order of 0.1 pix/hr (see also the [Monitoring page](#) on the [STIS website](#)).

To summarize, each set of spectroscopic scientific exposures taken at a given grating tilt (i.e., MSM position) will normally be accompanied by at least one automatically taken wavecal exposure. This auto-wavecal will be taken prior to the science exposure. Additional auto-wavecals will be taken at the first pause in data taking after ~2300 seconds of exposure time at that grating position have elapsed. For MAMA observations in particular, auto-wavecals can be forced into occultation by (1) keeping exposures in an orbit at the same grating setting, and implementing either (2a) a single long exposure that fills the visibility period or (2b) shorter exposures whose sum is less than ~2300 seconds since the last auto-wavecal, followed by an exposure that crosses the 2300 second boundary and fills the remainder of the visibility period. Similarly, if spectroscopic drifts are a concern, MAMA observations can be split into exposure sums that are ~2300 seconds in duration to maximize the occurrence of auto-wavecals. Multiple auto-wavecals occur more naturally for CCD observations which are usually CR-split into exposures of ~1000 seconds, or less, in duration.

These wavecal exposures will be processed along with the scientific data, and they will be used by the pipeline to automatically correct the zero-point offsets in the wavelength and spatial scales (see [Chapter 15](#)).

The automatic wavecals are designed to be of sufficient duration to produce spectrograms which contain at least 3 emission lines with 3 counts/pix and 50 counts summed over the line. In those regions of the spectrum where 3 lines are not obtainable, there will be at least 1 emission line with 18 counts/pix and 300 counts summed over the line. For the CCD, where integration times are short, the auto-wavecals will typically be taken to ensure roughly 8 times this signal. While the fading of the calibration lamps has reduced the count rates over time (particularly at the shortest wavelengths), the default auto-wavecals still appear to provide adequate zero points for nearly all combinations of grating, central wavelength, and aperture. Questions regarding particular configurations may be addressed to the STIS team via the [HST Help Desk](#).

The combination of thermal changes between the wavecal and scientific exposures, coupled with the ability to measure the zero points in the wavecal exposures, limits the accuracy of the absolute zero points to ≤ 0.2 pixels (see [Section 16.1](#)). Observers who desire more accurate wavelengths than will automatically be provided or who are particularly concerned about the time variation of the zero point may also take their own wavecal exposures, using the `WAVE` target option (see [GO Wavecals](#)), in addition to (or instead of) the default auto-wavecals. The auto-wavecals can be omitted by using the exposure level optional parameter `WAVECAL=NO`. Note, however, that using this option on *any* exposure in a visit will turn off the auto-wavecals for *all* exposures in that visit. The observer will then have to include sufficient GO wavecals to allow adequate wavelength calibration of their data. Beginning in Cycle 25, the `WAVECAL=NO` optional parameter was included as a supported availability mode, so that observers no longer need approval to disable auto-wavecals to reduce overhead during orbital visibility. Observers will be required, however, to include GO wavecals at each MSM position when using this option, and will need approval to use longer exposure times than the default values for their GO wavecals.

GO Wavecals

Only if you require particularly accurate wavelengths do you need to consider using the `TARGET=WAVE` option to insert additional wavecal exposures into your observing sequence.

The wavecals taken with `TARGET=WAVE` are identical to those taken automatically (i.e., the auto-wavecals) with two important exceptions. First, you can explicitly specify which aperture (slit) you wish to use for the `TARGET=WAVE` exposure (whereas for automatic wavecals the program slit or a pre-defined alternative for each grating is used). Second, you can take longer exposures, increasing the signal-to-noise of the lamp exposures or possibly saturating some lines to bring out weaker lines near astronomical lines of interest. While GO wavecals with the default exposure time are now supported, increasing the exposure time is an available-but-unsupported option (thus requiring justification and approval).

`TARGET=WAVE` exposures *cannot be taken with all slit-grating combinations*. In particular, the line lamps can be too bright for the MAMA detectors when used with wide slits. Therefore only certain aperture-grating combinations can be used for `TARGET=WAVE` observations. The complete list of allowed combinations is provided on the [GO Wavecal Aperture Selection](#) web page. When entering a GO Wavecal in `APT`, only the permitted slits will be displayed in the `APERTURE` menu.

Although the slit wheel repeatability is very high (see [Section Slit and Grating Wheels](#)), observers wishing particularly accurate wavelength calibrations may wish to use a slit for their scientific exposures for which there is an allowed slit-grating wavecal; otherwise, the slit wheel will be moved each time they take a wavecal exposure, producing a small additional uncertainty.

11.2.2 CR-SPLIT

In order to allow rejection of cosmic rays in post-observation data processing, observers using the STIS CCD should always try (as much as possible given signal-to-noise ratio constraints when in the read-noise-limited regime) to obtain at least two—preferably three or more—identical CCD exposures (see [Section 7.3.4](#)). In Phase II, the `CR-SPLIT` optional parameter (default value 2) allows easy scheduling of such multiple associated exposures. You specify the total exposure time and set `CR-SPLIT=n`, where n is the number of exposures to break the total observing time into. For example, if the total exposure time is 12 minutes and `CR-SPLIT=3`, then three 4-minute exposures will be taken. Those three exposures will be associated with one another, passed through the STScI calibration pipeline as a unit, and a cosmic-ray-free image will be produced during pipeline processing (see the "STIS Calibration" Chapter of the [STIS Data Handbook](#)). Allowed values of `CR-SPLIT` are integers from 1 to 8. Note that overheads are incurred for each `CR-SPLIT` subexposure.

11.2.3 Fringe Flat Fields

The STIS CCD exhibits fringing in the far red, limiting the signal-to-noise achievable at wavelengths longward of ~ 7500 Å in the `G750L` and `G750M` spectral modes. As discussed in [Section 7.2.6](#), the best way of eliminating the fringes in the far red is by obtaining contemporaneous flat fields along with the scientific observations. These "fringe flats" must be taken at the same position of the Mode Selection Mechanism as the scientific data. STIS users can insert such contemporaneous fringe flat fields into the same visits as their scientific data, as described below.

Designing Your Fringe Flat-Field Observations

Observers of extended sources will typically want to take their fringe flat fields using the same slits as they use for their scientific targets, since the flat-field lamp will then illuminate the detector in the most similar way to the targets. However, observers of point sources will typically fare better if they use small slits (e.g., those which are otherwise used for echelle observations) for their fringe flat fields. The main reason for this difference is that the PSF of the STIS CCD features a substantial halo in the far red containing up to 20% of the total source flux, which causes the fringes in lamp flat fields to behave differently from those of external sources, especially in the case of point sources (see also [Section 7.2.8](#)). Fringe flat fields taken with short slits simulate the spatial structure of point sources significantly better than those taken with long slits.

The slits supported for scientific observations with the G750L and G750M gratings and the associated slits to use for fringe flat fields in the cases of both extended- and point-source observations in the far red are listed in [Table 11.1](#).

Table 11.1: Slits for Extended-Source and Point Source Fringe Flat Fields.

| Supported Scientific Slit | Fringe Flat Slit for Extended-Source Observations | Fringe Flat Slit ¹ for Point-Source Observations |
|---------------------------|---|---|
| 52X2 | 52X2 | 0.3X0.09 |
| 52X2E1 | 52X2 | 52X0.1 |
| 52X2E2 | N/A | 52X0.1 |
| 52X0.5 | 52X0.5 | 0.3X0.09 |
| 52X0.5E1 | 52X0.5 | 52X0.1 |
| 52X0.5E2 | N/A | 52X0.1 |
| 52X0.2 | 52X0.2 | 0.3X0.09 |
| 52X0.2E1 | 52X0.2 | 52X0.1 |
| 52X0.2E2 | N/A | 52X0.1 |
| 52X0.2F1 | 52X0.2F1 | 52X0.2F1 <i>and</i> 0.3X0.09 (optional) |
| 52X0.1 | 52X0.1 | 0.2X0.06 |
| 52X0.1E1 | 52X0.1 | 52X0.1 |
| 52X0.05 | 52X0.05 | 0.2X0.06 |
| 52X0.05E1 | 52X0.05 | 52X0.05 |

¹ Short slits are chosen so as to be concentric with the matched long slit. E2 positions are chosen to be concentric with the 52X0.1 aperture at row 900.

A few notes are of importance on the use of short slits for obtaining fringe flat fields:

- Fringe removal for sources that are offset from the center of the long slit will not be possible with a short-slit fringe flat field; one has to use long-slit fringe flat fields for those cases. A special case in this respect is that of point-source spectra with the 52X0.2F1 slit, as the 0.3X0.09 slit (which is in principle the appropriate one to use for fringe flats in that case, cf. Table 11.1) is only a few CCD pixels larger than the occulting bar of the 52X0.2F1 slit. However, a short-slit fringe flat does give a somewhat better fringe correction for the area covered by both the short slit and the 52X0.2F1 slit, so if that area is of particular scientific interest, we recommend taking a short-slit fringe flat as well.
- The limited length of the short slits used for obtaining contemporaneous flat fields of point sources (0.2-0.3 arcseconds) does not allow one to sample the full PSF, so that absolute spectrophotometry cannot be performed with the short-slit fringe flat fields alone. However, a comparison with the pipeline-reduced point-source spectrograms will enable a proper flux calibration.
- At wavelengths longward of ~ 7500 , fringing is the dominant calibration concern at high S/N, whereas imperfect charge transfer efficiency (CTE) is the dominant concern at low S/N ratios. We therefore recommend using the E1 or E2 pseudo-apertures for faint sources and the normal aperture positions in the long slits for high S/N observations.
- The E2 aperture positions are, like the E1 aperture positions, located near row 900 of the detector, and are intended to be used to mitigate CTE effects. However, in order to better align with the 52X0.1 aperture, which is used for fringe flats near row 900, the targeted position is offset about 1 pixel in the dispersion direction from the physical center of each aperture. Fringe-flat alignment will be slightly better than when using the E1 positions, although for the 52X0.2E2 aperture, the throughput will be slightly reduced. The E2 positions should only be used for point source observations where fringe flats are needed and CTE is a concern. If a peakup is desired before using the E2 aperture positions, it should be done using the 52X0.1E1 aperture.
- The limited length of the short slits used for obtaining contemporaneous flat fields of point sources (0.2-0.3 arcseconds) imposes a minimum requirement on the accuracy of the acquisition of target point sources in the slit. The final accuracy should be of the order of 1 pixel (i.e., ~ 0.05 arcseconds). In case the observer has to use offset acquisition targets, it is therefore recommended that an ACQ/PEAK exposure in a short slit be performed to ensure centering in both directions (see [Section 8.3](#)).

Inserting Fringe Flat-Field Exposures in Phase II

A fringe flat-field exposure is specified in your Phase II proposal input as follows:

- Specify `Target_Name = CCDFLAT` to indicate the exposure as a fringe flat field. The flat-field exposure will automatically be taken at `-CCDGAIN=4`.
- Specify `Number_Of_Iterations = 2` (to allow cosmic-ray rejection and to obtain adequate signal-to-noise).
- Specify `Config`, `Opmode`, `Aperture`, `Sp_Element`, and `Wavelength`.
 - `Config` must be `STIS/CCD`.
 - `Opmode` must be `ACCUM`.
 - `Aperture` must be one of `52X2`, `52X0.5`, `52X0.2`, `52X0.2F1`, `52X0.1`, `52X0.05`, `0.3X0.09`, or `0.2X0.06`.
 - `Sp_Element` and `Wavelength` must be one of the following combinations:
`Sp_Element: G750L` and `Wavelength: 7751`

Sp_Element: G750M and Wavelength: one of 6768, 7283, 7795, 8311, 8561, 8825, 9286, 9336, 9806, or 9851.

- Specify `Time_Per_Exposure` as `DEF` (Default). The default exposure time is determined from in-flight calibration data and ensures a signal-to-noise of 100 to 1 per pixel for all settings mentioned above and `Number_Of_Iterations` = 2. For very high-S/N observations (e.g., using spatial scans), it may be useful to obtain fringe flats with longer exposure times; see [Section 12.12.3](#) for more details.
- If the scientific data are taken in binned mode, specify Optional Parameters `BINAXIS1` and `BINAXIS2` in the same way as for scientific observations. Supported binning factors are 1, 2, and 4.

Two very important issues for fringe flat fields:

- Fringe flat-field exposures are moved into the occulted period whenever they occur as the first or last exposure in an orbit. Thus you can fill the unocculted portion of your orbit with scientific observations and take the fringe flat during the occultation by placing it at the beginning or end of the orbit.
- Fringe flat fields are effective only if taken without a move of the Mode Selection Mechanism between the scientific exposure and the fringe flat field. Observers *must* ensure that if the spectral element or wavelength setting is changed during an orbit in which they wish to obtain a fringe flat. They then place the fringe flat-field exposure immediately before or after the scientific exposure(s) they wish to de-fringe. In some cases (e.g., for a long series of exposures), the observer may choose to bracket the scientific exposures with fringe flat-field exposures to be able to account for any thermal drifts.

Please refer to the [July 2021 STAN article](#) on defringing and choosing appropriate fringe flats; [STIS ISR 1997-15](#) for more details about NIR fringe flats; [STIS ISR 1997-16](#) for fringing in spectrograms of extended sources; and [STIS ISR 1998-19](#) (Revision A) for fringing in spectrograms of point sources as well as more general fringing analysis and details related to the 52X0.2F1 aperture. The [stistools defringe documentation](#) contains a full overview and user guide for the current defringing tool suite, recently ported from the original **IRAF** defringe tools into python.

11.2.4 Repeat Exposures

A series of multiple repeated identical exposures can be taken most easily using the `Number_Of_Iterations` optional parameter in Phase II. In this way, time-resolved observations at minimum time intervals of roughly 20 seconds for the CCD (if subarrays are used) and 30 seconds for the MAMA can be taken in `ACCUM` operating mode. The output of this mode is a series of identical exposures. If your exposure time is 60 seconds, and you set `Number_Of_Iterations`=20, you will obtain twenty 60-second exposures. These twenty exposures will be associated with one another and processed through the pipeline as a unit—the individual exposures will be fully calibrated and a summed image will also be produced for MAMA data as well as a cosmic-ray rejected image for CCD data (see also [Chapter 15](#)).

11.3 Patterns and Dithering

- [11.3.1 STIS Imaging Patterns](#)
- [11.3.2 STIS Spectroscopic Patterns](#)
- [11.3.3 Generic Patterns](#)
- [11.3.4 Combining Patterns](#)
- [11.3.5 Dither Strategies](#)

A *pattern* refers to a series of exposures of a single target taken at slightly different telescope pointings, with the same set of guide stars. For STIS, patterns are commonly used to:

- Dither to decrease the effects of small-scale detector nonuniformity, eliminate hot pixels, and /or increase the spatial resolution (the latter requires sub-pixel stepping) by offsetting the target along a long slit in the spatial direction for spectroscopic observations or by performing a small stepping pattern for imaging or slitless spectroscopic observations (see [Section 11.3.5](#)).
- Spectroscopically map out a two-dimensional region of the sky by stepping the slit across the object of interest.
- Spectroscopically subsample the line spread function by stepping a fraction of a pixel along the dispersion direction—see [Section 12.6](#).

In Cycles 9 through 11, patterns were defined and then added to exposures as special requirements. In the **APT** Orbit Planner, this approach was replaced by the use of pattern containers. The observer selects a pattern (or constructs a composite pattern) from a list of generic and instrument-specific patterns and then defines one or more pattern containers which use this selected pattern. The exposures to be dithered are then put into these containers.

The pre-defined STIS patterns have a number of adjustable parameters. All patterns allow the `Point_Spacing`, which is given in units of arcseconds, as well as the `Pattern_Orient`, given in units of degrees, to be adjusted by the observer. Specifying `Center_Pattern = YES`, will cause the pattern as a whole to be centered at the specified coordinates; otherwise, the given coordinates will apply to the first point in the pattern.

A full description of all patterns, including illustrations and a list of all adjustable parameters and default values for each pattern type, are given in the [HST Phase II Proposal Instructions](#). Additional examples and advice are given in the [Dither Handbook](#), the online [drizzlepac](#) documentation, [The DrizzlePac Handbook](#) (Hoffmann et al. 2021), and the other references listed at the end of this section.

11.3.1 STIS Imaging Patterns

`STIS-SPIRAL-DITH` can be used to make a mosaic of images. It performs a spiral dither pattern, starting at the center and moving outward counterclockwise. For this pattern, both the `Number_of_Points` and the `Point_Spacing` (in arcseconds) must be specified by the observer.

`STIS-CCD-BOX` and `STIS-MAMA-BOX` are parallelograms based on the `BOX` patterns used with WFPC2 and STIS in Cycle 8 to dither images. The default parameters for these two patterns give offsets in integer numbers of pixels along the X-axis and Y-axis, which can be used, for example, to dither hot pixels. By dividing the default point spacing by 2, one can achieve half-pixel shifts in each coordinate to improve spatial sampling.

11.3.2 STIS Spectroscopic Patterns

`STIS-ALONG-SLIT`, which steps the target along the slit, can be used to dither hot pixels (integer pixel steps) or to improve spatial sampling (fractional pixel steps) in spectroscopic images (see [Figure 11.7](#)).

`STIS-PERP-TO-SLIT` can be used to step the slit across an extended source to map the spectral characteristics of the source (see [Figure 11.8](#)). It can also be used to subsample the line spread function by moving a target by fractions of a pixel.

For both of these patterns, the `Point_Spacing` (in arcseconds) and the `Number_of_Points` must be specified by the observer.

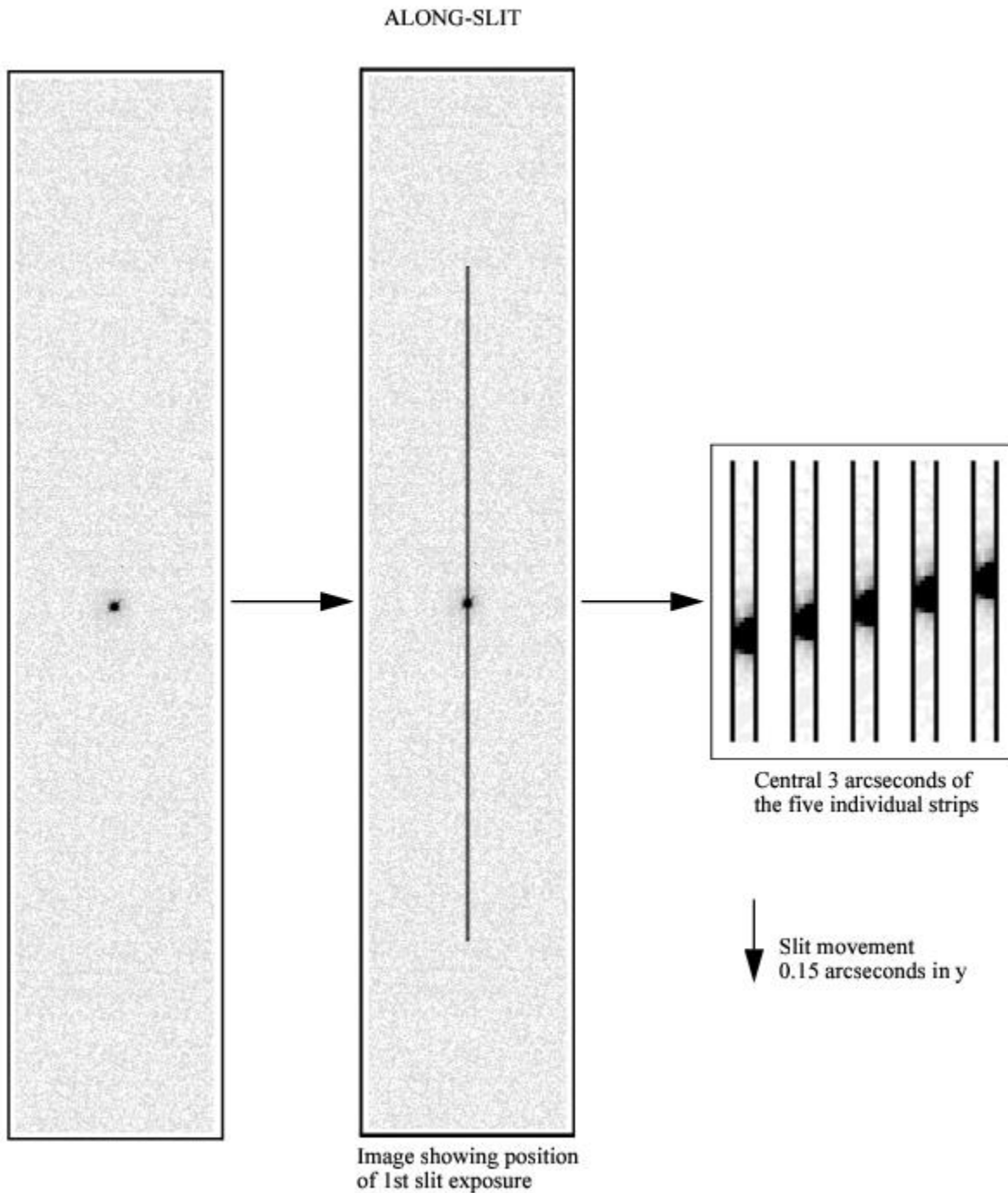
11.3.3 Generic Patterns

Generic patterns, available for all instruments, have been added for flexibility in pattern design. The generic `LINE` pattern allows for movement along a line at an arbitrary angle. The generic `SPIRAL` pattern is essentially the same as the `STIS-SPIRAL-DITH`.

11.3.4 Combining Patterns

In Cycle 9, the ability to combine two patterns was introduced. After selecting a pattern and defining its parameters, one can choose to add a secondary pattern, which is then executed at each point in the primary pattern. The secondary pattern can either be centered on the primary points or it can use the primary points as its initial points. For example, instead of just stepping a slit across an extended target at five points with `STIS-PERP-TO-SLIT`, you can add `STIS-ALONG-SLIT` with two points to make a 5×2 grid of observations. If `Center_Pattern=yes` for both patterns, the grid will be centered on the target position. To check that you have specified a pattern correctly, you can display it using the **APT**.

Figure 11.7: Stepping a Target Along a Long Slit to Dither Hot Pixels or Improve Spatial Sampling.



This example shows the pattern `STIS-ALONG-SLIT`, with `NUMBER_OF_POINTS = 5` and `POINT_SPACING = 0.15` (arcseconds).

Figure 11.8: Stepping Target Perpendicular to Slit to Map 2-D Region of Sky.

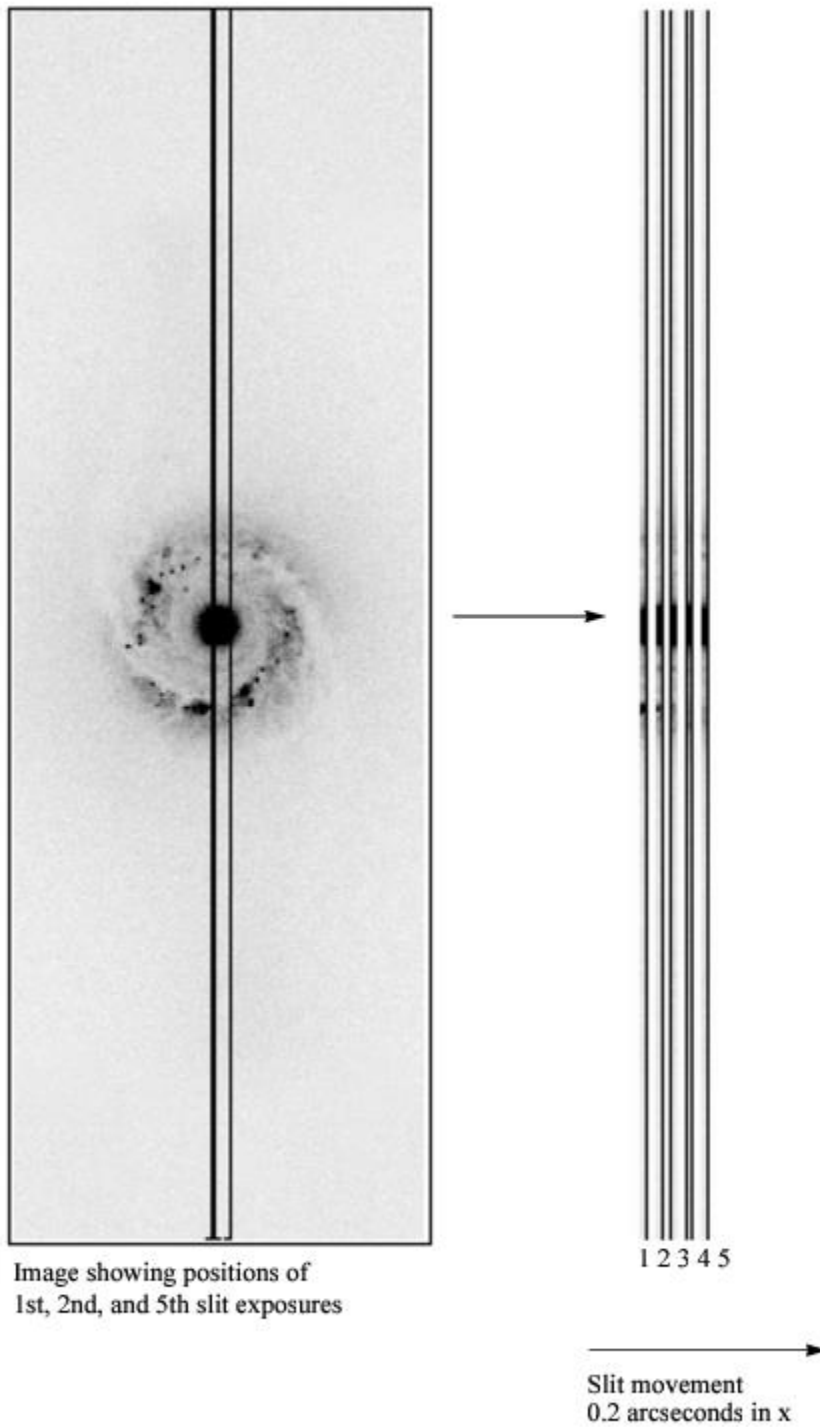


Image showing positions of 1st, 2nd, and 5th slit exposures

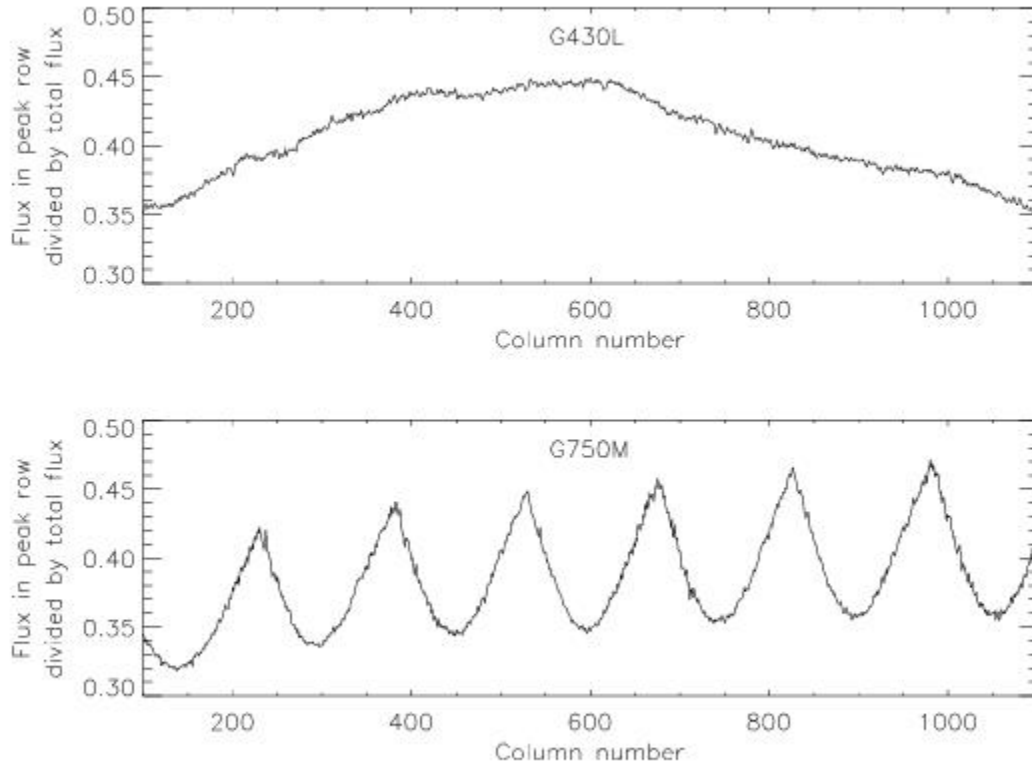
This example shows the pattern `STIS-PERP-TO-SLIT`, with `NUMBER_OF_POINTS = 5` and `POINT_SPACING = 0.2` (arcseconds).

11.3.5 Dither Strategies

There is no single observing strategy that is entirely satisfactory in all circumstances for STIS. One must consider cosmic rays, hot pixels (pixels with high, time-variable dark current), and spatial undersampling of the image. One strategy that can be used to minimize the effects of undersampling and to reduce the effects of hot pixels is to *dither*, that is, to offset the telescope between exposures by either integer or sub-pixel steps. The best choice for the number and size of the dithers depends on the amount of time available and the goals of the project. In the following we will address a few issues related to dithering:

- **Undersampling of images:** Individual images taken with sub-pixel offsets can be combined to form an image with higher spatial resolution than that of the original images. A single dither from the original pixel position, call it (0,0), to one offset by half a pixel in both x and y (0.5,0.5) will produce a gain in spatial information. On the other hand, very little extra information is gained from obtaining more than four positions. Therefore the recommended number of sub-pixel dither positions is between 2 and 4.
- **Undersampling of spectral images:** The spatial undersampling of compact sources in spectral images becomes apparent after the images are rectified. Interpolation during the rectification process spreads flux from the local peak row of the spectrum into adjacent rows. The result is undulation of the flux level in the individual spectral rows of the rectified image. If the spectrum is nearly horizontal on the detector (which is the case for gratings G140L, G230LB, G230MB, G430L, and G750L), the resulting undulation pattern is broad and irregular. On the other hand, if the spectrum has an appreciable tilt across the detector (as for gratings G140M, G230M, G230L, G430M, and G750M; see e.g., [STIS ISR 1998-19](#)), the undulation is quasi-periodic. Two representative cases are shown in [Figure 11.9](#), which displays the flux in the peak row in the rectified image normalized by the total flux for stellar observations taken with G430L (top) and G750M (bottom). Note that this effect is inconsequential in most cases: if the source is unresolved, several rows of the spectrum will be extracted to make a single spectrum, eliminating the effect; if the source is sufficiently extended to be well sampled, the undulations will not occur. A problematic situation is encountered when row-by-row spectral analyses are needed of an extended component which is affected by the undulations produced by a compact component (e.g., near the center of a galaxy containing an active nucleus). For example, kinematic measurements of spatially extended emission or absorption lines can be affected in cases where a compact continuum component produces a baseline that fluctuates rapidly across the spectral lines of interest. The amplitude of the fluctuations can be reduced by using the Python tool `wx2d` instead of `x2d`. (See [STIS ISR 2007-04](#), but note that this references the **PYRAF** version of the tool.) To obtain substantially greater improvement, one must combine data dithered by a non-integer number of pixels along the slit, (e.g., $N+0.5$ pixels), but be aware that spectroscopic data are not supported by [AstroDrizzle](#).

Figure 11.9: Undulations in the Flux Level of Individual Rows in Rectified Spectra of Point Sources, Caused by Rectification of Spatially Undersampled Spectral Images.



- **Hot Pixels in CCD Data:** There are three ways to deal with hot pixels: (1) Correct them using superdarks constructed from darks taken on the day of the observation. These can be created using [stistools weekdark](#) (similar to the previously recommended task `daydark` in **STSDAS**). (2) Dither by an integer number of pixels. Dithered images can be combined with **AstroDrizzle**; dithered spectral images can be aligned with the Python tool `sshift` before being combined with `occreject`. If three or more exposures are obtained, cold pixels that produce low fluxes can be rejected (e.g., with `mscombine`, which allows rejection of low fluxes as well as high fluxes). Alternatively, anomalously low fluxes can be set to very high values (e.g., as previously done with `imrepl`); they can then be rejected by `occreject` like hot pixels or cosmic rays. (3) Use a task such as **STSDAS warmpix** (no longer supported) to filter out the known hot pixels. Hot pixels are flagged in the data quality array during dark subtraction and propagate through to the output images.
- **Hot Pixels in MAMA data:** The MAMA detectors show few hot pixels and they appear to evolve slowly, thus they are usually not an issue. Nevertheless, dithering is an easy way to avoid them, and there is no read noise or cosmic-ray removal penalty for doing so.
- **Cosmic Rays:** Cosmic rays in the raw CCD images are most easily removed by running `occreject` on `CR-SPLIT` exposures. At least two exposures are needed, but more are recommended, especially for longer exposures where the possibility of cosmic ray coincidence in two exposures is greater. For spectroscopic observations, integer pixel dithers along the slit are recommended to aid in the rejection of hot and cold pixels along with cosmic rays, as discussed above. For imaging observations, dithered exposures are recommended for the same reasons,

but will have to be combined with a task like **AstroDrizzle**, a more resource-intensive and time-consuming process.

- **Dithering Spectroscopic Observations:** In the case of spectroscopic observations, extra care should be taken in choosing the optimum dither strategy, which depends on the spatial extent of the extractions and the nature of the science target. However, beware that dithering spectroscopic observations will only be useful if your exposure times are long enough, especially for CCD spectra that can become severely read noise limited (see [Section 7.3.4](#)).
 - **Spectra of Point Sources:** 1-D first-order spectra of point sources are usually extracted over 7 spatial pixels for the CCD, 11 spatial pixels for the MAMAs (during STIS pipeline processing). Hence, the effect of hot pixels is exacerbated compared to the case of imaging observations. The best practice is to dither the target by an offset large enough to avoid having the same hot pixels fall in the individual extracted spectra. This means that you should move the spectrum by more than 0.35 arcseconds (for a 7 pixel CCD extraction) along the slit between dither positions. Exposures with integer pixel shifts can be aligned with `sshift`. A pair of dithered exposures is preferable to a `CR-SPLIT=2` exposure, but more exposures (e.g., `CR-SPLIT` dithered exposures) will provide better cosmic ray rejection, especially for long exposure times.
 - **Spectra of Extended Sources:** For extended sources, one should consider the spatial size of the extractions to be made during post-observation analysis, or whether rectified spectral images will be analyzed instead of extracted spectra. To enable a proper rejection of hot pixels within broad extractions, the telescope move between dithers should be larger than the spatial size of the extractions made. If a spectral image is to be analyzed, and the region of interest is at or near a sharp peak in the surface brightness distribution, one should consider dithering by a non-integer number of pixels to deal with the undulation issue due to undersampling (see above).
 - **Dithering of Echelle Observations:** Because most echelle observations are done using small apertures, many of the dithering strategies recommended for 1st order spectra are not applicable to the echelle modes. However, there are still a number of ways to shift the spectrum on the detector to work around hot pixels or flat-fielding artifacts. For many observers, the simplest way to dither echelle data will be to observe using two or more different `CENWAVE` settings that each cover the wavelengths of interest; however, wavelengths near the ends of the wavelength ranges will then not be covered by all of the exposures. Another way is the use of `FP-SPLIT` apertures (see [Section FP-SPLIT Slits for Echelle Observations](#)), which are displaced along the dispersion direction. And observers using the echelle with a long slit can also dither up and down the length of the aperture. Observers should also remember that there is some overlap between many adjacent echelle orders, so some wavelengths will appear at two different locations in the same spectral image.
- **Accuracy of Dithering:** During the *Hubble* Deep Field campaign, nearly all dithers were placed to within 10 milliarcsec (mas) (during 1.3 arcsecond offsets and returns separated by multiple days), although in a few cases the dither was off by more than 25 mas, and on one occasion (out of 107 reacquisitions) the telescope locked on a secondary FGS peak – causing the pointing to be off by approximately 1 arcsecond and a field rotation of about 4 arcminutes. The software which was developed for the *Hubble* Deep Field was able to reconstruct images even for those non-optimal dithers, and still yielded gains in resolution over non-dithered data. Those capabilities are now available in [drizzlepac](#) (current successor to the **STSDAS dither** package), which is based on the variable-pixel linear-reconstruction technique developed by Fruchter and Hook (known as *drizzling*). STIS imaging data can be drizzled together provided several preparatory steps are taken: updating the WCS with the [stwcs.updatewcs](#) routine and accurately aligning the images to sub-pixel accuracy with the [drizzlepac.tweakreg](#) routine. For help with combining STIS images, contact the [Help Desk](#).
- **Flat-Field Accuracy:** For the MAMAs, dithering on scales of several pixels can help to smooth out pixel-to-pixel variations in detector sensitivity. For this purpose it is best to use dither steps

that are not integral multiples of half a pixel (the intrinsic high-resolution format of the MAMAs); integral pixel steps should be used instead.

Note that dark and flat-field reference files need to be applied before any shift-and-add procedures. This may require running the usual pipeline calibration in pieces with the combination of the different dither positions inserted in the middle. Once dark subtraction has been done, hot pixels are about as likely to be over-subtracted as under-subtracted in the image. In this case, those pixels should be treated as "cold" pixels (see section on Hot Pixels in CCD Data above).

Be sure to use the correct plate scales when calculating the along-the-slit pixel offsets a given dither size will produce. See [Table 14.38](#) for the pixel scales for each detector and [Section 13.2.4](#) for more information on the header PLATE_{SC} plate scales.

The simplest way to schedule dithers with STIS is to use the patterns `STIS-CCD-BOX` or `STIS-MAMA-BOX` (four-point parallelogram dithers, centering on fractional pixels to gain spatial resolution) or, for spectroscopic observations that use a long slit, the pattern `STIS-ALONG-SLIT` (for linear dithers in the `AXIS2` direction, with user-specified offsets). An alternate approach is to use `POS-TARGs`.

Note that large dithers will incur small errors due to the camera geometric distortion, which increases toward the CCD corners and alters the image scale by about 1% at the corners. For instance, a 20 pixel offset at the field center will suffer a 0.2 pixel error at the CCD corners. Large dithers may also occasionally require a different set of guide stars for each pointing, thus increasing the overhead for the observations and reducing the expected pointing accuracy.

For related articles on dither strategies, see the following papers (all available through the STScI webpages): [A Package for the Reduction of Dithered Undersampled Images](#) (Fruchter et al., in the 1997 *HST* Calibration Workshop Proceedings), the [WFPC2 ISR 98-04, Drizzle: A Method for the Linear Reconstruction of Undersampled Images](#) (Fruchter & Hook 2002, *PASP*, 114, 144), the [Dither Handbook](#) (Koekemoer et al.), the online [drizzlepac](#) documentation, and [The DrizzlePac Handbook](#) (Hoffmann et al. 2021).

A STIS DrizzlePac Tutorial Jupyter Notebook is now available from the [STIS-Notebooks](#) GitHub repository or the [STIS Data Analysis & Software Tools](#) webpage. The Notebook includes examples of aligning and combining images from all three STIS detectors using tools from [DrizzlePac](#), as well as an example of using the pixel-based CTI correction code `stis_cti` on STIS CCD images (see [Section 7.3.9](#)). Further details regarding the Notebook can be found in the [STIS April 2022 STAN](#).

11.4 Fixing Orientation on the Sky

STIS users, particularly those using the long slits to observe extended sources, commonly wish to specify the orientation of the slit on the sky. Specific orientations may also be used to place multiple point sources in a long slit (to be observed simultaneously) or to make sure that overly bright nearby stars are excluded. Observers planning coordinated parallel observations may also wish to specify the orientation of the *HST* focal plane, so as to place the appropriate instrument to cover a given patch of sky. When you set the orientation of the telescope, you effectively constrain the times when your observation can be scheduled, since *HST* must maintain a spacecraft orientation (sometimes called *roll angle*) which keeps its solar panels roughly perpendicular to the incoming sunlight. A roll ranges report, available in the **APT** Visit Planner, shows the range(s) of roll angle possible for a given observation as a function of observation date.

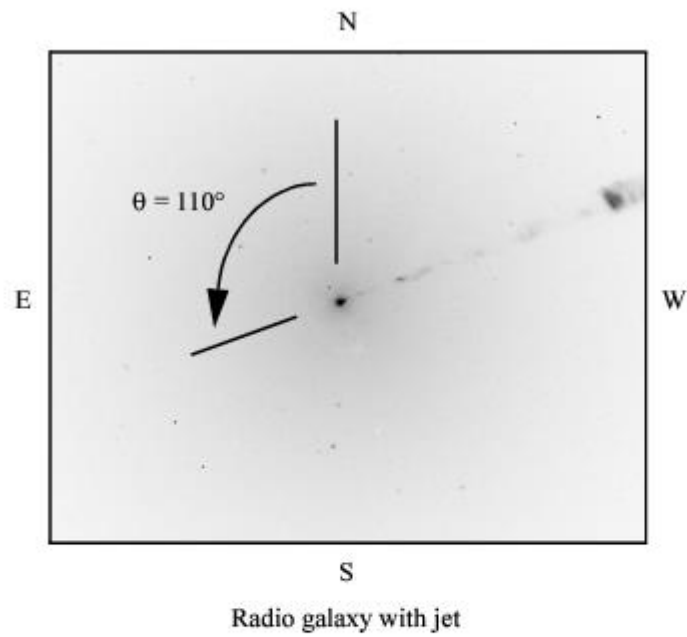
The orientation of the spacecraft (and therefore of the STIS long slits which are fixed in relation to the *HST* focal plane) is controlled by the **ORIENT** special requirement, which is entered during Phase II. The [Phase II Proposal Instructions](#) contain a detailed description of orientations and how to specify them. A specific orientation can be set, or a range of allowed orientations (e.g., 90–110 degrees) can be given. The tighter the constraints, the more difficult it will be to schedule the observation.

The **ORIENT** parameter gives the orientation of the *HST* focal plane projected onto the sky and is defined by the U2 and U3 axes. [Figure 3.2](#) shows the *HST* focal plane containing all the *HST* instruments, with the U2 and U3 axes defined. [Figure 11.1](#) shows the relationship between these axes and the position angle (PA) of the STIS long slits on the sky. Note that the long slits are approximately aligned with the detector's **AXIS2**, i.e., they are directly perpendicular to the dispersion axis (**AXIS1**). The important point to note is that if you fix the orientation of a long slit on the sky to be $PA = X$, where X is measured in degrees east of north, then the **ORIENT** parameter (which determines where the other *HST* instruments lie for parallel observations) is given as $X+45$ or $X+225$ degrees. Likewise, for **PRISM** mode observations, if you wish to fix the orientation of the spatial direction (i.e., perpendicular to the dispersion) to be X , then the **ORIENT** parameter should be set to $X+45$ or $X+225$ degrees. It is possible during Phase II to specify more than one permissible **ORIENT** range. The allowed and forbidden orientation ranges may be displayed in the Aladin image of the field in **APT**.

Users who wish to determine their orientation requirements using existing *HST* images should consult the *HST* Observatory website on [determining an observation's orientation](#). It is especially important to be careful when using *HST* data taken before 15 Sept. 1997, where there may be errors of ~ 0.5 degrees in the **ORIENT** and **PA_V3** header keywords.

We show two examples below. [Figure 11.10](#) illustrates how to set the **ORIENT** parameter to place the long slit along the M87 jet. [Figure 11.11](#) illustrates how to set the **ORIENT** parameter to fix the dispersion axis for **PRISM** observations to be perpendicular to a double star system.

Figure 11.10: Placing the STIS Long Slit Along the Jet of M87.



$\theta = \text{Angle of jet on sky} = 110^\circ$

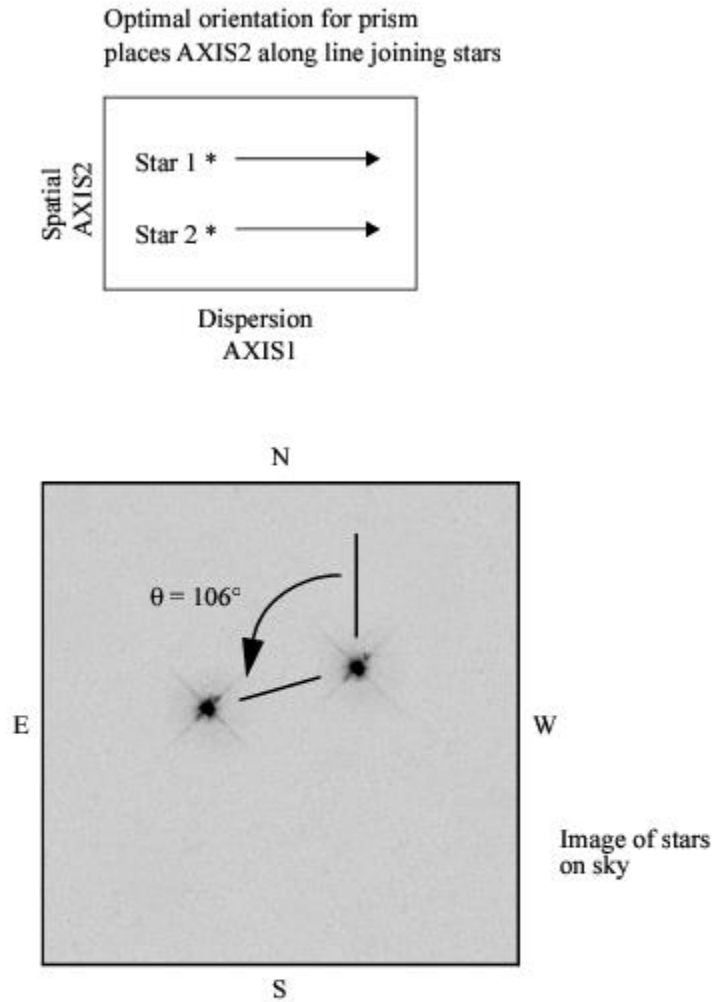
To place long slit axis (AXIS2 on the CCD) on jet:

Orient = $\theta + 45^\circ$ or $\theta + 225^\circ$

= $110^\circ + 45^\circ$ or $110^\circ + 225^\circ$

= 155° or 335°

Figure 11.11: Placing Dispersion Direction Perpendicular to a Binary Star System.



$\theta = \text{Angle of line joining stars on sky} = 106^\circ$

To place AXIS2 along θ :

$$\begin{aligned} \text{Orient} &= \theta + 45^\circ \text{ or } \theta + 225^\circ \\ &= 106^\circ + 45^\circ \text{ or } 106^\circ + 225^\circ \\ &= 151^\circ \text{ or } 331^\circ \end{aligned}$$

This relation between ORIENT and position angle will satisfy most needs. Observers with extremely stringent orientation requirements, however, should be aware that each STIS aperture has a specific U3 offset angle which is close to, *but not equal to*, 45° . In [Table 11.2](#) below we list the offset angles for all supported spectroscopic slits. If ultimate precision is required, observers may wish to use the

offset angles given in this table instead of the standard 45°. Observers should also note that the position angles for the 52" long slits have been revised by up to 0.33°.

Table 11.2: Offset Angles Between Supported STIS Slits and the Spacecraft Orientation Reference Vector U3.

| STIS Aperture | Offset Angle (degrees) |
|---------------|------------------------|
| 0.2X0.06 | 44.94 |
| 0.2X0.09 | 44.94 |
| 0.2X0.2 | 44.94 |
| 6X0.2 | 45.31 |
| 0.1X0.03 | 44.94 |
| 52X0.05 | 45.35 |
| 52X0.1 | 45.35 |
| 52X0.2 | 45.35 |
| 52X0.5 | 45.35 |
| 52X2 | 45.35 |
| 0.2X0.06FPA | 44.94 |
| 0.2X0.06FPB | 44.94 |
| 0.2X0.06FPC | 44.94 |
| 0.2X0.06FPD | 44.94 |
| 0.2X0.06FPE | 44.94 |
| 0.2X0.2FPA | 44.94 |
| 0.2X0.2FPB | 44.94 |
| 0.2X0.2FPC | 44.94 |
| 0.2X0.2FPD | 44.94 |
| 0.2X0.2FPE | 44.94 |
| 52X0.2F1 | 46.30 |
| 0.3X0.05ND | 44.95 |
| 0.2X0.05ND | 44.94 |
| 31X0.05NDA | 45.36 |

| | |
|------------|-------|
| 31X0.05NDB | 45.37 |
| 31X0.05NDC | 45.37 |

11.5 Target Positioning

11.5.1 POSition TARGet (POS TARG)

11.5.2 SAME POSition AS (SAME POS AS)

Target position special requirements are used to restrict the pointing of *HST* observations. Details on the different target position options and implementing these special requirements in Phase IIs can be found in [Section 6.3.3 of the *HST Phase II Proposal Instructions*](#) (P2PI). Below we summarize some STIS use cases for target position options.

11.5.1 POSition TARGet (POS TARG)

POS TARG specifies a non-default placement of the target, relative to the aperture fiducial point in the instrument field of view, for the current exposure, which must be on an external target. Changing the pointing in this way can cause overheads to be repeated at each POS TARG pointing. If a large number of pointings need to be obtained within one orbital visibility period, it may be more efficient to use a pattern designed for this purpose (see [Section 11.3](#)).

Below are some of the STIS use cases for POS TARG:

- **Custom dithering:** POS TARG is most commonly used in some special science cases for custom dithering with the STIS-ALONG-SLIT pattern or to implement a user-specified pattern (see [Section 11.3.2](#) for more details).
- **Crowded fields:** In overcrowded regions, POS TARG can be used to set a position relative to an acquisition/peakup of an isolated reference source. Though in many cases this can be accomplished without a POS TARG by using the preferred method of specifying an OFFSET reference star for the acquisition (see [Table 3.1](#) in the P2PI).
- **Spatial scanning:** For scanned observations with G750L or G750M, POS TARG can be used to better align the stellar scans (often taken with the 52x2 aperture) with the fringe flats (generally taken with 52x0.1) – to account for the slight difference in the X positions of the two apertures (as tabulated in the [Science Instrument Aperture File](#)). See [Section 12.12.3](#) for more details.
- **Coronagraphy:** Using POS TARG to adjust the positioning of a target behind coronagraphic bars is an [Available-but-Unsupported mode](#) (see [Sections 12.10](#) & [12.11](#) on coronagraphy).

11.5.2 SAME POSition AS (SAME POS AS)

SAME POS AS specifies that the current exposure be done at exactly the same position on the sky and with the same telescope roll as a reference exposure. Do not use SAME POS AS with dithering patterns (see [Section 11.3](#)), as it will negate them.

Chapter 12: Special Uses of STIS

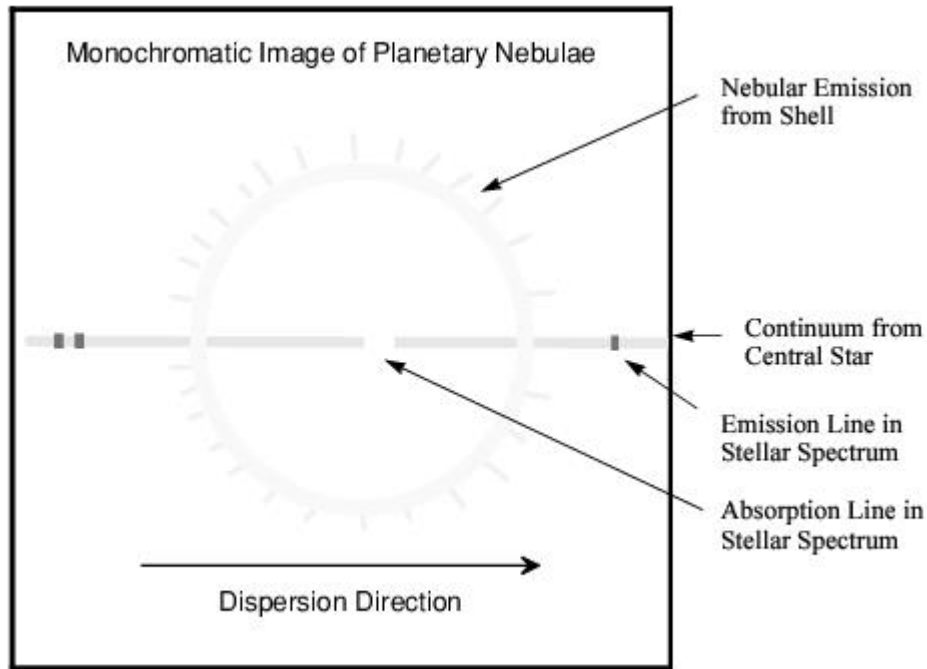
Chapter Contents

- [12.1 Slitless First-Order Spectroscopy](#)
- [12.2 Long-Slit Echelle Spectroscopy](#)
- [12.3 Time-Resolved Observations](#)
- [12.4 Observing Too-Bright Objects with STIS](#)
- [12.5 High Signal-to-Noise Ratio Observations](#)
- [12.6 Improving the Sampling of the Line Spread Function](#)
- [12.7 Considerations for Observing Planetary Targets](#)
- [12.8 Special Considerations for Extended Targets](#)
- [12.9 Parallel Observing with STIS](#)
- [12.10 Coronagraphic Spectroscopy](#)
- [12.11 Coronagraphic Imaging - 50CORON](#)
- [12.12 Spatial Scans with the STIS CCD](#)

12.1 Slitless First-Order Spectroscopy

The vast majority of STIS first-order grating mode observations use a long slit. The use of a long slit ensures a clean separation of emission lines arising from different spatial features. However, all of STIS' first-order gratings as well as the NUV PRISM (see [Table 4.1](#)) can also be used slitless or with a wide slit to obtain emission line images. [Figure 12.1](#) below shows a schematic example of a slitless spectrogram. [Figure 4.8](#) shows an image of SN1987A observed using the 52x2 aperture, and as the source is smaller than the slit, this is effectively a slitless image.

Figure 12.1: A Schematic slitless Spectrogram of a Planetary Nebula.



When STIS is used slitless (or with a wide slit), the image obtained will be the sum of a series of shifted monochromatic images of the field of view. The range of wavelengths covered in the series of monochromatic images is dictated by the spectral range of the grating. The result is that there is *not* a one-to-one mapping of pixel location to wavelength in your image or of pixel location to spatial location on the sky. Depending on the structure of your source and the grating you use, it may be easy to deconvolve the spatial and spectral information, or it may be very difficult.

Slitless spectroscopy can be employed either for prime or parallel STIS observing, (although MAMA pure parallels are not allowed). If you are designing a slitless spectroscopic observation there are a few important points to keep in mind:

- The more complex the emission line, velocity, and spatial structure of your target field, the more difficult it will be to deconvolve the spatial and spectral information. It is important to match the grating you choose to the structure of your source. Gratings which produce images of multiple, kinematically resolved emission lines will be the most challenging to deconvolve. At the other extreme, a grating which covers only a single strong emission line at a resolution where the lines are kinematically unresolved will produce a clean image of the source in the single emission line (see [Figure 12.1](#), above). You may also wish to specify the orientation for slitless spectroscopic observations to ensure that the most complex source structure is oriented perpendicular to the dispersion axis (see [Section 11.4](#)).
- Since each point in the sky emits geocoronal light, the background due to the geocoronal emission lines (Lyman- α λ 1216, O I λ 1302 triplet, and occasionally on the day side O I] λ 1356 and [O II] λ 2471; see [Section Geocoronal Emission and Shadow](#)) will be observed at all pixels in the image when a slitless spectrum is obtained which covers these wavelengths. This background must be taken into account in your signal-to-noise calculations. For this reason, you may wish to consider using one of the two longpass ultraviolet (UV) blocking filters (see

[Section 5.3.5](#)), instead of a clear aperture when performing UV slitless spectroscopy. Note that when a spectroscopic exposure is obtained with a slit, these sky emission lines are localized in the resulting image to the pixels at the corresponding wavelengths.

- Slitless spectroscopic data will not be fully calibrated by the STScI STIS pipeline. Slitless spectroscopic data will be passed through the first phase of calibration and a flat-fielded calibrated image will be produced; however, the pipeline will not attempt to spectroscopically calibrate the data. This process must be interactively done by the observer since, as described above, ambiguous overlap of spatial and spectral information will occur. Please contact the [Help Desk](#) if you have questions about calibrating your slitless spectroscopic data.

In order to properly calibrate slitless data it is necessary to know the position of each source along the dispersion direction. This usually requires a STIS, ACS, WFC3, or archival image at comparable spatial resolution and imaged with a comparable bandpass to the emission line structure that is being imaged with the slitless STIS spectroscopy. Obtaining the image during the same visit and at the same position angle as the slitless spectroscopy simplifies the image registration and analysis. Variations in the positioning of the Mode Select Mechanism (MSM), which contains the mirrors and gratings, can result in an uncertainty of the position of an image or spectrum on the detector by as much as five pixels, and an additional special calibration may be needed in order to fix the absolute offset between the images and the spectrograms. The standard STIS ACQ procedure automatically measures the offset between the location of a star and a reference aperture on the CCD detector and uses this to place the target accurately in the desired slit. So if the ACQ target appears in the field of view, there is no need for an additional image to calibrate the MSM offset, although a separate full field image may still be needed to measure the relative positions of other sources with respect to the ACQ target. In cases where no STIS ACQ exposure is done, an image of the field should be taken either immediately following or immediately preceding a lamp image taken through a narrow slit. For the CCD, a 1 second tungsten lamp exposure with the 52x0.1 slit will do nicely. This will allow the MSM offset for that image to be determined. It is important that no MSM motion (mirror or grating change) occur between the sky image and the lamp image of the slit. The MSM offset for the spectrographic exposure itself can usually be measured from the standard wavecal exposure. If extremely precise alignment between the spectrum and the field image in the cross dispersion direction is also required for source identification, this procedure may require some modifications, and observers should consult their contact scientist or the STScI [Help Desk](#).

Finally, we note that to achieve an accurate wavelength calibration for targets observed in slitless mode, when those targets are well displaced from the nominal AXIS1 center, the dispersion coefficients at the off-nominal centerings must be well known. Currently, the incidence-angle offset corrections are based on ground calibration data and are somewhat less accurate than the on-axis dispersion solutions. We recommend that observers consult the [Help Desk](#) if they are concerned about the calibration of observations taken of targets which are expected to be off-center by more than 1 arcsecond in the dispersion direction.

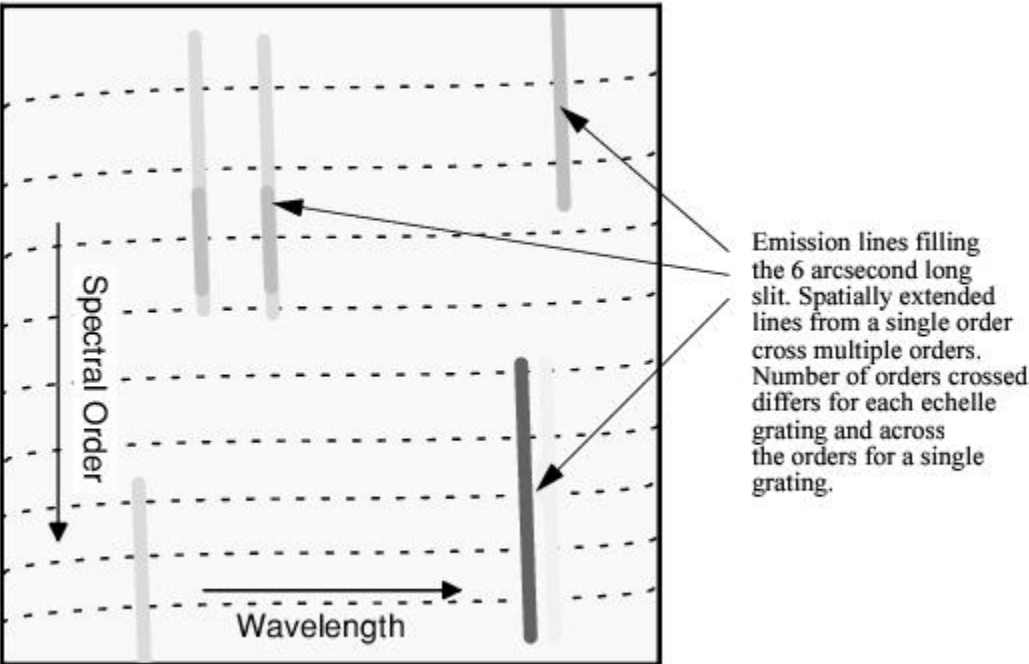
12.2 Long-Slit Echelle Spectroscopy

The STIS echelle gratings (see [Section 4.3.1](#)) were designed to maximize the spectral range covered in a single echellogram. The orders are therefore closely spaced, and to avoid overlap between orders, short echelle slits must be used. Indeed, the majority of STIS echelle observations are of point sources and use these customized echelle slits (see [Section 4.3.2](#)). Nevertheless, at the price of confusion due to order overlap, the echelle gratings can be used with a long slit to obtain high-resolution spectroscopy of extended objects, or they can be used slitless with a full clear, filtered, or ND aperture. An example of a scientific application that would benefit from long-slit echelle spectroscopy might be observations designed to map the kinematics of planetary nebulae and stellar outflows around young stars. Observers contemplating such observations should be aware that the problems of order overlap, scattered light, and the broad wings of the PSF from the Optical Telescope Assembly will make accurate calibration and line-profile work extremely complex for extended sources with a continuum (see [Section 13.7](#)). While the three 31X0.05ND(A-C) apertures provide a range of attenuation factors between those of the small clear apertures and the 0.2X0.05ND aperture (e.g., for maximizing the S/N for targets that are too bright for the small clear apertures), order overlap in those long slits will produce slight increases in the inter-order background even for point sources, which can complicate determination of the flux zero points.

The 6x0.2 slit (6 arcseconds in the spatial direction and 0.2 arcseconds wide in the dispersion direction) is supported for use with all four of the echelle gratings. However, observers should be aware of the ambiguous overlap in the resulting echellogram that makes the reduction of long-slit echelle data an inherently source-dependent and interactive process.

Observers should also note that, for long-slit echelle spectra, images of monochromatic lines on the detector are rotated by an angle that differs significantly from the physical angle of the slit, and which varies from one echelle grating to another. When using the 6x0.2 aperture with an echelle grating, the same aperture is also used for the auto-wavecal, and this wavecal image can be used to measure the change of the wavelength scale as a function of position along the slit. However, long-slit wavecal lines will overlap multiple orders, causing `calstis` to calculate incorrect wavelength and spatial offsets. Users may wish to consider adding an additional GO wavecal exposure using a smaller aperture (e.g., 0.2x0.2) to more easily derive an accurate wavelength scale for their science image. When using any other long-slit aperture with the echelle gratings, the auto-wavecal will be done by default with a small aperture. In such cases, the user may wish to add an additional GO wavecal with the 6x0.2 aperture in order to measure the change in the projected slit angle.

Figure 12.2: Echelle Long-Slit Spectrogram of Extended Emission Line Source Filling the Long Slit (partial image).



12.3 Time-Resolved Observations

There are two ways to obtain time-resolved spectroscopic and imaging observations with STIS:

- Use the MAMA `TIME-TAG` operating mode (described in [Section 11.1.3](#)) in the UV.
- Take a series of multiple, short, identical repeated observations (described in [Section 11.2.4](#)) of your target in `ACCUM` operating mode with either the CCD or the MAMAs.

Both the data products received (an event stream in the case of `TIME-TAG` and a series of individual images from each `ACCUM` mode exposure in a repeated sequence) and the basic parameters of the time-resolved observations (e.g., sample time, interval between samples, total number of samples or equivalently duration) differ dramatically in these modes. In [Table 12.1](#) we summarize and contrast the ranges of parameter space covered by the different methods of obtaining time-resolved observations.

The information presented in [Table 12.1](#) can be summarized into the following set of guidelines for performing time-resolved observations with STIS:

- If you wish to observe variability on second-or-less time-scales, observe in the UV using `TIME-TAG` mode. [Figure 12.3](#) shows an example of a time profile of the Crab Pulsar obtained with STIS `G140L` in `TIME-TAG` mode overlaid on prior HSP observations.
- In the optical, variability can be observed on tens-of-seconds time-scales using subarrays and multiple exposures with the CCD.
- In the UV, variability on the several-minute or more time-scale can be observed by multiple `ACCUM` mode exposures with the MAMAs or using `TIME-TAG` (subject to count rate limitations).
- A series of identical exposures that are each less than three minutes in length incurs additional data management overheads when compared to longer exposures (see [Table 9.2](#)).
- Single MAMA visits are limited to five orbits (see [Chapter 2.7](#)) so continuous variability (though interrupted by occultation for non-CVZ visits) can be tracked for only that duration with the MAMAs.
- Spatial scanning with the STIS CCD is another option in the optical/NUV – though apparent slight variations in the scan rate may limit both the useful time scales and the accuracy of the timing within individual scanned spectra (see results from test observations in the [March 2017 STAN](#), spatial scanning performance in the [September 2020 STAN](#), and detailed information on this mode in [Section 12.12](#)).

Table 12.1: Summary of Time-Resolved Imaging and Spectroscopy.

| Observation Type | Detector | Spectral Range (Å) | Minimum Sample Time (τ) | Interval Between Samples ($\Delta\tau$) | Total Duration of Uninterrupted Time Series ¹ |
|------------------------------|----------|--------------------|--------------------------------|---|---|
| Repeat <code>ACCUM</code> | CCD | 1,640–10,300 | 0 . 1 second | full frame: 45 second 1060 × 32 subarray: 20 second | For $\tau > 3$ minutes, no limit For $\tau < 3$ minutes: dur = $(\tau + \Delta\tau) \times 7$, full frame (1062 × 1044) dur = $(\tau + \Delta\tau) \times 256$, 1060 × 32 subarray |

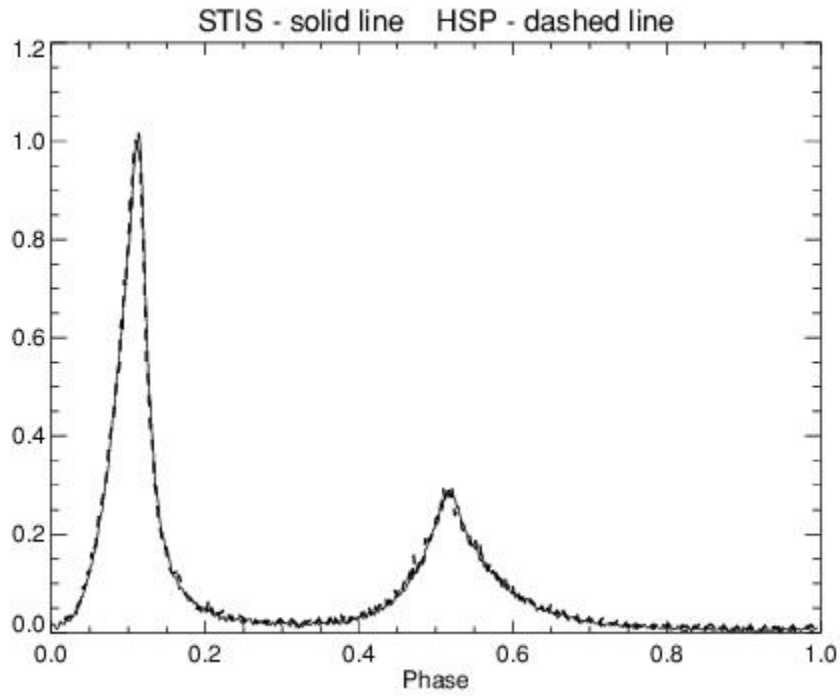
| | | | | | |
|-----------------------|-------|-----------------|---------------------|--|--|
| Repeat ACCUM | MAMAs | 1,150- 3,100 | 0 . 1 second | 30 second for $\tau > 3$ minutes 2 minutes for $\tau < 3$ minutes | No limit ² No limit |
| TIME-TAG ³ | MAMAs | 1,150- 3,100 | 125 μ second | 0 | $6.0 \times 10^7/R$ seconds if $R < 21,000$ counts/s or $4.0 \times 10^6/R$ sec if $R > 21,000$ counts/s, where R is rate in counts/s |

¹ τ = duration of an individual exposure.

² Note, with BINAXIS1=BINAXIS2=2, 7 images separated by 1 minute and each of duration $\tau < 3$ minutes can be obtained.

³ Above 30,000 counts/s timing accuracy suffers.

Figure 12.3: Crab Pulsar Observed Using the STIS FUV-MAMA with G140L in TIME-TAG Mode.



The resulting integrated time profile is shown superimposed on the early results from the HSP. The full period of the Crab pulsar is 33 milliseconds. (Figure courtesy of Don Lindler and Ted Gull, see also Gull et al. 1998, *ApJ*, 495, L51).

12.4 Observing Too-Bright Objects with STIS

As described in [Section 7.7](#), the STIS MAMA detectors are subject to damage at high local and global count rates. The MAMA detectors also suffer uncorrectable non-linearity at similar count rates (see [Section 7.5.4](#)). There are therefore configuration-specific count rate limits for all observations that use the MAMA detectors; sources brighter than allowed by the limits *cannot be observed* in that configuration.

The STIS CCDs are not subject to the same bright object constraints, as the CCD cannot be damaged by observations of bright sources. At high *accumulated* count/pix levels, however, the CCD saturates and charge bleeds along the columns. When `CCDGAIN=4`, the saturated counts can be recovered by summing over the pixels bled into, and this spatially integrated count rate remains linear with exposure level (see [STIS ISR 1999-05](#)). This is not true for `CCDGAIN=1`. The charge bleeding resulting from saturation does somewhat complicate flat fielding and removal of cosmic rays, however, as it changes the locations of some of the observed counts. As described previously (see [Section 7.3.2](#)), CCD saturation can be avoided by keeping exposure times short when observing bright targets. Spatial scanning with the CCD ([Section 12.12](#)) may also be employed. The minimum exposure time for CCD observations (0.1 second) dictates the maximum source brightness which can be observed without saturating.

The only way to use STIS to observe a source that is too bright is to use a configuration or observing mode which reduces the flux from the target (globally and/or locally), bringing it into the observable regime. The options available to achieve this reduction are:

- Use a smaller slit to reduce the transmitted light for spectroscopic observations (see [Section 13.4](#)—you will find there the percent flux transmitted through each slit as a function of wavelength).
- Select a more appropriate grating or filter configuration. The solution may be a configuration with higher resolving power if it is the local limit which is being violated, or a configuration that covers a smaller spectral range if the global limit is being violated. In more extreme cases, you may be forced to choose a grating (filter) that covers an entirely different region of the spectrum. Note that if you are observing in first order in the NUV, you can consider using the CCD NUV first-order spectroscopic modes `G230LB` and `G230MB` (see [Section 4.1.6](#)).
- Use a neutral-density-filtered full aperture. The neutral-density filters are described in [Section 5.4](#); they produce attenuations ranging by factors from 10^{-1} to 10^{-6} . Note, however, that the *ND* filters are located in the slit wheel. Thus, all supported *ND* full-filtered exposures will be slitless; i.e., you cannot use a slit and an *ND* full filter together. Similarly, you cannot use a *ND* full filter and another filter in imaging mode. Also note that the *NDQ1*, *NDQ2*, *NDQ3*, and *NDQ4* filters are four distinct quadrants of a single filter, all of which are simultaneously imaged. Note that *NDQ4* is of little use, as any target that requires this filter is too close to the *NDQ1* quadrant to pass bright-object screening.
- Use one of the echelle or long calibration slits which contain neutral-density filters. Supported neutral-density slits for the echelles are `0.2x0.05ND` (with $ND=2.0$) and `0.3x0.05ND` (with $ND=3.0$), where if $ND=x$, the flux is attenuated by approximately 10^{-x} . Supported neutral-density long-slits that can be used for first order or echelle observations are `31x0.05NDA` (with $ND=0.4$), `31x0.05NDB` (with $ND=0.8$), and `31x0.05NDC` (with $ND=1.2$). Use of these long slits with an echelle grating will cause order overlap problems (see [Section 12.2](#)), but for point sources the order separation may be adequate for many science programs. Use of the neutral-density long-slits with the PRISM remains "available-but-unsupported" at this time.
- Use spatial scanning (CCD only) to spread the exposure over a larger spatial extent (see [Section 12.12](#)).

12.5 High Signal-to-Noise Ratio Observations

The maximum achievable signal-to-noise (S/N) ratio of STIS observations for well exposed targets is, in general, limited by the S/N ratio and stability of the flat fields. CCD flat-field observations are obtained monthly. Ultimately, CCD reference flats in the pipeline should have an effective illumination of up to 10^6 e⁻/pix. Thus, it should be possible to achieve a S/N ratio of several hundred over larger spatial scales given sufficient source counts. The limitation is the temporal stability of the CCD reference flats, which show variations of a few tenths of a percent. Dithering techniques can and should be considered for high S/N CCD observations (see [Section 11.3](#)). The realizable S/N ratio for spectroscopy will be less in the far red due to fringing, unless appropriate fringe flats are applied (see the caveats on long-wavelength spectroscopy in the red in [Section 7.2.4](#)).

[12.5.1 Dithering](#)

[12.5.2 FP-SPLIT Slits for Echelle Observations](#)

Two observing techniques have been employed to obtain higher S/N ratios in STIS CCD spectra of relatively bright stars. In the first method, high total counts are built up by deliberate saturation of the detector at a fixed pointing. The excess charge "bleeds" along the columns, but, for GAIN=4, the total accumulated charge is preserved in each column. In this way, S/N ratios of order 1000 have been achieved ([Gilliland et al. 1999, PASP, 111, 1009](#); [Bohlin & Gilliland 2004, AJ, 127, 3508](#)). The second method uses spatial scanning - trailing the target along one of the long STIS slits, roughly perpendicular to the dispersion. The aim is again to build up high total counts in each spectral element, but without saturating the individual pixels in the detector. As discussed in more detail in [Section 12.12](#), spatial scanning can enable better flat fielding, more robust removal of cosmic rays, and more complete removal of the strong fringing seen in STIS CCD spectra at wavelengths longer than about 7000 Å. In a first application of this method, [Cordiner et al. \(2017, ApJ, 843, L2\)](#) achieved S/N ~ 600-800 in G750M spectra near 9300 Å, consistent with expectations based on photon statistics. Two subsequent special calibration programs have demonstrated total flux reproducibility at a level ~30 ppm in repeated G750L spatial scans of the relatively bright exoplanet host star 55 Cnc obtained over several *HST* orbits ([STIS September 2020 STAN](#)).

The S/N ratio of MAMA flat fields is limited by the long integration times needed to acquire them and the limited lamp lifetimes. (See [Section 16.1](#)). S/N ratios of ~100:1 should routinely be achievable for spectroscopic observations of bright sources with the MAMAs if supported by counting statistics. If a program requires high S/N ratios, we recommend using some form of dithering (described below) and co-adding the spectrograms to ameliorate the structure in the flat fields.

Kaiser et al. ([1998, PASP, 110, 978](#)) and Gilliland ([STIS ISR 1998-16](#)) reported quite high S/N ratios for spectrograms of bright standard stars obtained during a STIS commissioning program. The realizable S/N ratio depends on the technique used to correct for the flat-field variations, as shown in [Table 12.2](#). The S/N ratios quoted are for wavelength bins from an extraction box of 2x11 lowres pixels (2 in `AXIS1` or dispersion, 11 in `AXIS2` or across the dispersion). In the table, the Poisson limit is just the S/N ratio that would be expected on the basis of counting statistics alone; "No Flat" means the realized S/N ratio without applying any flat field to the data; "Reference Flat" means the realized S/N ratio after applying the best available reference flat, and the "Full FP-SPLIT Solution" is discussed under [Section 12.5.2](#) below. Clearly, S/N ratios in excess of 100:1 per resolution element are well within the capabilities of the MAMAs for spectroscopy.

Table 12.2: Results of S/N Ratio Tests with STIS MAMAs in Orbit.

| Grating | Poisson Limit | No Flat | Reference Flat | Full FP-Split Solution ¹ |
|---------|---------------|---------|------------------|-------------------------------------|
| E140M | 470 | 200 | 360 ² | 390 |
| G140L | 295 | 90 | 180 | N/A |
| E230M | 400 | 250 | 320 ³ | 380 |
| G230M | 200 | 100 | 150 | N/A |

¹ Results obtainable in echelle modes using the FP-SPLIT slits and an iterative solution for the spectrogram and flat field.

² Results obtained using the FP-SPLIT slits and simply shifting and co-adding the spectrograms after flat fielding.

³ Results obtained using the FP-SPLIT slits and simply shifting and co-adding the spectrograms after flat fielding.

12.5.1 Dithering

In first-order spectroscopic modes, improved S/N ratios can be achieved by stepping the target along the slit, taking separate exposures at each location, which are subsequently shifted and added in post-observation data processing (PATTERN=STIS-ALONG-SLIT, see [Section 11.3](#)). This stepping, or dithering, in the spatial direction effectively smooths the detector response over the number of steps, achieving a reduction of pixel-to-pixel nonuniformity by the square root of the number of steps, assuming the pixel-to-pixel deviations are uncorrelated on the scale of the steps. In imaging modes, the same dithering can be done in two dimensions, i.e., the steps need not be along a straight line (see [Section 11.3.5](#)). For echelle modes, stepping along the slit is possible only with a long echelle slit (e.g., the 6X0.2 or 52X0.1 apertures, or one of the available but unsupported long-slit apertures), but see [Section 12.2](#) above, and note the ameliorating effects of Doppler smearing as noted below. In practice, using the FP-SPLIT slits (see [Section 12.5.2](#)) provides a better means of dithering echelle observations.

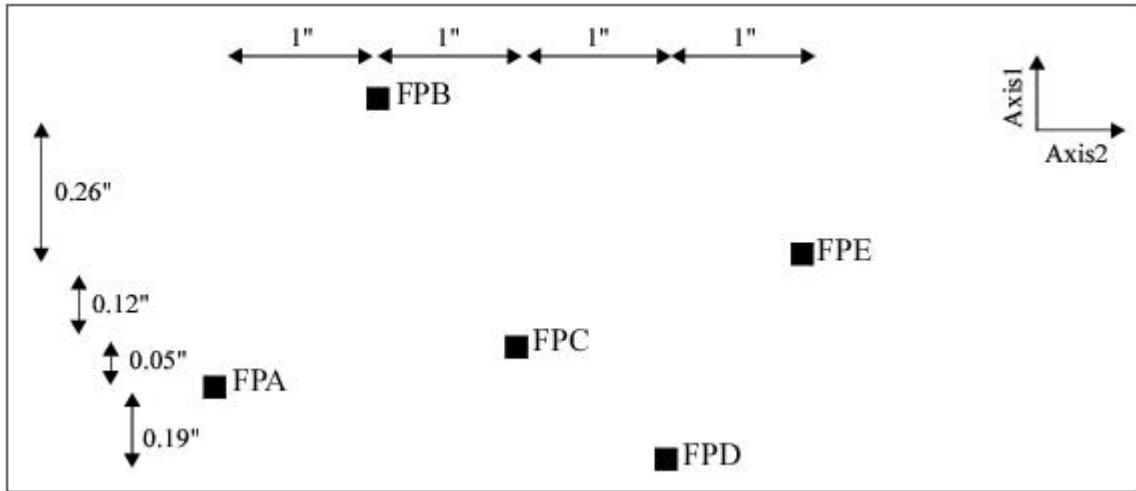
In a slitless or wide-slit mode, stepping along the dispersion direction provides another method to achieve high S/N ratio data. Data so obtained permit, at least in principle, an independent solution for spectrogram and flat field, but at a cost of lower spectral resolution and line profile confusion due to the wings of the LSFs transmitted through a wide slit (see [Section 13.7](#)). Such an approach for STIS data has not been attempted as of this writing.

The three scanned STIS echelle modes (E140H, E230H, and E230M), have a number of secondary wavelength settings defined with broad overlap in their wavelength coverage. Using two or more of these overlapping wavelength settings is another simple way to move a given feature to different parts of the detector.

12.5.2 FP-SPLIT Slits for Echelle Observations

A special kind of dithering in the spectral direction is possible for echelle mode observations with one of two sets of fixed-pattern (or FP-SPLIT) slits. These slit sets are each comprised of a mask with five apertures that are all either 0.2×0.2 or 0.2×0.06 in size. A schematic of the configuration is shown in [Figure 12.4](#). During a visit, the target is moved from one aperture to another, and the slit wheel is repositioned, so that the spectrogram is shifted (relative to the detector pixels) along the dispersion direction only. The slits are spaced to place the spectrogram at different detector locations, so that flat-field variations can be ameliorated by co-adding many such spectrograms. The FP-SPLIT slits can be a good choice for obtaining high S/N ratio echelle data, since it is usually not possible to dither in the spatial direction. However, since $S/N=100$ is routinely achieved using the normal echelle apertures, the FP-SPLIT slits are rarely used.

Figure 12.4: Schematic of the STIS Fixed-Pattern Slit Configuration.



axis1 corresponds to the dispersion direction, and **axis2** to the spatial direction. Dimensions are not to scale.

For the echelle modes, Doppler-induced spectral shifts, due to the variation of the projected *HST* spacecraft velocity along the line of sight to the target, move the spectrogram on the detector. Column 2 of Table 12.3 gives the maximum shift in highres pixels that would apply, based upon an *HST* orbital velocity of ~ 7.5 km/s during an orbit. The actual shift will depend upon the cosine of the target latitude, i , above or below the *HST* orbital plane, and upon the sine of the orbital phase at which the exposure is obtained. (Note that in general the observer can predict neither the latitude nor the orbit phase of the exposures in advance with any precision.) Column 3 gives, for a target lying in the *HST* orbital plane, the maximum duration of an exposure for which the Doppler shift will be one highres pixel or less; the actual duration will scale as $\sec(i)$, so that targets near the continuous viewing zone (CVZ) are scarcely affected by Doppler motion. This information on T_{max} is relevant only if one is trying to derive the flat-field response simultaneously with the source spectrogram (see below) and not for the straightforward flat field and shift-and-add methodology described above.

The STIS flight software automatically applies an onboard compensation for Doppler motion for echelle and MAMA medium resolution, first-order data taken in ACCUM mode (see Chapter 11). The MAMA control electronics correct (to the nearest highres pixel) the location of each event for the Doppler shift induced by the spacecraft motion prior to updating the counter in the image being collected. Thus, the flat-field correction for any image pixel would be an appropriately weighted average over a small range of nearby pixels and the effect of spacecraft-induced Doppler shifts is therefore to naturally provide some smoothing over the flat fields in the echelle modes.

Table 12.3: Effect of Doppler Shift on Exposure Times.

| Grating | Maximum Doppler Shift (hi-res pixels) | T_{max}^1 (minutes) |
|---------|---------------------------------------|-----------------------|
| E140H | 11.41 | 2.7 |
| E140M | 4.59 | 7.0 |

| | | |
|-------|-------|------|
| E230H | 11.41 | 2.7 |
| E230M | 3.00 | 11.3 |

¹ For inclination $i = 0$; actual duration will scale as $\sec(i)$. See text for details.

Obtaining the Highest S/N Ratio with the FP-SPLIT Slits

As described above, the FP-SPLIT slits have been used with the echelles to provide signal-to-noise as high as ~ 350 with the direct shift-and-add method. Additionally, data obtained with the FP-SPLIT slits make it possible to solve independently for the fixed-pattern (i.e., the flat-field variation) and the source spectrum. An iterative technique for combining FP-SPLIT data was applied successfully to data obtained with GHRIS (see Lambert et al., ApJ, 420, 756, 1994), based on a method described by Bagnuolo and Gies (ApJ, 376, 266, 1991). This same technique was applied by Gilliland (STIS ISR 1998-16) to STIS observations of a standard star. The S/N ratio that was achieved with these slits is summarized in the last column of Table 12.2, which shows that the FP-SPLIT slits can offer some advantage when one is attempting to achieve the highest possible S/N ratio. In general, though, it may be difficult to improve upon the S/N ratio that can be achieved by simply calibrating with the standard flat field and co-adding the spectrograms.

There are a number of caveats to the use of the FP-SPLIT slits to solve independently for the target spectrum and flat field. The most notable is that the targets must be relatively bright point sources. The restriction to bright targets results both from the need to limit the duration of individual exposures to keep the Doppler-induced spectral shifts to less than one highres pixel, and from the need to have appreciable counts in the individual exposures—at least in the orders of interest. Very high counts in the sum of all exposures are essential for a good (and stable) solution to both the target spectrum and the underlying flat field.

If one is using the FP-SPLIT slits to distinguish the signature of the flat field from the target spectrum, then Doppler smearing (and the discrete compensation for that smearing) will defeat that solution. In this case, the exposures must be kept as short as if there were no Doppler compensation at all if the goal is to solve for the pixel-to-pixel variation at a precision higher than that of the available flat-field reference files.

The utility of FP-SPLIT observations is also limited by the modest range of slit offsets in wavelength space, and by the distribution and character of the features in the target spectrum itself. That is, if the spectrum in the order(s) of interest is dominated by absorption over a width comparable to or larger than the largest offset range, the solution may not be stable or unique. A corollary is that some of the spectral orders must contain moderately prominent spectral features with good signal in order to distinguish the spectrum from flat-field variations. Table 12.4 gives the FP-SPLIT offsets for each grating, including offsets in Ångstroms for typical central-wavelength settings.

Table 12.4: Magnitude of Spectrogram Offset for the FP-SPLIT Slits.

| Grating | Minimum Offset (hires pix) | Maximum Offset (hires pix) | CENWAVE (Å) | Max. Offset @CENWAVE (Å) |
|---------|----------------------------|----------------------------|-------------|--------------------------|
| E140H | 2.128 | 26.383 | 1416 | 0.164 |
| E140M | 2.778 | 34.444 | 1425 | 0.535 |
| E230H | 2.128 | 26.383 | 2390 | 0.277 |

| | | | | |
|-------|-------|--------|------|-------|
| E230M | 2.857 | 35.429 | 2340 | 1.382 |
|-------|-------|--------|------|-------|

12.6 Improving the Sampling of the Line Spread Function

In most configurations the point source spectral line FWHM is slightly less than two detector pixels (see [Section 13.6](#)). Most observations should not be affected, but if one is observing lines which are near to being unresolved in the grating of interest and requires accurate line profiles, the following techniques may be useful:

- Stepping of the target in the dispersion direction in a wide slit or slitless aperture to subsample the line spread function by displacing the spectrogram. This technique can also be used to increase the signal-to-noise (see above). Note that in employing this strategy, one will have to trade off the benefits of the sampling with the negative impact of increased wings in the line spread function with a wide slit, particularly for MAMA observations (see [Section 13.7](#)).
- For MAMA observations, *highres* pixels may provide twice the sampling; however, flat-field variability may make it difficult to realize the benefit in resolution (see [Highres Section in 3.2](#)). Note that all STIS data are taken by default in highres format, and then binned in calibration on the ground, so all one needs to do is to recalibrate the data, changing the switch settings (see "[STIS Calibration](#)" chapter in the [STIS Data Handbook](#)) to fully exploit the highres data.
- For MAMA echelle observations, one can use the very small 0.1x0.03 aperture. When used with high signal-to-noise data in the highres format and with specialized data reduction techniques, resolutions as high as 200,000 are possible with the E140H and E230H echelle gratings ([Jenkins & Tripp 2001, ApJS, 137, 297](#)). See [Section 3.1](#) on the smallest STIS apertures (with caveat detailed in the footnote) and details about throughput losses given in [ISR 2017-01](#). The [STIS Throughput Curves](#) are available on the [STIS Performance](#) website.
- Use of a higher resolution grating mode in which the intrinsic line width of the source is well sampled.

12.7 Considerations for Observing Planetary Targets

12.7.1 Slit Orientation

STIS' FUV solar-blind and NUV solar-insensitive MAMA detectors make it particularly well suited to slitted spectroscopic and imaging planetary observations. In addition, the 52x2 long slit (2 arcseconds wide in the dispersion direction) is particularly well suited to the "slitless" UV spectroscopic study of small planetary bodies (using a slit limits the background continuum contribution; see [Section 6.5.2](#)). STIS has been used successfully to perform long-slit and echelle spectroscopy and UV imaging of a number of solar system objects including comets, planetary satellites, and planets.

Planetary observers may wish to use the sequence `PATTERN=STIS-PERP-TO-SLIT` (see [Section 11.3](#)) to map out the surface of a planet by taking a series of long-slit observations, each one stepped by the slit width perpendicular to the slit's long dimension, relative to the previous exposure. Advice on performing target acquisitions for solar system targets is provided in [Chapter 8](#).

12.7.1 Slit Orientation

Planetary observers requiring specific long-slit orientations will want to be aware of the tight scheduling constraints of specific orientations for observations of targets in the ecliptic plane (see discussion in the [Phase II Proposal Instructions](#)).

For example, say an observer wanted to orient the STIS long (52 arcsecond) slit in the north-south direction on Jupiter. For a Jupiter north-pole position angle of $\sim 20^\circ$ from celestial north, an `ORIENT` constraint of $\sim 65-70^\circ$ or $\sim 270-275^\circ$ would be required. These values take into account the $\sim 45^\circ$ rotation between the `ORIENT` frame and the STIS slit. See [Section 11.4](#) for a more extended discussion about fixing the orientation of the detector and slit on the sky. The nominal roll angle (orientation) for Jupiter varies from $\sim 250^\circ$ before opposition to $\sim 70^\circ$ after opposition, and it goes through the intervening 180° range during a four-day period centered on opposition. Deviations from nominal roll are allowed as follows:

- 5° when the sun-target angle is $50-90^\circ$.
- Up to $15-30^\circ$ when the sun-target angle is $90-178^\circ$.
- Unlimited when the sun-target angle is $178-180^\circ$.

Thus orientation of the long slit in a north-south direction on Jupiter is possible only during a single four-day period near Jovian opposition, since no allowable deviation from nominal roll is large enough at any other time to permit a north-south orientation of the slit on the planet. Although the situation for Saturn is not nearly as extreme, observers should be aware of the tight scheduling constraints on observations requiring specific slit orientations. Additional information on the placement of a long slit on extended sources can be found in [Section 12.8](#).

Observers should also be aware that other operational constraints, such as the lack of suitably positioned guide stars, may place additional restrictions beyond those listed above on the range of orientations that are available for a particular observation.

12.8 Special Considerations for Extended Targets

Special care should be taken when determining the placement of a long slit on an extended source. Observers should take into account the following:

- **Slit lengths using the MAMA in First-Order Spectroscopy:** Although the full 52 arcsecond length of the long slits is imaged on to the CCD, light from only a portion of these slits reaches the MAMA detector. Twenty-five arcseconds are available for G230L and G140L, and 28 arcseconds can be used for G230M and G140M. See [Table 4.1](#) and [Section 4.2.2](#) for details of these apertures.
- **Fiducial Bars in the Long Slits:** The STIS long slits have fiducial bars which will block light from two regions along the length of the slit. [Section 13.2.6](#) and [Figure 13.1](#) describe the bars and their location.
- **Pseudo-Aperture Positions:** Choosing one of the pseudo-apertures described in [Section 4.2.3](#) will result in the target being off-center in the aperture.
- **Offset of G140L and G140M Spectra to Avoid the Repeller Wire:** First-order MAMA spectra in these modes are shifted by ~ 3.25 arcseconds to avoid the shadow of the repeller wire ([Section 7.6](#)). These shifts are done by adjusting the grating angle and so the spectrum is shifted on the detector, even though the target remains at the requested location in the aperture.
- **Monthly Offsets of First-Order MAMA Spectra:** Monthly offsets of up to about ± 1 arcsec are applied to both FUV and NUV first-order spectra ([Section 7.6](#)).

12.9 Parallel Observing with STIS

12.9.1 Coordinated Parallels: Using STIS in Parallel with Other Instruments

The second Servicing Mission installed solid-state data recorders on *HST*. The volume capacity of these recorders is roughly ten times that of the mechanical tape recorders in use for Cycles 1 through 6. Coupled with changes to the ground system and the flight software of the second-generation instruments designed to fully exploit this capability, this translates into a greatly increased capability for parallel observing.

STIS can be used to observe simultaneously with ACS, COS, WFC3, or FGS. [Figure 3.2](#) shows the *HST* field of view following the installation of COS and WFC3 during the *HST* Servicing Mission 4. STIS, ACS, COS, and WFC3 are shown, with their fields of view drawn to scale, in their relative focal plane positions. The three STIS cameras share a common field of view; only one can be used at a time.

The policy for proposing for parallel observations and technical advice on parallel observing are provided in the [Call for Proposals/Phase II Proposal Instructions](#). We remind you that there are two types of parallel observations:

- Coordinated parallels, in which you explicitly link the taking of exposures in parallel to your own prime scientific exposures.
- Pure parallels, in which exposures are taken in parallel with other observers' prime exposures. For Cycle 31 only pure parallel proposals using WFC3 or ACS CCDs will be considered by the TAC. See the [HST Call for Proposals](#) for more details.

Both coordinated and pure parallels must be explicitly proposed in Phase I. Implementing parallels requires significant resources; only those recommended by the TAC process will be implemented. If you are considering coordinated parallels, you may wish to consider constraining the orientation of *HST*, to place an object of interest in the parallel instrument's field of view. `ORIENT` constraints do affect observation scheduling, however, and should not be entered lightly (see [Chapter 11](#)).

12.9.1 Coordinated Parallels: Using STIS in Parallel with Other Instruments

Observations for which STIS is the parallel instrument are likely to be most useful when the full STIS field of view is used. If you wish to use a small slit, then STIS should be used as prime, and the other imaging instruments used in parallel with it.

If STIS is used as the secondary instrument in coordinated parallel observations, the STIS exposures cannot contain both external and internal exposures. Assuming the first exposure is external, all STIS exposures will be declared external. Therefore no internal exposures are allowed. This includes any user-specified internals, such as fringe flat fields, as well as automatic internals, such as auto-wavecal. If STIS is used as the prime instrument, this restriction does not apply.

For coordinated parallels where STIS is prime, automatic wavecalls occur during the visibility period—not during occultation. Since many CCD observations request `CR-SPLITS`, in general, this is not an impact for STIS CCD coordinated parallels. However for long MAMA exposures, auto-wavecalls that would have occurred during occultation in the absence of coordinated parallels are now shifted into the visibility period. This reduces the time available for science exposures. In addition, the buffer management overhead associated with the last MAMA science exposure now occurs prior to the auto-wavecall, further reducing the time available on target.

CCDFLATs for fringe correction of long wavelength CCD exposures can be taken in the same orbit as the coordinated parallel and forced into the occultation period when the prime STIS CCD exposures fill the visibility period. The CCDFLAT exposures are required to be specified outside the Prime + Parallel Group. However, they should be specified immediately after the last parallel exposure and they can be grouped as a non-interruptible sequence with the Prime + Parallel Group by highlighting both the Prime + Parallel Group and the CCDFLAT exposures then selecting Edit-Group-New Sequence in the **APT** menu toolbar and specifying that the CCDFLAT sub-exposures occur during the same orbit as the STIS observation they will correct.

The MAMA detectors cannot be used for pure parallel observing. For Cycle 31, coordinated parallels will not be allowed with STIS MAMA imaging modes and the STIS NUV-MAMA PRISM mode. However, coordinated parallels will be allowed with other STIS MAMA spectroscopic modes, provided that an explicit `ORIENT` is specified and precise RA and Dec coordinates for the parallel field are given.

The MAMA detectors are subject to bright object protection limits; see [Section 2.8](#).

Three types of STIS exposures which have particular scientific utility with STIS as the parallel instrument are:

- Optical imaging taking advantage of the ability to go deep very fast with the 50CCD wide-open mode.
- Optical slitless spectroscopy.
- UV slitless spectroscopy (available only for coordinated parallels with exact `ORIENT` specification).

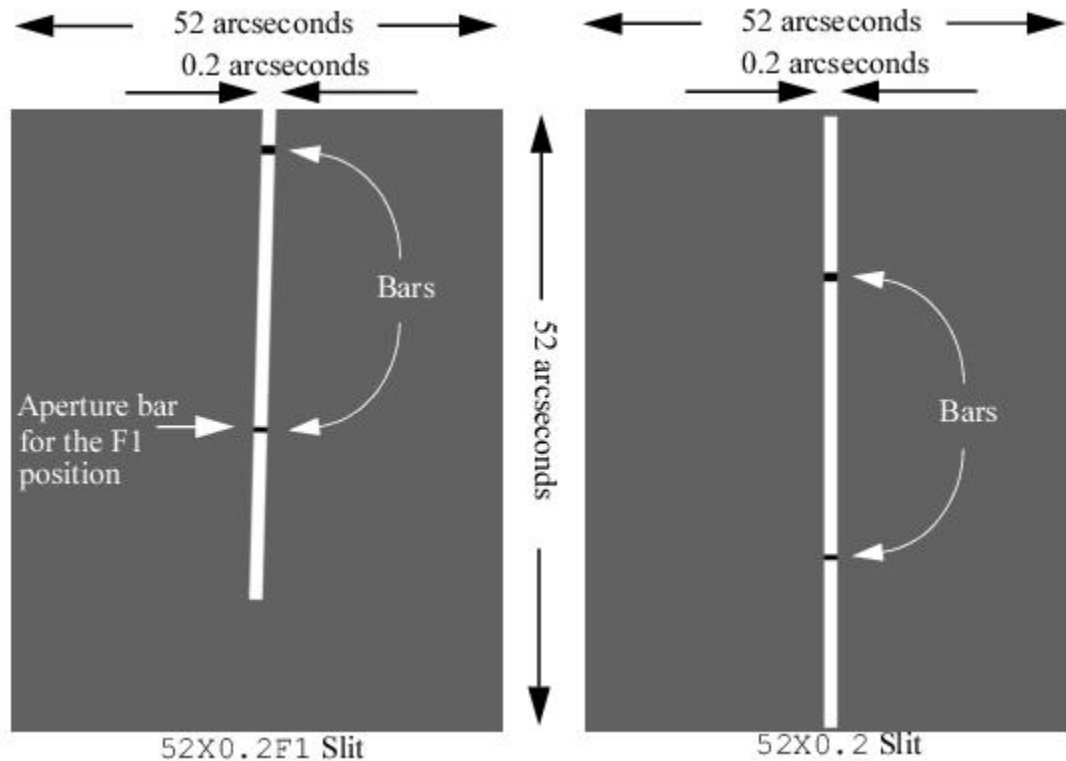
12.10 Coronagraphic Spectroscopy

STIS offers the capability to perform spectroscopic observations with occulting bars located in the long slits, and imaging observations with occulting bars in the coronagraphic mask 50CORON. Coronagraphic imaging is described in detail in [Section 12.11](#).

Barred Spectroscopy

The 52X0.2F1 aperture is the same physical slit as 52X0.2 with the target centered on the smaller of the two occulting bars (i.e., 0.5 arcseconds), instead of at the center of the 52X0.2 long slit. When this aperture is specified the slit wheel is rotated slightly to bring the bar into the center of the detector's field of view. This results in a tilt of 1.30° with respect to AXIS2 (i.e., the spatial axis perpendicular to the dispersion). Also, the full 52 arcseconds length of the long-slit field of view is decreased by about 20% for CCD spectroscopy.

Figure 12.5: A cartoon illustrating the 1.30° tilt of the 52x0.2F1 aperture.



This occulting bar is well suited to scientific programs conducting spectroscopy of faint extended material around a bright central source. Typical examples of such a program include QSO host galaxies, dynamics of jets in young stellar objects, spectroscopic characterization of circumstellar disk material, and spectroscopy of resolved binaries and companions. Observers performing barred spectroscopy should be sure to consult [Section 13.7.3](#). Spectroscopic observations with the 0.5 arcsecond occulting bar are limited to first-order spectroscopic modes.

Aperture 52X0.2F1 refers to the occulting bar itself, while 52X0.2F1-R represents a reference position offset from the bar. The reference aperture was designed to allow the observer to pickup on the target prior to moving it behind the occulting bar. But because pickups are not recommended for apertures larger than 0.1 arcsecond in width, the 52X0.2F1-R is no longer used. The occulting bar is even wider (0.5 arcsecond), so a simple ACQ exposure should suffice to center the target in the 52X0.2F1 aperture.

[Table 12.5](#) below shows the complete set of aperture names and their application for the 0.5 arcsecond fiducial bar on the 52x0.2 slit. An example of an acquisition into the 52X0.2F1 aperture is provided in [Chapter 8](#).

Table 12.5: Aperture Names and Applications on 52x0.2 Slit.

| Aperture Name | Description | Destination | Application |
|---------------|--------------------------------|--------------------------|-------------------------|
| 52x0.2 | Slit (width=0."2, length=52"). | Target centered in slit. | Long-slit spectroscopy. |

| | | | |
|------------|---|--|---|
| 52X0.2F1 | Slit (width=0."2, length=52"). Fiducial=0."5. | Target centered in slit and located under fiducial bar. | Locates target under bar ready for occulted observation. |
| 52X0.2F1-R | Slit (width=0."2, length=52"). Fiducial=0."5. Reference point off-fiducial. | Target centered in slit at reference position, offset from fiducial bar. | Locates target at reference position ready for pickup in slit, but is no longer in use. |

There are two important ramifications you should be aware of when using the 52X0.2F1 aperture: (1) ORIENT specification and (2) fringing correction.

Specifying ORIENT with the 52X0.2F1 Aperture

The ORIENT special requirement parameter is a specified position angle of the orientation reference vector U3, which is offset by 45° from the STIS detector spatial axis (AXIS2), in the direction North through East. Given a position angle on the sky of θ and taking into account the additional 1.30° offset for the 52X0.2F1 aperture (see [Figure 12.5](#)):

ORIENT = $\theta + 46.30^\circ$
or
ORIENT = $\theta + 226.30^\circ$.

For example, if we want to place the STIS 52X0.2F1 aperture along the jet of M87 (the example in [Figure 11.10](#) for a standard slit), we would do the following. Given a position angle of 110° on the sky:

ORIENT = $110^\circ + 46.30^\circ = 156.3^\circ$
or
ORIENT = $110^\circ + 226.30^\circ = 336.3^\circ$.

Correcting Fringing for the 52X0.2F1 Aperture

The STIS CCD shows fringing for wavelengths longward of 7000 Å with the G750L and G750M gratings, limiting the signal-to-noise that can be obtained in these modes. The fringing is caused by interference of multiple reflections between the two surfaces of the CCD. (See [Chapter 7](#) for details.) The recommended way to correct for fringing is by using contemporaneous fringe flats in conjunction with your science observations. Contemporaneous flat-field exposures need to be budgeted in the Phase I time request and specified more fully during the Phase II proposal generation process with APT. Section 13.11.2, entitled "Target_Name=CCDFLAT", of the [HST Phase II Instructions](#) provides a description of the parameter settings necessary to obtain contemporaneous flat-field exposures. It is the observer's responsibility to include contemporaneous flat fields in their Phase II proposals.

For spectra of point sources, contemporaneous fringe flats are normally taken using a short slit which is concentric with the long slit used for the science exposures. When point source fringe flats are taken at or near a standard aperture position near the center of the detector, the best alignment between science image and fringe flat will usually be for fringe flats taken using the 0.3x0.09 aperture. In the special case of the 52x0.2F1 aperture, however, we recommend obtaining long slit fringe flats to fully sample the PSF, since the spatial coverage of the short slit is only a few CCD pixels larger than that of the occulting bar of the 52x0.2F1 slit. A short slit fringe flat does give a somewhat better fringe correction for point sources than a long slit fringe flat. Consequently, if you are also taking an unocculted image of your star with the 52x0.2 aperture, we recommend obtaining a short slit flat as well as a long slit flat to rectify that image.

Optimization of the instrument configuration for the acquisition of fringe flats, the subsequent data reduction, and fringing analysis are described in more detail in a series of STIS Instrument Science Reports and in the *STIS Data Handbook*. [STIS ISR 1997-15 \(Revision A\)](#) provides a general overview of fringing. [STIS ISR 1997-16](#) discusses fringing in spectra of extended sources. [STIS ISR 1998-19 \(Revision A\)](#) discusses fringing associated with point sources, fringing analysis, and details related to the 52x0.2F1 aperture. [STIS ISR 1998-29](#), [STIS ISR 2021-01](#), and the [stistools defringe documentation](#) provide detailed descriptions of the STIS tasks (`normspflat`, `mkfringeflat`, `defringe`, and `prepspec`) in the `stistools` package that use contemporaneous flat-field images to remove infrared (IR) fringing from STIS G750L and G750M spectra. [Section 3.5.5](#) of the *STIS Data Handbook* provides guidance and updates to the instructions for removing near-infrared (NIR) fringing presented in [STIS ISR 1998-29](#) and [STIS ISR 2021-01](#).

12.11 Coronagraphic Imaging - 50CORON

STIS has a single coronagraphic mask aperture for direct imaging. The aperture (50CORON) contains two occulting bars and two intersecting wedges and is shown in [Figure 12.6](#). This illustration of the coronagraphic aperture is derived from an on-orbit lamp flat. The approximate positions of the predefined aperture locations are marked. The wedges vary in width from 0.5 to 3.0 arcseconds over their 50 arcseconds length, while the larger rectangular bar (BAR10) measures 10 by 3 arcseconds. The small occulting finger on the right (BAR5) was damaged during assembly of STIS and was not used until Cycle 25, when its performance was tested. Now, the STIS team recommends using BAR5 as a fully supported capability for coronagraphic science. See [STIS ISR 2017-03](#) for more details. The entire coronagraphic aperture measures 50×50 arcseconds, slightly smaller than the size of the unobstructed CCD aperture. The parallel readout of the CCD is along the `AXIS2` direction, and heavily saturated images will bleed in this direction (vertically in this figure). Saturation near the top of the detector can result in serial transfer artifacts that produce tails in the `AXIS1` direction. The [December 2013 STScI Analysis Newsletters \(STAN\)](#) discusses additional details of this effect.

The aperture cannot be combined with a filter and so, when used with the CCD, yields a bandpass of $\sim 2000\text{--}10,300$ Å. See [Section 5.2.2](#) for the spectral properties of the images obtained. A number of locations on the occulting masks have been specified, to correspond to widths of 2.75, 2.5, 2.0, 1.75, 1.0, and 0.6^1 arcseconds on each wedge. The mask is not available for use with the MAMA detectors due to concerns about bright-object protection of the MAMAs.

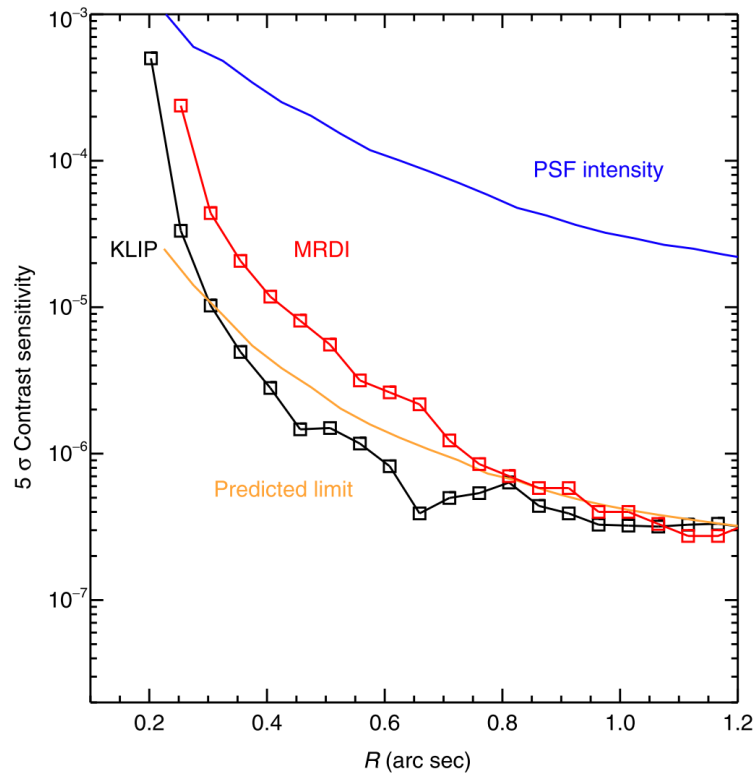
Figure 12.6: Design of the STIS Coronagraphic Mask.



In combination with the option of a coronagraphic mask, there is a limited amount of apodization via a Lyot stop which masks the outer perimeter of the re-imaged exit pupil. Consequently, diffraction from the secondary mirror assembly and the telescope spider is not apodized. The STIS coronagraphic imaging facility is well suited to imaging problems involving faint material surrounding a relatively bright source. Typical examples include circumstellar disks, such as β Pictoris, and the host galaxies of bright QSOs.

When imaging without the coronagraph, the CCD long wavelength halo from the central source is present as well as window reflection ghosts. In practice the coronagraph provides substantial additional suppression of the PSF wings, especially at wavelengths $>8000 \text{ \AA}$, where the halo of light scattered within the CCD itself dominates the far wings of the PSF. Observing with the coronagraphic aperture locations in concert with post-processing and the use of multiple spacecraft orientations can further improve contrast by orders of magnitude. [Figure 12.7](#), found in the [JATIS article by Debes, Ren, & Schneider \(2019\)](#), shows STIS' contrast performance for point sources in the visible interior to 1 arcsecond using the BAR5 aperture location and classical azimuthal differential imaging (ADI) or Karhunen-Loève Image Projection (KLIP) post processing. At distances beyond 6", contrasts of 10^{-9} are possible with STIS and other coronagraphic aperture locations. Due to STIS' broad bandpass, it still retains sensitivity to both stellar and substellar objects. For more information see the [JATIS article by Debes, Ren, & Schneider \(2019\), "Pushing the limits of the coronagraphic occulters on Hubble Space Telescope/Space Telescope Imaging Spectrograph"](#).

Figure 12.7: PSF Suppression with the STIS Coronagraph.



Due to the very broad bandpass of the unfiltered STIS CCD, the STIS coronagraphic PSF shape is very strongly dependent on the target's spectral energy distribution. When using the coronagraph to look for a point source or a localized structure that is strongly asymmetric (such as an edge-on disk), the best approach is to observe the target star at a minimum of two and preferably three different roll angles, and then compare the images to separate the stellar PSF from the real circumstellar structure. When looking for more diffuse or symmetric material, it will be necessary to use a separate comparison star. Here it is important to match the colors of the target and comparison star as closely as possible. We suggest that all the broadband *UVBRI* color differences be less than 0.08 magnitudes. In either case, it is also essential to compare stars at the same location on the coronagraphic mask.

Breathing and focus differences will also significantly affect the quality of such a subtraction, but the observer has only limited control over these parameters. The best alignment of STIS PSF images tends to occur when comparing images taken in the same part of adjacent orbits. When observing the same star at multiple roll angles, it is therefore often useful to do a sequence of adjacent one-orbit visits, each at a different roll angle. As large departures from the nominal roll angle can also affect the PSF shape, it may be helpful to keep the roll changes as small as is consistent with the structure to be imaged. When observing a separate comparison star, it is best if possible to observe a star in the same part of the sky, during an adjacent orbit, and at the same angle relative to the nominal spacecraft roll, as the observations of the prime target, but remember that picking a comparison star with a good color match must be the first priority.

An alternative strategy would be to take observations separated by several days, but constrained so that each observation is done at the nominal spacecraft roll. When very large roll changes or several orbit-long visits are required, this might give better results than doing the observations in adjacent orbits, but there is very little operational experience using this approach.

Attempting to observe multiple coronagraphic targets or the same target at different roll angles in a single orbit is not recommended. The overheads required to do separate visits in a single orbit are very large, and the PSF alignment between different parts of the same orbit are usually inferior to that obtained between the same part of adjacent orbits.

Coronagraphic images of stars of various colors have been obtained as parts of calibration programs 7151, 7088, 8419, 8842, and 8844 and are available from the archive. These images may be useful in providing comparison objects or in estimating exposure times. However, for the best PSF subtraction, we still recommend that each coronagraphic program include its own tailored PSF observations.

In planning any observing program with the 50CORON aperture, observers should carefully consider the required orientation of the target. The telescope's V2 and V3 axes are at 45° to the STIS AXIS1/AXIS2 coordinate system (see [Figure 11.1](#)) and so diffraction spikes further reduce the unocculted field of view.

A series of apertures has been defined for the coronagraphic mask so that targets can be placed on the 3 arcseconds wide bar and 5 locations on each of the two wedges. These apertures are summarized in [Table 12.6](#) below. We defined a special coronagraphic acquisition technique for placing stars at these predefined locations. This involves performing a bright-target acquisition with a filtered aperture, followed by a slew to the chosen location on the coronagraphic mask. An example of an acquisition into one of the bars on the 50CORON aperture is provided in [Section 8.5.6](#).

An outsourced Cycle 20 STIS calibration program, 12923 (PI: Gaspar), investigated new aperture locations near the corners of the coronagraphic bar (BAR10) as well as the "bent finger" occulter (BAR5). These new positions allow high contrast imaging at a minimum working angle of 0.15 arcseconds, with demonstrated performance to ~0.2 arcseconds—roughly 3λ/D, and close to a factor of two better than WEDGEA0.6. The BAR10 rounded-corner aperture is currently available-but-unsupported. Even though there are no current plans to incorporate this aperture into **APT**, it can be implemented using POS-TARGs from other aperture positions. BAR5 is now a currently-supported mode and is incorporated into **APT**. A summary of the initial results of this program, as well as detailed suggestions on how to implement observations using these new aperture positions, is available within [STIS ISR 2017-03](#) ("Enabling Narrow(est) IWA Coronagraphy with STIS BAR5 and BAR10 Occulters") and additional information on BAR5 may be found [here](#).

Users wishing to achieve a particular contrast are encouraged to read Sections 2.3-2.5 of [Debes, Ren, & Schneider 2019](#) (JATIS article) in order to predict the possible contrast performance for a star of a given magnitude. See the STIS Coronagraphic Visualization Tool available on the [Data Analysis and Software Tools page](#) for help with planning and preparing STIS coronagraphic observations.

Table 12.6: Apertures for Coronagraphic Mask.

| Proposal Instructions Aperture Name | Description |
|--|---|
| 50CORON | Coronagraphic mask—clear aperture in center of the field of view |
| BAR5 ² | Narrow occulter with a width of 0.3" |
| BAR10 | Coronagraphic bar of width 3.0" |
| WEDGEA2.8 | Coronagraphic Wedge A (vertical in AXIS1) Position 1: bar width = 2.75" |

| | |
|------------------------|---|
| WEDGEA2.5 | Coronagraphic Wedge A (vertical in AXIS1) Position. 2: bar width = 2.5" |
| WEDGEA2.0 | Coronagraphic Wedge A (vertical in AXIS1) Position 3: bar width = 2.0" |
| WEDGEA1.8 | Coronagraphic Wedge A (vertical in AXIS1) Position 4: bar width = 1.75" |
| WEDGEA1.0 | Coronagraphic Wedge A (vertical in AXIS1) Position 5: bar width = 1.0" |
| WEDGEA0.6 ¹ | Coronagraphic Wedge A (vertical in AXIS1) Position 6: bar width = 0.6" |
| WEDGEB2.8 | Coronagraphic Wedge B (vertical in AXIS2) Position 1: bar width = 2.75" |
| WEDGEB2.5 | Coronagraphic Wedge B (vertical in AXIS2) Position 2: bar width = 2.5" |
| WEDGEB2.0 | Coronagraphic Wedge B (vertical in AXIS2) Position 3: bar width = 2.0" |
| WEDGEB1.8 | Coronagraphic Wedge B (vertical in AXIS2) Position 4: bar width = 1.75" |
| WEDGEB1.0 | Coronagraphic Wedge B (vertical in AXIS2) Position 5: bar width = 1.0" |

¹ The 0.6 arcsecond location is on wedge A only and was added in Cycle 12.

² The BAR5 location was first supported in Cycle 24.

12.12 Spatial Scans with the STIS CCD

[12.12.1 Why Use Spatial Scans with STIS?](#)

[12.12.2 Possible STIS Spatial Scan Use Cases](#)

[12.12.3 Using STIS Spatial Scans](#)

Spatial scanning, which is a supported mode for WFC3 observations (see [WFC3 ISR 2012-08: Considerations for using Spatial Scans with WFC3](#)), can also be used with the STIS CCD as an available-but-unsupported mode. For a bright target this can potentially allow signal-to-noise levels of perhaps as high as a thousand to one to be obtained, even at wavelengths where the STIS CCD is affected by strong IR fringing. This can be especially valuable at wavelengths that are also strongly affected by telluric features in ground-based spectra. Many such regions can be observed with the STIS *G750M* at wavelengths up to 10140 Å (1.014 μm), with a resolving power close to 10000, allowing weak features such as diffuse interstellar bands to be observed with an accuracy not achievable by any other means. High-S/N ratio time series observations may also be obtained with spatial scans (e.g., for studies of exoplanets and their atmospheres).

Spatial scans are currently not available with STIS MAMA observations.

12.12.1 Why Use Spatial Scans with STIS?

Trailing an external point source in the spatial direction during a first-order STIS CCD spectral observation can spread the target's light over a much larger area of the detector than would be the case for a simple pointed observation. This has several potential advantages:

- Many more photons can be collected before reaching the detector full well saturation limit.
- Spreading the light over a larger fraction of the detector area will better average over flat field variations.
- Trailing along a long slit can result in IR fringing patterns that are significantly closer to the fringing patterns produced by the available contemporaneous tungsten lamp flats, leading to much improved near-IR fringe removal.
- A wider variety of algorithms can potentially be used to detect and remove hot pixels and cosmic rays.

However, spreading the source light over a larger area of the detector can also significantly increase the dark current and read-noise in the extraction region, so the advantages of spatially scanned spectra will be most significant for very bright targets.

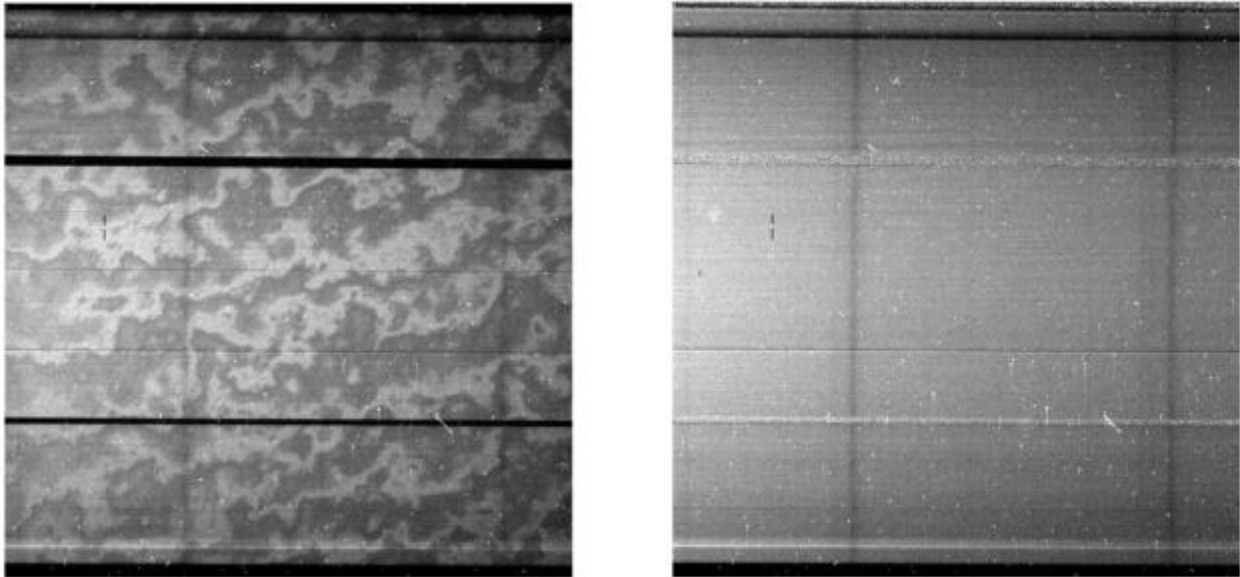
12.12.2 Possible STIS Spatial Scan Use Cases

Trailing along a Narrow Slit to Maximize S/N and Fringe Removal

The initial on-orbit applications of this technique were performed by *HST* programs 14705, 15429, and 15478, as reported by Cordiner et al. (2017, *Apj*, 843, L2; 2019, *Apj*, 875, L28). Signal-to-noise ratios in excess of 600:1 per resolution element were achieved for G750M spectral observations of moderately reddened stars near 9300 Å, enabling the detection of weak interstellar absorption lines attributed to C₆₀⁺. In this case, the narrow 52X0.1 aperture was used for both the trailed external observations and the internal lamp flats. As the STIS PSF near that wavelength is relatively wide compared to the slit, the fringing pattern from the lamp and the trailed external target are very similar, which greatly facilitates the fringing correction.

In [Figure 12.8](#), we show an example of one of the trailed spectral observations before and after a simple division by the contemporaneous fringe flat. The very effective removal of the fringing pattern allows detection of much weaker spectral features (vertical dark bands in the image) than would be possible for a simple pointed image.

Figure 12.8



The images above show the trailed $G750M$ exposure `od9d02vcq` of a bright star from program 14705, before (left) and after (right) dividing by a contemporaneous fringe flat image. In these images, wavelength increases to the right, and the star was scanned in the vertical direction along the length of the 52×0.1 aperture. This is highly effective at removing the fringing pattern, but does reveal that instability in the trail rate results in noticeable flux variations as a function of the position along the trail direction.

Trailing along a Wide Slit to Maximize Photometric Repeatability

While use of a narrow slit does ensure the best fringe removal and is recommended for programs aimed at measuring the absolute equivalent widths of weak features, it does compromise the absolute flux calibration of the observations.

STIS special calibration program 15383 recently obtained scanned $G750L$ observations of the known exoplanet host star 55 Cnc, including scans in both the narrow 52×0.1 and the wider 52×2 apertures. The second visit in the program included a series of repeated 12" long scans along the wider aperture, over the course of two successive orbits, that have yielded encouraging results on the absolute repeatability of flux measurements obtainable with scanned $G750L$ observations. Application of custom procedures for cosmic ray removal, the recently developed python defringe tool, and a de-trending procedure commonly used for analyses of spectral time series observations (e.g., [Sing et al. 2011, A&A, 527, A73](#)) yielded an rms scatter in the resulting total fluxes of order 30 ppm. That is comparable to the best precision previously obtained for time series photometry with *HST* via the more traditional technique of taking saturated spectra at a fixed pointing ([STIS ISR 1999-05](#)), which has commonly been used for transiting planet observations with STIS. Detailed analyses of the 15383 data are summarized in the [September 2020 STAN](#). A more detailed discussion, including results from a longer series of scans encompassing a transit of the super-Earth 55 Cnc e obtained under follow-on program 16442, will be given in a paper in preparation.

Variations in the trail rate are also visible during the wide aperture scans, and this will probably hinder any use of trailed STIS observations to model source flux variations during an individual scan; it remains to be determined what limits this may place on the accuracy and repeatability of the integrated flux for individual scanned exposures.

12.12.3 Using STIS Spatial Scans

As STIS spatial scans are an "available-but-unsupported" mode, only a limited amount of tuning has been done to optimize this mode. In brief, to scan along one of the long apertures, one must specify the starting location (in arcsec, relative to the aperture fiducial point; using the `POS TARG` special requirement), the scan rate (in arcsec s^{-1} ; see below), the scan orientation (nominally 90 degrees), the scan direction, and the total exposure time. The scan length is then given by the product of the scan rate and the exposure time; the Y coordinate of the starting location should be specified to position the scan as desired on the detector. Currently, "forward" scans place the spectra at close to the intended position, but there is apparently a timing error in the implementation of "reverse" scans that result in them being offset on the detector to higher than intended Y locations, with larger offsets at higher scan rates. As a result, we currently recommend that STIS observers use only "forward" scans and avoid both the "reverse" and "round-trip" options. Because different apertures can map to slightly different positions on the detector, when scanning up the 52X2 and doing fringe flats with the 52X0.1, the procedure should be to first peak up in the 52X0.1, and then add an X component to the `POS TARG` for the 52X2 scan to correct for the -0.049241721 " difference in SIAF X locations between the two apertures.

Visit 01 of program 15383 took scanned imaging observations to check the alignment of the default scan angle with the science apertures. This visit suggested a small correction to the default scan angle of $\sim +0.065$ degrees, but the repeatability of this correction has yet to be verified.

For more information about proposing for spatial scanning using STIS, please see [Section 6.3.1 in the Phase II Proposal Instructions](#).

Using the ETC to Estimate Scan Parameters

Currently the STIS **ETC** does not support calculations for scanned observations. However, to achieve the expected flat-fielding improvements, it is essential to avoid saturating the detector.

To estimate the expected peak flux levels, we recommend beginning with a spectroscopic **ETC** calculation of a pointed observation with `CR-SPLIT=1` for the requested total exposure time of an individual scan with all other parameters set as they will be for the actual observation. Then go to the "Table of Source and Noise Counts per Pixel" on the **ETC** results page. In this table, "pixel" refers to a pixel in the extracted 1D spectrum which is actually a sum in the original 2D image over 1 pixel in the dispersion direction and the extraction height (7 pixels by default for the STIS CCD), in the spatial direction, while the "counts" given in this table are always in units of electrons, regardless of the gain setting. The source counts/per pixel in this table have been scaled by the wavelength dependent fraction, E , of the total source flux at that wavelength that is expected to fall within the extraction height, and this excluded light in the wings of the PSF will contribute to the counts accumulated during the scan. For the [G750L](#) grating the encircled energy fraction in the 7 pixel region varies from ~ 0.8 at 6000 Å, to about 0.6 at 10000 Å. If S is the "Source Per Pixel" in the **ETC** table and L is the length of the scan in pixels (the scan length in arcseconds divided by 0.0508"/pixel), then the approximate local source count rate in electrons per second per pixel in the scanned 2D image will simply be $S/E/L$; this is the number that should be compared to the saturation limits.

Because the spectrum will be spread over a larger region of the detector than was assumed in the **ETC**, for obtaining a good S/N estimate for fainter targets it will also be necessary to scale the dark current, sky background, and the read-noise squared from the values calculated for the default extraction height to the actual area to be used in the final extraction. If these are significant compared to the source count rate, then the final signal-to-noise should be manually computed using the equations in [Section 6.4](#). If the read-noise and dark current are negligible compared to the Poisson noise of the source counts, then the S/N estimate in the original **ETC** calculation is probably as good an approximation as any available.

We can take as a concrete example one of the series of 218.1 s exposures done in the 2nd and 3rd orbits of visit 11 of 15383. The scan rate there was set to 0.055 arcsec/sec, which yielded a scan length of 12 arcseconds or about 236 pixels. An **ETC** calculation for a pointed exposure with the same parameters is given by <http://etc.stsci.edu/etc/results/STIS.sp.1044073/>. At 5828.9 Å, the tabular data page for this **ETC** calculation gives about 1.48e7 electrons as the "source per pixel". For the scanned observation, we would then predict about $1.48e7/0.8/(12/0.0508) = 78317 e^-$, or for GAIN=4 about 19500 DN in each pixel of the FLT image. The contribution from the dark current is negligible, and examination of the FLT file for exposure ODQF11UOQ shows that the mean count rate in the column corresponding to this wavelength is indeed very close to 19500 DN, although the actual value fluctuates from row-to-row by up to 10% due to variations in the scanning rate during the observation. To account for scan rate variations, fringing effects, and other approximations in the **ETC** calculations, we recommend keeping the planned peak source counts for GAIN=4 STIS CCD observations below about 100,000 e⁻ in each pixel of the 2D image.

Setting Fringe-Flat Exposures for Spatial Scans

The supported `TARGET=CCDFLAT` exposures available in **APT** to provide tungsten lamp IR fringe flats have relatively modest default exposure times, intended to support the S/N requirements of pointed observations. Using this option for the fringe flats prohibits exposure times greater than the default values from being used.

Since scanned observations can collect many more photons per resolution element than is possible in pointed observations, it may sometimes be useful to take deeper tungsten lamp images than are supported with `TARGET=CCDFLAT`. This can be done when available modes are enabled by setting `TARGET=NONE`, and adding the special requirement `LAMP=TUNGSTEN`. It is then the responsibility of the user, however, to set the exposure and instrument parameters, as the default settings differ from those used with `TARGET=CCDFLAT`. Note also that **APT** does not recognize `TARGET=NONE` exposures as `CCDFLAT` exposures and will complain of missing fringe flats, whether or not the parameters are set correctly. This warning will be spurious, however, when the appropriate `TARGET=NONE`, `LAMP=TUNGSTEN` exposures are actually there. It is important to note that setting `TARGET=NONE` is an available-but-unsupported mode and will require scientific justification and approval.

The overhead on each individual tungsten lamp exposure can be significant, and it will often be significantly more efficient to take a few deep lamp exposures rather than a number of shorter ones using the `CCDFLAT` default times. Observers must be careful to not saturate the longer fringe flat exposures, however.

The fringing correction is very sensitive to the exact distribution of wavelengths falling on each pixel of the detector, and shifts in instrument alignment can cause noticeable changes over the course of a single visibility period. For this reason, the science and fringe-flat exposures should be accurately registered (e.g., if taken through different apertures), and it may sometimes be useful to intermingle fringe-flat lamp exposures with the external science exposures, even if this reduces the time available to observe the external target.

Chapter 13: Spectroscopic Reference Material

Chapter Contents

- 13.1 Introduction
- 13.2 Using the Information in this Chapter
- 13.3 Gratings
 - First-Order Grating G750L
 - First-Order Grating G750M
 - First-Order Grating G430L
 - First-Order Grating G430M
 - First-Order Grating G230LB
 - Comparison of G230LB and G230L
 - First-Order Grating G230MB
 - Comparison of G230MB and G230M
 - First-Order Grating G230L
 - First-Order Grating G230M
 - First-Order Grating G140L
 - First-Order Grating G140M
 - Echelle Grating E230M
 - Echelle Grating E230H
 - Echelle Grating E140M
 - Echelle Grating E140H
 - PRISM
 - PRISM Wavelength Relationship
- 13.4 Apertures
 - 52X0.05 Aperture
 - 52X0.05E1 and 52X0.05D1 Pseudo-Apertures
 - 52X0.1 Aperture
 - 52X0.1E1 and 52X0.1D1 Pseudo-Apertures
 - 52X0.2 Aperture
 - 52X0.2E1, 52X0.2E2, and 52X0.2D1 Pseudo-Apertures
 - 52X0.5 Aperture
 - 52X0.5E1, 52X0.5E2, and 52X0.5D1 Pseudo-Apertures
 - 52X2 Aperture
 - 52X2E1, 52X2E2, and 52X2D1 Pseudo-Apertures
 - 52X0.2F1 Aperture
 - 0.2X0.06 Aperture
 - 0.2X0.2 Aperture
 - 0.2X0.09 Aperture
 - 6X0.2 Aperture
 - 0.1X0.03 Aperture
 - FP-SPLIT Slits 0.2X0.06FP(A-E) Apertures
 - FP-SPLIT Slits 0.2X0.2FP(A-E) Apertures
 - 31X0.05ND(A-C) Apertures
 - 0.2X0.05ND Aperture
 - 0.3X0.05ND Aperture
 - F25NDQ Aperture
- 13.5 Spatial Profiles
 - First-Order Spatial Profiles
 - Echelle Spatial Profiles
- 13.6 Line Spread Functions

- First-Order Line Spread Functions
- Echelle Line Spread Functions
- 13.7 Spectral Purity, Order Confusion, and Peculiarities
- 13.8 MAMA Spectroscopic Bright Object Limits

13.1 Introduction

The information in this chapter will help you select your grating configuration and observing slit and determine your observing plan (e.g., total required exposure time, and number of exposures). This chapter is basically organized by *grating and slit* (corresponding to *Spectral Element and Aperture* in the [Phase II Proposal Instructions](#).)

For each grating mode the following are provided:

- A brief description of the grating mode's specifications, including recommended uses and special considerations.
- The central-wavelength settings and range of wavelength covered at each setting, together with the dispersions and plate scales.
- Plots and tables of sensitivities and throughputs as a function of wavelength.
- Plots of signal-to-noise as a function of $V+STMAG_{\lambda}$ (the color-dependent correction from V magnitude to $STMAG$ at wavelength λ), F_{λ} , and exposure time.

For each slit the following are provided:

- A brief description of the slit's specifications, including recommended uses and special considerations.
- Plots and tables of relative throughputs as a function of wavelength.

For representative grating-slit combinations we provide:

- Tables of encircled energy for the flux in the default pipeline extraction aperture, and the percent flux contained in the peak pixel.
- Plots of representative spatial (perpendicular to the dispersion) profiles at selected wavelengths.
- Line spread functions and FWHM as a function of wavelength.

In addition,

- [Section 13.8](#) provides a summary of the screening brightness limits for the MAMA spectroscopic modes.

The sensitivities and dark currents adopted for calculating the figures and tables used in this chapter were projected before SM4 for a date of August 2008. Actual values for a given cycle will differ slightly. For the most up-to-date values, please consult the STIS [ETC](#).

The next section explains the plots and tables found in the grating sections in this chapter.

13.2 Using the Information in this Chapter

- [13.2.1 Wavelength Ranges](#)
- [13.2.2 Grating Sensitivities and Throughputs](#)
- [13.2.3 Signal-To-Noise Plots](#)
- [13.2.4 Plate Scales](#)
- [13.2.5 Apertures](#)
- [13.2.6 Fiducials on Bars](#)
- [13.2.7 Spatial Profiles](#)
- [13.2.8 Line Spread Functions \(Instrumental Profiles\)](#)

13.2.1 Wavelength Ranges

The complete wavelength range for each grating, as well as the wavelength coverage per tilt for the scanned grating modes, is shown in a table and graphically. The exact wavelengths at the ends of the ranges for the MAMA detectors will depend on the MAMA monthly offsetting. This procedure shifts the spectrogram so that it falls on slightly different parts of the MAMA detectors from month to month in order to minimize charge depletion in the microchannel plates and can cause the loss of ± 30 pixels from either end of the spectrogram in dispersion (AXIS1) and ± 80 pixels in cross-dispersion (AXIS2). Spectral format plots of the STIS grating and central wavelength settings are available to download from the STIS webpage under "[Instrument Design > Gratings/Prism](#)."

Monthly offsetting for the echelles was discontinued in August 2002. Prior to that, the monthly offsetting projected the extreme orders of formats off of the detector in some months. The wavelength ranges for the echelle gratings given in this chapter are those routinely falling on the detector since the discontinuation of the monthly offsets for the echelle modes, as measured from data obtained for the Cycle 17 Calibration Program 11866. The wavelength ranges of archival data taken before August 2002 may differ from those values given here. Users should also be aware that the past monthly offsets have influenced whether or not a given echelle order has a good sensitivity correction; therefore, not all echelle orders available on the detector will be flux calibrated. Users may refer to [STIS ISR 2012-01](#) for more information on the affected orders. Some of these affected orders are expected to be added back to the flux calibrated data products as the [flux recalibration effort](#) is completed. A recent example is order 86 for E140M ([STIS ISR 2022-04](#)).

Wavelengths in this handbook and in STIS data products are always measured in vacuum conditions.

13.2.2 Grating Sensitivities and Throughputs

This chapter contains plots and tables of sensitivities and throughputs for each grating mode. [Section 6.2](#) in the Exposure Time Calculation chapter explains how to use these sensitivities to calculate expected count rates from your source.

The total system¹ *spectroscopic point source sensitivity*, S_{λ}^p , has the unit:

counts/s/pix _{λ} per incident erg/cm²/s/Å for the MAMA and e⁻/s/pix _{λ} per incident erg/cm²/s/Å for the CCD, where:

- pix_λ = a pixel in the dispersion direction.
- counts refer to the total counts from the point source integrated over the PSF in the direction perpendicular to the dispersion (along the slit).

i Note that the spectroscopic point source sensitivity presented here does not include slit losses, CTI losses (on the CCD), or time-dependent or temperature-dependent variations. These corrections are made by pipeline calibration.

The spectroscopic diffuse source sensitivity, S_λ^d , has the units counts/s/ $\text{pix}_\lambda/\text{pix}_s$ per incident erg/s/cm²/Å/arcsec² for the MAMA and e⁻/s/ $\text{pix}_\lambda/\text{pix}_s$ per incident erg/s/cm²/Å/arcsec² for the CCD, where:

- pix_λ = a pixel in the dispersion direction.
- pix_s = a pixel in the spatial direction.

S_λ^p and S_λ^d are related through the relation:

$$S_\lambda^d \cong S_\lambda^p \times m_s \times W ,$$

where:

- m_s is the platescale in arcsec per pixel in the direction perpendicular to the dispersion.
- W is the width of the slit used in arcsec.

Here, we have assumed that the diffuse source has a uniform brightness over the area of interest and that the spectrum can be approximated as a continuum source. The throughput is defined as the end-to-end effective area divided by the geometric area of a filled, unobstructed 2.4 meter aperture (see [Chapter 6](#)).

i Note that the spectroscopic diffuse-source sensitivity presented here does not include CTI losses (on the CCD) or time-dependent or temperature-dependent variations. The last two corrections are made by pipeline calibration.

Tables of sensitivities and throughputs are given for a point source placed in the center of the largest clear aperture for each detector. Calibration data for measuring sensitivities and throughputs for a point source placed high on the CCD detector in the long-slit "E1" pseudo-apertures (see [Section 7.3.8](#)) were taken in Cycles 10 and 11. It was found that the overall low dispersion throughputs are decreased by 2-3%, and the medium dispersion throughputs are expected to show a similar reduction. The sensitivity plots give values for point and diffuse sources. In the plots in this chapter we show the diffuse source sensitivity for a 0.1 arcsec wide slit. For an extended continuum source,

S_{λ}^d scales directly with slit width, as above.

For the echelles, the sensitivities given were derived from fits of a smooth curve as a function of wavelength to the measured sensitivities at the central wavelength of each order (i.e., they do not include the effect of the echelle ripple). The [Spectroscopic Exposure Time Calculator \(ETC; see Chapter 6\)](#) will properly take the echelle ripple into account and should be used for more detailed S/N analysis.

Small but significant changes in the STIS sensitivity have been revealed by repeated observations of the same standard stars in the 52x2 slit. These changes are discussed in detail in [Section 7.2.4](#), and [Section 7.4.3](#), and the mean variations in sensitivity with time for some first order configurations are illustrated in [Figure 7.1](#) and in [Figure 7.15](#). Time- and temperature-dependent variations are discussed in [STIS ISR 2004-04](#) and the most recent measurements of these variations can be found in [STIS ISR 2017-06](#). The [ETC](#) accounts for the latest sensitivity trends, projected to the mid-point of the current HST Cycle.

13.2.3 Signal-To-Noise Plots

For each grating mode, a plot is provided to help you estimate the signal-to-noise (S/N) for a class of sources and a range of exposure times, corresponding to a fiducial taken at wavelengths near the peak of the responses. The fiducial wavelength is indicated in the ordinate label of each plot. To estimate signal-to-noise at alternate wavelengths, you can scale your source flux or magnitude by the relative sensitivities (or throughputs) at the wavelength of interest and at the fiducial. The point source plots show S/N as a function of F_{λ} and of V+STMAG(λ) for a range of exposure times; the

diffuse source plots show I_{λ} and V+STMAG(λ) per arcsec² for a range of exposure times. Using STMAG units is natural in this plot given that a particular STMAG value corresponds to a flux distribution with a constant value of F_{λ} . In producing these plots we assumed an average sky background (as described in [Chapter 6](#)) and the appropriate values for read noise and dark current for each detector. Note the following:

- The point source S/N has been calculated per two dispersion pixels and has been integrated over the PSF to contain 80% of the flux in the spatial direction.
- The point source S/N calculations assume the use of the 52x0.2 slit for the first-order modes and the use of the 0.2x0.2 slit for the echelle modes.
- The diffuse-source S/N is calculated with the 0.2 arcsecond wide slit and the assumption that the slit is fully filled by a diffuse continuum source. The S/N is given per 2 spatial pixels and 4 spectral pixels for the CCD and is given per 2 spatial pixels and 6 spectral pixels for the MAMA (these are the equivalent spectral resolution elements for these observations).
- For the CCD, the plots assume CR-SPLIT=2 and CCDGAIN=1.

- The different symbols in the S/N figures delineate regions where different sources of noise dominate. A particular source of noise (read noise for example) is presumed to dominate if it contributes more than half the total noise in the observations. Saturation is likewise indicated.
- The vertical dashed line indicates the MAMA bright object *observing limits*; if F_λ (or I_λ) exceeds the indicated value, the observation would exceed the observing limits (recall that the observing limits are at slightly higher count rates than the *screening* limits given in [Table 13.45](#)). For diffuse sources we indicate only the local rate limit, since the global limit is dependent on the source extent. If no line is seen on the plot, it indicates the limit is higher than the range of fluxes plotted.

These plots are meant to allow a general assessment of the feasibility of proposed scientific program. In situations requiring more detailed calculations (non-stellar spectra, extended sources, other sky background levels, full treatment of wavelength dependent sensitivity changes, etc.), we refer users to the STIS **ETC**, available at: <http://etc.stsci.edu/>.

Follow these steps to use the S/N plots:

1. Look up in [Table 13.1](#) the spectral type and wavelength region of interest of your target observation (e.g., G0 V @ 4300 Å). Interpolate in the table to get $STMAG_\lambda$.
2. Add the V magnitude of the target to the interpolated value of $STMAG_\lambda$ derived from the table.
3. Find the appropriate plot for the desired grating, and locate $V+STMAG_\lambda$ on the horizontal axis. Read off the S/N for the desired exposure time, or vice-versa. Alternatively use F_λ directly on the horizontal axis.
4. To get accurate values for repeated or CR-SPLIT exposures, one should use the sub-exposure

time when consulting the plot, and then multiply the resulting S/N by \sqrt{N} , where N is the number of sub-exposures to be averaged. Recall that these plots assume CR-SPLIT=2 for CCD observations.

We now give a sample S/N calculation using these plots. Consider a V = 18 star of spectral class B0 V, for which we want to derive the S/N for a 100 second CR-SPLIT exposure in G430L with the CCD. We look up the B0 V spectral class and interpolate in the table between 4000 Å ($STMAG_\lambda = -1.20$) and 4500 Å ($STMAG_\lambda = -0.78$) to obtain $STMAG_\lambda \sim -1$ at 4300 Å. We thus have $V+STMAG_\lambda = 17$. We look at [Figure 13.13](#) and find this value on the horizontal axis. We locate exposure time 100 and find $S/N \sim 10$. This exposure is well below the saturation lines in the plot, so saturation is not a concern.

13.2.4 Plate Scales

In the grating information section, the plate scale (units: arcsec/pix) is given in the table for each grating. The values used have been obtained from imaging observations and have been approximated at 0.05072 arcsec/pix for the CCD modes, and ~ 0.0246 and 0.0248 arcsec/pix respectively for the G140L and G230L MAMA modes (see [Section 14.6](#)). The other MAMA spectroscopy modes (G140M and G230M) operate at a lower magnification, yielding a cross-dispersion plate scale of ~ 0.029 arcsec/pix. Anamorphic magnification by the gratings further modifies the plate scales in the dispersion direction, particularly for the echelle modes. The relevant scales in both directions have been used in the generation of each grating's diffuse source sensitivity and signal-to-noise plots.

The exact level of anamorphic magnification is a function of grating and central wavelength. More detailed information on the CCD modes can be found in [STIS ISR 1998-23](#).

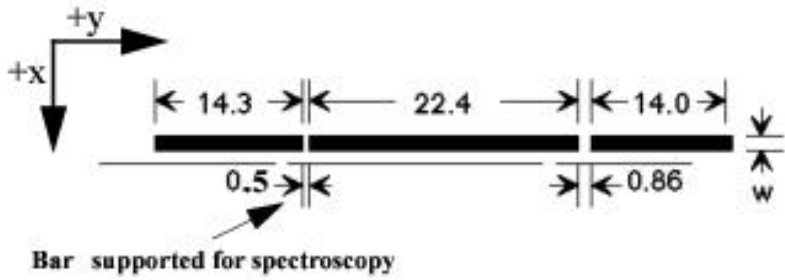
13.2.5 Apertures

For each supported slit (aperture) we provide a table giving the name of the slit, length (in the spatial direction) and width (in the dispersion direction) of the slit as well as a table and plot of the relative throughput of the slit (with respect to a large clear aperture) as a function of wavelength. Recall that the point source sensitivities that we have derived assume zero slit losses. Your calculations of exposure times must account for light losses for the desired slit. Aperture throughputs measured in orbit are given in [STIS ISR 1998-20](#) and [STIS ISR 1998-25](#). These measurements were used to revise pre-launch models of the aperture throughputs as a function of wavelength, and these revised models were then used to calculate the aperture throughput information given in this chapter and in the aperture throughputs (APER_{TAB}) reference file. Low order flat (LFL_{TFILE}) reference files are used to correct the system throughput as a function of position on the detector, as indicated in the descriptions of the E1, E2, and D1 pseudo-apertures. Since September 2005, additional wavelength-dependent corrections to the throughput have been made for grating-aperture combinations (gac) using the GAC_{TAB} reference file. (See [Section 3.4.13](#) in the [STIS Data Handbook](#).) This file currently has entries for the CCD L gratings and long-slit apertures, including the E1 apertures.

13.2.6 Fiducials on Bars

Each STIS long slit has two fiducial bars, located 11.2 arcseconds above and below the slit center, that are 0.86 and 0.5 arcseconds long, respectively (see [Figure 13.1](#) below). They have several purposes. First, the bars provide structural integrity for the long slits. Second, the image of the bars obtained in wavecal (and target acquisition) images is used by the calibration software to locate the projection of the aperture on the detector in post-observation data processing. Lastly, the bars can be used to occult a source thereby providing a coronagraphic spectroscopic capability for STIS. Use of the 0.5 arcsecond bar is supported only on the 52x0.2 slit (the 52x0.2F1 aperture) for coronagraphic observations. We refer you to [Section 12.10](#) for more information about performing coronagraphic spectroscopy, and [Section 13.7.3](#) for some caveats. As a reminder, for first-order MAMA modes, the projection of the aperture centers onto the detectors varies with the monthly offsetting, and the FUV modes are offset from the detector center by $\sim 3''$ (see [Section 7.6](#) for more details).

Figure 13.1: 52" Long Slits and Location of Fiducial Bars.



13.2.7 Spatial Profiles

For each grating mode, information about the cross dispersion (spatial) profiles is provided as follows:

- Plots of model fits to on-orbit data of the spectral profile in the cross dispersion (spatial) direction for a series of central wavelengths and gratings.
- A table of "encircled energies" containing two values: the percent of the total flux contained in the default calibration pipeline 1-D spectrum extraction aperture and the percent of the total flux contained in the central pixel.

13.2.8 Line Spread Functions (Instrumental Profiles)

We show plots of predicted line spread functions (LSFs) for CCD and MAMA spectroscopic modes (Section 13.6), as a function of wavelength and slit width. These plots are based on models of the PSFs at the aperture plane and detector PSFs that have been updated and verified using on-orbit data. Tabulations of the line spread functions may be found on the [STIS Spectral Resolution](#) web page.

Table 13.1: $STMAG_{\lambda}$ as a Function of Wavelength for Stellar Objects.

| Temp (K) | Wavelength (\AA) | | | | | | | | | | | | |
|----------|-----------------------------|-------|-------|-------|-------|------|------|------|------|------|------|------|-------|
| | 1500 | 2000 | 2500 | 3000 | 3500 | 4000 | 4500 | 5000 | 6000 | 7000 | 8000 | 9000 | 10000 |
| 50000 | -4.87 | -3.95 | -3.09 | -2.35 | -1.76 | - | - | - | 0.41 | 0.97 | 1.64 | 2.17 | 2.62 |
| | | | | | | 1.30 | 0.79 | 0.32 | | | | | |
| 30000 | -4.36 | -3.53 | -2.73 | -2.08 | -1.54 | - | - | - | 0.41 | 0.95 | 1.61 | 2.16 | 2.56 |
| | | | | | | 1.25 | 0.77 | 0.30 | | | | | |
| 20000 | -3.44 | -2.77 | -2.14 | -1.61 | -1.16 | - | - | - | 0.38 | 0.89 | 1.52 | 2.05 | 2.41 |
| | | | | | | 1.14 | 0.73 | 0.29 | | | | | |
| 15000 | -2.68 | -2.13 | -1.55 | -1.17 | -0.81 | - | - | - | 0.36 | 0.85 | 1.46 | 1.97 | 2.29 |
| | | | | | | 1.06 | 0.69 | 0.28 | | | | | |
| 10000 | -0.78 | -0.74 | -0.30 | -0.21 | -0.05 | | | | 0.32 | 0.76 | 1.34 | 1.85 | 2.09 |

| | | | | | | | | | | | | | | |
|------|-------|-------|-------|------|------|-------|-------|-------|-------|-------|-------|-------|-------|--|
| | | | | | | -0.82 | -0.62 | -0.25 | | | | | | |
| 9000 | 1.21 | -0.28 | 0.07 | 0.00 | 0.09 | -0.69 | -0.58 | -0.22 | 0.29 | 0.67 | 1.22 | 1.69 | 1.92 | |
| 8000 | 6.07 | 0.66 | 0.60 | 0.18 | 0.14 | -0.49 | -0.45 | -0.17 | 0.25 | 0.56 | 1.05 | 1.48 | 1.72 | |
| 7000 | 8.90 | 1.77 | 1.30 | 0.37 | 0.17 | -0.28 | -0.31 | -0.08 | 0.18 | 0.45 | 0.89 | 1.26 | 1.52 | |
| 6000 | 13.33 | 5.15 | 2.90 | 0.95 | 0.40 | -0.01 | -0.16 | 0.01 | 0.10 | 0.28 | 0.65 | 0.93 | 1.17 | |
| 5000 | 19.41 | 9.70 | 6.29 | 3.07 | 1.32 | 0.51 | 0.03 | 0.17 | -0.03 | 0.07 | 0.36 | 0.58 | 0.75 | |
| 4000 | 22.27 | 14.10 | 9.24 | 5.41 | 2.65 | 1.17 | 0.40 | 0.64 | -0.26 | -0.43 | -0.38 | -0.32 | -0.16 | |
| 3000 | 34.85 | 24.46 | 14.38 | 8.06 | 3.82 | 1.18 | 0.74 | 1.50 | -0.15 | -0.76 | -1.81 | -2.36 | -2.37 | |

$STMAG_{\lambda}$ is defined as the color-dependent correction from V magnitude to STMAG at wavelength λ . The results presented in this table are for Kurucz (1993), solar abundance main-sequence models. The spectral energy distributions of real stars can differ substantially, especially in the ultraviolet (UV), due to differences in chemical composition, surface gravity, and reddening. Also note that these models only include the photospheric continuum and not the chromospheric emission that dominates the flux of most cool stars in the FUV.

Table 13.2: $STMAG_{\lambda}$ as a Function of Wavelength for Non-Stellar Objects.

| Spectrum | Wavelength (Å) | | | | | | | | | | | | | |
|---------------------------|----------------|-------|-------|-------|-------|-------|-------|-------|-------|-------|-------|-------|-------|--|
| | 1500 | 2000 | 2500 | 3000 | 3500 | 4000 | 4500 | 5000 | 6000 | 7000 | 8000 | 9000 | 10000 | |
| Elliptical | 3.35 | 3.19 | 4.17 | 2.92 | 1.60 | 0.70 | 0.17 | 0.15 | -0.04 | -0.08 | -0.07 | -0.13 | n/a | |
| S0 | 4.63 | 3.95 | 3.27 | 2.23 | 1.61 | 0.71 | 0.18 | 0.13 | -0.03 | -0.13 | -0.02 | -0.08 | n/a | |
| Sa | 2.64 | 2.27 | 2.39 | 1.78 | 1.31 | 0.36 | 0.12 | 0.07 | -0.06 | -0.05 | -0.00 | 0.02 | n/a | |
| Sb | 1.70 | 2.59 | 2.04 | 1.32 | 1.12 | 0.43 | 0.17 | 0.10 | 0.02 | -0.05 | -0.01 | -0.04 | n/a | |
| Sc | -0.18 | 0.44 | -0.17 | -0.68 | -0.67 | -0.51 | -0.44 | -1.25 | 0.18 | 0.40 | n/a | n/a | n/a | |
| Starburst, $E(B-V) < 0.1$ | -1.71 | -1.15 | -0.68 | -0.43 | -0.13 | -0.42 | -0.23 | -1.24 | 0.21 | 0.40 | 0.70 | 0.85 | n/a | |
| | | | | | 0.08 | | | | 0.15 | 0.44 | 0.41 | 0.47 | n/a | |

| | | | | | | | | | | | | | |
|---------------------------------------|-----------|-----------|-----------|-----------|------|-----------|-----------|-----------|------|------|------|------|-----|
| Starburst, 0.25 < E(B-V) < 0.35 | - 0.95 | - 0.87 | - 0.33 | - 0.10 | | - 0.19 | - 0.19 | - 0.28 | | | | | |
| Starburst, 0.51 < E(B-V) < 0.60 | - 0.40 | - 0.18 | 0.01 | 0.23 | 0.03 | - 0.14 | - 0.12 | - 0.36 | 0.07 | 0.07 | 0.18 | 0.29 | n/a |
| Starburst, 0.61 < E(B-V) < 0.70 | 0.05 | 0.31 | 0.31 | 0.15 | 0.27 | - 0.17 | - 0.13 | - 0.11 | 0.06 | 0.17 | 0.26 | 0.24 | n/a |

$STMAG_{\lambda}$ is defined as the color-dependent correction from V magnitude to STMAG at wavelength λ .

How to Use the $STMAG_{\lambda}$ Tables

1. Interpolate in the table to get $STMAG_{\lambda}$ for the spectral type and wavelength region of your target observation (e.g., 6000K star @ 4300 Å).
2. Add the target V magnitude to the $STMAG_{\lambda}$ derived from Step 1.
3. Find the S/N plot for the grating you want to use.
4. Locate V+ $STMAG_{\lambda}$ on the horizontal axis and read off the S/N for the desired exposure time (or read off the exposure time for the desired S/N).

¹ STIS plus *HST* Optical Telescope Assembly (OTA).

13.3 Gratings

For each grating mode of STIS listed below, we provide the basic properties of the mode, wavelength ranges covered in each central wavelength setting, sensitivities, throughputs, dispersions and plate scales. Advice on usage is provided where appropriate, and comparisons of the G230L, G230M MAMA modes with their G230LB, G230MB CCD counterparts are shown.

Wavelengths in this handbook and in STIS data products are always measured in vacuum conditions.

- [First-Order Grating G750L](#)
- [First-Order Grating G750M](#)
- [First-Order Grating G430L](#)
- [First-Order Grating G430M](#)
- [First-Order Grating G230LB](#)
- [First-Order Grating G230MB](#)
- [First-Order Grating G230L](#)
- [First-Order Grating G230M](#)
- [First-Order Grating G140L](#)
- [First-Order Grating G140M](#)
- [Echelle Grating E230M](#)
- [Echelle Grating E230H](#)
- [Echelle Grating E140M](#)
- [Echelle Grating E140H](#)
- [PRISM](#)

First-Order Grating G750L

Description

The G750L grating is used with the CCD. It has high throughput but low resolving power (~ 500), and is designed for efficient, full spectral coverage. The grating has one supported prime tilt setting¹.

Recommended Uses

This grating is recommended for observations where high spectral resolution is not required, but efficient coverage in the red portion of the optical is desired.

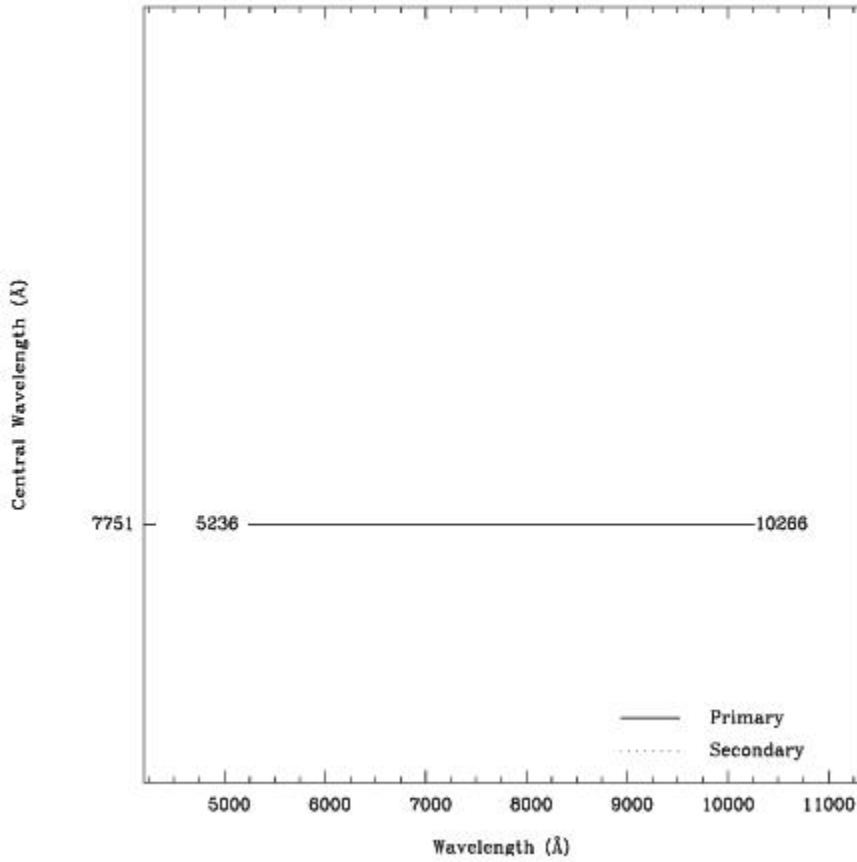
Special Considerations

Fringing in the CCD compromises the realizable signal-to-noise longward of 7500 Å if contemporaneous fringe flats are not obtained (see [Section 7.2.6](#)).

| Grating | Spectral Range | | Average Dispersion (Å/Pixel) | Plate Scale (arcsec/pixel) | Tilts | Central Wavelengths |
|---------|-------------------------|----------|------------------------------|----------------------------|-------|---------------------|
| | Complete | Per Tilt | | | | |
| G750L | 5240-10270 ¹ | 5030 | 4.92 | 0.05078 | Prime | 7751 |

¹ Coverage from about 6460-10331 Å is possible with the available-but-unsupported 8975 setting.

Figure 13.2: Wavelength Range for the G750L Grating Setting.



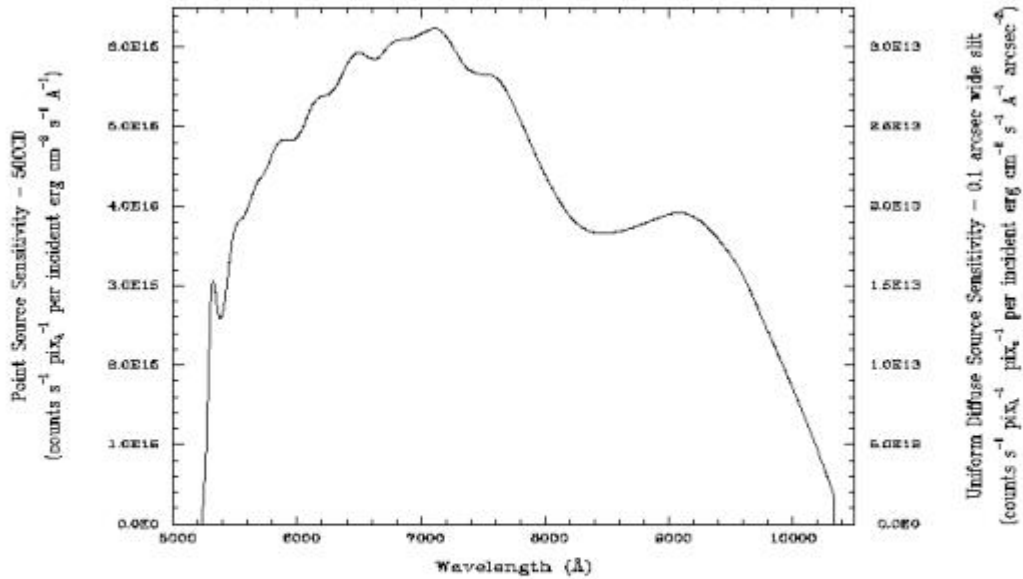
G750L Sensitivities

Table 13.3: G750L Sensitivities & Throughputs for a Point Source.

| λ | Sensitivity | % Throughput |
|-----------|-------------|--------------|
| 5500 | 3.4E15 | 5.5 |
| 6000 | 5.0E15 | 7.4 |
| 6500 | 5.8E15 | 8.0 |
| 7000 | 6.1E15 | 7.9 |
| 7500 | 5.7E15 | 6.8 |
| 8000 | 4.4E15 | 5.0 |
| 8500 | 3.7E15 | 3.9 |
| 9000 | 3.9E15 | 3.8 |

| | | |
|-------|--------|-----|
| 9500 | 3.3E15 | 3.1 |
| 10000 | 1.7E15 | 1.5 |
| 10500 | 8.5E13 | 0.1 |

Figure 13.3: G750L Point Source (left axis), and Diffuse Source (right axis) Sensitivities.



Note:

Point source sensitivity assumes full transmission (zero slit losses). Diffuse source sensitivity assumes a 0.1" wide slit. To convert point source sensitivities to diffuse source sensitivities multiply the point source values by the grating spatial (cross dispersion) plate scale in units of arcseconds per pixel and by the width of the desired slit in units of arcseconds.

G750L Signal-to-Noise

Note:

The top axis displays constant F_{λ} values corresponding to the STMAG units (V+STMAG $_{\lambda}$) on the bottom axis. Recall that STMAG=0 is equivalent to $F_{\lambda} = 3.63E-9 \text{ erg/cm}^2/\text{s}^{-1}/\text{\AA}$. The curves are labeled with exposure times in seconds.

Figure 13.4: Diffuse Source Signal-to-Noise as a Function of STMAG for G750L. λ Fiducial = 7500 Å.

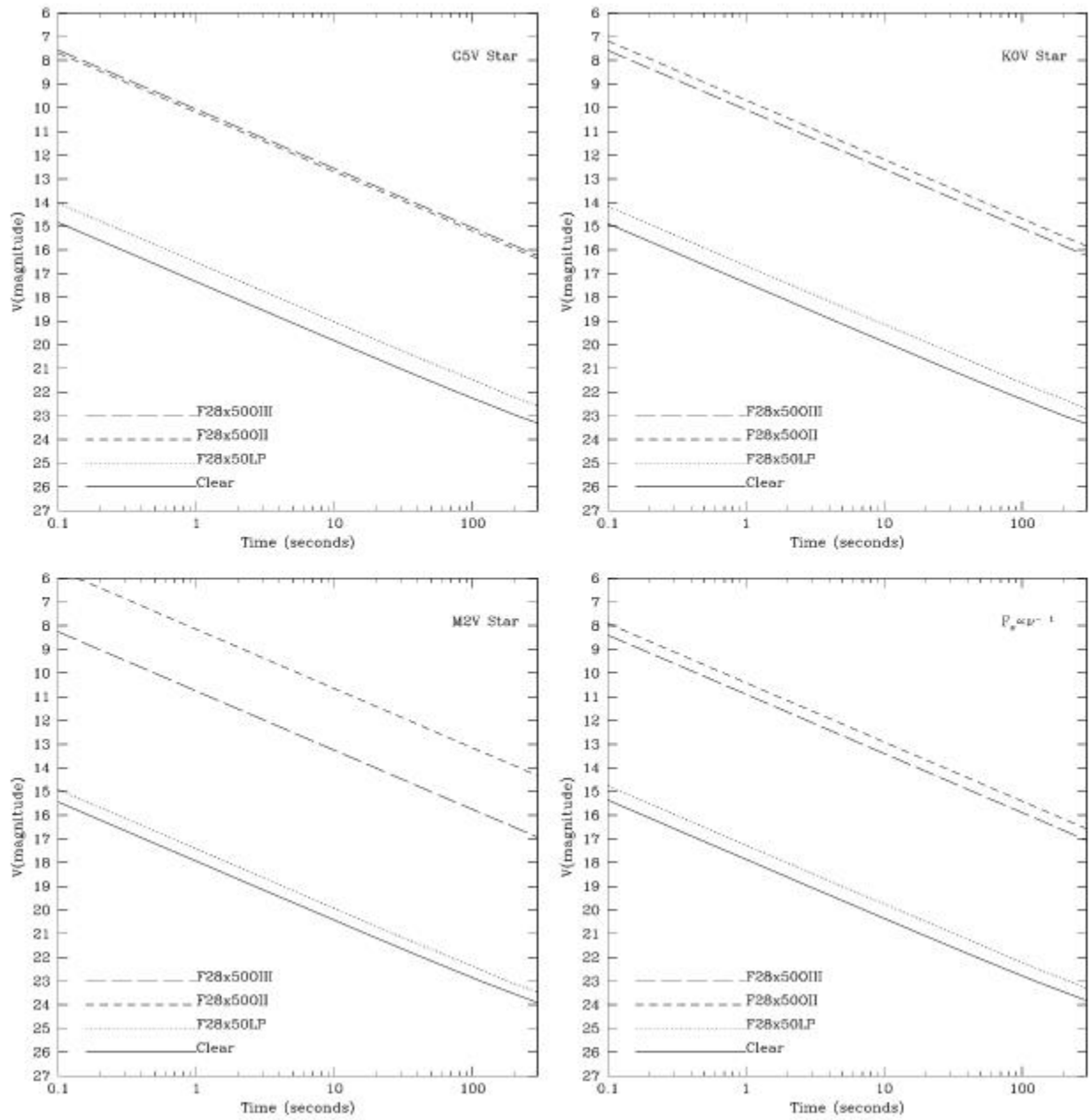
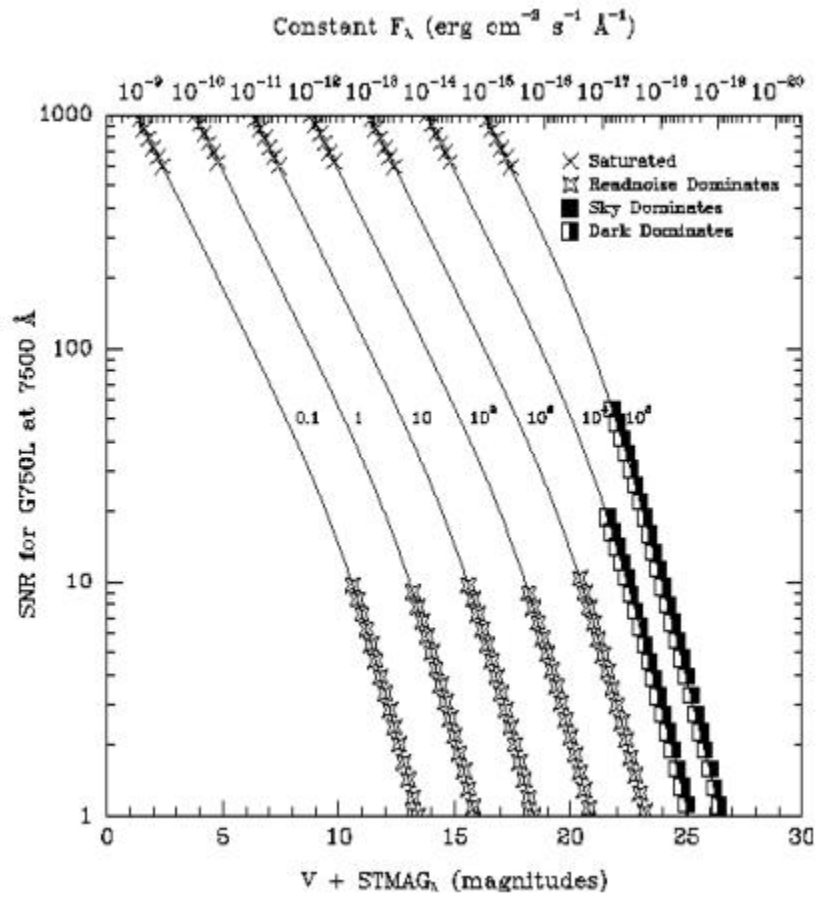


Figure 13.5: Point Source Signal-to-Noise as a Function of STMAG for G750L.



First-Order Grating G750M

Description

Like G750L, the G750M grating is used with the CCD and has a spectral range from 5500–10,000 Å. With a resolving power $R \sim 5000$, a single exposure with this grating covers only 570 Å, and the grating must be scanned, with a series of exposures taken at nine distinct settings to cover the full range of the grating.

Recommended Uses

This grating is designed for relatively high spectral resolution work centered on selected wavelength regions of the optical to near-infrared (NIR).

Special Considerations

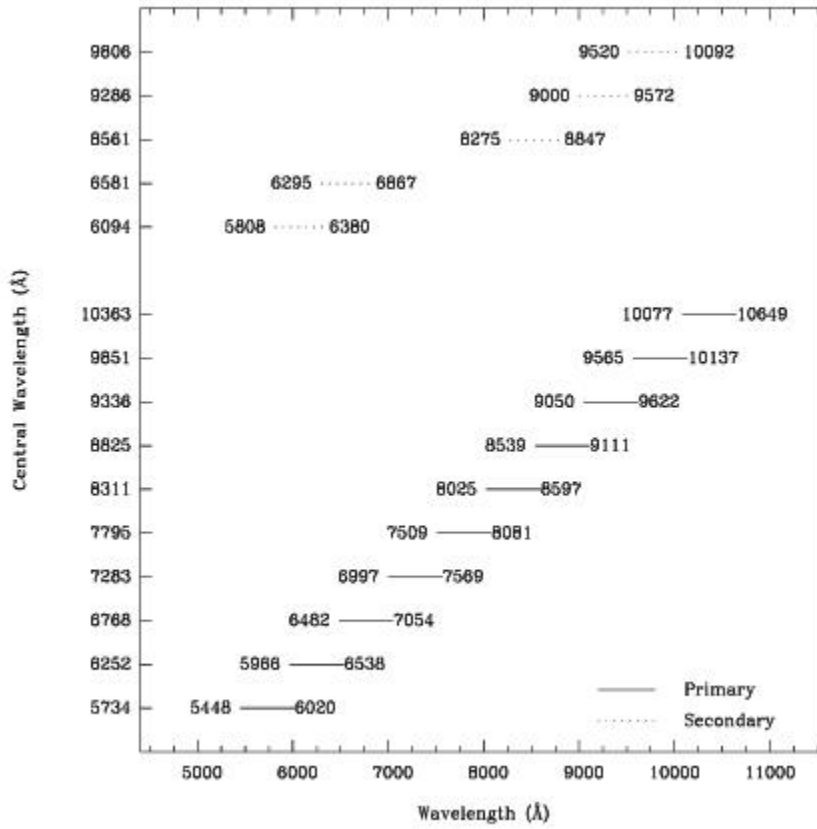
There is a partial ghost spectrum present in the $\lambda_c = 5734$ setting which is $\sim 1.2\%$ of the prime spectrum intensity and is both inverted with respect to the prime spectrum and offset by ~ 70 pixels. It arises from back reflections between the CCD and the order sorter.

Fringing in the CCD compromises the realizable signal-to-noise longward of 7500 Å if contemporaneous fringe flats are not obtained (see [Section 7.2.6](#)).

| Grating | Spectral Range | | Average Dispersion (Å per Pixel) | Plate Scale (arcsec /pixel) | Tilts | Central Wavelengths |
|---------|----------------|----------|----------------------------------|-----------------------------|-----------|--|
| | Complete | Per Tilt | | | | |
| G750M | 5450–10140 | 572 | 0.56 | 0.05078 | Prime | 5734, 6252, 6768, 7283, 7795, 8311, 8825, 9336, 9851, 10363 ¹ |
| | | | | | Secondary | 6094, 6581, 8561, 9286, 9806 |

¹ Setting 10363 is available-but-unsupported.

Figure 13.6: Wavelength Range for the G750M Grating Setting.



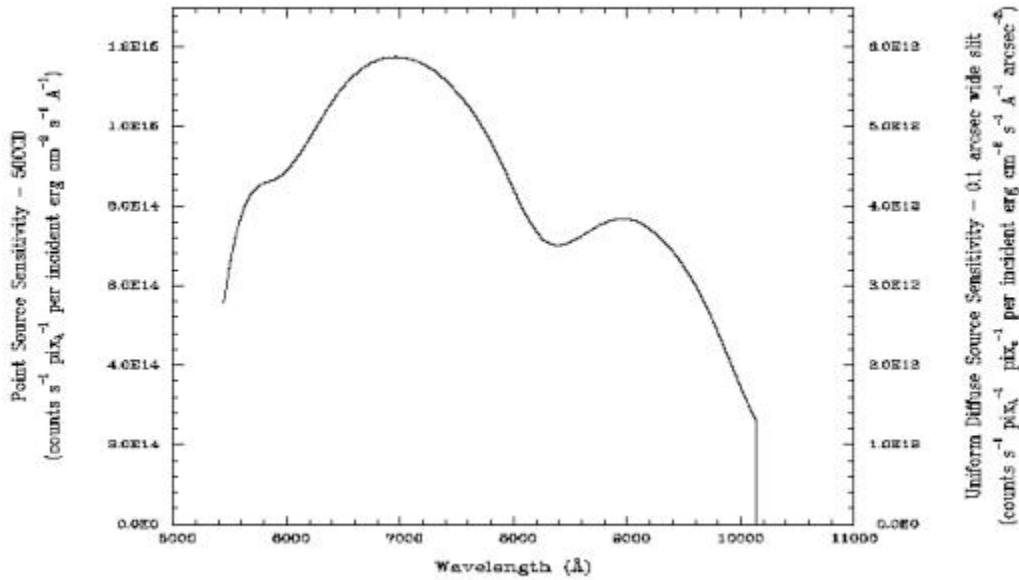
G750M Sensitivities

Table 13.4: G750M Sensitivities & Throughputs for a Point Source.

| λ | Sensitivity | % Throughput |
|-----------|-------------|--------------|
| 5500 | 6.6E14 | 9.5 |
| 6000 | 9.0E14 | 12.0 |
| 6500 | 1.1E15 | 13.4 |
| 7000 | 1.2E15 | 13.3 |
| 7500 | 1.1E15 | 11.5 |
| 8000 | 8.5E14 | 8.5 |
| 8500 | 7.2E14 | 6.7 |
| 9000 | 7.6E14 | 6.7 |
| 9500 | 6.4E14 | 5.4 |

| | | |
|-------|--------|-----|
| 10000 | 3.0E14 | 2.4 |
| 10500 | 0.0E0 | 0.0 |

Figure 13.7: G750M Point Source (left axis), and Diffuse Source (right axis) Sensitivities.



Note:

Point source sensitivity assumes full transmission (zero slit losses). Diffuse source sensitivity assumes a 0.1" wide slit. To convert point source sensitivities to diffuse source sensitivities multiply the point source values by the grating spatial (cross dispersion) plate scale in units of arcseconds per pixel and by the width of the desired slit in units of arcseconds.

G750M Signal-to-Noise

Note:

The top axis displays constant F_{λ} values corresponding to the STMAG units ($V+STMAG_{\lambda}$) on the bottom axis. Recall that $STMAG=0$ is equivalent to $F_{\lambda} = 3.63E-9 \text{ erg/cm}^2/\text{s}^{-1}/\text{\AA}$. The curves are labeled with exposure times in seconds.

Figure 13.8: Diffuse Source Signal-to-Noise as a Function of STMAG for G750M.

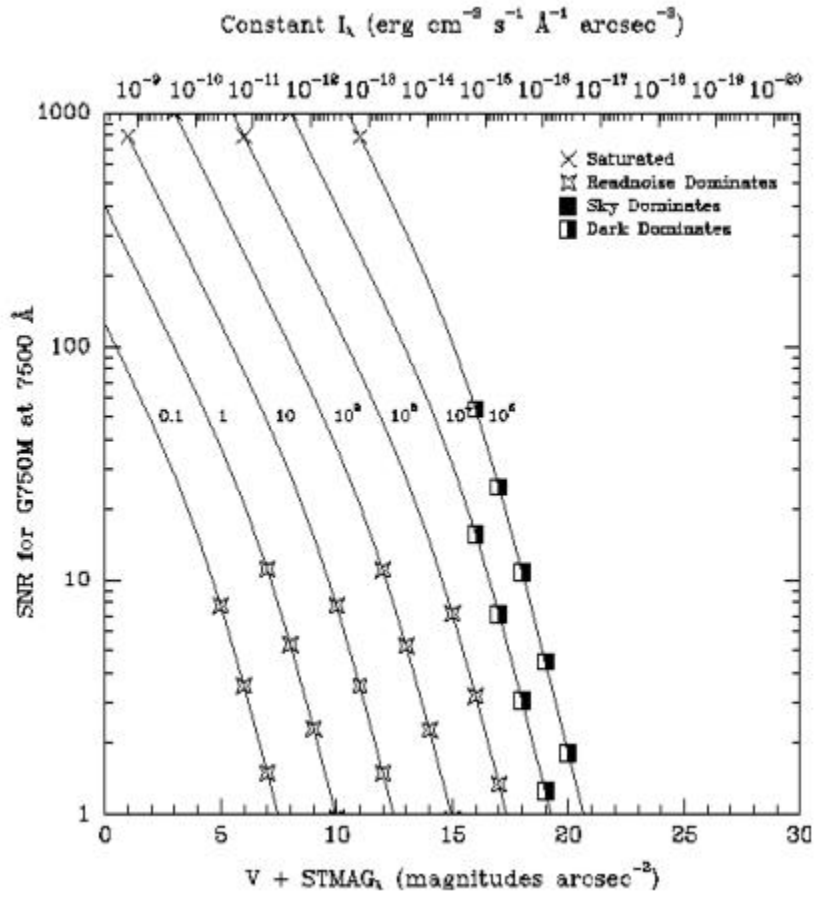
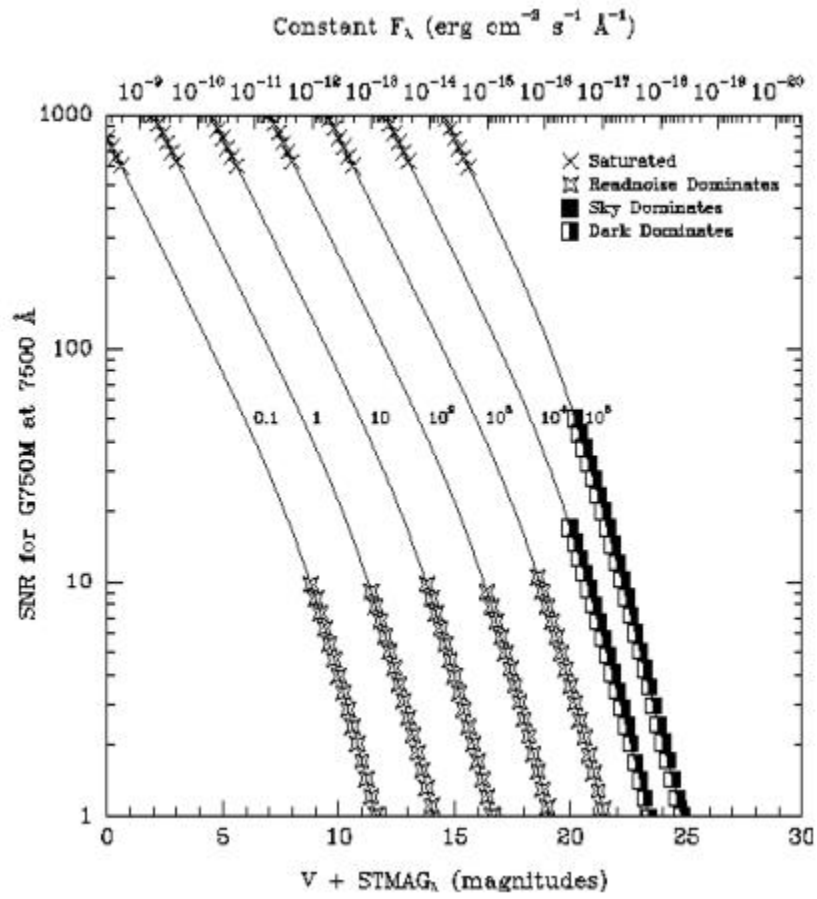


Figure 13.9: Point Source Signal-to-Noise as a Function of STAG for G750M.



First-Order Grating G430L

Description

G430L, used with the CCD, is a low resolution grating ($R \sim 500$) with a relatively high throughput. The grating has only a single setting.

Recommended Uses

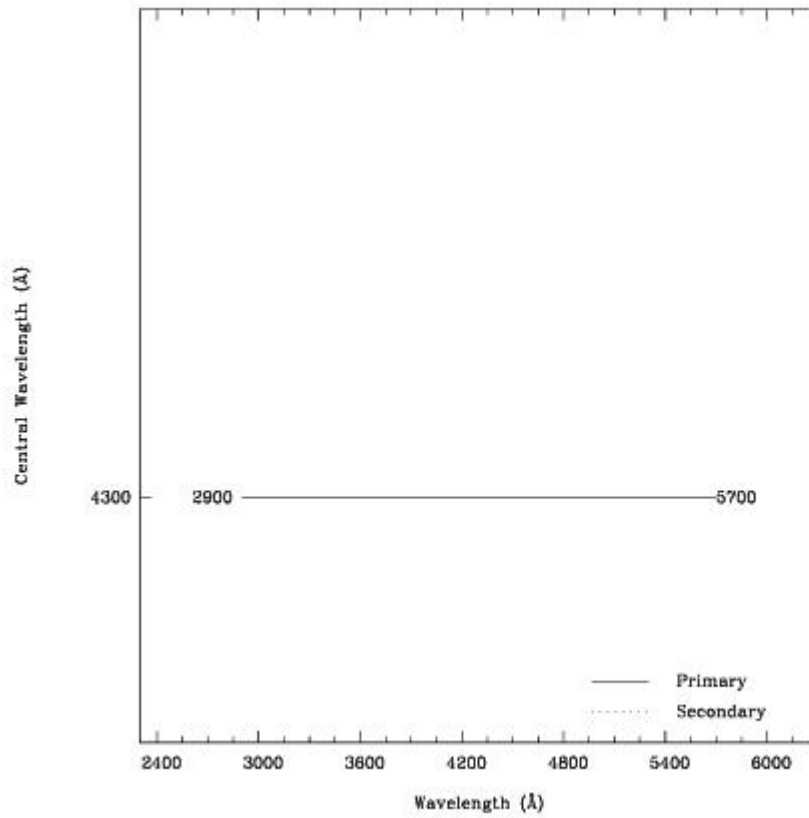
This grating is designed for observations where high spectral resolution is not required, but efficient spectral coverage in the blue portion of the optical is desired.

Special Considerations

By taking two observations, one with G750L and one with G430L, the full spectral region from the NIR at 10000 Å through the optical at 3000 Å can be efficiently observed at an $R \sim 500$.

| Grating | Spectral Range | | Average Dispersion (Å per Pixel) | Plate Scale (arcsec/pixel) | Tilts | Central Wavelengths |
|---------|----------------|----------|----------------------------------|----------------------------|-------|---------------------|
| | Complete | Per Tilt | | | | |
| G430L | 2900-5700 | 2800 | 2.73 | 0.05078 | Prime | 4300 |

Figure 13.10: Wavelength Ranges for the G430L Grating Setting.



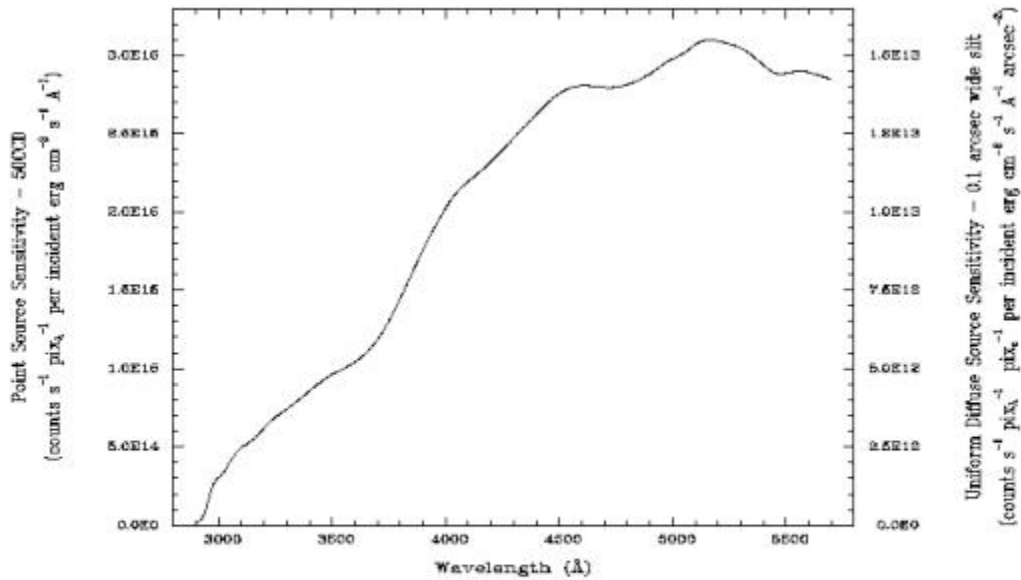
G430L Sensitivities

Table 13.5: G430L Sensitivities & Throughputs for a Point Source.

| λ | Sensitivity | % Throughput |
|-----------|-------------|--------------|
| 3000 | 2.7E14 | 1.4 |
| 3250 | 6.8E14 | 3.4 |
| 3500 | 9.5E14 | 4.4 |
| 3750 | 1.3E15 | 5.7 |
| 4000 | 2.0E15 | 8.1 |
| 4250 | 2.5E15 | 9.2 |
| 4500 | 2.7E15 | 9.9 |
| 4750 | 2.8E15 | 9.6 |
| 5000 | 3.0E15 | 9.7 |

| | | |
|------|--------|-----|
| 5250 | 3.1E15 | 9.5 |
| 5500 | 2.9E15 | 8.6 |

Figure 13.11: G430L Point Source (left axis), and Diffuse Source (right axis) Sensitivities.



Note:

Point source sensitivity assumes full transmission (zero slit losses). Diffuse source sensitivity assumes a 0.1" wide slit. To convert point source sensitivities to diffuse source sensitivities multiply the point source values by the grating spatial (cross dispersion) plate scale in units of arcseconds per pixel and by the width of the desired slit in units of arcseconds.

G430L Signal-to-Noise

Note:

The top axis displays constant F_{λ} values corresponding to the STMAG units (V+STMAG_λ) on the bottom axis. Recall that STMAG=0 is equivalent to $F_{\lambda} = 3.63E-9 \text{ erg/cm}^2/\text{s}/\text{Å}$. The curves are labeled with exposure times in seconds.

Figure 13.12: Diffuse Source Signal-to-Noise as a Function of STMAG for G430L.

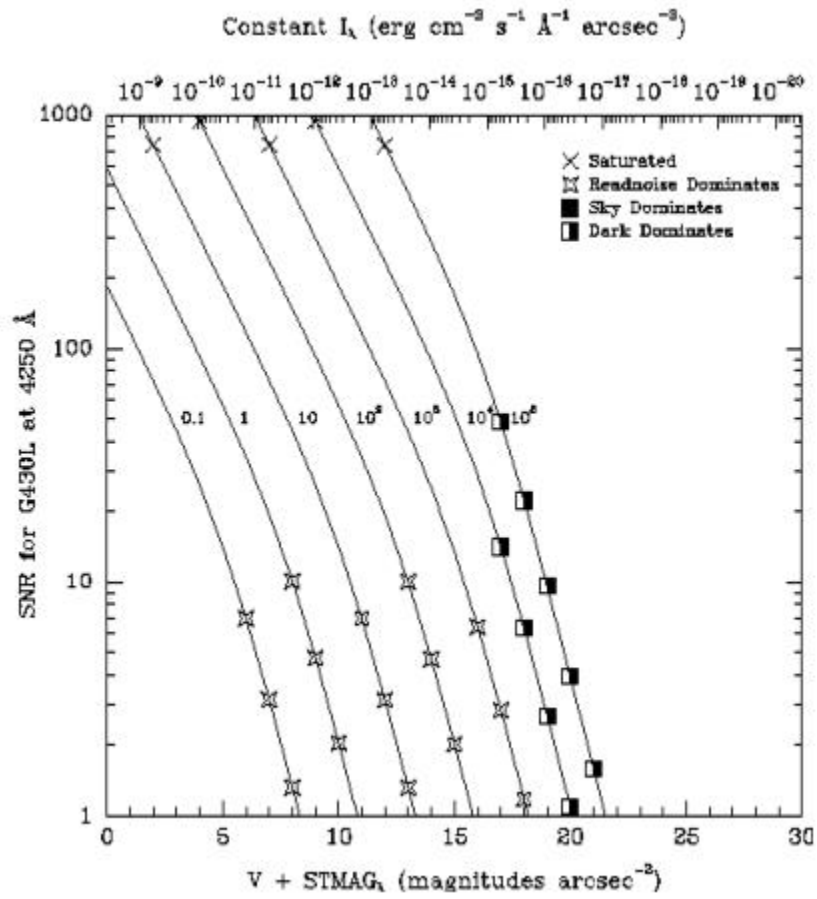
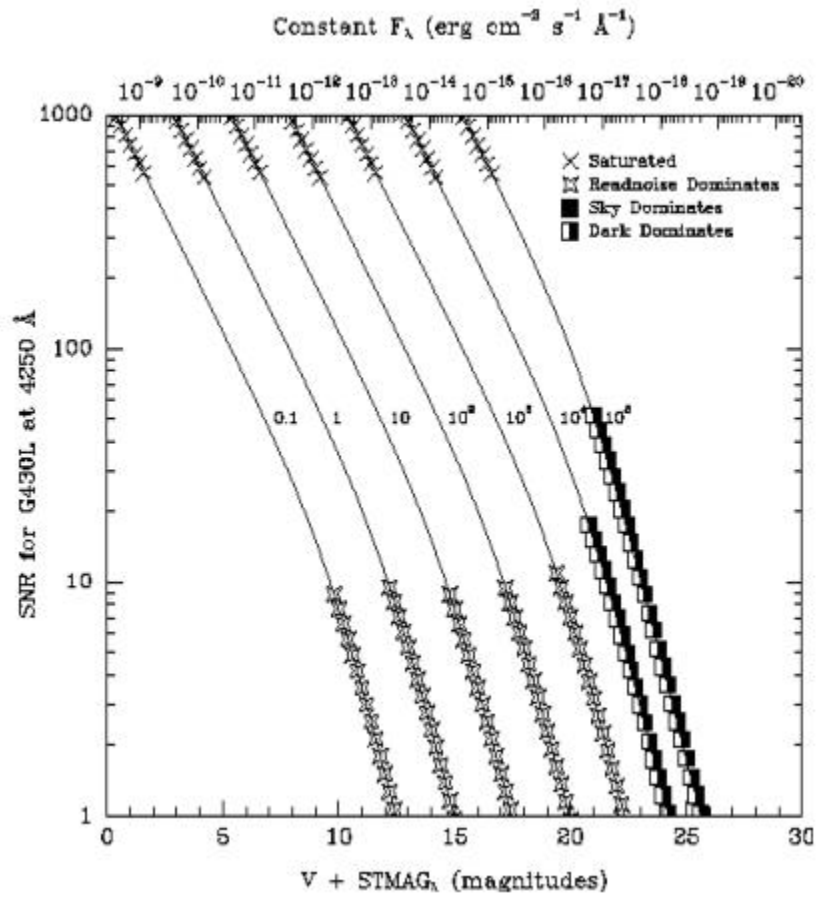


Figure 13.13: Point Source Signal-to-Noise as a Function of STMAG for G430L.



First-Order Grating G430M

Description

Like the G430L grating, the G430M grating is used with the CCD and has a spectral range from 3020–5600 Å.

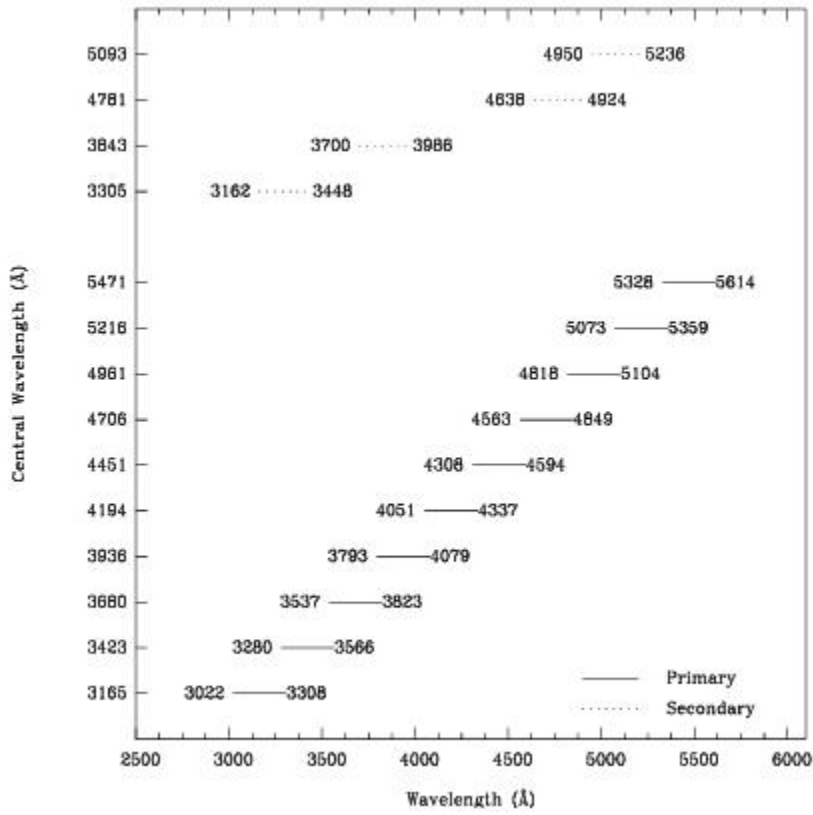
Since a single exposure taken with this grating covers only 286 Å the grating must be scanned, with a series of exposures taken at 10 distinct settings, to cover the full spectral range of the grating.

Recommended Uses

The G430M grating mode is designed for observations where spatially resolved, long slit spectroscopy is desired at relatively high spectral resolution ($R \sim 6000$) over a limited region of the NUV or optical spectrum.

| Grating | Spectral Range | | Average Dispersion (Å per Pixel) | Plate Scale (arcsec /pixel) | Tilts | Central Wavelengths |
|---------|----------------|----------|----------------------------------|-----------------------------|-----------|--|
| | Complete | Per Tilt | | | | |
| G430M | 3020–5610 | 286 | 0.28 | 0.05078 | Prime | 3165, 3423, 3680, 3936, 4194, 4451, 4706, 4961, 5216, 5471 |
| | | | | | Secondary | 3305, 3843, 4781, 5093 |

Figure 13.14: Wavelength Ranges for the G430M Grating Setting.



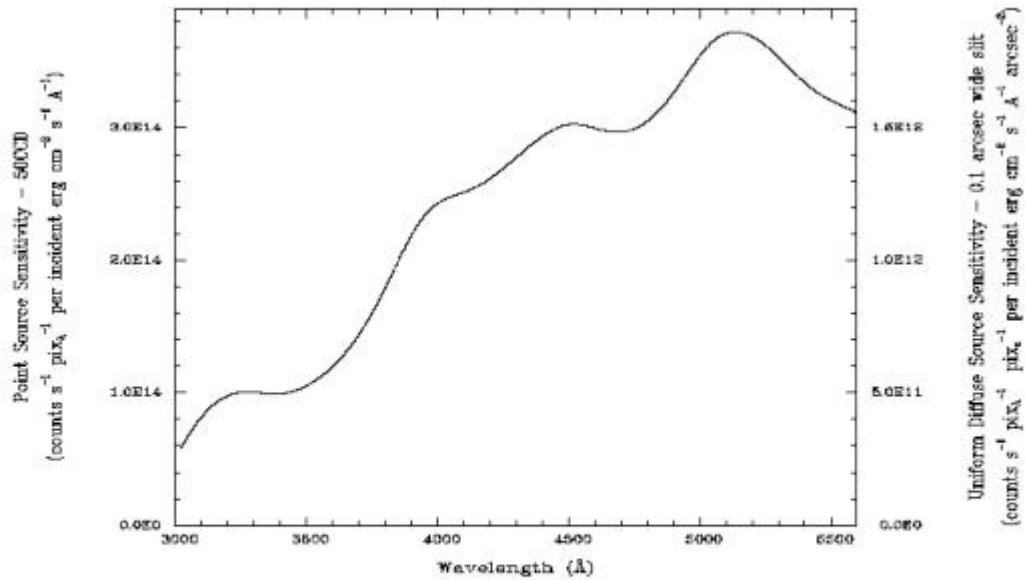
G430M Sensitivities

Table 13.6: G430M Sensitivities & Throughputs for a Point Source.

| λ | Sensitivity | % Throughput |
|-----------|-------------|--------------|
| 3050 | 6.7E13 | 3.5 |
| 3150 | 9.1E13 | 4.5 |
| 3250 | 1.0E14 | 4.8 |
| 3350 | 9.9E13 | 4.7 |
| 3450 | 1.0E14 | 4.6 |
| 3550 | 1.1E14 | 4.9 |
| 3650 | 1.3E14 | 5.6 |
| 3750 | 1.6E14 | 6.7 |
| 3850 | 2.0E14 | 8.1 |

| | | |
|------|--------|------|
| 3950 | 2.3E14 | 9.2 |
| 4050 | 2.5E14 | 9.6 |
| 4150 | 2.6E14 | 9.7 |
| 4250 | 2.7E14 | 9.9 |
| 4350 | 2.9E14 | 10.3 |
| 4450 | 3.0E14 | 10.5 |
| 4550 | 3.0E14 | 10.4 |
| 4650 | 3.0E14 | 10.0 |
| 4750 | 3.0E14 | 9.9 |
| 4850 | 3.1E14 | 10.2 |
| 4950 | 3.4E14 | 10.8 |
| 5050 | 3.6E14 | 11.3 |
| 5150 | 3.7E14 | 11.3 |
| 5250 | 3.6E14 | 10.8 |
| 5350 | 3.4E14 | 10.1 |
| 5450 | 3.3E14 | 9.4 |
| 5500 | 3.2E14 | 8.9 |

Figure 13.15: G430M Point Source (left axis), and Diffuse Source (right axis) Sensitivities.



Note:

Point source sensitivity assumes full transmission (zero slit losses). Diffuse source sensitivity assumes a 0.1" wide slit. To convert point source sensitivities to diffuse source sensitivities multiply the point source values by the grating spatial (cross dispersion) plate scale in units of arcseconds per pixel and by the width of the desired slit in units of arcseconds.

G430M Signal-to-Noise

Note:

The top axis displays constant F_{λ} values corresponding to the STMAG units ($V+STMAG_{\lambda}$) on the bottom axis. Recall that $STMAG=0$ is equivalent to $F_{\lambda} = 3.63E-9 \text{ erg/cm}^2/\text{s}^{-1}/\text{\AA}$. The curves are labeled with exposure times in seconds.

Figure 13.16: Diffuse Source Signal-to-Noise as a Function of STMAG for G430M.

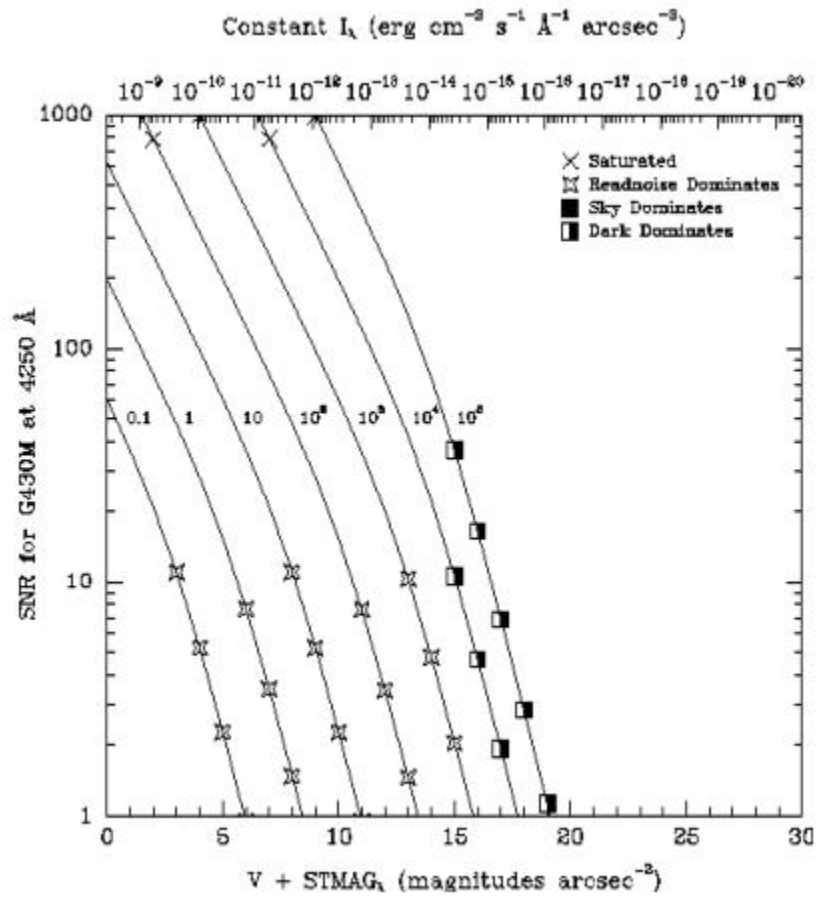
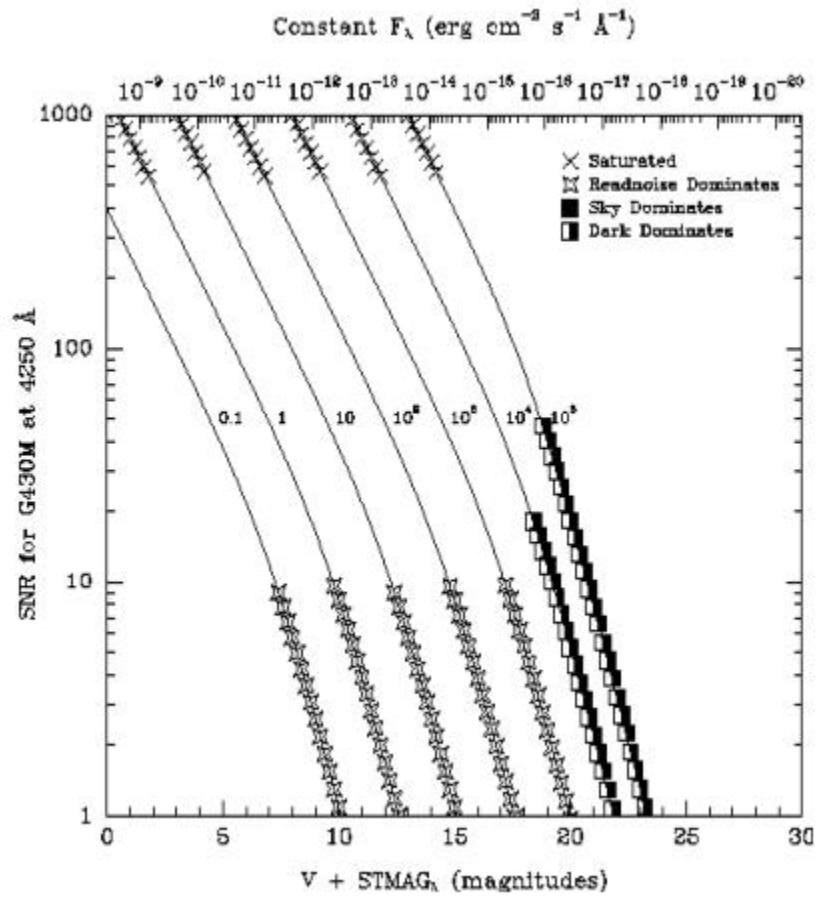


Figure 13.17: Point Source Signal-to-Noise as a Function of STMAG for G430M.



First-Order Grating G230LB

Description

The G230LB grating mode uses a backup low resolution grating originally designed for use with the STIS/NUV-MAMA, which has been repurposed for use with the STIS/CCD. It enables $R \sim 700$ spectroscopy in the near-ultraviolet (NUV) and takes advantage of the CCD's higher throughput and dynamic range longward of $\lambda = 2500 \text{ \AA}$.

Recommended Uses

The G230LB grating mode is designed for programs needing the highest available sensitivity in the NUV from ~ 2500 to 3100 \AA or more generally to allow observation of sources too bright for the MAMA in the NUV.

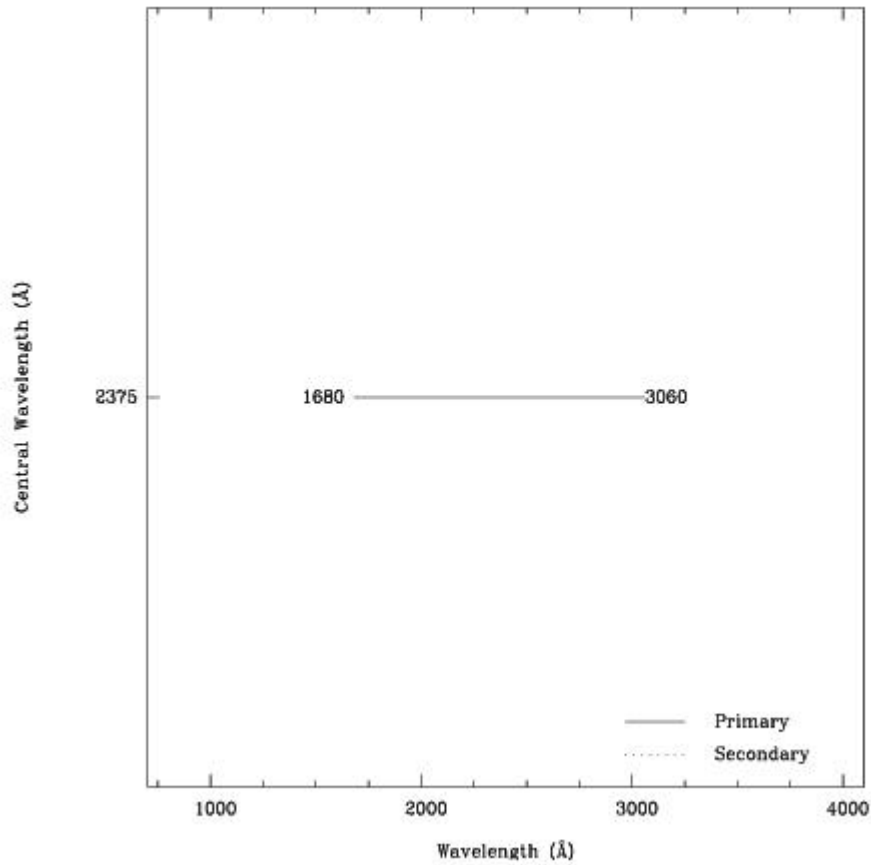
Special Considerations

In making the plots for the G230LB grating mode, we assumed that the CCD is subject to a change in the effective quantum yield resulting in the creation of multiple electron-hole pairs per photon for $\lambda < 3400 \text{ \AA}$.

Also be aware that because of the high sensitivity of the CCD to red light, observations of red stars with G230LB are more likely to be affected by scatter than observations of those stars using the MAMA G230L (see [ISR 2022-05](#) and [Section 4.1.6](#)).

| Grating | Spectral Range | | Average Dispersion (\AA per Pixel) | Plate Scale (arcsec/pixel) | Tilts | Central Wavelengths |
|---------|----------------|----------|--|----------------------------|-------|---------------------|
| | Complete | Per Tilt | | | | |
| G230LB | 1680-3060 | 1380 | 1.35 | 0.05078 | Prime | 2375 |

Figure 13.18: Wavelength Range for the G230LB Grating Setting.



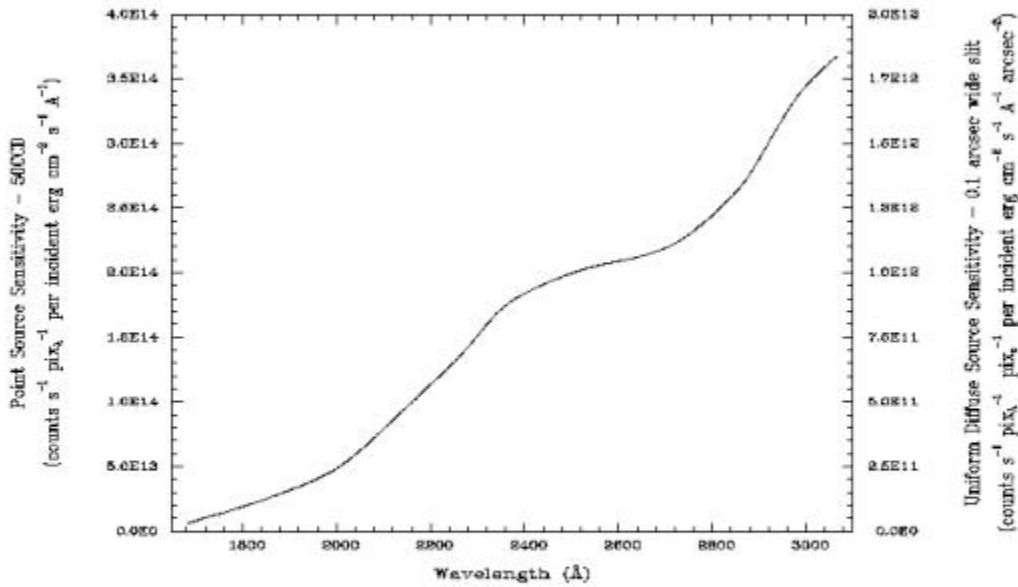
G230LB Sensitivities

Table 13.7: G230LB Sensitivities & Throughputs for a Point Source.

| λ | Sensitivity | % Throughput |
|-----------|-------------|--------------|
| 1750 | 1.3E13 | 0.3 |
| 1850 | 2.5E13 | 0.5 |
| 1950 | 3.9E13 | 0.7 |
| 2050 | 6.3E13 | 1.0 |
| 2150 | 9.9E13 | 1.5 |
| 2250 | 1.3E14 | 2.0 |
| 2350 | 1.7E14 | 2.4 |
| 2450 | 1.9E14 | 2.6 |

| | | |
|------|--------|-----|
| 2550 | 2.0E14 | 2.7 |
| 2650 | 2.1E14 | 2.7 |
| 2750 | 2.3E14 | 2.8 |
| 2850 | 2.6E14 | 3.1 |
| 2950 | 3.2E14 | 3.6 |
| 3050 | 3.6E14 | 4.0 |

Figure 13.19: G230LB Point Source (left axis), and Diffuse Source (right axis) Sensitivities.



Note:

Point source sensitivity assumes full transmission (zero slit losses). Diffuse source sensitivity assumes a 0.1" wide slit. To convert point source sensitivities to diffuse source sensitivities multiply the point source values by the grating spatial (cross dispersion) plate scale in units of arcseconds per pixel and by the width of the desired slit in units of arcseconds.

G230LB Signal-to-Noise

Note:

The top axis displays constant F_{λ} values corresponding to the STMAG units ($V+STMAG_{\lambda}$) on the bottom axis. Recall that $STMAG=0$ is equivalent to $F_{\lambda} = 3.63E-9 \text{ erg/cm}^2/\text{s}^{-1}/\text{\AA}$. The curves are labeled with exposure times in seconds.

Figure 13.20: Diffuse Source Signal-to-Noise as a Function of STMAG for G230LB.

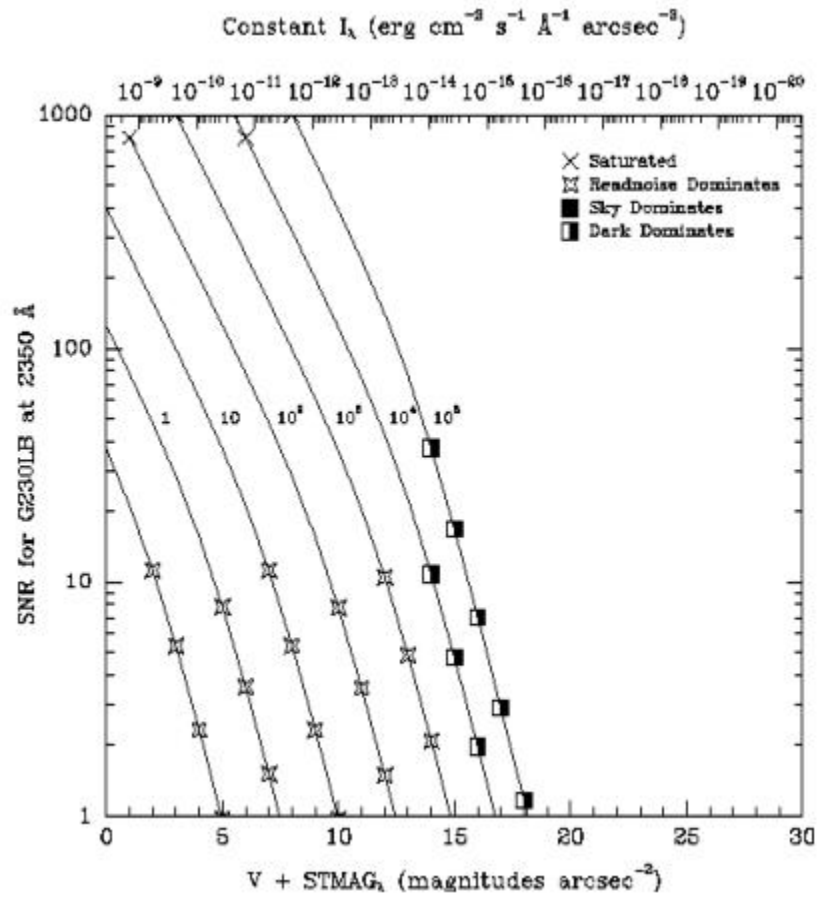
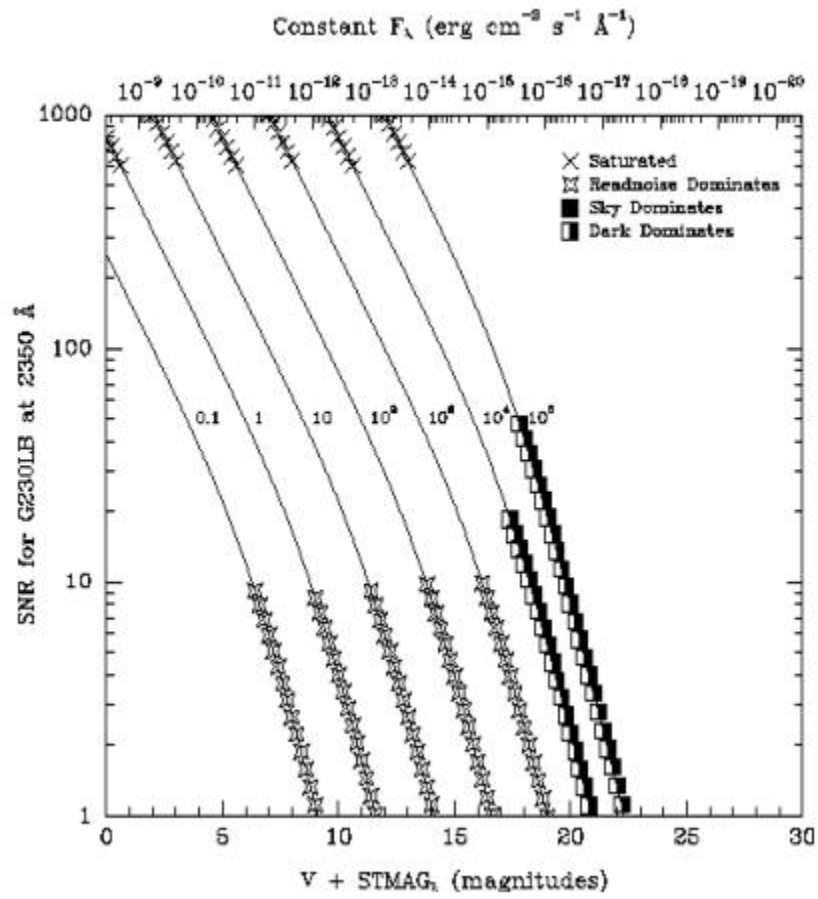


Figure 13.21: Point Source Signal-to-Noise as a Function of STMAG for G230LB.



Comparison of G230LB and G230L

The trade-off between using the G230LB or the G230L (which uses the NUV-MAMA), depends sensitively on the science goals and your source properties.

- The CCD has read noise, whereas the MAMA does not.
- The CCD suffers from charge transfer inefficiency (CTI), whereas the NUV-MAMA does not.
- The CCD does not have bright object limits, whereas the MAMA does.
- The NUV-MAMA is solar insensitive, whereas the CCD is not.
- The spatial sampling of the MAMA is better than that of the CCD.
- The CCD does not enable high time resolution ($Dt < 10$ seconds), whereas the MAMA does.
- For red objects, CCD data can suffer from scattered light problems, but the detector PSF of the CCD is much cleaner than that of the NUV-MAMA (see [ISR 2022-05](#) and [Section 4.1.6](#) discussion on scattered light).

Figure 13.22: Comparison of Limiting Magnitudes and Fluxes for G230LB and G230L. Plotted are the limiting source magnitudes and fluxes for G230LB and G230L to achieve a signal-to-noise ratio of 10 per 2-pixel spectral resolution element integrated across the PSF in 1 hour. The prediction due to the Charge Transfer Inefficiency (CTI) effect, computed for the year 2005, is also shown.

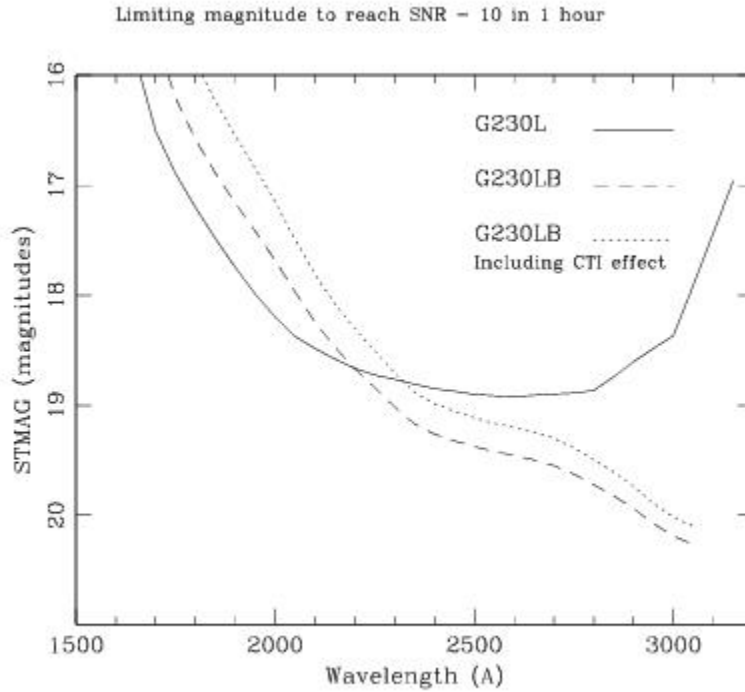
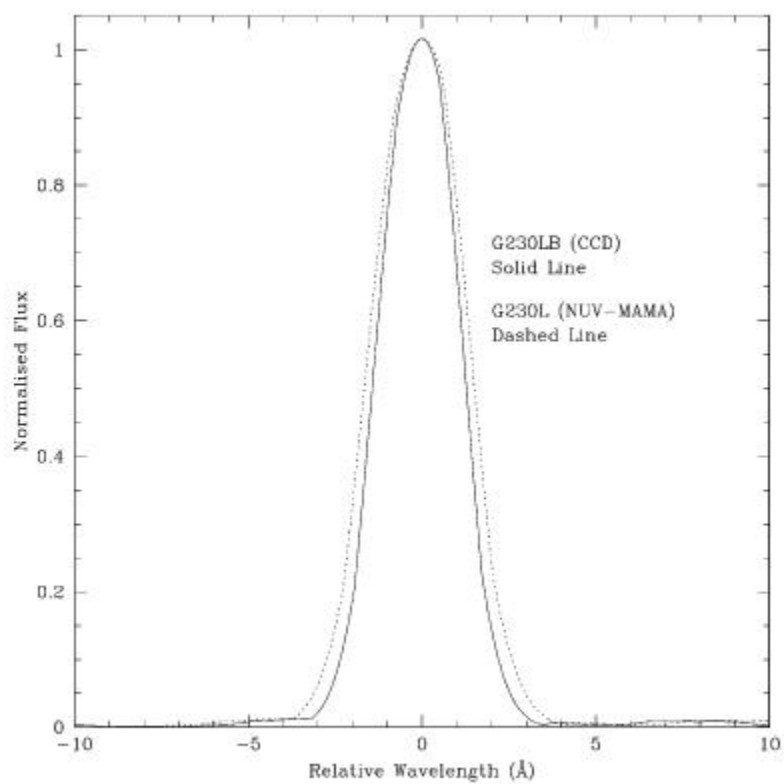


Figure 13.23: Comparison of LSFs for G230LB and G230L.



First-Order Grating G230MB

Description

The G230MB grating mode uses a backup intermediate-resolution grating originally designed for use with the NUV-MAMA which has been repurposed for use with the CCD. It provides $R \sim 6000$ spectroscopy in the NUV and takes advantage of the CCD's higher throughput longward of $\lambda = 2500 \text{ \AA}$. The G230MB grating mode has a spectral range from 1640–3190 \AA .

As a single exposure with this grating covers only 150 \AA , the grating must be scanned with a series of exposures taken at 11 distinct settings to cover the full spectral range of the grating.

Recommended Uses

The G230MB grating mode is designed for programs needing the highest available sensitivity in the NUV from ~ 2500 to 3100 \AA or more generally to allow observation of sources too bright for the MAMA in the NUV.

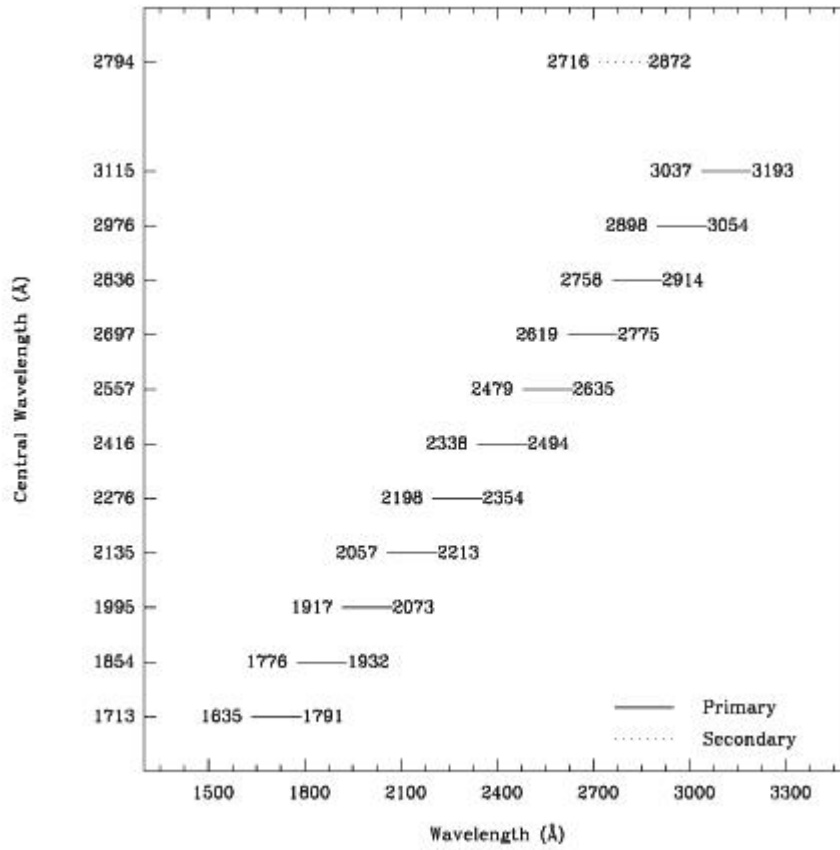
Special Considerations

In making the plots for the G230MB grating mode, we assumed that the CCD is subject to a change in the effective quantum yield resulting in the creation of multiple electron-hole pairs per photon for $\lambda < 3400 \text{ \AA}$.

Because of the high sensitivity of the CCD to red light, observations of red stars with G230MB are more likely to be affected by scattered light than observations of those stars using the NUV-MAMA G230M (see [Section 4.1.6](#)).

| Grating | Spectral Range | | Average Dispersion (\AA per Pixel) | Plate Scale (arcsec/pixel) | Tilts | Central Wavelengths |
|---------|----------------|----------|--|----------------------------|-----------|--|
| | Complete | Per Tilt | | | | |
| G230MB | 1640–3190 | 156 | 0.15 | 0.05078 | Prime | 1713, 1854, 1995, 2135, 2276, 2416, 2557, 2697, 2836, 2976, 3115 |
| | | | | | Secondary | 2794 |

Figure 13.24: Wavelength Ranges for the G230MB Grating Setting.



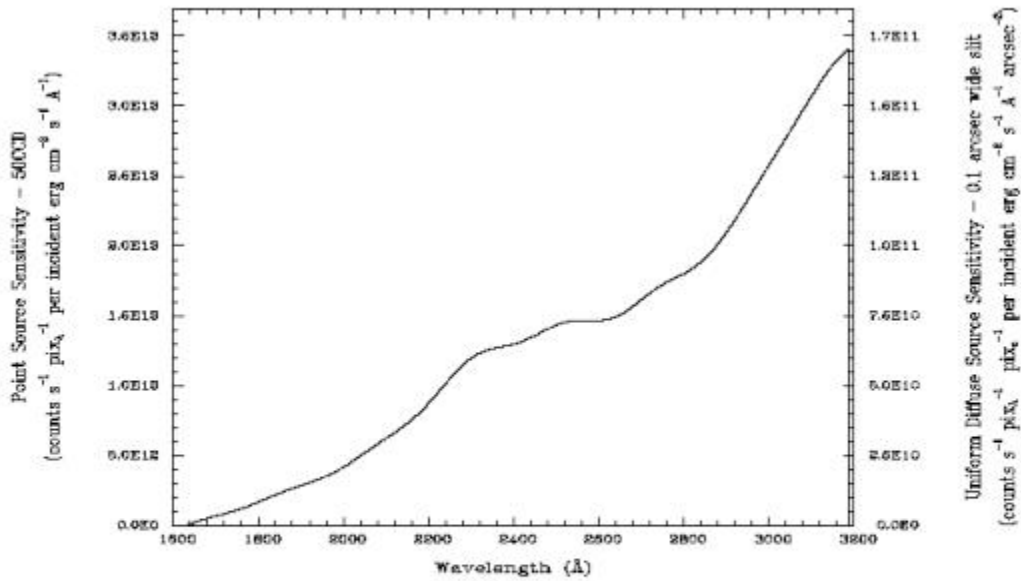
G230MB Sensitivities

Table 13.8: G230MB Sensitivities & Throughputs for a Point Source.

| λ | Sensitivity | % Throughput |
|-----------|-------------|--------------|
| 1700 | 6.5E11 | 0.1 |
| 1800 | 1.7E12 | 0.3 |
| 1900 | 2.8E12 | 0.4 |
| 2000 | 4.2E12 | 0.6 |
| 2100 | 6.2E12 | 0.9 |
| 2200 | 8.8E12 | 1.2 |
| 2300 | 1.2E13 | 1.5 |
| 2400 | 1.3E13 | 1.6 |
| 2500 | 1.4E13 | 1.7 |

| | | |
|------|--------|-----|
| 2600 | 1.5E13 | 1.7 |
| 2700 | 1.6E13 | 1.7 |
| 2800 | 1.8E13 | 1.9 |
| 2900 | 2.1E13 | 2.1 |
| 3000 | 2.6E13 | 2.5 |
| 3100 | 3.1E13 | 2.9 |

Figure 13.25: G230MB Point Source (left axis), and Diffuse Source (right axis) Sensitivities.



Note:

Point source sensitivity assumes full transmission (zero slit losses). Diffuse source sensitivity assumes a 0.1" wide slit. To convert point source sensitivities to diffuse source sensitivities multiply the point source values by the grating spatial (cross dispersion) plate scale in units of arcseconds per pixel and by the width of the desired slit in units of arcseconds.

G230MB Signal-to-Noise

Note:

The top axis displays constant F_{λ} values corresponding to the STMAG units ($V+STMAG_{\lambda}$) on the bottom axis. Recall that $STMAG=0$ is equivalent to $F_{\lambda} = 3.63E-9 \text{ erg/cm}^2/\text{s}^{-1}/\text{\AA}$. The curves are labeled with exposure times in seconds.

Figure 13.26: Diffuse Source Signal-to-Noise as a Function of STMAG for G230MB.

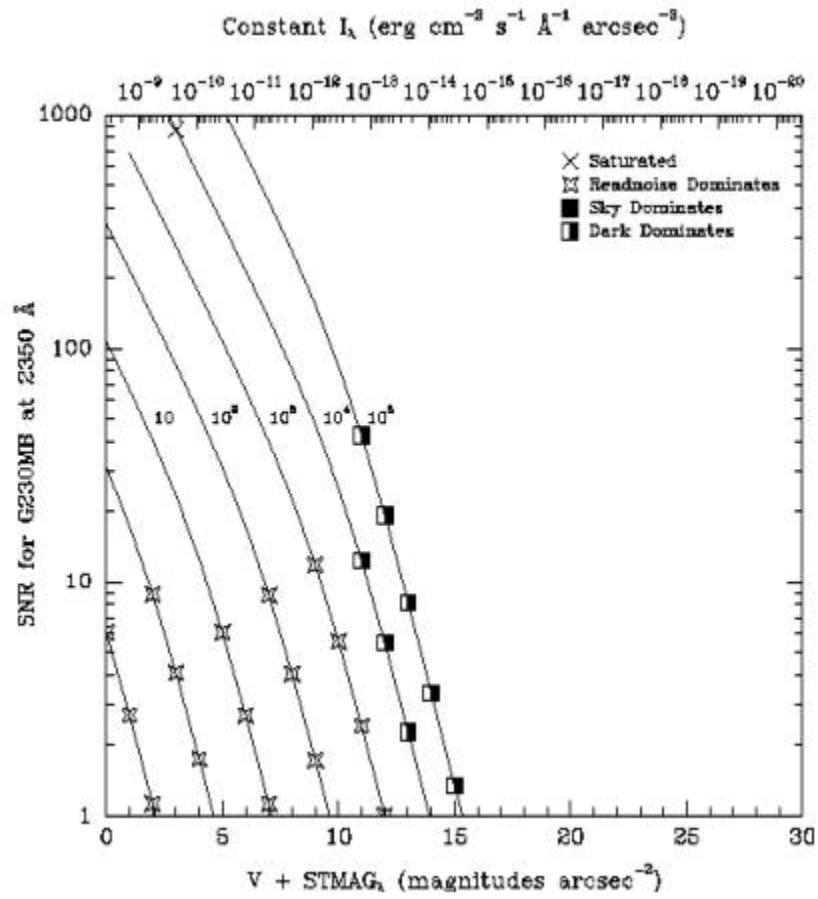
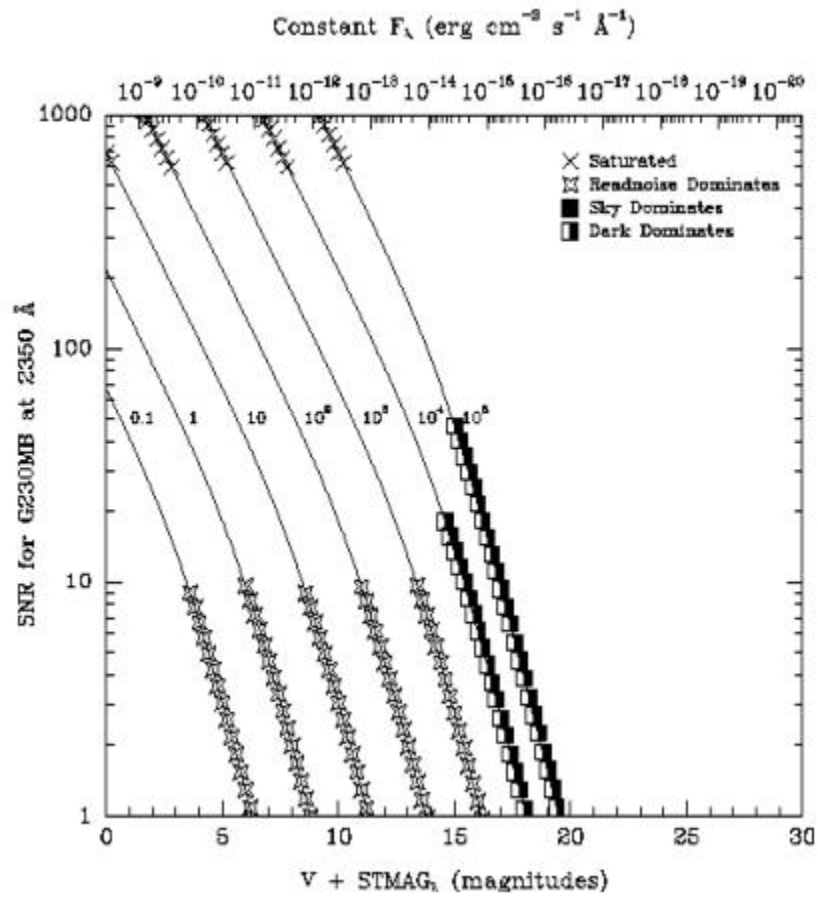


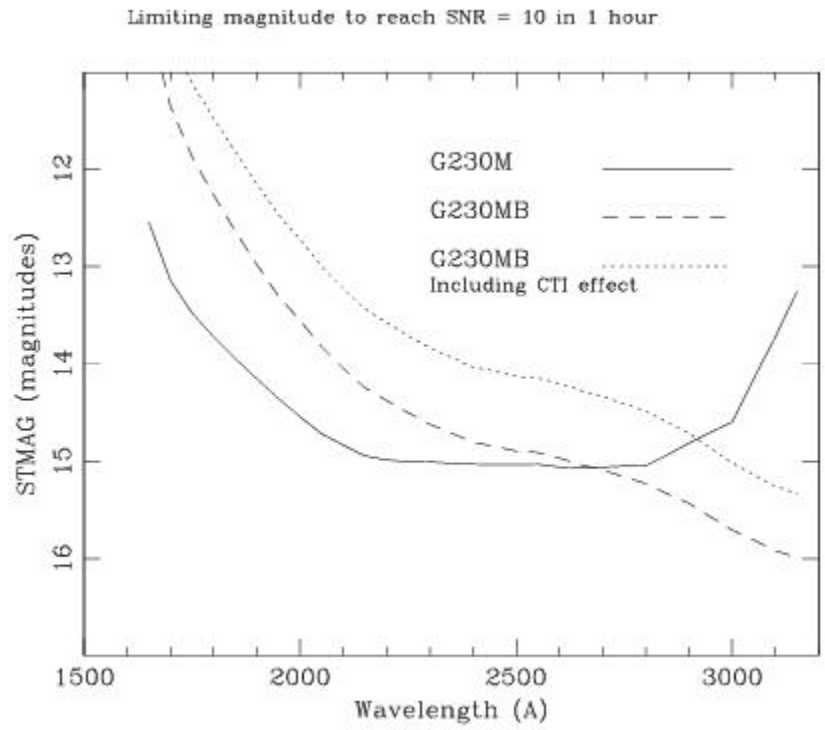
Figure 13.27: Point Source Signal-to-Noise as a Function of STMAG for G230MB.



Comparison of G230MB and G230M

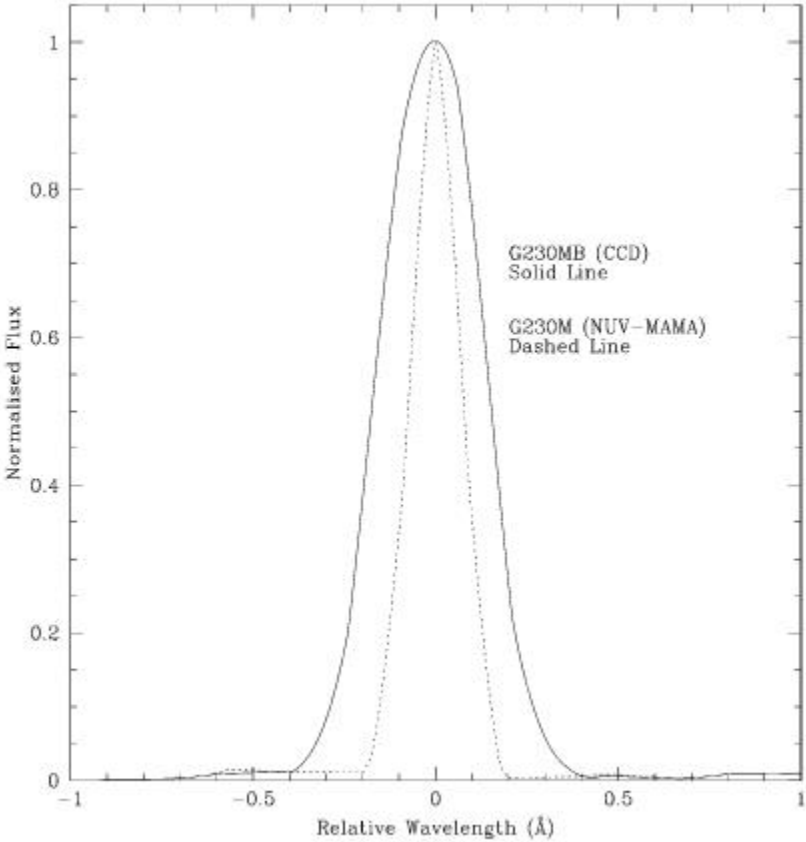
The trade-off between using the G230MB or the G230M (which uses the NUV-MAMA) grating modes, depends sensitively on the science goals and your source properties. Figures below show a direct comparison of some of the properties of the G230MB and G230M modes. For red objects, CCD data can suffer from scattered light problems (see [Section 4.1.6](#)). See also [Comparison of G230LB and G230L](#).

Figure 13.28: Comparison of Limiting Magnitudes and Fluxes for G230MB and G230M.



Plotted are the limiting source magnitudes and fluxes for G230MB and G230M to achieve a signal-to-noise ratio of 10 per 2-pixel spectral resolution element integrated across the PSF, in 1 hour. The prediction due to the Charge Transfer Inefficiency (CTI) effect, computed for the year 2005, is also shown.

Figure 13.29: Comparison of LSFs for G230MB and G230M.



First-Order Grating G230L

Description

The G230L grating is used with the NUV-MAMA and has a relatively high throughput and a resolving power of ~ 500 .

Recommended Uses

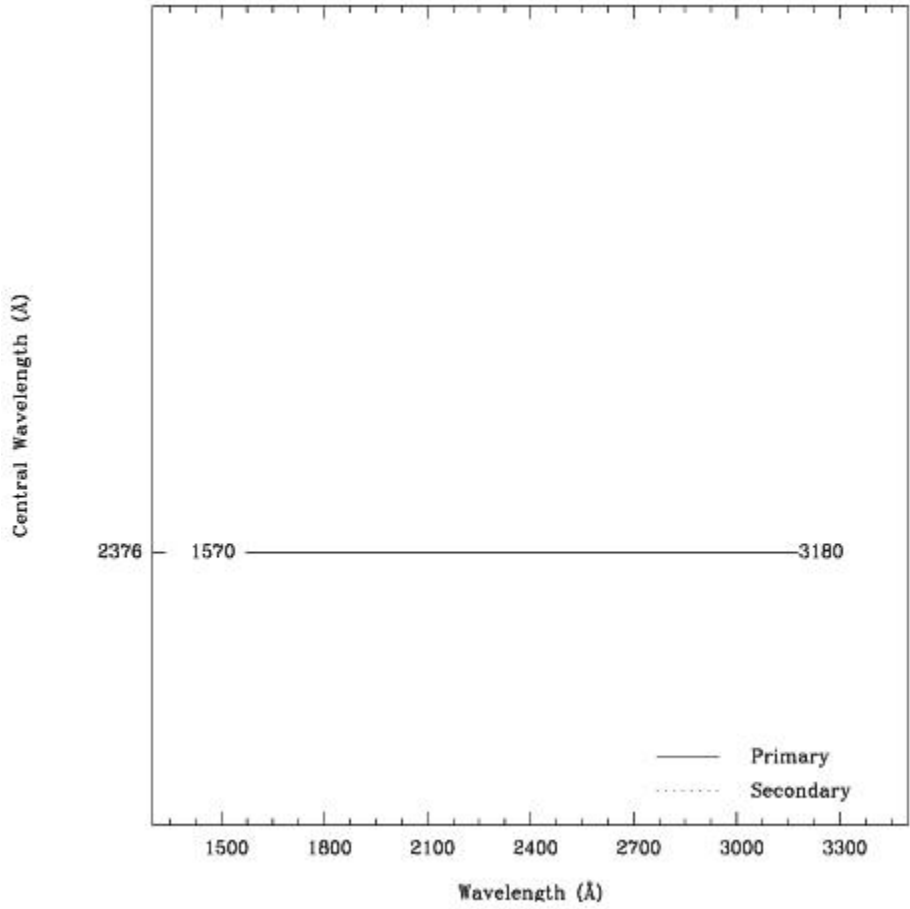
G230L is designed for observations where high spectral resolution is not required, but efficient, spatially resolved spectroscopy with full spectral coverage in the NUV is desired.

Special Considerations

Notice that the CCD G230LB grating mode also covers the NUV with comparable resolution; see [Comparison of G230LB and G230L](#) for a detailed comparison of these two grating modes in that wavelength regime.

| Grating | Spectral Range | | Average Dispersion (\AA per Pixel) | Plate Scale (arcsec/pixel) | Tilts | Central Wavelengths |
|---------|----------------|----------|--|----------------------------|-------|---------------------|
| | Complete | Per Tilt | | | | |
| G230L | 1570-3180 | 1616 | 1.58 | 0.025 | Prime | 2376 |

Figure 13.30: Wavelength Range for the G230L Grating Setting.



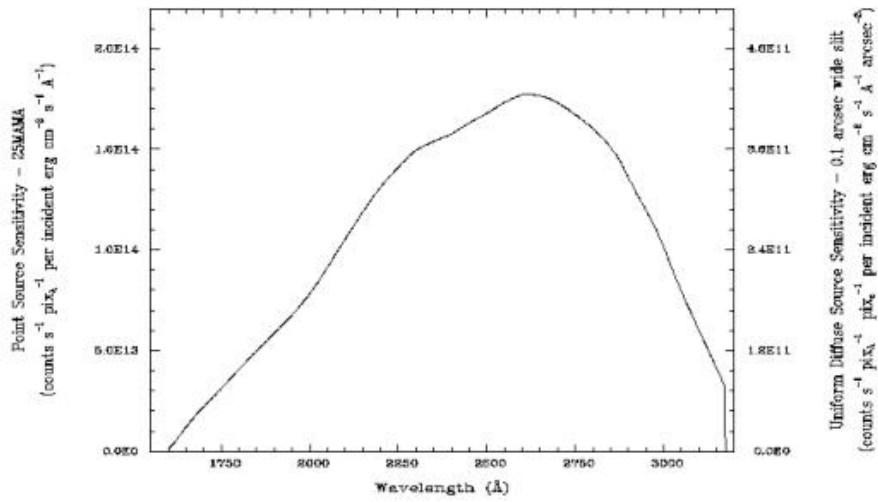
G230L Sensitivities

Table 13.9: G230L Sensitivities & Throughputs for a Point Source.

| λ | Sensitivity | % Throughput |
|-----------|-------------|--------------|
| 1600 | 2.4E12 | 0.0 |
| 1700 | 2.2E13 | 0.4 |
| 1800 | 4.1E13 | 0.6 |
| 1900 | 5.9E13 | 0.8 |
| 2000 | 7.9E13 | 1.1 |
| 2100 | 1.1E14 | 1.4 |
| 2200 | 1.3E14 | 1.6 |

| | | |
|------|--------|-----|
| 2300 | 1.5E14 | 1.8 |
| 2400 | 1.6E14 | 1.8 |
| 2500 | 1.7E14 | 1.8 |
| 2600 | 1.8E14 | 1.9 |
| 2700 | 1.7E14 | 1.8 |
| 2800 | 1.6E14 | 1.6 |
| 2900 | 1.4E14 | 1.3 |
| 3000 | 1.0E14 | 0.9 |
| 3100 | 6.0E13 | 0.5 |

Figure 13.31: G230L Point Source (left axis), and Diffuse Source (right axis) Sensitivities.



Note:

Point source sensitivity assumes full transmission (zero slit losses). Diffuse source sensitivity assumes a 0.1" wide slit. To convert point source sensitivities to diffuse source sensitivities multiply the point source values by the grating spatial (cross dispersion) plate scale in units of arcseconds per pixel and by the width of the desired slit in units of arcseconds.

G230L Signal-to-Noise

Note:

The top axis displays constant F_λ values corresponding to the STMAG units ($V+STMAG_\lambda$) on the bottom axis. Recall that $STMAG=0$ is equivalent to $F_\lambda = 3.63E-9 \text{ erg/cm}^2/\text{s}/\text{\AA}$. The curves are labeled with exposure times in seconds.

Figure 13.32: Diffuse Source Signal-to-Noise as a Function of STMAG for G230L.

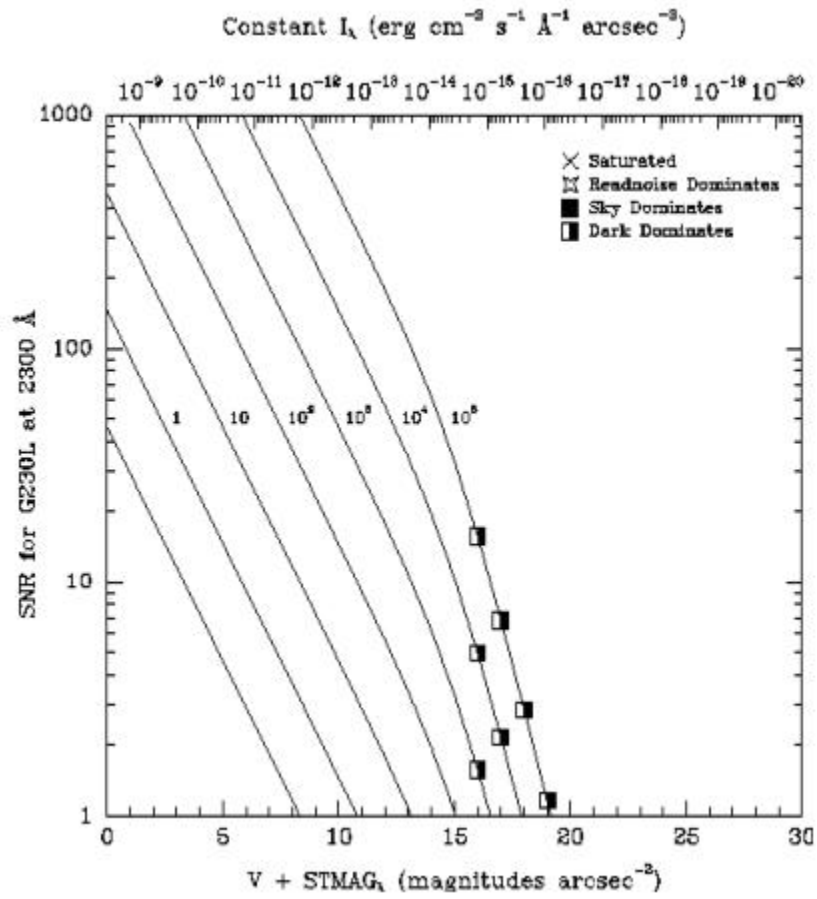
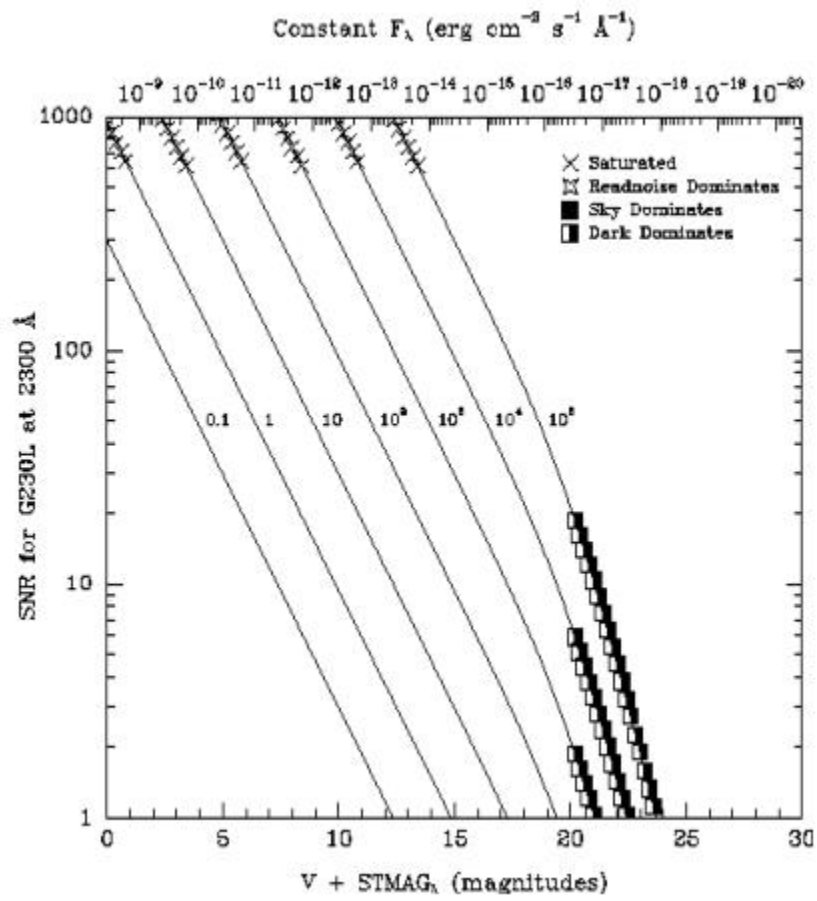


Figure 13.33: Point Source Signal-to-Noise as a Function of STMAG for G230L.



First-Order Grating G230M

Description

Like the G230L grating, the G230M grating is used with the NUV-MAMA. It has a spectral range from 1650–3100 Å; however, with a resolving power $R \sim 10,000$ a single exposure with the G230M grating covers only 90 Å. The grating must be scanned with a series of exposures taken at 18 distinct settings to cover the full spectral range.

Recommended Uses

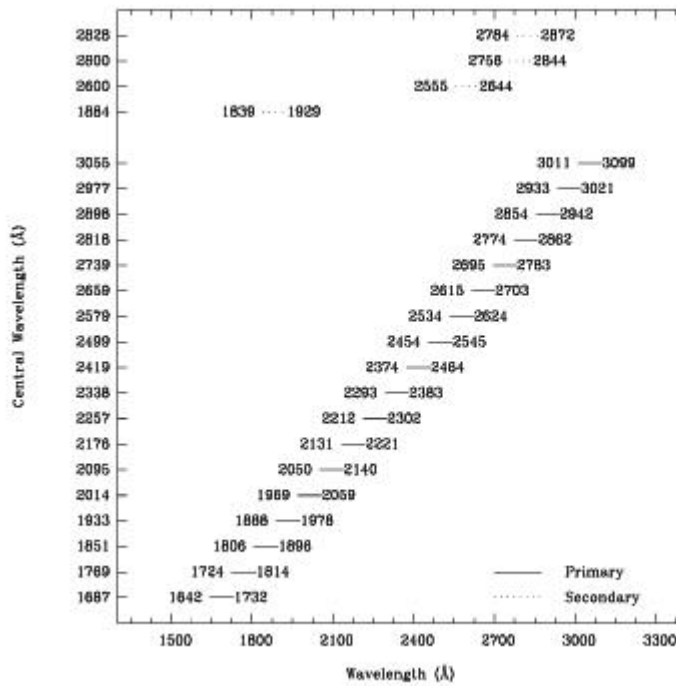
The G230M grating mode is designed for observations where spatially resolved, long slit, spectroscopy is desired at relatively high spectral resolution covering a limited region of the NUV spectrum.

Special Considerations

Notice that the CCD G230MB grating mode also covers the NUV with comparable resolution. See [Comparison of G230MB and G230M](#) for a detailed comparison of these two grating modes in that wavelength regime.

| Grating | Spectral Range | | Average Dispersion (Å/Pixel) | Plate Scale (arcsec/pixel) | Tilts | Central Wavelengths |
|---------|----------------|----------|------------------------------|----------------------------|-----------|--|
| | Complete | Per Tilt | | | | |
| G230M | 1640–3100 | 90 | 0.09 | 0.029 | Prime | 1687, 1769, 1851, 1933, 2014, 2095, 2176, 2257, 2338, 2419, 2499, 2579, 2659, 2739, 2818, 2898, 2977, 3055 |
| | | | | | Secondary | 1884, 2600, 2800, 2828 |

Figure 13.34: Wavelength Ranges for the G230M Grating Settings.



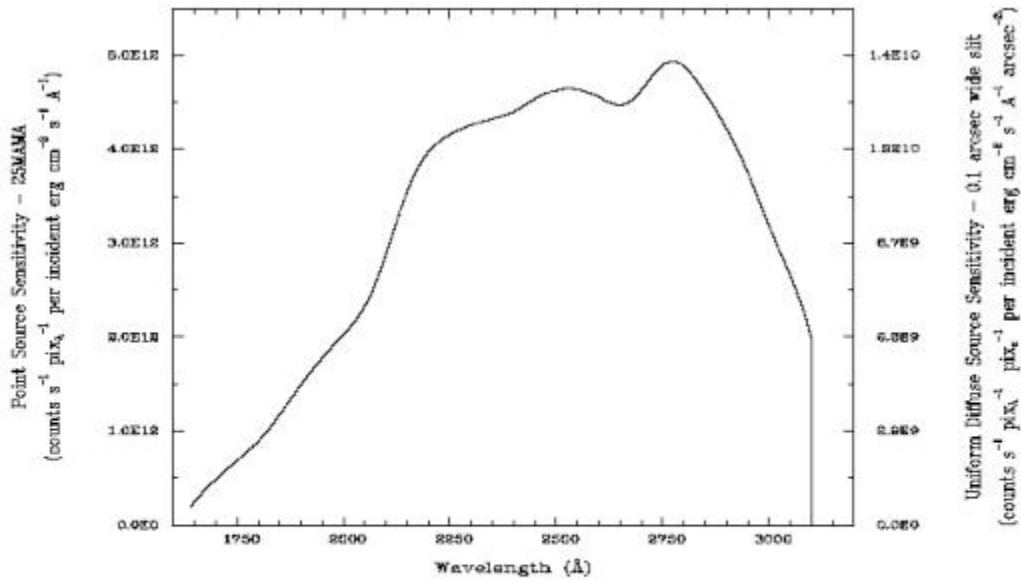
G230M Sensitivities

Table 13.10: G230M Sensitivities & Throughputs for a Point Source.

| λ | Sensitivity | % Throughput |
|-----------|-------------|--------------|
| 1700 | 4.8E11 | 0.1 |
| 1800 | 9.1E11 | 0.2 |
| 1900 | 1.5E12 | 0.4 |
| 2000 | 2.0E12 | 0.5 |
| 2100 | 2.9E12 | 0.7 |
| 2200 | 3.9E12 | 0.9 |
| 2300 | 4.2E12 | 0.9 |
| 2400 | 4.4E12 | 0.9 |
| 2500 | 4.6E12 | 0.9 |
| 2600 | 4.6E12 | 0.9 |
| 2700 | 4.6E12 | 0.8 |

| | | |
|------|--------|-----|
| 2800 | 4.8E12 | 0.8 |
| 2900 | 4.2E12 | 0.7 |
| 3000 | 3.2E12 | 0.5 |
| 3100 | 1.2E12 | 0.2 |

Figure 13.35: G230M Point Source (left axis), and Diffuse Source (right axis) Sensitivities.



Note:

Point source sensitivity assumes full transmission (zero slit losses). Diffuse source sensitivity assumes a 0.1" wide slit. To convert point source sensitivities to diffuse source sensitivities multiply the point source values by the grating spatial (cross dispersion) plate scale in units of arcseconds per pixel and by the width of the desired slit in units of arcseconds.

G230M Signal-to-Noise

Note:

The top axis displays constant F_{λ} values corresponding to the STMAG units ($V+STMAG_{\lambda}$) on the bottom axis. Recall that $STMAG=0$ is equivalent to $F_{\lambda} = 3.63E-9 \text{ erg/cm}^2/\text{s}^{-1}/\text{\AA}$. The curves are labeled with exposure times in seconds.

Figure 13.36: Diffuse Source Signal-to-Noise as a Function of STMAG for G230M.

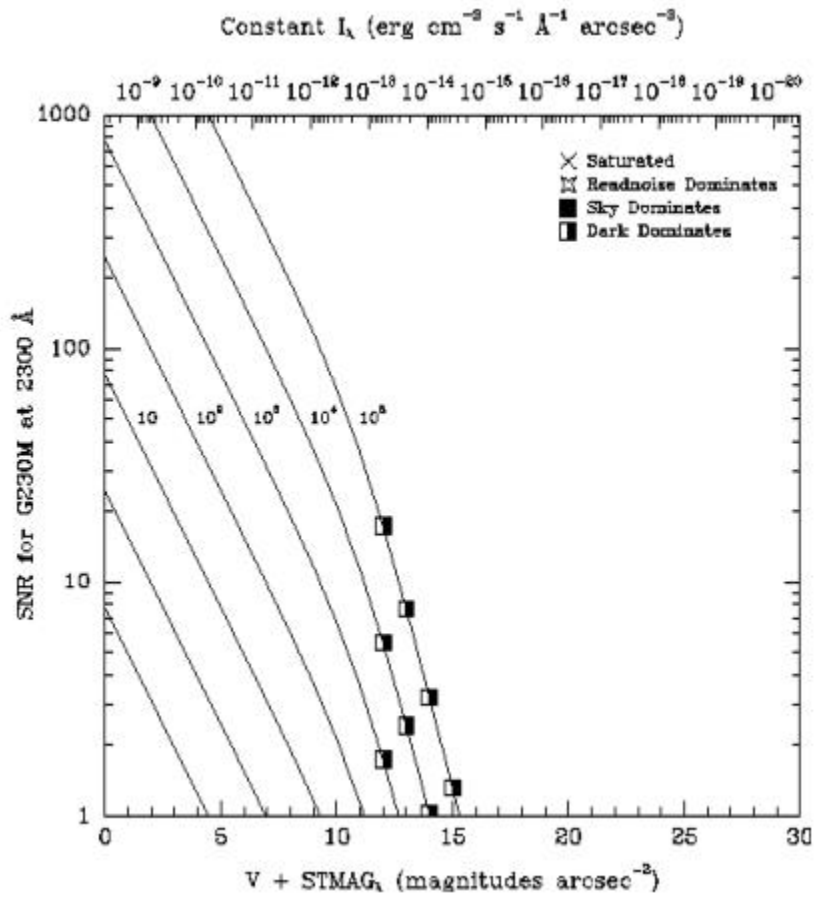
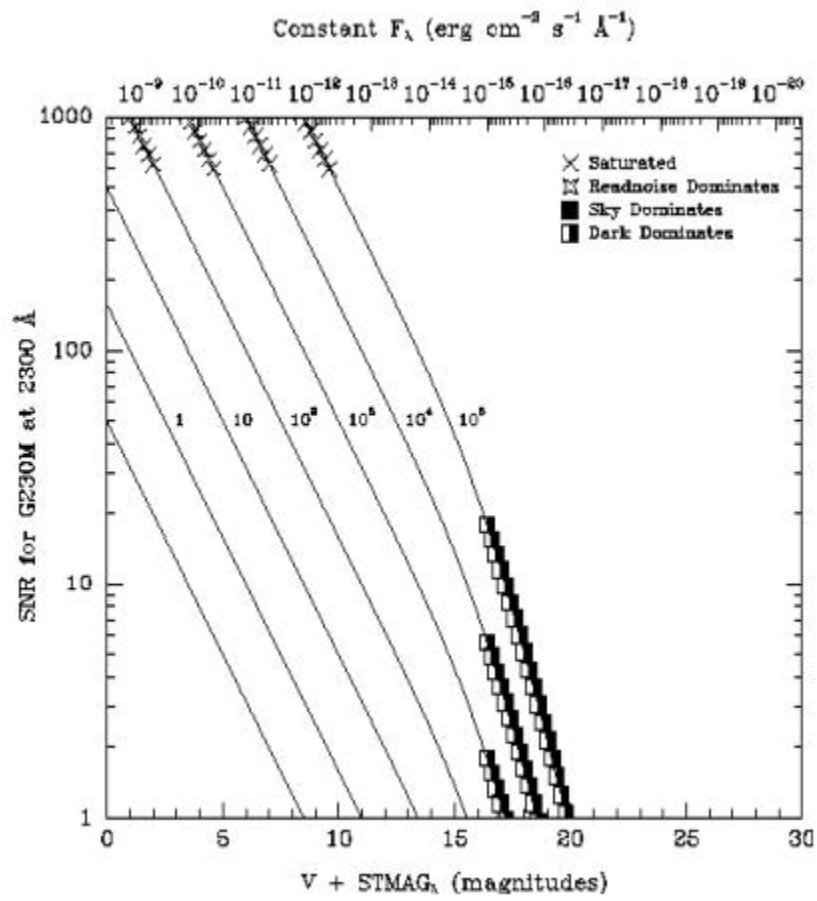


Figure 13.37: Point Source Signal-to-Noise as a Function of STMAG for G230M.



First-Order Grating G140L

Description

The G140L grating mode is used with the FUV-MAMA, has a resolving power $R \sim 1000$, and covers a spectral range from 1150 to 1700 Å in a single exposure.

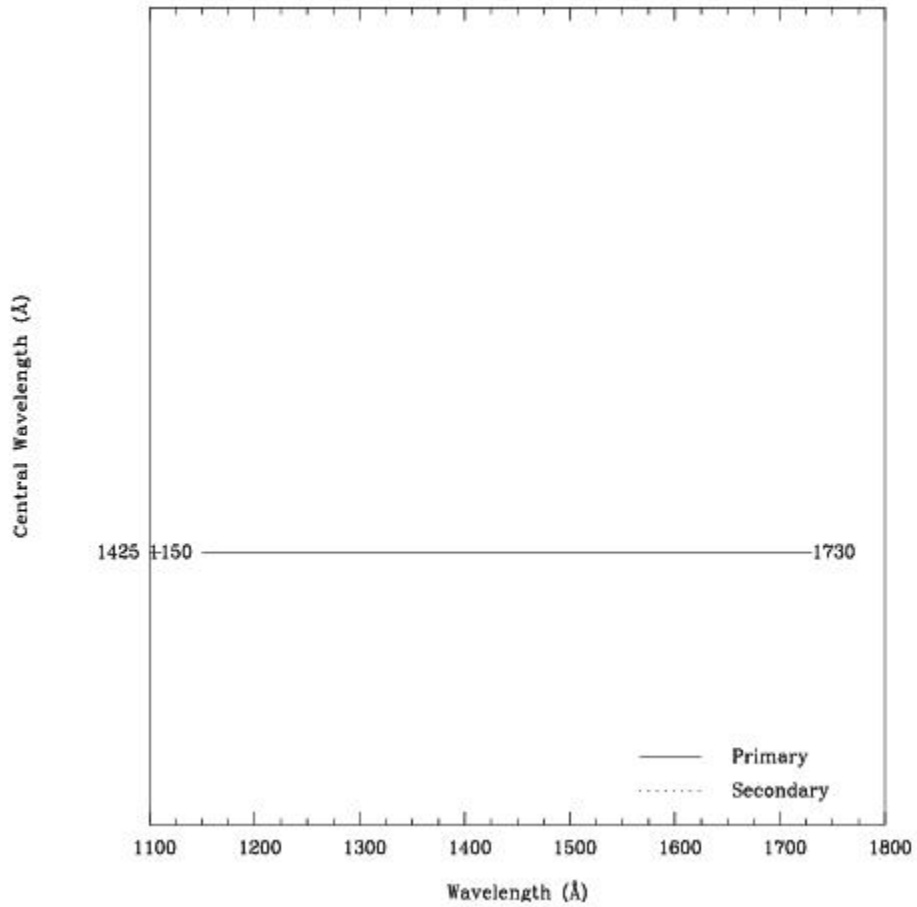
Note that with two observations, one with G140L and one with G230L, the full spectral region from 1150 to 3100 Å can be efficiently observed at an $R \sim 1000$.

Recommended Uses

The G140L grating mode is designed for observations where high spectral resolution is not required, but efficient, spatially resolved spectroscopy providing wide spectral coverage in the UV is desired.

| Grating | Spectral Range | | Average Dispersion (Å/Pixel) | Plate Scale (arcsec/pixel) | Tilts | Central Wavelengths |
|---------|----------------|----------|------------------------------|----------------------------|-------|---------------------|
| | Complete | Per Tilt | | | | |
| G140L | 1150-1730 | 590 | 0.6 | 0.0246 | Prime | 1425 |

Figure 13.38: Wavelength Range for the G140L Grating Setting.



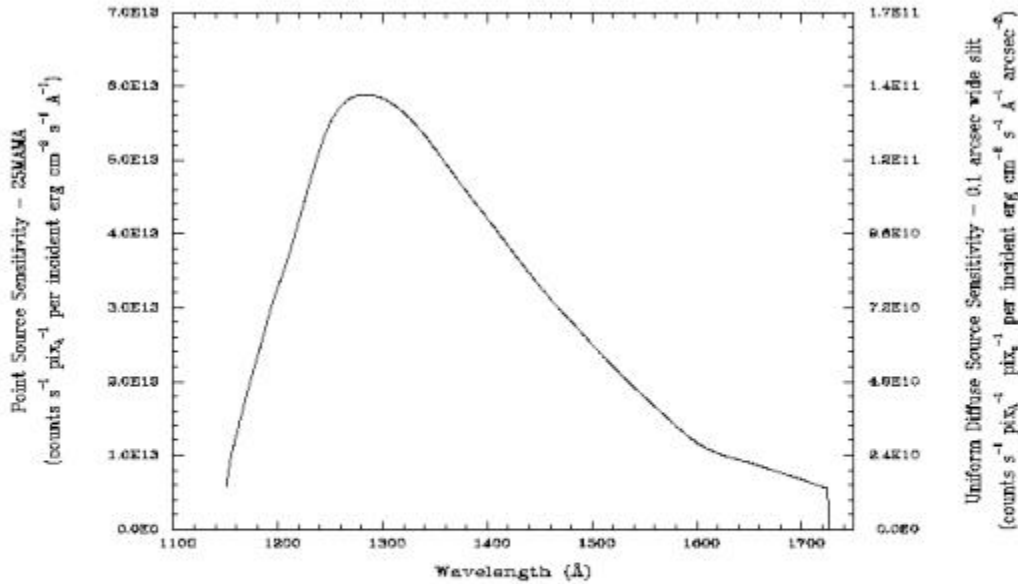
G140L Sensitivities

Table 13.11: G140L Sensitivities & Throughputs for a Point Source.

| λ | Sensitivity | % Throughput |
|-----------|-------------|--------------|
| 1200 | 3.3E13 | 2.0 |
| 1250 | 5.4E13 | 3.1 |
| 1300 | 5.8E13 | 3.3 |
| 1350 | 5.1E13 | 2.8 |
| 1400 | 4.2E13 | 2.2 |
| 1450 | 3.3E13 | 1.7 |
| 1500 | 2.5E13 | 1.2 |
| 1550 | 1.8E13 | 0.8 |

| | | |
|------|--------|-----|
| 1600 | 1.2E13 | 0.5 |
| 1650 | 9.0E12 | 0.4 |
| 1700 | 6.7E12 | 0.3 |

Figure 13.39: G140L Point Source (left axis), and Diffuse Source (right axis) Sensitivities.



Note:

Point source sensitivity assumes full transmission (zero slit losses). Diffuse source sensitivity assumes a 0.1" wide slit. To convert point source sensitivities to diffuse source sensitivities multiply the point source values by the grating spatial plate scale in units of arcseconds per pixel and by the width of the desired slit in units of arcseconds.

G140L Signal-to-Noise

Note:

The top axis displays constant F_{λ} values corresponding to the STMAG units ($V+STMAG_{\lambda}$) on the bottom axis. Recall that $STMAG=0$ is equivalent to $F_{\lambda} = 3.63E-9 \text{ erg/cm}^2/\text{s}^{-1}/\text{\AA}$. The curves are labeled with exposure times in seconds.

Figure 13.40: Diffuse Source Signal-to-Noise as a Function of STMAG for G140L.

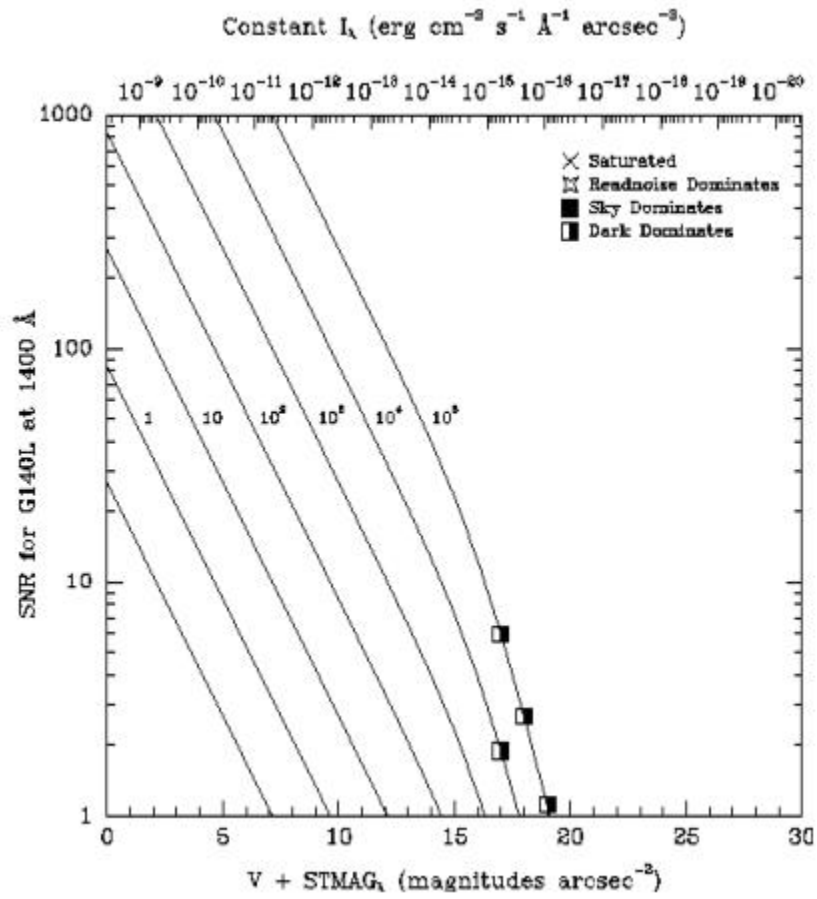
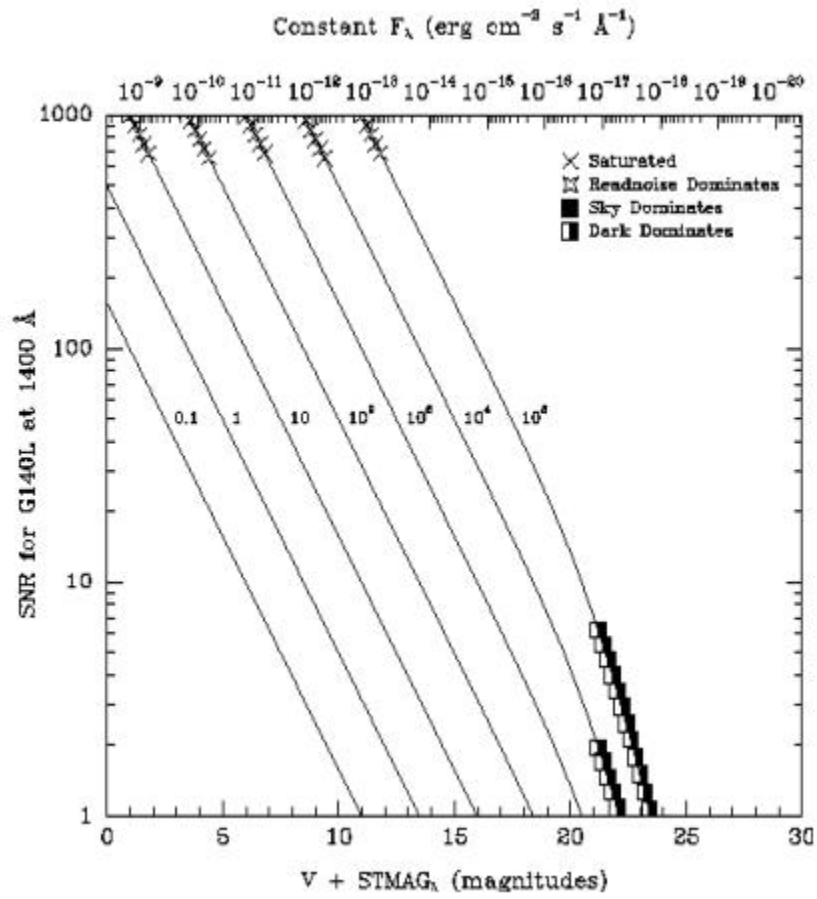


Figure 13.41: Point Source Signal-to-Noise as a Function of STMAG for G140L.



First-Order Grating G140M

Description

The G140M grating mode is used with the FUV-MAMA and has a spectral range from 1150 to 1700 Å.

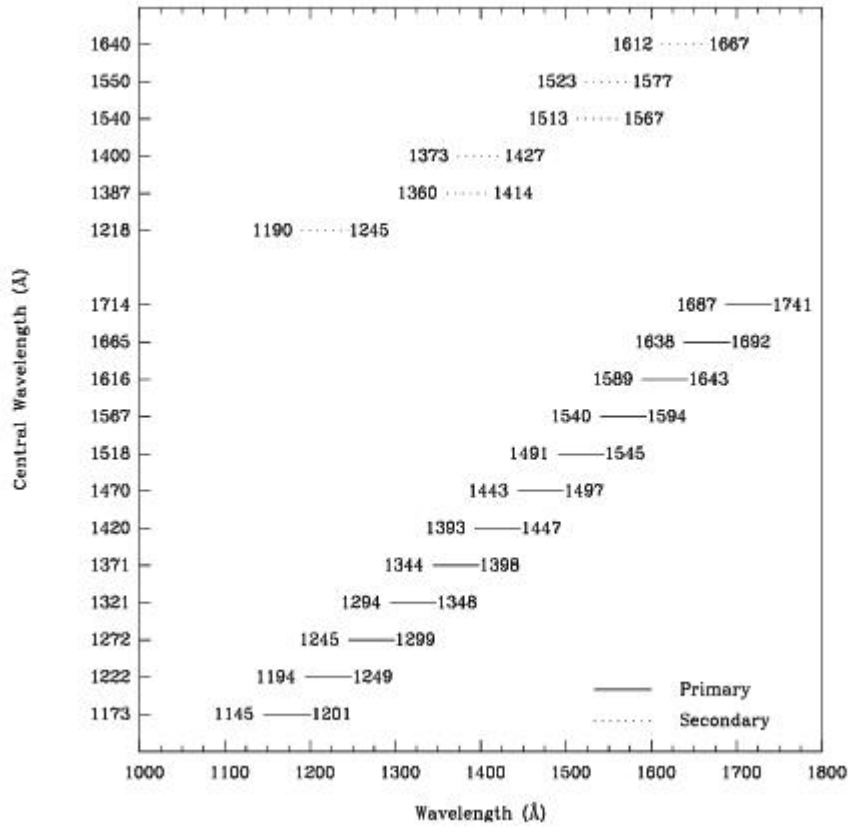
With a resolving power $R \sim 10,000$, a single exposure with this grating covers only 55 Å. The grating must be scanned, with a series of exposures taken at 12 distinct settings to cover the full spectral range.

Recommended Uses

The G140M grating mode is designed for observations where spatially resolved, long slit, spectroscopy is desired at relatively high spectral resolution over a limited region of the UV spectrum.

| Grating | Spectral Range | | Average Dispersion (Å/Pixel) | Plate Scale (arcsec/pixel) | Tilts | Central Wavelengths |
|---------|----------------|----------|------------------------------|----------------------------|-----------|--|
| | Complete | Per Tilt | | | | |
| G140M | 1140–1740 | 55 | 0.05 | 0.029 | Prime | 1173, 1222, 1272, 1321, 1371, 1420, 1470, 1518, 1567, 1616, 1665, 1714 |
| | | | | | Secondary | 1218, 1387, 1400, 1540, 1550, 1640 |

Figure 13.42: Wavelength Ranges for the G140M Grating Setting.



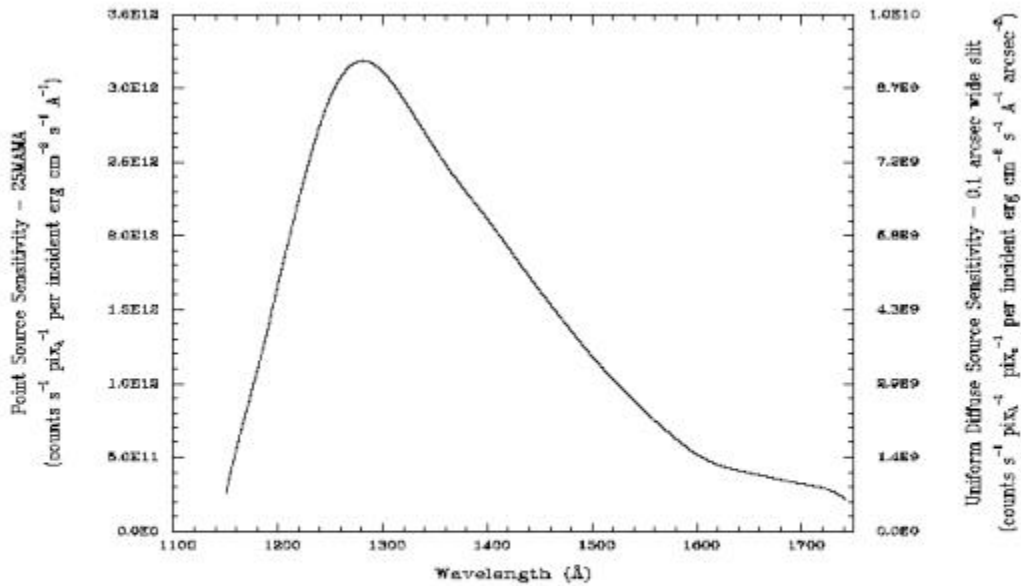
G140M Sensitivities

Table 13.12: G140M Sensitivities & Throughputs for a Point Source.

| λ | Sensitivity | % Throughput |
|-----------|-------------|--------------|
| 1200 | 1.7E12 | 1.2 |
| 1250 | 2.9E12 | 2.0 |
| 1300 | 3.1E12 | 2.1 |
| 1350 | 2.6E12 | 1.7 |
| 1400 | 2.1E12 | 1.3 |
| 1450 | 1.6E12 | 1.0 |
| 1500 | 1.2E12 | 0.7 |
| 1550 | 8.2E11 | 0.5 |
| 1600 | 5.3E11 | 0.3 |

| | | |
|------|--------|-----|
| 1650 | 3.9E11 | 0.2 |
| 1700 | 3.2E11 | 0.2 |

Figure 13.43: G140M Point Source (left axis), and Diffuse Source (right axis) Sensitivities.



Note:

Point source sensitivity assumes full transmission (zero slit losses). Diffuse source sensitivity assumes a 0.1" wide slit. To convert point source sensitivities to diffuse source sensitivities multiply the point source values by the grating spatial plate scale in units of arcseconds per pixel and by the width of the desired slit in units of arcseconds.

G140M Signal-to-Noise

Note:

The top axis displays constant F_{λ} values corresponding to the STAG units ($V+STAG_{\lambda}$) on the bottom axis. Recall that $STAG=0$ is equivalent to $F_{\lambda} = 3.63E-9 \text{ erg/cm}^2/\text{s}^{-1}/\text{\AA}$. The curves are labeled with exposure times in seconds.

Figure 13.44: Diffuse Source Signal-to-Noise as a Function of STMAG for G140M.

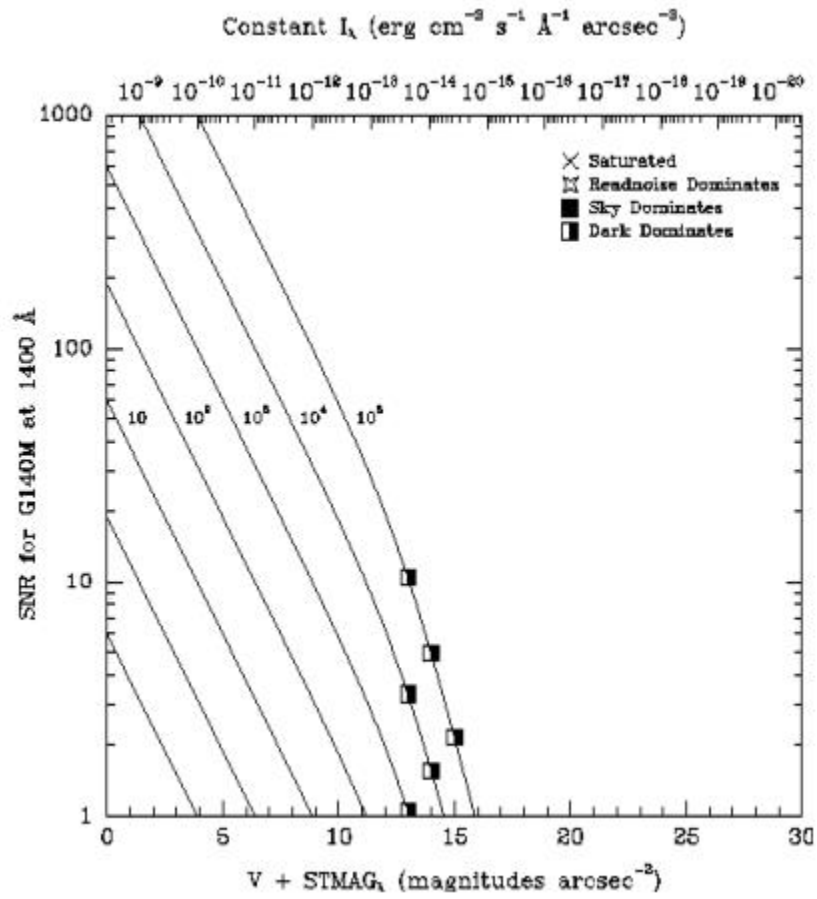
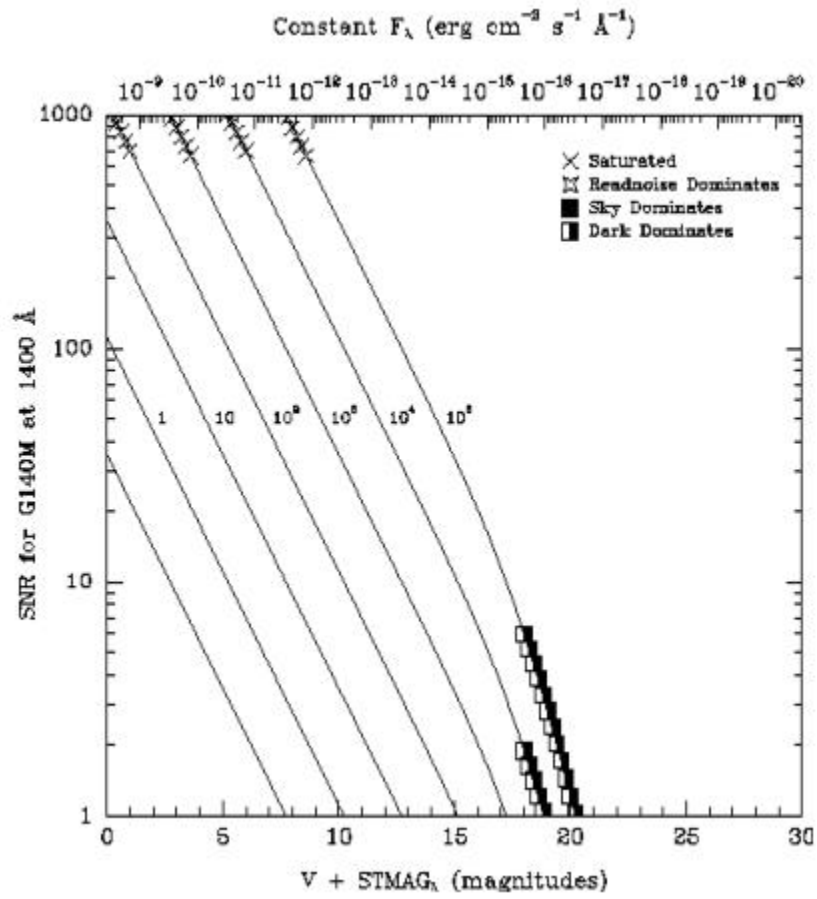


Figure 13.45: Point Source Signal-to-Noise as a Function of STMAG for G140M.



Echelle Grating E230M

Description

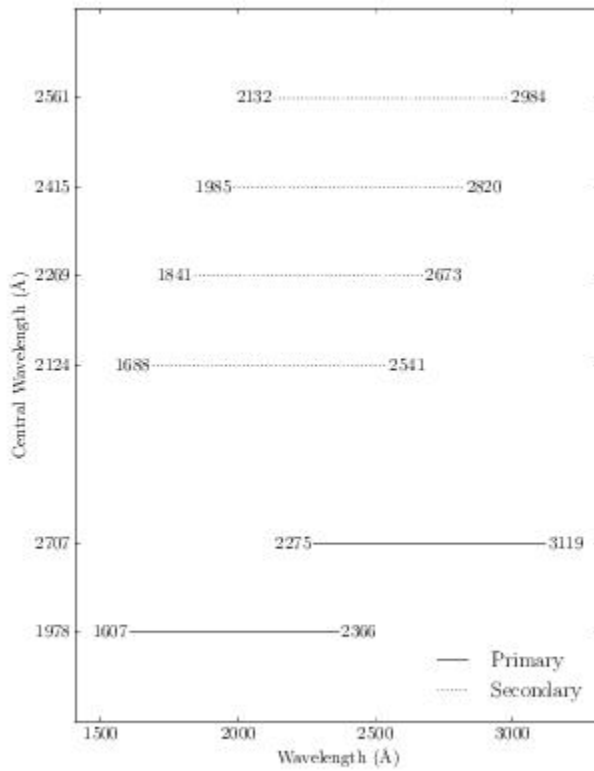
The E230M grating is used with the NUV-MAMA and provides echelle spectra at a resolving power of 30,000 from 1607 to 3129 Å.

Special Considerations

A single exposure with this grating covers 800 Å over ~20–40 orders. The interorder separation is ~18 pixels (0.52 arcseconds) at 1650 Å and 62.5 pixels (~1.8 arcseconds) at 3100 Å. The grating must be scanned, with exposures taken at two distinct settings to cover the full spectral range of the grating.

| Grating | Spectral Range | | Average Dispersion (Å/Pixel) | Dispersion, Cross Dispersion Plate Scales (arcsec/pixel) | Tilts | Central Wavelengths |
|---------|----------------|----------|------------------------------|--|-----------|------------------------|
| | Complete | Per Tilt | | | | |
| E230M | 1607–3129 | ~800 | $\lambda/60,000$ | 0.035,0.029 | Prime | 1978, 2707 |
| | | | | | Secondary | 2124, 2269, 2415, 2561 |

Figure 13.46: Wavelength Ranges for the E230M Grating Setting.



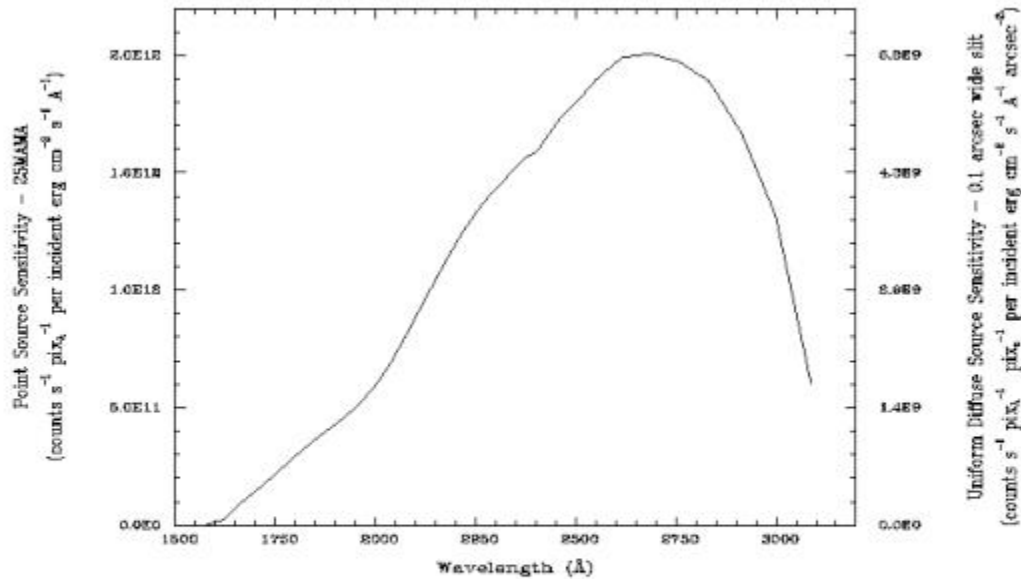
E230M Sensitivities

Table 13.13: E230M Sensitivities & Throughputs for a Point Source.

| λ | Sensitivity | % Throughput |
|-----------|-------------|--------------|
| 1700 | 1.2E11 | 0.1 |
| 1800 | 2.5E11 | 0.2 |
| 1900 | 3.7E11 | 0.2 |
| 2000 | 5.1E11 | 0.3 |
| 2100 | 7.6E11 | 0.4 |
| 2200 | 1.0E12 | 0.6 |
| 2300 | 1.3E12 | 0.7 |
| 2400 | 1.4E12 | 0.7 |
| 2500 | 1.6E12 | 0.7 |

| | | |
|------|--------|-----|
| 2600 | 1.7E12 | 0.7 |
| 2700 | 1.7E12 | 0.7 |
| 2800 | 1.7E12 | 0.7 |
| 2900 | 1.4E12 | 0.5 |
| 3000 | 1.1E12 | 0.4 |
| 3100 | 4.5E11 | 0.2 |

Figure 13.47: E230M Point Source (left axis), and Diffuse Source (right axis) Sensitivities.



Throughput curve traces the peaks of the blaze function for each order.

Note:

Point source sensitivity assumes full transmission (zero slit losses). Diffuse source sensitivity assumes a 0.1" wide slit. To convert point source sensitivities to diffuse source sensitivities multiply the point source values by the grating spatial (cross dispersion) plate scale in units of arcseconds per pixel and by the width of the desired slit in units of arcseconds.

E230M Signal-to-Noise

Note:

The top axis displays constant F_{λ} values corresponding to the STMAG units ($V+STMAG_{\lambda}$) on the bottom axis. Recall that $STMAG=0$ is equivalent to $F_{\lambda} = 3.63E-9 \text{ erg/cm}^2/\text{s}/\text{\AA}$. The curves are labeled with exposure times in seconds.

Figure 13.48: Diffuse Source Signal-to-Noise as a Function of STMAG for E230M.

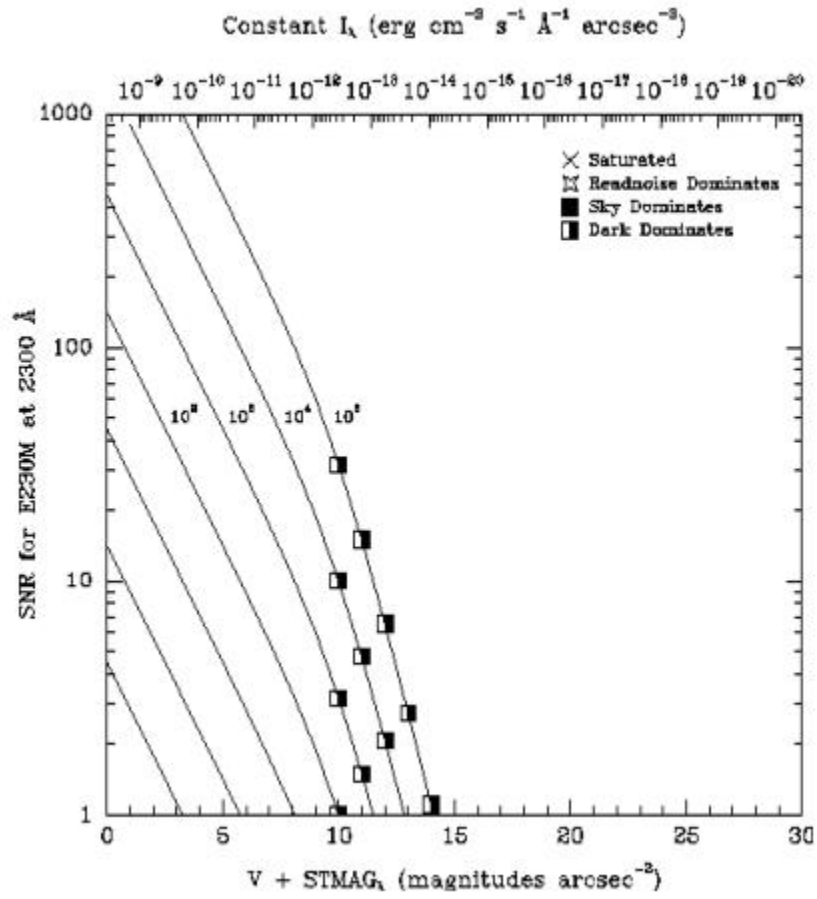
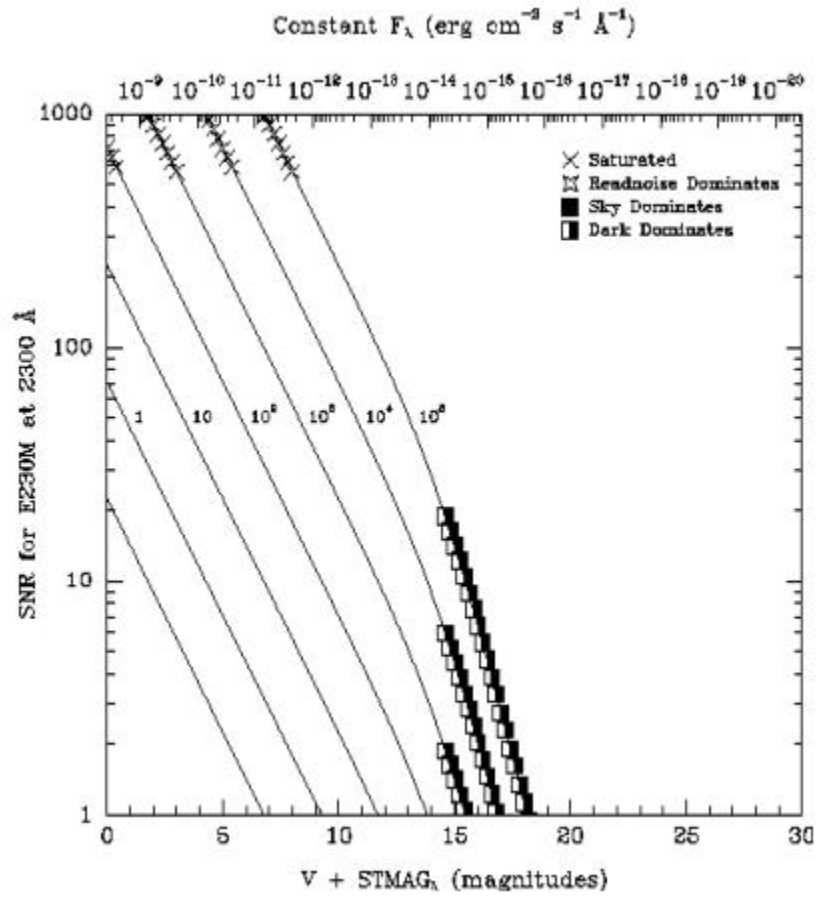


Figure 13.49: Point Source Signal-to-Noise as a Function of STMAG for E230M.



Echelle Grating E230H

Description

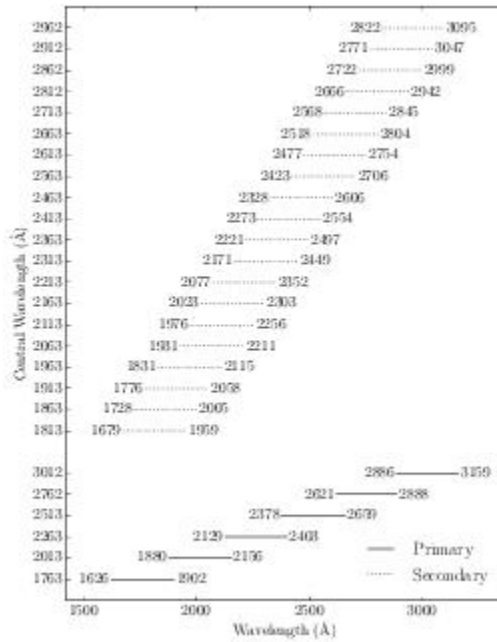
The E230H grating is used with the NUV-MAMA and provides echelle spectra at a resolving power of $\sim 114,000$ ¹ from 1626 to 3159 Å.

Special Considerations

A single E230H echellogram covers ~ 267 Å, over ~ 20 – 70 orders. The orders are spaced by only ~ 12 . 7 pixels (0.37 arcseconds) at 1650 Å and 47.2 pixels (~ 1.38 arcseconds) at 3100 Å. The grating must be scanned, with exposures taken at six distinct settings to cover the full spectral range of the grating.

| Grating | Spectral Range | | Average Dispersion (Å per Pixel) | Dispersion, Cross Dispersion Plate Scale (arcsec/pixel) | Tilts | Central Wavelengths |
|---------|----------------|------------|----------------------------------|---|-----------|--|
| | Complete | Per Tilt | | | | |
| E230H | 1626–3159 | ~ 267 | $\lambda/228,000$ | 0.047,0.029 | Prime | 1763, 2013, 2263, 2513, 2762, 3012 |
| | | | | | Secondary | 1813, 1863, 1913, 2063, 2113, 2213, 2163, 2413, 2313, 2463, 2563, 2613, 2663, 2713, 2812, 2862, 2912, 2962 |

Figure 13.50: Wavelength Ranges for the E230H Grating Setting.



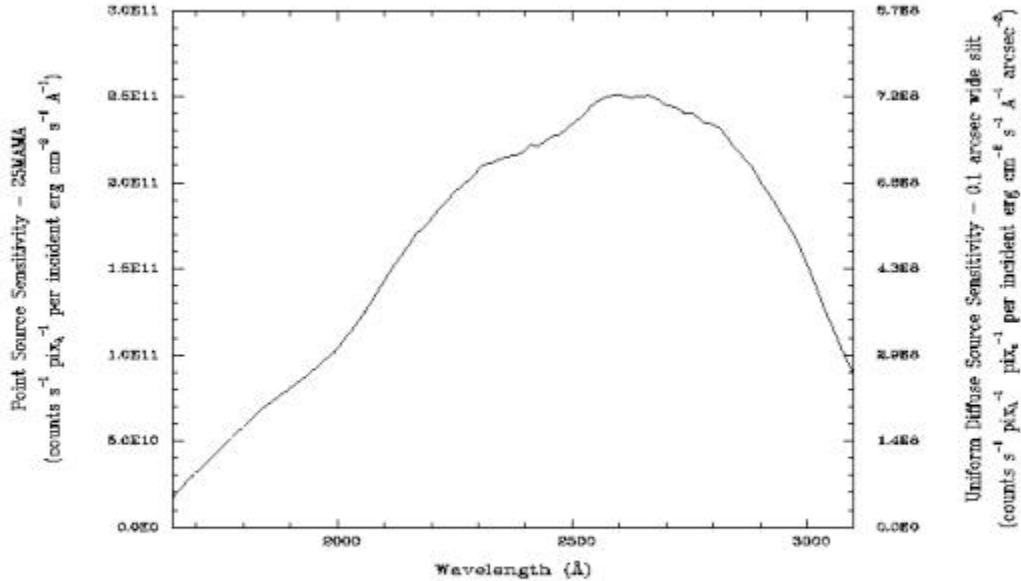
E230H Sensitivities

Table 13.14: E230H Sensitivities & Throughputs for a Point Source.

| λ | Sensitivity | % Throughput |
|-----------|-------------|--------------|
| 1700 | 3.1E10 | 0.1 |
| 1800 | 5.6E10 | 0.2 |
| 1900 | 7.8E10 | 0.2 |
| 2000 | 1.0E11 | 0.3 |
| 2100 | 1.4E11 | 0.4 |
| 2200 | 1.7E11 | 0.5 |
| 2300 | 2.0E11 | 0.5 |
| 2400 | 2.1E11 | 0.5 |
| 2500 | 2.2E11 | 0.5 |
| 2600 | 2.4E11 | 0.5 |
| 2700 | 2.3E11 | 0.5 |

| | | |
|------|--------|-----|
| 2800 | 2.2E11 | 0.4 |
| 2900 | 1.9E11 | 0.4 |
| 3000 | 1.4E11 | 0.2 |
| 3100 | 8.1E10 | 0.1 |

Figure 13.51: E230H Point Source (left axis), and Diffuse Source (right axis) Sensitivities.



Throughput curve traces the peaks of the blaze function for each order.

Note:

Point source sensitivity assumes full transmission (zero slit losses). Diffuse source sensitivity assumes a 0.1" wide slit. To convert point source sensitivities to diffuse source sensitivities multiply the point source values by the grating spatial (cross dispersion) plate scale in units of arcseconds per pixel and by the width of the desired slit in units of arcseconds.

E230H Signal-to-Noise

Note:

The top axis displays constant F_{λ} values corresponding to the STMAG units (V+STMAG $_{\lambda}$) on the bottom axis. Recall that STMAG=0 is equivalent to $F_{\lambda} = 3.63E-9$ erg/cm²/s/Å. The curves are labeled with exposure times in seconds.

Figure 13.52: Diffuse Source Signal-to-Noise as a Function of STMAG for E230H.

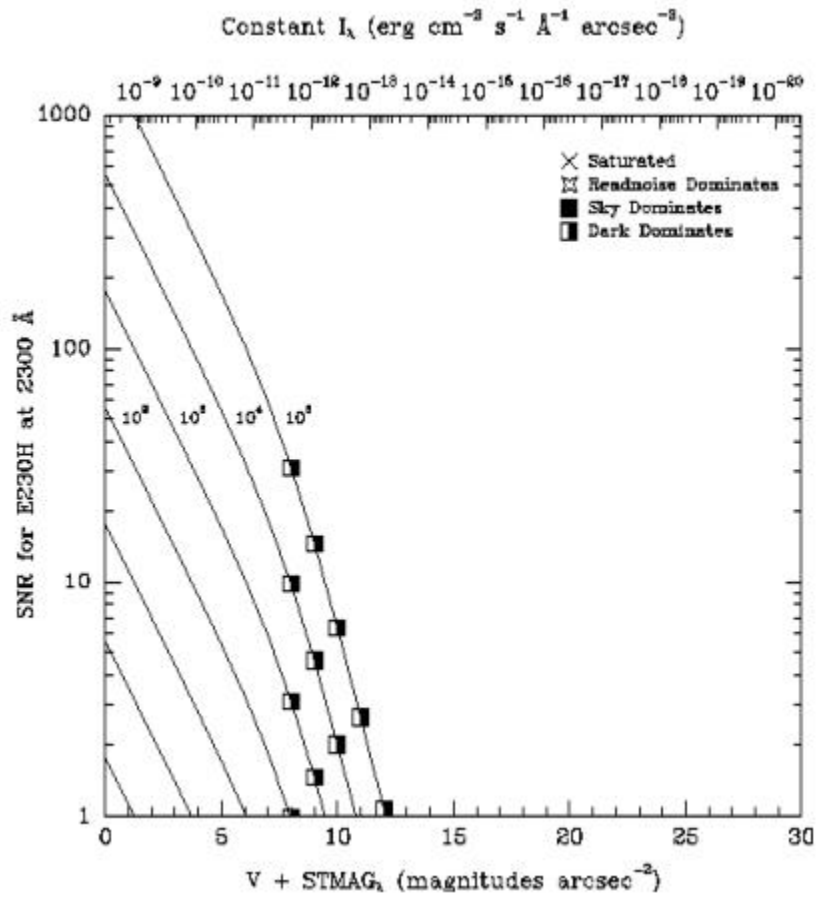
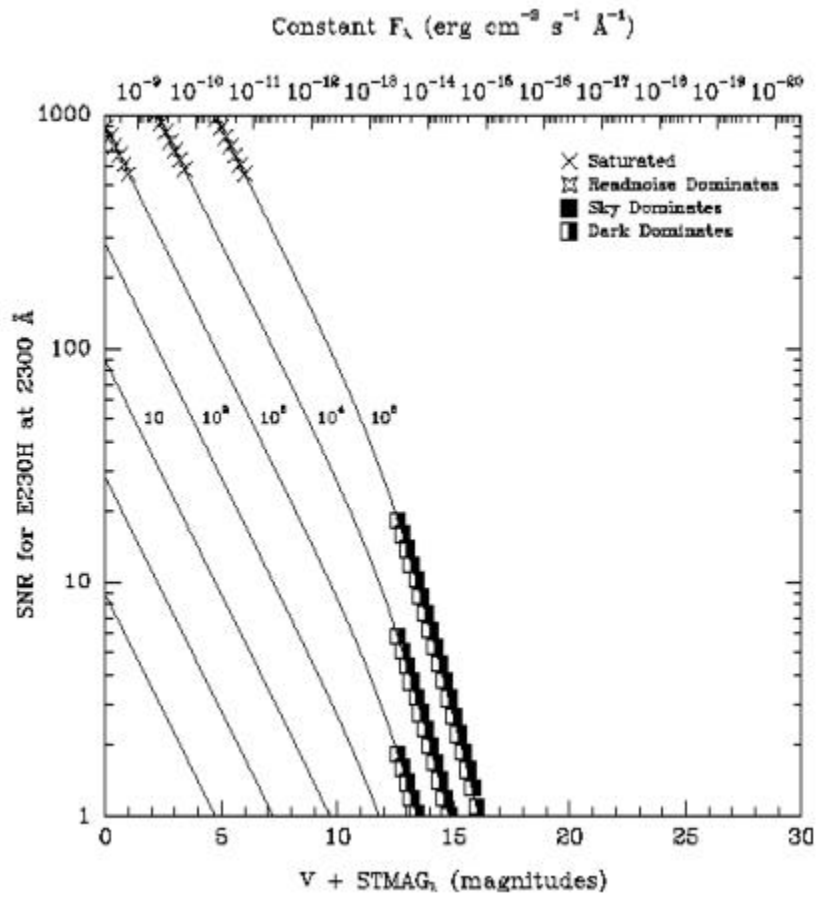


Figure 13.53: Point Source Signal-to-Noise as a Function of STMAG for E230H.



¹ R ~ 200,000 possible with the 0.1x0.03 aperture; see [Section 12.6](#).

Echelle Grating E140M

Description

The E140M grating is used with the FUV-MAMA and provides echelle spectra at a resolving power of 45,800 from ~1144-1729 Å.

Special Considerations

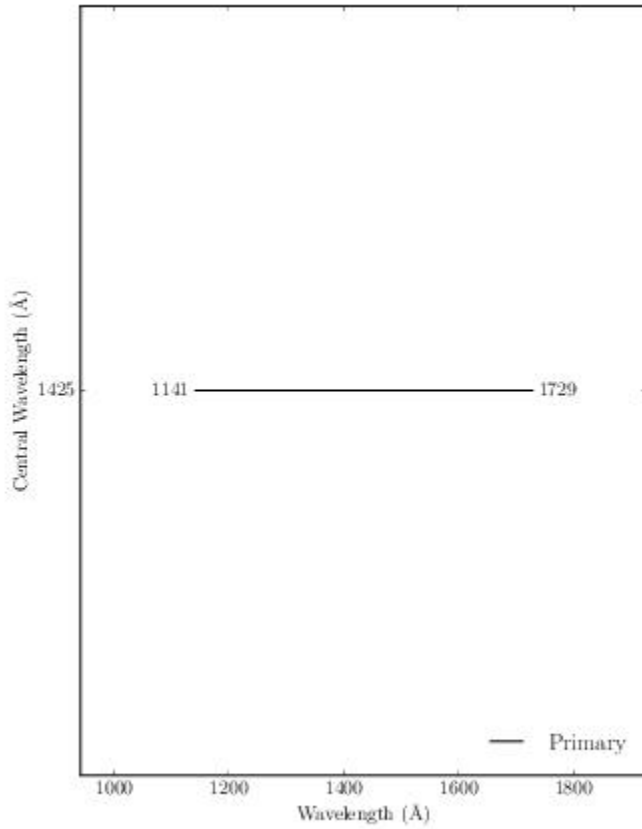
A single E140M echellogram covers ~600 Å, however at wavelengths longward of 1649 Å, the echelle orders overrun the width of the detector in the dispersion direction, so there will be three small gaps in the wavelength coverage. One gap of ~0.2 Å, one of ~0.4 Å, and one of ~0.7 Å occur between 1649 and 1700 Å.

The separation between orders is ~15 pixels (or 0.44 arcseconds) at 1150 Å and ~33 (0.96 arcseconds) at 1700 Å.

Also note that while the spectral format of the E140M extends down to 1123 Å, HST's total system throughput is extremely small below about 1144 Å.

| Grating | Spectral Range | | Average Dispersion (Å per Pixel) | Dispersion, Cross Dispersion Plate Scale (arcsec/pixel) | Tilts | Central Wavelengths |
|---------|----------------|----------|----------------------------------|---|-------|---------------------|
| | Complete | Per Tilt | | | | |
| E140M | 1144-1729 | 567 | $\lambda/91,700$ | 0.036,0.029 | Prime | 1425 |

Figure 13.54: Wavelength Ranges for the E140M Grating Setting.



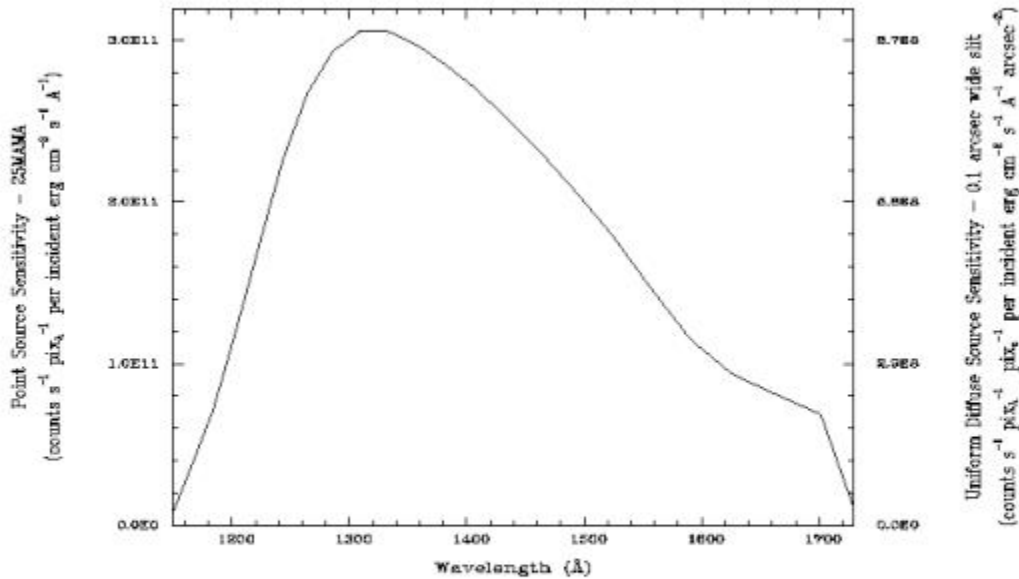
E140M Sensitivities

Table 13.15: E140M Sensitivities & Throughputs for a Point Source.

| λ | Sensitivity | % Throughput |
|-----------|-------------|--------------|
| 1200 | 1.0E11 | 0.3 |
| 1250 | 2.1E11 | 0.5 |
| 1300 | 2.6E11 | 0.6 |
| 1350 | 2.6E11 | 0.6 |
| 1400 | 2.4E11 | 0.5 |
| 1450 | 2.0E11 | 0.4 |
| 1500 | 1.7E11 | 0.3 |

| | | |
|------|--------|-----|
| 1550 | 1.3E11 | 0.2 |
| 1600 | 9.3E10 | 0.1 |
| 1650 | 7.4E10 | 0.1 |
| 1700 | 6.0E10 | 0.1 |

Figure 13.55: E140M Point Source (left axis), and Diffuse Source (right axis) Sensitivities.



Throughput curve traces the peaks of the blaze function for each order.

Note:

Point source sensitivity assumes full transmission (zero slit losses). Diffuse source sensitivity assumes a 0.1" wide slit. To convert point source sensitivities to diffuse source sensitivities multiply the point source values by the grating spatial (cross dispersion) plate scale in units of arcseconds per pixel and by the width of the desired slit in units of arcseconds.

E140M Signal-to-Noise

Note:

The top axis displays constant F_λ values corresponding to the STAG units ($V+STAG_\lambda$) on the bottom axis. Recall that $STAG=0$ is equivalent to $F_\lambda = 3.63E-9 \text{ erg/cm}^2/\text{s}/\text{\AA}$. The curves are labeled with exposure times in seconds.

Figure 13.56: Diffuse Source Signal-to-Noise as a Function of STMAG for E140M.

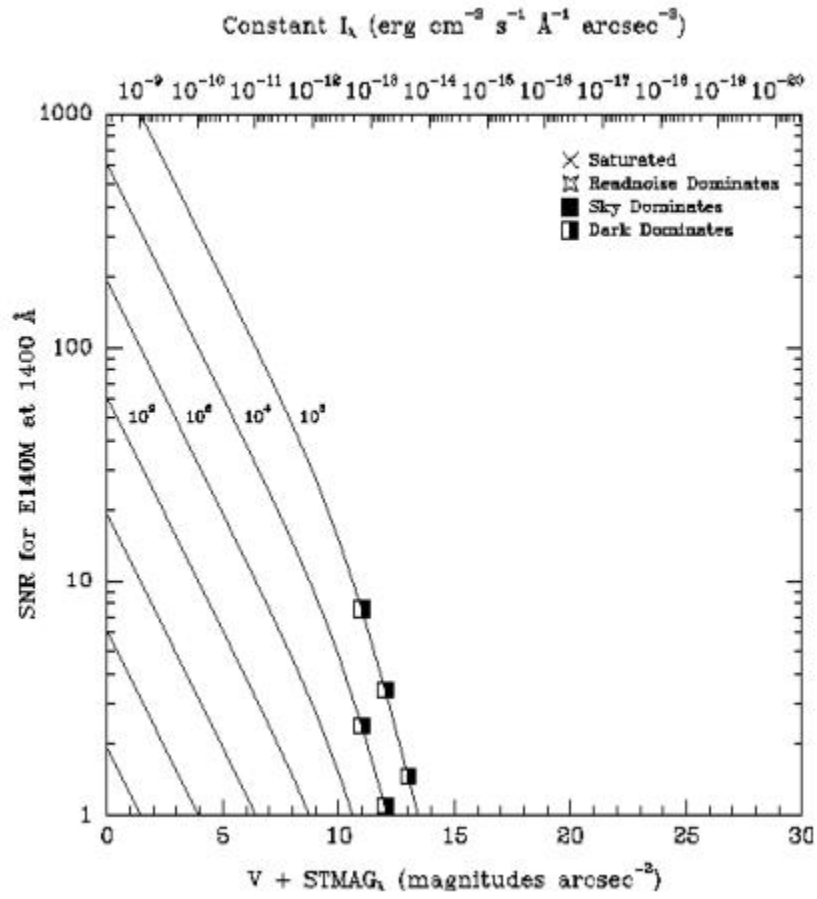
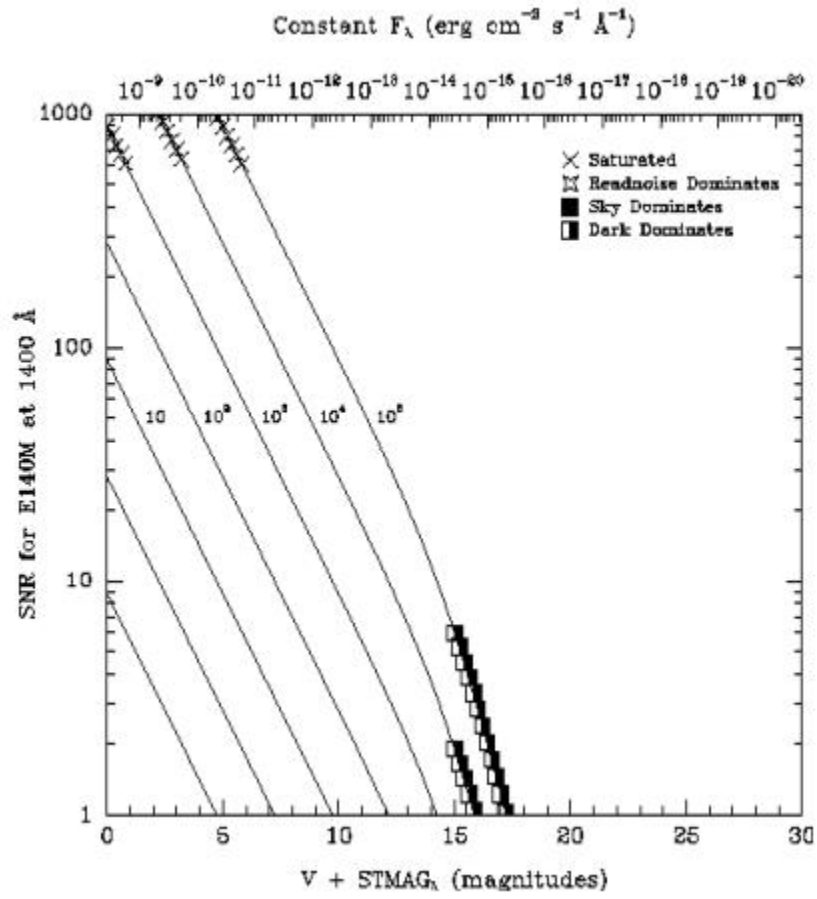


Figure 13.57: Point Source Signal-to-Noise as a Function of STMAG for E140M.



Echelle Grating E140H

Description

The E140H grating is used with the NUV-MAMA and provides echelle spectra at a resolving power of $\sim 114,000^1$ from ~ 1140 to 1700 \AA .

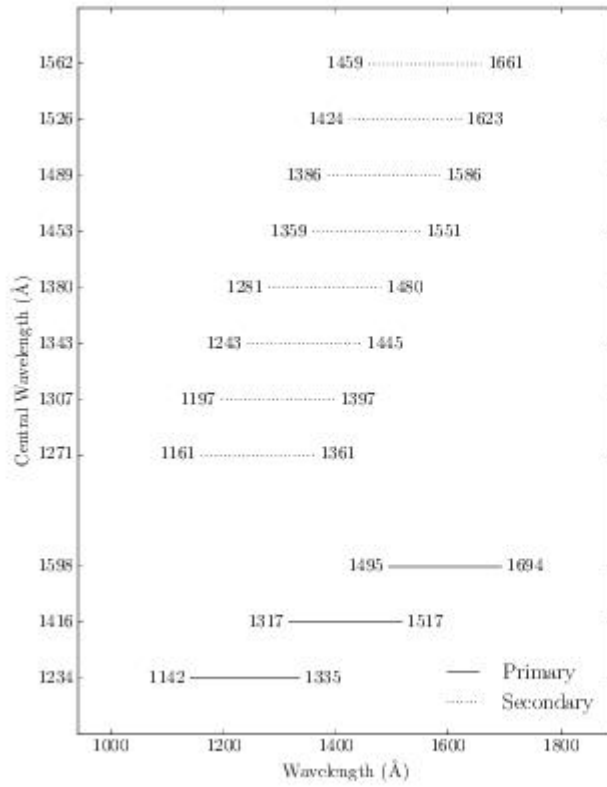
Special Considerations

A single E140H echellogram covers $\sim 210 \text{ \AA}$, over ~ 50 orders. The order separation is ~ 16 pixels (0.47 arcseconds) at 1150 \AA and ~ 36 pixels (1.05 arcseconds) at 1700 \AA . The grating must be scanned, with exposures taken at three distinct settings to cover the full spectral range of the grating.

Note that while the spectral format of the 1234 \AA setting extends down to 1133 \AA , the throughput becomes vanishingly small below about 1140 \AA .

| Grating | Spectral Range | | Average Dispersion (\AA per Pixel) | Dispersion, Cross Dispersion Plate Scale (arcsec/pixel) | Tilts | Central Wavelengths |
|---------|----------------|------------|--|---|-----------|--|
| | Complete | Per Tilt | | | | |
| E140H | 1140-1700 | ~ 210 | $\lambda/228,000$ | 0.047,0.029 | Prime | 1234, 1416, 1598 |
| | | | | | Secondary | 1271, 1307, 1343, 1380, 1453, 1489, 1526, 1562 |

Figure 13.58: Wavelength Ranges for the E140H Grating Setting.



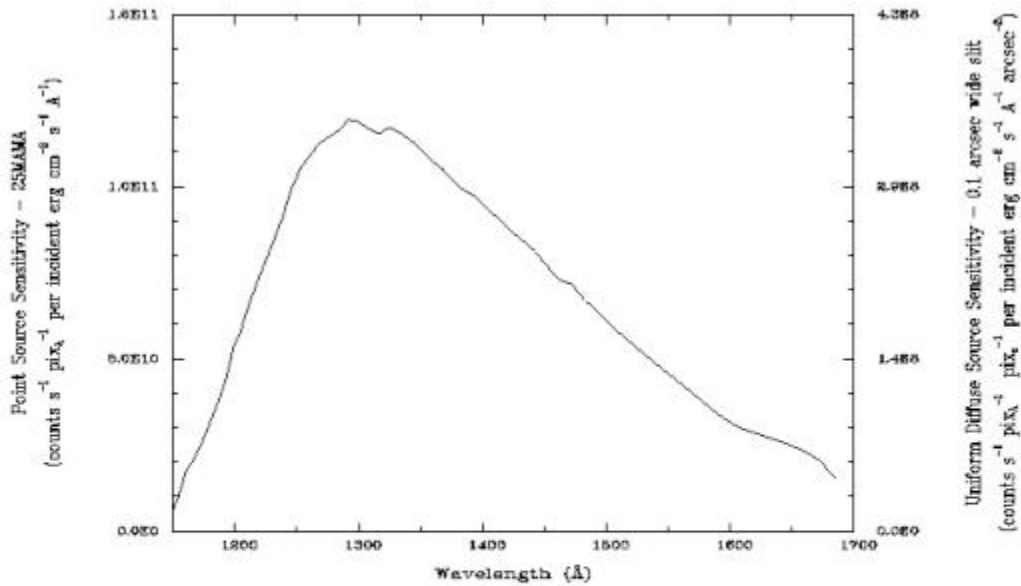
E140H Sensitivities

Table 13.16: E140H Sensitivities & Throughputs for a Point Source.

| λ | Sensitivity | % Throughput |
|-----------|-------------|--------------|
| 1200 | 5.0E10 | 0.4 |
| 1250 | 9.4E10 | 0.6 |
| 1300 | 1.1E11 | 0.7 |
| 1350 | 1.0E11 | 0.6 |
| 1400 | 8.9E10 | 0.5 |
| 1450 | 7.3E10 | 0.4 |
| 1500 | 5.7E10 | 0.3 |
| 1550 | 4.2E10 | 0.2 |
| 1600 | 2.9E10 | 0.1 |

| | | |
|------|--------|-----|
| 1650 | 2.2E10 | 0.1 |
|------|--------|-----|

Figure 13.59: E140H Point Source (left axis), and Diffuse Source (right axis) Sensitivities.



Throughput curve traces the peaks of the blaze function for each order.

Note:

Point source sensitivity assumes full transmission (zero slit losses). Diffuse source sensitivity assumes a 0.1" wide slit. To convert point source sensitivities to diffuse source sensitivities multiply the point source values by the grating spatial (cross dispersion) plate scale in units of arcseconds per pixel and by the width of the desired slit in units of arcseconds.

E140H Signal-to-Noise

Note:

The top axis displays constant F_λ values corresponding to the STAG units ($V+STAG_\lambda$) on the bottom axis. Recall that $STAG=0$ is equivalent to $F_\lambda = 3.63E-9 \text{ erg/cm}^2/\text{s}/\text{\AA}$. The curves are labeled with exposure times in seconds.

Figure 13.60: Diffuse Source Signal-to-Noise as a Function of STMAG for E1403H.

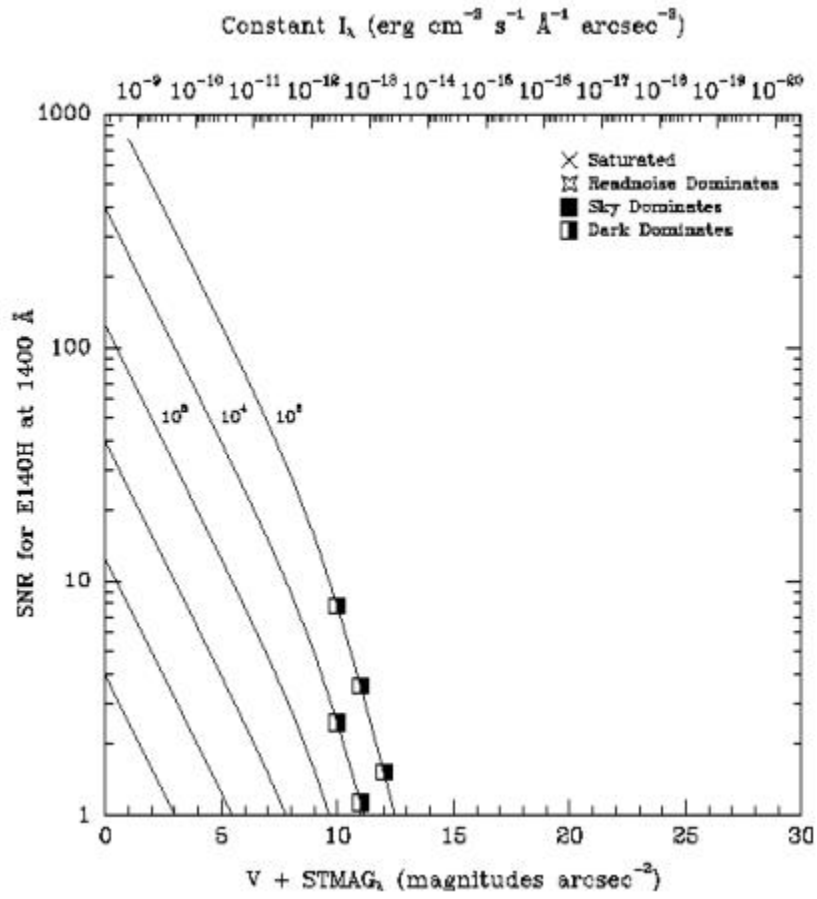
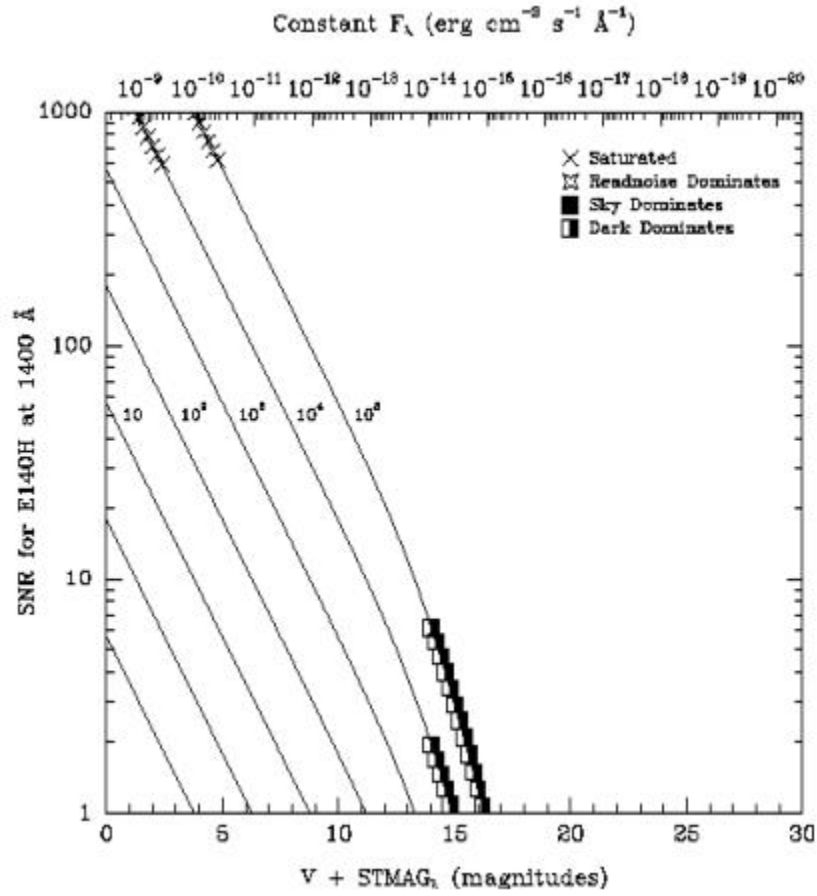


Figure 13.61: Point Source Signal-to-Noise as a Function of STMAG for E140H.



¹ R ~ 200,000 possible with the 0.1x0.03 aperture; see [Section 12.6](#).

PRISM

Description

The PRISM has two central wavelength settings optimized to cover the optical through the far-ultraviolet (FUV) tail down to 1150 Å. It is used with the `NUV-MAMA` detector. Beginning in Cycle 30, the use of the STIS PRISM will be an Available-but-Unsupported mode. See [Section 4.4](#) for more information.

Special Considerations

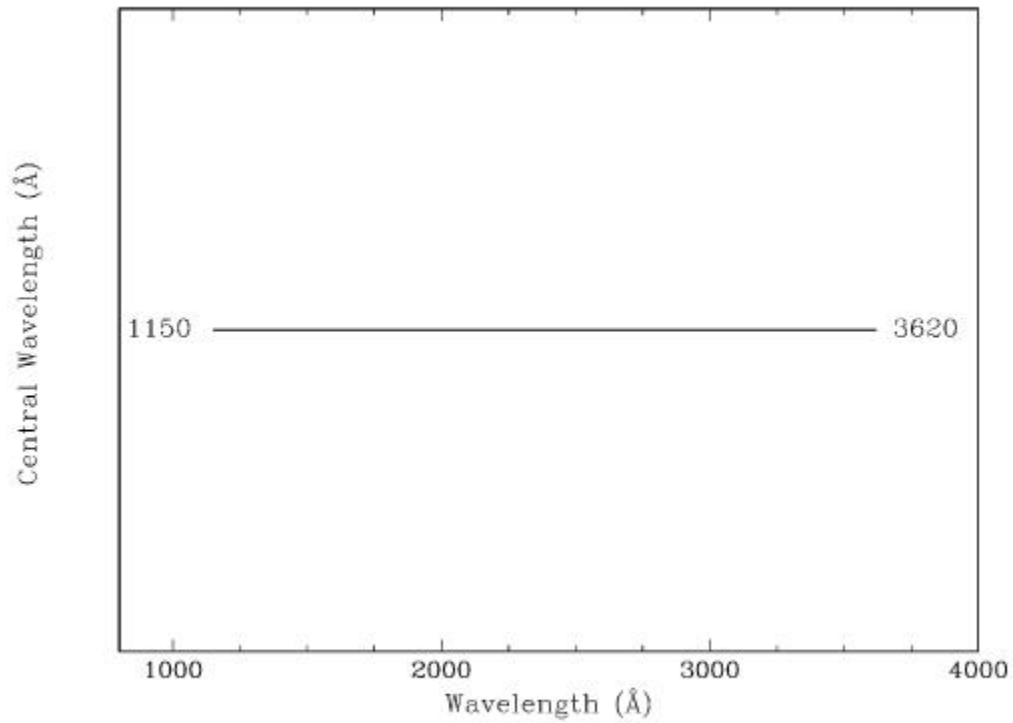
The full dispersion spreads over ~450 pixels with dispersion as shown in [Figure 13.64](#); thus if you have sources covering the field of view in the dispersion direction, the red tail will be lost for some targets with this setting. For a plot of wavelength vs. pixel no., see [Figure 4.12](#).

We note that the dispersion of the PRISM at wavelengths longer than ~2600 Å is very poorly known at this time.

Note also that the time-dependent sensitivity of PRISM does not follow that of the NUV gratings ([STIS ISR 2005-01](#)) and has not been measured since 2005. Its current sensitivity may be unknown by >~25% (see [STIS ISR 2017-06](#)). In view of the uncertainties in sensitivity, use of the PRISM has been designated as available-but-unsupported. Those who do use it will need to include observations of a standard star in their programs, in order to measure its current sensitivity.

| Grating | Spectral Range | | Average Dispersion (Å per Pixel) | Plate Scale (arcsec/pixel) | Tilts | Central Wavelength |
|---------|----------------|----------|----------------------------------|----------------------------|-------|--------------------|
| | Complete | Per Tilt | | | | |
| PRISM | 1150-3620 | 2470 | 0.2-72 | 0.029 | Prime | 1200/2125 |

Figure 13.62: Wavelength Range for the PRISM Setting.



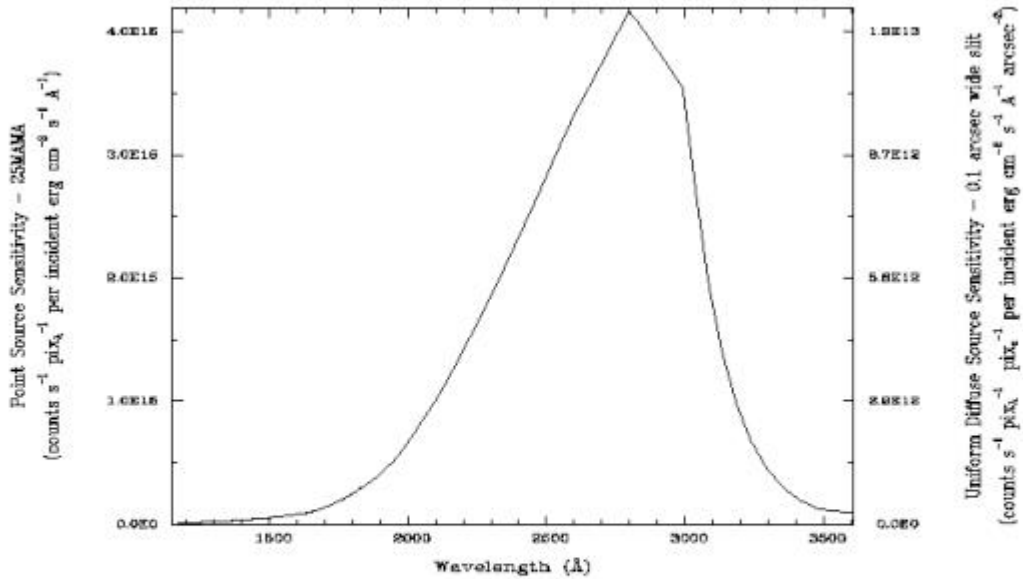
PRISM Sensitivities

Table 13.17: PRISM Sensitivities & Throughputs for a Point Source.

| λ | Sensitivity | % Throughput |
|-----------|-------------|--------------|
| 1250 | 1.3E13 | 0.6 |
| 1350 | 2.6E13 | 0.6 |
| 1450 | 4.1E13 | 0.5 |
| 1550 | 6.5E13 | 0.5 |
| 1650 | 1.0E14 | 0.6 |
| 1750 | 1.9E14 | 0.8 |
| 1850 | 3.2E14 | 1.0 |
| 1950 | 5.2E14 | 1.2 |

| | | |
|------|--------|-----|
| 2050 | 8.3E14 | 1.5 |
| 2150 | 1.2E15 | 1.8 |
| 2250 | 1.6E15 | 1.9 |
| 2350 | 2.1E15 | 2.0 |
| 2450 | 2.6E15 | 2.0 |
| 2550 | 3.1E15 | 2.0 |
| 2650 | 3.5E15 | 2.0 |
| 2750 | 4.0E15 | 1.9 |
| 2850 | 4.0E15 | 1.7 |
| 2950 | 3.7E15 | 1.3 |
| 3050 | 2.5E15 | 0.8 |
| 3150 | 1.3E15 | 0.4 |
| 3250 | 6.3E14 | 0. |
| 3350 | 3.1E14 | 0.1 |

Figure 13.63: PRISM Point Source (left axis), and Diffuse Source (right axis) Sensitivities.



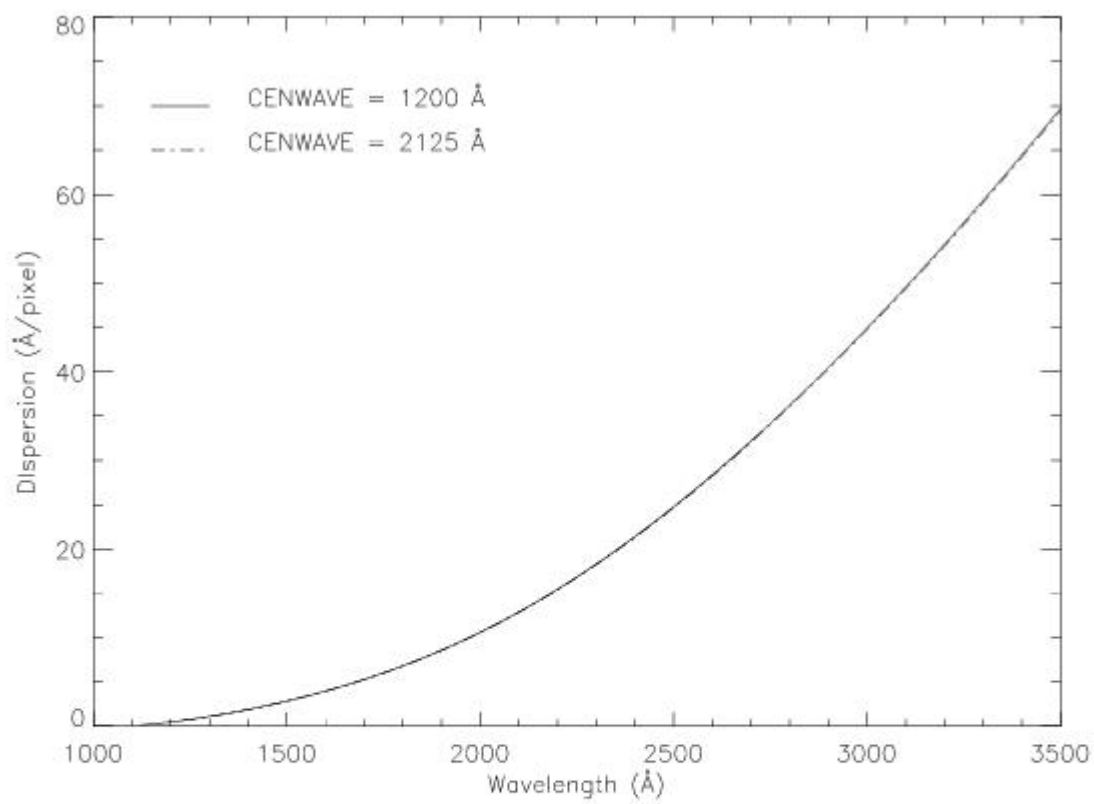
Note:

Point source sensitivity assumes full transmission (zero slit losses). Diffuse source sensitivity assumes a 0.1" wide slit. To convert point source sensitivities to diffuse source sensitivities multiply the point source values by the grating spatial (cross dispersion) plate scale in units of arcseconds per pixel and by the width of the desired slit in units of arcseconds.

PRISM Wavelength Relationship

The relationship between dispersion and wavelength for the PRISM is shown in [Figure 13.64](#). The relationships between the wavelength and the pixel number for the two wavelength settings are given in [Figure 4.12](#).

Figure 13.64: PRISM Dispersion-Wavelength Relationship.



13.4 Apertures

On the following pages we provide, for each supported aperture, a description of the aperture, the wavelength dependent point source throughput of the aperture, and some advice on its use. The current complete listing of STIS aperture + detector + grating combinations – supported, available-but-unsupported, or prohibited – may be found in [Table 8.7](#) of the [Phase II Proposal Instructions](#). The detailed locations, orientations, and scales of the apertures are given in the [SIAF table](#). A description and schematic of the long 52X apertures, showing the fiducial occulting bars, is given in [Section 13.2.6](#) and [Figure 13.1](#).

Wavelengths in this handbook and in STIS data products are always measured in vacuum conditions.

- [52X0.05 Aperture](#)
- [52X0.05E1 and 52X0.05D1 Pseudo-Apertures](#)
- [52X0.1 Aperture](#)
- [52X0.1E1 and 52X0.1D1 Pseudo-Apertures](#)
- [52X0.2 Aperture](#)
- [52X0.2E1, 52X0.2E2, and 52X0.2D1 Pseudo-Apertures](#)
- [52X0.5 Aperture](#)
- [52X0.5E1, 52X0.5E2, and 52X0.5D1 Pseudo-Apertures](#)
- [52X2 Aperture](#)
- [52X2E1, 52X2E2, and 52X2D1 Pseudo-Apertures](#)
- [52X0.2F1 Aperture](#)
- [0.2X0.06 Aperture](#)
- [0.2X0.2 Aperture](#)
- [0.2X0.09 Aperture](#)
- [6X0.2 Aperture](#)
- [0.1X0.03 Aperture](#)
- [FP-SPLIT Slits 0.2X0.06FP\(A-E\) Apertures](#)
- [FP-SPLIT Slits 0.2X0.2FP\(A-E\) Apertures](#)
- [31X0.05ND\(A-C\) Apertures](#)
- [0.2X0.05ND Aperture](#)
- [0.3X0.05ND Aperture](#)
- [F25NDQ Aperture](#)

52X0.05 Aperture

Description

This slit is supported with use of the first-order and echelle gratings and provides the best spatial and spectral resolution of the long slits. This aperture is the 2 pixel-wide slit in the dispersion direction for the MAMA first-order modes.

Special Considerations

Observations with this slit require a `PEAKUP` prior to science observations. The actual width of this aperture is 34 milliarcsec instead of 50 milliarcsec, the value suggested by its name. Special pseudo-apertures have been defined to minimize detector effects such as background and CTE. See next page for more information.

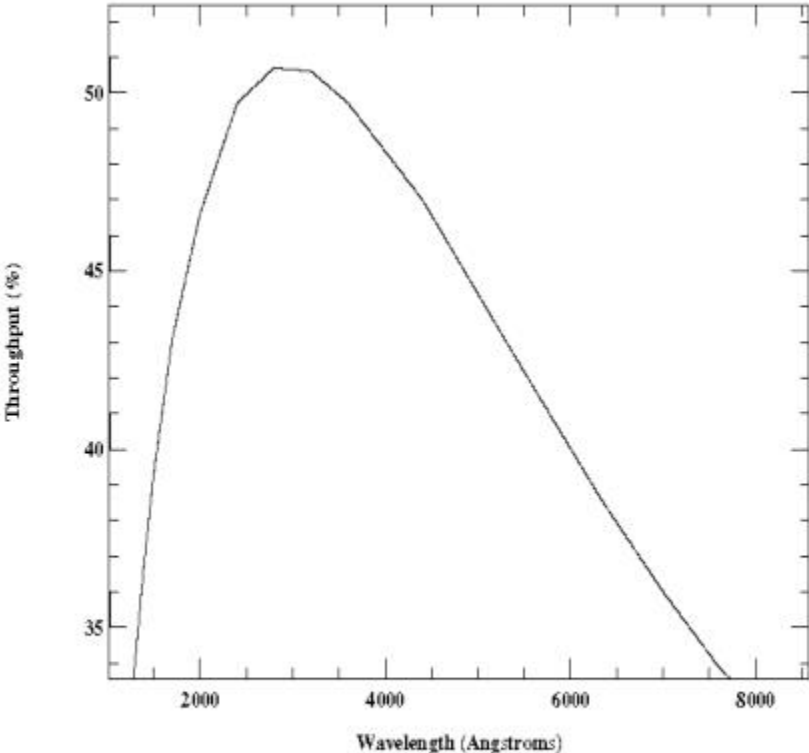
Table 13.18: 52x0.05 Throughputs.

| λ | % Throughput |
|-----------|--------------|
| 1200 | 31.0 |
| 1600 | 41.2 |
| 2000 | 46.6 |
| 2400 | 49.7 |
| 2800 | 50.7 |
| 3200 | 50.6 |
| 3600 | 49.7 |
| 4000 | 48.4 |
| 4400 | 47.0 |
| 4800 | 45.2 |
| 5200 | 43.5 |
| 5600 | 41.7 |
| 6000 | 40.0 |
| 6400 | 38.3 |
| 6800 | 36.8 |
| 7200 | 35.3 |
| 7600 | 33.9 |
| 8000 | 32.8 |

| | |
|------|------|
| 8400 | 31.7 |
|------|------|

| | Projected Length (arcsec) | | | |
|----------|---------------------------|----------------|----------------|----------------|
| Aperture | CCD | MAMA (M-modes) | MAMA (L-modes) | Width (arcsec) |
| 52x0.05 | 52.0 | 28.0 | 25.0 | 0.034 |

Figure 13.65: 52x0.05 Aperture Throughput as a Function of Wavelength.



52X0.05E1 and 52X0.05D1 Pseudo-Apertures

Description

These pseudo-apertures are the same physical aperture as the 52X0.05 aperture, but are used to place the target at different locations on the detectors to reduce CCD CTE loss (E1) or FUV-MAMA background (D1). The throughputs of the E1 and D1 apertures as a function of wavelength are similar to those of the corresponding regular positions. However, there is some vignetting of the gratings that changes the overall system throughput slightly with varying position along the slit. At the E1 positions, the overall low dispersion throughputs are decreased by 2 to 3%, while at the D1 position the G140L throughput is increased by 2 to 7%. Since these throughput changes depend on the grating and the position on the detector, they are handled in the pipeline calibration by the use of low-order flat fields (lfl files, only for the L-mode) rather than by a change in aperture throughput curve. Throughput changes for the medium resolution (M-mode) gratings are not well characterized, but should be similar. The usage of these slits is supported only for certain modes, as listed in the table below.

Special Considerations

Same special considerations as for the 52X0.05 aperture apply to these pseudo-apertures. See reference information on previous page.

| Aperture | Detector | Allowed Gratings | Usage |
|-----------|----------|------------------|---|
| 52X0.05E1 | CCD | All CCD gratings | Places the target at row ~900 to minimize CTE effects |
| 52X0.05D1 | FUV-MAMA | G140L & G140M | Places the target 2 ± 1 " (G140L) or 4 ± 1 " (G140M) above the bottom edge of FUV-MAMA; intended for observations of very faint targets where dark current contribution should be minimized |

52X0.1 Aperture

Description

This slit is supported with use of first-order and medium-resolution echelle gratings. This aperture is the 2 pixel-wide slit in the dispersion direction for the CCD first-order modes.

Special Considerations

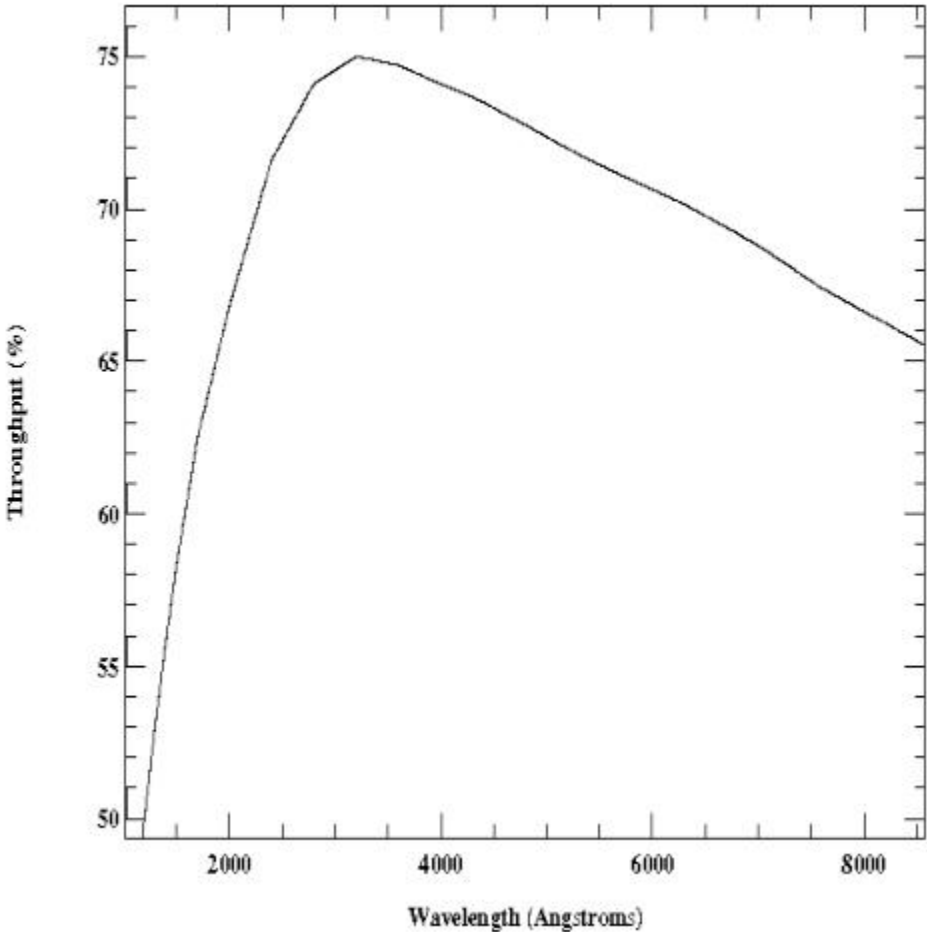
Observations with this slit require a `PEAKUP` prior to science observations.

Table 13.19: 52x0.1 Throughputs.

| λ | % Throughput |
|-----------|--------------|
| 1200 | 50.1 |
| 1600 | 60.4 |
| 2000 | 66.8 |
| 2400 | 71.6 |
| 2800 | 74.1 |
| 3200 | 75.0 |
| 3600 | 74.7 |
| 4000 | 74.1 |
| 4400 | 73.5 |
| 4800 | 72.7 |
| 5200 | 72.0 |
| 5600 | 71.3 |
| 6000 | 70.6 |
| 6400 | 70.0 |
| 6800 | 69.2 |
| 7200 | 68.3 |
| 7600 | 67.4 |
| 8000 | 66.6 |
| 8400 | 65.9 |

| | Projected Length (arcsec) | | | |
|----------|---------------------------|----------------|----------------|----------------|
| Aperture | CCD | MAMA (M-modes) | MAMA (L-modes) | Width (arcsec) |
| 52x0.1 | 52.0 | 28.0 | 25.0 | 0.1 |

Figure 13.66: 52x0.1 Aperture Throughput as a Function of Wavelength.



52X0.1E1 and 52X0.1D1 Pseudo-Apertures

Description

These pseudo-apertures are the same physical aperture as the 52x0.1 aperture, but are used to place the target at different locations on the detectors to reduce CCD CTE loss (E1) or FUV-MAMA background (D1). The throughputs of the E1 and D1 apertures as a function of wavelength are similar to those of the corresponding regular positions. However, there is some vignetting of the gratings that changes the overall system throughput slightly with varying position along the slit. At the E1 positions, the overall low dispersion throughputs are decreased by 2 to 3%, while at the D1 position the G140L throughput is increased by 2 to 7%. Since these throughput changes depend on the grating and the position on the detector, they are handled in the pipeline calibration by the use of low-order flat fields (lfl files, only for the L-mode) rather than by a change in aperture throughput curve. Throughput changes for the medium resolution (M-mode) gratings are not well characterized, but should be similar. The usage of these slits is supported only for certain modes, as listed in the table below.

Special Considerations

Same special considerations as for the 52x0.1 aperture apply to these pseudo-apertures. See reference information on previous page.

| Aperture | Detector | Allowed Gratings | Usage |
|----------|----------|------------------|--|
| 52X0.1E1 | CCD | All CCD gratings | Places the target at row ~900 to minimize CTE effects |
| 52X0.1D1 | FUV-MAMA | G140L & G140M | Places the target $2\pm 1'' \leq$ (G140L) or $4\pm 1''$ (G140M) above the bottom edge of FUV-MAMA; intended for observations of very faint targets where dark current contribution should be minimized |

52X0.2 Aperture

Description

This is the "utility" slit used with first-order gratings. It provides a good compromise between spectral resolution and photometric throughput.

Special Considerations

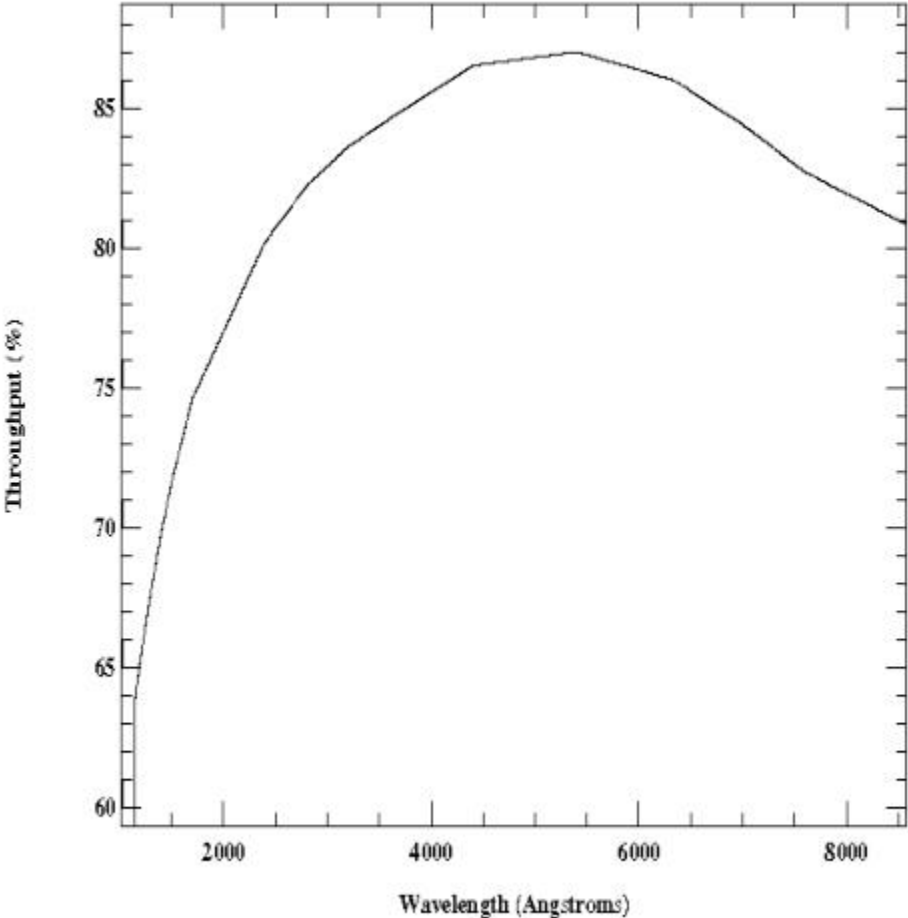
Observations using this slit do not need to be preceded by a PEAKUP.

Table 13.20: 52x0.2 Throughputs.

| λ | % Throughput |
|-----------|--------------|
| 1200 | 65.3 |
| 1800 | 75.4 |
| 2400 | 80.2 |
| 3000 | 82.9 |
| 3600 | 84.6 |
| 4200 | 86.0 |
| 4800 | 86.7 |
| 5400 | 87.0 |
| 6000 | 86.4 |
| 6600 | 85.4 |
| 7200 | 83.8 |
| 7800 | 82.3 |
| 8400 | 81.2 |

| | Projected Length (arcsec) | | | |
|----------|---------------------------|----------------|----------------|----------------|
| Aperture | CCD | MAMA (M-modes) | MAMA (L-modes) | Width (arcsec) |
| 52x0.2 | 52.0 | 28.0 | 25.0 | 0.2 |

Figure 13.67: 52X0.2 Aperture Throughput as a Function of Wavelength.



52X0.2E1, 52X0.2E2, and 52X0.2D1 Pseudo-Apertures

Description

These pseudo-apertures are the same physical aperture as the 52x0.2 aperture, but are used to place the target at different locations on the detectors to reduce CCD CTE loss (E1 and E2) or FUV-MAMA background (D1). The throughputs of the E1 and D1 apertures as a function of wavelength are similar to those of the corresponding regular positions. However, there is some vignetting of the gratings that changes the overall system throughput slightly with varying position along the slit. At the E1 positions, the overall low dispersion throughputs are decreased by 2 to 3%, while at the D1 position the G140L throughput is increased by 2 to 7%. Since these throughput changes depend on the grating and the position on the detector, they are handled in the pipeline calibration by the use of low-order flat fields (lfl files, only for the L-mode) rather than by a change in aperture throughput curve. Throughput changes for the medium resolution (M-mode) gratings are not well characterized, but should be similar. Throughput at the 52x0.2E2 position is about 20% lower than that at the 52x0.2E1 position. The usage of these slits is supported only for certain modes, as listed in the table below.

Special Considerations

Same special considerations as for the 52x0.2 aperture apply to these pseudo-apertures. See reference information on previous page.

| Aperture | Detector | Allowed Gratings | Usage |
|----------|----------|------------------|---|
| 52X0.2E1 | CCD | All CCD gratings | Places the target at row ~900 to minimize CTE effects |
| 52X0.2E2 | CCD | G750L & G750M | Places the target at row ~900 to minimize CTE effects; positions are offset from the center of the physical aperture in the dispersion direction, to give better alignment with fringe flats done using 52x0.1 aperture (see section 11.2.3) |
| 52X0.2D1 | FUV-MAMA | G140L & G140M | Places the target $2\pm 1''$ (G140L) or $4\pm 1''$ (G140M) above the bottom edge of FUV-MAMA; intended for observations of very faint targets where dark current contribution should be minimized |

52X0.5 Aperture

Description

This slit is designated for use with the first-order gratings and is a good slit for spectrophotometric observations of point sources.

Special Considerations

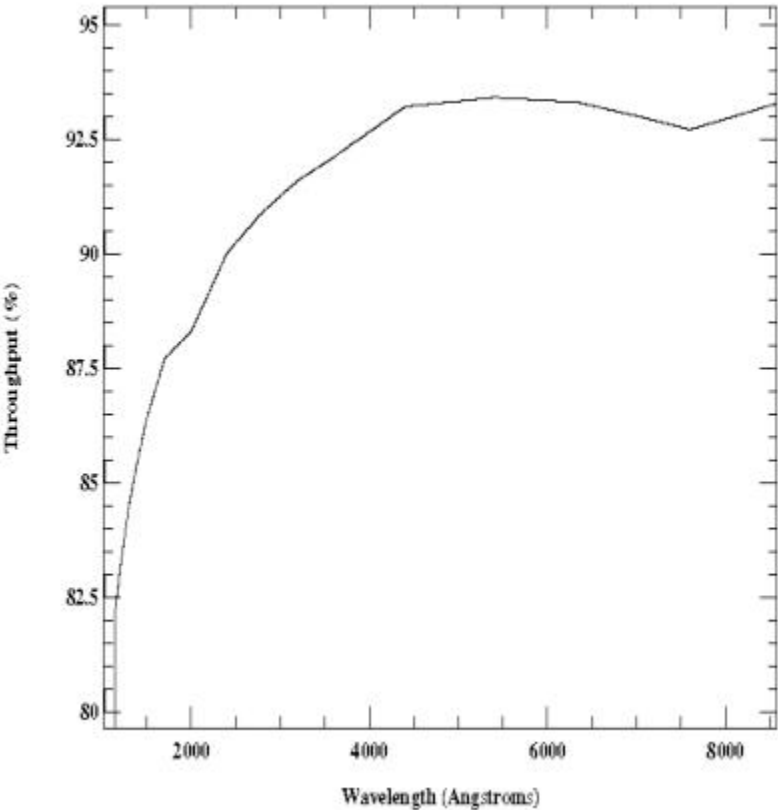
Observations using this slit do not need to be preceded by a PEAKUP. Be aware of effects of OTA scatter on the line profiles when observing point sources in wide slits (see [Section 13.7](#)). Targets not centered on the slit along the spatial direction can experience significant shifts in wavelength.

Table 13.21: 52x0.5 Throughputs.

| λ | % Throughput |
|-----------|--------------|
| 1200 | 83.1 |
| 1800 | 87.9 |
| 2400 | 90.0 |
| 3000 | 91.2 |
| 3600 | 92.1 |
| 4200 | 92.9 |
| 4800 | 93.3 |
| 5400 | 93.4 |
| 6000 | 93.3 |
| 6600 | 93.2 |
| 7200 | 92.9 |
| 7800 | 92.8 |
| 8400 | 93.2 |

| | Projected Length (arcsec) | | | |
|----------|---------------------------|----------------|----------------|----------------|
| Aperture | CCD | MAMA (M-modes) | MAMA (L-modes) | Width (arcsec) |
| 52x0.5 | 52.0 | 28.0 | 25.0 | 0.5 |

Figure 13.68: 52x0.5 Aperture Throughput as a Function of Wavelength.



52X0.5E1, 52X0.5E2, and 52X0.5D1 Pseudo-Apertures

Description

These pseudo-apertures are the same physical aperture as the 52x0.5 aperture, but are used to place the target at different locations on the detectors to reduce CCD CTE loss (E1 and E2) or FUV-MAMA background (D1). The throughputs of the E1 and D1 apertures as a function of wavelength are similar to those of the corresponding regular positions. However, there is some vignetting of the gratings that changes the overall system throughput slightly with varying position along the slit. At the E1 positions, the overall low dispersion throughputs are decreased by 2 to 3%, while at the D1 position the G140L throughput is increased by 2 to 7%. Since these throughput changes depend on the grating and the position on the detector, they are handled in the pipeline calibration by the use of low-order flat fields (lfl files, only for the L-mode) rather than by a change in aperture throughput curve. Throughput changes for the medium resolution (M-mode) gratings are not well characterized, but should be similar. Throughput at the 52x0.5E2 position is about 20% lower than that at the 52x0.5E1 position. The usage of these slits is supported only for certain modes, as listed in the table below.

Special Considerations

Same special considerations as for the 52x0.5 aperture apply to these pseudo-apertures. See reference information on previous page.

| Aperture | Detector | Allowed Gratings | Usage |
|----------|----------|------------------|---|
| 52X0.5E1 | CCD | All CCD gratings | Places the target at row ~900 to minimize CTE effects |
| 52X0.5E2 | CCD | G750L & G750M | Places the target at row ~900 to minimize CTE effects; positions are offset from the center of the physical aperture in the dispersion direction, to give better alignment with fringe flats done using 52x0.5E1 aperture (see section 11.2.3) |
| 52X0.5D1 | FUV-MAMA | G140L & G140M | Places the target $2\pm 1''$ (G140L) or $4\pm 1''$ (G140M) above the bottom edge of FUV-MAMA; intended for observations of very faint targets where dark current contribution should be minimized |

52X2 Aperture

Description

The last in the series of supported long slits used with the first-order gratings and is a good slit for spectrophotometric observations of point sources. The small dip in throughput seen at 2000 Å is likely due to uncertainties in the numerical calculation, and will not affect the absolute flux calibration.

Special Considerations

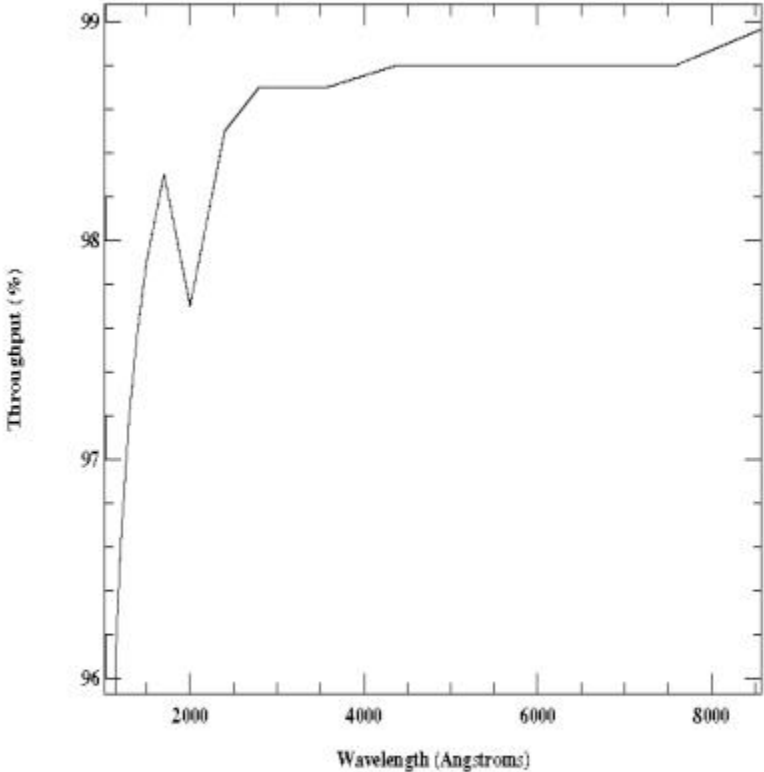
Observations using this slit do not need to be preceded by a PEAKUP. Be aware of effects of OTA scatter on the line profiles when observing point sources in wide slits (see [Section 13.7](#)). Targets not centered on the slit along the spatial direction can experience significant shifts in wavelength.

Table 13.22: 52x2 Throughputs.

| λ | % Throughput |
|-----------|--------------|
| 1200 | 96.6 |
| 1800 | 98.1 |
| 2400 | 98.5 |
| 3000 | 98.7 |
| 3600 | 98.7 |
| 4200 | 98.8 |
| 4800 | 98.8 |
| 5400 | 98.8 |
| 6000 | 98.8 |
| 6600 | 98.8 |
| 7200 | 98.8 |
| 7800 | 98.8 |
| 8400 | 98.9 |

| | Projected Length (arcsec) | | | |
|----------|---------------------------|----------------|----------------|----------------|
| Aperture | CCD | MAMA (M-modes) | MAMA (L-modes) | Width (arcsec) |
| 52x2 | 52.0 | 28.0 | 25.0 | 2.0 |

Figure 13.69: 52x2 Aperture Throughput as a Function of Wavelength.



52X2E1, 52X2E2, and 52X2D1 Pseudo-Apertures

Description

These pseudo-apertures are the same physical aperture as the 52x2 aperture, but are used to place the target at different locations on the detectors to reduce CCD CTE loss (E1 and E2) or FUV-MAMA background (D1). The throughputs of the E1 and D1 apertures as a function of wavelength are similar to those of the corresponding regular positions. However, there is some vignetting of the gratings that changes the overall system throughput slightly with varying position along the slit. At the E1 positions, the overall low dispersion throughputs are decreased by 2 to 3%, while at the D1 position the G140L throughput is increased by 2 to 7%. Since these throughput changes depend on the grating and the position on the detector, they are handled in the pipeline calibration by the use of low-order flat fields (lfl files, only for the L-mode) rather than by a change in aperture throughput curve. Throughput changes for the medium resolution (M-mode) gratings are not well characterized, but should be similar. Throughput at the 52X2E2 position is about 20% lower than that at the 52X2E1 position. The usage of these slits is supported only for certain modes, as listed in the table below.

Special Considerations

Same special considerations as for the 52x2 aperture apply to these pseudo-apertures. See reference information on previous page.

| Aperture | Detector | Allowed Gratings | Usage |
|----------|----------|------------------|---|
| 52X2E1 | CCD | All CCD gratings | Places the target at row ~900 to minimize CTE effects |
| 52X2E2 | CCD | G750L & G750M | Places the target at row ~900 to minimize CTE effects; positions are offset from the center of the physical aperture in the dispersion direction, to give better alignment with fringe flats done using 52X0.1 aperture (see section 11.2.3) |
| 52X2D1 | FUV-MAMA | G140L & G140M | Places the target $2\pm 1''$ (G140L) or $4\pm 1''$ (G140M) above the bottom edge of FUV-MAMA; intended for observations of very faint targets where dark current contribution should be minimized |

52X0.2F1 Aperture

Description

The same physical aperture as the 52x0.2 but used at the position of the smaller of the two fiducial bars, which can be used for spectroscopic coronagraphic observations. The throughput for the unocculted 52x0.2 aperture is given below.

Special Considerations

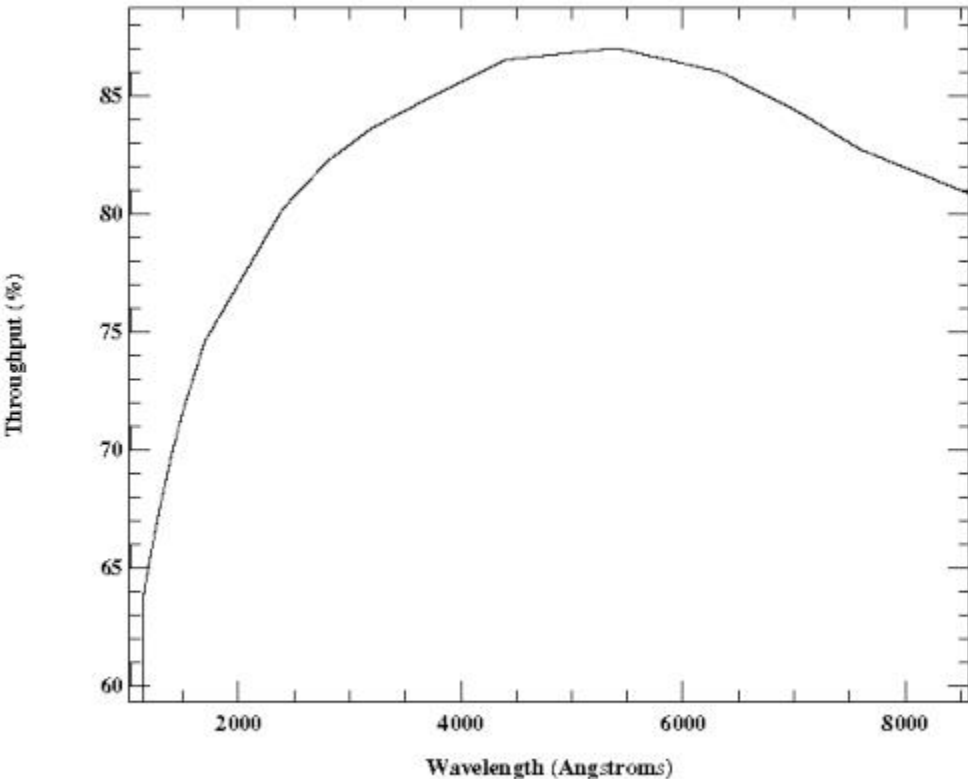
Observations using this slit do not need to be preceded by a PEAKUP.

Table 13.23: 52x0.2 Throughputs.

| λ | % Throughput |
|-----------|--------------|
| 1200 | 65.3 |
| 1600 | 73.1 |
| 2000 | 77.0 |
| 2400 | 80.2 |
| 2800 | 82.2 |
| 3200 | 83.6 |
| 3600 | 84.6 |
| 4000 | 85.6 |
| 4400 | 86.5 |
| 4800 | 86.7 |
| 5200 | 86.9 |
| 5600 | 86.8 |
| 6000 | 86.4 |
| 6400 | 85.8 |
| 6800 | 84.9 |
| 7200 | 83.8 |
| 7600 | 82.7 |
| 8000 | 81.9 |
| 8400 | 81.2 |

| | Projected Length (arcsec) | | | |
|----------|---------------------------|----------------|----------------|----------------|
| Aperture | CCD | MAMA (M-modes) | MAMA (L-modes) | Width (arcsec) |
| 52X0.2F1 | 52.0 | 28.0 | 25.0 | 0.2 |
| Fiducial | 0.5 | 0.5 | 0.5 | 0.2 |

Figure 13.70: 52x0.2 Aperture Throughput as a Function of Wavelength.



0.2X0.06 Aperture

Description

This slit is supported for use with the medium resolution echelle gratings, and available (but unsupported) for other gratings according to P2PI. It is two pixels wide in the dispersion direction for the MAMA echelle gratings, providing optimal spectral resolution and line profiles.

Special Considerations

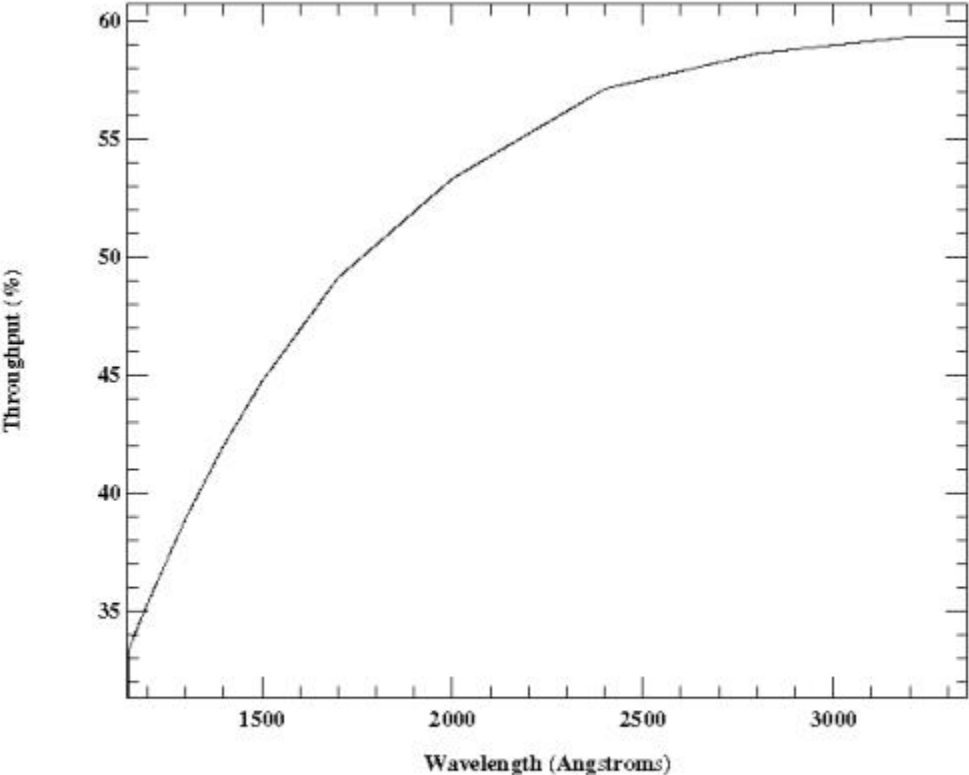
Used primarily with the E230M and E140M gratings. Observations with this slit require a prior PEAKUP.

Table 13.24: 0.2x0.06 Throughputs.

| λ | % Throughput |
|-----------|--------------|
| 1200 | 35.3 |
| 1800 | 50.5 |
| 2400 | 57.1 |
| 3000 | 59.0 |
| 3600 | 59.3 |
| 4200 | 58.7 |
| 4800 | 57.2 |
| 5400 | 55.2 |
| 6000 | 52.4 |

| Projected Length (arcsec) | | |
|---------------------------|----------------|----------------|
| Aperture | MAMA (E-modes) | Width (arcsec) |
| 0.2x0.06 | 0.2 | 0.06 |

Figure 13.71: 0.2x0.06 Aperture Throughput as a Function of Wavelength.



0.2X0.2 Aperture

Description

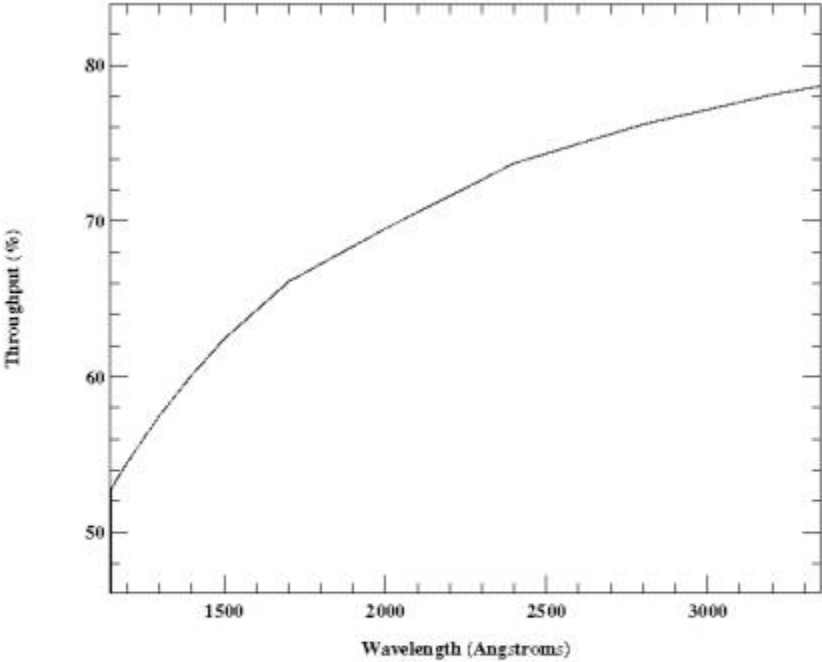
The "utility" slit for the echelle gratings. This slit is the most photometric of the supported echelle slits and has the highest throughput for photon statistics. Starting in Cycle 12, this slit is also supported for use with the first order gratings, and it is the recommended aperture for first order MAMA snapshot and survey programs that do not have a scientific need for a long-slit (see [Section 2.9](#)).

Table 13.25: 0.2x0.2 Throughputs.

| λ | % Throughput |
|-----------|--------------|
| 1200 | 54.5 |
| 1800 | 67.2 |
| 2400 | 73.7 |
| 3000 | 77.2 |
| 3600 | 79.6 |
| 4200 | 81.6 |
| 4800 | 82.6 |
| 5400 | 83.2 |
| 6000 | 81.7 |

| Projected Length (arcsec) | | |
|---------------------------|----------------|----------------|
| Aperture | MAMA (E-modes) | Width (arcsec) |
| 0.2x0.2 | 0.2 | 0.2 |

Figure 13.72: 0.2x0.2 Aperture Throughput as a Function of Wavelength.



0.2X0.09 Aperture

Description

This slit is supported for use with the high resolution echelle gratings, and available (but unsupported) for use with other gratings according to P2PI. It is two pixels wide in the dispersion direction for the MAMA echelle gratings, providing optimal spectral resolution and line profiles.

Special Considerations

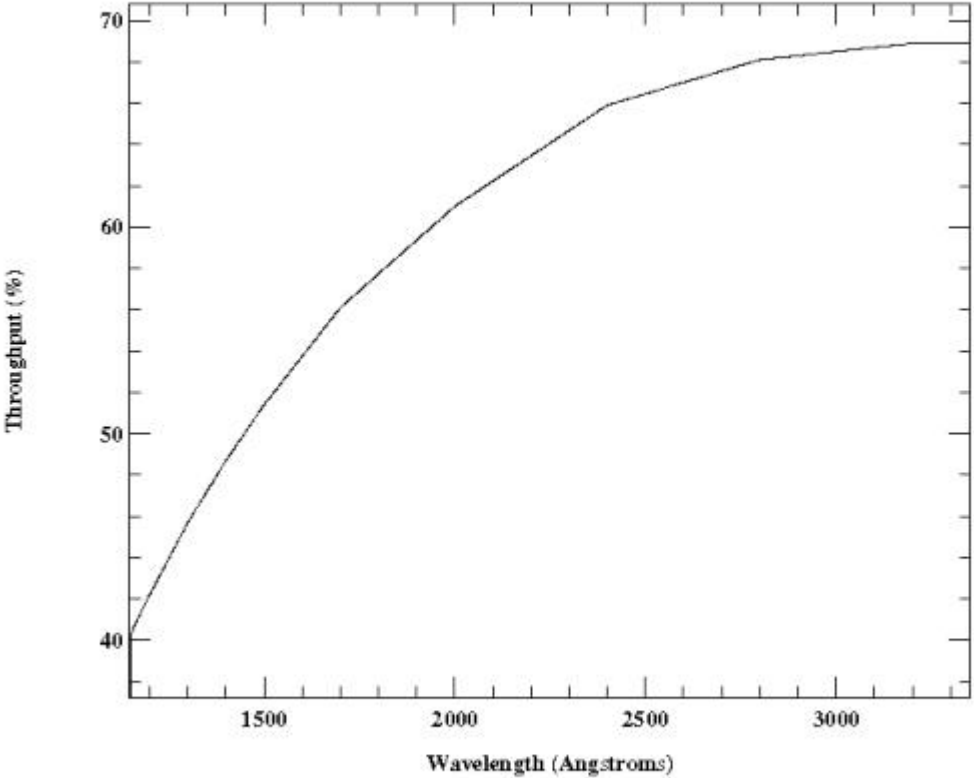
Used primarily with the E140H and E230H gratings. Observations with this slit require a prior PEAKUP.

Table 13.26: 0.2x0.09 Throughputs.

| λ | % Throughput |
|-----------|--------------|
| 1200 | 42.2 |
| 1800 | 57.7 |
| 2400 | 65.9 |
| 3000 | 68.5 |
| 3600 | 68.9 |
| 4200 | 68.6 |
| 4800 | 67.8 |
| 5400 | 66.8 |
| 6000 | 64.9 |

| Projected Length (arcsec) | | |
|---------------------------|----------------|----------------|
| Aperture | MAMA (E-modes) | Width (arcsec) |
| 0.2x0.09 | 0.2 | 0.09 |

Figure 13.73: 0.2x0.09 Aperture Throughput as a Function of Wavelength.



6X0.2 Aperture

Description

This slit is supported for use with the echelle gratings, and available (but unsupported) for use with other gratings according to P2PI.

Recommended Uses

A good slit for echelle observations of extended sources with isolated emission lines.

Special Considerations

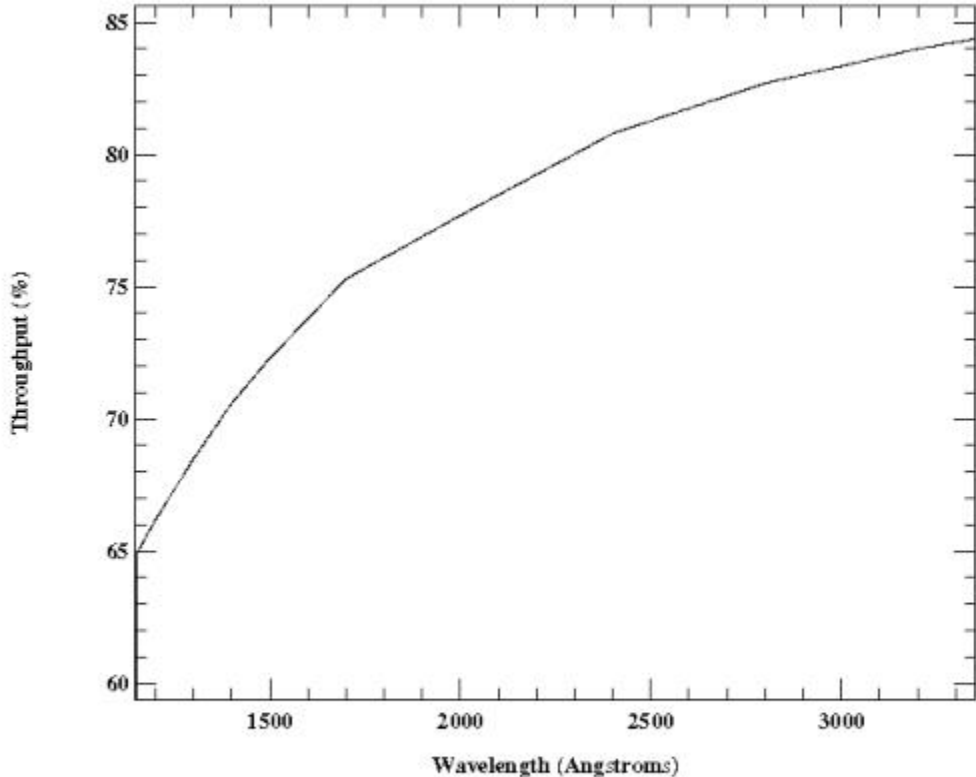
This slit can be used with all echelle gratings. Please note that use of this slit with an extended source will produce order overlap and may make analysis difficult (see also [Section 13.7](#)).

Table 13.27: 6x0.2 Throughputs.

| λ | % Throughput |
|-----------|--------------|
| 1200 | 66.2 |
| 1400 | 70.6 |
| 1600 | 73.8 |
| 1800 | 76.1 |
| 2000 | 77.7 |
| 2200 | 79.3 |
| 2400 | 80.8 |
| 2600 | 81.8 |
| 2800 | 82.7 |
| 3000 | 83.3 |
| 3200 | 84.0 |
| 3400 | 84.5 |

| Projected Length (arcsec) | | |
|---------------------------|----------------|----------------|
| Aperture | MAMA (E-modes) | Width (arcsec) |
| 6x0.2 | 6.0 | 0.2 |

Figure 13.74: 6x0.2 Aperture Throughput as a Function of Wavelength.



0.1X0.03 Aperture

Description

This slit is supported for use with the high resolution echelle gratings, and available (but unsupported) for use with other gratings according to P2PI. During ground calibration, test observations of a mono-isotopic platinum lamp source with this slit and the high resolution echelle gratings exhibited resolving powers in excess of 200,000 – the highest available with STIS.

Special Considerations

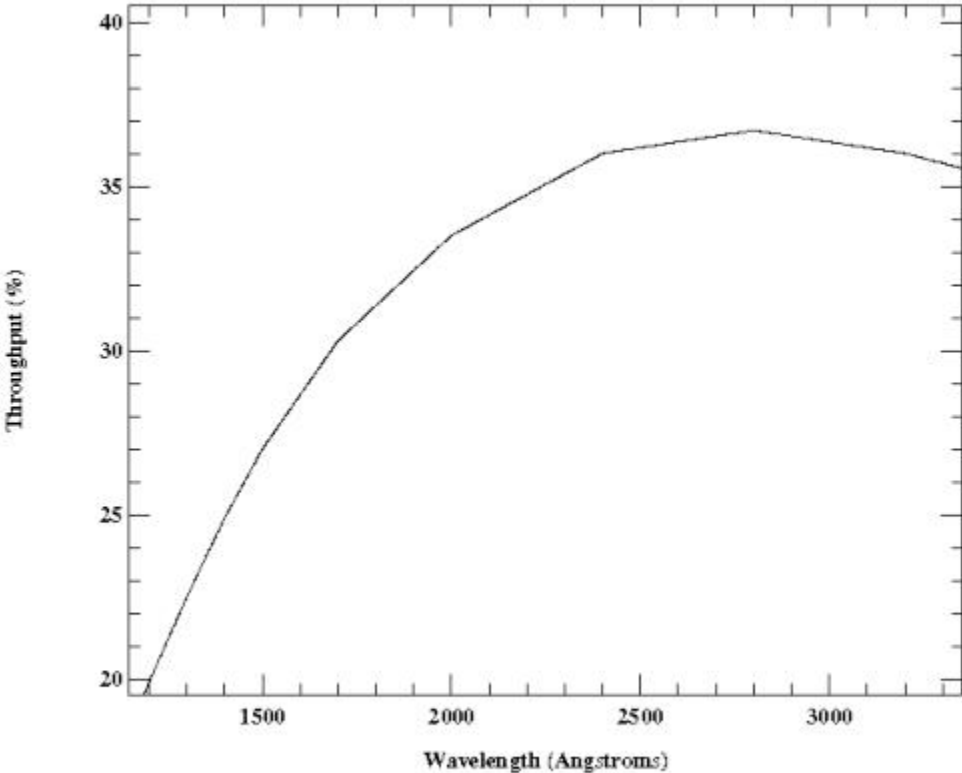
Observations with this slit require a prior PEAKUP. The PEAKUP is performed in two stages—first with the 0.2x0.09 aperture (or one of the small neutral density apertures), and then with the 0.1x0.03 aperture (see [Section 8.3](#), [Table 8.5](#)). The throughput can be particularly sensitive to degraded focus ([ISR 2017-01](#)), and specialized data reduction techniques are required to correct for fixed pattern noise in the MAMA highres format ([Jenkins & Tripp 2001](#), [ApJS, 137, 297](#)).

Table 13.28: 0.1x0.03 Throughputs.

| λ | % Throughput |
|-----------|--------------|
| 1200 | 19.9 |
| 1800 | 31.4 |
| 2400 | 36.0 |
| 3000 | 36.4 |
| 3600 | 34.8 |
| 4200 | 32.8 |
| 4800 | 30.9 |
| 5400 | 28.9 |
| 6000 | 27.0 |

| Projected Length (arcsec) | | |
|---------------------------|----------------|----------------|
| Aperture | MAMA (E-modes) | Width (arcsec) |
| 0.1x0.03 | 0.1 | 0.025 |

Figure 13.75: 0.1x0.03 Aperture Throughput as a Function of Wavelength.



FP-SPLIT Slits 0.2X0.06FP(A-E) Apertures

Description

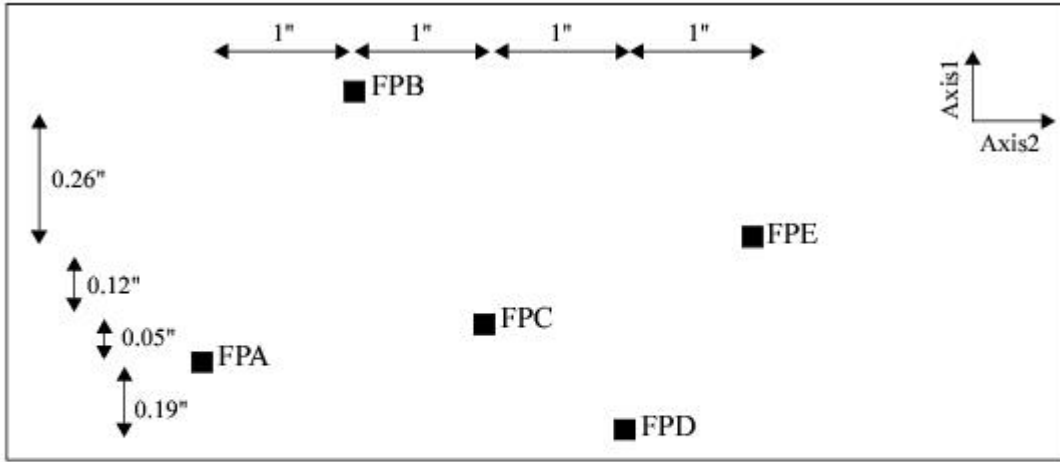
The FP-SPLIT slits consist of two sets of five slits; in each set the slits are all the same size. They are for use with the MAMA echelle gratings. It is possible to achieve high S/N data for bright targets, independently of the quality of the flat-field, by means of a special observing strategy wherein multiple spectrograms are obtained through these slits.

Special Considerations

See [Section 12.5.2](#) for more details on obtaining high S/N spectral data. Observations with this slit require a prior PEAKUP.

| Aperture | Projected Length (arcsec) | Width (arcsec) |
|-------------|---------------------------|----------------|
| 0.2X0.06FPA | 0.2 | 0.06 |
| 0.2X0.06FPB | 0.2 | 0.06 |
| 0.2X0.06FPC | 0.2 | 0.06 |
| 0.2X0.06FPD | 0.2 | 0.06 |
| 0.2X0.06FPE | 0.2 | 0.06 |

Figure 13.76: Schematic of the STIS Fixed-Pattern Slit Configuration. AXIS1 corresponds to the dispersion direction, and AXIS2 to the spatial direction. Dimensions are not to scale.

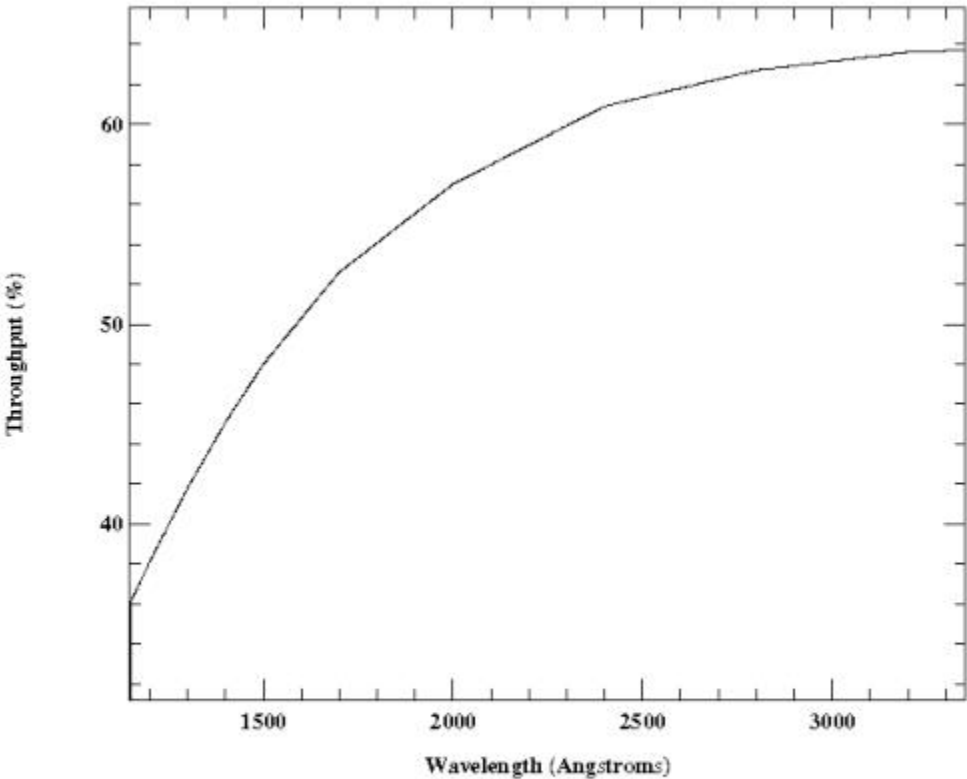


FP-SPLIT Throughputs

Table 13.29: Throughput for 0.2x0.06FP (A-E).

| λ | % Throughput |
|-----------|--------------|
| 1200 | 38.1 |
| 1800 | 54.1 |
| 2400 | 60.9 |
| 3000 | 63.1 |
| 3600 | 63.9 |
| 4200 | 63.8 |
| 4800 | 62.5 |
| 5400 | 60.8 |
| 6000 | 58.0 |

Figure 13.77: 0.2x0.06FP (A-E) Aperture Throughput as a Function of Wavelength.



FP-SPLIT Slits 0.2X0.2FP(A-E) Apertures

Description

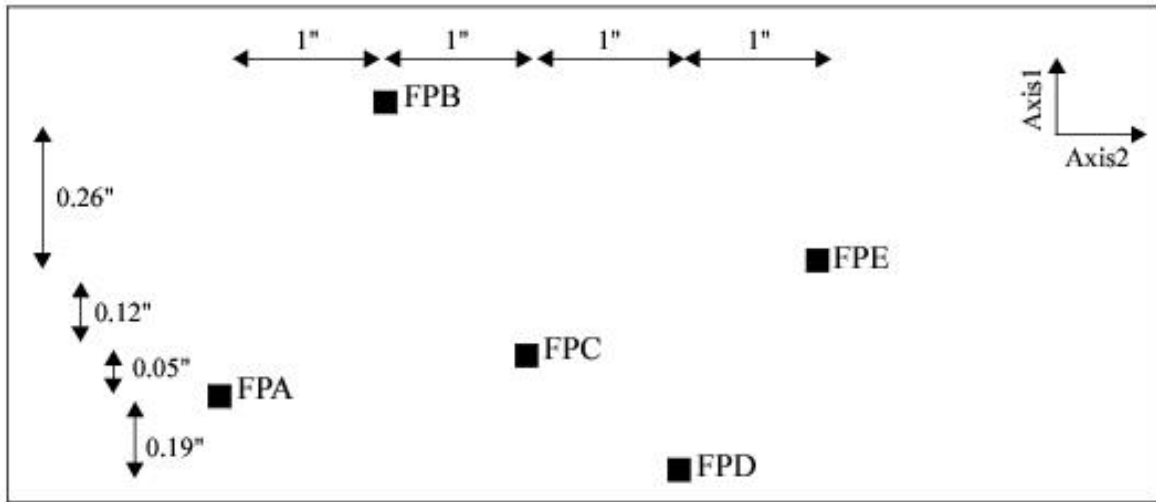
The FP-SPLIT slits consist of two sets of five slits; in each set the slits are all the same size. They are for use with the MAMA echelle gratings. It is possible to achieve high S/N data for bright targets, independently of the quality of the flat-field, by means of a special observing strategy wherein multiple spectrograms are obtained through these slits.

Special Considerations

See [Section 12.5.2](#) for more details on obtaining high S/N spectral data.

| Aperture | Projected Length (arcsec) | Width (arcsec) |
|------------|---------------------------|----------------|
| 0.2X0.2FPA | 0.2 | 0.2 |
| 0.2X0.2FPB | 0.2 | 0.2 |
| 0.2X0.2FPC | 0.2 | 0.2 |
| 0.2X0.2FPD | 0.2 | 0.2 |
| 0.2X0.2FPE | 0.2 | 0.2 |

Figure 13.78: Schematic of the STIS Fixed-Pattern Slit Configuration. AXIS1 corresponds to the dispersion direction, and AXIS2 to the spatial direction. Dimensions are not to scale.



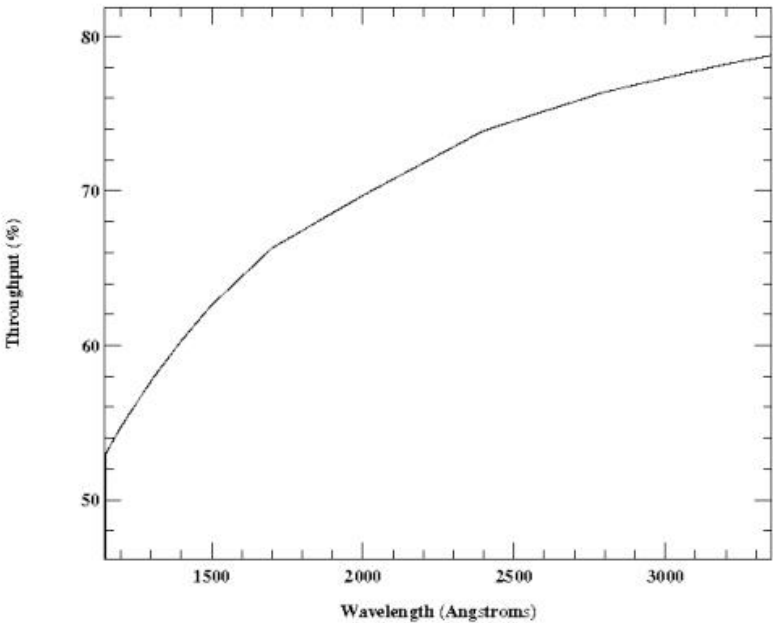
FP-SPLIT Throughputs

Table 13.30: Throughput for 0.2X0.2FP (A-E).

| λ | % Throughput | | | | |
|-----------|--------------|------------|------------|------------|------------|
| | 0.2X0.2FPA | 0.2X0.2FPB | 0.2X0.2FPC | 0.2X0.2FPD | 0.2X0.2FPE |
| 1200 | 54.7 | 54.8 | 54.7 | 55.0 | 55.1 |
| 1800 | 67.4 | 67.5 | 67.4 | 67.6 | 67.7 |
| 2400 | 73.9 | 73.9 | 73.9 | 74.0 | 74.1 |
| 3000 | 77.3 | 77.3 | 77.3 | 77.3 | 77.4 |
| 3600 | 79.7 | 79.7 | 79.7 | 79.7 | 79.8 |
| 4200 | 81.7 | 81.7 | 81.7 | 81.7 | 81.7 |

| | | | | | |
|------|------|------|------|------|------|
| 4800 | 82.7 | 82.7 | 82.7 | 82.7 | 82.8 |
| 5400 | 83.3 | 83.4 | 83.3 | 83.4 | 83.5 |
| 6000 | 82.0 | 82.2 | 82.0 | 82.2 | 82.5 |

Figure 13.79: 0.2x0.2FP (A-E) Aperture Throughput as a Function of Wavelength.



31X0.05ND(A-C) Apertures

Description

Set of three supported neutral-density filtered slits for use with first-order or echelle observations. The approximate dex ND factors are 0.4, 0.8, and 1.2, for 31X0.05NDA, 31X0.05NDB, and 31X0.05NDC, respectively. Their use for PRISM observations is "available-but-unsupported" at this time.

Special Considerations

Observations with this slit require a PEAKUP prior to science observations. Use of these long slits with an echelle grating will cause order overlap problems (particularly for the most closely spaced orders; see [Section 12.2](#)), but for point sources the order separation may be adequate for many science programs.

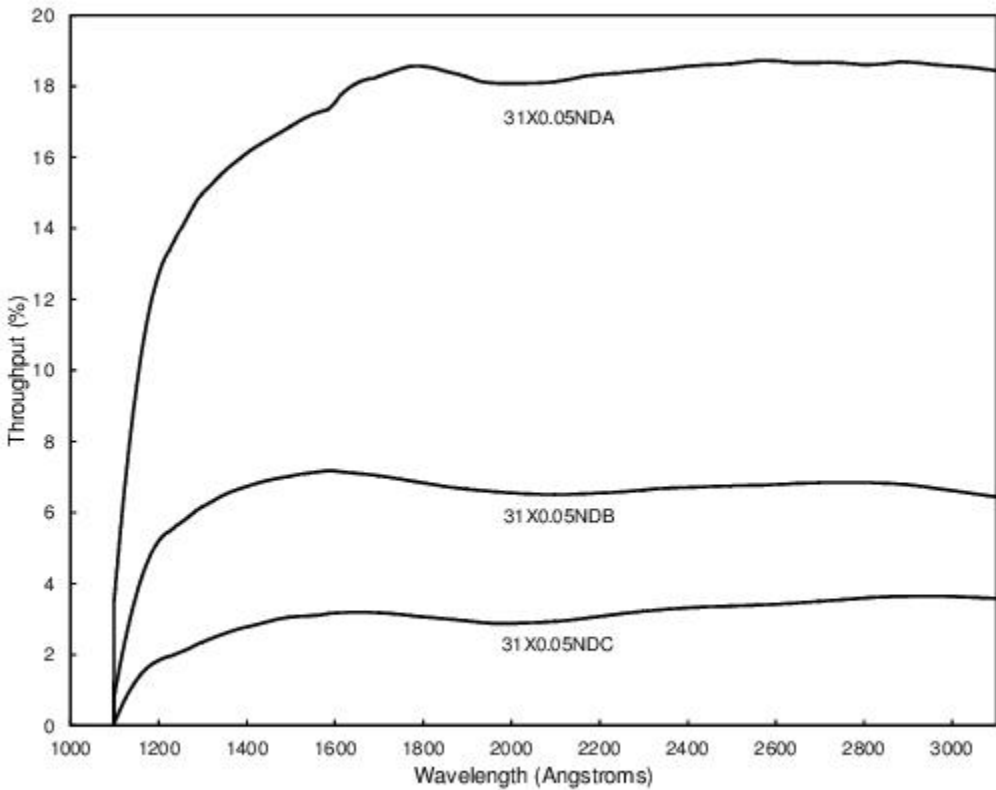
Table 13.31: 31X0.05ND(A-C) Throughputs (%).

| λ | 31X0.05NDA | 31X0.05NDB | 31X0.05NDC |
|-----------|------------|------------|------------|
| 1100 | 3.6 | 0.9 | 0.09 |
| 1150 | 9.5 | 3.7 | 1.28 |
| 1200 | 12.7 | 5.2 | 1.83 |
| 1300 | 15.0 | 6.2 | 2.36 |
| 1400 | 16.1 | 6.7 | 2.78 |
| 1500 | 16.9 | 7.0 | 3.06 |
| 1600 | 17.5 | 7.2 | 3.17 |
| 1700 | 18.3 | 7.0 | 3.18 |
| 1800 | 18.6 | 6.8 | 3.06 |
| 1900 | 18.3 | 6.7 | 2.95 |
| 2000 | 18.1 | 6.6 | 2.88 |
| 2100 | 18.1 | 6.5 | 2.93 |
| 2200 | 18.3 | 6.5 | 3.08 |
| 2300 | 18.4 | 6.6 | 3.22 |
| 2400 | 18.6 | 6.7 | 3.32 |
| 2500 | 18.6 | 6.8 | 3.37 |
| 2600 | 18.7 | 6.8 | 3.42 |
| 2700 | 18.7 | 6.8 | 3.50 |
| 2800 | 18.6 | 6.8 | 3.59 |

| | | | |
|-------|------|-----|------|
| 2900 | 18.7 | 6.8 | 3.64 |
| 3000 | 18.6 | 6.6 | 3.64 |
| 3100 | 18.4 | 6.4 | 3.59 |
| 4400 | 14.4 | 4.2 | 2.66 |
| 8800 | 8.7 | 2.6 | 1.61 |
| 12400 | 4.4 | 1.3 | 0.81 |

| Aperture | Projected Length (arcsec) | Width (arcsec) |
|------------|---------------------------|----------------|
| 31X0.05NDA | 31 | 0.048 |
| 31X0.05NDB | 31 | 0.048 |
| 31X0.05NDC | 31 | 0.048 |

Figure 13.80: 31x0.05ND(A-C) Aperture Throughput as a Function of Wavelength.



0.2X0.05ND Aperture

Description

Supported neutral-density-filtered slit for use with bright objects with the echelle gratings; also available (but unsupported) for other gratings according to P2PI. The dex ND factor is 2.0.

Special Considerations

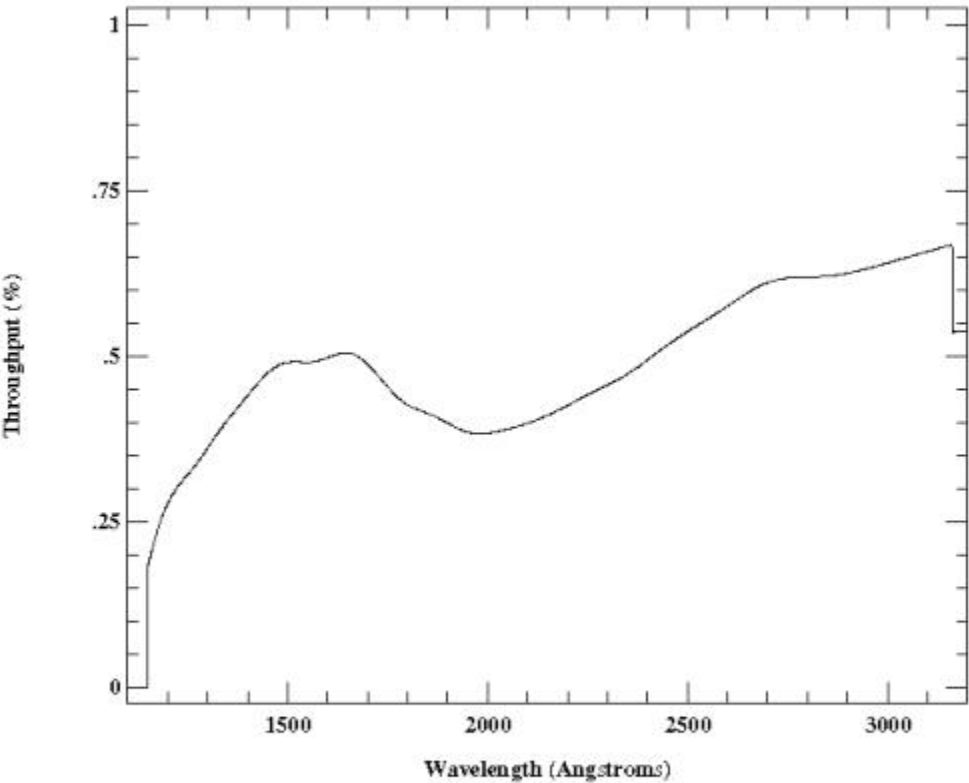
Observations with this slit require a prior PEAKUP. This aperture can also be used with the CCD for ACQ /PEAKS.

Table 13.32: 0.2x0.05ND Throughputs.

| λ | % Throughput |
|-----------|--------------|
| 1150 | 0.18 |
| 1350 | 0.40 |
| 1550 | 0.49 |
| 1750 | 0.45 |
| 1950 | 0.38 |
| 2150 | 0.41 |
| 2350 | 0.47 |
| 2550 | 0.56 |
| 2750 | 0.62 |
| 2950 | 0.63 |
| 3150 | 0.67 |

| Projected Length (arcsec) | | |
|---------------------------|----------------|----------------|
| Aperture | MAMA (E-modes) | Width (arcsec) |
| 0.2X0.05ND | 0.2 | 0.05 |

Figure 13.81: 0.2x0.05ND Aperture Throughput as a Function of Wavelength.



0.3X0.05ND Aperture

Description

Supported neutral-density-filtered slit for use with bright objects with the echelle gratings; also available (but unsupported) with other gratings according to P2PI. The dex ND factor is 3.0.

Special Considerations

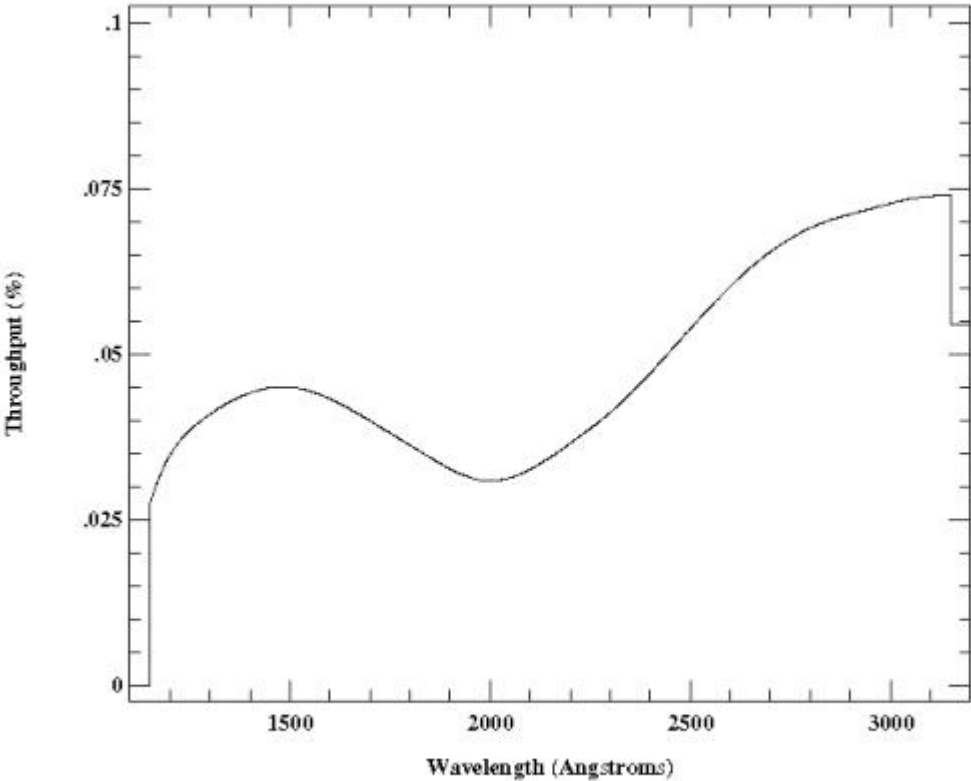
Observations with this slit require a prior `PEAKUP`. This aperture can also be used with the CCD for `ACQ` / `PEAKS`.

Table 13.33: 0.3x0.05ND Throughputs.

| λ | % Throughput |
|-----------|--------------|
| 1151 | 0.028 |
| 1350 | 0.043 |
| 1550 | 0.044 |
| 1750 | 0.038 |
| 1950 | 0.031 |
| 2150 | 0.034 |
| 2350 | 0.044 |
| 2550 | 0.057 |
| 2750 | 0.067 |
| 2950 | 0.072 |
| 3150 | 0.074 |

| Projected Length (arcsec) | | |
|---------------------------|----------------|----------------|
| Aperture | MAMA (E-modes) | Width (arcsec) |
| 0.3X0.05ND | 0.3 | 0.05 |

Figure 13.82: $0.3 \times 0.05 \text{ND}$ Aperture Throughput as a Function of Wavelength.



F25NDQ Aperture

Description

Supported neutral-density-filtered aperture for slitless 1st order MAMA spectroscopy of targets too bright to be observed with a clear aperture. The F25NDQ filter is unique in that it is divided into four quadrants, each having a different neutral density factor. In clockwise order starting from the upper left, these are F25NDQ1, F25NDQ2, F25NDQ3, and F25NDQ4, where the number appended to each name is the approximate dex ND factor. Approximate dimensions of each quadrant and the default location of an external target in each quadrant are given in [Table 13.34](#).

Special Considerations

The default aperture locations where the target is placed in each quadrant are significantly offset from the center of the detector in both the spatial and the dispersion directions. For observations at these nominal aperture locations, this will cause a significant shift in the wavelength coverage for any given grating setting. For example, when observing with G140L in F25NDQ1, wavelengths shorter than about 1330 Å will fall off the detector. Users may wish to use a POS-TARG to bring the target back closer to the center line of the detector. However, if the target would violate BOP restrictions in any quadrant of the aperture, the restrictions regarding pointing close to objects violating safety limits discussed in [Chapter 7](#) and [STIS ISR 2000-01](#) will apply. This latter rule renders the F25NDQ4 quadrant mostly useless, and the F25NDQ3 quadrant is redundant with the full field F25ND3 aperture, so in practice only the F25NDQ1 and F25NDQ2 quadrants are commonly used. Also the dividing lines between the quadrants are somewhat displaced from the center of the detector and are not quite parallel to the detector edges (see [Figure 13.83](#)), so observers for whom the exact locations of the quadrant boundaries are important should consult the [Help Desk](#).

Table 13.34: NDQ Quadrant Dimensions and the Default Locations at which a Target Is Placed in Each Quadrant.

| Aperture | Projected Length (arcsec) | Projected Width (arcsec) | Target X location (pixels) | Target Y location (pixels) |
|----------|---------------------------|--------------------------|----------------------------|----------------------------|
| F25NDQ1 | 13.4 | 9.7 | 198 | 756 |
| F25NDQ2 | 13.8 | 15.1 | 712 | 753 |
| F25NDQ3 | 11.4 | 15.3 | 686 | 254 |
| F25NDQ4 | 11.8 | 9.5 | 195 | 248 |

Figure 13.83: A CCD lamp image taken through the NDQ filter. Note the unequal sizes of the four quadrants.

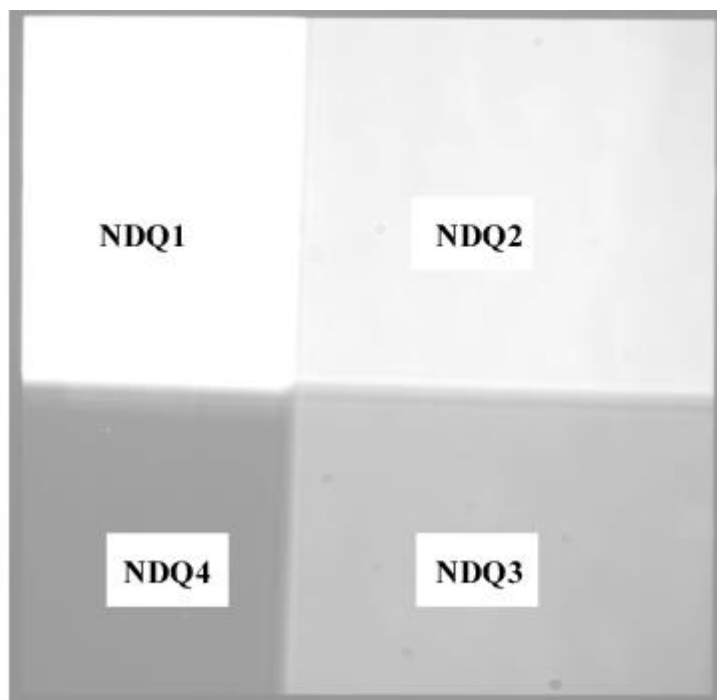
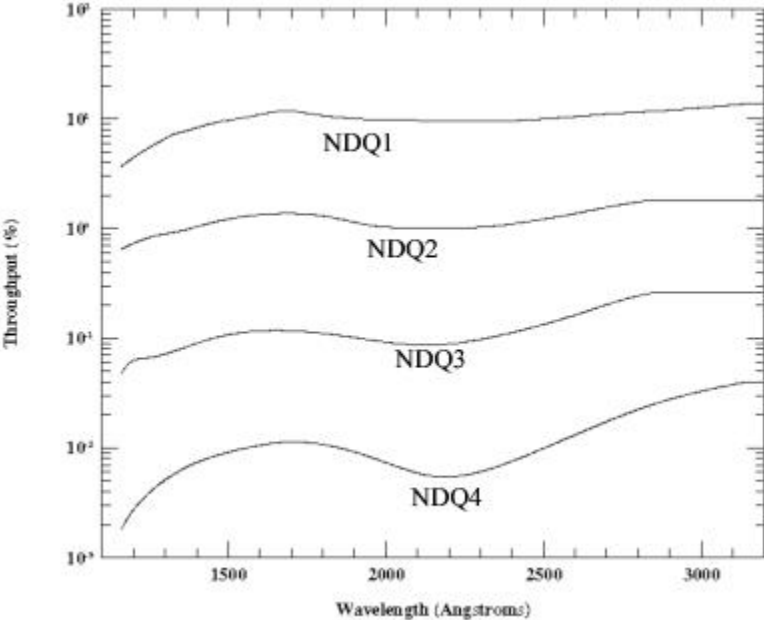


Table 13.35: F25NDQ Throughputs (%)

| λ | F25NDQ1 | F25NDQ2 | F25NDQ3 | F25NDQ4 |
|-----------|---------|---------|---------|---------|
| 1161 | 3.69 | 0.65 | 0.05 | 0.002 |
| 1350 | 7.54 | 0.95 | 0.08 | 0.006 |
| 1550 | 10.24 | 1.29 | 0.11 | 0.010 |
| 1750 | 11.26 | 1.35 | 0.11 | 0.011 |
| 1950 | 9.88 | 1.07 | 0.10 | 0.008 |
| 2150 | 9.66 | 1.01 | 0.09 | 0.006 |
| 2350 | 9.54 | 1.06 | 0.10 | 0.007 |
| 2550 | 10.22 | 1.29 | 0.15 | 0.011 |
| 2750 | 11.30 | 1.66 | 0.22 | 0.020 |
| 2950 | 12.29 | 1.79 | 0.26 | 0.030 |
| 3150 | 13.73 | 1.79 | 0.26 | 0.040 |

Note: Aperture throughputs values for NDQ1 and NDQ4 at $\lambda < 1330 \text{ \AA}$ and for NDQ2 and NDQ3 at $\lambda > 2850 \text{ \AA}$ are extrapolated.

Figure 13.84: F25NDQ Aperture Throughputs vs. Wavelength.



13.5 Spatial Profiles

In this section, we provide encircled energy tables for each grating mode, giving the fraction of the total flux contained in the default point source extraction aperture (which is not the same as the physical aperture used for the observation) during pipeline processing. The pipeline code, **calstis**, sums a number of pixels (given by the "extraction height") to obtain the spectral flux; the default values are 11 pixels for the MAMAs and 7 pixels for the CCD. The tables also give the fractional flux in the peak pixels. Accompanying figures show sample spatial profiles (i.e., in the direction perpendicular to the dispersion), given in terms of the encircled energies. See [ISR 2018-06](#) for a recent discussion of the encircled energies.

First-Order Spatial Profiles

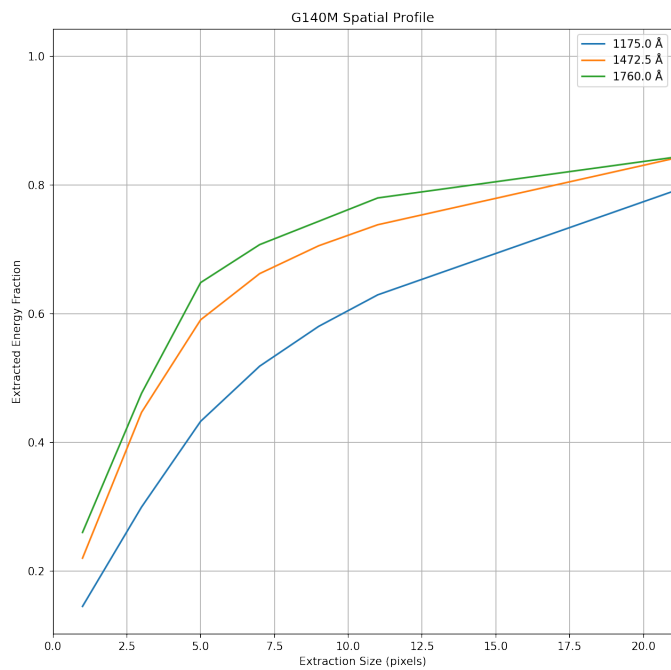
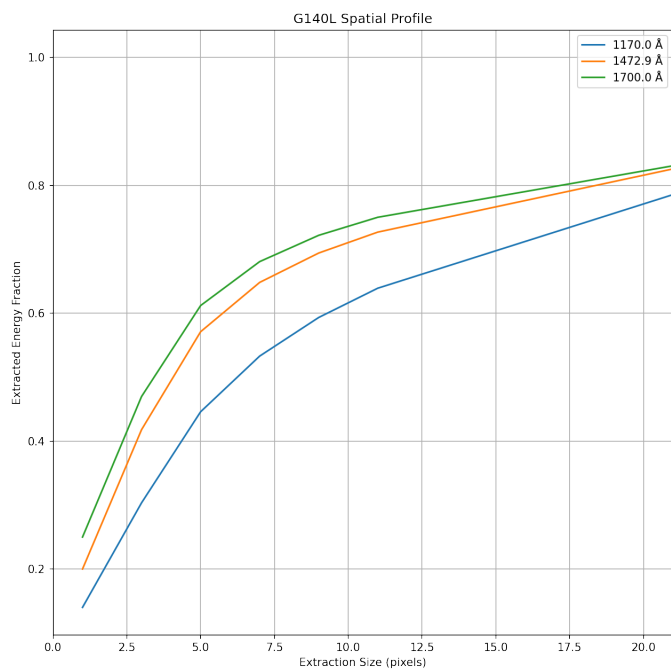
Table 13.36: Encircled Energies for G140L, G140M, G230L, G230M

| Grating | λ | Slit ¹ | Extraction Height (pixels) | Flux in Center Pixel ² | Flux in Extraction Aperture ² |
|---------|-----------|-------------------|----------------------------|-----------------------------------|--|
| G140L | 1170.0 | 52x0.2 | 11 | 0.140 | 0.6393 |
| | 1472.9 | | | 0.200 | 0.7270 |
| | 1700.0 | | | 0.250 | 0.7502 |
| G140M | 1175.0 | 52x0.2 | 11 | 0.145 | 0.6295 |
| | 1472.5 | | | 0.220 | 0.7385 |
| | 1760.0 | | | 0.260 | 0.7802 |
| G230L | 2037.1 | 52x0.2 | 11 | 0.260 | 0.7721 |
| | 2474.3 | | | 0.310 | 0.8001 |
| | 3130.0 | | | 0.330 | 0.7966 |
| G230M | 1968.0 | 52x0.2 | 11 | 0.260 | 0.7732 |
| | 2535.0 | | | 0.300 | 0.7870 |
| | 3021.0 | | | 0.340 | 0.8253 |

¹ Values are only weakly dependent on observing slit.

² From [ISR 2018-06](#)

Figure 13.85: G140L, G140M, G230L, G230M Spatial Profiles.



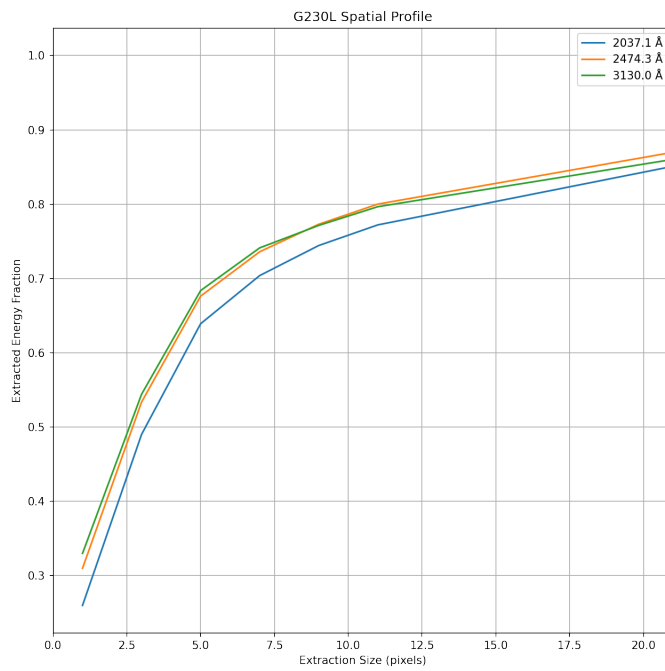
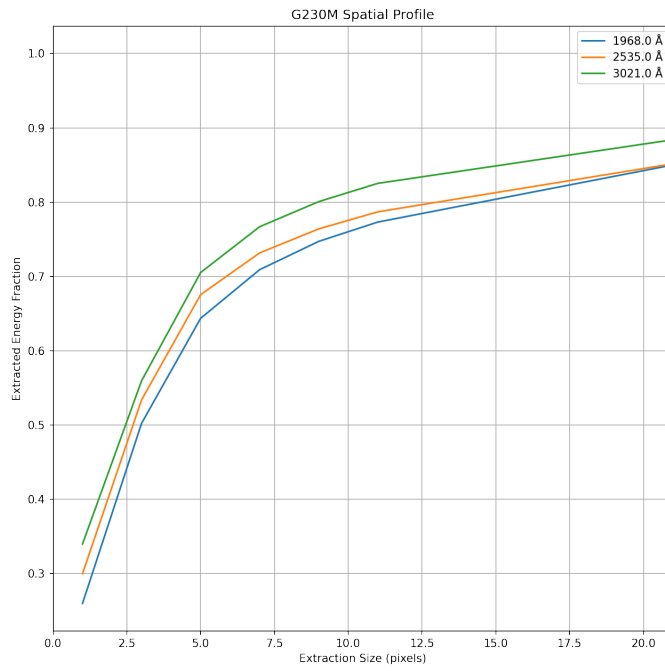


Table 13.37: Encircled Energies for G230LB and G230MB.

| Grating ¹ | λ | Slit ² | Extraction Height (pixels) | Flux in Center Pixel | Flux in Extraction Aperture |
|----------------------|-----------|-------------------|----------------------------|----------------------|-----------------------------|
| G230LB & G230MB | 2000 | 52X2 | 7 | 0.3008 | 0.8130 |
| | 2500 | | | 0.3390 | 0.8475 |
| | 3000 | | | 0.3017 | 0.8621 |

¹ M mode profiles are assumed to be identical to L mode profiles.

² Values are only weakly dependent on observing slit.

Figure 13.86: G230LB and G230MB Spatial Profiles.

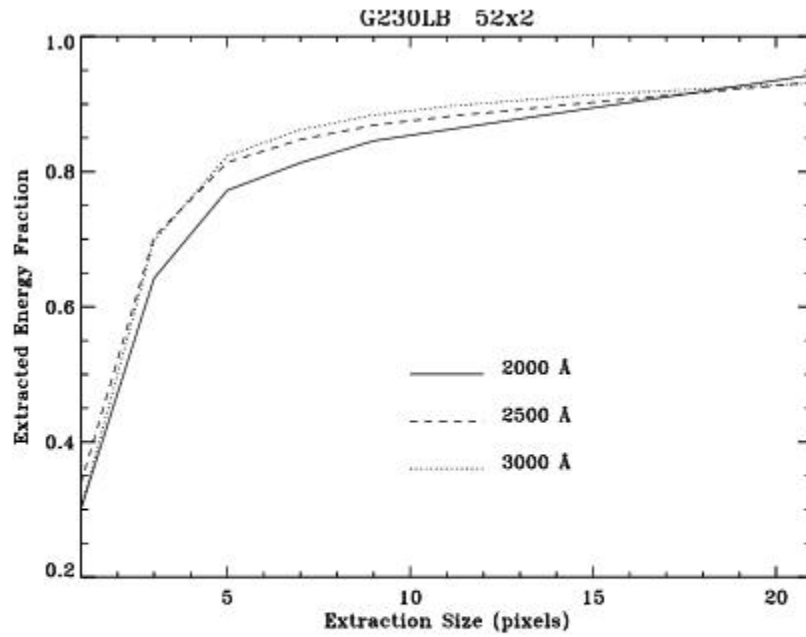


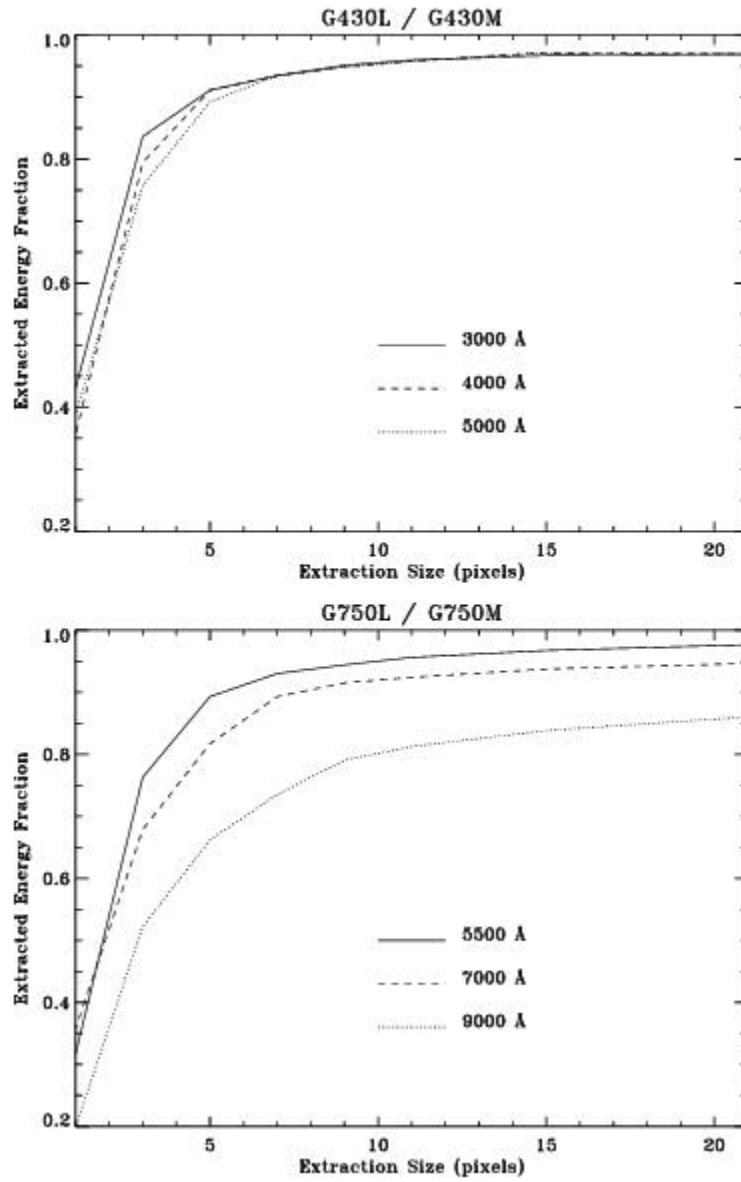
Table 13.38: Encircled Energies for G430L, G430M, G750L, G750M

| Grating ¹ | λ | Slit ² | Extraction Height (pixels) | Flux in Center Pixel | Flux in Extraction Aperture |
|----------------------|-----------|-------------------|----------------------------|----------------------|-----------------------------|
| G430L & G430M | 3000 | 52X0.2 | 7 | 0.4299 | 0.9348 |
| | 4000 | | | 0.3551 | 0.9346 |
| | 5000 | | | 0.3879 | 0.9346 |
| G750L & G750M | 5500 | 52X0.2 | 7 | 0.3163 | 0.9302 |
| | 7000 | | | 0.3571 | 0.8929 |
| | 9000 | | | 0.1985 | 0.7353 |

¹ M mode profiles are assumed to be identical to L mode profiles.

² Values are only weakly dependent on observing slit.

Figure 13.87: G430L, G430M, G750L, and G750M Spatial Profiles.



Echelle Spatial Profiles

Table 13.39: Encircled Energies for Echelle M Modes.

| Grating | λ | Slit ¹ | Extraction Height (pixels) | Flux in Center Pixel | Flux in Extraction Aperture |
|---------|-----------|-------------------|----------------------------|----------------------|-----------------------------|
| E140M | 1170 | 0.2x0.2 | 7 | 0.274 | 0.944 |
| | 1400 | | | 0.308 | 0.959 |
| | 1600 | | | 0.331 | 0.961 |
| E230M | 1900 | 0.2x0.2 | 7 | 0.347 | 0.973 |
| | 2550 | | | 0.359 | 0.947 |
| | 3000 | | | 0.391 | 0.949 |

¹ Values are only weakly dependent on observing slit.

Figure 13.88: Echelle M Mode Spatial Profiles.

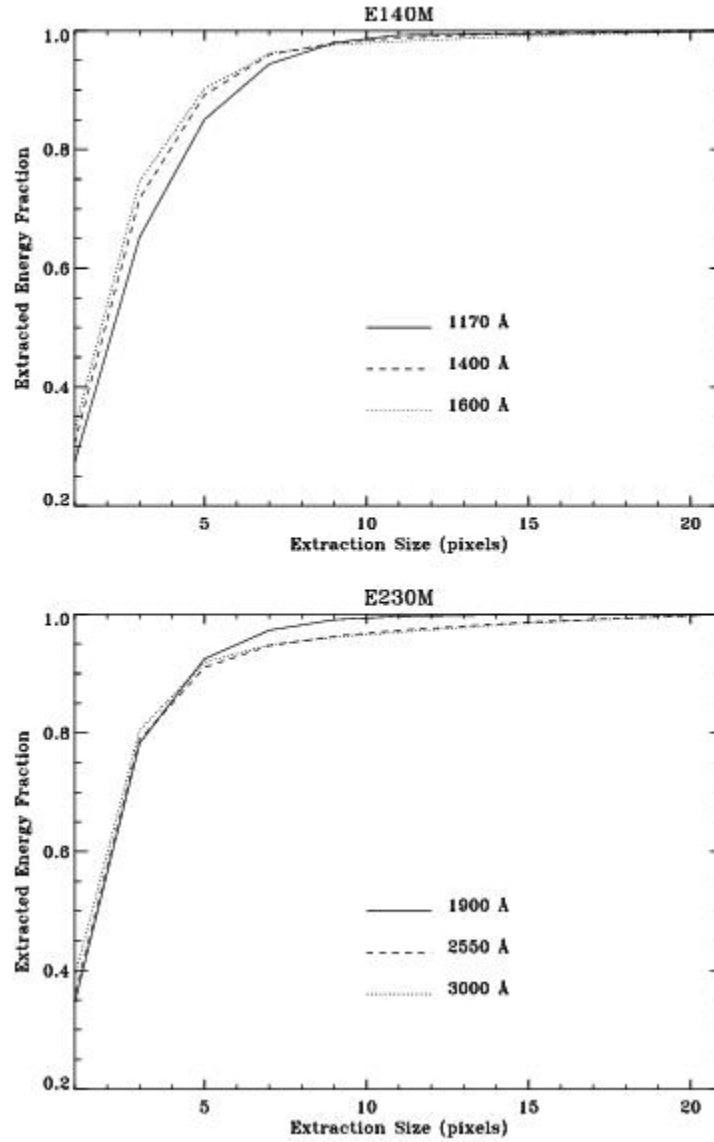


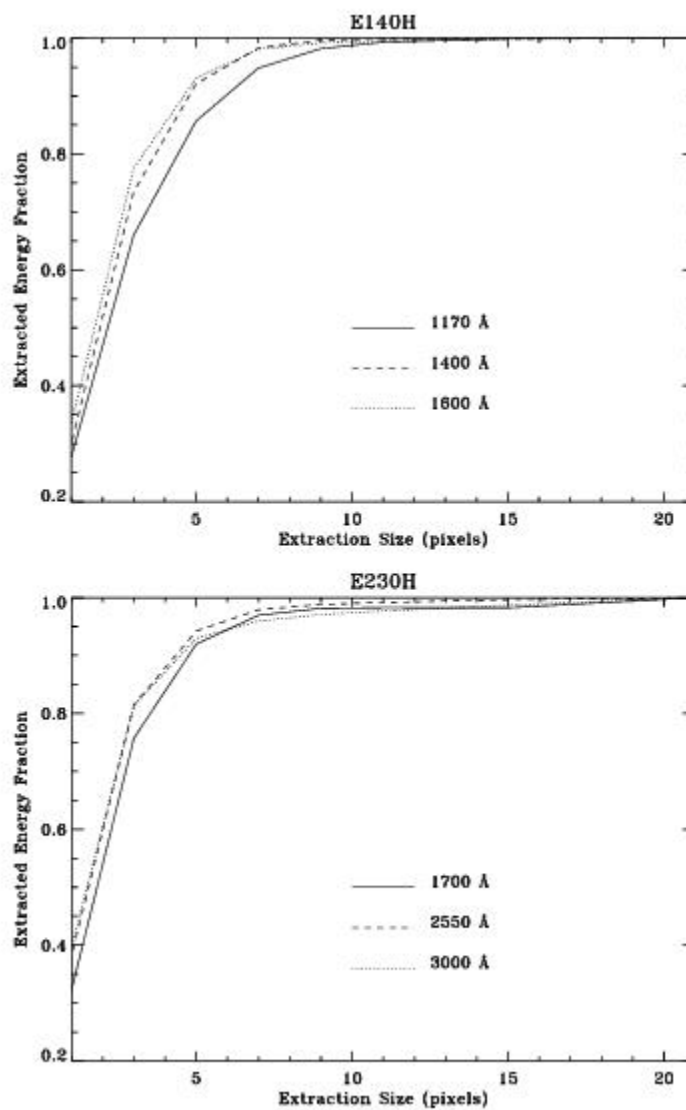
Table 13.40: Encircled Energies Echelle H Modes.

| Grating | λ | Slit ¹ | Extraction Height (pixels) | Flux in Center Pixel | Flux in Extraction Aperture |
|---------|-----------|-------------------|----------------------------|----------------------|-----------------------------|
| E140H | 1170 | 0.2X0.2 | 7 | 0.276 | 0.948 |
| | 1400 | | | 0.300 | 0.983 |
| | 1600 | | | 0.335 | 0.981 |

| | | | | | |
|-------|------|---------|---|-------|-------|
| E230H | 1700 | 0.2x0.2 | 7 | 0.323 | 0.970 |
| | 2550 | | | 0.382 | 0.979 |
| | 2700 | | | 0.342 | 0.968 |

¹ Values are only weakly dependent on observing slit.

Figure 13.89: Echelle H Mode Spatial Profiles.



13.6 Line Spread Functions

In this section, we provide model line spread functions (LSFs, i.e., instrumental profiles) for point source observations through a sample of supported slits in first-order and echelle modes as a function of observing wavelength. Internal lamp observations and on-orbit data for external targets have been used to confirm and revise the original pre-flight models of the STIS LSFs. Tabulated LSFs can be found on the [STIS spectral resolution webpage](#).

These plots and the derived FWHM presented below in tabular form show that increasing the slit width for point source observations has very little effect on the FWHM of the observed lines but does broaden the wings of the LSFs. This occurs because a wider aperture allows more of the wings of the *HST* Optical Telescope Assembly PSF to enter, but does not change the shape of the inner part of the PSF which is quite narrow. The implications of the LSF wings on line profile and equivalent width measures are discussed in more detail in [Section 13.7](#). For diffuse source observations, don't forget that widening the slit, while it allows more light to enter, also will degrade the spectral resolution obtained.

First-Order Line Spread Functions

Table 13.41: Spectral Resolution for CCD First-Order Modes

| Slit | Spectral Resolution (FWHM in pixels) | | | | |
|---------|--------------------------------------|--------|--------|---------|-----------------|
| | Point Source | | | | Extended Source |
| | 3200 Å | 5500 Å | 7000 Å | 10000 Å | |
| 52X0.05 | 1.3 | 1.4 | 1.5 | 1.7 | 2 |
| 52X0.1 | 1.3 | 1.4 | 1.5 | 1.7 | ~2-3 |
| 52X0.2 | 1.3 | 1.5 | 1.6 | 2.0 | ~4 |
| 52X0.5 | 1.3 | 1.5 | 1.6 | 2.0 | ~10 |
| 52X2 | 1.3 | 1.5 | 1.6 | 2.0 | ~40 |

Figure 13.90: CCD First-Order L-Mode Line Spread Functions.

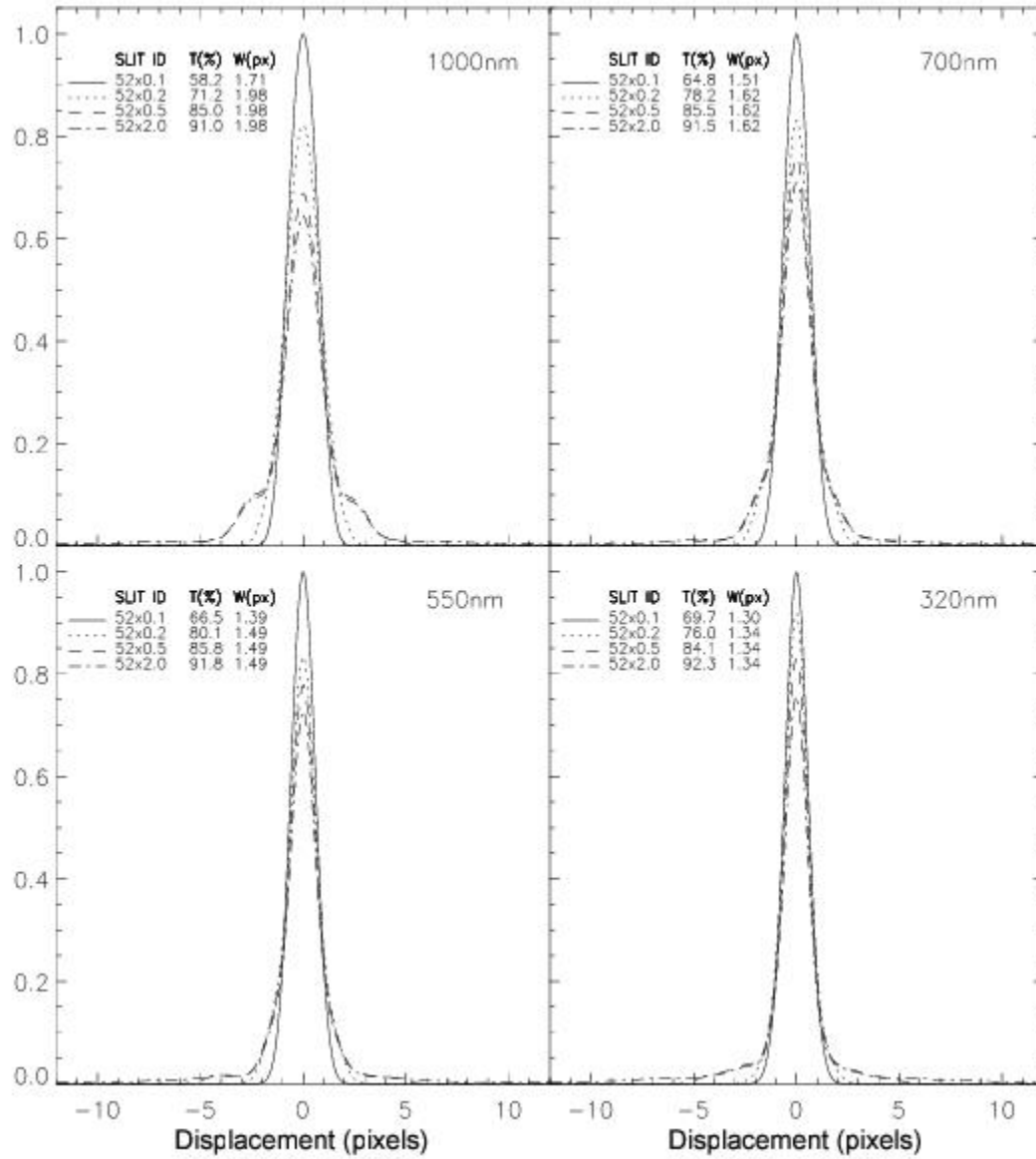


Table 13.42: Spectral Resolution for MAMA First-Order Modes.

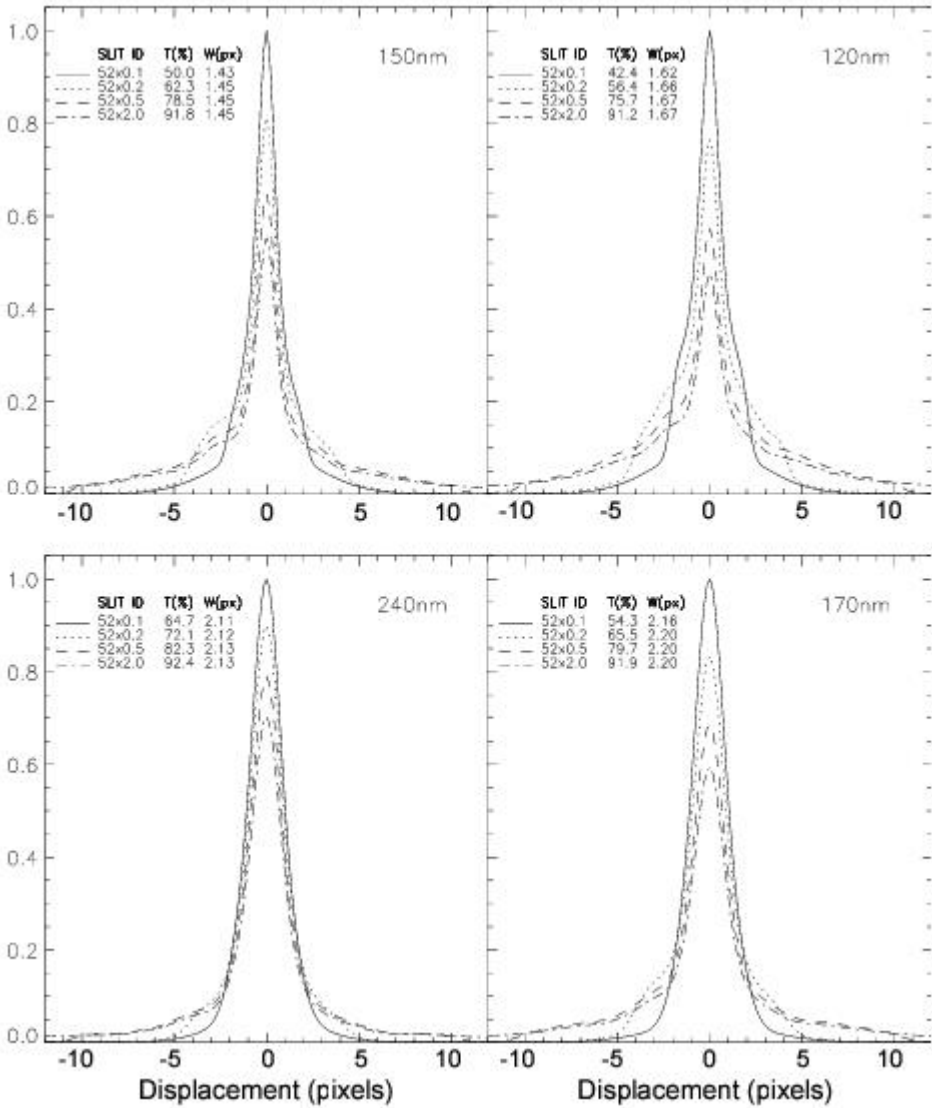
| Slit | Spectral Resolution (FWHM in pixels) | | | | | |
|---------|--------------------------------------|--------|---------------------|---------------------|--------|-----------------|
| | Point Source | | | | | Extended Source |
| | 1200 Å | 1500 Å | 1700 Å ¹ | 1700 Å ² | 2400 Å | |
| 52X0.05 | 1.6 | 1.5 | 1.4 | 2.2 | 2.1 | ~2 |
| 52X0.1 | 1.6 | 1.5 | 1.4 | 2.2 | 2.1 | ~4 |

| | | | | | | |
|--------|-----|-----|-----|-----|-----|-----|
| 52X0.2 | 1.7 | 1.5 | 1.4 | 2.2 | 2.1 | ~8 |
| 52X0.5 | 1.7 | 1.5 | 1.4 | 2.2 | 2.1 | ~20 |
| 52X2 | 1.7 | 1.5 | 1.4 | 2.2 | 2.1 | ~80 |

¹ FWHM with FUV-MAMA (G140L, G140M).

² FWHM with NUV-MAMA (G230L, G230M).

Figure 13.91: MAMA First-Order Line Spread Functions. Top G140L and G140M, bottom G230L and G230M.



Echelle Line Spread Functions

Table 13.43: Spectral Resolution for Echelle Medium-Resolution Modes (E230M, E140M).

| Slit | Spectral Resolution (FWHM in pixels) | | | | | |
|----------|--------------------------------------|--------|---------------------|---------------------|--------|-----------------|
| | Point Source | | | | | Extended Source |
| | 1200 Å | 1500 Å | 1700 Å ¹ | 1700 Å ² | 2400 Å | |
| 0.1x0.03 | 0.9 | 0.9 | 1.0 | 1.6 | 1.6 | ~1 |
| 0.2x0.2 | 1.4 | 1.3 | 1.1 | 2.0 | 1.9 | ~6 |
| 0.2x0.06 | 1.3 | 1.2 | 1.1 | 1.8 | 1.7 | ~2 |
| 6x0.2 | 1.6 | 1.4 | 1.2 | 2 | 1.9 | ~6 |

¹ FWHM with FUV-MAMA (E140M).

² FWHM with NUV-MAMA (E230M).

Figure 13.92: Echelle Line Spread Functions. E140M (top) and E230M (bottom).

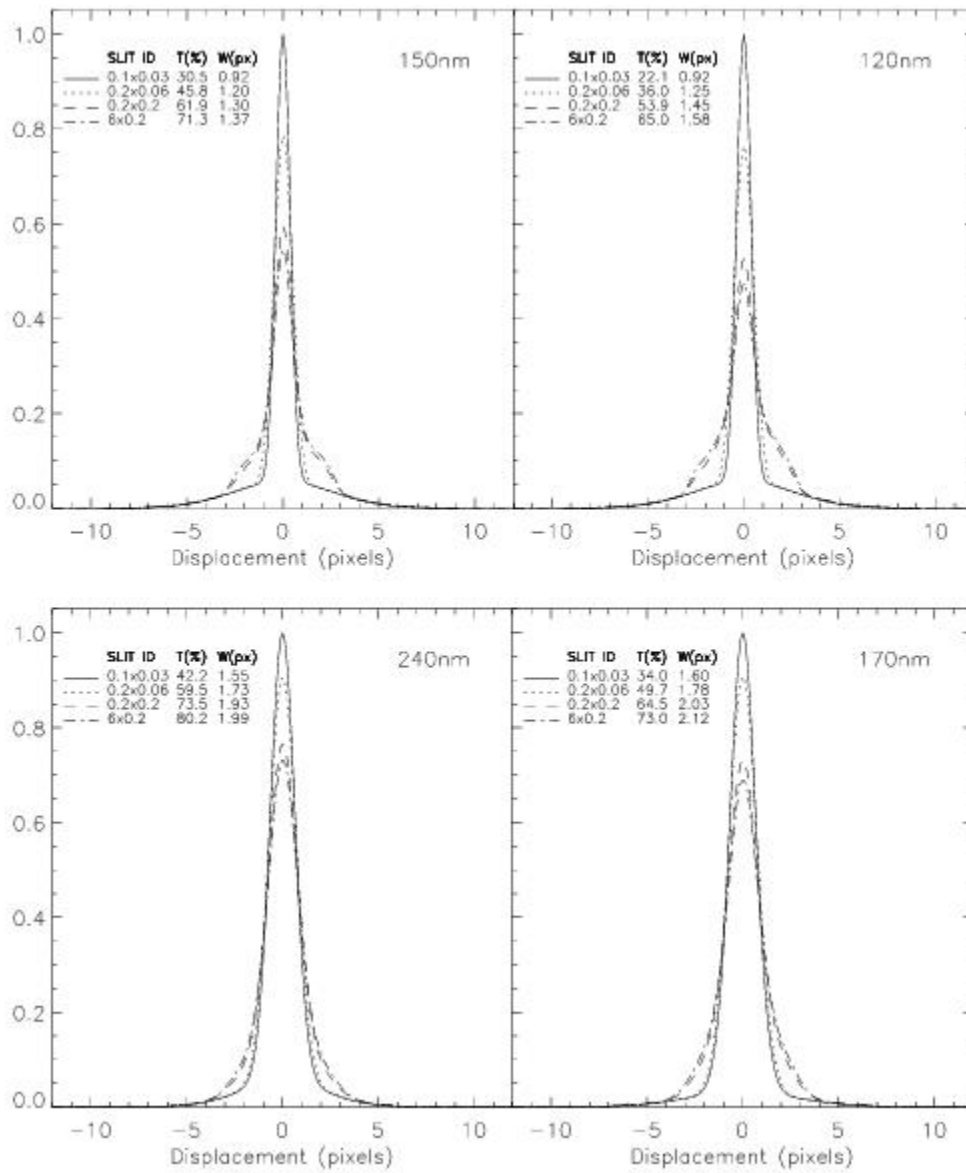


Table 13.44: Spectral Resolution for Echelle High-Resolution Modes (E140H, E230H).

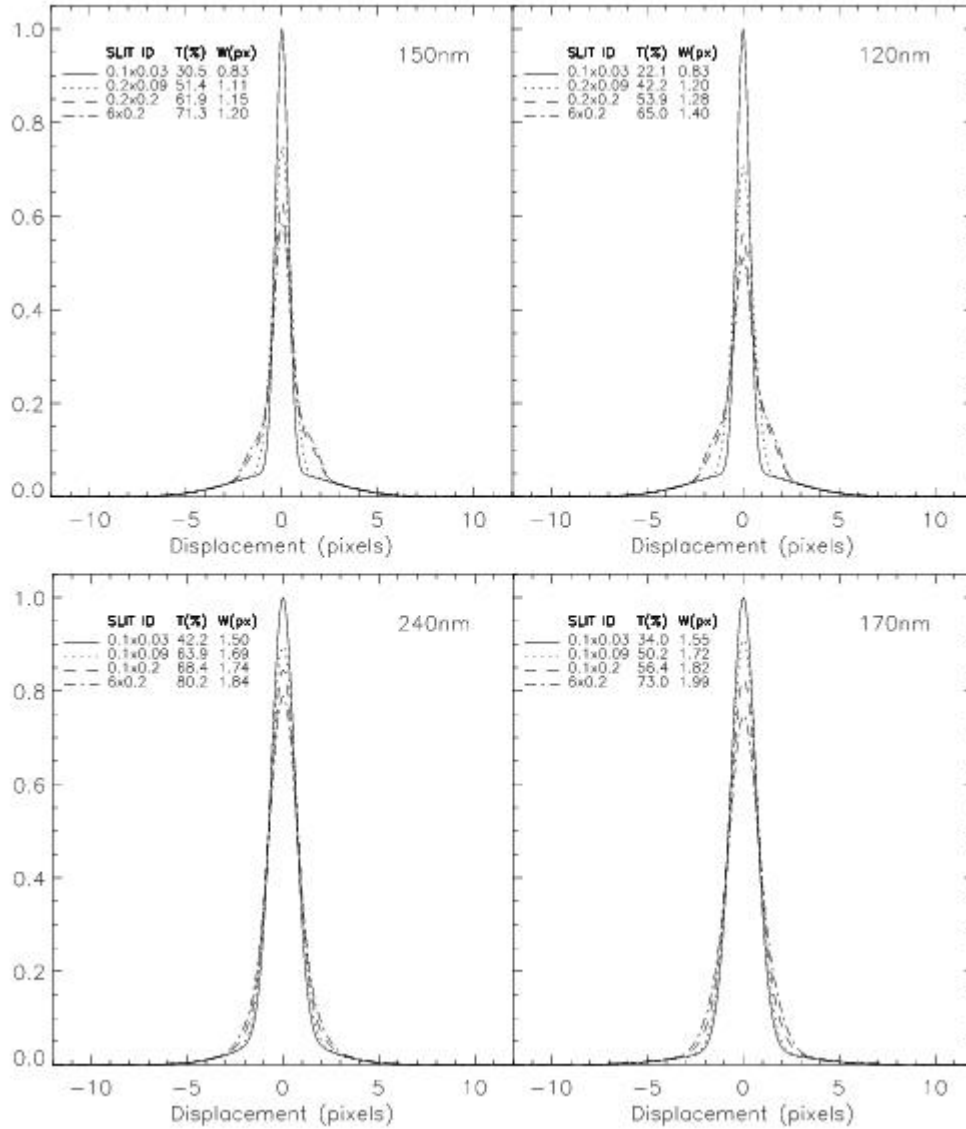
| Slit | Spectral Resolution (FWHM in pixels) | | | | | Extended Source |
|----------|--------------------------------------|--------|---------------------|---------------------|--------|-----------------|
| | Point Source | | | | | |
| | 1200 Å | 1500 Å | 1700 Å ¹ | 1700 Å ² | 2400 Å | |
| 0.1x0.03 | 0.8 | 0.8 | 1 | 1.5 | 1.5 | ~1 |
| 0.2x0.2 | 1.3 | 1.1 | 1 | 1.8 | 1.7 | ~6 |

| | | | | | | |
|----------|-----|-----|-----|-----|-----|----|
| 0.2x0.09 | 1.2 | 1.1 | 1 | 1.7 | 1.7 | ~2 |
| 6x0.2 | 1.4 | 1.2 | 1.2 | 2 | 1.8 | ~5 |

¹ FWHM with FUV-MAMA (E140H).

² FWHM with NUV-MAMA (E230H).

Figure 13.93: Echelle Line Spread Functions. $\Xi 140\text{H}$ (top) and $\Xi 230\text{H}$ (bottom). LSFs for $\Xi 230\text{H}$ were derived using the 0.1×0.2 and 0.1×0.09 apertures; results for 0.2×0.2 and 0.2×0.09 should be similar.



13.7 Spectral Purity, Order Confusion, and Peculiarities

- [13.7.1 Recommendations for Stellar Observations with Narrow Slits](#)
- [13.7.2 Order Overlap and Scattered Light for Echelle Gratings](#)
- [13.7.3 Spectroscopic Mode Peculiarities](#)
- [13.7.4 Railroad Tracks](#)

If the PSF had an infinitely small FWHM and no extended wings, a point source would produce a spectrogram with infinitesimal extension in the spatial direction. Furthermore, the spectral resolution would be essentially the theoretical limit of the spectrograph, independent of the entrance slit. In practice, the Optical Telescope Assembly PSF is wider and more complex, and there is scattered light from both the gratings and the detector itself, leading to decreased spectral resolution and spectral purity.

In [Figure 13.94](#) we have plotted H β in the white dwarf Feige 110 observed with the G430L grating and five entrance slits with widths between 2" and 0."05. The spectrum observed through the 0."05 and 0."1 slits can be considered spectrally pure (remember 0."1 maps to 2 pixels on the CCD and 0."05 maps to 2 pixels on the MAMAs). Observations with the 0."2 slits are still reasonably pure but larger slit widths lead to significant impurity. This becomes evident from the increasing flux in the line core with increasing slit width. The maximum spectral purity is achieved with entrance slits of 0."2 width or smaller. Similar results can be seen in [Figure 13.95](#) which shows the calcium triplet regions. Observers wishing to study spectral lines of continuum sources should always consider using small entrance slits.

Figure 13.94: H β in the White Dwarf Feige 110 Observed with G430L and 5 Entrance Slits.

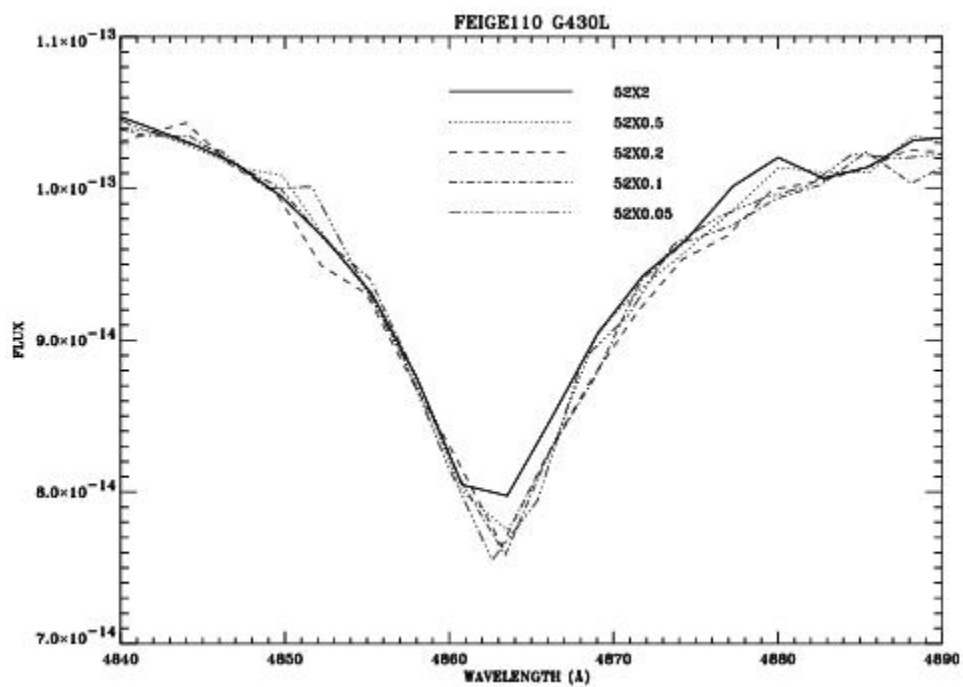
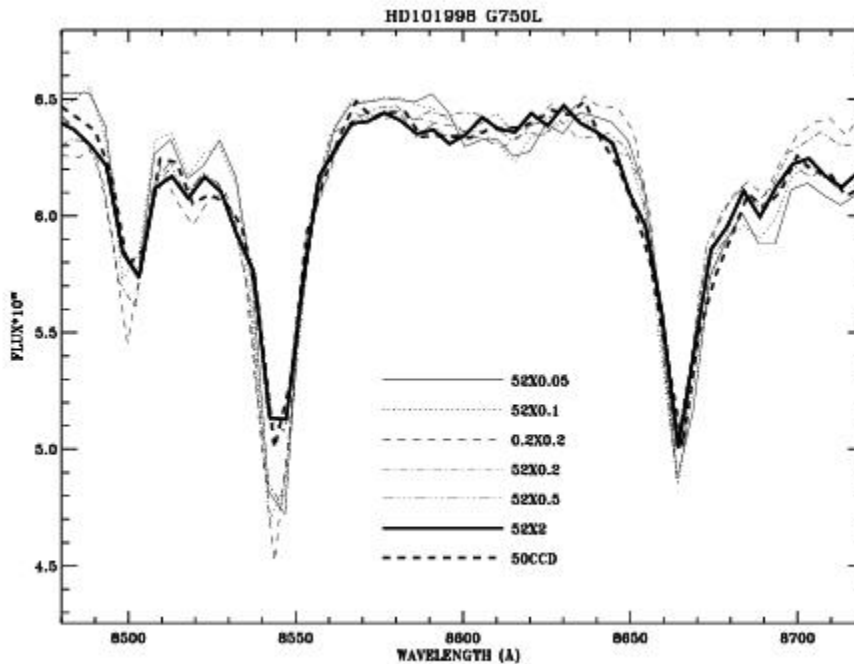


Figure 13.95: Calcium Triplet Observed with G750L and 7 Entrance Slits.



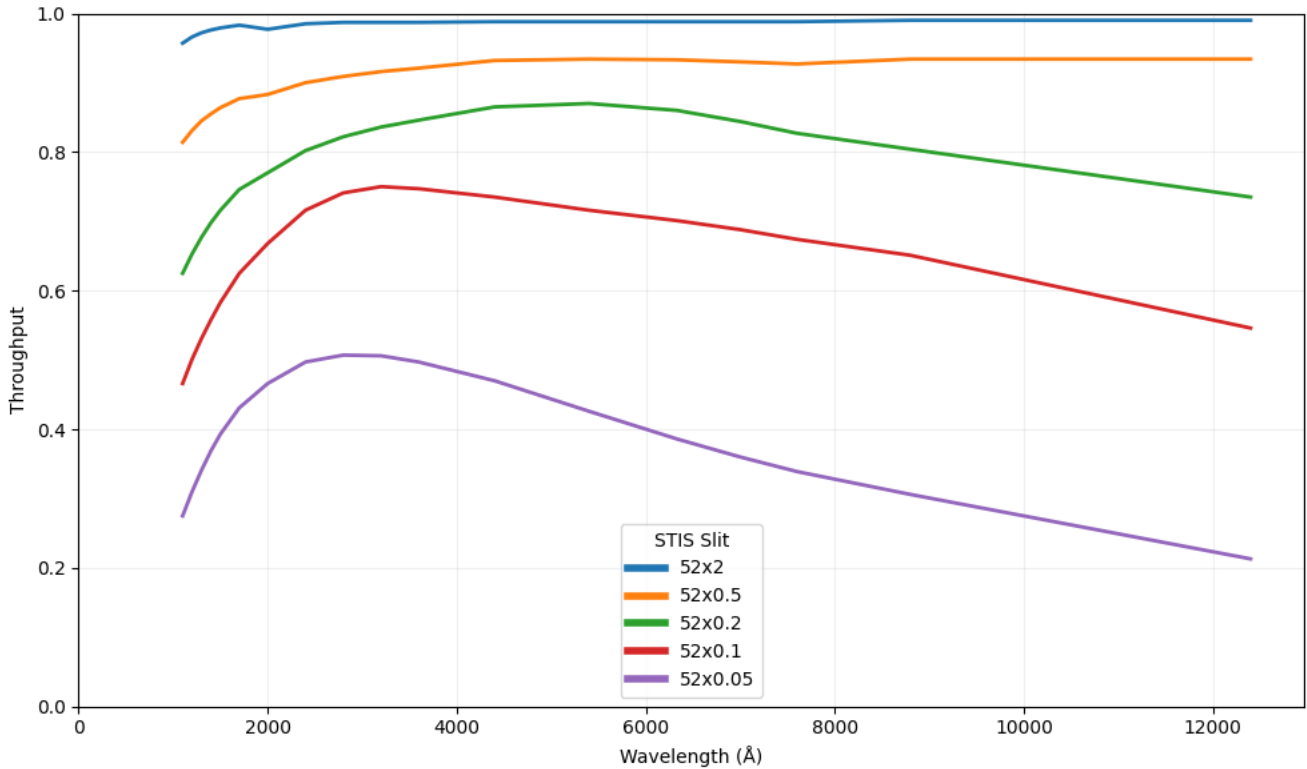
13.7.1 Recommendations for Stellar Observations with Narrow Slits

In assessing the trade between the better spectral purity of small slits and the higher throughput and photometric precision of larger slits, the following should be kept in mind:

1. Choose a slit that meets your requirements for photometric precision.
2. Avoid the 52x0.05 slit with the G750 modes, since the Airy core of the point spread function is much larger than the slit size and the resulting light losses may exceed a factor of 5 in comparison with the 52x2 slit. Furthermore, the nominal resolution of 2 pixels is a match to a 0.1 arcsec slit width for the CCD modes.
3. Longer wavelength observations require wider slits to avoid light loss problems as the point spread function enlarges. Beyond ~ 5000 Å, a rapid loss of light is possible even when a 52x0.1 slit is used (see [Figure 13.95b](#)). In a test of medium dispersion modes, a loss of 10% was found near 4000 Å, but this increased to 25% by 8500 Å.
4. As a stellar target may not be perfectly centered, pipeline fluxes may, in general, be treated as lower limits. Exceptions are the CCD G430L and G750L modes which utilize a Lyot stop.

More complete details on these points can be found in [STIS ISR 1998-20](#) by R. Bohlin and G. Hartig. Regardless of the size of the slit, remember that a pickup will ensure the greatest wavelength accuracy, since an offset of the target in the dispersion direction will be miscalibrated as an offset of the wavelength scale (see [Section 8.1.1](#) and [Section 8.3.1](#)).

Figure 13.95b: Throughputs of STIS long slits from stsynphot data.

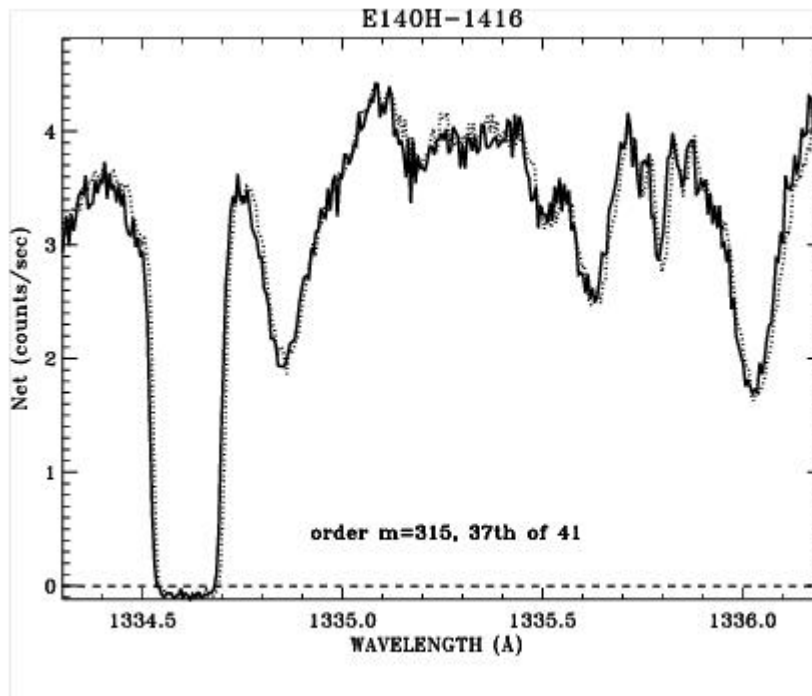


13.7.2 Order Overlap and Scattered Light for Echelle Gratings

As with most other echelle spectrographs, STIS echelle data are affected by spectral order overlap at the shortest wavelengths where adjacent spectral orders are not well separated. Echelle observations of continuum sources taken slitless or with a 2x2 entrance slit suffer from severe order overlap. Therefore, an entrance slit of 0."2 or smaller height should be used.

Figure 13.96 demonstrates the difference in resolution for a narrow absorption line for BD+75°325 observed in the 0.2x0.2 slit vs. a 0.2x0.09 slit. Any difference in the effect of impure light on the depth of the line profiles is less than ~1% of the continuum. An extraction height of 7 pixels is used, and the 0.2x0.09 aperture spectrum is multiplied by 1.28 to compensate for the lower transmission. A slight wavelength shift is maintained to improve visibility.

Figure 13.96: Comparison Between 0.2x0.2 (solid line) and 0.2x0.09 (dotted line) Aperture Spectra of BD+75°325 in the E140H-1416 Mode.



Note the "oversubtraction" of the black line. This is a ramification of oversubtraction of the background; light which is scattered from the echelle, the OTA PSF, and the detector into the interorder area is being oversubtracted from the science spectrum in the straightforward background subtraction procedure used. The E230M and E230H gratings are only a little affected by this scatter (7% of the light is scattered at $\sim 2000 \text{ \AA}$, 4% at 2500 \AA). However, the E140M and E140H modes do have appreciable scatter; 33% of the light scattered at 1235 \AA for E140M and 15% for E140H; at 1600 \AA this drops to $\sim 12\%$ and 8% , respectively. The STScI provides an [ETC](#), which predicts global and net countrates to sufficient accuracy for planning purposes. An estimate of the *net* S/N and the *net + scattered light* in an echelle observation are produced for a specified input spectrum, including an approximation to the scattered component.

An "algorithm" parameter has been added to the `x1d` spectral extraction task in `calstis`. Changing this parameter from "unweighted" to `sc2d` enables a new two-dimensional background subtraction algorithm that was designed by Don Lindler (Sigma Space Corporation) and Chuck Bowers (Goddard Space Flight Center). Alternatively, you can run `calstis` on the new data with `SC2DCORR` set to `PERFORM` in the primary header. (See Section 3.4.20 of the [STIS Data Handbook](#).) [Figure 13.97](#) shows the dramatic improvement achieved with the use of this new algorithm. [Figure 13.98](#) summarizes the fractional error in saturated line cores as a function of wavelength and grating for both algorithms. Errors for the medium-resolution gratings are comparable to errors for the high-resolution gratings.

Figure 13.97: Comparison Between the Standard 1-D and the New 2-D Background Subtraction.

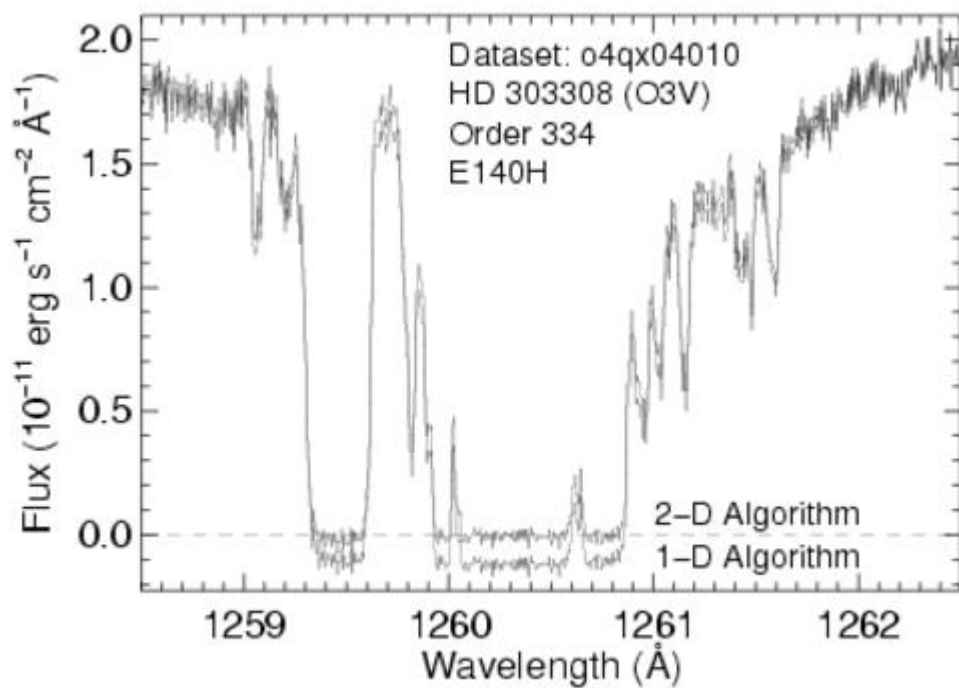
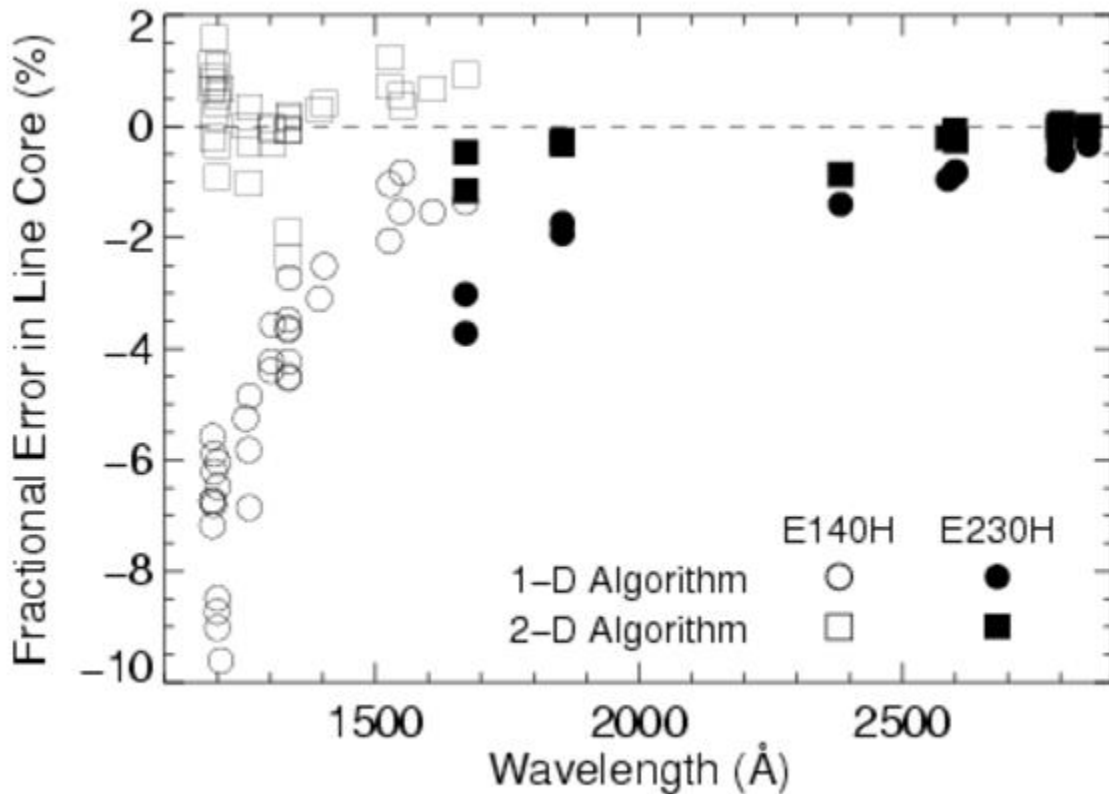


Figure 13.98: Comparison Between the Errors of the Two Methods.



Since early 2001, all STIS echelle data obtained from the archive have been processed using the new two-dimensional background subtraction algorithm.

Briefly, the new algorithm works as follows: a 2-D raw image is fit with a 2-D model, reconstructed at each iteration from the best current estimate of the extracted spectrum folded through a semi-empirical simulation of STIS optical properties. Self-consistency between the 2-D model and the extracted spectrum is achieved via iteration. An analogous model containing only scattered light is then constructed using only the echelle scatter light outside an 11 pixel-wide vertical window centered on each order. This 2-D scattered-light model is subtracted from the raw data and the final spectrum is obtained using standard 1-D extraction.

Construction of the 2-D model during each iteration involves several steps. Counts in the 1-D extracted spectrum are mapped back to their idealized origin in hypothetical echelle orders that extend beyond the edge of the physical detector. Echelle scatter is modelled by redistributing extracted counts along diagonal lines of constant wavelength, using echelle line spread functions. Post-echelle smearing along columns is modelled by independently convolving each column with a smoothing kernel. Scattering due to the aperture-truncated telescope PSF, isotropic detector halo, and pre-echelle scattering by the cross-disperser are treated by 2-D convolution with a kernel constructed from these components.

13.7.3 Spectroscopic Mode Peculiarities

During the original SMOV and initial observations, a number of first-order mode spectra have been obtained that show additional features that may affect the scientific goals of the observations. One class of spectroscopic images shows diffraction structure of the PSF re-imaged at the various STIS detectors. A second class, commonly referred to as railroad tracks, displays additional "spectra" displaced from and parallel to the primary spectrum. Some examples and impacts are presented below.

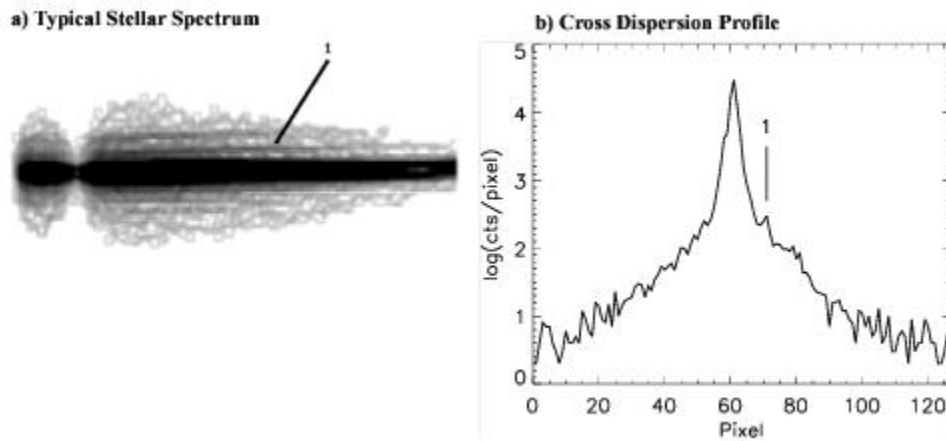
PSF Re-Imaging

The STIS corrector mirrors re-image the OTA PSF at an intermediate focus within STIS at the location of the slit wheel. This intermediate image is re-imaged to one of the detectors via the selected mode, either imaging or spectroscopic. Any PSF structure present in the slit plane image will be re-imaged at the detectors; however, its appearance in a final spectrum or image depends on the selected mode and the slit or aperture used.

In the imaging modes, little PSF diffraction structure is apparent, since the available filters are typically relatively broad band, smoothing out any structure. The spectroscopic modes, however, create a series of near monochromatic images at the detector plane and the PSF diffraction structure can be detected with the two dimensional STIS detectors.

Point Source: [Figure 13.99](#) shows the spectrum of a point source target, using G140L and slit 52X0.05.

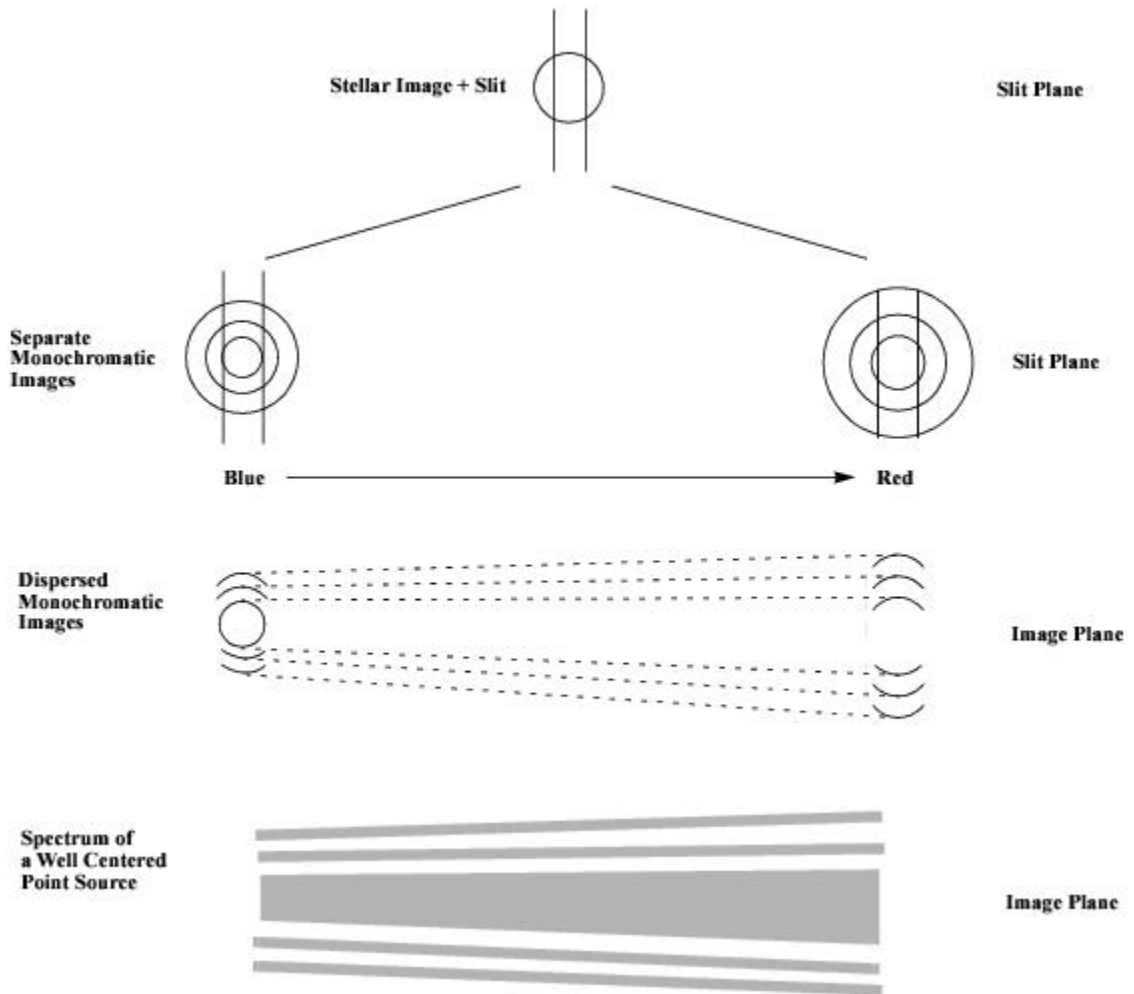
Figure 13.99: Spectrum of a Point Source (Stellar) Target.



This typical stellar spectrum (1150–1700 Å) shown in panel a, was of a white dwarf for instrument calibration. The Lyman- α absorption feature is apparent near the left end. This image was processed and log stretched to enhance the "fringes" seen above and below the stellar spectrum. These fringes are weak, diverge from the spectrum proportionally to wavelength, and are not present in the Lyman- α gap, indicating they are connected with the source at the slit plane and are not the result of STIS internal scatter. Panel b shows a cross dispersion profile of the original image, cut near the center of the spectrum at about 1430 Å. The brightest fringe (labelled "1") is indicated; the peak of the fringe is roughly 0.005 times the peak of the stellar spectrum.

Figure 13.100 illustrates how such fringes are created at the detector. At each wavelength, the portion of the PSF at the slit plane which passes the slit is re-imaged onto the detector. The envelope of all such PSF portions forms the complete image at the detector, as shown. The characteristic fringe separation, proportional to wavelength, is expected as the diffraction structure in the PSF increases with wavelength as shown. In the medium-resolution modes, with much less bandpass than the low-resolution modes, the tilt of the fringes is much less—they are nearly parallel to the primary spectrum.

Figure 13.100: How Fringes are Created.



The fringe visibility is decreased with increasing slit width. Figure 13.100 illustrates this—as the slit broadens, more of a curved portion of the diffraction rings is transmitted. The envelope of these more curved sections is broader with lower contrast compared to the sharp segments visible with a narrow slit.

Out of slit point source: Figure 13.101 shows the spectrum (G140L) of a stellar source, in which the target was mis-located and not nominally in the 52x0.05 slit. While the target center was not located in the slit, the extended PSF structure did cover the slit opening and was transmitted and re-imaged at the detector plane. This image has been processed and log stretched to enhance the faint fringe structure which is apparent.

Figure 13.101: Mis-Located Target—Stellar Source.

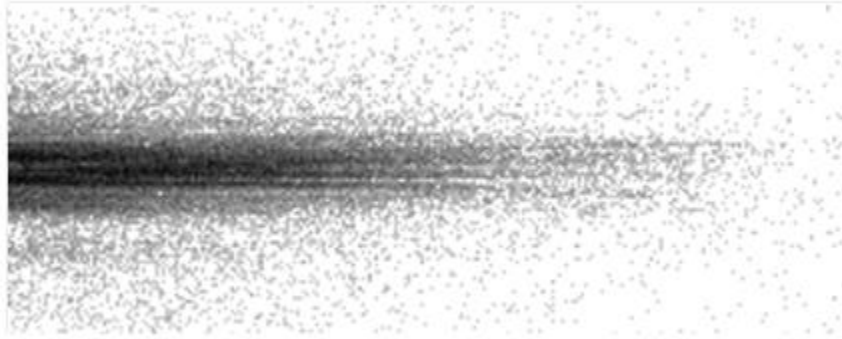
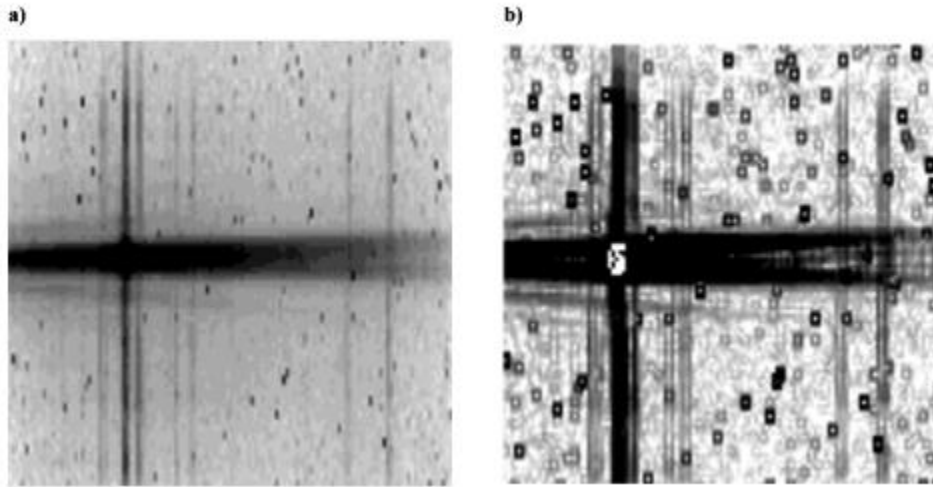


Figure 13.102 shows a similar case in which the spectrum of a galaxy with a very bright core was obtained with the core located roughly 0.1" from the center of the 0.1" wide slit in the visible mode G750L. The images were processed and log stretched to enhance the fringe appearance. Divergent fringes are apparent above and below the spectrum. A principal component of the "spectrum" consists of changes in the upper and lower portions of the first Airy ring, seen clearly separated at the long wavelength end of the spectrum. (See [STIS ISR 2006-02](#).) These two fringes converge at shorter wavelengths forming a single fringe which overlies the much fainter, off-core portion of the galaxy. The evident blueness of the core spectrum in this particular source makes the combined blue fringes much brighter than the combination of the separated red fringes.

Figure 13.102: Mis-Centered Spectrum of Galaxy with Bright Core.



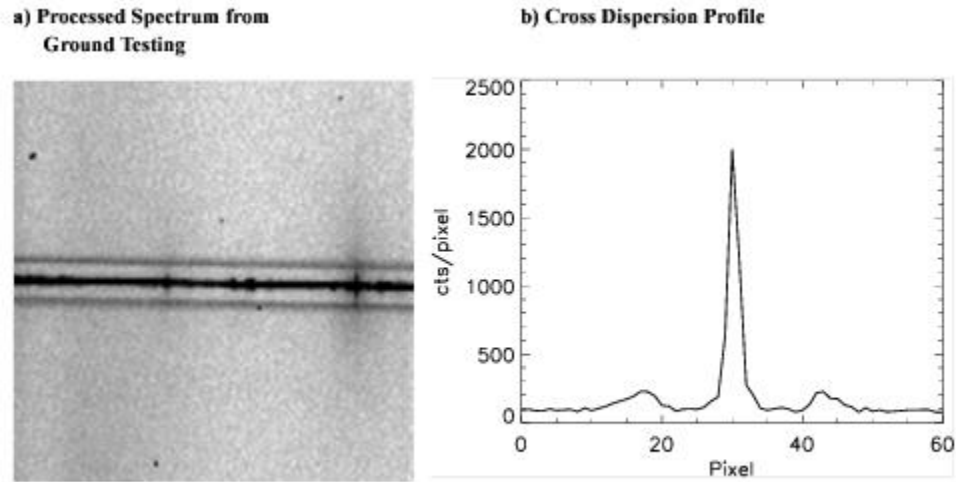
Impact

Diffraction structure in the PSF will set a limit to extracting spectra near a bright source. Blocking the bright source, either by using a coronagraphic aperture or by moving the bright source out of the slit does not remove the inherent, adjacent PSF or diffraction structure. In the case of a faint companion adjacent to a bright, primary source, note that the spectra of the primary and companion will be parallel while the PSF fringes will be tilted. This is especially true in the low resolution modes and may allow the unambiguous identification of a faint companion even in the presence of comparably bright PSF structure.

13.7.4 Railroad Tracks

Figure 13.103 (panel a) shows a processed spectrum of a continuum lamp in mode G750M, $\lambda_C = 10,363$ and slit 0.1×0.2 obtained during ground testing. Beside the spectrum, two adjacent, parallel, secondary spectra are seen symmetrically displaced about 13 pixels from the lamp spectrum. Panel b shows a cross dispersion profile illustrating the magnitude and shape of the spectra. The secondary spectra have peak intensities about 8% of the primary spectrum but are broader and asymmetric. This was the only example of this peculiar condition noticed during ground testing; however, subsequent review showed one additional example also obtained during ground testing. This second case was a similar continuum lamp spectrum using G750M, $\lambda_C = 7795$, with the same slit. Secondary spectra were $\sim 8\%$ and 3% (peak intensity) of the primary peak intensity.

Figure 13.103: Railroad Tracks.



One similar example has been obtained in flight to date, with the UV mode G230LB and the CCD. The target was a very red star. The parallel, secondary spectra are visible at a level of about 8% of peak intensity.

The cause of these secondary spectra in these three observations is not known. The three cases observed have all been with the CCD; no MAMA examples have been obtained. Other observations in these modes under similar conditions have not shown such effects. In all cases, a red source was observed. The broad profile and relatively bright intensity of the secondary spectra suggest a multiple reflection instead of a diffraction origin, but no way of producing dual, symmetric features has yet been proposed which is consistent with these observations.

13.8 MAMA Spectroscopic Bright Object Limits

As described in [Section 7.7](#), the MAMAs are subject to absolute brightness limits, above which sources cannot be observed or they would potentially damage the detectors. In [Table 13.45](#), we present the complete set of absolute bright object point source spectroscopic screening magnitudes and fluxes for the MAMA spectroscopic modes. These screening magnitudes are presented as a guide. Whether an individual source can be observed is ultimately determined by whether, in the desired configuration, the spectrum of that source is predicted to exceed the global and local observing count rate limits, as described in [Chapter 7](#). The information presented here should be used in conjunction with the material presented in [Chapter 7](#). Remember, sources cannot be observed in configurations where they exceed the absolute bright object limits. A few important points to note are:

- The screening limits are given either as *V* magnitude or CGS units as indicated.
- The screening limits for first order modes and the PRISM in this table have been calculated assuming zero slit losses. For Echelle modes, the 0.2x0.2 aperture was assumed unless otherwise noted. To determine if your source will violate the limits in this table, you must first correct the magnitude limit for the aperture throughput for your chosen slit. The maximum magnitude correction achieved without use of a neutral density filter using a supported slit is ~0.75 magnitudes. An exception to this are the values for the local surface brightness limits in row 1 of [Table 13.45](#). They were calculated for a 52x2 slit.
- The screening limits in the tables assume zero extinction. To determine if your source will violate the limits in this table, correct the magnitude limit for the extinction of your source.
- The peak flux from an emission line or from the continuum from your source must be less than the flux limit given in row two (for point sources—remember to correct for your aperture throughput) and row one for diffuse sources (remember to correct for the width of your source by scaling by your slit width in arcseconds divided by 2.0).
 - For echelle observations, the global limit of 200,000 counts/s over the detector sets the magnitude limits, but you must also assure that your source does not violate the local limit, e.g., if it had a bright emission line.
 - If you are observing a source which has high equivalent width line emission (i.e., whose flux is dominated by line emission), you must assure that the *line emission* does not exceed the limits. This may be a concern for stars with strong emission lines, such as Wolf-Rayet or T Tauri stars.
- If you plan to place multiple bright stars in the long slit, or observe slitless, you must also assure that the sum from all targets imaged on the detector does not exceed the applicable global limit.
- The limits in this table are the worst case limits for the scanned gratings; use of a less sensitive central wavelength may have a brighter true limit, allowing you to observe your target. The STIS [ETC](#) should always be used to verify the safety of your detailed target and configuration specifications.

Table 13.45: Approximate MAMA Spectroscopic Bright-Object Limits (*V* mags. and cgs units).

| Spectral Type | G140L | G140M | E140M | E140H | G230L | G230M | E230M | E230H | PRISM |
|---|----------------------------|----------------------------|---------------------------|---------------------------|----------------------------|----------------------------|---------------------------|---------------------------|----------------------------|
| Local limit ¹ surface brightness | 2.6 × 10 ⁻¹¹ | 4.0 × 10 ⁻¹⁰ | 3.4 × 10 ⁻⁸ | 6.7 × 10 ⁻⁸ | 8.7 × 10 ⁻¹² | 2.6 × 10 ⁻¹⁰ | 5.0 × 10 ⁻⁹ | 3.1 × 10 ⁻⁸ | 7.4 × 10 ⁻¹³ |

| Local limit ² point source flux | 5.0×10^{-12} | 9.4×10^{-11} | 1.1×10^{-9} | 2.2×10^{-9} | 1.4×10^{-12} | 5.0×10^{-11} | 1.0×10^{-10} | 6.9×10^{-10} | 5.9×10^{-14} |
|--|-----------------------|-----------------------|----------------------|----------------------|-----------------------|-----------------------|-----------------------|-----------------------|-----------------------|
| O5 V ³ | 14.3 | 11.9 | 10.13 | 9.49 | 13.6 | 10.3 | 9.87 | 8.65 | 14.7 |
| B1 V | 13.5 | 11.1 | 9.33 | 8.59 | 13.1 | 9.8 | 9.37 | 8.15 | 14.2 |
| B3 V | 12.6 | 10.2 | 8.53 | 7.69 | 12.5 | 9.2 | 8.87 | 7.55 | 13.8 |
| B5 V | 11.9 | 9.4 | 7.83 | 7.19 | 12.1 | 8.7 | 8.37 | 7.05 | 13.4 |
| B8 V | 10.7 | 8.2 | 6.73 | 6.19 | 11.3 | 7.9 | 7.67 | 6.25 | 12.7 |
| A1 V | 8.4 | 5.3 | 4.43 | 3.79 | 10.4 | 6.9 | 6.67 | 5.35 | 11.9 |
| A3 V | 6.9 | 4.2 | 3.13 | 2.49 | 10.1 | 6.7 | 6.47 | 5.15 | 11.7 |
| A5 V | 5.1 | 3.8 | 1.43 | 0.89 | 9.9 | 6.5 | 6.37 | 4.95 | 11.6 |
| F0 V | 2.1 | 1.1 | -1.47 | <-1.61 | 9.4 | 6.3 | 5.97 | 4.65 | 11.5 |
| F2 V | 1.1 | 0.1 | <-1.77 | <-1.61 | 9.1 | 6.2 | 5.77 | 4.45 | 11.4 |
| F5 V | -1.1 | <-2.0 | <-1.77 | <-1.61 | 8.7 | 6.0 | 5.37 | 4.25 | 11.2 |
| F8 V | <-2.0 | <-2.0 | <-1.77 | <-1.61 | 8.4 | 5.8 | 5.17 | 4.05 | 11.0 |
| G2 V ⁴ | 0.5 | -1.3 | <-1.77 | <-1.61 | 7.8 | 5.3 | 4.57 | 3.55 | 10.6 |
| G8 V ⁵ | 2.6 | -0.2 | <-1.77 | <-1.61 | 7.3 | 4.8 | 4.70 | 3.15 | 10.1 |
| K2 V ⁶ | 4.0 | 1.3 | <-1.77 | <-1.61 | 6.5 | 4.0 | 3.27 | 2.35 | 9.4 |
| KM III ⁷ | 2.2 | -0.9 | <-1.77 | <-1.61 | 6.1 | 3.7 | 2.87 | 2.15 | 9.1 |
| T~50000 K ⁸ | 14.2 | 11.8 | 10.0 | 9.29 | 13.6 | 10.2 | 9.77 | 8.65 | 14.6 |
| (λ^{-1}) ⁹ | 9.2 | 6.6 | 6.63 | 4.39 | 10.4 | 7.8 | 6.87 | 6.25 | 12.7 |

- ¹ Peak surface brightness in $\text{ergs/s/cm}^2/\text{\AA}/\text{arcsec}^2$ of the continuum or of an emission line from a diffuse source. For first-order and PRISM spectra, the calculation was done assuming use of the 52x2 aperture, while for echelle modes, the 6x0.2 aperture was used.
- ² Peak flux in $\text{ergs/s/cm}^2/\text{\AA}$ of an emission line from a point source.
- ³ Limits are *V* magnitudes, assuming zero reddening. Results for first-order gratings assume slitless spectra but neglect geocoronal lines. For echelles, the 0.2x0.2 aperture throughput is assumed.
- ⁴ The magnitudes listed for G2 V are for the Solar template in the STIS **ETC**.
- ⁵ The magnitudes listed for G8V are from *IUE* data for the star Tau Ceti.
- ⁶ The magnitudes listed for K2 V are from *IUE* data for the star Epsilon Eri.
- ⁷ The magnitudes listed for KM III are from *IUE* data for 9 stars of these types.
- ⁸ Limits for a black body with a temperature of 50,000 K.
- ⁹ Limits for a source with a spectrum F_λ proportional to λ^{-1} .

Chapter 14: Imaging Reference Material

Chapter Contents

- 14.1 Introduction
- 14.2 Using the Information in this Chapter
- 14.3 CCD
 - CCD Clear Imaging - 50CCD
 - CCD Long-Pass Imaging F28X50LP
 - F28X50OIII - CCD
 - F28X50OII - CCD
 - 50CORON - Clear CCD
- 14.4 NUV-MAMA
 - 25MAMA - NUV-MAMA, Clear
 - F25ND3 - NUV-MAMA
 - F25ND5 - NUV-MAMA
 - F25NDQ - NUV-MAMA
 - F25QTZ - NUV-MAMA, Longpass
 - F25SRF2 - NUV-MAMA, Longpass
 - F25MGII - NUV-MAMA
 - F25CN270 - NUV-MAMA
 - F25CIII - NUV-MAMA
 - F25CN182 - NUV-MAMA
- 14.5 FUV-MAMA
 - 25MAMA - FUV-MAMA, Clear
 - 25MAMAD1 - FUV-MAMA Pseudo-Aperture
 - F25ND3 - FUV-MAMA
 - F25ND5 - FUV-MAMA
 - F25NDQ - FUV-MAMA
 - F25QTZ - FUV-MAMA, Longpass
 - F25QTZD1 - FUV-MAMA, Longpass Pseudo-Aperture
 - F25SRF2 - FUV-MAMA, Longpass
 - F25SRF2D1 - FUV-MAMA, Longpass Pseudo-Aperture
 - F25LYA - FUV-MAMA, Lyman-alpha
- 14.6 Image Mode Geometric Distortion
- 14.7 Spatial Dependence of the STIS PSF
- 14.8 MAMA Imaging Bright Object Limits

14.1 Introduction

This chapter provides reference material to help you select your filter and detector configuration and determine your observing plan (e.g., total required exposure time, and number of exposures). This chapter is, for the most part, organized by *filter and detector*. For each imaging mode the following are provided:

- A table of integrated system efficiencies and zero points.
- Plots and tables of throughput and sensitivity as a function of wavelength.
- Where useful, plots of throughput on a logarithmic scale to show out-of band throughput (red leak or blue leak) for the different filters.
- Plots of the time needed to achieve a desired signal-to-noise ratio vs. magnitude for broadband filters and vs. line flux for narrowband filters.
- Plots of the PSF and encircled energies, along with a logarithmic-scale image of the PSF.

In addition, we provide the following sections:

- [Section 14.6](#) presents information on the geometry of the MAMA and CCD imaging modes.
- [Section 14.7](#) presents information on the changes of the PSF with position in the STIS field of view.
- [Section 14.8](#) presents screening tables of bright object magnitudes for sources of different spectral type, for use in deciding if a MAMA imaging observation is safe.

The sensitivities and dark currents adopted for calculating the figures and tables used in this chapter were projected before SM4 for a date of August 2008. Actual values for Cycle 32 will differ slightly. For the most up-to-date values, please consult the STIS [ETC](#).

14.2 Using the Information in this Chapter

- [14.2.1 Sensitivity Units and Conversions](#)
- [14.2.2 Signal-To-Noise](#)
- [14.2.3 Point Spread Functions](#)

14.2.1 Sensitivity Units and Conversions

This chapter contains plots of throughputs and tables of sensitivities and throughputs for each grating mode. [Section 6.2](#) explains how to use these sensitivities to calculate expected counts rates from your source.

The first table for each filter provides the following quantities:

| | |
|-------------------------------|--|
| Pivot wavelength ¹ | <p>Source-independent measure of the characteristic wavelength of the bandpass, defined such that it is the same if the input spectrum is in units of f_λ or f_ν:</p> $\lambda_p = \sqrt{\frac{\int T(\lambda)d\lambda}{\int T(\lambda)((d\lambda)/\lambda)}}$ |
| FWHM ¹ | Full-width at half-maximum of the throughput $T(\lambda)$. |
| AB mag zero point | AB magnitude of a source that produces a flux of one count per second. |
| S_{peak}^P | Peak sensitivity ($e^-/s/\text{\AA}$ per incident $\text{erg/cm}^2/\text{s}/\text{\AA}$) |
| B_λ ¹ | <p>Equivalent bandpass of filter, defined such that</p> $\int S_\lambda^P d\lambda = S_{peak}^P B_\lambda$ <p>(see Chapter 6.2.2).</p> |
| R_{80} | Radius in arcseconds of an aperture that encloses 80% of the flux of a point source. |

| | |
|-------------------------|--|
| % flux in central pixel | Percentage of the flux of a point source that falls within the central pixel (this estimate is accurate to about 10%). |
|-------------------------|--|

¹For filters with red leaks, the pivot wavelength, $B\lambda$, and FWHM correspond to the "in-band" region, and do not include the red leak.

The first figure for each imaging mode gives the integrated system throughput. This is the combination of the efficiencies of the detector and of the optical elements in the light path. The bottom section of the throughput figures includes wavelengths beyond the nominal passband of that mode, showing any red or blue "leak" on a log scale (dotted sections are manufacturer's lab measurements). The throughput is defined as the number of detected counts per second per cm^2 of telescope area relative to the incident flux in photons per cm^2 per second. For the CCD "counts" is the number of electrons detected. For the MAMA, "counts" is the number of valid events processed by the detector electronics after passing through the various pulse-shape and anti-coincidence filters. In both cases the detected counts obey Poisson statistics. The throughput includes all obscuration effects in the optical train (e.g., due to the *HST* secondary and due to the STIS CCD Lyot stops). The "effective area" of the mode can be computed from the throughput by multiplying by the physical area of the *HST* primary mirror (45238.93416 cm^2). This is shown on the ordinate label on the right side of each plot.

The table for each mode gives the throughput and the point source sensitivity as a function of wavelength. Throughput has the meaning described above. The *imaging point source sensitivity* S_{λ}^p has units of counts/s/Å per incident $\text{erg}/\text{cm}^2/\text{s}/\text{Å}$ for the MAMAs, and $\text{e}^-/\text{s}/\text{Å}$ per incident $\text{erg}/\text{cm}^2/\text{s}/\text{Å}$ for the CCD. Counts and electrons refer to the total counts from the point source integrated over the PSF.

The imaging diffuse source sensitivity S_{λ}^d , has the units: counts/s/Å/pix per incident $\text{erg}/\text{cm}^2/\text{s}/\text{Å}$ /arcsec² for the MAMAs and $\text{e}^-/\text{s}/\text{Å}/\text{pix}$ per incident $\text{erg}/\text{cm}^2/\text{s}/\text{Å}/\text{arcsec}^2$ for the CCD.

Thus S_{λ}^p and S_{λ}^d are related through the relation:

$$S_{\lambda}^d \cong (S_{\lambda}^p \times m^2)$$

where m is the plate-scale in arcsec per pixel. Here, we have assumed that the diffuse source has a uniform brightness over the area of interest.

14.2.2 Signal-To-Noise

For each imaging mode, plots are provided to estimate the signal-to-noise (S/N) for a representative source. The first figure shows S/N for point sources (for two different gains for the CCD). The second figure shows S/N for uniform extended sources of area 1 arcsec^2 and 0.2 arcsec^2 .

The different line styles in the S/N figures delineate regions where different sources of noise dominate. A particular source of noise (read noise for example) is presumed to dominate if it contributes more than half the total noise in the observations. For the CCD, the “x” characters at the top of each plot indicate the onset of saturation for gain=1, while solid dots indicate saturation for gain=4. For the MAMAs, the “x” characters show where the total number of counts exceeds the 16-bit buffer size of 65,535.

To the left of the vertical line in the MAMA S/N plots, the count rate from the source exceeds the 100 counts/s/pix local count rate limit (see [Table 7.8](#)). This is computed from the on-orbit measured PSF, which gives 6 to 14% of the flux in the central pixel. The bright object screening limits in [Table 14.40](#) use the more conservative (for this purpose) estimate of 25% of the flux in the central pixel.

The point source S/N figures are shown for average sky levels (i.e., the ‘average zodiacal+average earthshine’ background level used in the STIS ETC), and for sky levels during orbital night (i.e., average zodiacal + low earth). For the CCD the read noise has been computed assuming a number of readouts $N_{READ} = \text{integer}(t / 1000 \text{ s})$, where t is the exposure time, with a minimum $N_{READ}=2$. That is, each exposure has a minimum $CR-SPLIT=2$.

For the CCD, the dominant sources of sky background are zodiacal light (see [Table 6.2](#)) and scattered earthshine. The `LOW-SKY` requirement can be used to ensure that these backgrounds are kept as low or lower than the rates assumed for these plots. If your source falls within the sky-dominated portion of the figures, you may want to consider imposing the `LOW-SKY` requirement.

For the `NUV-MAMA` the sky background has different contributions which can dominate depending on the filter used and on whether the observation takes place on the day or night sides of the orbit. The FUV geocoronal lines dominate on the day side if `CLEAR`, `F25SRF2`, or a neutral-density filter are used due to the strength of those lines (see [Table 6.5](#)) and to the significant sensitivity of the detector at FUV wavelengths (see [25MAMA - NUV-MAMA, Clear](#) and [F25SRF2 - NUV-MAMA, Longpass](#)). The NUV [O II] 2471 Å geocoronal line is the second most important contribution and dominates on the day side of the orbit if `F25QTZ` is used. Zodiacal light provides the largest contribution for the rest of the filters on the day side of the orbit and for most of them on the night side, where geocoronal emission is greatly reduced. The dark current is larger than the sky background in all cases except for `CLEAR` observations in the day side of the orbit.

For the `FUV-MAMA`, the dominant source of background is geocoronal emission (see [Tables 6.3, 6.4](#) and [6.5](#)). The lines vary strongly from the day to night side of the orbit. For broad-band the contribution from the geocoronal lines can be minimized by using the `F25QTZ` filter, or observing with the `DARKTIME` special requirement.

Follow these steps to use the signal-to-noise plots:

1. Determine the AB magnitude of your source at the wavelength of interest. There are several ways to do this.
 - Examine [Table 14.1](#) and find AB_V for the desired temperature and filter. Sum the V magnitude of the target and AB_V .
 - Alternatively, compute $ABMAG (=V+AB_V)$ from the source flux, using the relation:

$$ABMAG = -2.5 \log f_v - 48.60$$

or

$$ABMAG = -2.5 \log f_{\lambda} - 5 \log \lambda - 2.406$$

- Find the appropriate plot for the filter in question, and locate $V+AB_V$ on the horizontal axis. Then read off the signal-to-noise ratio for the desired exposure time, or vice-versa.

We now give a sample S/N calculation using these plots. Consider a $V=27$ star of spectral class G2V, for which we want to obtain $S/N = 20$ with F28X50LP observing with the CCD. From Table 14.1 we find a correction $AB_V = -0.21$ to go from V magnitude to AB magnitude near the center of the F28X50LP bandpass. We thus have $V+AB_V=26.79$. We look at Figure 14.8 and find this value on the horizontal axis and read up to find the curve that intersects the desired S/N. We find $\sim 10,000$ seconds are needed to reach $S/N = 20$ in conditions of low sky background.

In situations requiring more detailed calculations (non-stellar spectra, extended sources, other sky background levels, unknown target V magnitude, etc.), the STIS Exposure Time Calculator (ETC) should be used.

14.2.3 Point Spread Functions

The final figures and table for each imaging mode contain information on the point spread function. The encircled energy plots and tables are normalized to 1 at a radius of 1 arcsecond. In actuality about 10% of the light from a point source falls beyond this radius; however, high S/N observations extending out to large radius exist for only a few modes from on-orbit data. The intensity vs. radius plots are normalized to a total integrated flux of 1. The PSF image is shown on a logarithmic intensity scale to enhance faint features in the wings of the PSF. Note the stellar like ‘ghost’ at approximately 45 pixels left of the peak pixel in all NUV-MAMA+Filter images, e.g., Figure 14.38. The ghost is a few tenths of a percent of the psf peak intensity. See Bowers (1997 HST Calibration Workshop) for a discussion of HST “breathing” effects on the PSF. Additional information about the STIS PSF and color dependent aperture corrections can be found in STIS ISR 2003-01.

Table 14.1: Color Corrections AB_V to convert from Johnson V Magnitude to AB Magnitude. Values were calculated using solar metallicity Lejeune models with $\log g = 5.0$.

| CCD Modes | AB_V as a Function of Temperature | | | | | | | | | | | |
|----------------|-------------------------------------|---------|---------|---------|---------|--------|--------|--------|--------|--------|--------|--------|
| | 50000 K | 30000 K | 20000 K | 15000 K | 10000 K | 9000 K | 8000 K | 7000 K | 6000 K | 5000 K | 4000 K | 3000 K |
| F28x50LP | 0.48 | 0.47 | 0.41 | 0.38 | 0.30 | 0.23 | 0.23 | 0.02 | -0.15 | -0.37 | -0.90 | -2.2 |
| 50CCD | -0.29 | -0.17 | 0.00 | 0.11 | 0.26 | 0.27 | 0.27 | 0.26 | 0.23 | 0.17 | -0.19 | -1.4 |
| F28X50OIII | -0.01 | 0.01 | 0.02 | 0.02 | 0.03 | 0.04 | 0.07 | 0.11 | 0.13 | 0.14 | -0.01 | -1.9 |
| F28X50OII | -0.64 | -0.42 | -0.08 | 0.22 | 0.88 | 0.99 | 1.01 | 1.03 | 1.31 | 2.38 | 3.36 | 4.21 |
| NUV-MAMA Modes | AB_V as a Function of Temperature | | | | | | | | | | | |
| | | | | | | | | | | | | |

| | 50000 K | 30000 K | 20000 K | 15000 K | 10000 K | 9000 K | 8000 K | 7000 K | 6000 K | 5000 K | 4000 K | 3000 K |
|---------------------------|---|------------|------------|------------|------------|-----------|-----------|-----------|-----------|-----------|-----------|-----------|
| 25MAMA | -1.62 | -1.23 | -0.49 | 0.18 | 1.54 | 1.98 | 2.56 | 3.12 | 4.06 | 5.92 | 7.63 | 8.14 |
| F25ND3 | -1.57 | -1.19 | -0.47 | 0.18 | 1.50 | 1.91 | 2.41 | 2.90 | 3.73 | 5.53 | 7.25 | 7.80 |
| F25ND5 | -1.40 | -1.06 | -0.41 | 0.16 | 1.34 | 1.66 | 1.99 | 2.31 | 2.93 | 4.49 | 6.03 | 6.44 |
| F25QTZ | -1.53 | -1.16 | -0.46 | 0.16 | 1.45 | 1.85 | 2.42 | 2.97 | 3.91 | 5.76 | 7.47 | 8.00 |
| F25SRF2 | -1.58 | -1.20 | -0.48 | 0.17 | 1.50 | 1.93 | 2.50 | 3.05 | 3.99 | 5.84 | 7.55 | 8.10 |
| F25CN182 | -1.73 | -1.32 | -0.54 | 0.15 | 1.58 | 2.08 | 3.00 | 3.91 | 5.62 | 8.36 | 10.95 | 12.00 |
| F25CIII | -1.71 | -1.28 | -0.52 | 0.12 | 1.50 | 1.95 | 2.87 | 3.88 | 5.90 | 7.60 | 8.55 | 9.10 |
| F25CN270 | -1.24 | -0.95 | -0.38 | 0.16 | 1.32 | 1.32 | 2.04 | 2.51 | 3.33 | 5.17 | 6.44 | 6.80 |
| F25MGII | -1.16 | -0.89 | -0.35 | 0.18 | 1.33 | 1.65 | 2.01 | 2.43 | 3.10 | 4.04 | 4.53 | 4.80 |
| FUV-MAMA Modes | AB_V as a Function of Temperature | | | | | | | | | | | |
| | 50000 K | 30000 K | 20000 K | 15000 K | 10000 K | 9000 K | 8000 K | 7000 K | 6000 K | 5000 K | 4000 K | 3000 K |
| 25MAMA | -2.16 | -1.67 | -0.61 | 0.42 | 2.86 | 4.61 | 7.10 | 9.19 | 13.49 | 18.09 | 21.70 | 23.00 |
| F25ND3 | -2.15 | -1.67 | -0.62 | 0.41 | 2.84 | 4.63 | 7.21 | 9.34 | 13.65 | 18.09 | 21.41 | 22.00 |
| F25ND5 | -2.15 | -1.66 | -0.61 | 0.41 | 2.80 | 4.49 | 6.98 | 9.12 | 13.44 | 17.35 | 20.01 | 20.00 |
| F25QTZ | -1.98 | -1.46 | -0.60 | 0.17 | 1.96 | 3.07 | 5.26 | 7.29 | 11.59 | 16.15 | 19.72 | 21.00 |
| F25RF2 | -2.09 | -1.64 | -0.68 | 0.20 | 2.35 | 4.03 | 6.49 | 8.57 | 12.86 | 17.44 | 21.01 | 22.00 |
| F25LYA | -2.25 | -2.25 | -1.68 | 0.98 | 4.70 | 7.34 | 10.50 | 12.83 | 17.26 | 22.24 | 26.81 | 29.00 |

14.3 CCD

This section provides the basic properties of the filters available for use with the CCD detector. The field of view for the CCD is 52" × 52", unless otherwise noted. Also note that the sensitivities given are projected values for 2008 August. For more up-to-date values, please see the [STIS ETC](#).

- [Section CCD Clear Imaging—50CCD](#)
- [Section CCD Long-Pass Imaging F28X50LP](#)
- [Section F28X50OIII—CCD](#)
- [Section F28X50OII—CCD](#)
- [Section 50CORON—Clear CCD](#)

CCD Clear Imaging - 50CCD

Description

The 50CCD mode is very sensitive for broad-band optical imaging. For a fixed exposure time, the ACS WFC with the F606W or F814W will be a better choice for most users.

Recommended Uses

This filter is recommended for deep imaging where detailed color information is not needed. In most cases the ACS WFC will be a better choice.

Special Considerations

Very red sources may show significant wings from detector halo (see [Section 7.2.8](#)).

| Pivot λ (Å) | FWHM (Å) | AB mag zero point | S_{peak} | B_{λ} | R_{80} (arcsec) | Flux in central pixel |
|---------------------|----------|-------------------|-------------------|---------------|-------------------|-----------------------|
| 5754.1 | 4333.0 | 26.295 | 2.03e+15 | 4930.6 | 0.16 | 14% |

Figure 14.1: Throughput for 50CCD

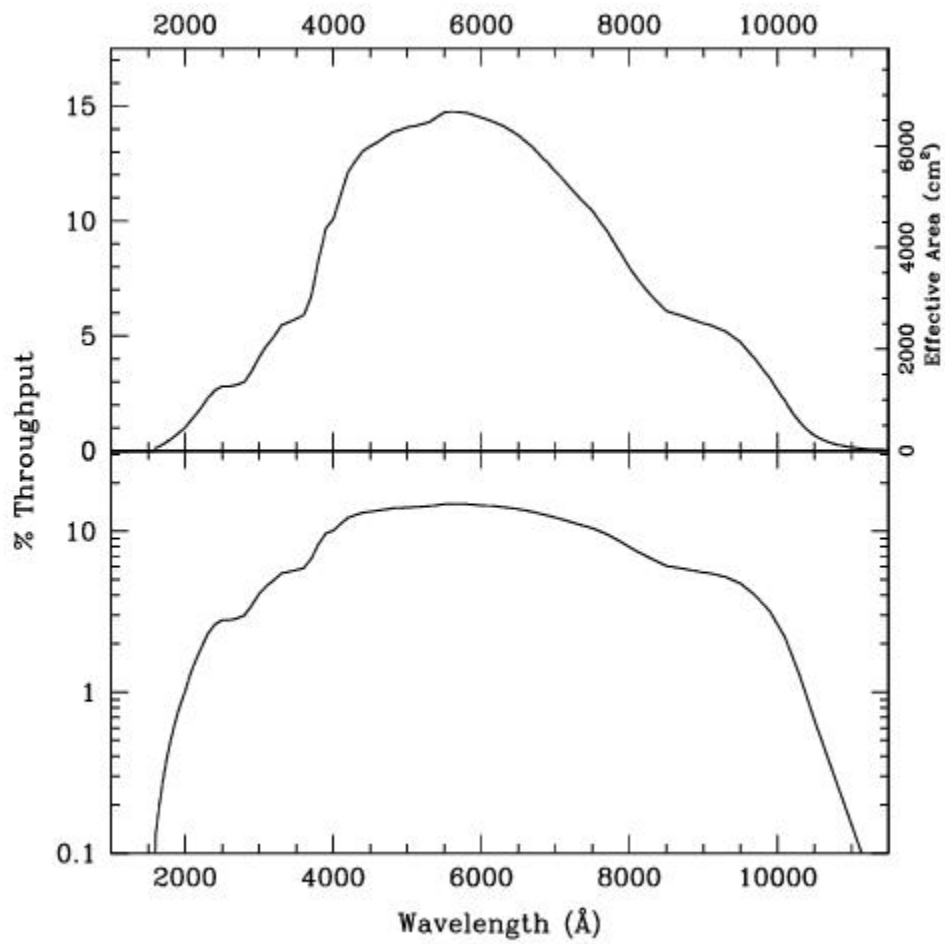


Table 14.2: 50CCD Sensitivity & Throughput

| λ | Sensitivity | % Throughput |
|-----------|-------------|--------------|
| 2400. | 1.41E14 | 2.59 |
| 2800. | 1.97E14 | 3.08 |
| 3200. | 3.64E14 | 4.99 |
| 3600. | 5.01E14 | 6.05 |
| 4000. | 9.33E14 | 10.24 |
| 4200. | 1.15E15 | 12.00 |

| | | |
|--------|---------|-------|
| 4400. | 1.30E15 | 12.98 |
| 4600. | 1.41E15 | 13.44 |
| 4800. | 1.51E15 | 13.83 |
| 5000. | 1.60E15 | 14.06 |
| 5200. | 1.68E15 | 14.21 |
| 5400. | 1.79E15 | 14.52 |
| 5600. | 1.88E15 | 14.74 |
| 5800. | 1.94E15 | 14.68 |
| 6000. | 1.98E15 | 14.50 |
| 6200. | 2.01E15 | 14.26 |
| 6400. | 2.03E15 | 13.93 |
| 6600. | 2.02E15 | 13.45 |
| 6800. | 1.99E15 | 12.84 |
| 7000. | 1.94E15 | 12.16 |
| 7200. | 1.88E15 | 11.45 |
| 7400. | 1.81E15 | 10.76 |
| 7600. | 1.73E15 | 9.99 |
| 7800. | 1.60E15 | 9.02 |
| 8000. | 1.46E15 | 7.99 |
| 8200. | 1.33E15 | 7.12 |
| 8400. | 1.23E15 | 6.41 |
| 8600. | 1.17E15 | 5.98 |
| 9000. | 1.14E15 | 5.55 |
| 9400. | 1.06E15 | 4.96 |
| 9800. | 7.95E14 | 3.56 |
| 10200. | 3.93E14 | 1.69 |

Figure 14.2: Point Source S/N vs. AB magnitude in the V-band for the 50CCD filter. Top curves are for low sky; bottom curves are for average sky. Curves are labeled by required exposure time (seconds).

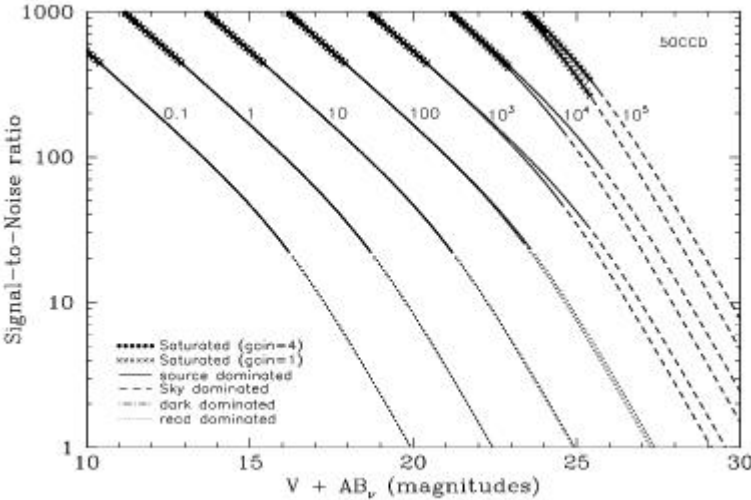


Figure 14.3: Extended Source S/N vs. AB magnitude in the V-band for the 50CCD filter for gain=1. Top curves are for a source area of 0.2 arcsec²; bottom curves are for 1 arcsec². Average sky assumed. Curves are labeled by required exposure time (seconds).

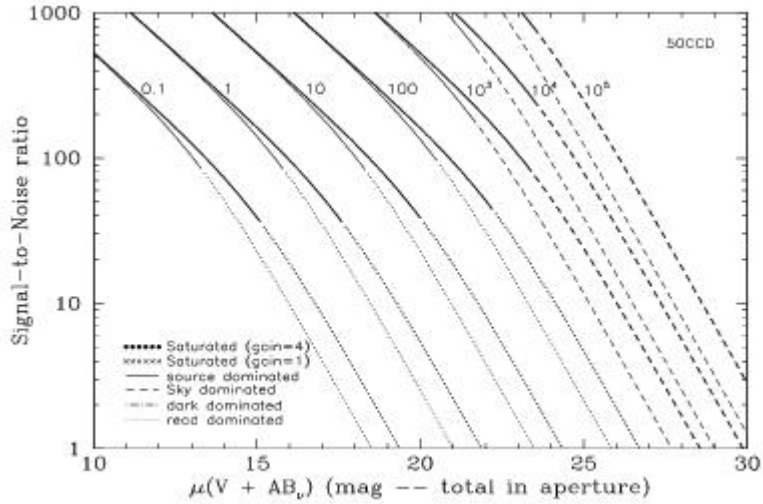


Table 14.3: Radial Profile for 50CCD

| Radius | | Intensity | Fraction of Energy Encircled |
|--------|--------|-----------|------------------------------|
| Pixels | Arcsec | | |
| 1 | 0.050 | 1.614e-02 | 0.321 |
| 1.5 | 0.075 | 7.765e-03 | 0.495 |
| 2 | 0.100 | 4.320e-03 | 0.621 |
| 3 | 0.150 | 1.629e-03 | 0.787 |
| 4 | 0.200 | 4.904e-04 | 0.868 |
| 5 | 0.250 | 1.978e-04 | 0.902 |
| 10 | 0.500 | 2.499e-05 | 0.964 |
| 15 | 0.750 | 7.654e-06 | 0.986 |
| 20 | 1.000 | 2.687e-06 | 0.996 |

Figure 14.4: Point Source PSF for 50CCD, 7."5 square (at pixel 518,517, log scaled, B-V=-0.25).

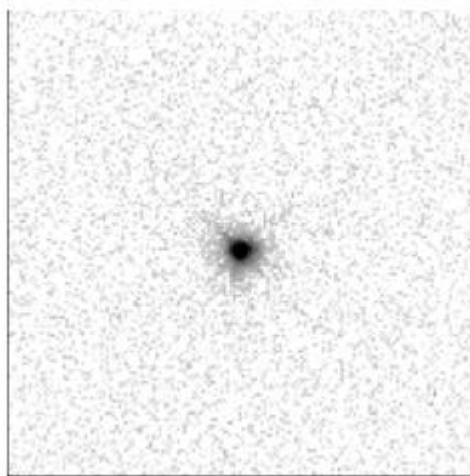


Figure 14.5: Point Source Encircled Energy for 50CCD

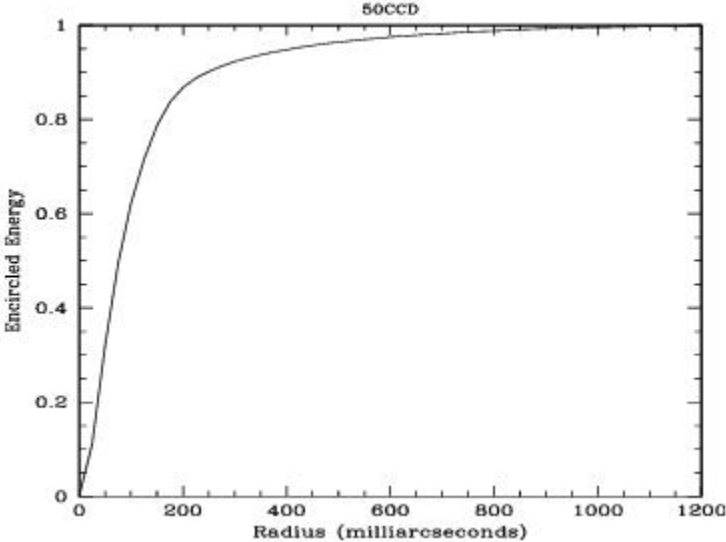
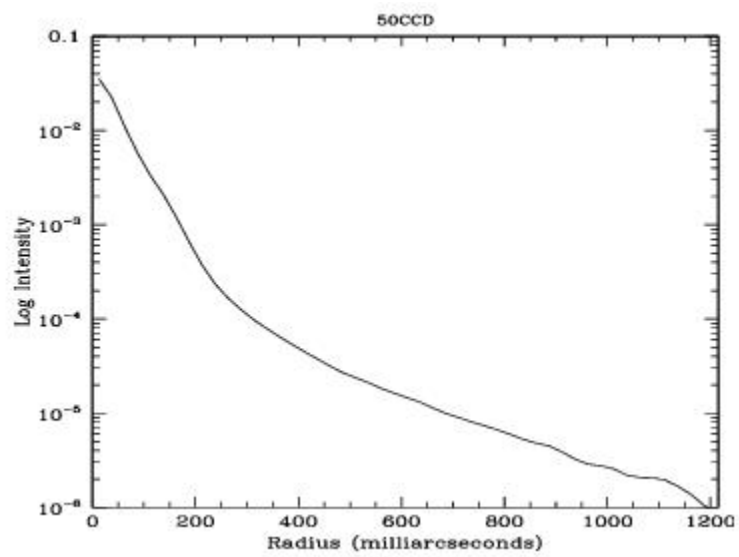


Figure 14.6: Point Source Intensity vs. Radius for 50CCD



CCD Long-Pass Imaging F28X50LP

Description

The F28X50LP mode is useful for deep imaging longward of 5500 Å. The field of view is 28" × 50". The ACS/WFC with the F814W filter will be more appropriate for most programs.

Recommended Uses

This filter is recommended for deep high-resolution imaging between 5500 Å and 10,000 Å. Default aperture for target acquisitions.

Special Considerations

Very red sources may show significant wings from detector halo (see [Section 7.2.8](#)).

| Pivot λ (Å) | FWHM (Å) | AB mag zero point | S_{peak} | B_{λ} | R_{80} (arcsec) | Flux in central pixel |
|---------------------|----------|-------------------|-------------------|---------------|-------------------|-----------------------|
| 7223.4 | 2693.2 | 25.266 | 1.76e+15 | 3486.8 | 0.15 | 14% |

Figure 14.7: Throughput for F28X50LP

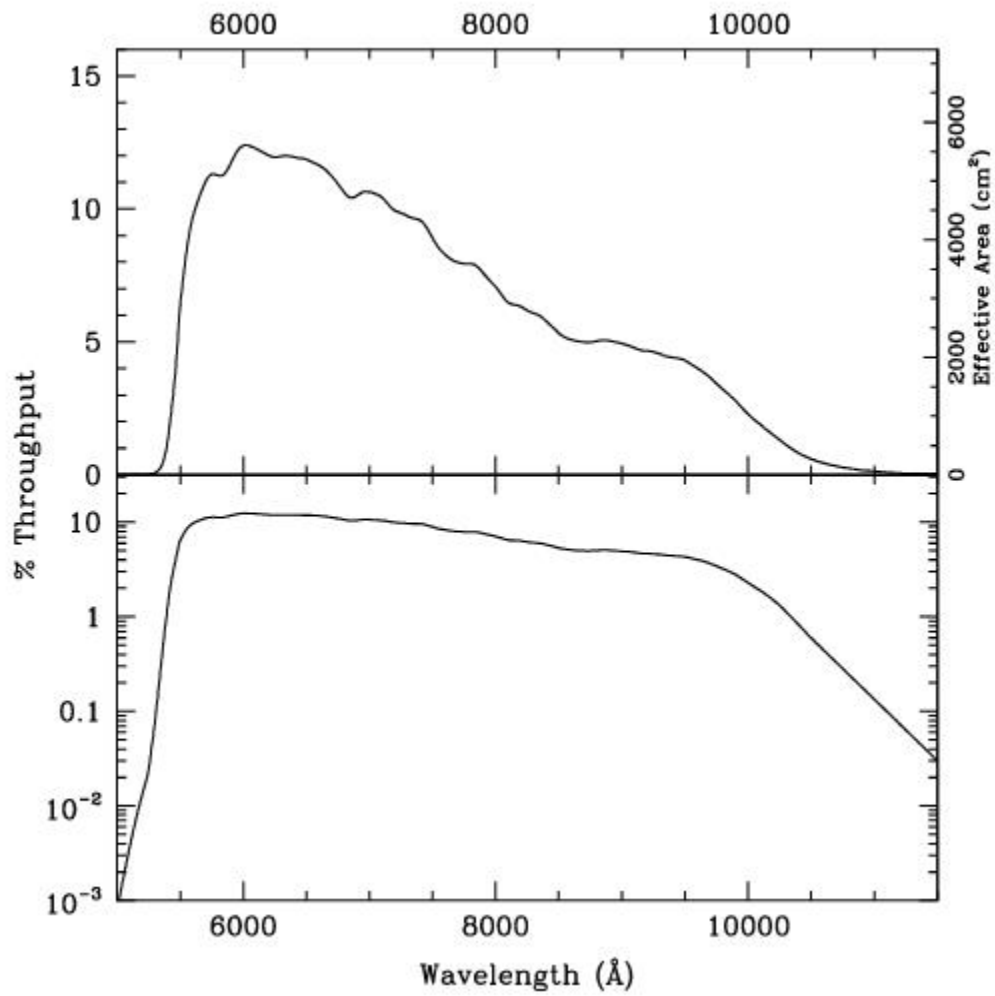


Table 14.4: F28X50LP Sensitivity & Throughput

| λ | Sensitivity | % Throughput |
|-----------|-------------|--------------|
| 5400. | 2.38E14 | 1.93 |
| 5600. | 1.19E15 | 9.32 |
| 5800. | 1.49E15 | 11.30 |
| 6000. | 1.67E15 | 12.23 |
| 6200. | 1.70E15 | 12.05 |
| 6400. | 1.74E15 | 11.95 |

| | | |
|--------|---------|-------|
| 6600. | 1.75E15 | 11.61 |
| 6800. | 1.66E15 | 10.71 |
| 7000. | 1.69E15 | 10.58 |
| 7200. | 1.64E15 | 10.01 |
| 7400. | 1.60E15 | 9.47 |
| 7600. | 1.44E15 | 8.33 |
| 7800. | 1.40E15 | 7.89 |
| 8000. | 1.28E15 | 7.04 |
| 8200. | 1.18E15 | 6.29 |
| 8400. | 1.10E15 | 5.76 |
| 8600. | 1.00E15 | 5.11 |
| 8800. | 1.01E15 | 5.03 |
| 9000. | 1.01E15 | 4.93 |
| 9200. | 9.76E14 | 4.66 |
| 9400. | 9.46E14 | 4.42 |
| 9600. | 8.74E14 | 4.00 |
| 9800. | 7.19E14 | 3.22 |
| 10000. | 5.25E14 | 2.30 |

Figure 14.8: Point Source S/N vs. AB magnitude in the V-band for the F28X50LP filter. Top curves are for low sky; bottom curves are for average sky. Curves are labeled by required exposure time (seconds).

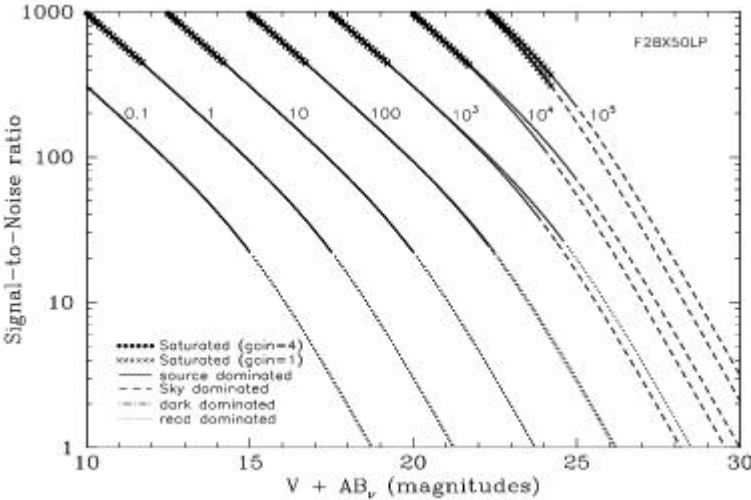


Figure 14.9: Extended Source S/N vs. AB magnitude in the V-band for the F28X50LP filter for gain=1. Top curves are for a source area of 0.2 arcsec²; bottom curves are for 1 arcsec². Average sky assumed. Curves are labeled by required exposure time (seconds).

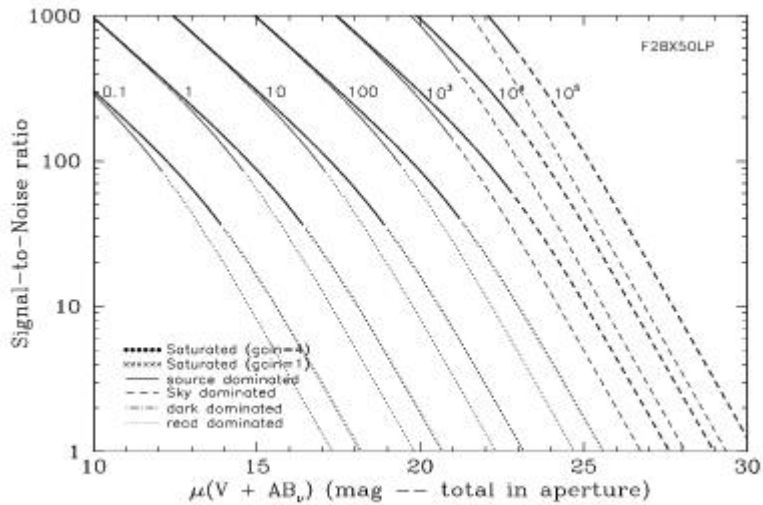


Table 14.3: Radial Profile for 50CCD

| Radius | | Intensity | Fraction of Energy Encircled |
|--------|--------|-----------|------------------------------|
| Pixels | Arcsec | | |
| 1 | 0.050 | 1.703e-02 | 0.337 |
| 1.5 | 0.075 | 7.468e-03 | 0.512 |
| 2 | 0.100 | 4.196e-03 | 0.632 |
| 3 | 0.150 | 1.733e-03 | 0.804 |
| 4 | 0.200 | 4.246e-04 | 0.883 |
| 5 | 0.250 | 1.660e-04 | 0.911 |
| 10 | 0.500 | 2.469e-05 | 0.976 |
| 15 | 0.750 | 5.360e-06 | 0.996 |
| 19.25 | 0.963 | 3.333e-07 | 1.000 |

Figure 14.10: Point Source Encircled Energy for F28X50LP

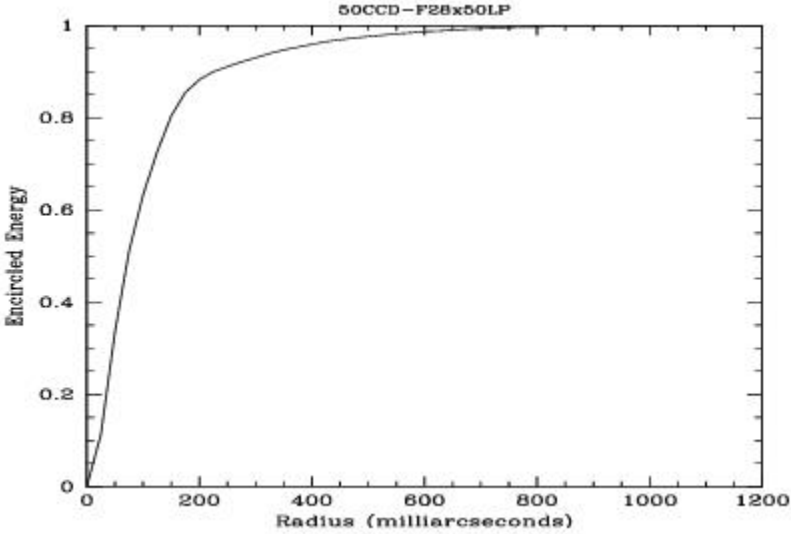
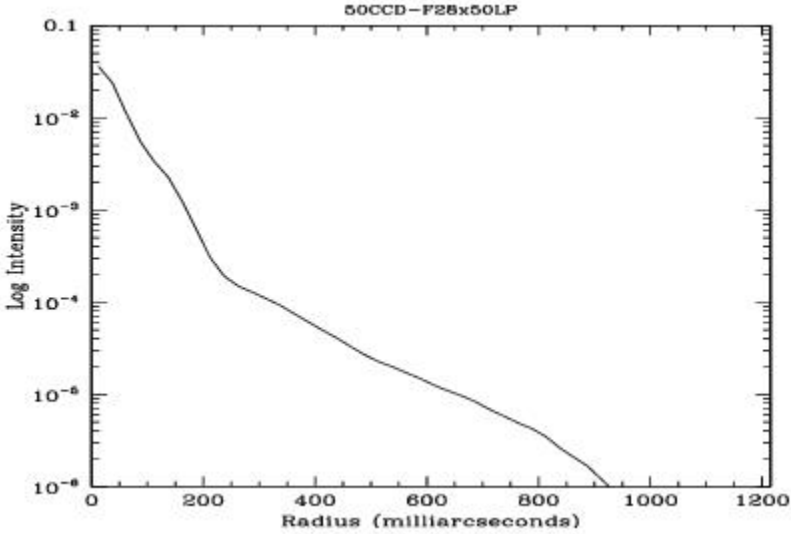


Figure 14.11: Point Source Intensity vs. Radius for F28X50LP



F28X500III - CCD

Description

The F28X5020III mode is useful for narrow-band imaging of O III 5007 Å. The field of view is 28" × 50".

Recommended Uses

This filter is recommended for deep high-resolution O III imaging.

Special Considerations

This filter has a significant red leak longward of 1 micron. Depending on the source spectrum, the contribution from red leak may swamp the contribution from line emission.

| Pivot λ (Å) | FWHM (Å) | AB mag zero point | S_{peak} | B_{λ} | R_{80} (arcsec) | Flux in central pixel |
|---------------------|----------|-------------------|-------------------|---------------|-------------------|-----------------------|
| 5005.8 | 6.2 | 18.755 | 1.16e+15 | 6.3 | 0.13 | 17% |

Figure 14.12: Throughput for F28x50OIII.

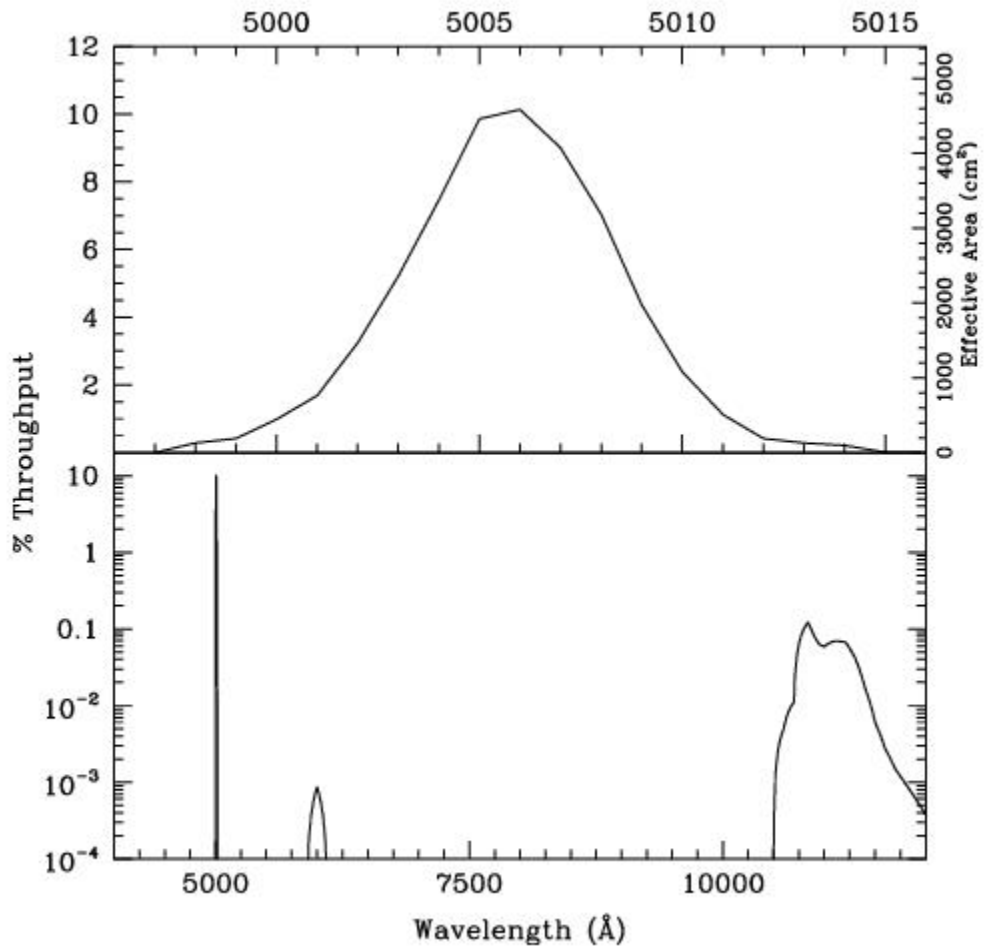


Table 14.6: F28X50OIII Sensitivity & Throughput

| λ | Sensitivity | % Throughput |
|-----------|-------------|--------------|
| 4999. | 4.81E13 | 0.42 |
| 5000. | 1.12E14 | 0.99 |
| 5001. | 1.92E14 | 1.69 |
| 5002. | 3.69E14 | 3.24 |
| 5003. | 5.93E14 | 5.21 |
| 5004. | 8.50E14 | 7.46 |
| 5005. | 1.12E15 | 9.85 |

| | | |
|-------|---------|-------|
| 5006. | 1.16E15 | 10.13 |
| 5007. | 1.03E15 | 9.01 |
| 5008. | 8.03E14 | 7.04 |
| 5009. | 4.98E14 | 4.36 |
| 5010. | 2.73E14 | 2.39 |
| 5011. | 1.29E14 | 1.13 |
| 5012. | 4.82E13 | 0.42 |

Figure 14.13: Point Source S/N vs. AB magnitude in the V-band for the F28X50OIII filter. Top curves are for low sky; bottom curves are for average sky. Curves are labeled by required exposure time (seconds).

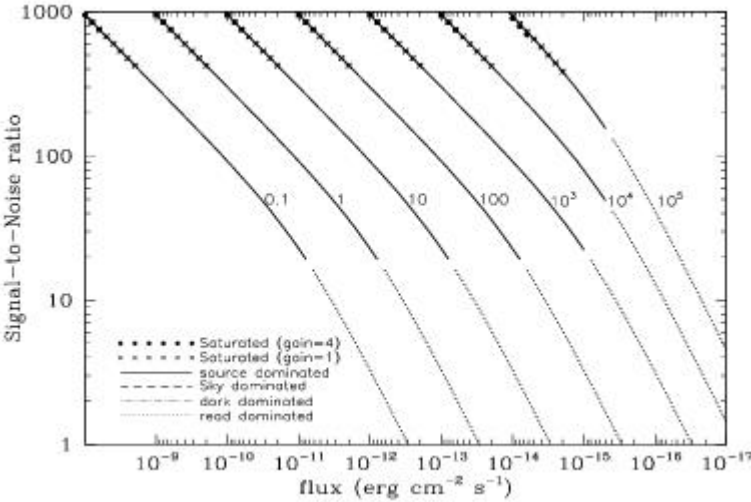


Figure 14.14: Extended Source S/N vs. AB magnitude in the V-band for the F28X50OIII for gain=1. Top curves are for a source area of 0.2 arcsec²; bottom curves are for 1 arcsec². Average sky assumed. Curves are labeled by required exposure time (seconds).

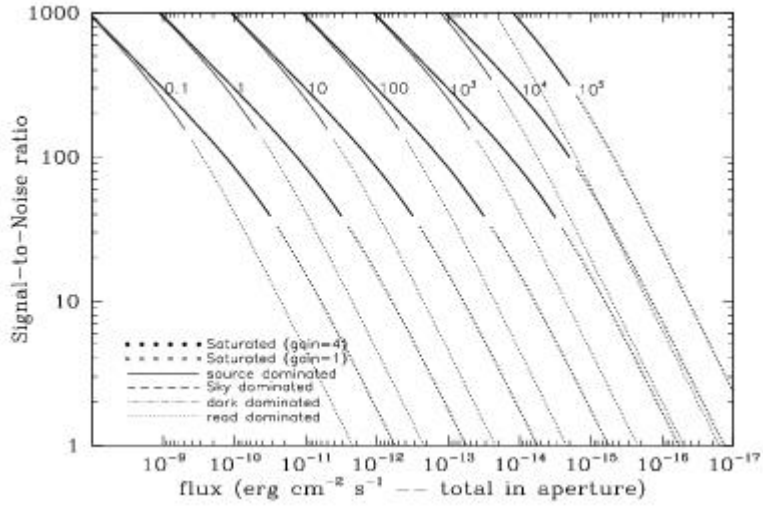


Table 14.7: Radial Profile for F28X50OIII

| Radius | | Intensity | Fraction of Energy Encircled |
|--------|--------|-----------|------------------------------|
| Pixels | Arcsec | | |
| 1 | 0.050 | 1.750e-02 | 0.358 |
| 1.5 | 0.075 | 9.783e-03 | 0.574 |
| 2 | 0.100 | 4.193e-03 | 0.711 |
| 3 | 0.150 | 8.194e-04 | 0.844 |
| 4 | 0.200 | 3.245e-04 | 0.884 |
| 5 | 0.250 | 2.403e-04 | 0.916 |
| 10 | 0.500 | 2.049e-05 | 0.979 |
| 15 | 0.750 | 4.391e-06 | 0.995 |
| 20 | 1.000 | 8.462e-07 | 1.000 |

Figure 14.15: Point Source PSF for F28X50OIII, 7."5 square (pixel 493,542, log scaled, B-V=-0.34)

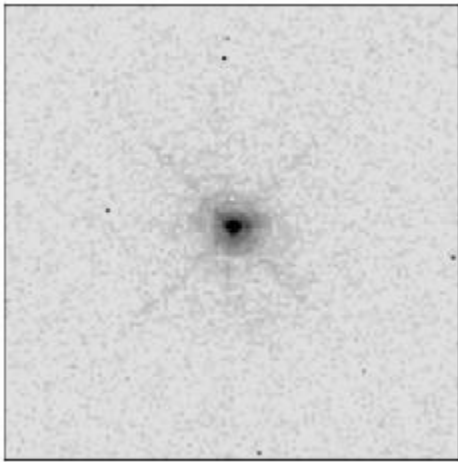


Figure 14.16: Point Source Encircled Energy for F28X50OIII

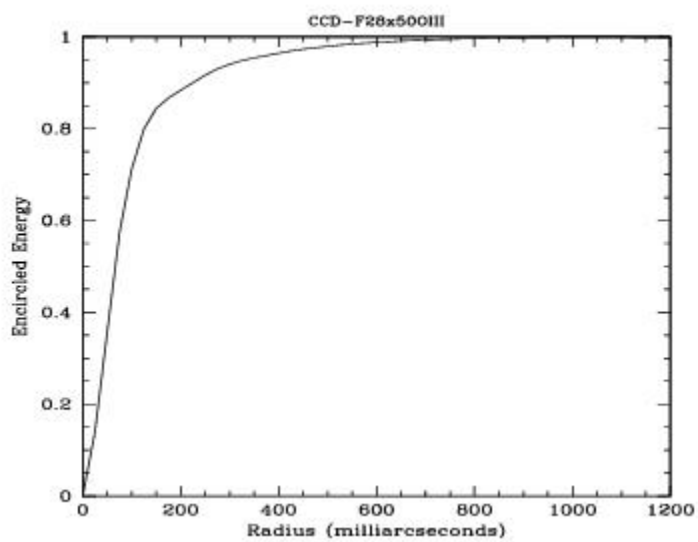
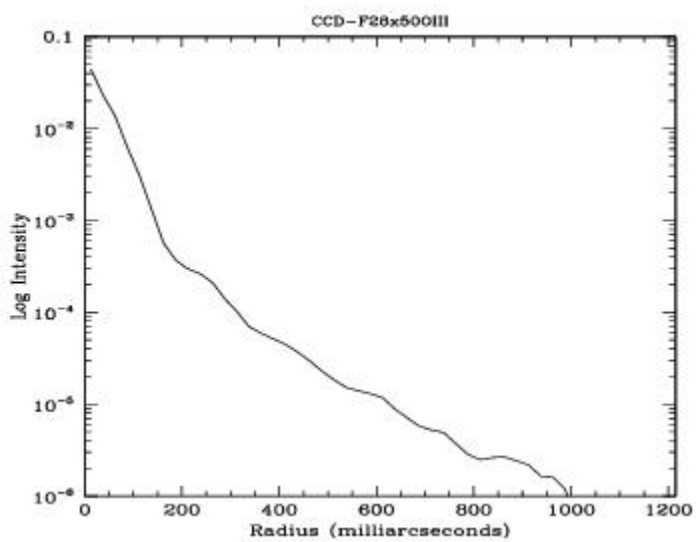


Figure 14.17: Point Source Intensity vs. Radius for F28X50OIII



F28X50OII - CCD

Description

The F28X50OII mode is useful for narrow-band imaging of OII 3727 Å. The narrow bandpass may offer some advantages over the ACS WFC with the [O II] ramp filter. The field of view is 28" x 50".

Recommended Uses

This filter is recommended for deep high-resolution O II imaging.

Special Considerations

Flat field images taken through this filter show scattered light at the top and bottom of the frame. This is not expected to be a problem for astronomical targets.

| Pivot λ (Å) | FWHM (Å) | AB mag zero point | S_{peak} | B_{λ} | R_{80} (arcsec) | Flux in central pixel |
|---------------------|----------|-------------------|-------------------|---------------|-------------------|-----------------------|
| 3738.1 | 56.9 | 20.522 | 3.43e+14 | 60.5 | 0.12 | 17% |

Figure 14.18: Throughput for F28x50OII

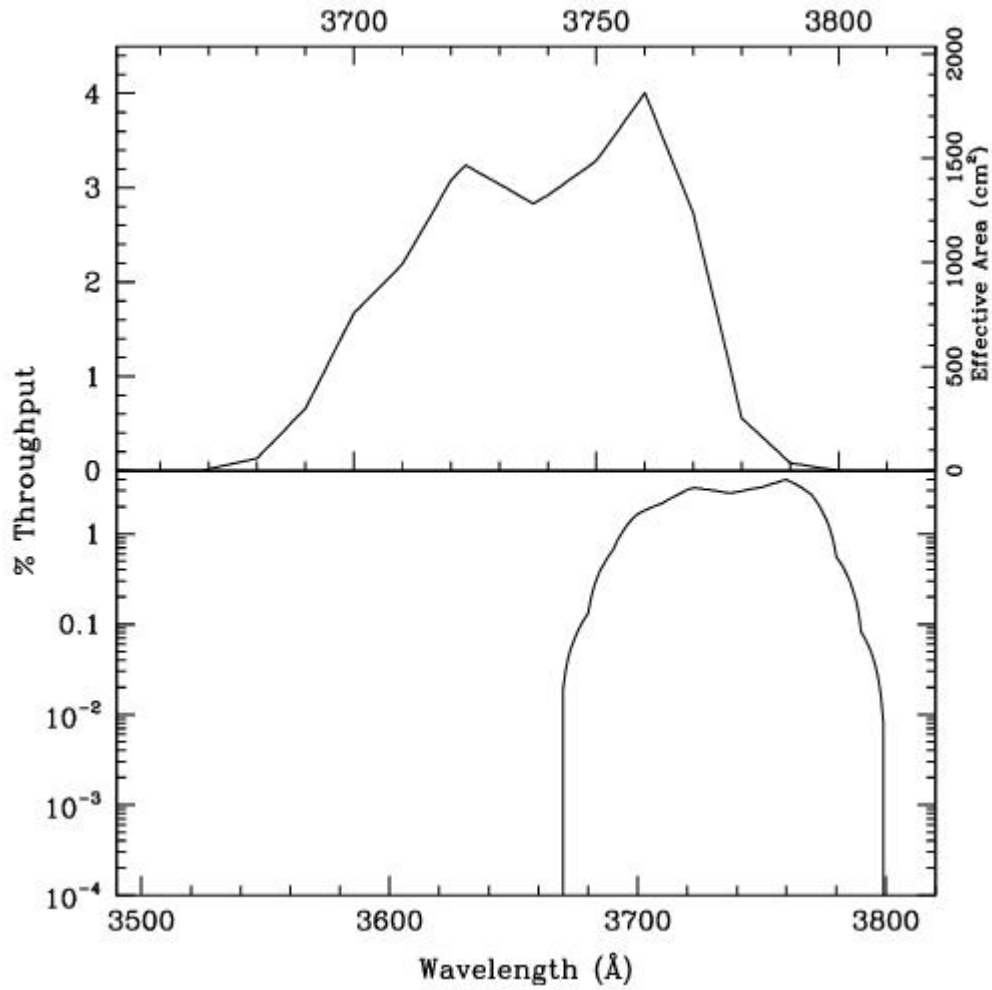


Table 14.8: F28X50OII Sensitivity & Throughput

| λ | Sensitivity | % Throughput |
|-----------|-------------|--------------|
| 3675. | 6.26E12 | 0.07 |
| 3685. | 3.31E13 | 0.39 |
| 3695. | 9.81E13 | 1.17 |
| 3705. | 1.63E14 | 1.93 |
| 3715. | 2.23E14 | 2.63 |
| 3725. | 2.67E14 | 3.14 |
| 3735. | 2.48E14 | 2.91 |

| | | |
|-------|---------|------|
| 3745. | 2.65E14 | 3.10 |
| 3755. | 3.12E14 | 3.64 |
| 3765. | 2.89E14 | 3.37 |
| 3775. | 1.42E14 | 1.65 |
| 3785. | 2.77E13 | 0.32 |

Figure 14.19: Point Source S/N vs. Line Flux for the F28X500II filter. Top curves are for low sky; bottom curves are for average sky. Curves are labeled by required exposure time (seconds).

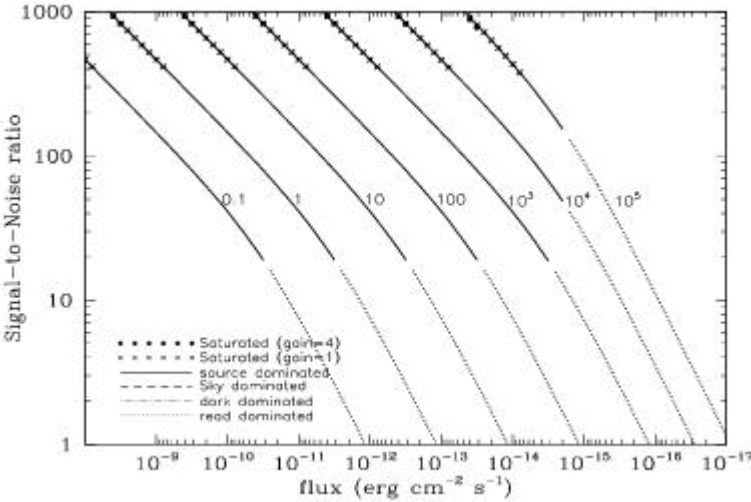


Figure 14.20: Extended Source S/N vs. total line flux for the F28X500II for gain =1. Top curves are for an area of 0.2 arcsec²; bottom curves are for 1 arcsec². Average sky assumed. Curves are labeled by required exposure time (seconds).

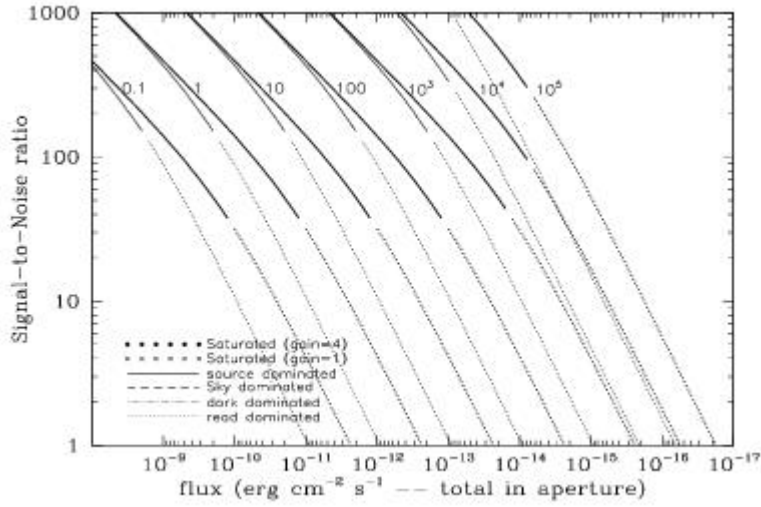


Table 14.9: Radial Profile for F28X500II

| Radius | | Intensity | Fraction of Energy Encircled |
|--------|--------|-----------|------------------------------|
| Pixels | Arcsec | | |
| 1 | 0.050 | 1.945e-02 | 0.405 |
| 1.5 | 0.075 | 9.266e-03 | 0.622 |
| 2 | 0.100 | 3.589e-03 | 0.750 |
| 3 | 0.150 | 7.742e-04 | 0.849 |
| 4 | 0.200 | 3.628e-04 | 0.895 |
| 5 | 0.250 | 1.826e-04 | 0.924 |
| 10 | 0.500 | 1.966e-05 | 0.982 |
| 15 | 0.750 | 4.876e-06 | 0.997 |
| 20 | 1.000 | 5.800e-07 | 1.000 |

Figure 14.21: Point Source Encircled Energy for F28X500II

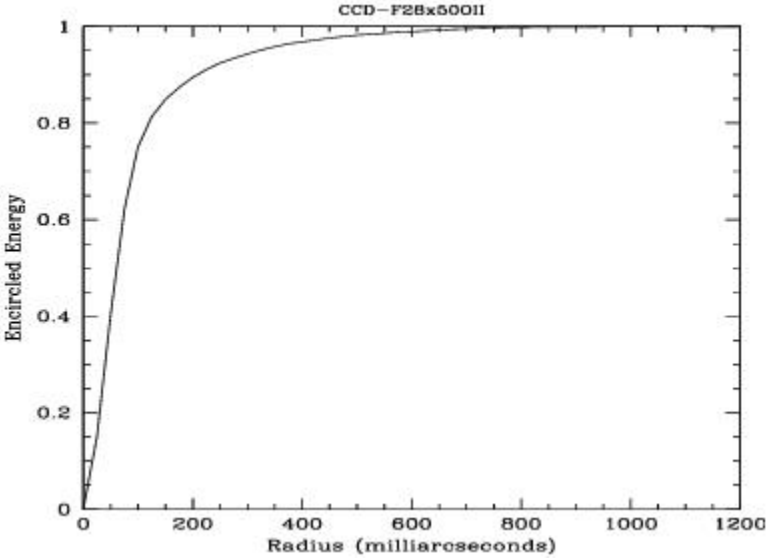
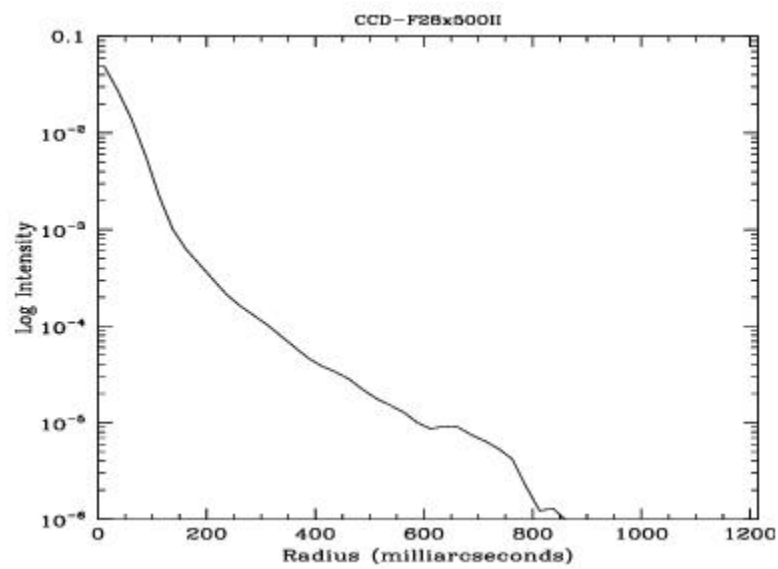


Figure 14.22: Point Source Intensity vs. Radius for F28X500II



50CORON - Clear CCD

Description

The 50CORON imaging mode is useful for imaging faint targets situated next to bright ones. The STIS CCD optics include a Lyot stop, which suppresses the wings of the PSF. See [Section CCD Clear Imaging—50CCD](#) for sensitivities, throughputs, and encircled energies. See [Section 12.11](#) for the PSF and for a discussion of coronagraphic imaging. [Figure 12.6](#) shows the layout of the 50CORON aperture and the positions of the wedges.

Recommended Uses

This filter is recommended for broad-band coronagraphic imaging.

| Pivot λ (Å) | FWHM (Å) | AB mag zero point | S_{peak} | B_{λ} | R_{80} (arcsec) | Flux in central pixel |
|---------------------|----------|-------------------|-------------------|---------------|-------------------|-----------------------|
| 5754.1 | 4333.0 | 26.295 | 2.03e+15 | 4930.6 | 0.16 | 14% |

14.4 NUV-MAMA

This section provides the basic properties of the filters available for use with the NUV-MAMA detector.

The field of view for the NUV-MAMA is 25 arcsec × 25 arcsec, unless otherwise stated. Note that the sensitivities given are projected values for August 2008. For more up-to-date values, please see the [STIS ETC](#).

Users should also consider whether the ACS SBC or WFC3 detector with an ultraviolet (UV) filter might be better for their particular imaging needs.

- [Section 25MAMA—NUV-MAMA, Clear](#)
- [Section F25ND3—NUV-MAMA](#)
- [Section F25ND5—NUV-MAMA](#)
- [Section F25NDQ - NUV-MAMA](#)
- [Section F25QTZ—NUV-MAMA, Longpass](#)
- [Section F25SRF2—NUV-MAMA, Longpass](#)
- [Section F25MGII—NUV-MAMA](#)
- [Section F25CN270—NUV-MAMA](#)
- [Section F25CIII—NUV-MAMA](#)
- [Section F25CN182—NUV-MAMA](#)

25MAMA - NUV-MAMA, Clear

Description

The 25MAMA mode with the NUV-MAMA provides high-throughput broad-band near-ultraviolet (NUV) imaging with excellent pixel sampling and very high throughput at $\sim 2500 \text{ \AA}$.

Recommended Uses

This filter is available for broad-band NUV imaging, but not recommended; see below.

Special Considerations

NUV-MAMA clear images are marginally defocused because the mirror optimally focuses for use of a filter. Whenever possible, use F25SRF2 or F25Q TZ instead of 25MAMA for NUV-MAMA imaging.

For long exposures of faint targets, sky background is likely to be a limiting factor. Observers should consider the use of DARKTIME or (preferably) use the F25Q TZ filter, which has nearly the same throughput but rejects geocoronal Lyman- α and O I 1302 \AA triplet air glow.

Users should also consider whether WFC3 with the F225W, the F300X or the F275W filters might be a better choice for their science goals.

| Pivot λ (\AA) | FWHM (\AA) | AB mag zero point | S_{peak} | B_{λ} | R_{80} (arcsec) | Flux in central pixel |
|----------------------------------|-----------------------|-------------------|-------------------|---------------|-------------------|-----------------------|
| 2260.6 | 1209.1 | 23.994 | 1.60e+14 | 1162.5 | 0.32 | 8% |

Figure 14.23: 25MAMA NUV-MAMA Integrated System Throughput and Redleak

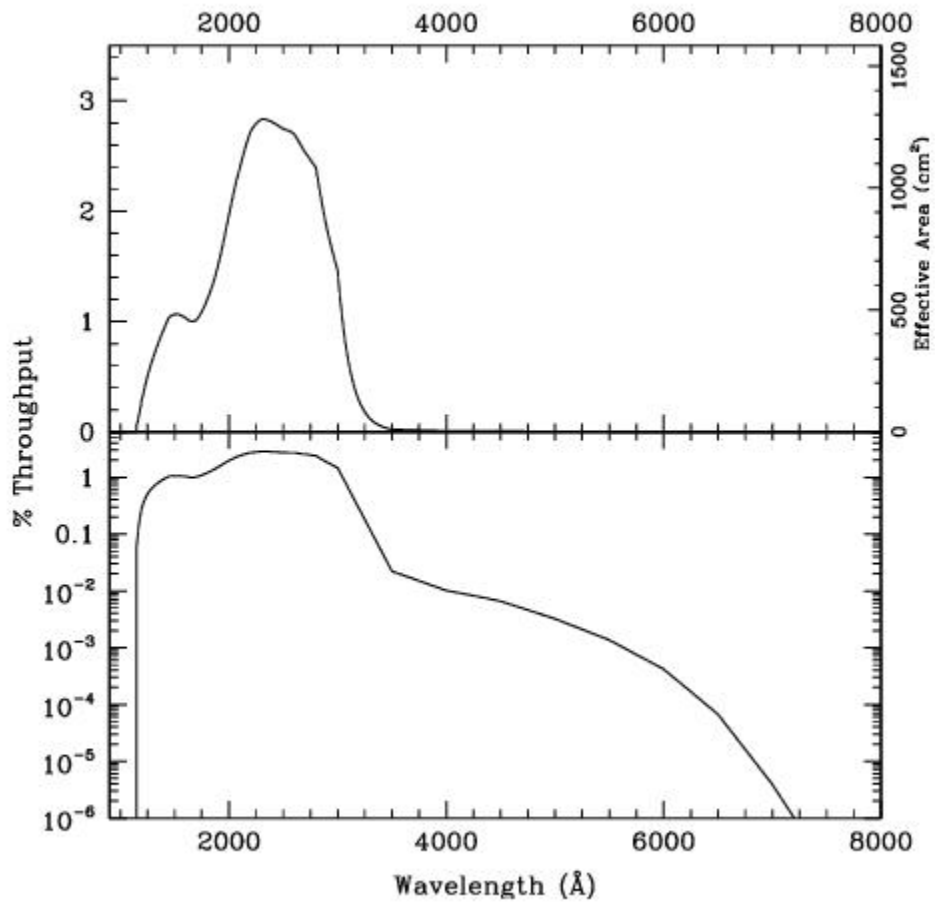


Table 14.10: 25MAMA NUV-MAMA Sensitivity & Throughput

| λ | Sensitivity | % Throughput |
|-----------|-------------|--------------|
| 1200. | 7.83E12 | 0.29 |
| 1300. | 1.96E13 | 0.66 |
| 1400. | 2.96E13 | 0.93 |
| 1500. | 3.62E13 | 1.06 |
| 1600. | 3.76E13 | 1.03 |
| 1700. | 3.98E13 | 1.03 |
| 1800. | 4.93E13 | 1.20 |

| | | |
|-------|---------|------|
| 1900. | 6.57E13 | 1.52 |
| 2000. | 8.95E13 | 1.96 |
| 2100. | 1.14E14 | 2.39 |
| 2200. | 1.36E14 | 2.71 |
| 2300. | 1.48E14 | 2.82 |
| 2400. | 1.53E14 | 2.81 |
| 2500. | 1.57E14 | 2.75 |
| 2600. | 1.59E14 | 2.69 |
| 2700. | 1.56E14 | 2.54 |
| 2800. | 1.49E14 | 2.34 |
| 2900. | 1.23E14 | 1.86 |
| 3000. | 9.38E13 | 1.37 |
| 3100. | 4.61E13 | 0.65 |

Figure 14.24: Point Source S/N vs. AB magnitude in the V-band for the 25MAMA NUV-MAMA mode. Top curves are for DARKTIME. Bottom curves are for average sky. Curves are labeled by required exposure time (sec.).

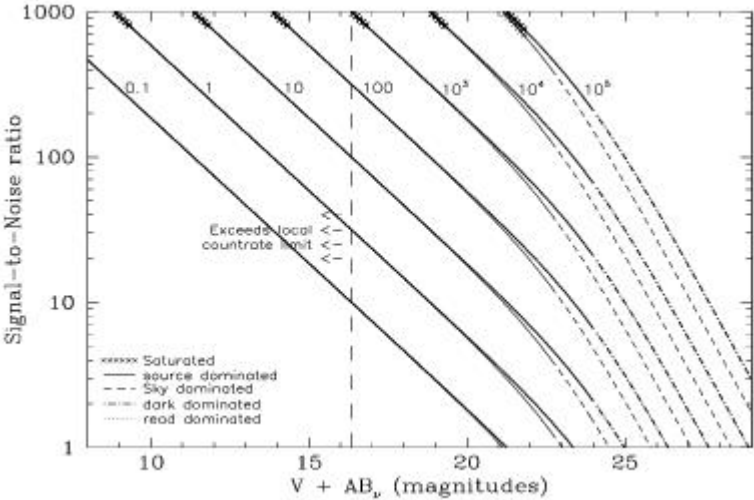


Figure 14.25: Extended Source S/N vs. AB magnitude in the V-band for the 25MAMA NUV-MAMA mode. Top curves are for an area of 0.2 arcsec²; bottom curves are for 1 arcsec². Average sky assumed. Curves are labeled by required exposure time (seconds).

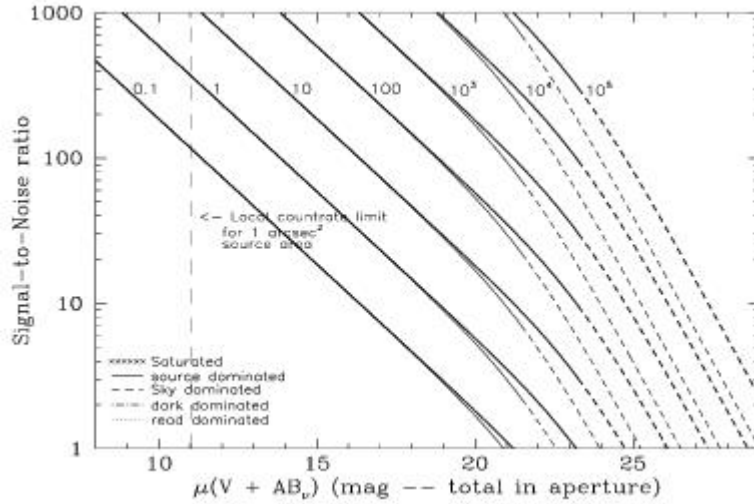


Table 14.11: Radial Profile for 25MAMA*

| Radius | | | Fraction of Energy Encircled |
|--------|--------|-----------|------------------------------|
| Pixels | Arcsec | Intensity | |
| 1 | 0.024 | 3.267e-02 | 0.141 |
| 1.5 | 0.037 | 2.107e-02 | 0.236 |
| 2 | 0.049 | 1.345e-02 | 0.331 |
| 3 | 0.073 | 6.141e-03 | 0.467 |
| 4 | 0.098 | 2.981e-03 | 0.557 |
| 5 | 0.122 | 1.485e-03 | 0.614 |
| 10 | 0.245 | 3.377e-04 | 0.746 |
| 15 | 0.367 | 1.676e-04 | 0.834 |
| 20 | 0.490 | 9.542e-05 | 0.900 |
| 25 | 0.613 | 4.543e-05 | 0.947 |
| 30 | 0.735 | 2.065e-05 | 0.972 |
| 40 | 0.980 | 5.088e-06 | 0.994 |

*See [STIS ISR 2003-01](#).

Figure 14.26: Point Source Encircled Energy for 25MAMA NUV-MAMA

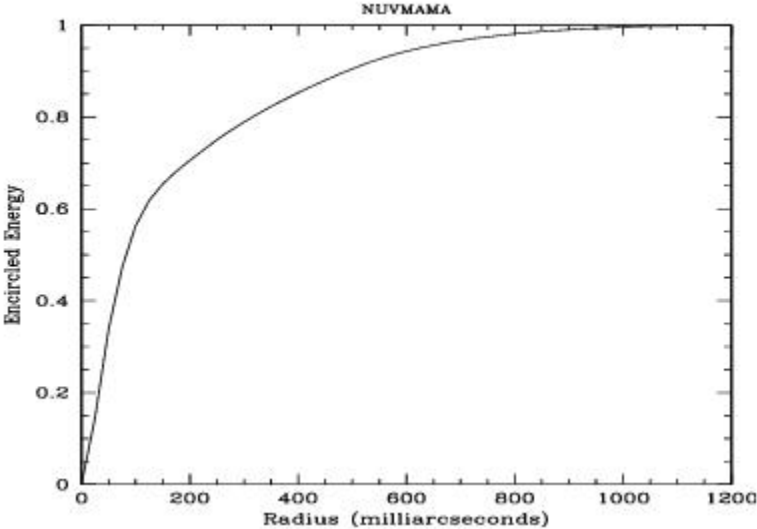
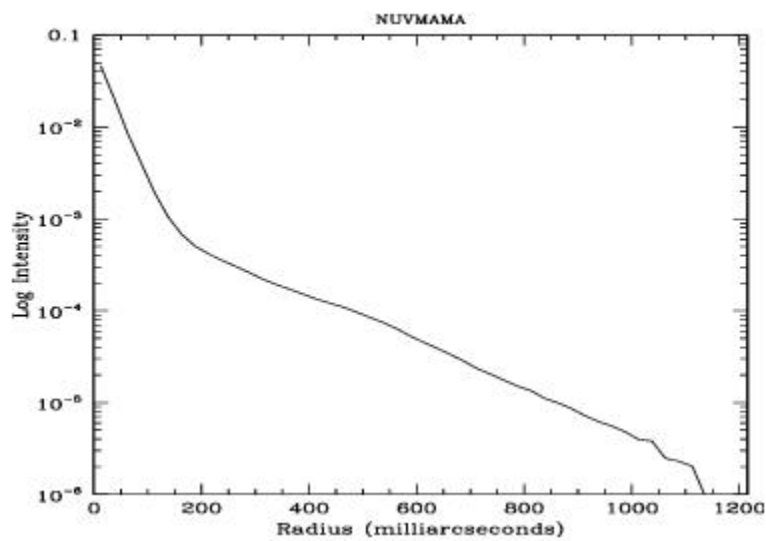


Figure 14.27: Point Source Intensity vs. Radius for 25MAMA NUV-MAMA



F25ND3 - NUV-MAMA

Description

The F25ND3 mode with the NUV-MAMA provides broad-band imaging with an attenuation of 10^{-3} . The value of R_{80} and the central pixel flux are unmeasured but assumed to be approximately the same as produced by the F25QTZ filter.

Recommended Uses

This filter is recommended for broad-band NUV imaging of objects that are too bright by a factor of 10^3 for the 25MAMA "clear" filter.

| Pivot λ (Å) | FWHM (Å) | AB mag zero point | S_{peak} | B_{λ} | R_{80} (arcsec) | Flux in central pixel |
|---------------------|----------|-------------------|-------------------|---------------|-------------------|-----------------------|
| 2360.7 | 1344.5 | 16.62 | 2.38e+11 | 942.0 | 0.32 | 8% |

Figure 14.28: F25ND3 NUV-MAMA Integrated System Throughput and Redleak

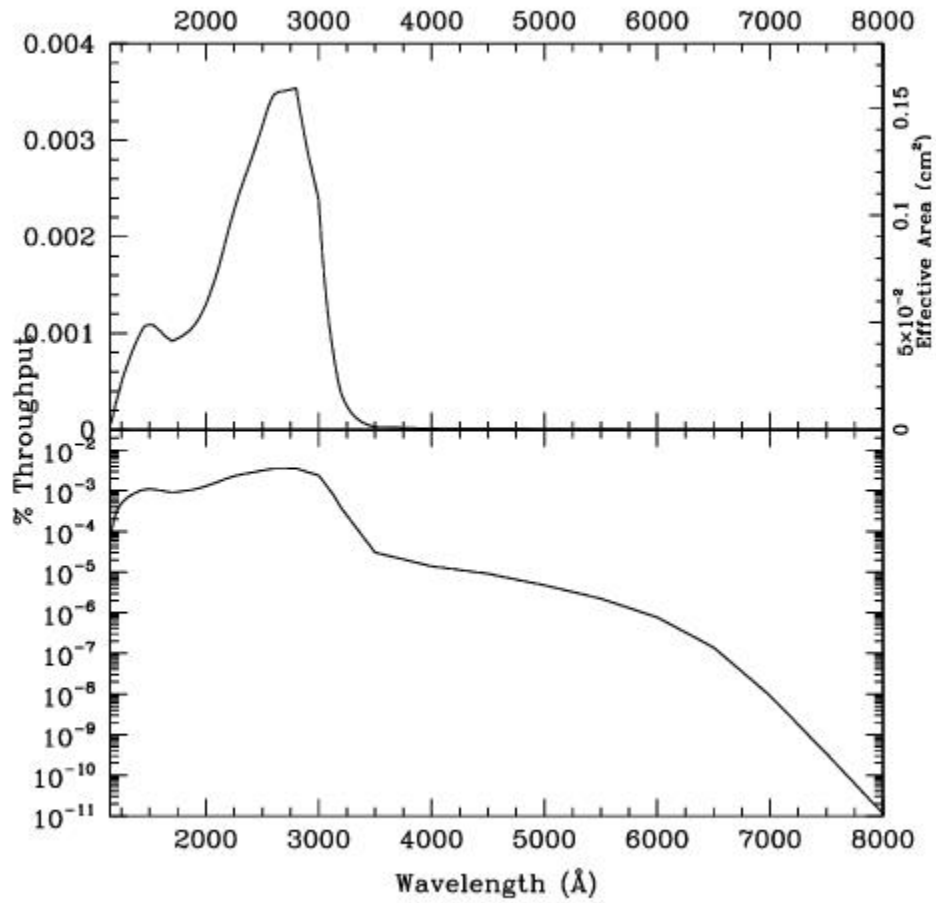


Table 14.12: Throughput and Sensitivity for F25ND3 NUV-MAMA

| λ | Sensitivity | % Throughput |
|-----------|-------------|--------------|
| 1200. | 7.12E9 | 2.6e-4 |
| 1300. | 1.95E10 | 6.6e-4 |
| 1400. | 3.03E10 | 9.5e-4 |
| 1500. | 3.70E10 | 1.1e-3 |
| 1600. | 3.70E10 | 1.0e-3 |
| 1700. | 3.62E10 | 9.4e-4 |
| 1800. | 4.03E10 | 9.8e-4 |

| | | |
|-------|---------|--------|
| 1900. | 4.73E10 | 1.1e-3 |
| 2000. | 5.95E10 | 1.3e-3 |
| 2100. | 7.84E10 | 1.6e-3 |
| 2200. | 1.03E11 | 2.1e-3 |
| 2300. | 1.29E11 | 2.5e-3 |
| 2400. | 1.53E11 | 2.8e-3 |
| 2500. | 1.79E11 | 3.1e-3 |
| 2600. | 2.04E11 | 3.4e-3 |
| 2700. | 2.16E11 | 3.5e-3 |
| 2800. | 2.20E11 | 3.4e-3 |
| 2900. | 1.92E11 | 2.9e-3 |
| 3000. | 1.52E11 | 2.2e-3 |
| 3100. | 7.44E10 | 1.1e-3 |

Figure 14.29: Point Source S/N vs. AB magnitude in the V-band for the F25ND3 NUV-MAMA mode. Top curves are for DARKTIME. Bottom curves are for average sky. Curves are labeled by required exposure time (sec.).

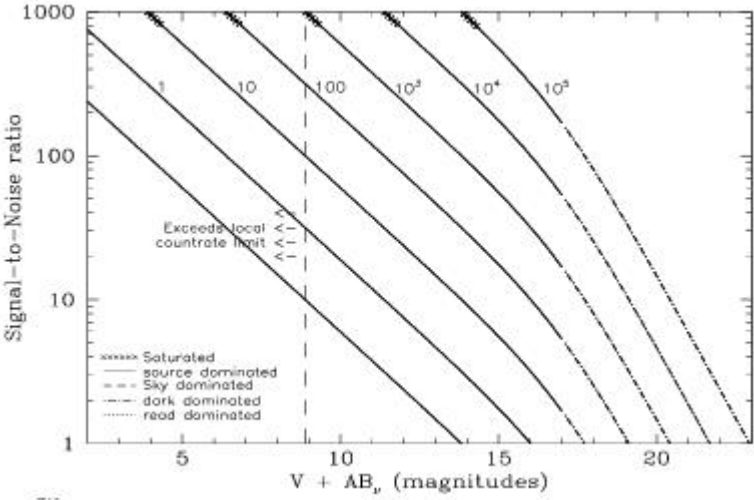
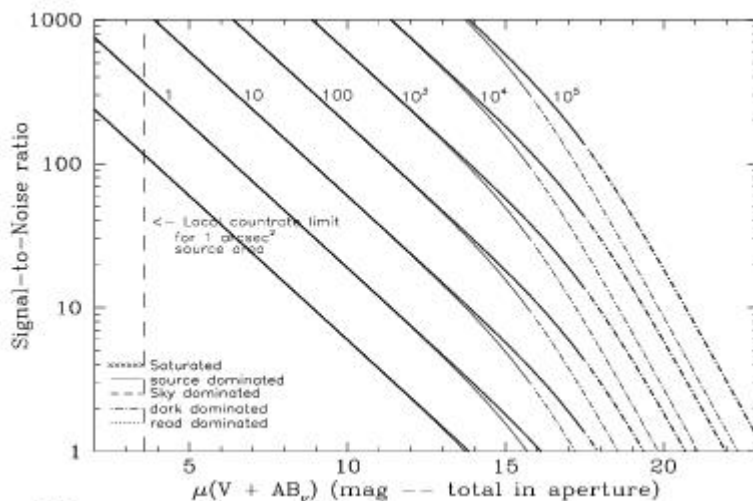


Figure 14.30: Extended Source S/N vs. AB magnitude in the V-band for the F25ND3 NUV-MAMA mode. Top curves are for an area of 0.2 arcsec²; bottom curves are for 1 arcsec². Average sky assumed. Curves are labeled by required exposure time (seconds).



F25ND5 - NUV-MAMA

Description

The F25ND5 mode with the NUV-MAMA provides broad-band imaging with an attenuation of 5×10^{-6} . The value of R80 and the central pixel flux are unmeasured but assumed to be approximately the same as produced by the F25Q1Z filter.

Recommended Uses

This filter is recommended for broad-band NUV images that are too bright by a factor of 2×10^5 for the 25MAMA "clear" filter.

Special Considerations

The throughput of the ND5 filter and NUV-MAMA combination relative to the unfiltered NUV-MAMA varies strongly as a function of wavelength. At wavelengths between 3000 and 5000 Å the attenuation factor is close to 5×10^{-6} . At shorter wavelengths the relative throughput can be a factor of ten or more smaller, while at longer wavelengths it is considerably larger, so special care should be taken for red sources. To make an accurate prediction of the expected count rate, observers should use a good approximation of the source spectrum as input for the [STIS ETC](#).

| Pivot λ (Å) | FWHM (Å) | AB mag zero point | S_{peak} | B_{λ} | R_{80} (arcsec) | Flux in central pixel |
|---------------------|----------|-------------------|-------------------|---------------|-------------------|-----------------------|
| 2633.8 | 1514.7 | 9.185 | 5.01e+8 | 594.3 | 0.32 | 8% |

Figure 14.31: F25ND5 NUV-MAMA Integrated System Throughput and Redleak

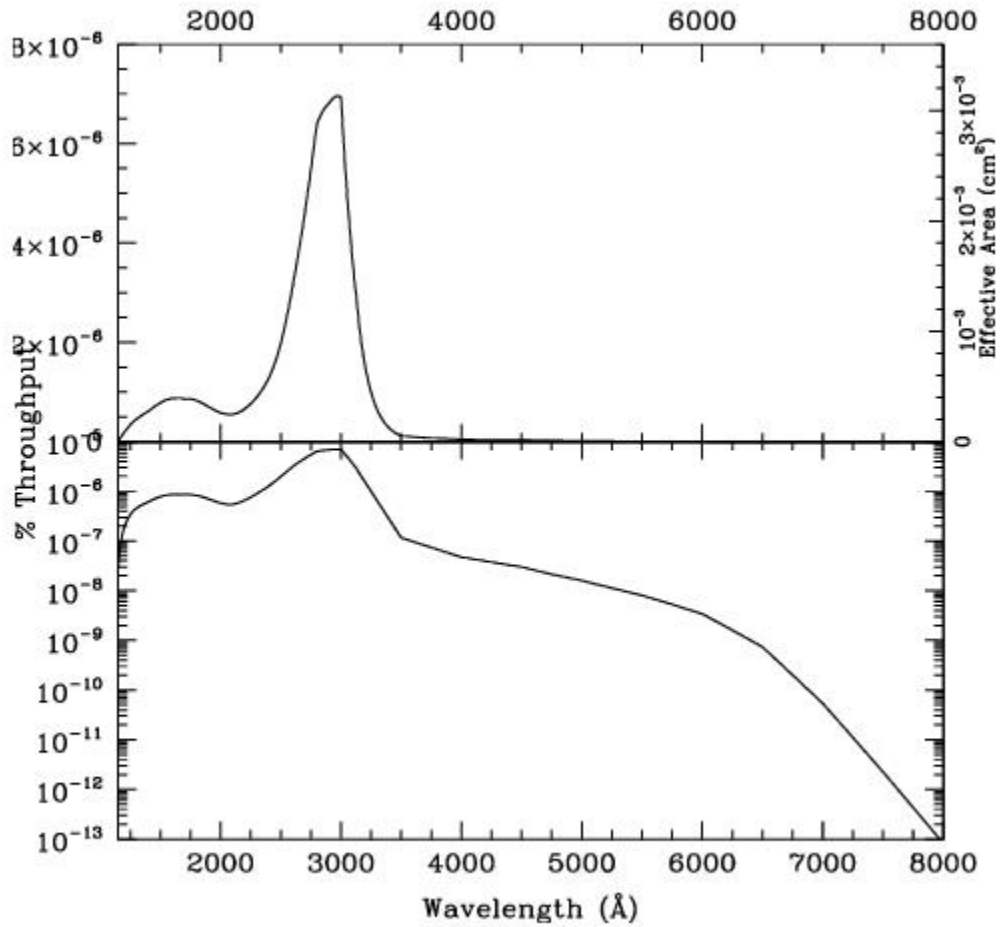


Table 14.13: Throughput and Sensitivity for F25ND5 NUV-MAMA

| λ | Sensitivity | % Throughput |
|-----------|-------------|--------------|
| 1200. | 4.99E6 | 1.8e-7 |
| 1300. | 1.32E7 | 4.5e-7 |
| 1400. | 1.97E7 | 6.2e-7 |
| 1500. | 2.66E7 | 7.8e-7 |
| 1600. | 3.15E7 | 8.6e-7 |
| 1700. | 3.35E7 | 8.7e-7 |
| 1800. | 3.38E7 | 8.3e-7 |

| | | |
|-------|--------|--------|
| 1900. | 3.04E7 | 7.0e-7 |
| 2000. | 2.67E7 | 5.9e-7 |
| 2100. | 2.67E7 | 5.6e-7 |
| 2200. | 3.33E7 | 6.6e-7 |
| 2300. | 4.72E7 | 9.0e-7 |
| 2400. | 7.06E7 | 1.3e-6 |
| 2500. | 1.14E8 | 2.0e-6 |
| 2600. | 1.87E8 | 3.2e-6 |
| 2700. | 2.85E8 | 4.6e-6 |
| 2800. | 3.98E8 | 6.2e-6 |
| 2900. | 4.50E8 | 6.8e-6 |
| 3000. | 4.40E8 | 6.4e-6 |
| 3100. | 2.54E8 | 3.6e-6 |

Figure 14.32: Point Source S/N vs. AB magnitude in the V-band for the F25ND5 NUV-MAMA mode. Top curves are for DARKTIME. Bottom curves are for average sky. Curves are labeled by required exposure time (sec.).

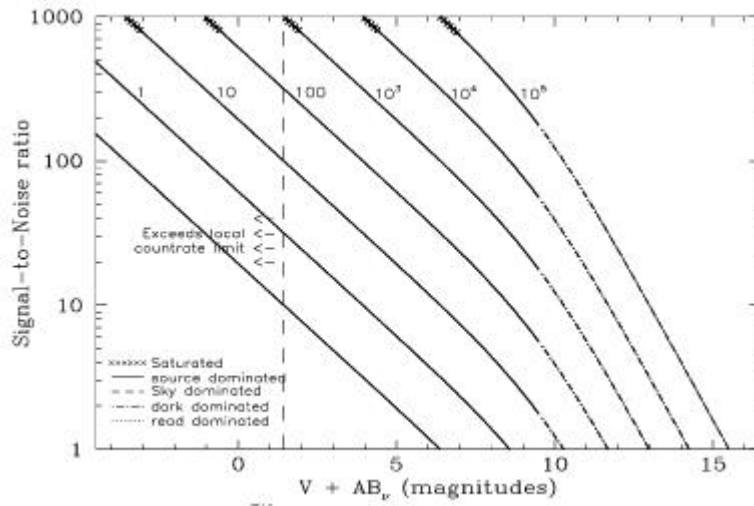
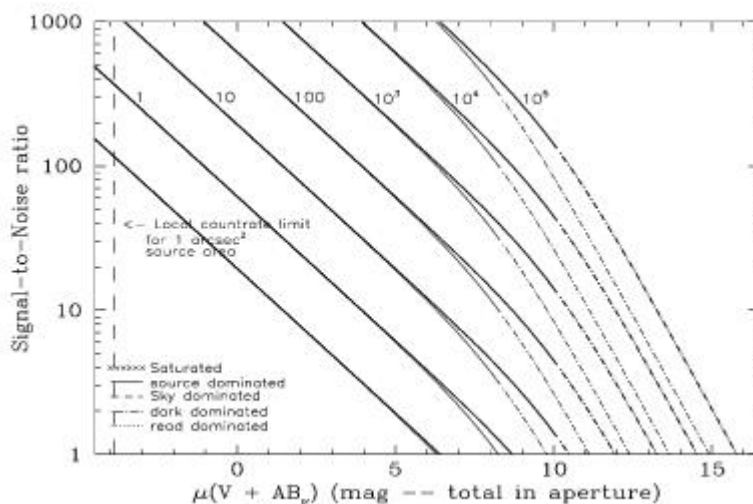


Figure 14.33: Extended Source S/N vs. AB magnitude in the V-band for the F25ND5 NUV-MAMA mode. Top curves are for an area of 0.2 arcsec²; bottom curves are for 1 arcsec². Average sky assumed. Curves are labeled by required exposure time (seconds).



F25NDQ - NUV-MAMA

Description

The F25NDQ mode with the NUV-MAMA detector provides broad-band imaging with attenuation factors that vary between 10^{-1} and 10^{-4} . The full field of view is 25 arcsec \times 25 arcsec, but the F25NDQ filter is unique in that it is divided into four quadrants, each having a different neutral density factor. Thus, the field of view for each quadrant is 12 arcsec \times 12 arcsec. In clockwise order starting from the upper left these are F25NDQ1, F25NDQ2, F25NDQ3, and F25NDQ4, where the number appended to each name is the approximate dex ND factor. The R_{80} and central pixel flux are unmeasured but assumed to be approximately the same as produced by the F25SRF2 filter.

Recommended Uses

Recommended for broad-band imaging of bright objects which require attenuation of between 10^{-1} and 10^{-4} to meet NUV-MAMA bright object limits.

Special Considerations

If a target would violate BOP restrictions in any quadrant of the F25NDQ aperture, the restrictions regarding pointing close to objects violating safety limits discussed in [Chapter 7](#) and [STIS ISR 2000-01](#) apply. Also the dividing lines between the quadrants are somewhat displaced from the center of the detector and are not quite parallel to the detector edges (see [Figure 13.83](#)), so observers for whom the exact locations of the quadrant boundaries are important should consult the [Help Desk](#).

| Aperture | Pivot λ (Å) | FWHM (Å) | AB mag zero point | S_{peak} | B_{λ} | R_{80} (arcsec) | Flux in central pixel |
|----------|---------------------|----------|-------------------|-------------------|---------------|-------------------|-----------------------|
| F25NDQ1 | 2277.46 | 1126 | 21.583 | 1.86 e+13 | 1263 | 0.32 | 8% |
| F25NDQ2 | 2318.08 | 1036 | 19.326 | 2.82 e+12 | 1098 | 0.32 | 8% |
| F25NDQ3 | 2417.84 | 756 | 16.906 | 3.92 e+11 | 889 | 0.32 | 8% |
| F25NDQ4 | 2450.14 | 607 | 14.207 | 3.63 e+10 | 814 | 0.32 | 8% |

Figure 14.34: F25NDQ Integrated System Throughputs.

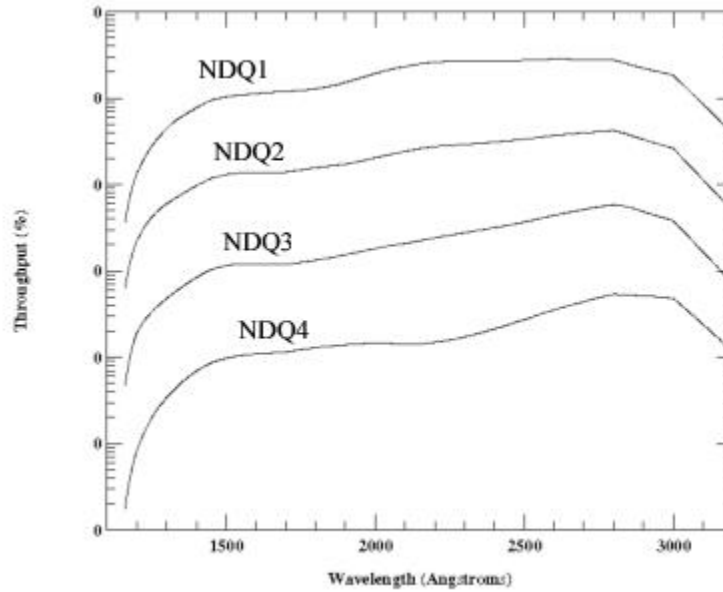


Table 14.14: Throughputs and Sensitivities for F25NDQ NUV-MAMA quadrants.

| λ | Sensitivities | | | | Throughputs | | | |
|-----------|---------------|----------|----------|----------|-------------|----------|----------|----------|
| | F25NDQ1 | F25NDQ2 | F25NDQ3 | F25NDQ4 | F25NDQ1 | F25NDQ2 | F25NDQ3 | F25NDQ4 |
| 1200 | 3.67e+11 | 5.89e+10 | 4.88e+09 | 2.39e+08 | 1.32e-02 | 2.12e-03 | 1.76e-04 | 8.60e-06 |
| 1300 | 1.31e+12 | 1.77e+11 | 1.43e+10 | 1.02e+09 | 4.41e-02 | 5.94e-03 | 4.82e-04 | 3.44e-05 |
| 1400 | 2.47e+12 | 3.10e+11 | 2.36e+10 | 2.19e+09 | 7.74e-02 | 9.68e-03 | 8.37e-04 | 6.85e-05 |
| 1500 | 3.51e+12 | 4.40e+11 | 3.88e+10 | 3.30e+09 | 1.03e-01 | 1.29e-02 | 1.14e-03 | 9.66e-05 |
| 1600 | 4.11e+12 | 5.01e+11 | 4.36e+10 | 3.96e+09 | 1.13e-01 | 1.37e-02 | 1.20e-03 | 1.09e-04 |
| 1700 | 4.63e+12 | 5.44e+11 | 4.63e+10 | 4.49e+09 | 1.19e-01 | 1.40e-02 | 1.20e-03 | 1.16e-04 |
| 1800 | 5.29e+12 | 6.40e+11 | 5.46e+10 | 5.28e+09 | 1.29e-01 | 1.56e-02 | 1.33e-03 | 1.29e-04 |
| 1900 | 6.61e+12 | 7.50e+11 | 6.66e+10 | 6.02e+09 | 1.53e-01 | 1.73e-02 | 1.54e-03 | 1.39e-04 |
| 2000 | 8.77e+12 | 9.27e+11 | 8.26e+10 | 6.57e+09 | 1.92e-01 | 2.03e-02 | 1.81e-03 | 1.44e-04 |
| 2100 | 1.11e+13 | 1.15e+12 | 9.97e+10 | 6.79e+09 | 2.32e-01 | 2.41e-02 | 2.08e-03 | 1.42e-04 |
| 2200 | 1.30e+13 | 1.37e+12 | 1.21e+11 | 7.47e+09 | 2.60e-01 | 2.73e-02 | 2.41e-03 | 1.49e-04 |
| 2300 | 1.41e+13 | 1.53e+12 | 1.45e+11 | 9.04e+09 | 2.69e-01 | 2.91e-02 | 2.76e-03 | 1.72e-04 |
| 2400 | 1.48e+13 | 1.69e+12 | 1.73e+11 | 1.17e+10 | 2.71e-01 | 3.10e-02 | 3.17e-03 | 2.13e-04 |

| | | | | | | | | |
|------|----------|----------|----------|----------|----------|----------|----------|----------|
| 2500 | 1.56e+13 | 1.91e+12 | 2.10e+11 | 1.56e+10 | 2.75e-01 | 3.35e-02 | 3.68e-03 | 2.73e-04 |
| 2600 | 1.67e+13 | 2.18e+12 | 2.60e+11 | 2.10e+10 | 2.82e-01 | 3.69e-02 | 4.39e-03 | 3.54e-04 |
| 2700 | 1.72e+13 | 2.44e+12 | 3.16e+11 | 2.71e+10 | 2.80e-01 | 3.96e-02 | 5.41e-03 | 4.41e-04 |
| 2800 | 1.72e+13 | 2.60e+12 | 3.62e+11 | 3.33e+10 | 2.69e-01 | 4.07e-02 | 5.67e-03 | 5.23e-04 |
| 2900 | 1.47e+13 | 2.19e+12 | 3.20e+11 | 3.39e+10 | 2.23e-01 | 3.32e-02 | 4.85e-03 | 5.13e-04 |
| 3000 | 1.18e+13 | 1.68e+12 | 2.45e+11 | 3.06e+10 | 1.74e-01 | 2.46e-02 | 3.59e-03 | 4.49e-04 |
| 3100 | 6.12e+12 | 8.23e+11 | 1.20e+11 | 1.72e+10 | 8.68e-02 | 1.17e-02 | 1.70e-03 | 2.44e-04 |

F25QTZ - NUV-MAMA, Longpass

Description

The F25QTZ filter with the NUV-MAMA provides high-throughput broad-band NUV imaging with better rejection of geocoronal emission than the F25MAMA or F25SRF2 modes, the same field of view, and the same high spatial resolution.

Recommended Uses

This filter is recommended for broad-band NUV imaging of faint targets.

Special Considerations

Sky background on the day side of the orbit contains a significant contribution from [O II] air glow emission at 2471 Å. In high-background conditions, the sky background can contribute a significant amount to the detector background. Observers can limit the background (with some cost to the total amount of observing time per orbit) by using the DARKTIME special requirement.

| Pivot λ (Å) | FWHM (Å) | AB mag zero point | S_{peak} | B_{λ} | R_{80} (arcsec) | Flux in central pixel |
|---------------------|----------|-------------------|-------------------|---------------|-------------------|-----------------------|
| 2359.3 | 998.7 | 23.713 | 1.42e+14 | 1099.6 | 0.32 | 8% |

Figure 14.35: F25QTZ NUV-MAMA Integrated System Throughput and Redleak

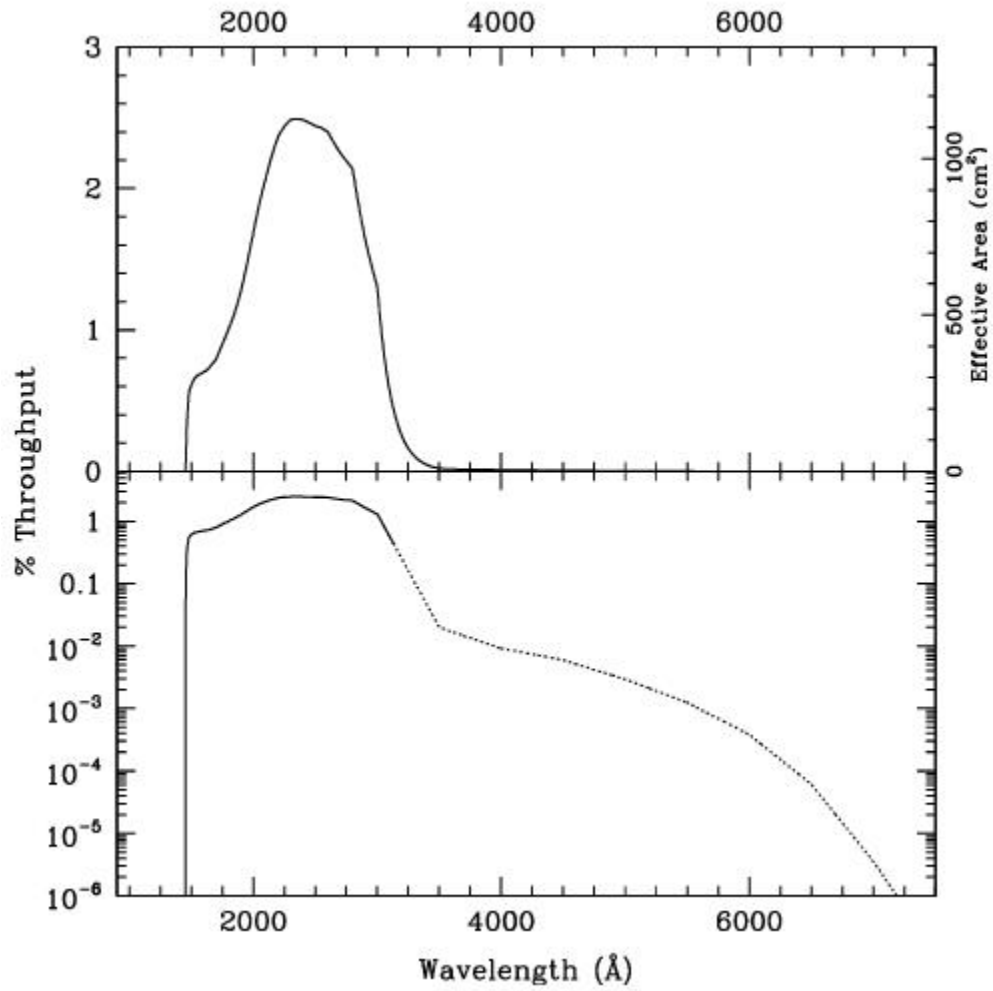


Table 14.15: F25QTZ NUV-MAMA Sensitivity & Throughput

| λ | Sensitivity | % Throughput |
|-----------|-------------|--------------|
| 1500. | 1.83E13 | 0.54 |
| 1600. | 2.57E13 | 0.79 |
| 1700. | 3.12E13 | 0.81 |
| 1800. | 4.13E13 | 1.01 |
| 1900. | 5.57E13 | 1.29 |
| 2000. | 7.69E13 | 1.69 |
| 2100. | 9.91E13 | 2.07 |

| | | |
|-------|---------|------|
| 2200. | 1.18E14 | 2.35 |
| 2300. | 1.30E14 | 2.48 |
| 2400. | 1.36E14 | 2.48 |
| 2500. | 1.39E14 | 2.44 |
| 2600. | 1.41E14 | 2.39 |
| 2700. | 1.39E14 | 2.25 |
| 2800. | 1.33E14 | 2.09 |
| 2900. | 1.09E14 | 1.66 |
| 3000. | 8.35E13 | 1.22 |

Figure 14.36: Point Source S/N vs. AB magnitude in the V-band for the F25QTZ NUV-MAMA mode. Top curves are for DARKTIME. Bottom curves are for average sky. Curves are labeled by required exposure time (seconds).

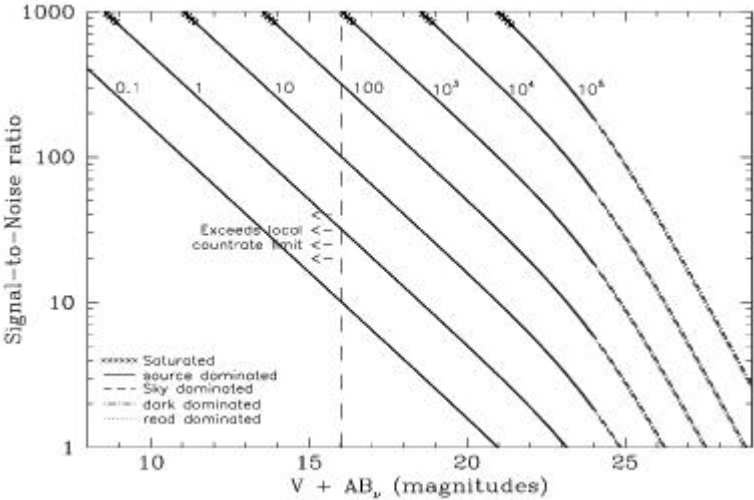


Figure 14.37: Extended Source S/N vs. AB magnitude in the V-band for the F25QTZ NUV-MAMA mode. Top curves are for an area of 0.2 arcsec²; bottom curves are for 1 arcsec². Average sky assumed. Curves are labeled by required exposure time (seconds).

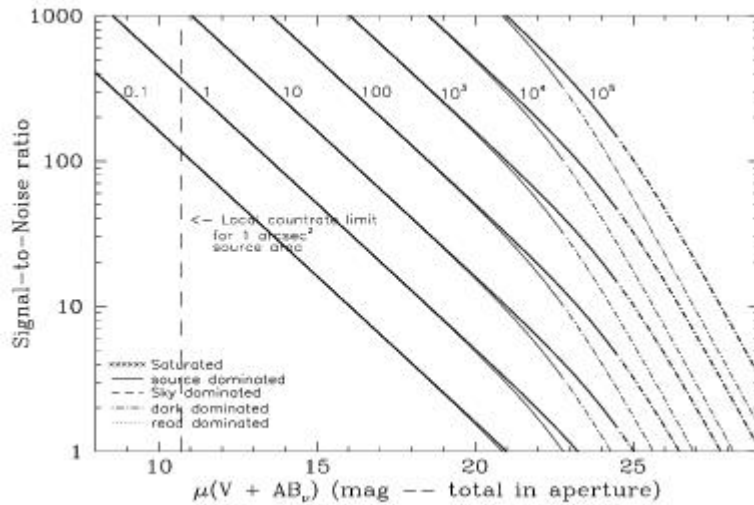


Table 14.16: Radial Profile for F25QTZ (see [STIS ISR 2003-01](#))

| Radius | | Intensity | Fraction of Energy Encircled |
|--------|--------|-----------|------------------------------|
| Pixels | Arcsec | | |
| 1 | 0.024 | 6.046e-02 | 0.210 |
| 1.5 | 0.037 | 4.292e-02 | 0.328 |
| 2 | 0.049 | 2.825e-02 | 0.440 |
| 3 | 0.073 | 1.036e-02 | 0.591 |
| 4 | 0.098 | 4.085e-03 | 0.667 |
| 5 | 0.122 | 1.839e-03 | 0.718 |
| 10 | 0.245 | 2.099e-04 | 0.820 |
| 15 | 0.367 | 9.929e-05 | 0.874 |
| 20 | 0.490 | 4.775e-05 | 0.911 |
| 25 | 0.613 | 2.706e-05 | 0.934 |
| 30 | 0.735 | 1.876e-05 | 0.953 |
| 40 | 0.980 | 8.441e-06 | 0.983 |

Figure 14.38: Point Source PSF for F25QTZ NUV-MAMA, 7."5 square (at pixel 606,649, log scaled). Note PSF ghost ~ 45 pixels left of peak pixel and a few 10^{-3} of the peak

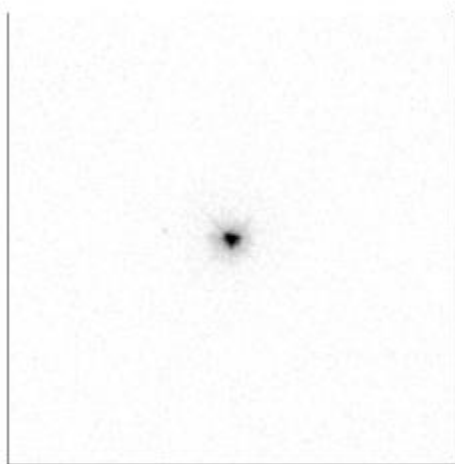


Figure 14.39: Point Source Encircled Energy for F25QTZ NUV-MAMA

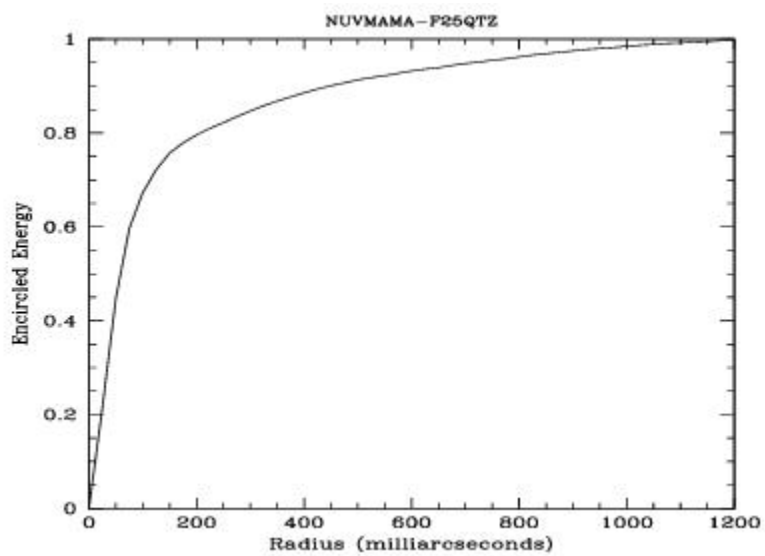
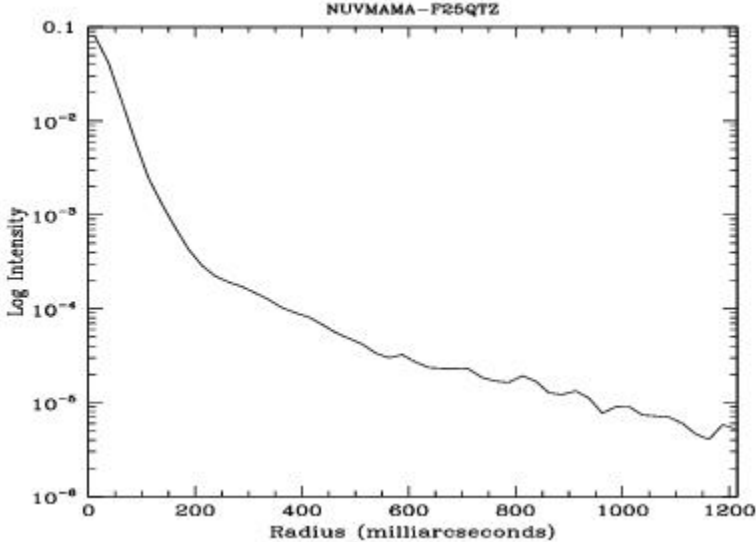


Figure 14.40: Point Source Intensity vs. Radius for F25QTZ NUV-MAMA



F25SRF2 - NUV-MAMA, Longpass

Description

The F25SRF2 filter with the NUV-MAMA provides high-throughput broad-band NUV imaging with better rejection of geocoronal emission than the F25MAMA but worse than the F25QIZ mode. It provides the same field of view and high spatial resolution.

Recommended Uses

This filter has slightly higher throughput than F25QIZ, but lets in geocoronal O I 1302 Å triplet. In most cases the sky background will still be lower than the detector background.

Special Considerations

Sky background on the day side of the orbit contains a significant contributions from [OII] air glow emission at 2471 Å and O I 1302 Å triplet air glow. In high-background conditions, the sky background can dominate the detector background. In average day-side observing conditions the background from the sky is approximately half of the background coming from the detector dark current. Also, the background through F25SRF2 will be about 10% higher than through F25QIZ. Observers can limit the background by using the DARKTIME special requirement.

| Pivot λ (Å) | FWHM (Å) | AB mag zero point | S_{peak} | B_{λ} | R_{80} (arcsec) | Flux in central pixel |
|---------------------|----------|-------------------|-------------------|---------------|-------------------|-----------------------|
| 2302.7 | 1138.4 | 23.834 | 1.47e+14 | 1129.8 | 0.32 | 8% |

Figure 14.41: F25SRF2 NUV-MAMA Integrated System Throughput and Redleak

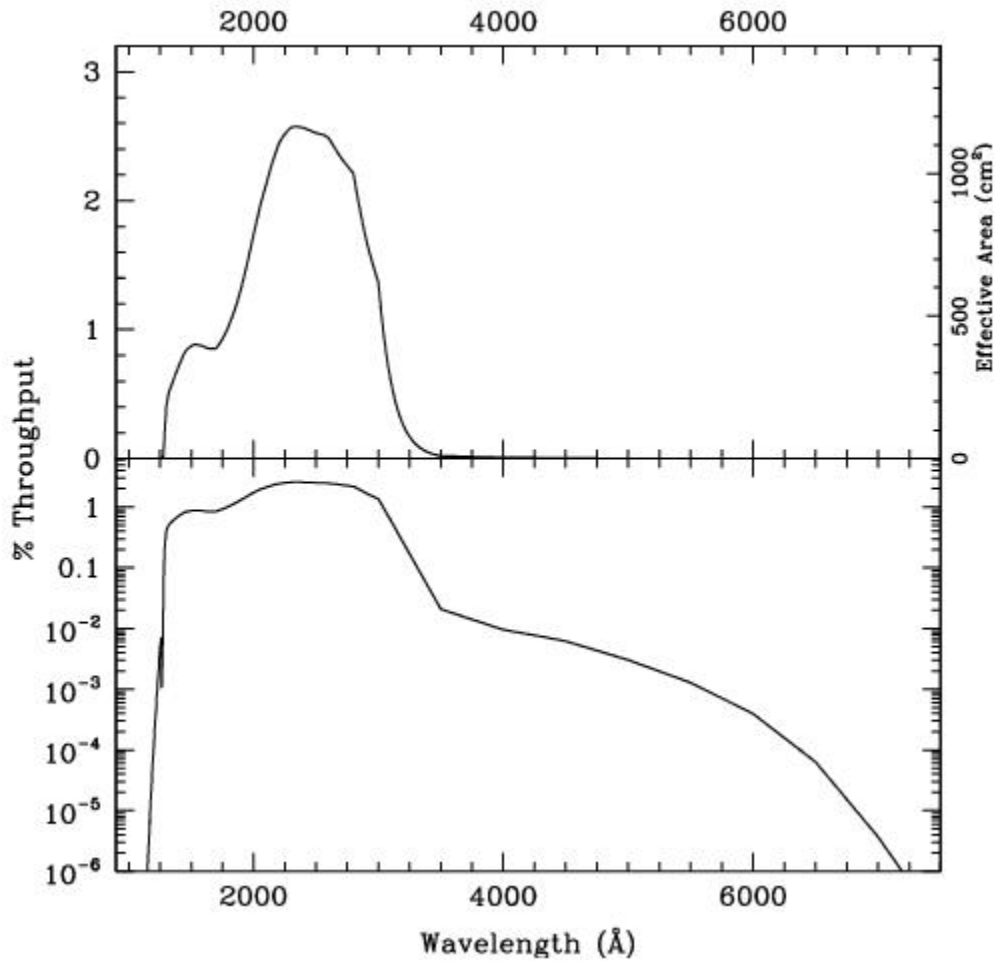


Table 14.17: F25SRF2 NUV-MAMA Sensitivity & Throughput

| λ | Sensitivity | % Throughput |
|-----------|-------------|--------------|
| 1300. | 8.93E12 | 0.30 |
| 1400. | 2.27E13 | 0.71 |
| 1500. | 2.96E13 | 0.87 |
| 1600. | 3.16E13 | 0.87 |
| 1700. | 3.37E13 | 0.87 |
| 1800. | 4.23E13 | 1.03 |
| 1900. | 5.73E13 | 1.32 |

| | | |
|-------|----------|------|
| 2000. | 7.90E13 | 1.73 |
| 2100. | 1.02E14 | 2.12 |
| 2200. | 1.21E14 | 2.42 |
| 2300. | 1.340E14 | 2.56 |
| 2400. | 1.40E14 | 2.56 |
| 2500. | 1.44E14 | 2.53 |
| 2600. | 1.47E14 | 2.48 |
| 2700. | 1.44E14 | 2.34 |
| 2800. | 1.38E14 | 2.16 |
| 2900. | 1.13E14 | 1.72 |
| 3000. | 8.74E13 | 1.28 |
| 3100. | 4.33E13 | 0.61 |
| 3200. | 1.93E13 | 0.27 |

Figure 14.42: Point Source S/N vs. AB magnitude in the V-band for the F25SRF2 NUV-MAMA mode. Top curves are for DARKTIME. Bottom curves are for average sky. Curves are labeled by required exposure time (sec.).

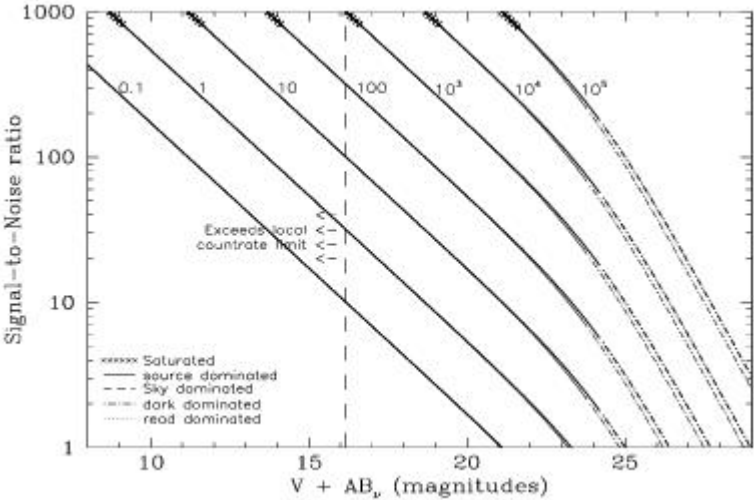
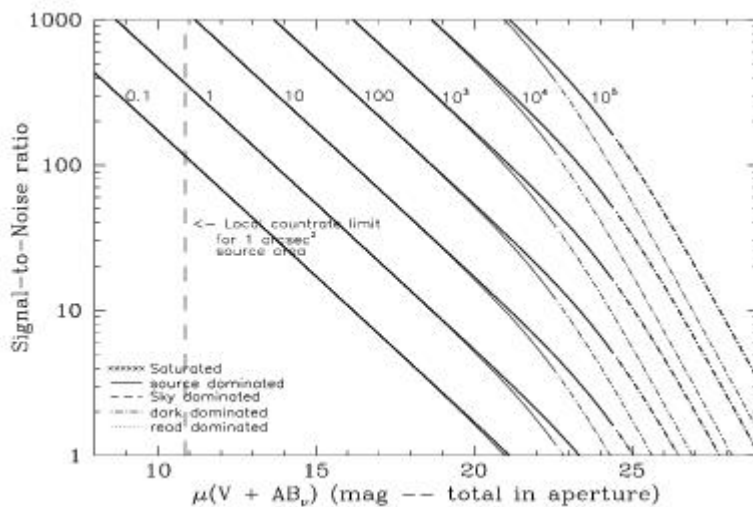


Figure 14.43: Extended Source S/N vs. AB magnitude in the V-band for the F25SRF2 NUV-MAMA mode. Top curves are for an area of 0.2 arcsec²; bottom curves are for 1 arcsec². Average sky assumed. Curves are labeled by required exposure time (seconds).



F25MGII - NUV-MAMA

Description

The F25MGII filter with the NUV-MAMA provides narrow-band imaging centered on the Mg II 2798 Å feature.

Recommended Uses

This filter is recommended for narrow-band imaging of the Mg II 2798 Å line.

Special Considerations

There is a substantial red leak in this filter. Sources with a red underlying continuum may be difficult to observe. Users should be careful to take into account the underlying continuum in estimating whether the observation will fall within the bright object protection limits. This filter also has a complex PSF and exhibits several ghosts.

| Pivot λ (Å) | FWHM (Å) | AB mag zero point | S_{peak} | B_{λ} | R_{80} (arcsec) | Flux in central pixel |
|---------------------|----------|-------------------|-------------------|---------------|-------------------|-----------------------|
| 2801.7 | 47.7 | 19.449 | 7.78e+13 | 55.8 | 0.18 | 14% |

Figure 14.44: Point Source PSF for F25MGII NUV-MAMA 7."5 square (at pixel 316,658, log scaled, B-V=-0.04). Note PSF ghost ~ 45 pixels left of peak pixel with a brightness of several thousandths of the peak, as well as the much more complex ghost about 10 pixels to the right of the central pixel.

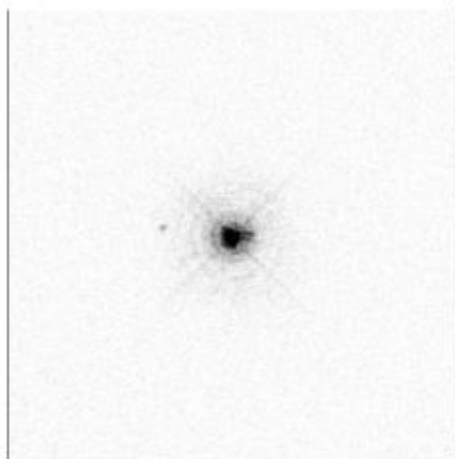


Figure 14.45: F25MGII NUV-MAMA Integrated System Throughput and Redleak

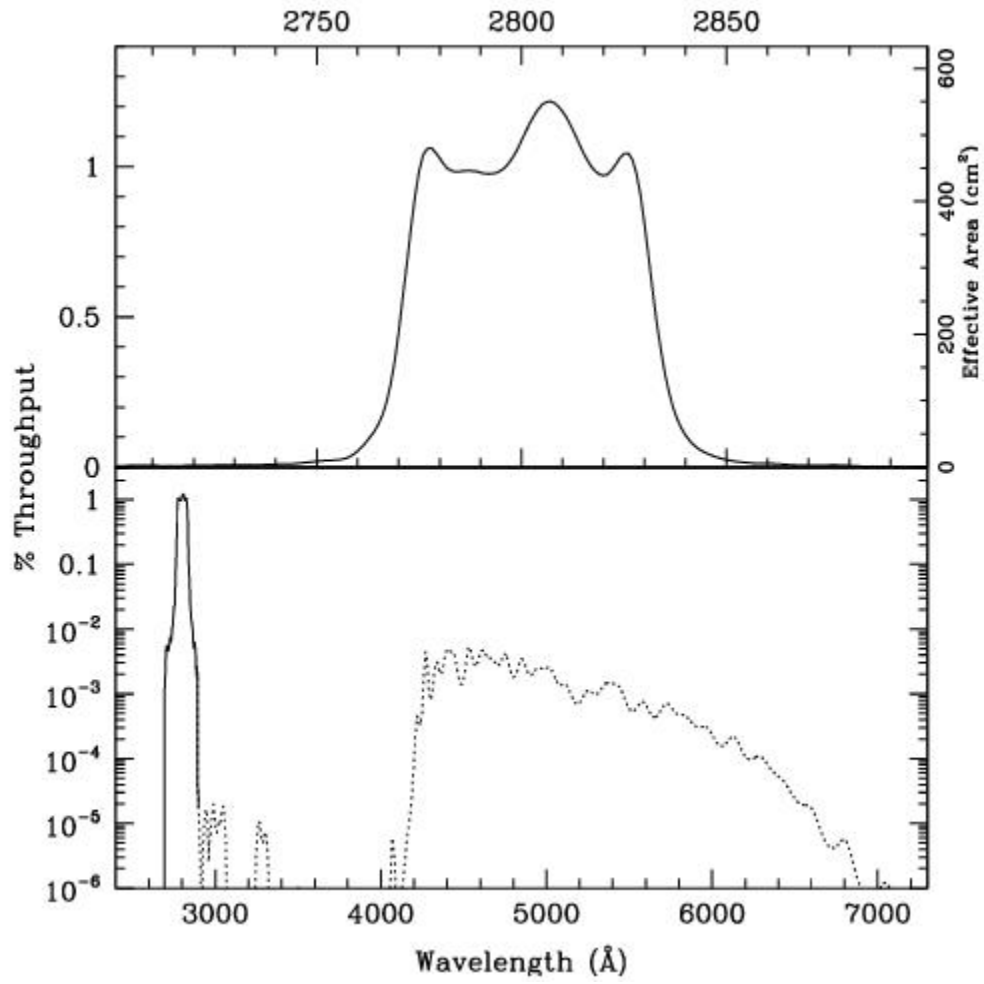


Table 14.8: F25MGII Sensitivity & Throughput

| λ | Sensitivity | % Throughput |
|-----------|-------------|--------------|
| 2765. | 9.39E12 | 0.15 |
| 2770. | 2.92E13 | 0.46 |
| 2775. | 6.05E13 | 0.96 |
| 2780. | 6.51E13 | 1.03 |
| 2785. | 6.25E13 | 0.98 |
| 2790. | 6.23E13 | 0.98 |
| 2795. | 6.31E13 | 0.99 |

| | | |
|-------|---------|------|
| 2800. | 6.94E13 | 1.09 |
| 2805. | 7.66E13 | 1.20 |
| 2810. | 7.54E13 | 1.18 |
| 2815. | 6.74E13 | 1.05 |
| 2820. | 6.28E13 | 0.98 |
| 2825. | 6.62E13 | 1.03 |
| 2830. | 5.13E13 | 0.80 |
| 2835. | 2.09E13 | 0.32 |
| 2840. | 7.23E12 | 0.11 |
| 2845. | 3.13E12 | 0.05 |
| 2850. | 1.64E12 | 0.03 |

Figure 14.46: Point Source S/N vs. line flux for the F25MGII NUV-MAMA mode. Curves are labeled by required exposure time (seconds).

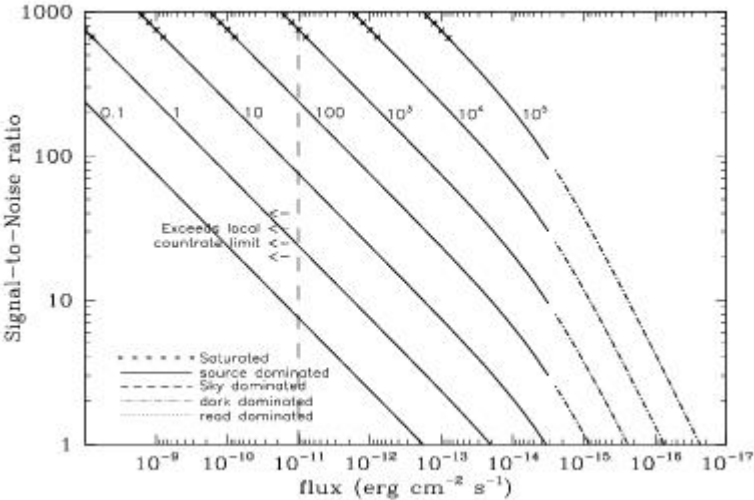


Figure 14.47: Extended Source S/N vs. line flux for the F25MGII NUV-MAMA mode. Top curves are for an area of 0.2 arcsec²; bottom curves are for 1 arcsec². Average sky assumed. Curves are labeled by required exposure time (seconds).

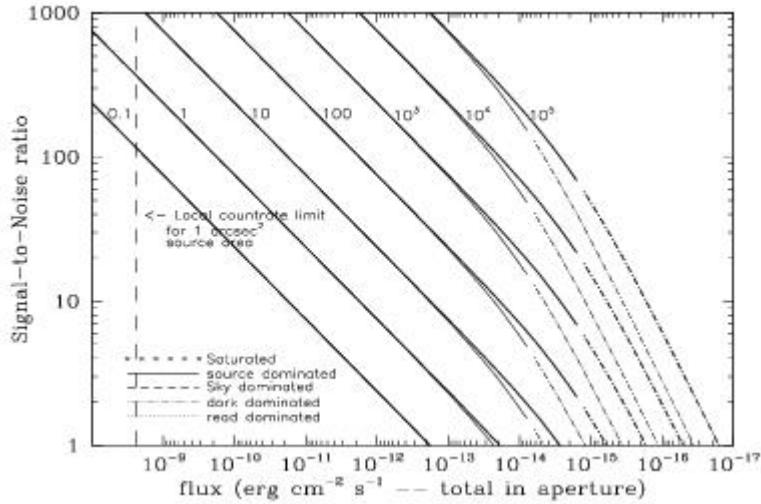


Table 14.19: Radial Profile for F25MGII*

| Radius | | Intensity | Fraction of Energy Encircled |
|--------|--------|-----------|------------------------------|
| Pixels | Arcsec | | |
| 1 | 0.024 | 5.302e-02 | 0.257 |
| 1.5 | 0.037 | 2.834e-02 | 0.391 |
| 2 | 0.049 | 1.466e-02 | 0.510 |
| 3 | 0.073 | 4.989e-03 | 0.641 |
| 4 | 0.098 | 1.739e-03 | 0.697 |
| 5 | 0.122 | 1.302e-03 | 0.738 |
| 10 | 0.245 | 2.035e-04 | 0.843 |
| 15 | 0.367 | 1.119e-04 | 0.899 |
| 20 | 0.490 | 3.763e-05 | 0.932 |
| 25 | 0.613 | 2.057e-05 | 0.949 |
| 30 | 0.735 | 1.692e-05 | 0.965 |
| 40 | 0.980 | 6.931e-06 | 0.988 |

* See [STIS ISR 2003-01](#).

Figure 14.48: Point Source Encircled Energy for F25MGII NUV-MAMA

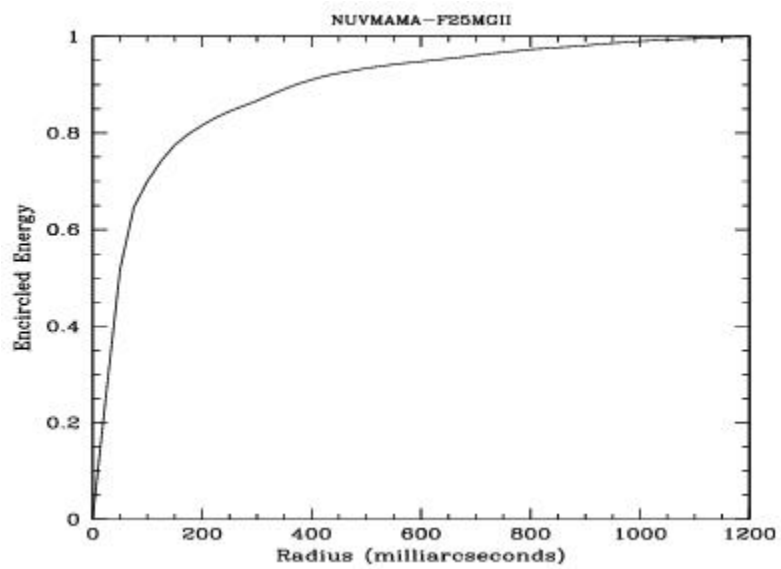
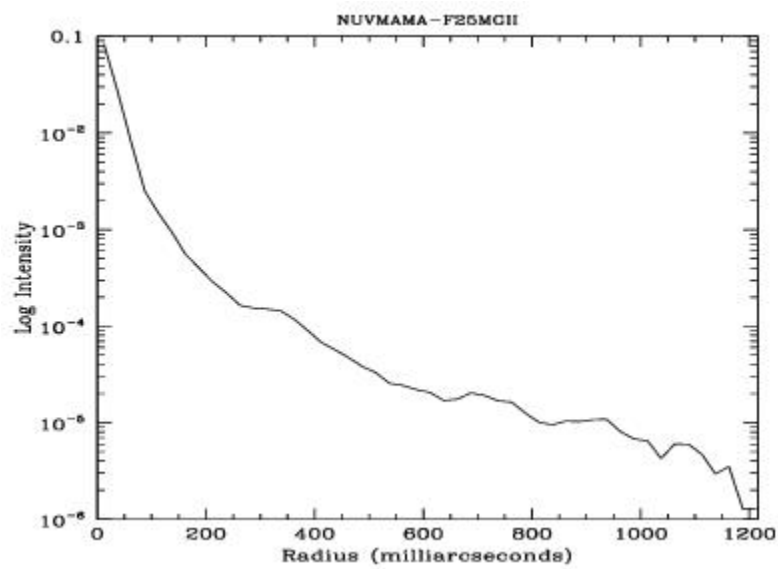


Figure 14.49: Point Source Intensity vs. Radius for F25MGII NUV-MAMA



F25CN270 - NUV-MAMA

Description

The F25CN270 filter with the NUV-MAMA provides medium bandwidth imaging near the Mg II 2798 Å feature.

Recommended Uses

This filter is recommended for imaging Mg II 2798 Å line emission and its local continuum.

Special Considerations

There is a substantial red leak in this filter. Sources with a red underlying continuum may be difficult to observe. Users should be careful to take into account the underlying continuum in estimating whether the observation will fall within the bright object protection limits.

| Pivot λ (Å) | FWHM (Å) | AB mag zero point | S_{peak} | B_{λ} | R_{80} (arcsec) | Flux in central pixel |
|---------------------|----------|-------------------|-------------------|---------------|-------------------|-----------------------|
| 2710.9 | 161.8 | 21.360 | 1.17e+14 | 202.3 | 0.17 | 14% |

Figure 14.50: F25CN270 NUV-MAMA Integrated System Throughput and Red Leak

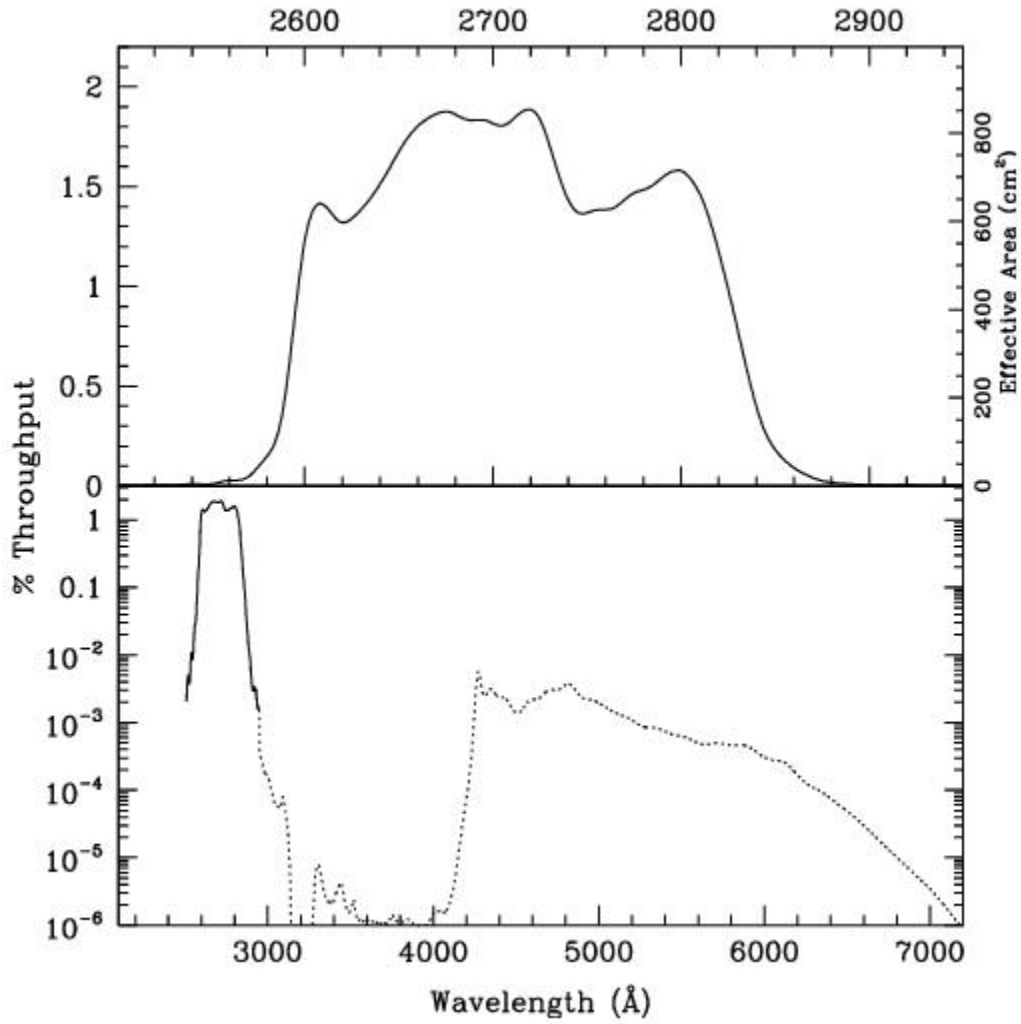


Table 14.20: F25CN270 NUV-MAMA Sensitivity & Throughput

| λ | Sensitivity | % Throughput |
|-----------|-------------|--------------|
| 2575. | 6.70E12 | 0.11 |
| 2600. | 6.37E13 | 1.08 |
| 2625. | 8.19E13 | 1.37 |
| 2650. | 1.01E14 | 1.67 |
| 2675. | 1.13E14 | 1.86 |
| 2700. | 1.12E14 | 1.82 |

| | | |
|-------|---------|------|
| 2725. | 1.10E14 | 1.77 |
| 2750. | 8.70E13 | 1.39 |
| 2775. | 9.22E13 | 1.46 |
| 2800. | 9.81E13 | 1.54 |
| 2825. | 6.27E13 | 0.97 |
| 2850. | 1.40E13 | 0.21 |

Figure 14.51: Point Source S/N vs. AB magnitude in the V-band for the F25CN270 NUV-MAMA mode. Curves are labeled by required exposure time (seconds).

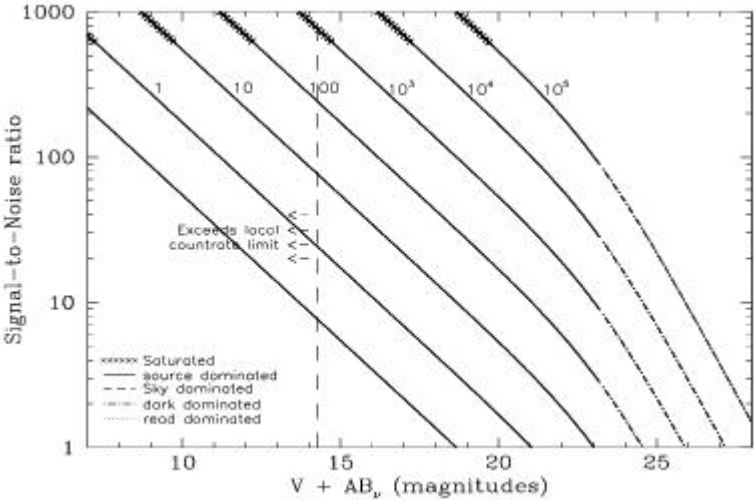


Figure 14.52: Extended Source S/N vs. AB magnitude in the V-band for the F25CN270 NUV-MAMA mode. Top curves are for an area of 0.2 arcsec²; bottom curves are for 1 arcsec². Average sky assumed. Curves are labeled by required exposure time (seconds).

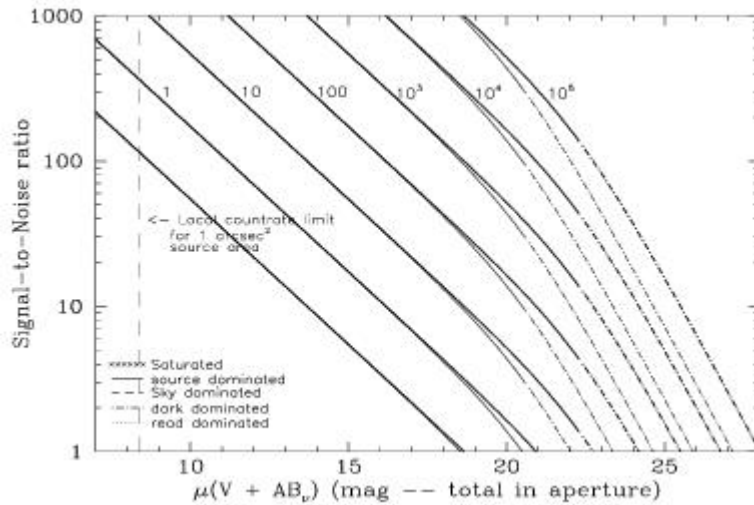


Table 14.21: Radial Profile for F25CN270*

| Radius | | Intensity | Fraction of Energy Encircled |
|--------|--------|-----------|------------------------------|
| Pixels | Arcsec | | |
| 1 | 0.024 | 5.158e-02 | 0.240 |
| 1.5 | 0.037 | 2.953e-02 | 0.378 |
| 2 | 0.049 | 1.608e-02 | 0.504 |
| 3 | 0.073 | 5.260e-03 | 0.643 |
| 4 | 0.098 | 2.022e-03 | 0.708 |
| 5 | 0.122 | 1.215e-03 | 0.750 |
| 10 | 0.245 | 2.048e-04 | 0.854 |
| 15 | 0.367 | 9.848e-05 | 0.908 |
| 20 | 0.490 | 4.138e-05 | 0.942 |
| 25 | 0.613 | 1.817e-05 | 0.960 |
| 30 | 0.735 | 1.440e-05 | 0.974 |
| 40 | 0.980 | 4.656e-06 | 0.994 |

* See [STIS ISR 2003-01](#).

Figure 14.53: Point Source Encircled Energy for F25CN270 NUV-MAMA

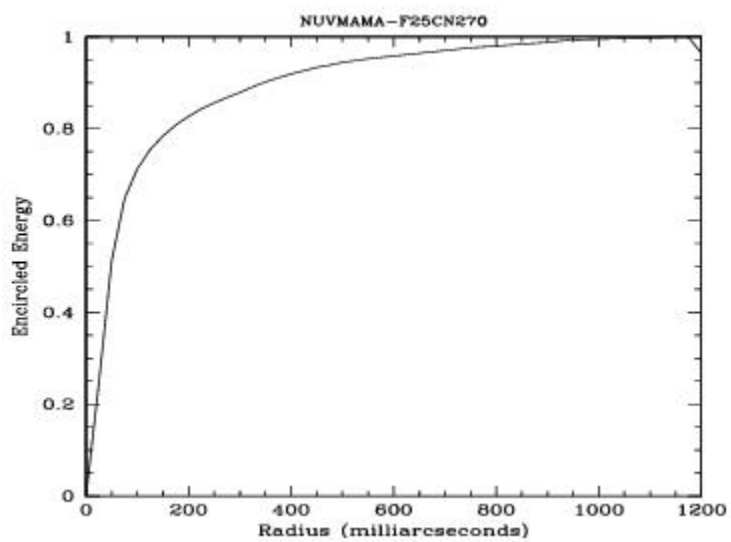
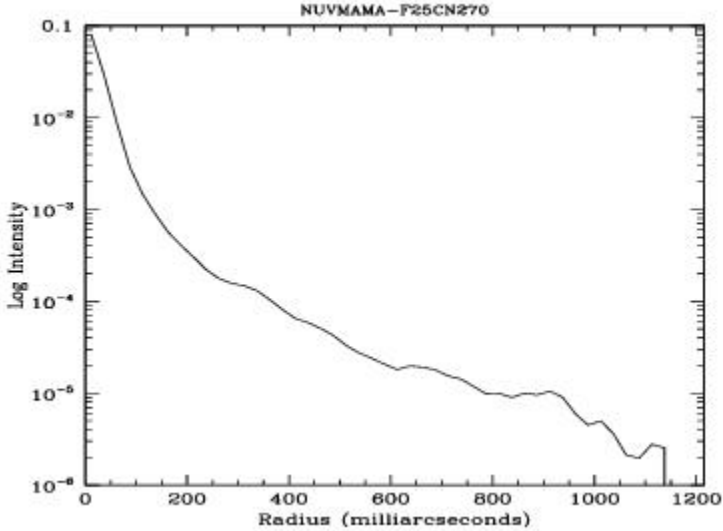


Figure 14.54: Point Source Intensity vs. Radius for F25CN270 NUV-MAMA



F25CIII - NUV-MAMA

Description

The F25CIII filter with the NUV-MAMA provides narrow-band imaging of the C III] 1907 + 1909 Å feature.

Recommended Uses

This filter is recommended for narrow-band imaging of the C III] 1907, 1909 Å features.

| Pivot λ (Å) | FWHM (Å) | AB mag zero point | S_{peak} | B_{λ} | R_{80} (arcsec) | Flux in central pixel |
|---------------------|----------|-------------------|-------------------|---------------|-------------------|-----------------------|
| 2011.0 | 389.3 | 19.371 | 1.01e+13 | 205.6 | 0.23 | 10% |

Figure 14.55: F25CIII NUV-MAMA Integrated System Throughput and Redleak

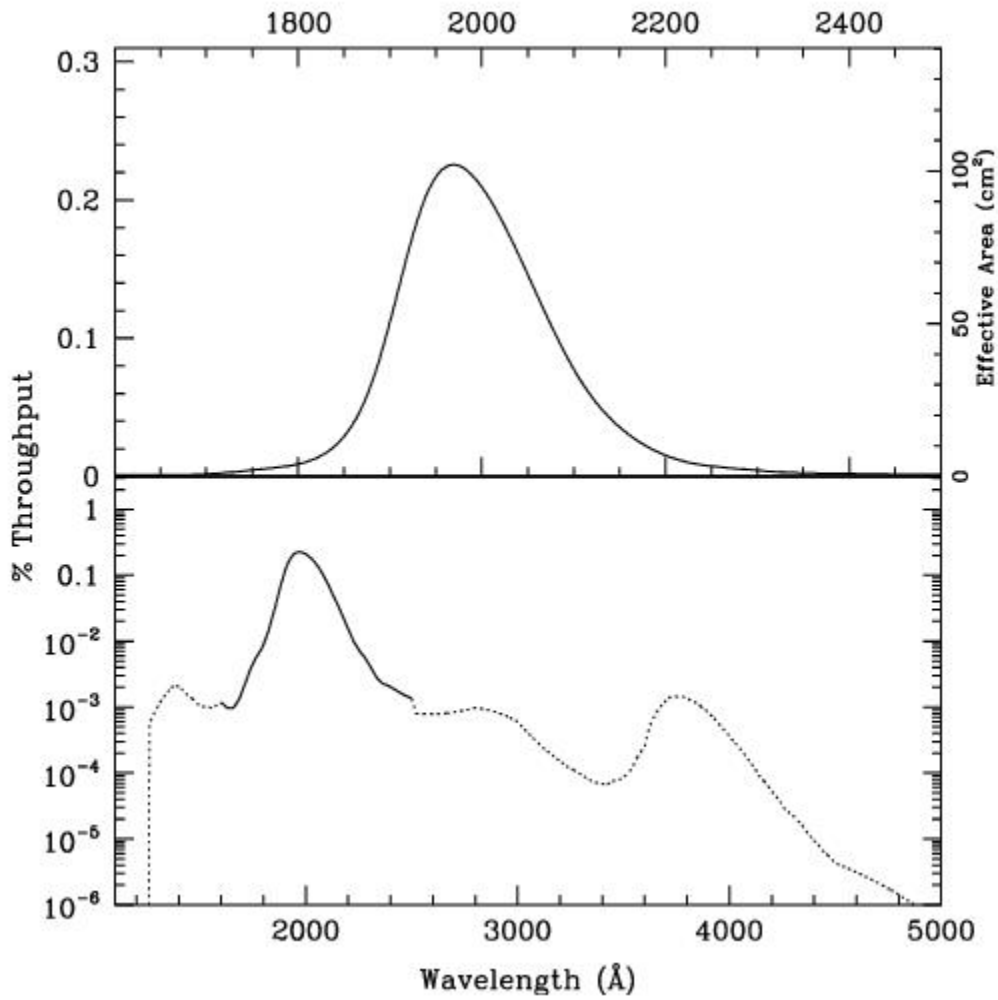


Table 14.22: F25CIII NUV-MAMA Sensitivity & Throughput

| λ | Sensitivity | % Throughput |
|-----------|-------------|--------------|
| 1750. | 1.82E11 | 0.00 |
| 1800. | 3.89E11 | 0.01 |
| 1850. | 1.33E12 | 0.03 |
| 1900. | 4.91E12 | 0.11 |
| 1950. | 9.37E12 | 0.21 |
| 2000. | 9.44E12 | 0.21 |
| 2050. | 6.81E12 | 0.15 |

| | | |
|-------|---------|------|
| 2100. | 3.78E12 | 0.08 |
| 2150. | 1.79E12 | 0.04 |
| 2200. | 7.92E11 | 0.02 |
| 2250. | 3.89E11 | 0.01 |

Figure 14.56: Point Source S/N vs. total line flux for the F25CIII NUV-MAMA mode. Curves are labeled by required exposure time (seconds).

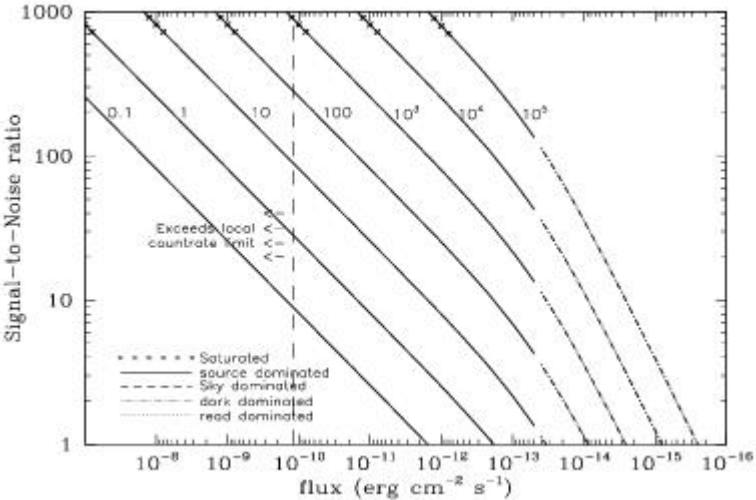


Figure 14.57: Extended Source S/N vs. total line flux for the F25CIII NUV-MAMA mode. Top curves are for an area of 0.2 arcsec²; bottom curves are for 1 arcsec². Average sky assumed. Curves are labeled by required exposure time (seconds).

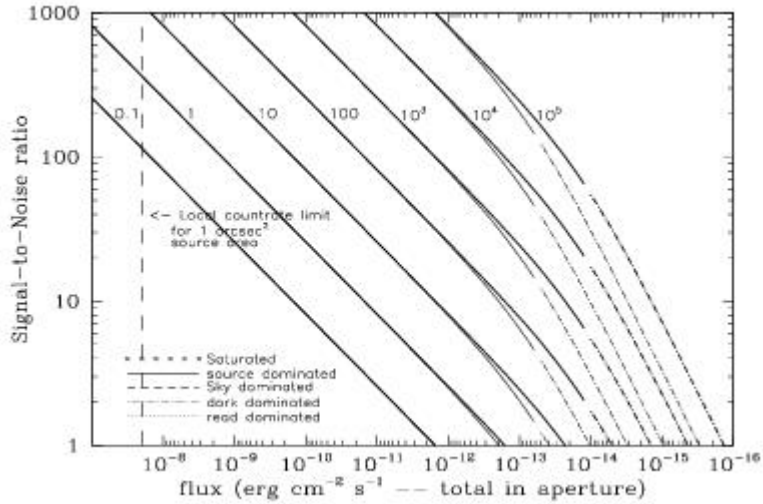


Table 14.23: Radial Profile for F25CIII (see [STIS ISR 2003-01.](#))

| Radius | | Intensity | Fraction of Energy Encircled |
|--------|--------|-----------|------------------------------|
| Pixels | Arcsec | | |
| 1 | 0.024 | 4.859e-02 | 0.173 |
| 1.5 | 0.037 | 3.660e-02 | 0.284 |
| 2 | 0.049 | 2.557e-02 | 0.392 |
| 3 | 0.073 | 9.899e-03 | 0.528 |
| 4 | 0.098 | 3.609e-03 | 0.598 |
| 5 | 0.122 | 1.832e-03 | 0.649 |
| 10 | 0.245 | 2.759e-04 | 0.753 |
| 15 | 0.367 | 1.339e-04 | 0.822 |
| 20 | 0.490 | 7.056e-05 | 0.873 |
| 25 | 0.613 | 4.358e-05 | 0.911 |
| 30 | 0.735 | 3.353e-05 | 0.944 |
| 40 | 0.980 | 1.002e-05 | 0.981 |

Figure 14.58: Point Source PSF for F25CIII NUV-MAMA, 7."5 square (at pixel 741,402, log scaled, B-V=-0.04). Note PSF ghost ~45 pixels left of peak and a few 10^{-3} of the peak

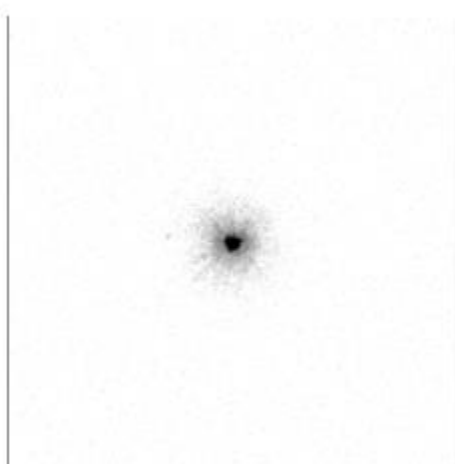


Figure 14.59: Point Source Encircled Energy for F25CIII NUV-MAMA

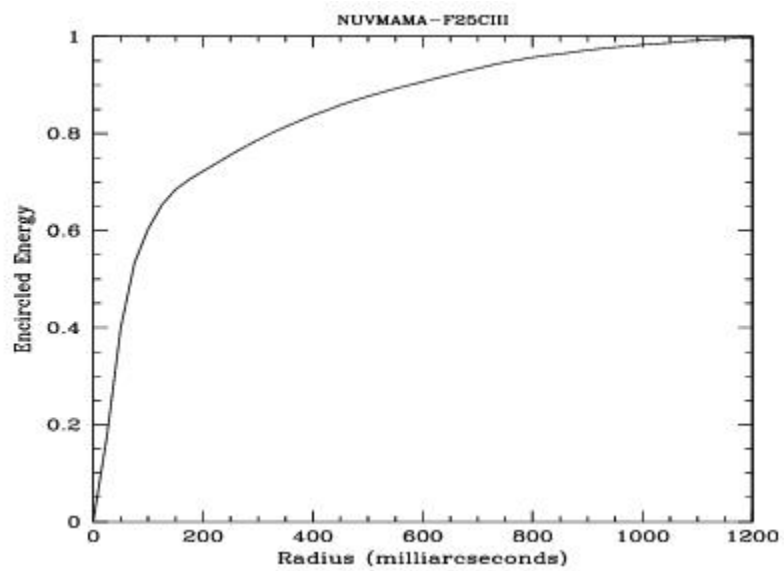
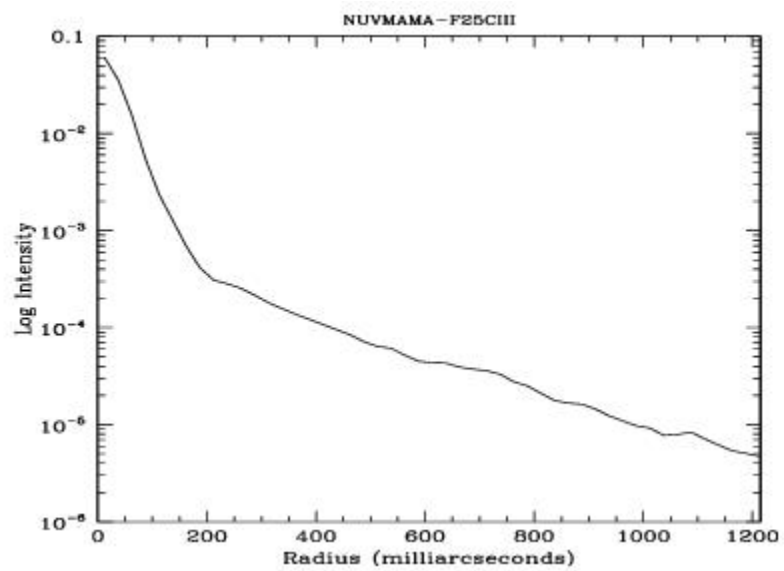


Figure 14.60: Point Source Intensity vs. Radius for F25CIII NUV-MAMA



F25CN182 - NUV-MAMA

Description

The F25CN182 filter with the NUV-MAMA provides medium bandwidth imaging of the continuum near 1900 Å.

Recommended Uses

This filter is recommended for medium-band imaging of line and continuum emission in the vicinity of 1900 Å.

| Pivot λ (Å) | FWHM (Å) | AB mag zero point | S_{peak} | B_{λ} | R_{80} (arcsec) | Flux in central pixel |
|---------------------|----------|-------------------|-------------------|---------------|-------------------|-----------------------|
| 2004.5 | 677.9 | 21.558 | 2.42e+13 | 641.6 | 0.23 | 10% |

Figure 14.61: F25CN182 NUV-MAMA Integrated System Throughput and Redleak

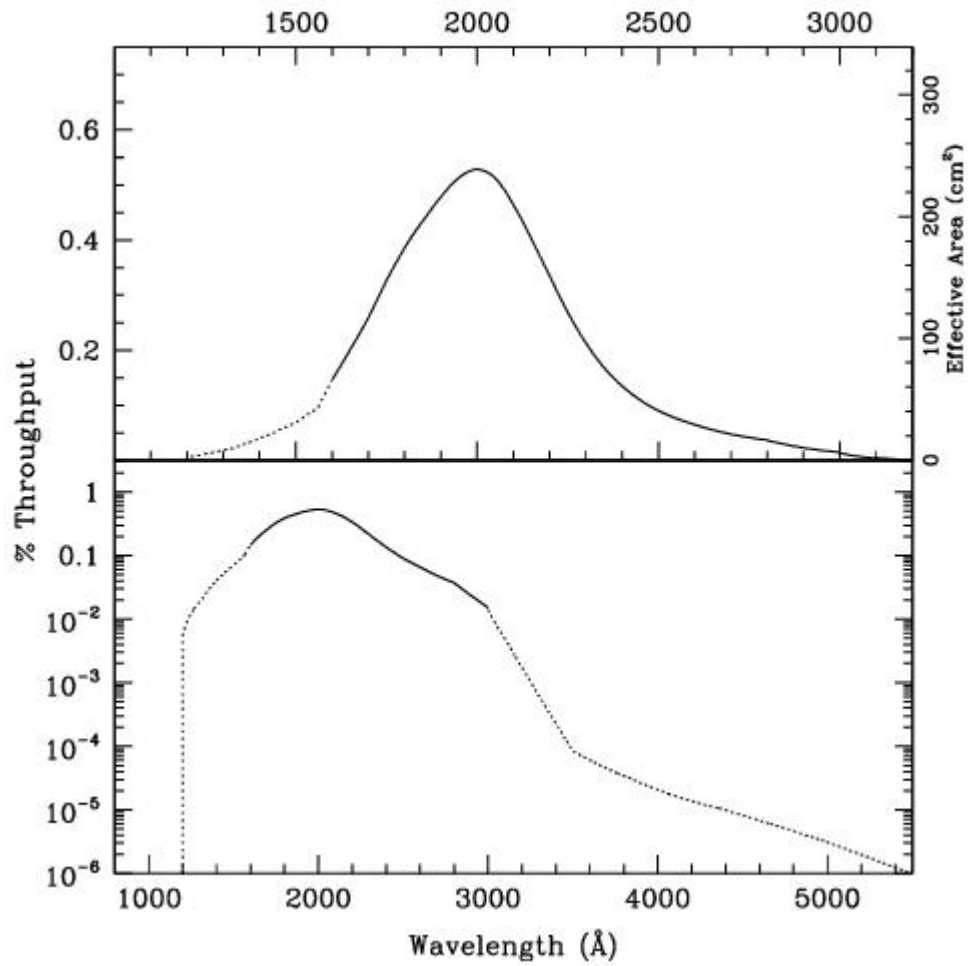


Table 14.24: F25CN182 NUV-MAMA Sensitivity & Throughput

| λ | Sensitivity | % Throughput |
|-----------|-------------|--------------|
| 1300. | 5.7E11 | 0.02 |
| 1400. | 1.29E12 | 0.04 |
| 1500. | 2.43E12 | 0.07 |
| 1600. | 5.26E12 | 0.14 |
| 1700. | 1.01E13 | 0.26 |
| 1800. | 1.57E13 | 0.38 |
| 1900. | 2.06E13 | 0.48 |

| | | |
|-------|---------|------|
| 2000. | 2.38E13 | 0.52 |
| 2100. | 2.21E13 | 0.46 |
| 2200. | 1.68E13 | 0.34 |
| 2300. | 1.13E13 | 0.22 |
| 2400. | 7.47E12 | 0.14 |
| 2500. | 5.21E12 | 0.09 |
| 2600. | 3.89E12 | 0.07 |
| 2700. | 2.98E12 | 0.05 |
| 2800. | 2.32E12 | 0.04 |

Figure 14.62: Point Source S/N vs. AB magnitude in the V-band for the F25CN182 NUV-MAMA mode. Curves are labeled by required exposure time (seconds).

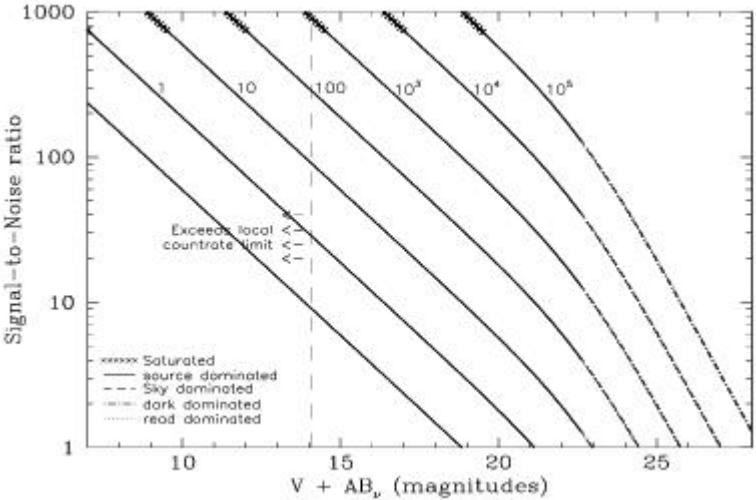


Figure 14.63: Extended Source S/N vs. AB magnitude in the V-band for the F25CN182 NUV-MAMA mode. Top curves are for an area of 0.2 arcsec²; bottom curves are for 1 arcsec². Average sky assumed Curves are labeled by required exposure time (seconds).

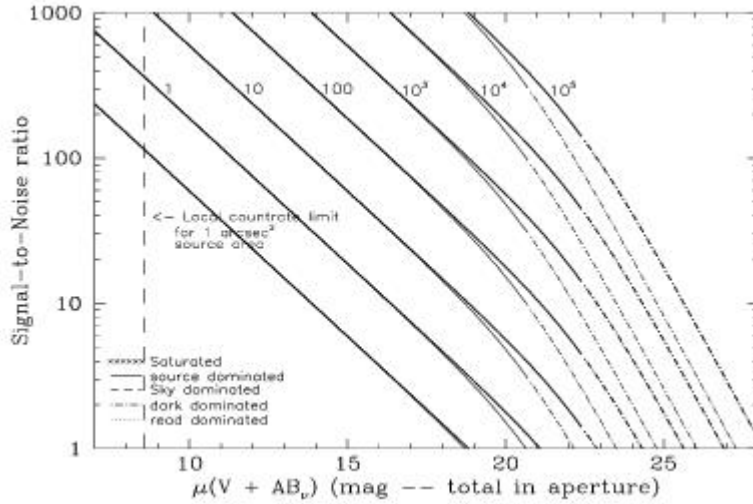


Table 14.25: Radial Profile for F25CN182*

| Radius | | Intensity | Fraction of Energy Encircled |
|--------|--------|-----------|------------------------------|
| Pixels | Arcsec | | |
| 1 | 0.024 | 4.177e-02 | 0.179 |
| 1.5 | 0.037 | 2.686e-02 | 0.302 |
| 2 | 0.049 | 1.620e-02 | 0.422 |
| 3 | 0.073 | 5.757e-03 | 0.565 |
| 4 | 0.098 | 2.720e-03 | 0.647 |
| 5 | 0.122 | 1.425e-03 | 0.700 |
| 10 | 0.245 | 2.600e-04 | 0.810 |
| 15 | 0.367 | 1.234e-04 | 0.876 |
| 20 | 0.490 | 6.357e-05 | 0.925 |
| 25 | 0.613 | 3.483e-05 | 0.956 |
| 30 | 0.735 | 2.099e-05 | 0.979 |
| 40 | 0.980 | 2.113e-06 | 0.999 |

* See [STIS ISR 2003-01](#).

Figure 14.64: Point Source Encircled Energy for F25CN182 NUV-MAMA

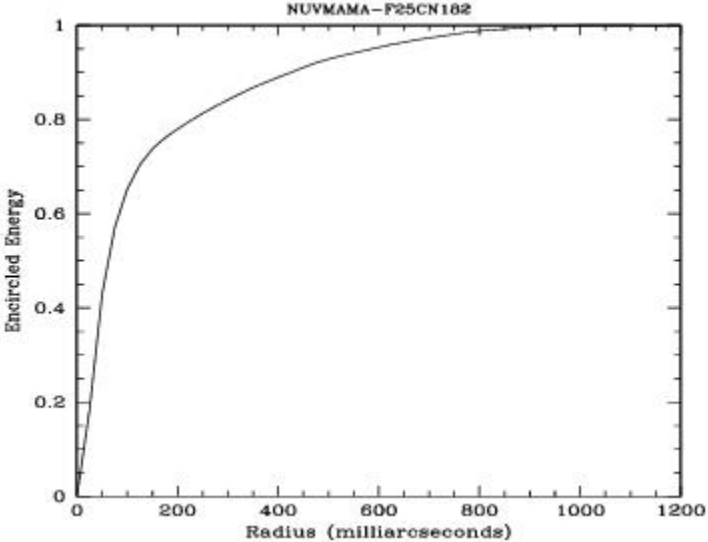
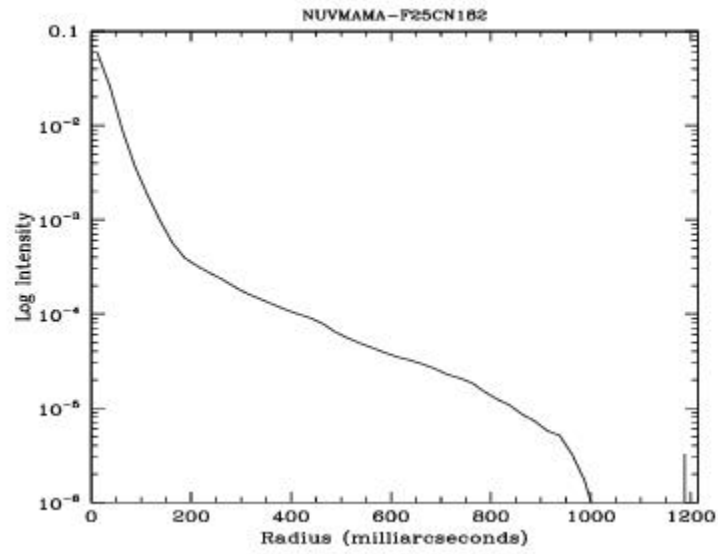


Figure 14.65: Point Source Intensity vs. Radius for F25CN182 NUV-MAMA



14.5 FUV-MAMA

This section provides the basic properties of the filters available for use with the `FUV-MAMA` detector. The field of view of the FUV-MAMA is 25 arcsec × 25 arcsec, unless otherwise stated. The FUV imaging sensitivity has been decreasing with time, with a time dependence very similar to that seen for the `G140L` mode (see [Figure 7.15](#)). Note that the sensitivities given are projected values for August 2008.

Users may also want to consider whether the ACS SBC detector might be better for their observing program. The SBC has a slightly larger field-of-view, a wider selection of filters, and better throughput at most wavelengths.

- [Section 25MAMA—FUV-MAMA Clear](#)
- [Section 25MAMAD1—FUV-MAMA Pseudo-Aperture](#)
- [Section F25ND3—FUV-MAMA](#)
- [Section F25ND5—FUV-MAMA](#)
- [Section F25NDQ - FUV-MAMA](#)
- [Section F25QTZ—FUV-MAMA, Longpass](#)
- [Section F25QTZD1—FUV-MAMA, Longpass Pseudo-Aperture](#)
- [Section F25SRF2—FUV-MAMA, Longpass](#)
- [Section F25SRF2D1—FUV-MAMA, Longpass Pseudo-Aperture](#)
- [Section F25LYA—FUV-MAMA, Lyman- \$\alpha\$](#)

25MAMA - FUV-MAMA, Clear

Description

The 25MAMA mode with the FUV-MAMA detector provides high-throughput broad-band far-ultraviolet (FUV) imaging with the highest available throughput at $\sim 1500 \text{ \AA}$ and the highest possible spatial resolution.

Recommended Uses

This filter is recommended for FUV imaging of sources for which sky background is not a consideration.

Special Considerations

For long exposures of faint targets, sky background is likely to be a limiting factor. Observers should consider the use of DARKTIME or (preferably) use the F25Q1Z filter, which has nearly the same throughput but rejects geocoronal Lyman- α and O I 1302 \AA triplet air glow.

Users may also want to consider whether the ACS SBC detector might be better for their observing program.

| Pivot λ (\AA) | FWHM (\AA) | AB mag zero point | S_{peak} | B_{λ} | R_{80} (arcsec) | Flux in central pixel |
|----------------------------------|-----------------------|-------------------|-------------------|---------------|-------------------|-----------------------|
| 1367.5 | 316.5 | 23.457 | 1.21e+14 | 341.9 | 0.32 | 8% |

Figure 14.66: 25MAMA FUV-MAMA Integrated System Throughput and Redleak

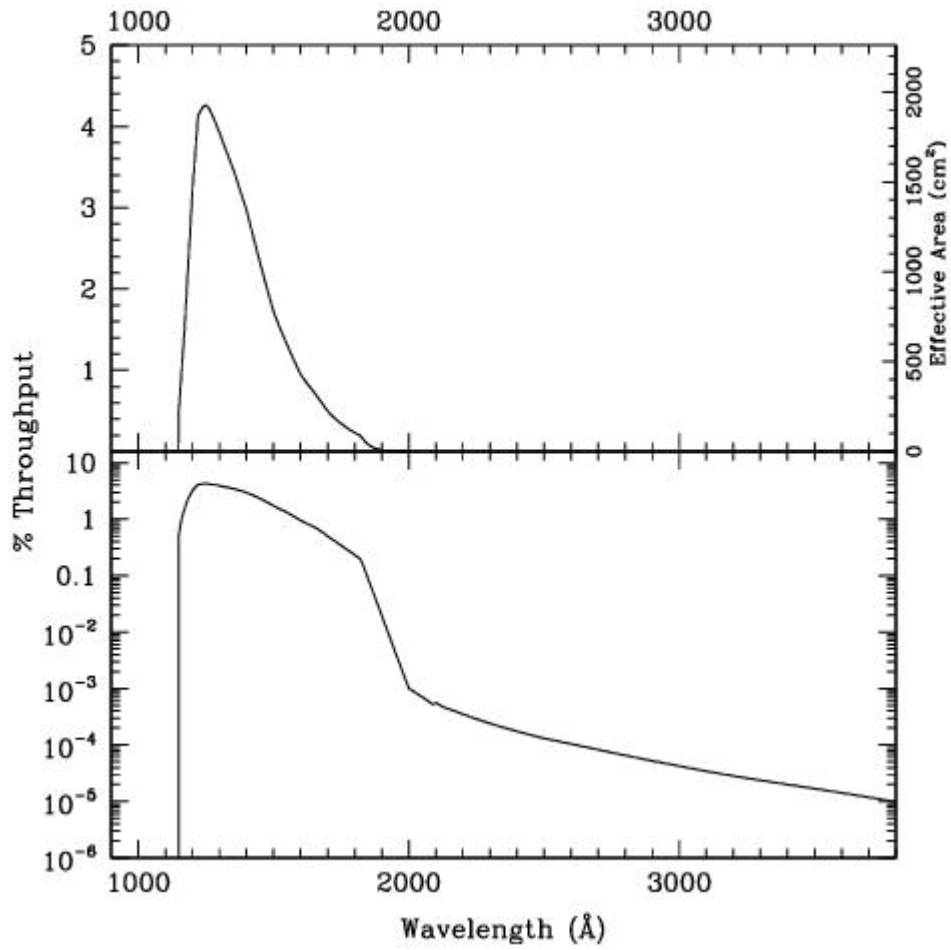


Table 14.26: 25MAMA FUV-MAMA Sensitivity & Throughput

| λ | Sensitivity | % Throughput |
|-----------|-------------|--------------|
| 1150. | 1.08E13 | 0.41 |
| 1175. | 4.69E13 | 1.75 |
| 1200. | 8.61E13 | 3.15 |
| 1225. | 1.15E14 | 4.11 |
| 1250. | 1.21E14 | 4.24 |
| 1275. | 1.20E14 | 4.12 |
| 1300. | 1.16E14 | 3.92 |

| | | |
|-------|---------|------|
| 1325. | 1.12E14 | 3.70 |
| 1350. | 1.07E14 | 3.48 |
| 1375. | 1.01E14 | 3.23 |
| 1400. | 9.44E13 | 2.96 |
| 1425. | 8.58E13 | 2.64 |
| 1450. | 7.68E13 | 2.32 |
| 1475. | 6.77E13 | 2.02 |
| 1500. | 5.92E13 | 1.73 |
| 1525. | 5.24E13 | 1.51 |
| 1550. | 4.64E13 | 1.31 |
| 1575. | 4.04E13 | 1.13 |
| 1600. | 3.49E13 | 0.96 |
| 1625. | 3.08E13 | 0.83 |
| 1650. | 2.74E13 | 0.73 |
| 1675. | 2.34E13 | 0.61 |
| 1700. | 1.94E13 | 0.50 |
| 1725. | 1.63E13 | 0.41 |
| 1750. | 1.37E13 | 0.34 |
| 1775. | 1.14E13 | 0.28 |
| 1800. | 9.55E12 | 0.23 |
| 1825. | 7.29E12 | 0.18 |
| 1850. | 3.76E12 | 0.09 |

Figure 14.67: Point Source S/N vs. AB magnitude in the V-band for the 25MAMA FUV-MAMA mode. Curves are labeled by required exposure time (seconds).

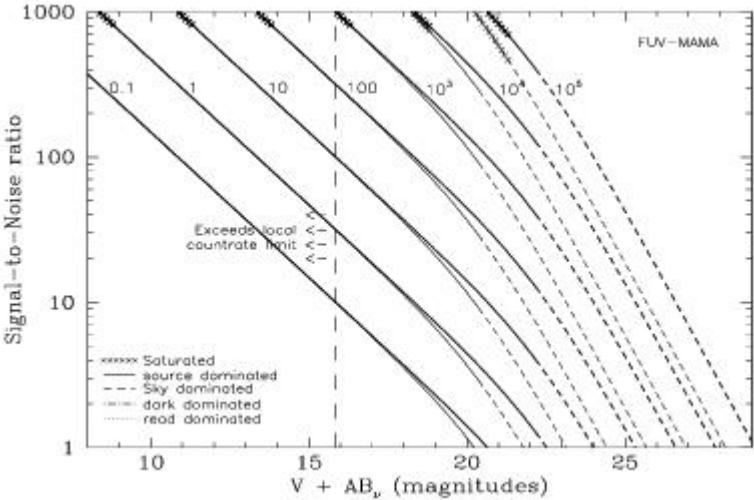


Figure 14.68: Extended Source S/N vs. AB magnitude in the V-band for the 25MAMA FUV-MAMA mode. Top curves are for an area of 0.2 arcsec²; bottom curves are for 1 arcsec². Average sky assumed. Curves are labeled by required exposure time (seconds).

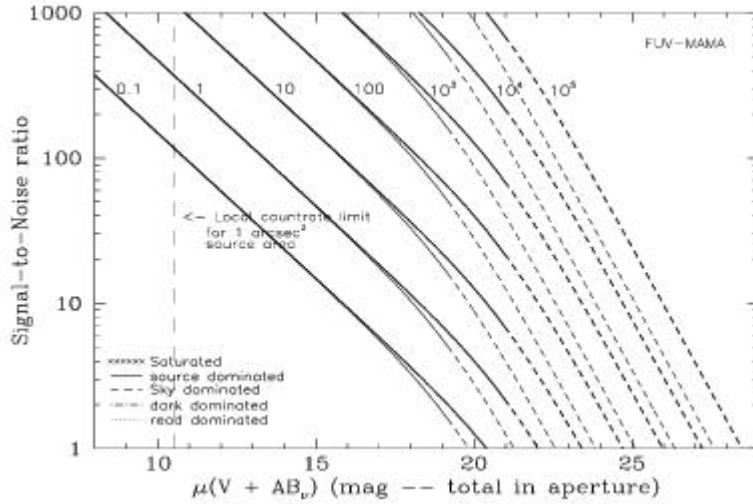


Table 14.27: Radial Profile for 25MAMA*

| Radius | | Intensity | Fraction of Energy Encircled |
|--------|--------|-----------|------------------------------|
| Pixels | Arcsec | | |
| 1 | 0.024 | 3.267e-02 | 0.141 |
| 1.5 | 0.037 | 2.107e-02 | 0.236 |
| 2 | 0.049 | 1.345e-02 | 0.331 |
| 3 | 0.073 | 6.141e-03 | 0.467 |
| 4 | 0.098 | 2.981e-03 | 0.557 |
| 5 | 0.122 | 1.485e-03 | 0.614 |
| 10 | 0.245 | 3.377e-04 | 0.746 |
| 15 | 0.367 | 1.676e-04 | 0.834 |
| 20 | 0.490 | 9.542e-05 | 0.900 |
| 25 | 0.613 | 4.543e-05 | 0.947 |
| 30 | 0.735 | 2.065e-05 | 0.972 |
| 40 | 0.980 | 5.088e-06 | 0.994 |

* See [STIS ISR 2003-01](#).

Figure 14.69: Point Source Encircled Energy for 25MAMA FUV-MAMA

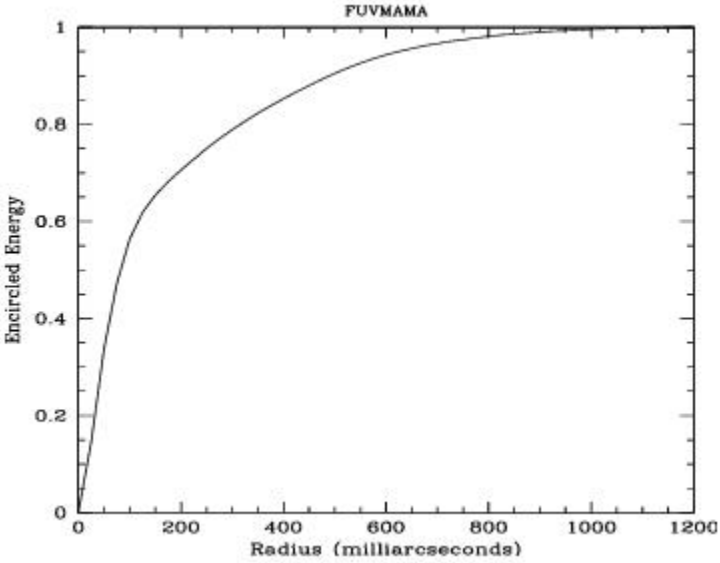
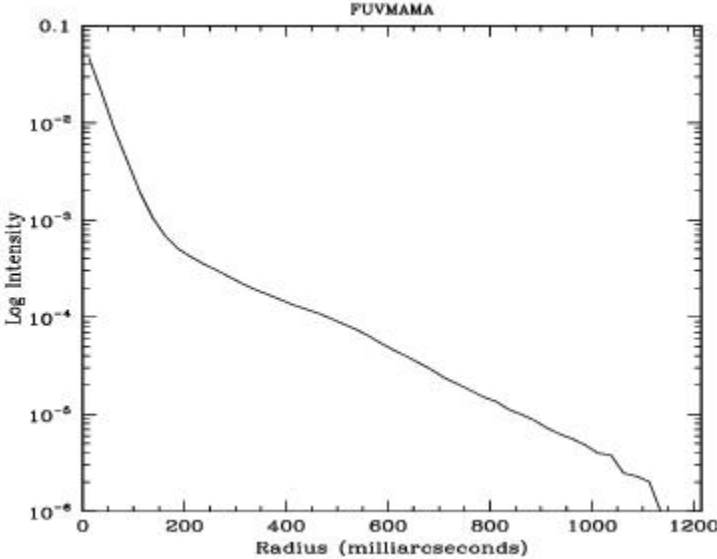


Figure 14.70: Point Source Intensity vs. Radius for 25MAMA FUV-MAMA



25MAMAD1 - FUV-MAMA Pseudo-Aperture

Description

The 25MAMAD1 filter is intended to be used for spectroscopic observations with the G140L and G140M gratings. Although it is the same optical element as 25MAMA, it should be used when the target has been offset to the D1 position, away from the region of amplifier "glow" in the FUV-MAMA to minimize the contribution from the dark current when observing very faint targets. This aperture moves the target 2 arcseconds above the bottom edge of the FUV-MAMA to avoid the detector glow region. It is yet to be determined if the throughput for a target at this position is significantly different from that obtained at the standard position.

Special Considerations

Refer to [Section 25MAMA—FUV-MAMA Clear](#) for information concerning the properties of the 25MAMAD1 filter. Note that it can only be used with the G140L and G140M gratings.

F25ND3 - FUV-MAMA

Description

The F25ND3 mode with the FUV-MAMA detector provides broad-band imaging with an attenuation of 10^{-3} . The R_{80} and central pixel flux are unmeasured but assumed to be approximately the same as produced by the F25QIZ filter.

Recommended Uses

This filter is recommended for broad-band imaging of objects that require attenuation by a factor of 10^3 to meet the FUV-MAMA bright object protection limits.

| Pivot λ (Å) | FWHM (Å) | AB mag zero point | S_{peak} | B_{λ} | R_{80} (arcsec) | Flux in central pixel |
|---------------------|----------|-------------------|-------------------|---------------|-------------------|-----------------------|
| 1376.0 | 316.2 | 16.070 | 1.26e+11 | 368.9 | 0.28 | 10% |

Figure 14.71: F25ND3 FUV-MAMA Integrated System Throughput and Redleak

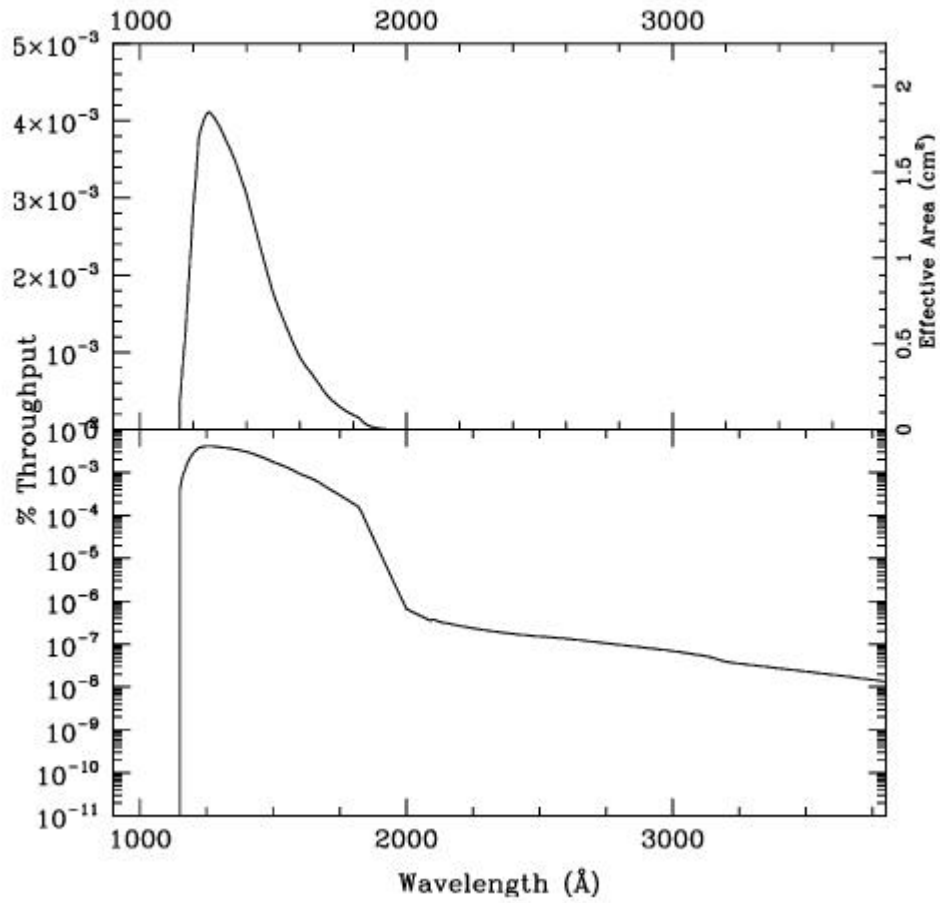


Table 14.28: Throughputs and Sensitivities for F25ND3 FUV-MAMA

| λ | Sensitivity | % Throughput |
|-----------|-------------|--------------|
| 1150. | 1.00E10 | 3.8E-4 |
| 1200. | 7.62E10 | 2.8E-3 |
| 1250. | 1.15E11 | 4.0E-3 |
| 1300. | 1.16E11 | 3.9E-3 |
| 1350. | 1.08E11 | 3.5E-3 |
| 1400. | 9.64E10 | 3.0E-3 |
| 1450. | 7.88E10 | 2.4E-3 |

| | | |
|-------|---------|--------|
| 1500. | 6.09E10 | 1.8E-3 |
| 1550. | 4.68E10 | 1.3E-3 |
| 1600. | 3.46E10 | 9.5E-4 |
| 1650. | 2.61E10 | 6.9E-4 |
| 1700. | 1.79E10 | 4.6E-4 |
| 1750. | 1.19E10 | 3.0E-4 |
| 1800. | 7.84E9 | 1.9E-4 |
| 1850. | 3.11E9 | 7.4E-5 |

Figure 14.72: Point Source S/N vs. AB magnitude in the V-band for the F25ND3 FUV-MAMA mode. Curves are labeled by required exposure time (seconds).

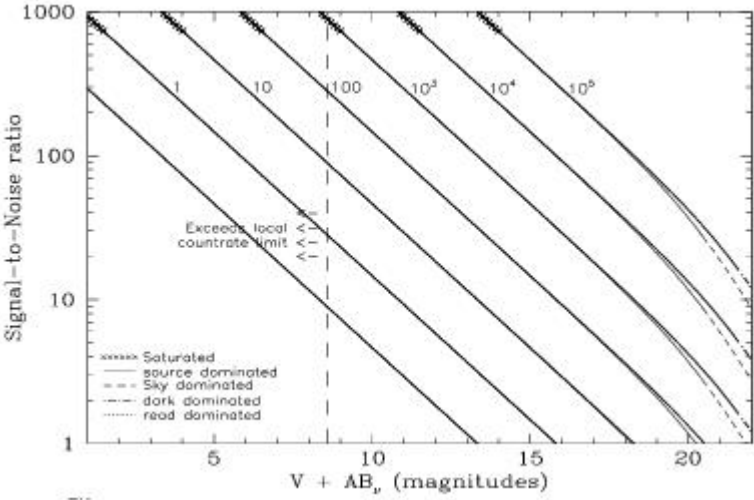
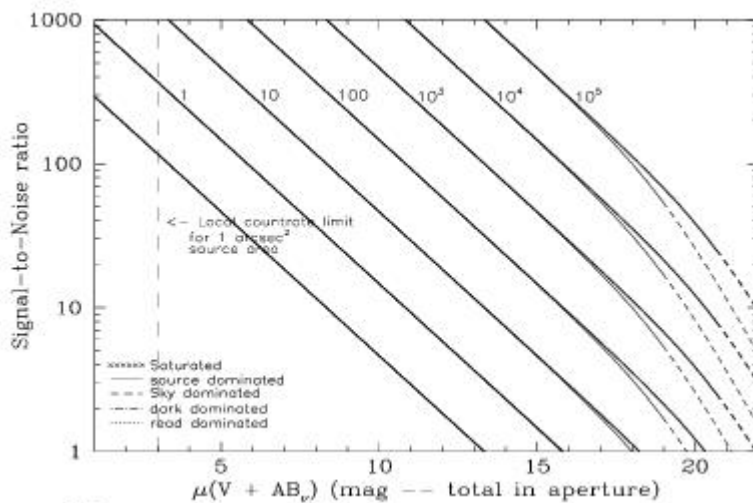


Figure 14.73: Extended Source S/N vs. AB magnitude in the V-band for the F25ND3 FUV-MAMA mode. Top curves are for an area of 0.2 arcsec²; bottom curves are for 1 arcsec². Average sky assumed. Curves are labeled by required exposure time (seconds).



F25ND5 - FUV-MAMA

Description

The F25ND5 mode with the FUV-MAMA detector provides broad-band imaging with an attenuation of 7×10^{-7} . The R_{80} and central pixel flux are unmeasured but assumed to be approximately the same as produced by the F25Q1Z filter.

Recommended Uses

This filter is recommended for broad-band imaging of objects that are brighter than the FUV-MAMA BOP limits by a factor of 1.4E6.

Special Considerations

At FUV wavelengths the attenuation is closer to a factor of 10^6 rather than the nominal 10^5 , but the attenuation factor decreases at longer wavelengths, so special care should be taken for red sources. To make an accurate prediction of the expected count rate, observers should use a good approximation of the source spectrum as input for the [STIS ETC](#).

| Pivot λ (Å) | FWHM (Å) | AB mag zero point | S_{peak} | B_{λ} | R_{80} (arcsec) | Flux in central pixel |
|---------------------|----------|-------------------|-------------------|---------------|-------------------|-----------------------|
| 1385.1 | 333.6 | 8.188 | 8.81e7 | 377.2 | 0.28 | 10% |

Figure 14.74: F25ND5 FUV-MAMA Integrated System Throughput and Redleak

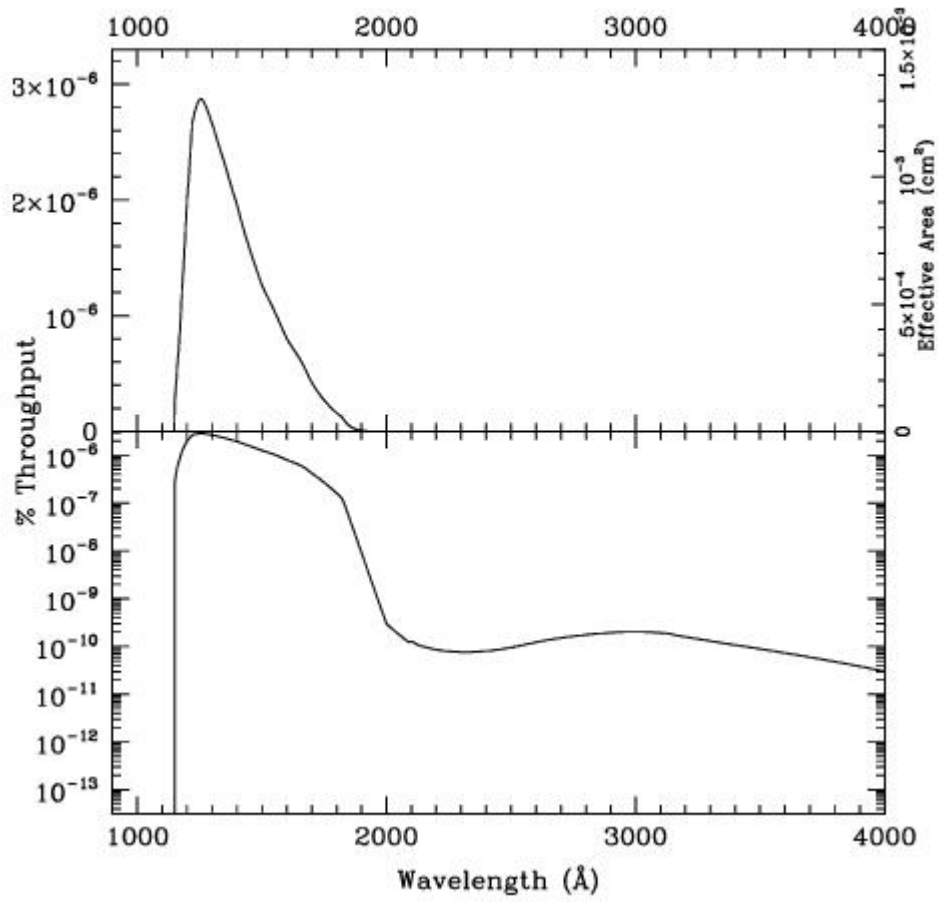


Table 14.29: Throughput and Sensitivity for F25ND5 FUV-MAMA

| λ | Sensitivity | % Throughput |
|-----------|-------------|--------------|
| 1150. | 6.52E6 | 2.5E-7 |
| 1200. | 5.34E7 | 2.0E-6 |
| 1250. | 8.05E7 | 2.8E-6 |
| 1300. | 7.87E7 | 2.7E-6 |
| 1350. | 7.11E7 | 2.3E-6 |
| 1400. | 6.22E7 | 2.0E-6 |
| 1450. | 5.23E7 | 1.6E-6 |

| | | |
|-------|--------|--------|
| 1500. | 4.36E7 | 1.3E-6 |
| 1550. | 3.67E7 | 1.0E-6 |
| 1600. | 2.95E7 | 8.1E-7 |
| 1650. | 2.37E7 | 6.3E-7 |
| 1700. | 1.66E7 | 4.3E-7 |
| 1750. | 1.09E7 | 2.7E-7 |
| 1800. | 6.65E6 | 1.6E-7 |
| 1850. | 2.38E6 | 5.6E-8 |

Figure 14.75: Point Source S/N vs. AB magnitude in the V-band for the F25ND5 FUV-MAMA mode. Curves are labeled by required exposure time (seconds).

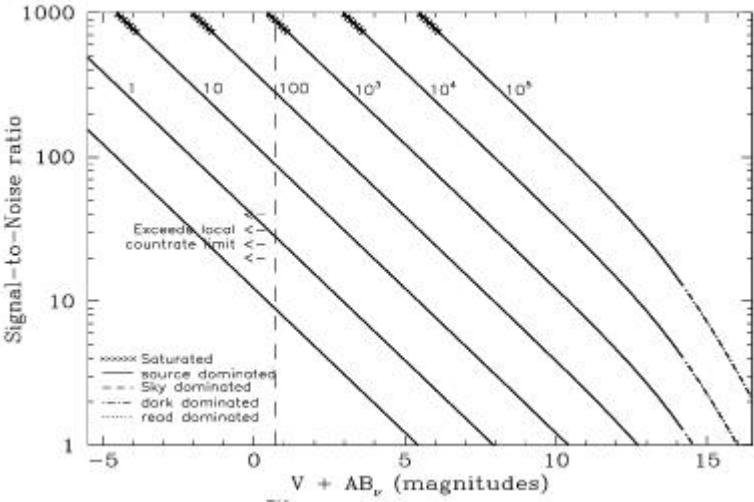
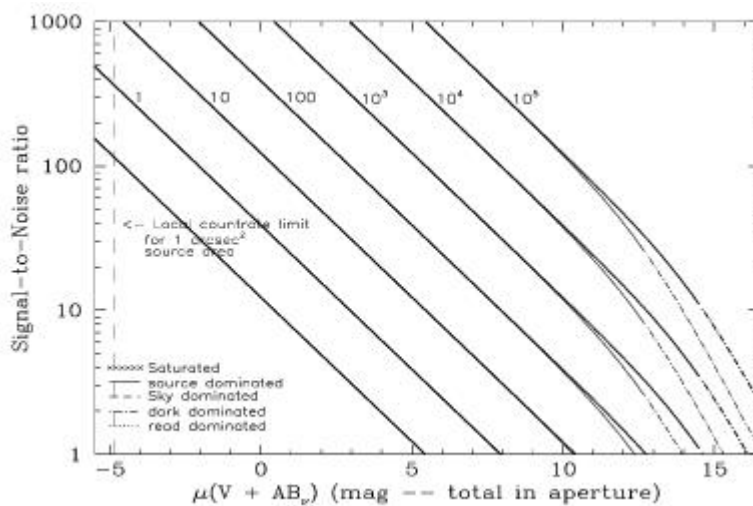


Figure 14.76: Extended Source S/N vs. AB magnitude in the V-band for the F25ND5 FUV-MAMA mode. Top curves are for an area of 0.2 arcsec²; bottom curves are for 1 arcsec². Average sky assumed. Curves are labeled by required exposure time (seconds).



F25NDQ - FUV-MAMA

Description

The **F25NDQ** mode with the **FUV-MAMA** detector provides broad-band imaging with attenuation factors that vary between 10^{-1} and 10^{-4} . The full field of view is 25 arcsec \times 25 arcsec, but the **F25NDQ** filter is unique in that it is divided into four quadrants, each having a different neutral density factor. Thus, the field of view for each quadrant is 12 arcsec \times 12 arcsec. In clockwise order starting from the upper left these are **F25NDQ1**, **F25NDQ2**, **F25NDQ3**, and **F25NDQ4**, where the number appended to each name is the approximate dex ND factor. The R_{80} and central pixel flux are unmeasured but assumed to be approximately the same as produced by the **F25SRF2** filter. Approximate dimensions of each quadrant and the default target location in each quadrant are given in [Table 14.30](#).

Recommended Uses

This filter is recommended for broad-band imaging of objects that are brighter than the **FUV-MAMA** BOP limits by factors between 10 and 10^4 .

Special Considerations

If a target violates BOP restrictions in any quadrant of the **F25NDQ** aperture, the restrictions regarding pointing close to objects violating safety limits discussed in [Chapter 7](#) and [STIS ISR 2000-01](#) apply. This rule renders the **F25NDQ4** quadrant rather useless, and the **F25NDQ3** quadrant is redundant with the full field **F25ND3** aperture. Also the dividing lines between the quadrants are somewhat displaced from the center of the detector and are not quite parallel to the detector edges (see [Figure 13.83](#) for a lamp image taken through this filter), so observers for whom the exact locations of the quadrant boundaries are important should contact the [Help Desk](#).

Table 14.30: NDQ quadrant dimensions and the default locations at which a target is placed in each quadrant

| Aperture | Pivot λ (Å) | FWHM (Å) | AB mag zero point | S_{peak} | B_{λ} | R_{80} (arcsec) | Flux in central pixel |
|----------|---------------------|----------|-------------------|-------------------|---------------|-------------------|-----------------------|
| F25NDQ1 | 1416.0 | 384 | 20.775 | 8.95 e+12 | 393 | 0.3 | 9% |
| F25NDQ2 | 1403.9 | 384 | 18.580 | 1.13 e+12 | 394 | 0.3 | 9% |
| F25NDQ3 | 1407.3 | 401 | 15.898 | 9.68 e+10 | 415 | 0.3 | 9% |
| F25NDQ4 | 1433.7 | 391 | 13.091 | 7.95 e+09 | 393 | 0.3 | 9% |

Figure 14.77: Integrated System Throughputs for F25NDQ FUV-MAMA.

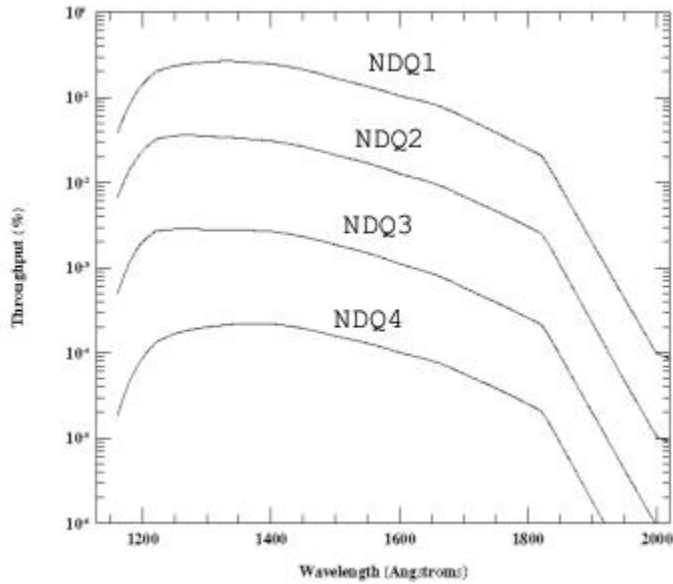


Table 14.31: Sensitivities and Throughputs for F25NDQ aperture with FUV-MAMA.

| λ | Sensitivities | | | | Throughputs (%) | | | |
|-----------|---------------|----------|----------|----------|-----------------|----------|----------|----------|
| | F25NDQ1 | F25NDQ2 | F25NDQ3 | F25NDQ4 | F25NDQ1 | F25NDQ2 | F25NDQ3 | F25NDQ4 |
| 1150 | 3.97e+11 | 6.88e+10 | 5.32e+09 | 2.05e+08 | 1.49e-02 | 2.54e-03 | 2.00e-04 | 7.71e-06 |
| 1200 | 3.85e+12 | 6.30e+11 | 5.34e+10 | 2.40e+09 | 1.40e-01 | 2.30e-02 | 1.95e-03 | 8.74e-05 |
| 1250 | 6.58e+12 | 9.94e+12 | 8.00e+10 | 4.70e+09 | 2.31e-01 | 3.49e-02 | 2.81e-03 | 1.65e-04 |
| 1300 | 7.76e+12 | 1.04e+12 | 8.33e+10 | 5.91e+09 | 2.58e-01 | 3.50e-02 | 2.81e-03 | 1.99e-04 |
| 1350 | 8.05e+12 | 1.02e+12 | 8.54e+10 | 6.69e+09 | 2.62e-01 | 3.31e-02 | 2.78e-03 | 2.18e-04 |
| 1400 | 7.80e+12 | 9.76e+11 | 8.43e+10 | 6.92e+09 | 2.45e-01 | 3.06e-02 | 2.65e-03 | 2.17e-04 |
| 1450 | 6.97e+12 | 8.69e+11 | 7.61e+10 | 6.36e+09 | 2.11e-01 | 2.63e-02 | 2.31e-03 | 1.93e-04 |
| 1500 | 5.76e+12 | 7.23e+11 | 6.38e+10 | 5.41e+09 | 1.69e-01 | 2.12e-02 | 1.87e-03 | 1.59e-04 |

| | | | | | | | | | |
|------|----------|----------|----------|----------|--|----------|----------|----------|----------|
| 1550 | 4.74e+12 | 5.95e+11 | 5.24e+10 | 4.57e+09 | | 1.34e-01 | 1.69e-02 | 1.49e-03 | 1.30e-04 |
| 1600 | 3.83e+12 | 4.68e+11 | 4.08e+10 | 3.70e+09 | | 1.05e-01 | 1.29e-02 | 1.12e-03 | 1.02e-04 |
| 1650 | 3.15e+12 | 3.72e+11 | 3.20e+10 | 3.02e+09 | | 8.40e-02 | 9.91e-03 | 8.53e-04 | 8.05e-05 |
| 1700 | 2.29e+12 | 2.68e+11 | 2.28e+10 | 2.22e+09 | | 5.93e-02 | 6.93e-03 | 5.90e-04 | 5.73e-05 |
| 1750 | 1.54e+12 | 1.86e+11 | 1.57e+10 | 1.54e+09 | | 3.89e-02 | 4.66e-03 | 3.94e-04 | 3.87e-05 |
| 1800 | 1.03e+12 | 1.25e+11 | 1.06e+10 | 1.03e+09 | | 2.50e-02 | 3.05e-03 | 2.59e-04 | 2.52e-05 |
| 1850 | 4.15e+11 | 4.95e+10 | 4.28e+09 | 4.06e+08 | | 9.87e-03 | 1.18e-03 | 1.02e-04 | 9.68e-06 |

F25QTZ - FUV-MAMA, Longpass

Description

The F25QTZ filter with the FUV-MAMA provides high-throughput broad-band FUV imaging with better rejection of geocoronal emission than the F25MAMA or F25SRF2 modes and the same field of view and spatial resolution.

Recommended Uses

This filter is recommended for broad-band FUV imaging of faint targets.

Special Considerations

With this filter the background is dominated by detector dark current. The dark current is not constant across the detector and not constant in time. This could limit the sensitivity for very extended faint targets, however, note that the FUV-MAMA dark is extremely low.

Users may also want to consider whether the ACS SBC detector might be better for their observing program.

| Pivot λ (Å) | FWHM (Å) | AB mag zero point | S_{peak} | B_{λ} | R_{80} (arcsec) | Flux in central pixel |
|---------------------|----------|-------------------|-------------------|---------------|-------------------|-----------------------|
| 1596.2 | 231.6 | 21.303 | 3.46e+13 | 224.5 | 0.28 | 10% |

Figure 14.78: F25QTZ FUV-MAMA Integrated System Throughput and Redleak

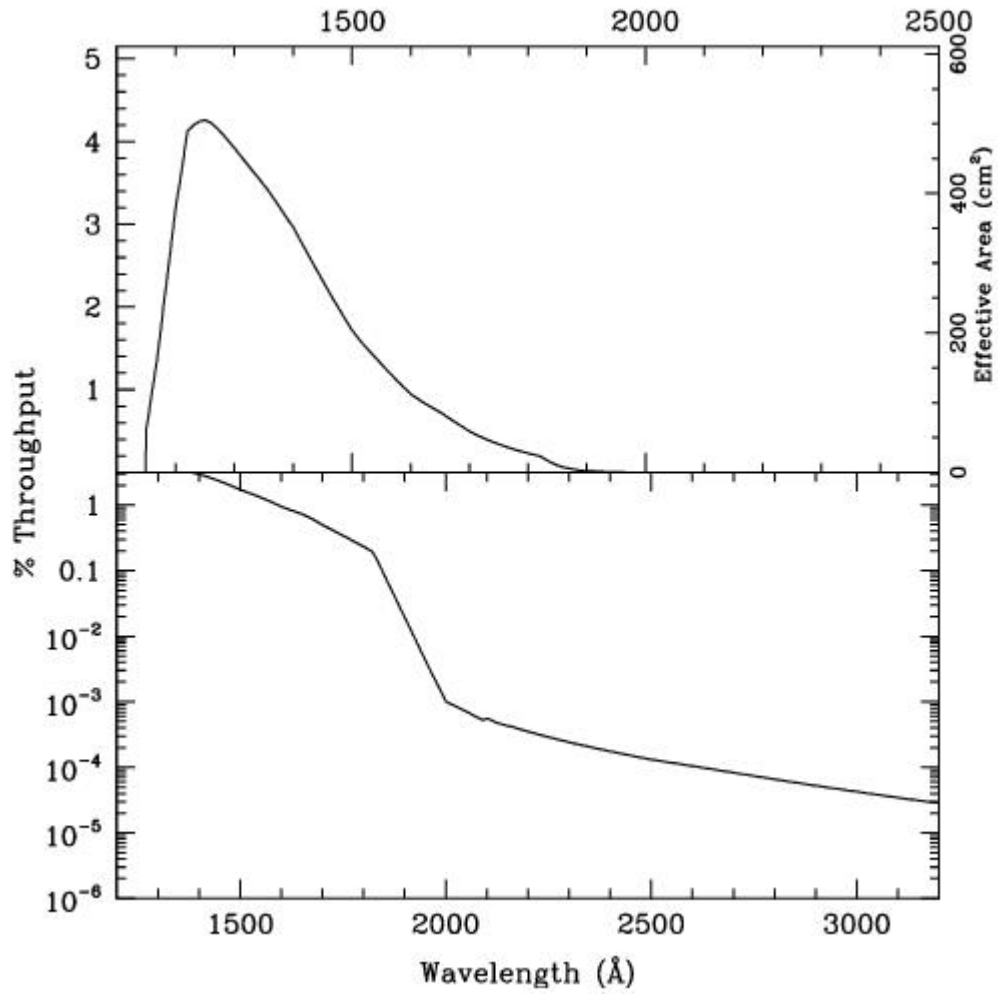


Table 14.32: F25QTZ FUV-MAMA Sensitivity & Throughput

| λ | Sensitivity | % Throughput |
|-----------|-------------|--------------|
| 1475. | 6.77E13 | 2.02 |
| 1500. | 5.92E13 | 1.73 |
| 1525. | 5.24E13 | 1.51 |
| 1550. | 4.64E13 | 1.31 |
| 1575. | 4.04E13 | 1.13 |
| 1600. | 3.49E13 | 0.96 |
| 1625. | 3.08E13 | 0.83 |

| | | |
|-------|---------|------|
| 1650. | 2.74E13 | 0.73 |
| 1675. | 2.34E13 | 0.61 |
| 1700. | 1.94E13 | 0.50 |
| 1725. | 1.63E13 | 0.41 |
| 1750. | 1.37E13 | 0.34 |
| 1775. | 1.14E13 | 0.28 |
| 1800. | 9.55E12 | 0.23 |
| 1825. | 7.29E12 | 0.18 |
| 1850. | 3.76E12 | 0.09 |
| 1875. | 1.81E12 | 0.04 |
| 1900. | 8.69E11 | 0.02 |

Figure 14.79: Point source S/N vs. AB magnitude in the V-band for the F25QTZ FUV-MAMA mode. Curves are labeled by required exposure time (seconds).

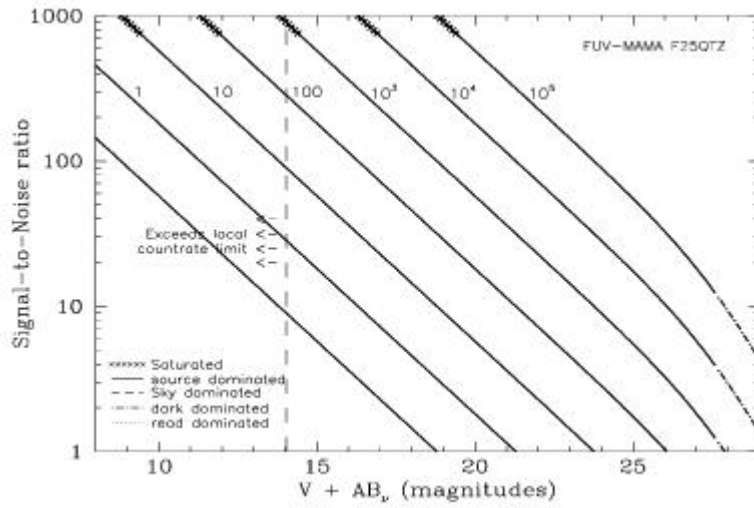


Figure 14.80: Extended source S/N vs. AB magnitude in the V-band for the F25QTZ FUV-MAMA mode. Top curves are for an area of 0.2 arcsec²; bottom curves are for 1 arcsec². Average sky assumed. Curves are labeled by required exposure time (seconds).

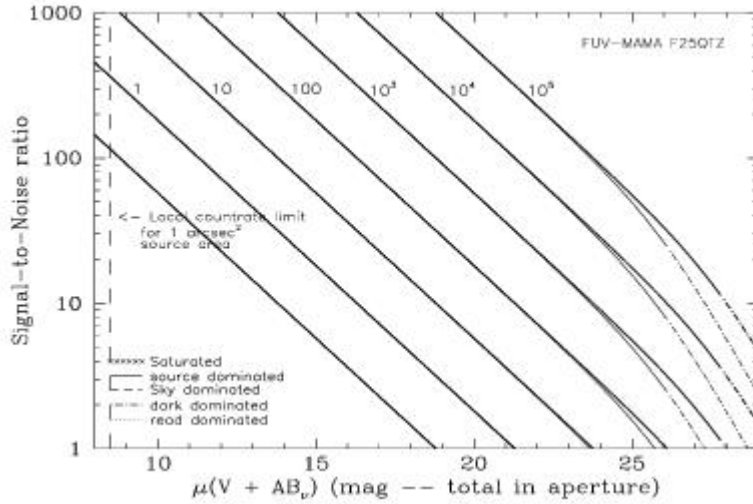


Table 14.33: Radial Profile for F25QTZ*

| Radius | | Intensity | Fraction of Energy Encircled |
|--------|--------|-----------|------------------------------|
| Pixels | Arcsec | | |
| 1 | 0.024 | 3.961e-02 | 0.172 |
| 1.5 | 0.037 | 2.515e-02 | 0.287 |
| 2 | 0.049 | 1.505e-02 | 0.398 |
| 3 | 0.073 | 5.412e-03 | 0.532 |
| 4 | 0.098 | 2.570e-03 | 0.609 |
| 5 | 0.122 | 1.373e-03 | 0.659 |
| 10 | 0.245 | 2.735e-04 | 0.778 |
| 15 | 0.367 | 1.447e-04 | 0.851 |
| 20 | 0.490 | 7.887e-05 | 0.909 |
| 25 | 0.613 | 4.703e-05 | 0.953 |
| 30 | 0.735 | 2.117e-05 | 0.980 |
| 40 | 0.980 | 1.135e-05 | 1.000 |

* See [STIS ISR 2003-01](#).

Figure 14.81: Point Source Encircled Energy for F25QTZ FUV-MAMA

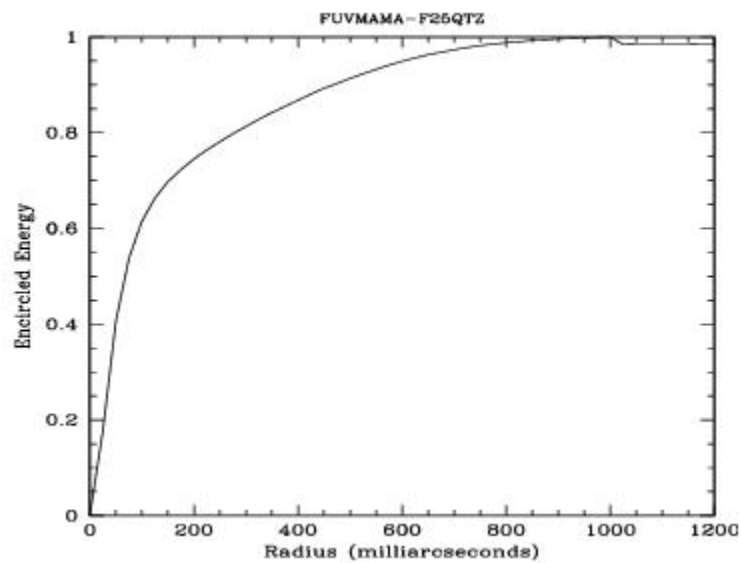
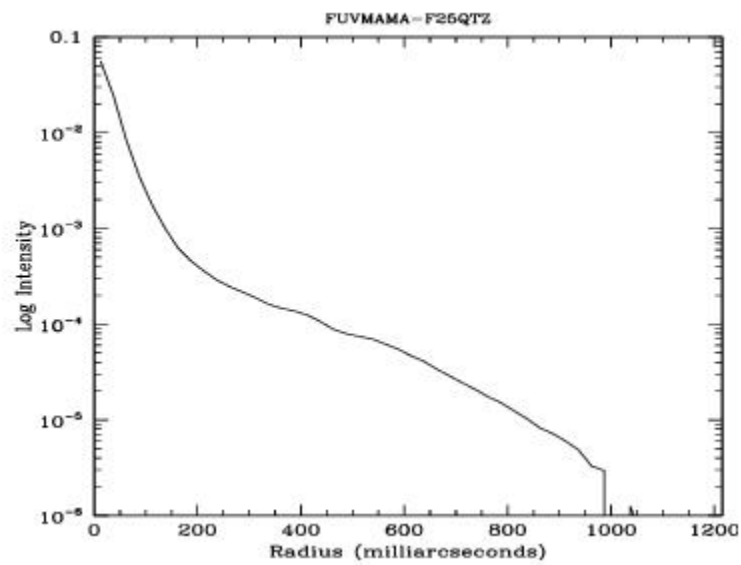


Figure 14.82: Point Source Intensity vs. Radius for F25QTZ FUV-MAMA



F25QTZD1 - FUV-MAMA, Longpass Pseudo-Aperture

Description

The F25QTZD1 filter is intended to be used with the G140L and G140M gratings for spectroscopic observations of very faint targets at the D1 position that require better rejection of geocoronal emission than provided by F25MAMAD1 or F25SRF2D1. It is the same optical element as the F25QTZ filter. This aperture moves the target 2 arcseconds above the bottom edge of the FUV-MAMA. It is yet to be determined if the throughput for a target at this position is significantly different from that obtained at the standard position.

Special Considerations

Refer to [Section F25QTZ—FUV-MAMA](#) for information concerning the properties of the F25QTZD1 filter. Note that it can only be used with the G140L and G140M gratings.

F25SRF2 - FUV-MAMA, Longpass

Description

The F25SRF2 filter with the FUV-MAMA provides high-throughput broad-band FUV imaging with an intermediate degree of rejection of geocoronal emission: better than F25MAMA, but worse than F25QTZ. It provides the same field of view and spatial resolution as these modes.

Recommended Uses

This filter has slightly higher throughput than F25QTZ, but admits light from the geocoronal O I 1302 Å triplet. For sky-limited imaging F25QTZ is usually a better choice.

Special Considerations

Sky background on the day side of the orbit contains a significant contributions from O I] 1356 Å and O I 1302, 1304, 1306 Å air glow emission. In high-background conditions, the sky background can dominate the detector background. In average day-side observing conditions the sky background through this filter will be about a factor of 100 higher than for F25QTZ. Observers can limit the background (with some cost to the total amount of observing time per orbit) by using the DARKTIME special requirement.

Users may also want to consider whether the ACS SBC detector might be better for their observing program.

| Pivot λ (Å) | FWHM (Å) | AB mag zero point | S_{peak} | B_{λ} | R_{80} (arcsec) | Flux in central pixel |
|---------------------|----------|-------------------|-------------------|---------------|-------------------|-----------------------|
| 1451.7 | 282.0 | 22.656 | 7.88e+13 | 283.6 | 0.30 | 9% |

Figure 14.83: F25SRF2 FUV-MAMA Integrated System Throughput and Redleak

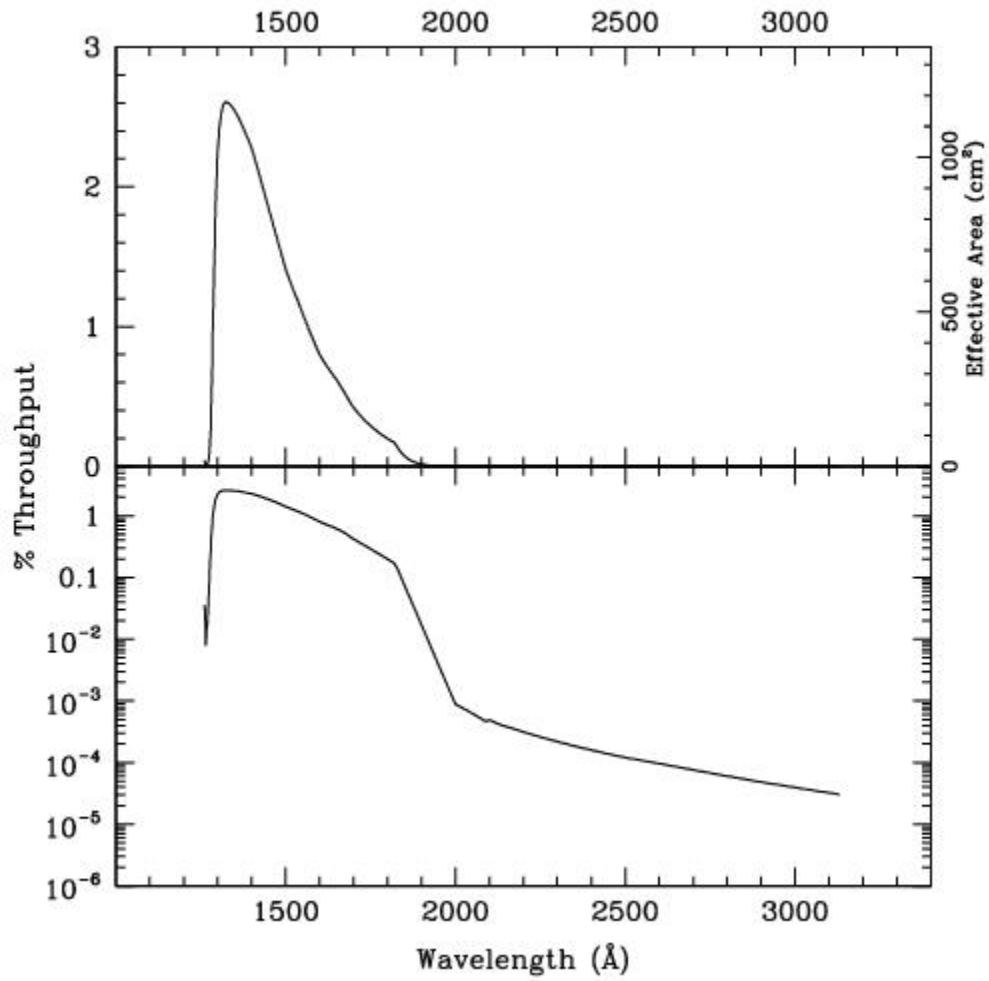


Table 14.34: F25SRF2 FUV-MAMA Sensitivity & Throughput

| λ | Sensitivity | % Throughput |
|-----------|-------------|--------------|
| 1300. | 6.21E13 | 2.10 |
| 1325. | 7.82E13 | 2.59 |
| 1350. | 7.82E13 | 2.54 |
| 1375. | 7.58E13 | 2.42 |
| 1400. | 7.24E13 | 2.27 |
| 1425. | 6.71E13 | 2.07 |
| 1450. | 6.10E13 | 1.85 |

| | | |
|-------|---------|------|
| 1475. | 5.47E13 | 1.63 |
| 1500. | 4.85E13 | 1.42 |
| 1525. | 4.34E13 | 1.25 |
| 1550. | 3.87E13 | 1.10 |
| 1575. | 3.39E13 | 0.94 |
| 1600. | 2.94E13 | 0.81 |
| 1625. | 2.61E13 | 0.71 |
| 1650. | 2.32E13 | 0.62 |
| 1675. | 1.99E13 | 0.52 |
| 1700. | 1.64E13 | 0.42 |
| 1725. | 1.38E13 | 0.35 |
| 1750. | 1.16E13 | 0.29 |
| 1775. | 9.76E12 | 0.24 |
| 1800. | 8.18E12 | 0.20 |
| 1825. | 6.27E12 | 0.15 |

Figure 14.84: Point Source S/N vs. AB magnitude in the V-band for the F25SRF2 FUV-MAMA mode. Curves are labeled by required exposure time (seconds).

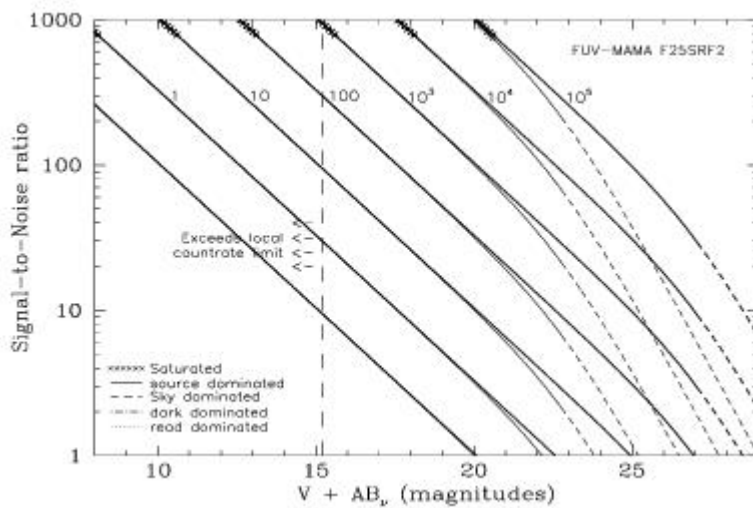


Figure 14.85: Extended Source S/N vs. AB magnitude in the V-band for the F25SRF2 FUV-MAMA mode. Top curves are for an area of 0.2 arcsec²; bottom curves are for 1 arcsec². Average sky assumed. Curves are labeled by required exposure time (seconds).

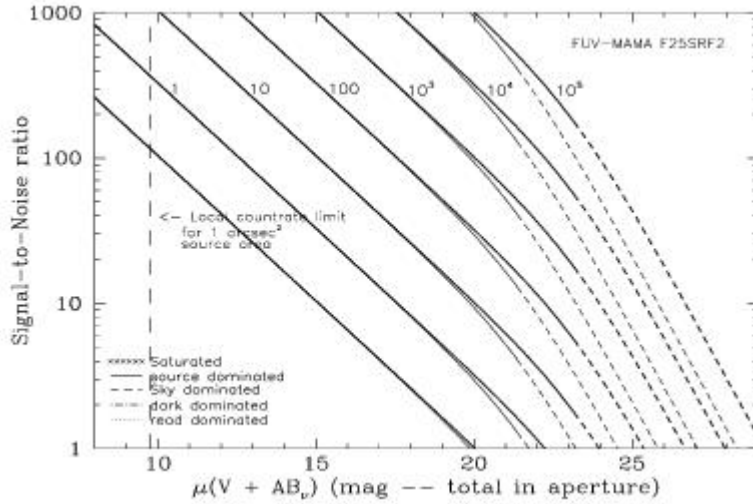


Table 14.35: Radial Profile for F25SRF2*

| Radius | | Intensity | Fraction of Energy Encircled |
|--------|--------|-----------|------------------------------|
| Pixels | Arcsec | | |
| 1 | 0.024 | 3.544e-02 | 0.154 |
| 1.5 | 0.037 | 2.268e-02 | 0.256 |
| 2 | 0.049 | 1.408e-02 | 0.358 |
| 3 | 0.073 | 5.787e-03 | 0.493 |
| 4 | 0.098 | 2.765e-03 | 0.576 |
| 5 | 0.122 | 1.514e-03 | 0.630 |
| 10 | 0.245 | 3.098e-04 | 0.762 |
| 15 | 0.367 | 1.677e-04 | 0.847 |
| 20 | 0.490 | 8.854e-05 | 0.910 |
| 25 | 0.613 | 4.487e-05 | 0.954 |
| 30 | 0.735 | 2.080e-05 | 0.980 |
| 40 | 0.980 | 1.510e-06 | 0.999 |

* See [STIS ISR 2003-01](#).

Figure 14.86: Point Source Encircled Energy for F25SRF2 FUV-MAMA

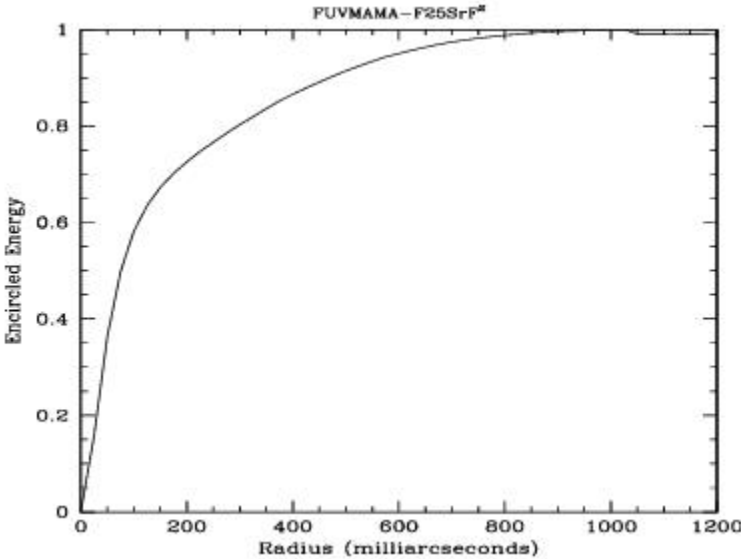
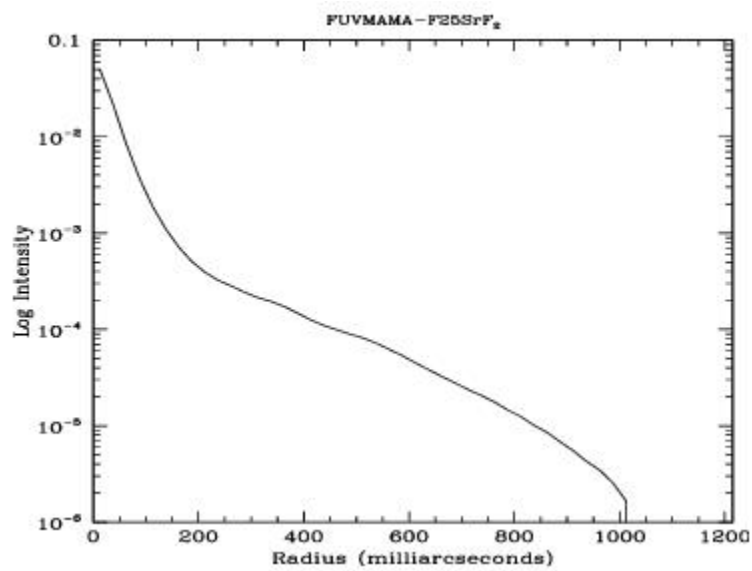


Figure 14.87: Point Source Intensity vs. Radius for F25SRF2 FUV-MAMA



F25SRF2D1 - FUV-MAMA, Longpass Pseudo-Aperture

Description

The F25SRF2D1 filter is intended to be used with the G140L and G140M gratings for spectroscopic observations of very faint targets at the D1 position. It provides an intermediate degree of rejection of geocoronal emission: better than F25MAMAD1, but worse than F25QTZD1. This is the same physical aperture as the F25SRF2 aperture and is available for use with the FUV-MAMA detector to minimize the contribution from the dark current when observing very faint targets. This aperture moves the target 2 arcseconds above the bottom edge of the FUV-MAMA to avoid the detector glow region. It is yet to be determined if the throughput for a target at this position is significantly different from that obtained at the standard position.

Special Considerations

Refer to [Section F25SRF2—FUV-MAMA](#) for information concerning the properties of the F25SRF2D1 filter. Note that it can only be used with the G140L and G140M gratings.

F25LYA - FUV-MAMA, Lyman-alpha

Description

The F25LYA filter with the FUV-MAMA provides narrowband imaging of the HI 1216 Å Lyman-α line.

Recommended Uses

This filter is recommended for imaging Lyman-α emission. Differencing two images taken with 25MAMA and F25SRF2 is another option.

Special Considerations

Sensitivity is limited by geocoronal Lyman-α. Observers can limit the background (with some cost to the total amount of observing time per orbit) by using the DARKTIME special requirement.

Users may also want to consider whether the ACS SBC detector with the F122M filter might be a better choice for their observing program.

| Pivot λ (Å) | FWHM (Å) | AB mag zero point | S _{peak} | B _λ | R ₈₀ (arcsec) | Flux in central pixel |
|-------------|----------|-------------------|-------------------|----------------|--------------------------|-----------------------|
| 1242.8 | 141.2 | 19.470 | 8.76e+12 | 99.5 | 0.35 | 6% |

Figure 14.88: F25LYA FUV-MAMA Integrated System Throughput and Redleak

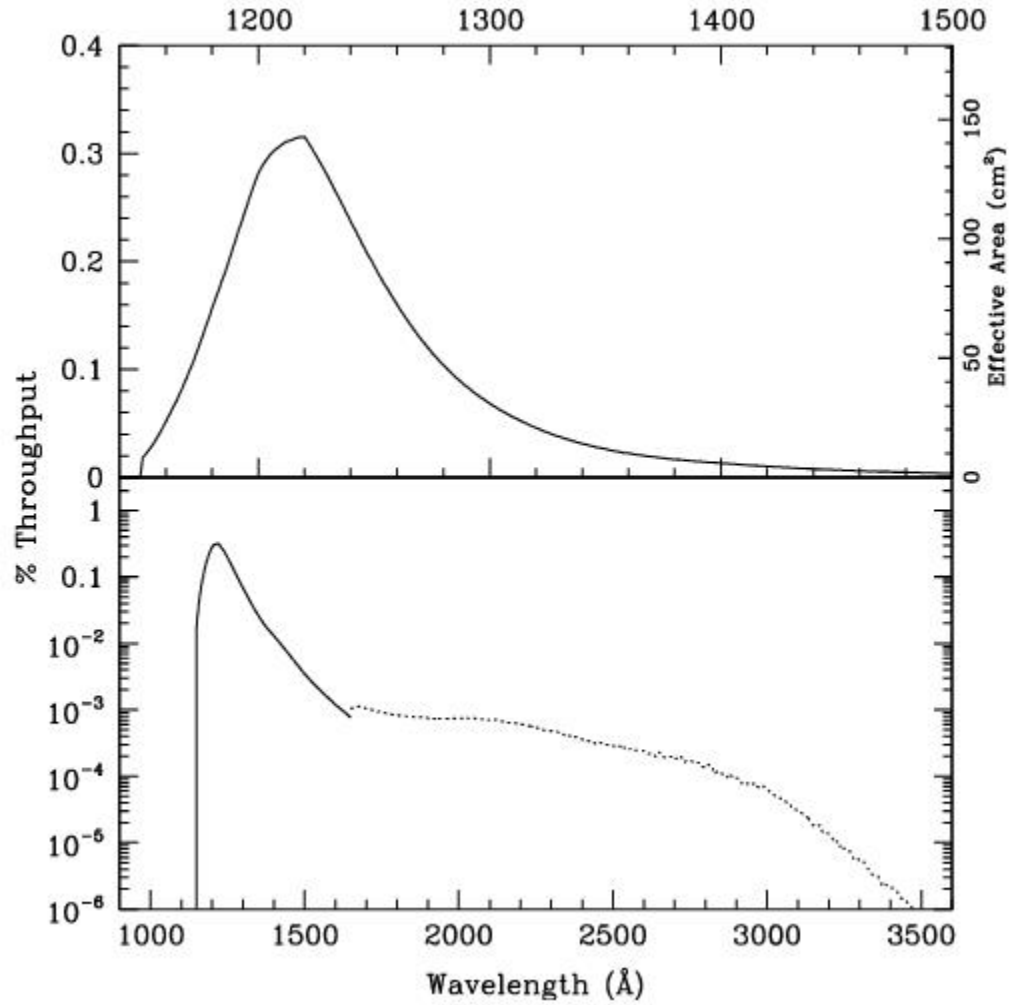


Table 14.36: F25LYA FUV-MAMA Sensitivity & Throughput

| λ | Sensitivity | % Throughput |
|-----------|-------------|--------------|
| 1150. | 5.06E11 | 0.02 |
| 1175. | 3.42E12 | 0.13 |
| 1200. | 7.42E12 | 0.27 |
| 1225. | 8.15E12 | 0.29 |
| 1250. | 5.62E12 | 0.20 |
| 1275. | 3.40E12 | 0.12 |
| 1300. | 2.05E12 | 0.07 |

| | | |
|-------|---------|------|
| 1325. | 1.27E12 | 0.04 |
| 1350. | 8.13E11 | 0.03 |
| 1375. | 5.62E11 | 0.02 |

Figure 14.89: Point Source S/N vs. flux for the F25LYA FUV-MAMA mode. Curves are labeled by required exposure time (seconds).

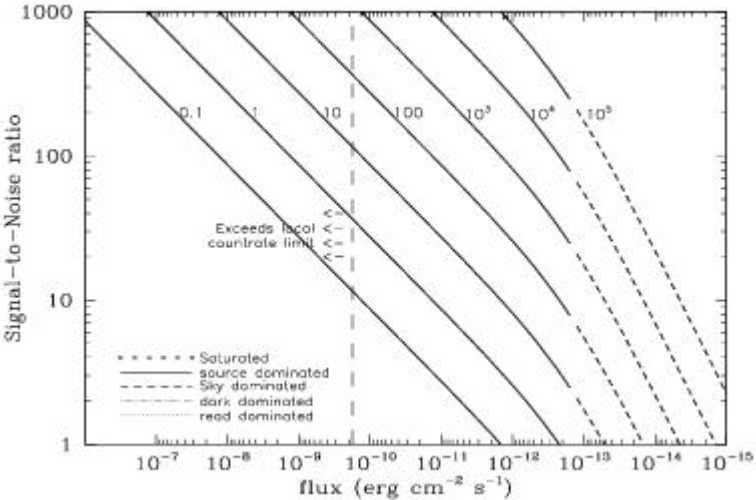


Figure 14.90: Extended Source S/N vs. flux for the F25LYA FUV-MAMA mode. Top curves are for an area of 0.2 arcsec²; bottom curves are for 1 arcsec². Average sky assumed. Curves are labeled by required exposure time (seconds).

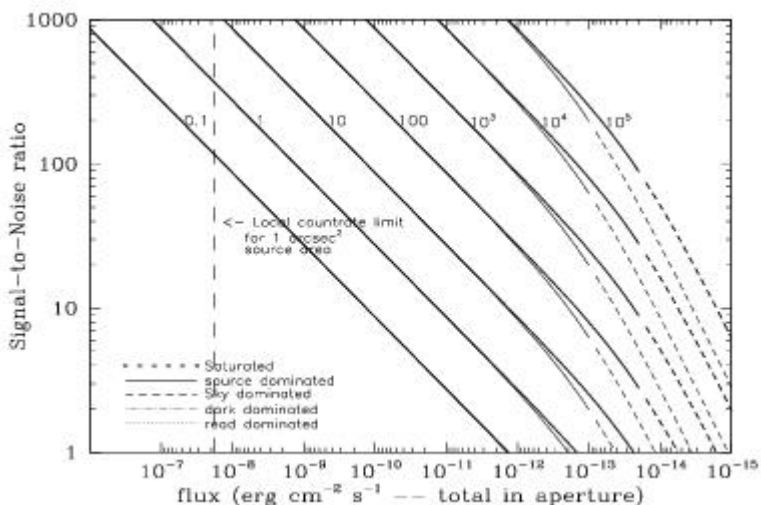


Table 14.37: Radial Profile for F25LYA*

| Radius | | Intensity | Fraction of Energy Encircled |
|--------|--------|-----------|------------------------------|
| Pixels | Arcsec | | |
| 1 | 0.024 | 2.440e-02 | 0.100 |
| 1.5 | 0.037 | 1.702e-02 | 0.174 |
| 2 | 0.049 | 1.199e-02 | 0.254 |
| 3 | 0.073 | 6.423e-03 | 0.387 |
| 4 | 0.098 | 3.326e-03 | 0.485 |
| 5 | 0.122 | 1.718e-03 | 0.549 |
| 10 | 0.245 | 3.888e-04 | 0.712 |
| 15 | 0.367 | 2.140e-04 | 0.816 |
| 20 | 0.490 | 1.044e-04 | 0.895 |
| 25 | 0.613 | 4.910e-05 | 0.943 |
| 30 | 0.735 | 1.741e-05 | 0.968 |
| 40 | 0.980 | 8.124e-06 | 0.994 |

* See [STIS ISR 2003-01](#).

Figure 14.91: Point Source PSF for F25LYA FUV-MAMA, 7."5 square (at pixel 739, 368, log scaled, B-V=-0.04)

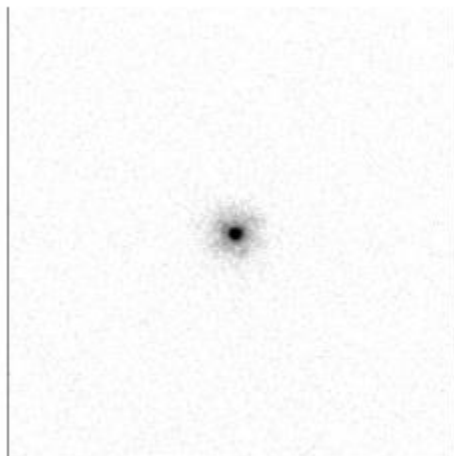


Figure 14.92: Point Source Encircled Energy for F25LYA FUV-MAMA

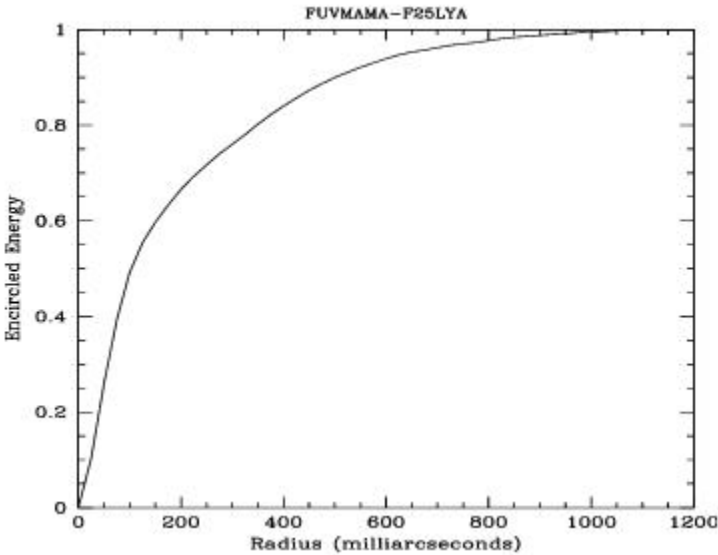
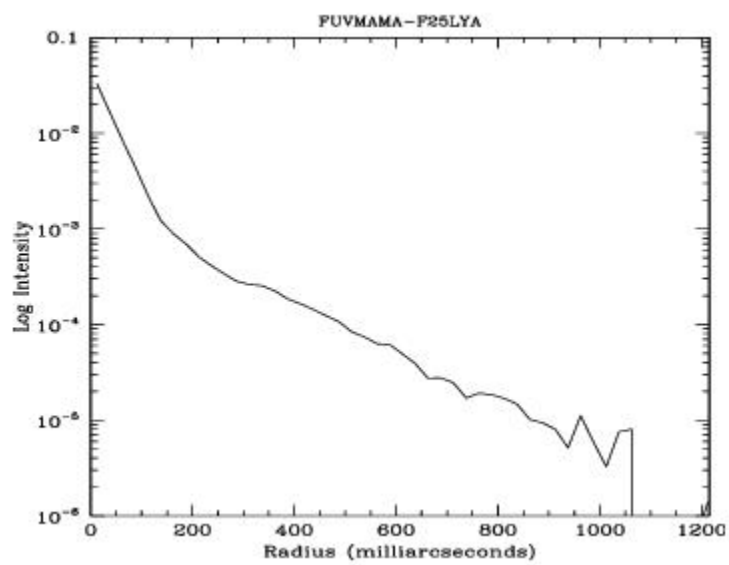


Figure 14.93: Point Source Intensity vs. Radius for F25LYA FUV-MAMA



14.6 Image Mode Geometric Distortion

The STIS cameras have significant geometric distortion that not only affects astrometry, but also in principle affects photometry (because the extended sources used to generate flat fields have an induced change in the apparent surface brightness). For the CCD the image distortions are less than one pixel across the whole detector, and can often be ignored. For the MAMA the distortions are larger, approaching 3 pixels at the corners of cameras.

Geometric distortion and plate scales for the STIS imaging configurations have been measured on-orbit by observing star fields shifted to different positions in the field, following a procedure similar to that used for WFPC-2 (Holtzman et al., 1995, *PASP*, 107, 156). The geometric distortion data also allowed a determination of the mean plate scale at the center of the field for each detector. These plate scales, for unfiltered CCD exposures and filtered MAMA exposures (see *ISR STIS 2001-02*), are given in [Table 14.38](#). The quoted errors are formal random errors derived from the uncertainties in measuring the positions of the sources. The STIS team has determined that the plate scale for unfiltered FUV-MAMA images (25MAMA) is 1.0031 times larger than for filtered images (F25QTZ and F25SRF2); the plate scale for unfiltered NUV-MAMA images (25MAMA) is 1.0008 times smaller than for filtered images (F25QTZ and F25CN182).

Table 14.38: Mean pixel scales for STIS detectors.

| Detector | X scale (arcsec/pix) | X error (arcsec/pix) | Y scale (arcsec/pix) | Y error (arcsec/pix) | Corrected mean scale |
|-------------------|-------------------------|-------------------------|-------------------------|-------------------------|-------------------------|
| Unfiltered CCD | 0.050716 | 0.000072 | 0.050735 | 0.000087 | 0.050725 |
| Filtered FUV-MAMA | 0.024328 | 0.000025 | 0.024608 | 0.000086 | 0.024468 |
| Filtered NUV-MAMA | 0.024526 | 0.000120 | 0.024829 | 0.000126 | 0.024677 |

Distortion solutions have been implemented in the IDCTAB reference files (see *ACS ISR 2001-08*). The equations which relate the true x_i, y_i positions of the stars with the observed positions x, y are as follows (*STIS ISR 2004-01*):

$$x_i - x_r = \sum_{i=0}^k \sum_{j=0}^i c_{x,i,j} (x - x_r)^j (y - y_r)^{i-j}$$

$$y_i - y_r = \sum_{i=0}^k \sum_{j=0}^i c_{y,i,j} (x - x_r)^j (y - y_r)^{i-j}$$

where x_r and y_r are the coordinates of the central pixel.

Maíz-Apellániz & L. Úbeda discovered that the coefficients for the `NUV-MAMA` had been incorrectly implemented in the original IDCTAB reference file and performed a revised analysis ([ISR STIS 2004-01](#)). A similar re-analysis for the `FUV-MAMA` has recently been performed by Sohn ([STIS ISR 2018-02](#)). Both analyses employ a fourth-order transformation between raw and rectified coordinates, using the mean plate scales given in [Table 14.38](#). The plate scales imposed on rectified images produced by `calstis` using the latest IDCTABs (column "SCALE") are given in [Table 14.39](#).

Table 14.39: Plate scales of rectified and drizzled images.

| Detector | IDCTAB | Plate Scale (arcsec/pixel) | |
|----------|---------------|----------------------------|----------|
| | | Clear | Filtered |
| CCD | o8g1508do_idc | 0.05072 | 0.05075 |
| FUV-MAMA | 1771408ro_idc | 0.024395 | 0.024468 |
| NUV-MAMA | o8g1508fo_idc | 0.024604 | 0.024678 |

14.7 Spatial Dependence of the STIS PSF

The STIS PSF varies across the field of view. Observations of Omega Cen and NGC 6681 have been used to study the PSF variations, and confirm the behavior expected from the optics. One way of characterizing the spatial variation is to measure the flux in a fixed aperture. [Figure 14.94](#) through [Figure 14.97](#) show the fraction of the flux enclosed within a 0.05 arcsec radius aperture. This parameter is relatively constant for the CCD, but is more variable for the MAMA detectors. For example, the 0.05" encircled energy varies from 47% to 31% across the NUV-MAMA with the F25CN182 filter.

See [Bowers \(1997 HST Calibration Workshop\)](#) for a discussion of *HST* "breathing" effects on the PSF.

Figure 14.94: Fraction of the total flux of a point source that passes through an aperture of 0.05" radius for the CCD and a clear aperture (50CCD). The data were obtained from observations of the Omega Cen star cluster. Crosses represent stars that have little or no contamination from other sources, while triangles are sources that were marginally contaminated in the region outside the PSF core. No objects were used that had contamination within 0.15" of the center.

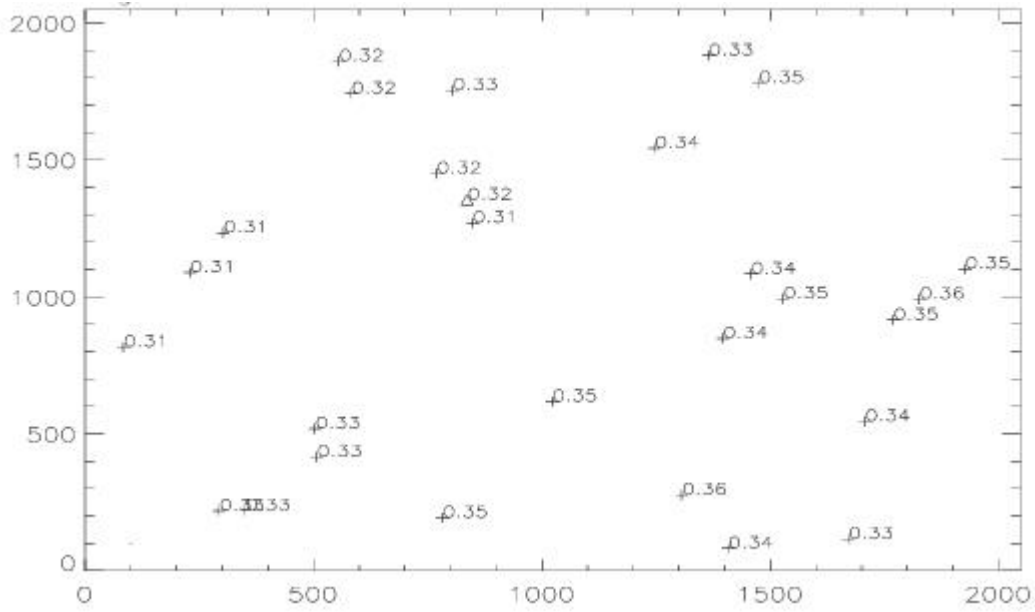


Figure 14.95: Fraction of the total flux of a point source that passes through an aperture of 0.05" radius for the NUV-MAMA with the F25CN182. The data were obtained from observations of the star cluster NGC 6881. Crosses represent stars that have little or no contamination from other sources, while triangles are sources that were marginally contaminated in the region outside the PSF core. No objects were used that had contamination within 0.15" of the center.

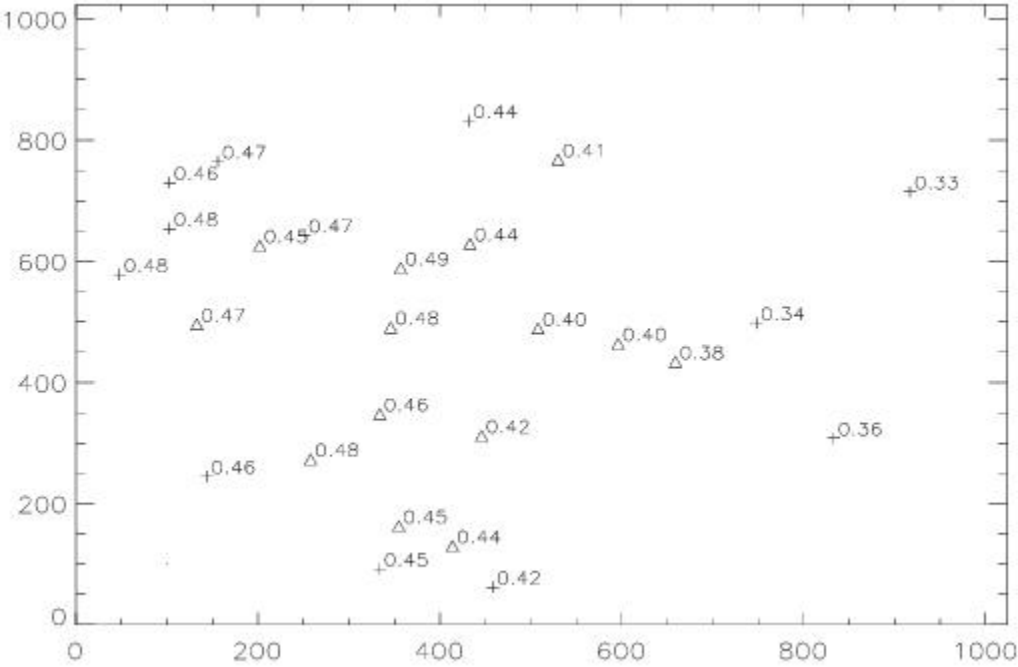


Figure 14.96: Fraction of the total flux of a point source that passes through an aperture of 0.05" radius for the NUV-MAMA with the F25CN270 filter. The data were obtained from observations of the star cluster NGC 6881. Crosses represent stars that have little or no contamination from other sources, while triangles are sources that were marginally contaminated in the region outside the PSF core. No objects were used that had contamination within 0.15" of the center.

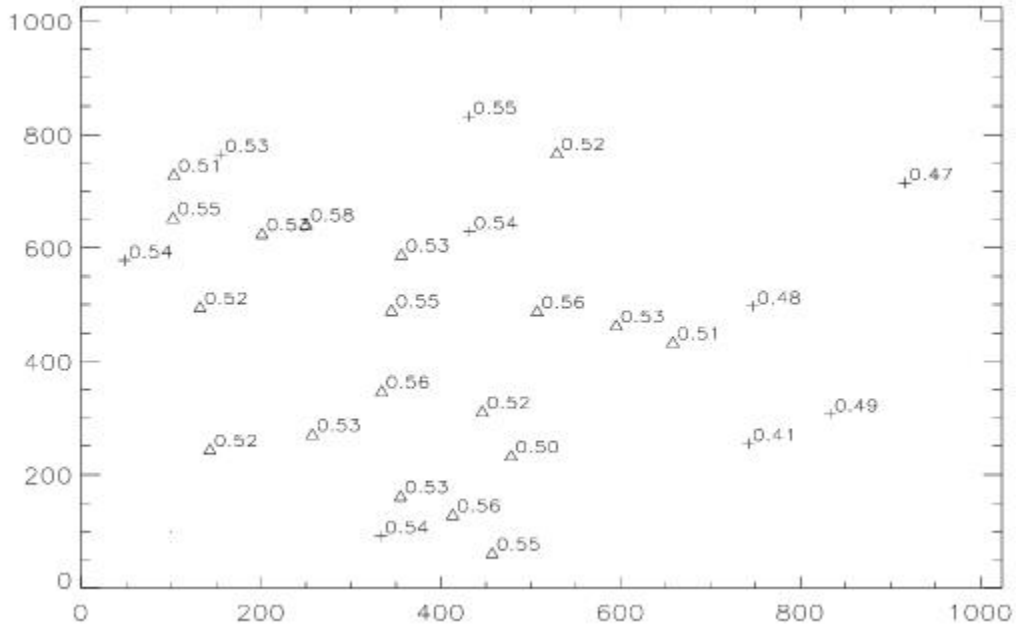
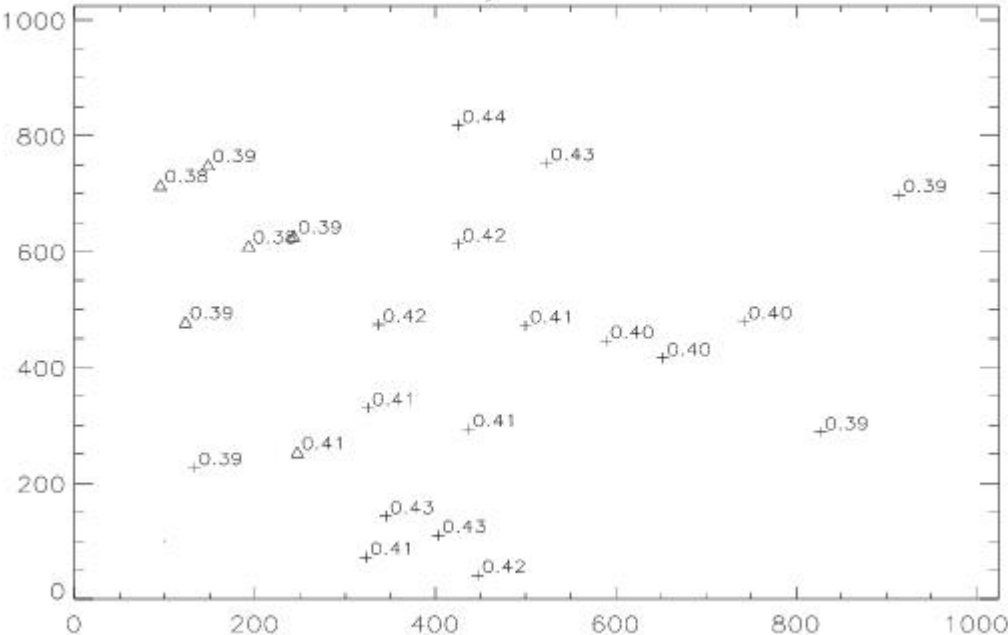


Figure 14.97: Fraction of the total flux of a point source that passes through an aperture of 0.05" radius for the FUV-MAMA with the F25QTZ filter. The data were obtained from observations of the star cluster NGC 6881. Crosses represent stars that have little or no contamination from other sources, while triangles are sources that were marginally contaminated in the region outside the PSF core. No objects were used that had contamination within 0.15" of the center.



14.8 MAMA Imaging Bright Object Limits

As described in [Section 7.7](#), the MAMAs are subject to absolute brightness limits, above which sources cannot be observed or they would potentially damage the detectors. In [Table 14.40](#), we present the complete set of bright object point source and integrated magnitude screening limits for the MAMA imaging modes. These screening magnitudes are presented as a guide. Whether or not an individual source can be observed is determined by whether the desired configuration and the spectrum of that source is predicted to exceed the global and local absolute observing count rate limits, as described in [Chapter 7](#). Remember, sources cannot be observed in configurations where they exceed the absolute bright object limits. The information presented here should be used in conjunction with the material presented in [Chapter 7](#).

A few important points to note:

- Limits are given as Johnson V Vega magnitudes, $\text{ergs/s/cm}^2/\text{\AA}$, or $\text{ergs/s/cm}^2/\text{\AA}/\text{arcsec}^2$.
- The limits were derived assuming zero slit loss.
- The imaging table includes a single point source limit. No single source in the field of view can exceed this limit.
- The limits in the tables assume zero extinction. If your source, when corrected for interstellar extinction, does not exceed the absolute limits, then you will be allowed to observe your source.
- The imaging table also includes an integrated magnitude limit. Remember that the global limit of 200,000 counts/s applies to all sources imaged onto the MAMA detector. The integrated magnitude limit gives the total magnitude from all stars (or galaxies, or diffuse objects) of spectral type O which can appear in the MAMA field of view. Initial screening of all MAMA imaging observations will be done assuming all stars are O stars, however, ultimately for the final decision, the colors of the stars are taken into account whenever such information is available (see [Chapter 7](#)).
- Be aware of the additional limitations that exist for crowded fields and slightly-resolved stellar clusters (see [Section 7.7.3](#)).
- M dwarf flaring is a potential issue for MAMA imaging observations. For more information, see [STIS ISR 2017-02](#).
- This table is provided for general guidance, but deference should be given to **ETC** calculations, particularly for stars which deviate significantly from the spectral type template (e.g., accretion, chromospheric emission, etc.).

Table 14.40: MAMA Bright-Object limits (V magnitudes and cgs units). V magnitudes include NO additional safety factor to account for extrapolation uncertainties from the optical to the UV spectral range.

| Spectral Type | FUV-MAMA | | | | NUV-MAMA | | | | | |
|---------------------------------|-----------------------|-----------------------|-----------------------|-----------------------|-----------------------|-----------------------|-----------------------|-----------------------|-----------------------|--------|
| | 25MAMA | F25SRF2 | F25QTZ | F25LYA | 25MAMA | F25SRF2 | F25QTZ | F25CN182 | F25CIII | F25CII |
| Flat, point source ¹ | 9.6×10^{-15} | 1.7×10^{-14} | 5.1×10^{-14} | 4.5×10^{-13} | 2.1×10^{-15} | 2.4×10^{-15} | 2.5×10^{-15} | 2.5×10^{-14} | 1.9×10^{-13} | 1. |

| | | | | | | | | | | |
|---|-----------------------|-----------------------|-----------------------|-----------------------|-----------------------|-----------------------|-----------------------|-----------------------|-----------------------|----|
| Flat, extended, peak² | 4.0×10^{-12} | 7.5×10^{-12} | 2.1×10^{-11} | 1.9×10^{-10} | 9.0×10^{-13} | 1.0×10^{-12} | 1.0×10^{-12} | 1.0×10^{-11} | 8.0×10^{-11} | 7. |
| O5 V³ | 19.1 | 18.3 | 16.8 | 15.2 | 19.2 | 19.0 | 18.8 | 16.8 | 14.6 | |
| O7 V | 18.9 | 18.1 | 16.6 | 15.0 | 19.1 | 18.9 | 18.7 | 16.7 | 14.5 | |
| O9 V | 18.7 | 17.9 | 16.4 | 14.7 | 18.9 | 18.7 | 18.6 | 16.6 | 14.4 | |
| B0 V | 18.6 | 17.8 | 16.3 | 14.6 | 18.8 | 18.7 | 18.5 | 16.5 | 14.3 | |
| B1 V | 18.3 | 17.4 | 16.0 | 14.3 | 18.6 | 18.4 | 18.2 | 16.2 | 14.0 | |
| B3 V | 17.4 | 16.7 | 15.3 | 13.3 | 17.9 | 17.8 | 17.7 | 15.5 | 13.3 | |
| B5 V | 16.7 | 16.1 | 14.8 | 12.3 | 17.5 | 17.3 | 17.2 | 15.1 | 12.9 | |
| B8 V | 15.5 | 15.1 | 13.8 | 10.6 | 16.7 | 16.6 | 16.5 | 14.3 | 12.1 | |
| A1 V | 13.3 | 13.0 | 12.3 | 7.2 | 15.6 | 15.5 | 15.5 | 13.1 | 11.0 | |
| A3 V | 12.1 | 11.9 | 11.5 | 5.4 | 15.4 | 15.3 | 15.2 | 12.8 | 10.8 | |
| A5 V | 10.7 | 10.6 | 10.4 | 3.4 | 15.1 | 15.0 | 15.0 | 12.4 | 10.4 | |
| F0 V | 8.5 | 8.3 | 8.3 | 0.9 | 14.6 | 14.5 | 14.4 | 11.5 | 9.4 | |
| F2 V | 7.7 | 7.5 | 7.4 | 0.0 | 14.3 | 14.2 | 14.2 | 11.1 | 8.9 | |
| F5 V | 5.8 | 5.7 | 5.6 | -2.0 | 13.9 | 13.8 | 13.8 | 10.3 | 8.0 | |
| F8 V | 4.7 | 4.6 | 4.5 | <-2.0 | 13.7 | 13.6 | 13.5 | 9.8 | 7.4 | |
| G2 V⁴ | 4.8 | 3.9 | 3.6 | 1.4 | 12.9 | 12.8 | 12.8 | 8.7 | 6.5 | |
| G8 V⁵ | 4.2 | 3.3 | 3.0 | 0.8 | 12.5 | 12.4 | 12.4 | 8.1 | 6.0 | |
| K2 V⁶ | 5.7 | 3.9 | 3.2 | 2.6 | 11.8 | 11.7 | 11.7 | 7.2 | 5.6 | |
| KM III⁷ | 4.2 | 3.6 | 2.5 | 1.1 | 11.5 | 11.4 | 11.4 | 6.9 | 5.6 | |
| Integrated V magnitude⁸ | 13.4 | 12.6 | 11.2 | 9.6 | 13.5 | 13.3 | 13.1 | 11.2 | 8.9 | |
| Flat, extended, all detector⁹ | 7.2×10^{-15} | 1.4×10^{-14} | 4.1×10^{-14} | 3.6×10^{-13} | 1.7×10^{-15} | 1.9×10^{-15} | 2.0×10^{-15} | 2.0×10^{-14} | 1.5×10^{-13} | 1. |

¹ Maximum allowed flux for a point source in $\text{ergs/s/cm}^2/\text{\AA}$.

² Maximum peak allowed flux for an extended source in $\text{ergs/s/cm}^2/\text{\AA}/\text{arcsec}^2$.

- ³ V magnitude limit for unreddened single stars. O5 V through F8 V are based on Kurucz (1993) models.
- ⁴ The magnitudes listed for G2 V are for the Solar template in the STIS **ETC**.
- ⁵ The magnitudes listed for G8 V are from IUE data for the star Tau Ceti.
- ⁶ The magnitudes listed for K2 V are from IUE data for the star Epsilon Eri.
- ⁷ The magnitudes listed for KM III are from IUE data for 9 stars of these types.
- ⁸ Maximum integrated V magnitude for stars in the field assuming all are of O5 V spectral type.
- ⁹ Maximum allowed flux for an extended source which covers the full detector in $\text{erg/s/cm}^2/\text{\AA}/\text{arcsec}^2$

Chapter 15: Overview of Pipeline Calibration

Chapter Contents

- [15.1 Pipeline Processing Overview](#)
- [15.2 How Phase II Parameter Choices Affect Calibration](#)
- [15.3 More Detailed Information](#)

15.1 Pipeline Processing Overview

Here, we briefly summarize the basic reductions and calibrations that are performed in the STScI STIS pipeline, and summarize the effects that particular Phase II proposal parameter choices have on calibration. The material in this chapter is intended to provide only enough background to develop robust observing proposals. A series of [STIS Instrument Science Reports](#) (see a listing in [Section 15.3](#)) and the [STIS Data Handbook](#) provide the more detailed information needed for analyzing your data.

Data taken with STIS are initially received by the Space Telescope Data Capture Facility at NASA's Goddard Space Flight Center before being sent to STScI. Once at STScI, the data are reformatted and repackaged into raw (uncalibrated) Flexible Image Transport System (FITS) files by the generic conversion process, which includes populating header keywords with information extracted from the telemetry stream. All STIS data products are FITS files. Most of them are stored as images, with separate FITS extensions holding the science, error, and data quality arrays in a single file. Uncalibrated FITS files are the input to the **calstis** software package, which produces calibrated FITS files for subsequent analysis. Consult the [STIS Data Handbook](#) for more details concerning the structure and naming conventions for the files produced by **calstis**.

Calstis performs the following calibrations for an input file (*rootname_raw.fits*):

- Basic, two-dimensional image reduction producing a flat-fielded output image (*rootname_fit.fits*), which, depending on whether the data are from the MAMA detectors or the CCD and whether they are imaging or spectroscopic data, includes the following: data quality initialization, dark subtraction, bias subtraction, non-linearity flagging, flat fielding, and photometric calibration.
- Two-dimensional spectral extraction producing a flux-calibrated, rectified spectroscopic image (usually *rootname_x2d.fits* for MAMA data, *rootname_sx2.fits* for CCD) with distance along the slit running linearly along the Y axis and wavelength running linearly along the X axis, for spectroscopic first-order mode data. See Table 2.2 in the [STIS Data Handbook](#).
- One-dimensional spectral extraction producing a one-dimensional spectrum of flux versus wavelength (usually *rootname_x1d.fits* for MAMA data, *rootname_sx1.fits* for CCD), uninterpolated in wavelength space, but integrated across an extraction aperture in the spatial direction, for first-order and echelle spectroscopic data. See Table 2.2 in the [STIS Data Handbook](#).
- Data taken in `TIME-TAG` mode are corrected for the Doppler shift from the spacecraft motion and output as an uncalibrated event stream by the pipeline in a FITS binary table (*rootname_tag.fits*). The time-tag data stream is subsequently integrated in time to produce an uncalibrated `ACCUM` mode image (*rootname_raw.fits*) which is then passed through standard calibration. To correct `TIME-TAG` spacecraft times to heliocentric times, refer to Section 5.6.1 in the [STIS Data Handbook](#).

In addition, **calstis** performs two types of *contemporaneous calibrations*:

- For CCD exposures which have been `CR-SPLIT` or when multiple exposures have been taken, **calstis** combines the exposures, producing a cosmic ray rejected image (*rootname_crj.fits*) which is then passed through subsequent calibration steps (e.g., spectral -extraction).
- For spectroscopic exposures, **calstis** processes the associated wavecal exposure (see [Section 3.3 Routine Wavecals](#)) to determine the zero point offset of the wavelength and spatial scales in the science image, thereby correcting for thermal drifts and the lack of repeatability of the mode select mechanism. Raw wavecal data are stored in the file *rootname_wav.fits* to distinguish them from the uncalibrated science data in *rootname_raw.fits*.

Figure 15.1 through Figure 15.3 show example outputs from the **calstis** pipeline. The **calstis** program propagates statistical errors and tracks data quality flags through the calibration process. Although **calstis** is written in C, convenient Python wrapper programs are available as part of the **stenv** environment. These routines may be used to recreate the results of the pipeline (e.g., by re-running **calstis** in its entirety) or to customize the processing by running modular components such as basic two-dimensional image reduction (**basic2d**), two-dimensional spectral extraction (**x2d**), one-dimensional spectral extraction (**x1d**), or cosmic ray rejection (**ocrreject**). Users can manually update the reference files listed in FITS headers by using the **crds.bestrefs** script. The calibration steps that **calstis** performs depends on the type of data. The action of each processing step is controlled by the value of a keyword flag in the FITS header. However, data obtained by available-but-unsupported-modes are calibrated only through flat-fielding in the pipeline.

Observers can retrieve STIS data from the [MAST Portal](#), the [HST Archive](#), or can use the Astropy module [astroquery.mast](#) to query and download data.

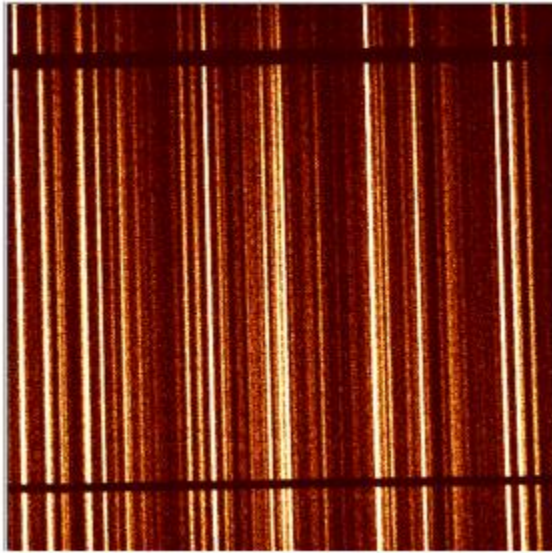
Between Spring 2001 and Fall 2016, calibrated data products for STIS were available through on-the-fly-reprocessing (OTFR), which replaced on-the-fly-calibration (OTFC). The OTFR system started with raw telemetry products, converted these to FITS files, and added the latest instrument calibrations.

Currently, the MAST archive maintains a cache of all STIS data that has been uniformly processed with the current instrumental calibration files. When new reference files become available, all affected data sets are promptly reprocessed and the cache is updated. This approach occasionally results in a delay between the submission of revised reference files and their application to the cached data. Users who require data calibrated with the most recently updated reference files may wish to consult with the STIS team to verify via the [HST Help Desk](#) when calibrated products made using these updated files will be available.

Calstis evolves and improves with time as we understand and characterize the on-orbit performance of STIS more fully. For details about the various changes made to the STIS calibration processes, please refer to the [STIS Data Handbook](#).

Figure 15.1: Two-Dimensional Rectification

INPUT: rootname_fit.fits or rootname_crj.fits



OUTPUT: rootname_x2d.fits

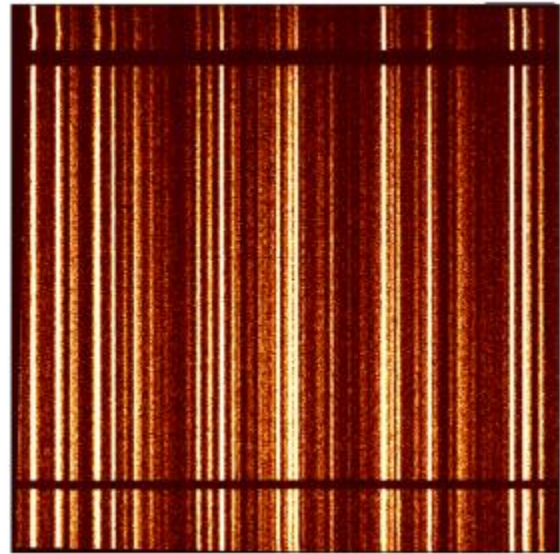


Figure 15.2: Cosmic Ray Rejection

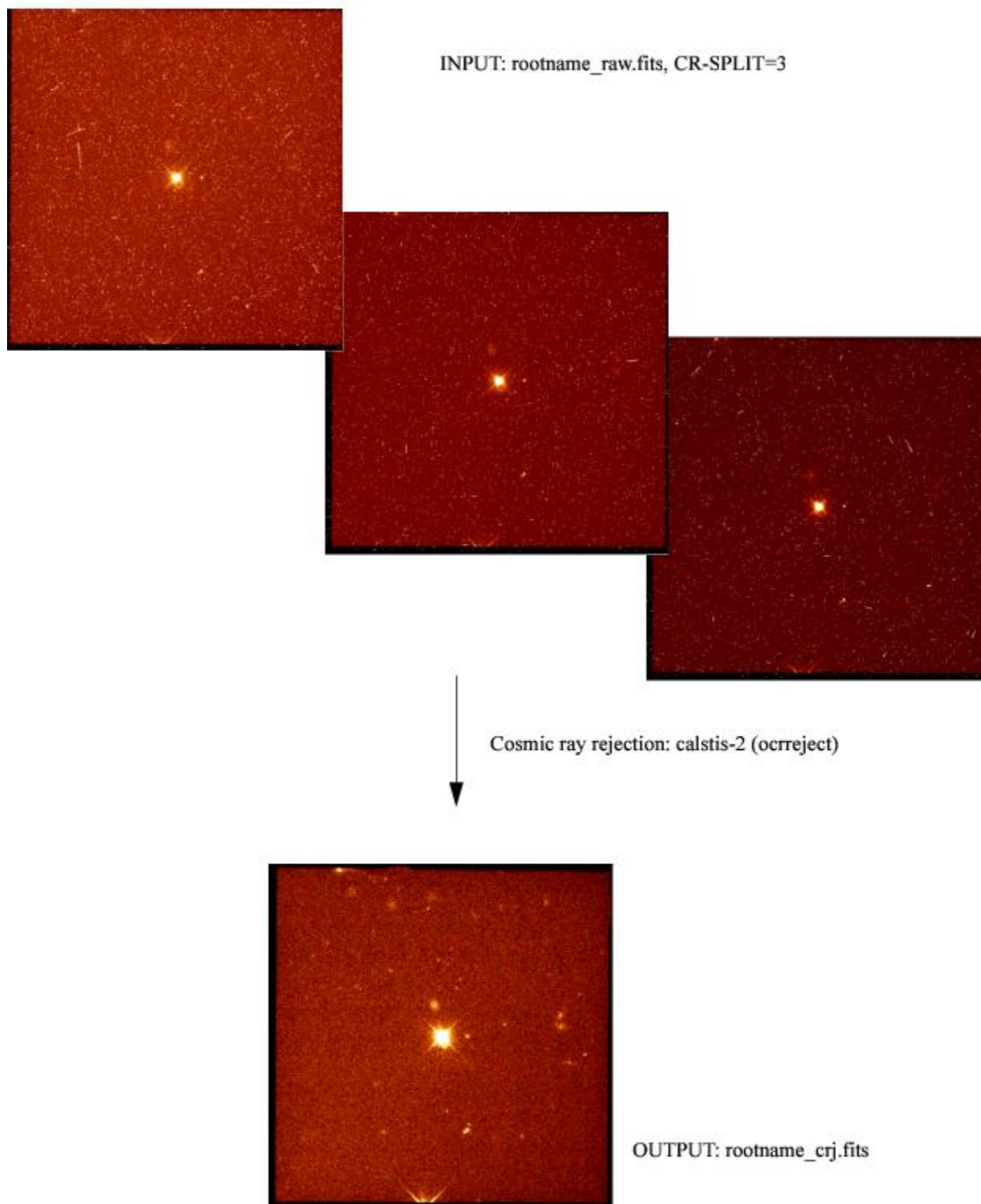
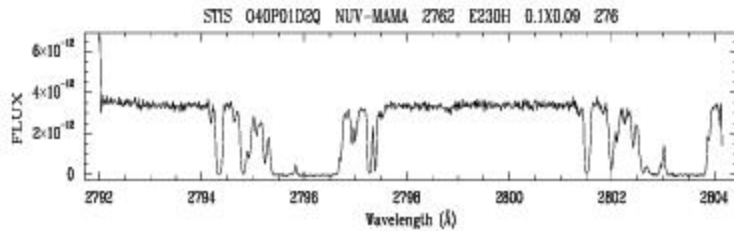
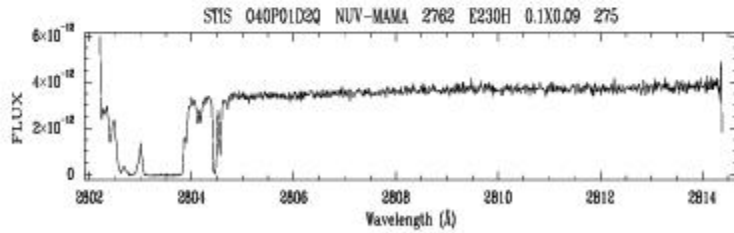
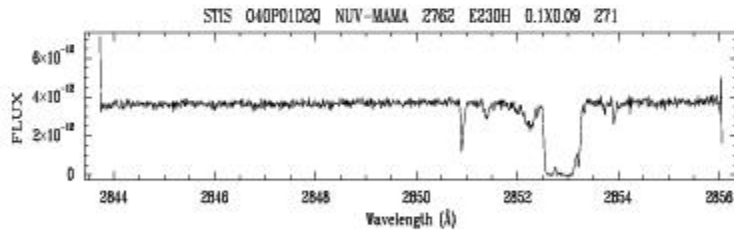
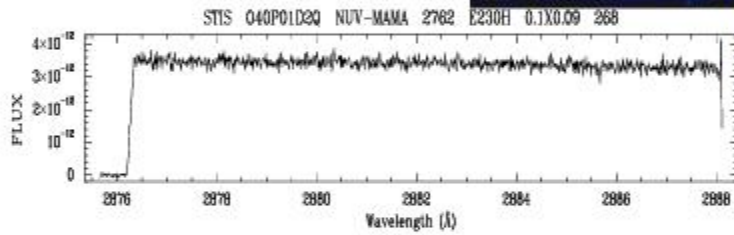
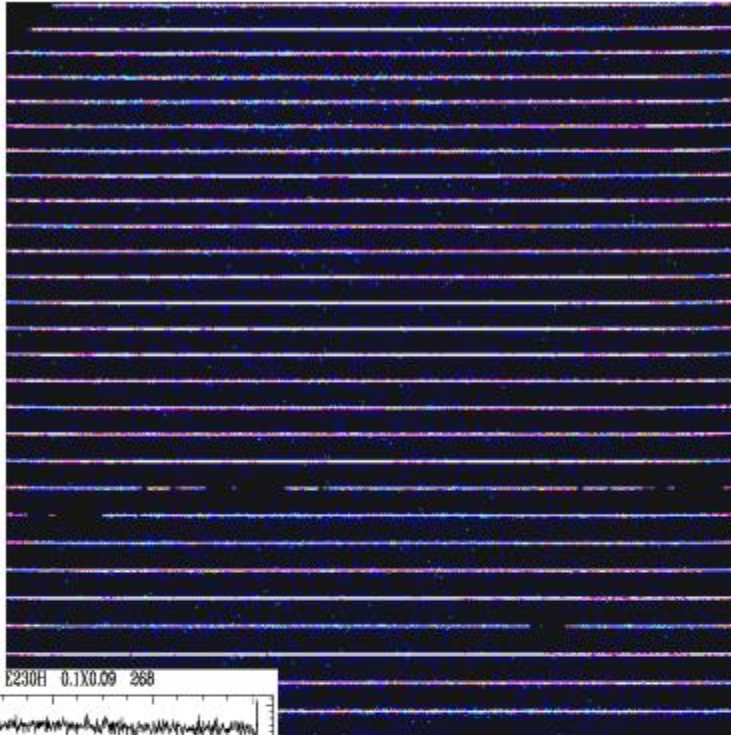


Figure 15.3: One-Dimensional Spectral Extraction

INPUT: rootname_raw.fits,
NUV-MAMA, E230H, cenwave=2762



OUTPUT: rootname_x1d.fits, plotted
by echplot (only a few spectral
orders are plotted)

15.2 How Phase II Parameter Choices Affect Calibration

Table 15.1: Calibration Dependencies on Phase II Parameter Choices.

| Parameter | Effect in Pipeline Calibration |
|--|--|
| Engineering MODE | Not calibrated; receive raw data files only. |
| Available-but-unsupported MODE | Calibrated through flat fielding only; no 2-D rectification, cosmic ray rejection (if applicable), flux calibration, or 1-D extraction. |
| MODE=ACQ or ACQ/PEAK | Not calibrated; receive raw data files only. |
| MODE=TIME-TAG | Data events are tabulated in <i>rootname_tag.fits</i> file with one binary table extension for each buffer read (determined by exposure time and BUFFER-TIME parameters). All raw data events are gathered into a single image, <i>rootname_raw.fits</i> , which is then passed through the normal calibration steps. |
| CCD only CR-SPLIT > 1 or Number_of_Iterations > 1 | The number of imsets in the raw file equals CR-SPLIT or Number_of_Iterations. Raw file imsets are cosmic ray rejected and summed before the bias, dark, and flat-fielding corrections are made, producing a <i>rootname_crj.fitsfile</i> . The individual imsets are also flagged for cosmic rays and processed without summing to produce a <i>rootname_flat.fits</i> file. |
| MAMA only Number_of_Iterations > 1 | The raw file contains Number_of_Iterations imsets, as do the flat-fielded and 2-D rectified files; the 1-D extracted files contain Number_of_Iterations tables. Repeat exposure imsets are summed after flat-fielding and 2-D rectification producing files <i>rootname_sfl.fits</i> and <i>rootname_x2d.fits</i> respectively (this is also true for imaging data). Note that for the MAMA detectors, 1-D spectral extraction data are not summed even when there are repeat exposures. |
| POS-TARG | Normal calibration processing. |
| PATTERN | Separate PATTERN step exposures are not associated with each other. Each PATTERN step exposure is processed through calibration independently. |
| WAVECAL=NO | If GO wavecals (i.e., TARGET=WAVE exposures) are obtained at the same MSM position instead of autowavecals, full pipeline spectral calibration is performed. If no onboard wavecals are obtained, 1-D extraction and 2-D rectification of spectral data will not be done, because the associated wavelengths would be incorrect and therefore misleading. |
| Target_Name=CCDFLAT | An internal STIS CCD flat-field lamp exposure useful in post-pipeline processing to correct for fringing above $\sim 7000 \text{ \AA}$ with gratings G750L and G750M. Users must apply fringe flats corrections themselves using the defringing tools in the stistools package. |

15.3 More Detailed Information

More detailed descriptions of the **calstis** software and its modular components are available in [Chapter 3](#) of the *STIS Data Handbook*, and in a series of STIS documents, listed below, and accessible via the [STIS webpages](#).

- [STIS ISR 1998-10](#): “Calstis0: Pipeline Calibration of STIS Data—A Detailed View”
- [STIS ISR 1998-26](#): “Calstis1: Basic Two-Dimensional Image Reduction”
- [STIS ISR 1998-11](#): “Calstis2: Cosmic Ray Rejection in the STIS Calibration Pipeline”
- [STIS ISR 1998-22](#): “Cosmic Ray Rejection in STIS CCD Images”
- [STIS ISR 1998-12](#): “Calstis4, Calstis11, Calstis12: Wavecal Processing in the STIS Calibration Pipeline”
- [STIS ISR 1999-03](#): “Calstis6: “Extraction of 1-D Spectra in the STIS Calibration Pipeline”
- [STIS ISR 1998-13](#): “Calstis7: Two-dimensional rectification of spectroscopic data in the STIS Calibration Pipeline”
- [STIS ISR 1998-28](#): “The STIS Pipeline - Determination of Calibration Switch Settings”
- [STIS ISR 2002-01](#): “2-D Algorithm for Removing Scattered Light from STIS Echelle Data”
- [STIS ISR 2003-03](#): “An Algorithm for Correcting CTE Loss in Spectrophotometry of Point Sources with the STIS CCD”
- [STIS ISR 2006-03](#): “A new CTE Correction Algorithm for Point Source Spectroscopy with the STIS CCD: Correcting for charge trap filling by the “red halo” of the CCD Point Spread Function redward of 8000 Å”
- [STIS ISR 2007-03](#): “Time Dependent Trace Angles for the STIS First Order Modes”
- [STIS ISR 2007-04](#): “wx2d: A PyRAF Routine to Resample Spectral Images”
- [STIS ISR 2018-01](#): “A Python Script for Aligning the STIS Echelle Blaze Function”
- [Pixel-based CTI Corrections for STIS CCD Data](#)

The ISRs currently contain the most up-to-date descriptions of the calibration software. New releases of **calstis** are accompanied by updates under the [“Software Tools”](#) page on the [STIS website](#).

A series of Jupyter notebooks available on the [HST Notebooks Repository](#) provide examples on using different modules of **calstis** and working with STIS data:

- [calstis 2D CCD Calibration Steps](#)
- [1D Spectral Extraction](#)
- [Viewing STIS Data](#)
- [Custom CCD Darks](#)
- [Correcting for Missing Wavecalcs with Cross-Correlation](#)

Chapter 16: Accuracies

Chapter Contents

- [16.1 Summary of Accuracies](#)

16.1 Summary of Accuracies

In this chapter we summarize the typical accuracies achieved by the STIS photometric, spectral, and astrometric calibrations. Tables 16.1 through 16.5 list the expected accuracies for each of the basic STIS observation modes: CCD spectroscopy, MAMA spectroscopy, CCD imaging, MAMA imaging, and target acquisition. All the accuracies correspond to 2-sigma limits; for the MAMA detectors, the pixels are the "native" low-resolution pixels. The specific values given in the tables are those characterizing the "close-out" calibration of data obtained prior to the suspension of STIS operations early in Cycle 13, reflecting our understanding of STIS as of 2010 August. The listed values thus are those to be expected for the pre-SM4 data that were delivered to the archive under that close-out calibration. Following the repair of STIS in SM4, both the CCD and the MAMA detectors have exhibited somewhat [increased dark rates](#), (continued) slow declines in sensitivity, and (for the CCD) reduced charge transfer efficiency (Sections 7.2 through 7.4). After accounting for those effects, however, similar accuracies generally have also been achieved for post-SM4 STIS data. The sources of inaccuracy are described in [Chapter 4](#) of the *STIS Data Handbook*, which includes discussions of various instrumental phenomena and the creation of reference files that characterize those phenomena. More detailed discussions may be found in various [STIS Instrument Science Reports](#) (ISRs) and [STScI Analysis Newsletters](#) (STANs).

The absolute and relative flux accuracies quoted in Tables 16.1 and 16.2 apply only to spectroscopic observations using relatively large apertures ($52 \times 2''$ for 1st order modes; $0.2 \times 0.2''$ for the echelle modes). For smaller apertures, however, the reliability and repeatability of the throughput has been less well quantified. There is some evidence that the average STIS focus, relative to that of other *HST* instruments, changed between 2013 and 2015 ([STIS ISR 2017-01](#)). For apertures less than or equal to about $0.1''$ in size, that change in focus appears to have resulted in both decreased average throughput and increased throughput variability. Analysis of echelle observations taken through the $0.2 \times 0.06''$ and $0.2 \times 0.09''$ apertures indicated that the average throughput was only about 80% of nominal, with some individual exposures showing as much as a 40% throughput loss; for the smallest aperture ($0.1 \times 0.03''$), the average throughput was typically only half its nominal value. (Note that for these apertures, throughput variations of order 10% due to telescope breathing have been commonly observed throughout the lifetime of STIS.) After 2016, however, the average STIS focus appears to have recovered somewhat ([STIS ISR 2019-01](#)). Because the throughput losses can vary significantly from observation to observation, it is not possible to simply update the ETC throughputs, as the ETC must also warn against observations which are too bright or which may cause saturation, and must therefore adopt the highest throughput that might reasonably be obtained. Focus offsets can also affect the relative flux calibration as a function of wavelength within a given observation. For modes covering a wide range of wavelengths, relative flux errors of 10% over the wavelength span of E140M and E230M observations done with the $0.2 \times 0.06''$ aperture are not uncommon. If combined with small aperture centering errors, the relative throughput errors can sometimes increase to as much as 25%. The most up-to-date information about STIS focus can be found at [HST's Focus page](#), which includes a link to an interactive focus model.

Many significant changes in pipeline calibration have been made during the lifetime of STIS—reflecting both better understanding of the instrument and compensation for observed changes in its behavior; see [Chapter 3](#) of the *STIS Data Handbook* for details. Extracted spectra and rectified spectral images from all three STIS detectors are now corrected for both time-dependent and temperature-dependent variations in sensitivity (*STIS Data Handbook Section 3.4.13*; [STIS ISR 2017-06](#)). Extracted CCD spectra are corrected for CTE losses ([STIS ISR 2022_07](#)) and are adjusted for the formerly neglected interdependence of grating and aperture throughputs. Time-dependent rotation of the spectral traces is applied to the most commonly used first order modes during spectral extraction and spectral image rectification ([STIS ISR 2007-03](#)). Both the echelle blaze shift correction (for spectral extractions) and the echelle flux calibration have recently been substantially improved (e.g., [2017 August STAN](#); [STIS ISR 2022-04](#)). The flat-field reference files have also been revised (*STIS Data Handbook Section 4.1.4*). Recent improvements to the stellar atmospheric models for the primary flux standard stars, incorporated into the [CALSPECv11 database](#), have prompted an effort to update the flux calibration and zero points for all of the STIS spectroscopic and imaging modes. The revised calibrations for the highest priority spectroscopic modes were delivered in 2022 April, and work is continuing on the rest of the modes (see <https://www.stsci.edu/hst/instrumentation/stis/flux-recalibration>).

We remind users that calibration data have always been immediately non-proprietary. If users have a need for higher accuracy or urgent results, they may wish to consider direct, custom analysis of the calibration data for their particular observing mode. See also [Chapter 17](#) of this handbook for a description of our regular on-orbit calibration program.

Table 16.1: CCD Spectroscopic Accuracies

| Attribute | | Accuracy | Limiting Factors |
|--|---------|---------------|---|
| Relative wavelength ¹ | | 0.1-0.4 pixel | Stability of optical distortion Accuracy of dispersion solutions |
| Absolute wavelength ¹ (across exposures) | | 0.2-0.5 pixel | Thermal stability Derivation of wavecal zero point Accuracy of dispersion solutions |
| Absolute photometry ² | | | Instrument stability Correction of charge transfer efficiency Time dependent photometric calibration Fringe correction (for $\lambda > 7500 \text{ \AA}$) |
| | L modes | 5% | |
| | M modes | 5% | |
| Relative photometry ² (within an exposure) | | | Instrument stability Correction of charge transfer efficiency Time dependent photometric calibration Fringe correction (for $\lambda > 7500 \text{ \AA}$) |
| | L modes | 2% | |
| | M modes | 2% | |

¹ For more recent analyses of wavelength accuracy, see [STIS ISR 2011-01](#), [STIS ISR 2015-02](#), and [STIS ISR 2018-04](#). Note that the wavelength accuracies will also depend on the accuracies of the rest wavelengths used in calculating the dispersion relations. The quoted accuracies refer to spectra obtained at the nominal (central) locations; the wavelength zero points may be somewhat less accurate for recent spectra obtained at the E1 pseudo-aperture.

² Assumes star is well centered in slit and use of a 2 arcseconds wide photometric slit. See the [STIS Data Handbook](#) for a more complete description of the impact of centering and slit width on accuracies. This accuracy excludes the G230LB and G230MB modes when used with red targets, for which grating scatter can cause large inaccuracies in the flux calibration at the shortest wavelengths; see [Gregg et al. 2006](#) (HST Calibration Workshop) and [STIS ISR 2022-05](#). Photometric accuracies referenced are for continuum sources; equivalent width and line profile measures are subject to other uncertainties (such as spectral purity and background subtraction).

Table 16.2: MAMA Spectroscopic Accuracies

| Attribute | Accuracy | Limiting Factors |
|--|-----------------------------|---|
| Relative wavelength ¹ (within an exposure) | 0.25–0.5 pixel ² | Stability of small scale geometric distortion Optical distortion Accuracy of dispersion solutions |
| Absolute wavelengths ² (across exposures) | 0.5–1.0 pixel ² | Thermal stability Derivation of wavecal zero point Accuracy of dispersion solutions |
| Absolute photometry ³ | | Instrument stability Time dependent photometric calibration |
| L modes | 4% | |
| M modes | 5% | |
| Echelle modes ⁴ | 8% | |
| Relative photometry (within an exposure) ⁴ | | Instrument stability Flat fields Echelle modes: Blaze shift correction accuracy Scattered light subtraction |
| L modes | 2% | |
| M modes | 2% | |
| Echelle modes ^{4,5} | 5% | |

¹ For more recent analyses of wavelength accuracy, see [STIS ISR 2011-01](#), [STIS ISR 2015-02](#), [STIS ISR 2018-04](#), and [Ayres 2022](#). Note that the wavelength accuracies will also depend on the accuracies of the rest wavelengths used in calculating the dispersion relations.

² A pixel for the MAMA refers to 1024 × 1024 native format pixels.

³ Assumes star is well centered in slit and use of a wide photometric slit.

⁴ For 0.2 × 0.2 arcsecond slit. These are typical accuracies (which can be 2 to 3 times better or worse as a function of wavelength; see [STIS ISR 1998-18](#) for details).

⁵ Quoted relative flux accuracies of echelle spectra assume that the time dependent shifts in the echelle blaze function are properly corrected. Recent improvements to the blaze shift correction yield agreement in the order overlap regions to better than 5% for E140H (see [August 2017 STAN](#)).

Table 16.3: CCD Imaging Accuracies

| Attribute | Accuracy | Limiting Factors |
|-------------------------------------|-----------|---------------------------------|
| Relative astrometry within an image | 0.1 pixel | Stability of optical distortion |
| Absolute photometry | 5% | Instrument stability |
| Relative photometry within an image | 5% | External illumination pattern |

Table 16.4: MAMA Imaging Accuracies

| Attribute | Accuracy | Limiting Factors |
|-------------------------------------|----------------------------|---------------------------------------|
| Relative astrometry within an image | 0.25 pixel ^{1, 2} | Small scale distortion stability |
| Absolute photometry | 5% | Instrument stability and calibration |
| Relative photometry within an image | 5% | Flat-fields and external illumination |

¹ A pixel for the MAMA refers to 1024 × 1024 native format pixels.

² A recent re-analysis of the FUV-MAMA geometric distortion has yielded rms residuals of 4mas (0.16 pix) in each coordinate, compared to the positions in an astrometric standard catalog based on WFC3 /UVIS imaging data see ([August 2017 STAN](#) and [STIS ISR 2018-02](#)).

Table 16.5: Target Acquisition Accuracies

| Attribute | Accuracy | Limiting Factors |
|---------------------------------------|----------------------|---|
| Guide star acquisition | 1-2" 0.2-0.3" | GSC1 catalog uncertainties GSC2 catalog uncertainties accuracy of input target coordinates See Section 8.1.1 |
| Following target acquisition exposure | | Signal to noise Source structure |
| Point sources Diffuse sources | 0.01" 0.01-0.1" | Centering accuracy plus plate scale accuracy to convert pixels to arcseconds See Sections 8.1.3 and 8.2 . |
| Following pickup acquisition exposure | 5% of the slit width | Signal to noise Source structure Number of steps in scan and PSF See Sections 8.1.3 and 8.3 . |

| | | |
|--------------------------------|--------|---|
| Following aperture/slit change | 0.005" | Accuracy of slit positioning See Section 8.3.1 |
|--------------------------------|--------|---|

Chapter 17: Calibration Status and Plans

Chapter Contents

- 17.1 Introduction
- 17.2 Ground Testing and Calibration
- 17.3 STIS Installation and Verification (SMOV2)
- 17.4 Cycle 7 Calibration
- 17.5 Cycle 8 Calibration
- 17.6 Cycle 9 Calibration
- 17.7 Cycle 10 Calibration
- 17.8 Cycle 11 Calibration
- 17.9 Cycle 12 Calibration
- 17.10 SM4 and SMOV4 Calibration
- 17.11 Cycle 17 Calibration Plan
- 17.12 Cycle 18 Calibration Plan
- 17.13 Cycle 19 Calibration Plan
- 17.14 Cycle 20 Calibration Plan
- 17.15 Cycle 21 Calibration Plan
- 17.16 Cycle 22 Calibration Plan
- 17.17 Cycle 23 Calibration Plan
- 17.18 Cycle 24 Calibration Plan
- 17.19 Cycle 25 Calibration Plan
- 17.20 Cycle 26 Calibration Plan
- 17.21 Cycle 27 Calibration Plan
- 17.22 Cycle 28 Calibration Plan
- 17.23 Cycle 29 Calibration Plan
- 17.24 Cycle 30 Calibration Plan
- 17.25 Cycle 31 Calibration Plan

17.1 Introduction

In this chapter we give a brief guide to the calibration observations obtained during ground testing, the original period of Servicing Mission Orbital Verification (SMOV2), Cycles 7 through 13, the post-SM4 repair verification (SMOV4), and Cycles 17 through 31. Details of improvements made to the pipeline calibration of STIS data after the failure of the STIS Side-2 electronics in August 2004 are discussed in [Section 15.1](#). Further information on calibration, including detailed descriptions of the proposals, can be found on the [STIS Calibration page](#).

STIS provides a large number of available-but-unsupported capabilities ([Appendix A](#)) beyond those which are routinely supported. Observers should remember that *STScI will not normally undertake additional calibrations for these available-but-unsupported instrument configurations*. Observers wishing to use non-standard instrument configurations should assess their specific calibration needs and include time in their Phase I proposal for any additional calibrations that are required. Proposers who believe that more extensive calibration observations or analysis may be of benefit to users of STIS should consider submitting a Cycle 32 Calibration Outsourcing Proposal (see the [Cycle 32 "Call for Proposals"](#) for details).

17.2 Ground Testing and Calibration

The STIS Instrument Definition Team (STIS IDT, Principal Investigator, Bruce Woodgate, GSFC) was responsible for the ground testing and ground calibration of STIS. Most of the ground test data were obtained in late 1996, during thermal vacuum testing at Ball Aerospace in Colorado, and during subsequent testing in a dry-nitrogen environment at GSFC. These tests characterized the basic properties of the optics, the detectors, and the mechanisms. Certain measurements (e.g., measurements of the quantum efficiency of the STIS detectors vs. wavelength) cannot be repeated in orbit. However, most of the ground test data have been superseded by on-orbit measurements.

17.3 STIS Installation and Verification (SMOV2)

The primary goal of the Second Servicing Mission’s Observatory Verification (SMOV2) was the timely commissioning of the HST observatory for normal science operations. For STIS, just installed at this time, this included testing the focus (internal and external), verifying the target acquisition procedures, monitoring instrument stability (both in terms of image motions and sensitivity), and measuring selected characteristics: plate scales, slit throughputs, line spread functions, etc. SMOV2 observations were complete by the summer of 1997. Most of the results of the calibrations were presented in the [1997 HST Calibration Workshop](#). A high level summary was provided in the [Kimble et al. 1998](#) (ApJ, 492, L83) paper on STIS on-orbit performance. For an update including early Cycle 7 calibration, see also [Baum et al. 1998](#) (SPIE, 3356, 271). Brief descriptions of the SMOV2 proposals are given in [Table 17.1](#). Data from calibration proposals are non-proprietary, and can be obtained from the archive with the proposal IDs listed in the table.

Table 17.1: STIS SMOV2 Proposals

| ID | Title |
|------------|---|
| 7058 | STIS Memory Load and Dump |
| 7059 | Science Data Buffer Check with Self-Test |
| 7061 | CCD Functional |
| 7062 | CCD Temperature Set Point Determination |
| 7063, 7064 | STIS SMOV Contamination Monitor |
| 7065 | STIS to FGS Alignment |
| 7066 | STIS Acquisition Aperture and Slit Location |
| 7067 | STIS CCD Point Source Acquisition |
| 7068 | STIS CCD Diffuse Source Acquisition |
| 7070 | STIS CCD Coronagraphic Acquisition |
| 7071 | CCD Target Centering |
| 7073 | CCD Peakdowns for Coronagraphic Acquisition |
| 7075 | STIS Corrector Alignment, Coarse |
| 7076 | STIS Corrector Alignment, Fine |
| 7077, 7078 | Spectroscopic Mode Image Quality |
| 7079, 7080 | Camera Mode Image Quality |
| 7081, 7082 | Repeatability of Image Positions for STIS Modes |
| 7083, 7084 | Verification of Optical Format of STIS Modes |
| 7085, 7086 | STIS Slit to Detector Internal Stability |

| | |
|------------|--|
| 7087 | OTA-STIS Pointing and Throughput Stability |
| 7088, 7089 | Occulting Bar Scattered Light |
| 7090 | PSF measurement for MAMAs |
| 7091 | STIS Pixel-To-Pixel Response Stability |
| 7092 | CCD Dark Rate and Read Noise |
| 7093 | Dark Measurement for MAMAs |
| 7094, 7096 | STIS Sensitivity On-Axis |
| 7095, 7097 | STIS Sensitivity (Vignetting) |
| 7098 | MAMA Flat-field Uniformity |
| 7099 | CCD Flat-field Stability |
| 7100 | SMOV Slit Transmission |
| 7101 | SMOV Slit Transmission |
| 7103 | STIS Mechanism Mini-Functional |
| 7104 | STIS Onboard Doppler Processing Checkout |
| 7105 | MAMA Turn-On |
| 7106 | STIS MAMA Fold Distribution |
| 7107 | STIS CCD Hot Pixel Annealing |
| 7108 | STIS MAMA Time Tag Mode |
| 7131, 7132 | STIS Imaging Mode Geometric Distortion |
| 7133 | STIS to FGS alignment |
| 7142 | CCD Flat-field Monitoring |
| 7143 | CCD Internal Image stability with LVPS cycling |
| 7144 | STIS Thermal Stability with LVPS cycling |
| 7147 | STIS Fine Corrector Alignment with CCD |
| 7148 | STIS CCD Target Acquisition Workout |
| 7151 | STIS CCD V2V3 Aperture Verification |
| 7159 | NUV-MAMA Dark Current vs. Time from SAA |
| 7160 | CCD Reconfiguration Effects |

17.4 Cycle 7 Calibration

[17.4.1 Calibration Priorities](#)

[17.4.2 Calibration Status](#)

The [STIS Cycle 7 calibration plan](#) included additional characterization of STIS performance, along with periodic monitoring of sensitivity, flat fields, dark current, gain, etc. Because it is not feasible to calibrate the instrument in all possible observing modes, the calibration emphasizes measurements in all the supported modes. The results of all Cycle 7 calibration programs are presented in the close-out report [STIS ISR 2000-04](#).

17.4.1 Calibration Priorities

The task of calibrating STIS involves a number of important trade-offs. HST calibration observations are planned to use a limited number of orbits (no more than about 10% of the total science time allocated in the Cycle), and to stretch out through each Cycle so that the observing schedule is not too heavily front-loaded with calibrations. The allocation of spacecraft and staff resources to the calibration effort for STIS has followed roughly the following set of priorities:

1. *Monitor the health and safety of STIS.* Carry out the necessary periodic monitoring of STIS to ensure that it is operating correctly. Revise operations as necessary to ensure that it will maintain its scientific performance over its lifetime.
2. *Update and Maintain Pipeline Reference files.* This includes things such as darks, biases, flats, and sensitivities. Information on newly released files is announced via the Reference Files Update mailing list ([stis_reffiles_upd](#)), the [Space Telescope Analysis Newsletters \(STANs\)](#), and is posted to the [STIS webpages](#). To subscribe to the [stis_reffiles_upd](#) mailing list, send an email to listserv@stsci.edu with a blank subject line and “subscribe stis_reffiles_upd” in the body of the email. As new reference files are incorporated into the pipeline, the “recommended reference files” are updated as appropriate for each dataset in the HST Archive.
3. *Basic sensitivity calibration of spectroscopic modes.* The majority of STIS science observations use the spectroscopic modes. Sensitivity calibration is important for instrument safety, science optimization, and data analysis. The sensitivity calibration includes basic measurements of on-orbit throughput, and monitoring of time variations either due to contamination or due to gain variations in the detectors.
4. *Characterization of optical performance.* This includes point spread functions (PSFs), line spread functions, aperture throughputs, enclosed energy for different spectral extraction heights, and imaging and spectroscopic geometric distortion calibrations. Detailed characterization of scattering (e.g., in wavelength in the gratings, or in the far wings of the imaging PSF) is included, but is orbit-intensive and therefore will be carried out over a longer time scale.
5. *Characterization of detector and observation specific peculiarities.* This includes detector nonlinearities, charge transfer effects, fringing, long-wavelength scattering within the CCD, grating scatter and extended PSF wings, etc.
6. *Calibration and testing of future observing mode strategies.* The original goals to test cross-dispersed gratings and other operating modes were scaled back through the course of Cycle 7 due to the press of the higher priority calibrations.

Within each of these priority groups, calibration priority is in the following order by observing mode:

1. First order prime L grating modes (G140L, G230L, G430L, G750L).
2. Echelle spectroscopy.

3. First- order M-mode gratings.
4. CCD imaging (broad band first, then narrow band).
5. MAMA imaging (broad band first, then narrow band).
6. G230LB and G230MB backup modes, including analysis of scattered red light.

In addition, on-axis calibrations have higher priority than off-axis calibrations. That is, we sought first to establish the calibrations at the field/slit center and thereafter, to expand the calibration to two dimensions.

17.4.2 Calibration Status

The overall status of STIS calibration was summarized in the STScI Newsletter in October 1998 and in the Cycle 7 Calibration Close-out Report ([STIS ISR 2000-04](#)). Many reference files were updated with new calibrations from on-orbit data. The HISTORY and PEDIGREE fields of the calibration reference files should be consulted if you are in doubt about the origin of the calibration. HISTORY keywords contain commentary on the file's creation. The PEDIGREE keyword describes the type of data (GROUND , INFLIGHT) and gives the date range over which the calibration data were taken.

17.5 Cycle 8 Calibration

The [Cycle 8 calibration plan](#) was modeled closely on the Cycle 7 calibration plan. Once again, *supported* modes were monitored for such things as sensitivity changes, flat-field evolution, and dispersion solutions. No additional calibrations were taken for most *available-but-unsupported* configurations.

In addition to monitoring instrument health and safety and maintaining the overall calibration of STIS supported modes, our special goals were as follows:

1. To improve the imaging throughput calibration accuracy (to better than the current 5% systematic uncertainty);
2. To improve PSF characterization in imaging mode and in coronagraphic mode;
3. To improve CCD hot pixel and bias subtraction;
4. To improve the CCD charge transfer efficiency (CTE) characterization for sparse fields at low count levels;
5. To calibrate the dispersion as a function of position for MAMA slitless spectroscopy with the L-mode gratings;
6. To characterize observations with the FUV-MAMA repeller wire turned off, with the aim of possibly making this available for Cycle 10. This should improve the spectral resolution at the expense of a ~35% loss of sensitivity.

The results of all the Cycle 8 calibration programs are presented in the close-out report [STIS ISR 2001-04](#).

17.6 Cycle 9 Calibration

The [STIS Cycle 9 calibration plan](#) was modeled closely on the Cycle 8 calibration plan. *Supported* modes were monitored for items such as sensitivity changes, flat-field evolution, and dispersion solutions.

In addition to monitoring instrument health and safety and maintaining the overall calibration of STIS supported modes at the accuracies as established during Cycles 7 and 8, a few special calibration programs were added for Cycle 9, with the following goals:

1. To improve the charge transfer efficiency (CTE) characterization for the CCD, i.e., its dependences on time, source intensity, source nature (point source vs. extended source), and sky background;
2. To quantify the remanence intensity level after over-illumination of the CCD as a function of time after saturation and of number of readouts after saturation. The remanence level may well have increased since STIS was installed on HST due to the degraded CTE;
3. To improve PSF characterization for the CCD in imaging mode, coronagraphic mode, and spectroscopic mode as a function of source color;
4. To improve the dispersion solutions for the reddest settings of the G750M grating;
5. To model the ghosts (which are caused by multiple reflections in the CCD window) in the G750M grating mode.

The results of all the Cycle 9 calibration programs are presented in the close-out report [STIS ISR 2003-02](#).

17.7 Cycle 10 Calibration

The [STIS Cycle 10 calibration plan](#) was very similar to the Cycle 9 calibration program. Supported modes continued to be monitored for items such as sensitivity changes, flat-field evolution, dispersion solutions, and evolution of charge transfer efficiency (CTE) of the CCD detector.

In addition to monitoring instrument health and safety and maintaining the overall calibration of STIS supported modes at the accuracies as established during Cycles 7 through 9, a few new calibration programs were added for Cycle 10, with the following goals.

1. To obtain exposures of primary spectrophotometric standard stars in *every single* supported spectroscopic mode of STIS, including the echelle and first-order medium-resolution modes;
2. To characterize the effect of the presence of bright stars outside the field of view of the STIS CCD on the amount of scattered light;
3. To further improve PSF characterization for the CCD in imaging and coronagraphic mode as a function of source color;
4. To finalize the accurate determination of the throughput curve of the longpass filter used for CCD imaging;
5. To monitor the throughput curves of the broad-band and medium-band imaging filters used with the MAMA detectors and the CCD;
6. To characterize STIS spectroscopic performance at the recently defined “pseudo-apertures” located near row 900 of the CCD (see [Section 7.3.8](#)) that have been defined to reduce losses due to the decreasing CTE of the CCD with time. Spectroscopic sensitivity, PSFs, and LSFs will be measured at the pseudo-apertures using all supported long slits.

The results of all the Cycle 9 calibration programs are presented in the close-out report [STIS ISR 2004-06](#).

17.8 Cycle 11 Calibration

The [Cycle 11 calibration plan](#) closely follows the plans for previous Cycles. Supported modes continue to be monitored for sensitivity changes, flat-field evolution, dispersion solutions, and the evolution of the charge transfer efficiency (CTE) of the CCD detector. Existing monitor programs have been expanded to include routine sensitivity measurements at the E1 aperture positions, to include an annual NUV-PRISM flux monitor observation (which was stopped after Cycle 17), and to more thoroughly check the adopted STIS dispersion solutions. The frequency of some other monitors has been decreased, as our improved understanding of STIS allows us to predict future trends with greater confidence.

In addition to monitoring instrument health and safety and maintaining the overall calibration of STIS supported modes at the accuracies established during Cycles 7 through 10, a few special calibration programs have been added for Cycle 11, with the following goals:

1. To improve the calibration of detector sensitivity, aperture throughputs, and the PSF at the E1 positions that were defined to mitigate CTE effects;
2. To better test the effects of the monthly MSM offsetting on echelle sensitivity;
3. To verify models of the PSF for first order G750L and G750M observations that are critical for many programs targeted at determining rotation curves of galaxies and black hole masses;
4. To re-measure, with improved accuracy, the ratio between CCDGAIN=1 and CCDGAIN=4 observations;
5. To define additional faint spectroscopic flux standards to support calibration of ACS (especially the ACS Sloan filters), and COS.

A detailed summary of the calibration plans can be found on the [STIS Calibration page](#).

17.9 Cycle 12 Calibration

The [Cycle 12 calibration plan](#) continues the routine monitoring programs of Cycle 11, with reductions in observing time where less data or less frequent monitoring are now sufficient. As before, much of the program is devoted to producing timely darks, biases, flats, and sensitivity corrections, and to monitoring basic instrument characteristics and performance. Characterization of CTE remains a high priority, to support upcoming CTE correction of fluxes in extracted CCD spectra in the pipeline.

Additional or modified observations were made to meet specific needs in some continuing programs, and some new observations were made, as follows:

1. CCD spectroscopic sensitivity was monitored more frequently so that dependence on detector temperature can be modelled more accurately, along with tracking temporal dependence.
2. Deeper MAMA wavecal exposures were made to support physical modelling that will lead to better dispersion solutions.
3. Spectroscopic observations were made of a star stepped along the slit, achieving low signal and background levels, to improve our characterization of the large CTE losses that occur at these low levels.
4. New “apertures” (target locations in existing apertures) were defined to improve observations high on the CCD detector (where CTE losses are less) and low on the FUV-MAMA detector (where dark current is less), and to provide a new coronagraphic aperture (see [Section 12.11](#)). The locations of the new apertures were verified.

The STIS Side-2 electronics failure occurred very early in Cycle 13, before the Cycle 13 calibration plan commenced. However, routine monitoring observations from the STIS Cycle 12 calibration plan were still ongoing, and provided the necessary calibration data for the Cycle 13 STIS GO data that were collected. A detailed summary of the calibration plans can be found on the [STIS Calibration page](#).

17.10 SM4 and SMOV4 Calibration

After the successful repair of STIS during Servicing Mission 4 (SM4), a plan for verification and preliminary calibration was executed during the subsequent period of Servicing Mission Observatory Verification (SMOV4). The SMOV4 plan for STIS focused on ensuring that observers can obtain data of sufficient quality to meet their scientific goals, but some of the more time consuming calibration observations that do not affect the planning of observations and which can be applied retroactively, (e.g., high signal-to-noise pixel-to-pixel flats and high precision sensitivity determinations for all central wavelength settings), were deferred and included in the Cycle 17 calibration plan. As a result the initial calibration precision for STIS data products delivered early in Cycle 17 is less than that which will ultimately be obtainable when the final calibration reference files become available for those observations. Significant updates to the calibration will be announced on the [STIS webpages](#).

A summary of preliminary STIS SMOV4 activities follows.

STIS-01: Modes and Data Interface Checks

- Includes turn-on and telemetry checks that verify the capability to enter required instrument and detector states during normal operations.
- Includes the initial turn-on of the MAMA low voltage (LV) and checks of the MAMA readout electronics that can be made with the high voltage (HV) off.
- Includes the initial turn-on of the CCD thermal electric cooler (TEC).

STIS-02: Memory Load and Dump

- Loads, dumps and compares sections of memory with stored images to verify operations.

STIS-03: Science Data Buffer Check with Self-Test

- Loads a test pattern into the science data buffer. The buffer contents are subsequently examined using memory and exposure dumps.

STIS-04: Mechanism Mini-Functional

- Initializes all mechanisms, except the focus and corrector mechanism, commands them to selected positions, and moves them over the full range necessary for normal operations. Commanded motions are verified using telemetry.

STIS-05: CCD Anneal

- The CCD is warmed from $\sim -80\text{C}$ to $\sim +5\text{C}$ to repair hot pixels. A series of darks and biases are taken to monitor and evaluate CCD performance before and after the anneal process.

STIS-06: CCD Functional

- Bias, dark, and tungsten lamp exposures are taken, using various gains and binning, to measure the baseline CCD performance.

STIS-07: CCD Bias and Dark Monitor

- Acquisition of sufficient dark and bias frames to permit construction of superbias and superdark frames needed for pipeline image reduction.

STIS-08: Aperture Wheel and Lamp Functional Tests

- Aperture positions are checked using tungsten lamp images through several slits.
- Thermal drifts are measured using repeated observations of the 0.2X0.2 aperture interspersed throughout the test.
- Pt/Cr-Ne lamp functionality is checked by obtaining images with the HITM1, HITM2, and LINE lamps.

STIS-09: STIS to FGS Alignment

- Target positioning accuracy in the STIS aperture plane using fine guidance sensors (FGS) guiding is measured using star field and lamp images illuminating the 50CCD aperture.

STIS-10: CCD Optical Format Verification

- Measurement of the location of the CCD spectra and images on the detector for each CCD spectral element (G230LB, G230MB, G430L, G430M, G750M, G750) and MIRVIS using the HITM calibration lamps.

STIS-11: External Focus Check

- Evaluation of the STIS PSF at the aperture plane using small slit (0.1X0.09) ACQ/PEAK images and point source images with the F28X500II filter.
- Determination of the shape of the PSF at ultraviolet (UV) wavelengths from spectra acquired using the G230LB grating.
- Estimation of the STIS focus through comparison of the aperture throughputs and PSF shape with previous values.

STIS-12: Corrector and Focus Alignment

- Coarse and/or fine adjustments of the STIS focus are made if STIS-11 finds a significantly degraded PSF. If a focus adjustment is necessary, then the STIS CM1 mirror will be adjusted in tip/tilt and focus to optimize the PSF. Coarse adjustments optimize the encircled energy of an isolated star observed through the 50CCD aperture while fine adjustment sweeps optimize the small aperture throughputs.

STIS-13: CCD Spectroscopic Image Quality and ACQ Tests

- Checks the cross dispersion PSF using point source spectra obtained at multiple positions along a long slit.
- Peak-ups are executed to check target centering at the E1 slit location.

STIS-14: CCD CTE Check

- Lamp exposures are taken at multiple positions along the 0.05X31ND slit, and read-out using amplifiers D and B, to search for, and compare, CTE losses as a function of Y-position on the detector.

STIS-15: CCD Spectroscopic Throughputs

- Determination of the throughput of each spectroscopic CCD mode from observations of the standard high-latitude sdO-type star AGK+81D266.

STIS-16: CCD Image and Pointing Stability

- The pointing stability is assessed after execution of a large pointing maneuver selected to apply a significant thermal change to STIS. Star field images and lamp images of an aperture are interspersed to measure the image stability at detector and aperture planes.

STIS-17: FUV-MAMA HV Recovery

- The FUV-MAMA voltage is ramped-up in stages while taking dark exposures and using on-board count rate monitors to protect against anomalies. Fold analysis is performed after it has been verified that the voltage can be safely ramped-up to the required level.

STIS-18: NUV-MAMA HV Recovery

- The NUV-MAMA voltage is ramped-up in stages while taking dark exposures and using on-board count rate monitors to protect against anomalies. A fold analysis is performed after it has been verified that the voltage can be safely ramped-up to the required level.

STIS-19: FUV-MAMA Dark Measure

- Characterization of the FUV-MAMA glow as a function of detector warm-up through the acquisition of a series of darks spanning the 5-orbit SAA-free period.

STIS-20: NUV Dark Monitor

- Monitoring of the NUV phosphorescent window glow to determine the equilibrium behavior and the onset of science observations.

STIS-21: FUV-MAMA Optical Format Verification

- Measurement of the location of the FUV spectra on the detector for each FUV-MAMA spectral element (G140L, G140M, E140M, and E140H) using the HITM calibration lamps.

STIS-22: NUV-MAMA Optical Format Verification

- Measurement of the location of the NUV spectra on the detector for each NUV-MAMA spectral element (G230L, G230M, E230M, E230H, and PRISM) using the HITM calibration lamps.

STIS-23: FUV-MAMA Image Quality

- Checks the cross dispersion PSF using point source spectra of G140L obtained at multiple positions along a long slit.

STIS-24: NUV-MAMA Image Quality

- Checks the cross dispersion PSF using point source spectra of G230L obtained at multiple positions along a long slit.

STIS-25: MAMA Spectroscopic Throughputs

- Determination of the throughput of each spectroscopic MAMA mode, except the NUV PRISM, from standard star observations (preferably GRW+70D5824, AGK+81D266, or BD+28D4211).

STIS-26: MAMA Image Stability

- The pointing stability is assessed after the execution of a large pointing maneuver selected to apply a significant thermal change to STIS. Repeated lamp images of an aperture are obtained to measure the image stability at detector over a two orbit period.

17.11 Cycle 17 Calibration Plan

The [STIS Cycle 17 calibration plan](#) includes the usual routine calibration and monitoring observations performed in previous Cycles. However, because of the long gap in STIS operations, and changes in STIS usage, the emphasis on some activities have changed:

- Programs to derive new pixel-to-pixel flat fields for both the MAMA (programs 11861 and 11862) and CCD (programs 11852 and 11853) detectors were a high priority for early in Cycle 17.
- New flux calibrations for all STIS echelle central wavelength settings have also been included early in the Cycle, in order to measure changes in the echelle blaze function (program 11866).
- Special calibration programs to improve the cross-calibration between STIS, COS, and other space-based instrumentation (programs 11865 and 11999) were also executed.
- New supplemental Cycle 17 calibration programs were added to follow up on the results of earlier SMOV4 and Cycle 17 calibration observations. Specifically, program 12078: to verify the adjustment of two STIS MSM positions and 12079: to study the calibration lamp ratios at all wavelengths.
- Observations were added as part of the Cycle 17 supplemental calibration plan to programs 11861, 11857, and 11860 to improve the characterization of the FUV-MAMA flat fields, the MAMA dark rate, and the echelle time-dependent sensitivity.

The results of all the Cycle 17 calibration programs are presented in the close-out report [STIS ISR 2012-03](#). A detailed summary of the calibration plans can be found on the [STIS Calibration web page](#).

17.12 Cycle 18 Calibration Plan

The [Cycle 18 calibration plan](#) continues the Cycle 17 monitoring programs adjusting observing times as necessary to better characterize the instrument. This calibration plan takes into account the Cycle 18 GO calibration requirements for the CCD and MAMA detectors.

For Cycle 18, separate calibration data will no longer be routinely collected to support on-chip binning, as this option is rarely used. A new special calibration program, 12418, will evaluate the use of the DB white dwarf star WD0308-566 as a possible flux standard for COS and STIS. A DB-type white dwarf would provide a useful cross-check on the DA white dwarf standards normally used, especially for wavelengths near Lyman-alpha.

A detailed summary of the calibration plans can be found on the [STIS Calibration web page](#).

17.13 Cycle 19 Calibration Plan

The [Cycle 19 calibration plan](#) continues the standard monitoring programs established in previous Cycles, while adjustments are being made as necessary to better characterize the instrument and to meet Cycle 19 GO calibration requirements.

In addition to the new and modified calibration programs, the following areas are under study for possible improvement.

- Pixel based CTE correction.
- Revised CCD dark temperature scaling relation.
- The CCD and $FUV-MAMA$ distortion solution.

A detailed summary of the calibration plans can be found on the [STIS Calibration web page](#).

17.14 Cycle 20 Calibration Plan

The [Cycle 20 calibration plan](#) continues the standard monitoring programs established in previous Cycles, while adjustments are being made as necessary to better characterize the instrument and to meet Cycle 20 GO calibration requirements. A special program was added to study CCD residual images after over-illumination.

A detailed summary of the calibration plans can be found on the [STIS Calibration web page](#).

17.15 Cycle 21 Calibration Plan

The [Cycle 21 calibration plan](#) continues the standard monitoring programs established in previous Cycles, while adjustments are being made as necessary to better characterize the instrument and to meet Cycle 21 GO calibration requirements. A special program was added to study the CCD saturation limits.

A detailed summary of the calibration plans can be found on the [STIS Calibration web page](#).

17.16 Cycle 22 Calibration Plan

The [Cycle 22 calibration plan](#) continues the standard monitoring programs established in previous Cycles, while adjustments are being made as necessary to better characterize the instrument and to meet Cycle 22 GO calibration requirements.

A detailed summary of the calibration plans can be found on the [STIS Calibration web page](#).

17.17 Cycle 23 Calibration Plan

The [Cycle 23 calibration plan](#) continues the standard monitoring programs established in previous Cycles, while adjustments are being made as necessary to better characterize the instrument and to meet Cycle 23 GO calibration requirements. A special program was added to study the coronagraphic capabilities of BAR5 and to remeasure the CCD gain values of Amps A, C, and D. Extra observations were added to enhance the calibration of CTI effects and to monitor the focus offset between STIS and the other HST instruments. Additionally, a special program was carried out to assess the fading of the HITM2 calibration lamp at the bluest FUV wavelength settings.

A detailed summary of the calibration plans can be found on the [STIS Calibration web page](#).

17.18 Cycle 24 Calibration Plan

The [Cycle 24 calibration plan](#) continues the standard monitoring programs established in previous Cycles, while adjustments are being made as necessary to better characterize the instrument and to meet Cycle 24 GO calibration requirements. A special program was added to observe three HST white dwarf standard stars to verify the spectrophotometric stability of the stars observed for the MAMA and CCD spectroscopic sensitivity monitors. Simultaneous parallel observations with the STIS/CCD, WFC3/UVIS, and ACS/WFC detectors were included to monitor the focus offsets between the three HST instruments.

A detailed summary of the calibration plans can be found on the [STIS Calibration web page](#).

17.19 Cycle 25 Calibration Plan

The [Cycle 25 calibration plan](#) continues the standard monitoring programs established in previous Cycles, with minor adjustments to improve characterization of the instrument and meet Cycle 25 GO calibration requirements. A special program was added to optimize STIS spatial scans by determining the scan angle alignment and testing the flux repeatability of trailed observations in a wide aperture. Additionally, a special program was included to derive a new set of sensitivity curves for the E140M grating.

A detailed summary of the calibration plans can be found on the [STIS Calibration web page](#).

17.20 Cycle 26 Calibration Plan

The [Cycle 26 calibration plan](#) continues the standard monitoring programs established in previous Cycles, with minor adjustments to improve characterization of the instrument and to meet Cycle 26 GO calibration requirements. Special programs were added to assess the impact of increased spacecraft jitter on BAR5 coronagraphic exposures and to monitor the three primary white dwarf standard stars used for flux calibration.

A detailed summary of the calibration plans can be found on the [STIS Calibration web page](#).

17.21 Cycle 27 Calibration Plan

The [Cycle 27 calibration plan](#) continues the standard monitoring programs established in previous Cycles, with minor adjustments to improve characterization of the instrument and to meet Cycle 27 GO calibration requirements. A special program was added to enable more reliable cross correlation with COS by obtaining high signal-to-noise spectral energy distributions of white dwarfs used as standards for COS.

A detailed summary of the calibration plans can be found on the [STIS Calibration web page](#).

17.22 Cycle 28 Calibration Plan

The [Cycle 28 calibration plan](#) continues the standard monitoring programs established in previous Cycles, with minor adjustments to improve characterization of the instrument and to meet Cycle 28 GO calibration requirements. Also included are the biennial monitoring of the three primary white dwarf (WD) flux standards and four new special calibration programs: absolute flux measurements for several fainter WD standards (in order to improve cross-calibration with other instruments), an investigation of FUV flux variations at off-nominal detector positions, a more extensive assessment of the flux reproducibility obtainable with STIS spatial scans, and a NUV flat field monitor program to probe the current brightness of the Deuterium lamp (was approved in the middle of Cycle 28).

A detailed summary of the calibration plans can be found on the [STIS Calibration web page](#).

17.23 Cycle 29 Calibration Plan

The [Cycle 29 calibration plan](#) continues the standard monitoring programs established in previous Cycles, with minor adjustments to improve characterization of the instrument and to meet Cycle 29 GO calibration requirements. No additional special calibration programs were performed during Cycle 29.

A detailed summary of the calibration plans can be found on the [STIS Calibration web page](#).

17.24 Cycle 30 Calibration Plan

The [Cycle 30 calibration plan](#) continues the standard monitoring programs established in previous Cycles, with minor adjustments to improve characterization of the instrument and to meet Cycle 30 GO calibration requirements. Biennial monitoring of the three primary white dwarf flux standard stars (G191-B2B, GD71, GD153) -- done as special programs in cycles 24, 26, and 28 -- was incorporated into the regular calibration program. No additional special calibration programs are currently planned for Cycle 30.

A detailed summary of the calibration plans can be found on the [STIS Calibration web page](#).

17.25 Cycle 31 Calibration Plan

The [Cycle 31 calibration plan](#) continues the standard monitoring programs established in previous Cycles, with minor adjustments to improve characterization of the instrument and to meet Cycle 31 GO calibration requirements. Also included is a special calibration program to supplement the NUV spectroscopic sensitivity monitoring observations through solar maximum. This program increases the cadence of monitoring observations with the NUV-MAMA and CCD to better track sensitivity changes between 1800 and 2100 Angstroms.

A detailed summary of the calibration plans can be found on the [STIS Calibration web page](#).

Appendix A: Available-But-Unsupported Spectroscopic Capabilities

Appendix Contents

- [A.1 Introduction](#)
- [A.2 Full Aperture Complement](#)
- [A.3: Additional Available-but-Unsupported Options](#)

A.1 Introduction

STIS provides additional *Available-but-Unsupported* capabilities beyond those which will be routinely *supported*. [Section 2.4](#) describes the distinctions between supported and available-but-unsupported modes and the policies regarding use of the latter. A mode is a combination of aperture, optical element (and central wavelength setting), and detector.

This appendix to the *STIS Instrument Handbook* indicates which modes are supported and gives information about the additional Available-but-Unsupported modes of STIS. Since all of the imaging capabilities are supported (apart from special use case of coronagraphic imaging, see [Section 12.11](#)), it contains information relevant to spectroscopic observations only. As detailed in [Section A.2](#), numerous entrance slits or apertures are supported for a limited set of optical elements and available for others, or are used in available mode only. A small number of central wavelength settings have been removed from the set of supported settings due to difficulties with them (e.g., order overlap). [Section A.3](#) lists several additional available-but-unsupported capabilities that have been used in some recent programs.

A.2 Full Aperture Complement

The STIS aperture wheel has 65 positions, several of which correspond to multiple slits or masks. Only a small fraction of the full complement of spectroscopic apertures is currently supported. [Table A.1](#) and [Table A.2](#) provide complete lists of STIS apertures for spectroscopy, together with comments regarding their characteristics or purposes. For most apertures, the aperture name gives the length in the spatial direction by the width in the dispersion direction in arcseconds. Schematics of three complex apertures are given in [Figure A.1](#), [Figure A.2](#), and [Figure A.3](#).

Note that all set-ups with the NUV-PRISM are available-but-unsupported starting Cycle 30.

Table A.1: STIS Spectroscopic Apertures. Supported apertures are in boldface.

| Apertures that can be used with the Echelle Gratings | |
|---|--|
| Apertures | Comments |
| 0.1X0.03 0.1X0.06 0.1X0.09 0.1X0.2 | The latter two are supported with E230H only. The 0.1X0.03 is supported with all echelle gratings. |
| 0.2X0.06 0.2X0.09 0.2X0.2 0.2X0.5 | 0.2X0.2 is supported with all echelle modes, while 0.2X0.09 is supported with E230H and E140H, and 0.2X0.06 is only supported on E230H |
| 0.2X0.06FP 0.2X0.2FP | Masks with five apertures, suffixed A through E, for reduction of fixed-pattern noise; see Figure A.3 . |
| 0.2X0.05ND 0.3X0.05ND | Neutral-density slits. Dex ND factors are 2.0 and 3.0, respectively. |
| 0.3X0.06 0.3X0.09 0.3X0.2 0.5X0.5 1X0.06 1X0.2 | Miscellaneous available-but-unsupported echelle apertures. |
| 2X2 6X0.06 6X0.2 6X0.5 6X6 | The 6X0.2 long slit is supported with the echelles. |
| 52X0.05 52X0.1 52X0.2 52X0.5 52X2 | Long slits for use with the echelles. 52X0.05 is supported, and the others are available-but-unsupported with the echelle gratings. |
| 52X0.05F1 52X0.05F2 52X0.1F1 52X0.1F2 52X0.2F1 52X0.2F2 52X0.5F1 52X0.5F2 52X2F1 52X2F2 | The fiducial bar slits are available-but-unsupported with the echelle gratings. |
| 52X0.1B0.5 52X0.1B1.0 52X0.1B3.0 | A long slit with 3 fiducial bars. The bar length in arcseconds is given by the third dimension. See Figure A.1 . |
| 31X0.05NDA 31X0.05NDB 31X0.05NDC | Neutral-density-filtered long slits, which may be used for bright objects. The dex ND factors are 0.4, 0.8, and 1.2, respectively. |
| 25MAMA | Full-field clear aperture. |
| F25QTZ F25SRF2 | Supported long-pass filters, with all echelles. |

| | |
|--|---|
| F25ND3 F25ND5 F25NDQ1 F25NDQ2 F25NDQ3 F25NDQ4 | Supported neutral-density filters for MAMA detectors. The numbers give the dex ND factors. |
| F25MGII F25CN270 F25CIII F25CN182 | Narrow-band filters. F25MGII is supported for E230H and E230M. Others are available with the NUV-MAMA only. |
| F25LYA | Available-but-unsupported with the FUV-MAMA only. |
| 36X0.05P45 36X0.05N45 36X0.6P45 36X0.6N45 | Long slits which are inclined at $\pm 45^\circ$ to facilitate observations of moving targets at off-nominal rolls. See Figure A.2 . |

Table A.2: STIS Spectroscopic Apertures. Supported apertures are in boldface.

| Apertures that can be used with the First-Order Gratings | |
|--|--|
| Apertures | Comments |
| 52X0.05 52X0.1 52X0.2 52X0.5 52X2 | Long slits. |
| 52X0.05E1 52X0.1E1 52X0.2E1 52X0.5E1 52X2E1 | Long slits centered at 19.7 arcseconds in +Y position. (Places compact target at row ~ 900 on the CCD to reduce CTE losses.). Supported with all CCD gratings. Use with the MAMAs is not allowed. |
| 52X0.2E2 52X0.5E2 52X2E2 | These CTE aperture positions are centered near row 900 on the STIS CCD detector; however, the positions are offset from the physical aperture centers to give better alignment with fringe flats done using the 52X0.1 aperture. The E2 positions are supported for the G750L and G750M gratings only. |
| 52X0.05D1 52X0.1D1 52X0.2D1 52X0.5D1 52X2D1 | These aperture positions put a target near the bottom edge of the FUV-MAMA and are intended for observation of very faint targets where it is necessary to minimize the contribution of the FUV-MAMA dark current. They are all supported with the G140L and G140M gratings. 52X0.05D1 and 52X0.1D1 are also supported for CCD peakups. |
| 52X0.05F1 52X0.05F2 52X0.1F1 52X0.1F2 52X0.2F1 52X0.2F2 52X0.5F1 52X0.5F2 52X2F1 52X2F2 | Fiducial bars on the long slits which can be used for coronagraphic spectroscopy. The 52X0.2F1 is supported for all first-order gratings and is available-but-unsupported for the PRISM. The other fiducial bars are available-but-unsupported with all gratings and the PRISM. The F1 and F2 bars are 0.5 arcseconds and 0.86 arcseconds long, respectively (see Figure 13.1). |
| 52X0.1B0.5 52X0.1B1.0 52X0.1B3.0 | A long slit with 3 fiducial bars where the bar length in arcseconds is given by the third dimension. See Figure A.1 . |
| 31X0.05NDA 31X0.05NDB 31X0.05NDC | Neutral-density-filtered long slits of the given dimensions in arcseconds, which may be used for bright objects or flat-field calibration. The dex ND factors are 0.4, 0.8, and 1.2, respectively. Use with the NUV-PRISM is “available-but-unsupported.” |

| | |
|---|---|
| 0.5x0.5 2X2 6X6 | Square apertures of the given dimensions in arcsec. |
| 0.1X0.03 0.1X0.06 0.1X0.09 0.1X0.2 0.2X0.06 0.2X0.09 0.2X0.2 0.2X0.5 0.3X0.06 0.3X0.09 0.3X0.2 1X0.06 1X0.2 6X0.06 6X0.2 6X0.5 0.2X0.05ND 0.3X0.05ND | As of Cycle 12, the 0.2x0.2 aperture is supported for use with all first-order gratings; it is available-but-unsupported with the PRISM. While not supported for first-order observations, the other echelle apertures can be used in first order as available-but-unsupported apertures. This includes the echelle neutral-density slits 0.2x0.05ND and 0.3x0.05ND with dex ND factors of 2.0 and 3.0, respectively. |
| 25MAMA 50CCD | Supported full-field clear apertures. |
| F25QTZ F25SRF2 | F25QTZ and F25SRF2 are supported for all MAMA gratings, but are unavailable with the CCD and no longer supported for PRISM. |
| 25MAMAD1 F25SRF2D1 F25QTZD1 | These aperture positions put a target near the bottom edge of the FUV-MAMA and are intended for observation of very faint targets where it is necessary to minimize the contribution of the FUV-MAMA dark current. They are all supported with the G140L and G140M gratings. |
| F25ND3 F25ND5 F25NDQ1 F25NDQ2 F25NDQ3 F25NDQ4 | Supported neutral-density filters for MAMA detectors. Can be used as available-but-unsupported apertures with the CCD gratings. The numbers give the dex ND factors. |
| F25MGII F25CN270 F25CIII F25CN182 | F25MGII is supported and these other filters are available-but-unsupported with the NUV-MAMA gratings and PRISM only. |
| F25LYA | The F25LYA filter is available-but-unsupported with the G140L, G140M, E140H, and E140M gratings only. |
| F28X50LP F28X50OII F28X50OIII | These CCD imaging filters are available-but-unsupported with the CCD gratings, but are unavailable with the MAMA detectors. |
| 36X0.05P45 36X0.05N45 36X0.6P45 36X0.6N45 | Long slits of given dimensions in arcseconds, inclined at $\pm 45^\circ$ to facilitate observations of moving targets at off-nominal rolls. See Figure A.1 . |

Figure A.1: Schematic Showing the 52x 0.1 arcsecond Long Slit with 3 Occulting Bars.

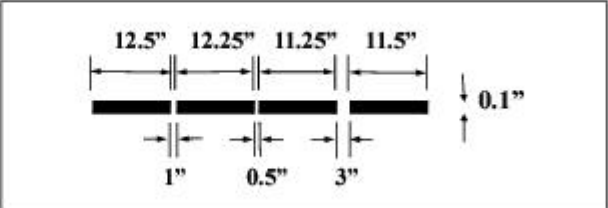


Figure A.2: Schematic Showing the 45° Slits Design. A second pair has the same morphology but widths of 0.6 arcsecond (central) and 2.0 arcsecond (peripheral).

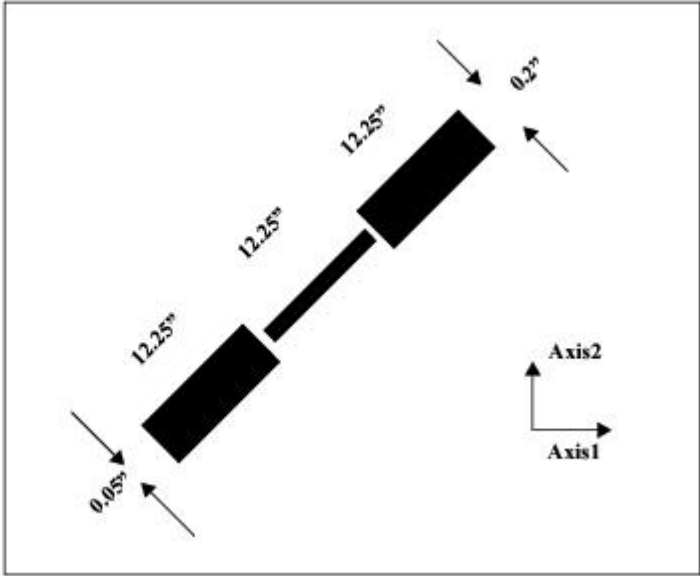
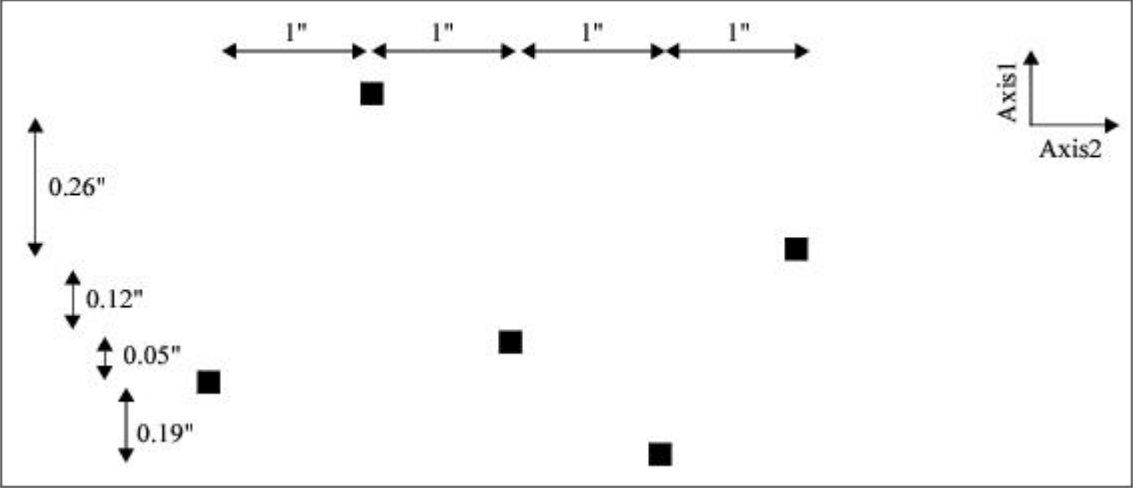


Figure A.3: Schematic Showing the Configuration of the Fixed-Pattern Slits. There are two sets, with slit widths of 0.06 arcsecond and 0.2 arcsecond, and lengths of 0.2 arcsecond in both cases. Axis1 corresponds to the dispersion direction.



A.3: Additional Available-but-Unsupported Options

There are a few additional available-but-unsupported capabilities that can be used (upon justification and approval) for certain applications:

- Spatial scans, which are a supported mode for WFC3 observations (see [WFC3 ISR 2012-08: Considerations for using Spatial Scans with WFC3](#)), can also be used with the STIS CCD as an available-but-unsupported mode. For more information on the potential advantages of spatial scanning and instructions on its implementation, please refer to the dedicated section [12.12 Spatial Scans with the STIS CCD](#).
- While the use of [GO wavecal](#)s employing the default exposure times is supported, there are cases where longer exposure times may be needed. Some programs (e.g., where extremely precise wavelength zero points are required) or ones using settings where the fading of the emission lines in the calibration lamps has been most severe (e.g., [STIS ISR 2017-04](#)) may benefit from somewhat longer wavecal exposures times. Because the calibration lamps have limited lifetimes, the use of longer wavecal exposures requires adequate justification and approval.
- `POS TARGS` (see [Section 11.5](#)) may be used to adjust the placement of targets behind the coronagraphic bars.
- Some programs requiring very high photometric accuracy and reproducibility in first-order spectra obtained with the FUV and NUV MAMAs (e.g., in comparisons between data from multiple epochs) may benefit from disabling the default monthly positional offsets applied in executing such observations. Starting in Cycle 30, this previously restricted capability (using the `MSMOFF` mode) will become available-but-unsupported; users for whom this option may be beneficial should consult the [Help Desk](#).
- Due to lack of recent use and to significant uncertainties in its current sensitivity, use of the NUV PRISM will be considered as available-but-unsupported starting in Cycle 30.
- Programs using G750L or G750M and need high signal-to-noise may ask for longer fringe flat exposure times. Since the lamps have a limited lifetime, this is an available-but-unsupported mode (see [Section 11.2.3](#)).

Glossary

The following terms and acronyms are used in this Handbook.

| | |
|-----------------|---|
| A-D | Analog to Digital |
| ACS | Advanced Camera for Surveys |
| ABMAG | $-2.5 \log (F_{\nu}) - 48.60$ where F_{ν} is the flux from the source in $\text{erg}/\text{cm}^2/\text{s}/\text{Hz}$ |
| APT | Astronomer's Proposal Tool. Used to construct Phase I and Phase II observing proposals: https://www.stsci.edu/scientific-community/software/astromers-proposal-tool-apt |
| BOP | Bright-Object Protection |
| CALSTIS | STIS calibration pipeline software: https://stistools.readthedocs.io/en/latest/calstis.html |
| CCD | Charge Coupled Device. Solid-state photon counting device |
| CDBS | Calibration Data Base. System for maintaining reference files and tables used to calibrate <i>HST</i> observational datasets. |
| CIM | Calibration insert mechanism |
| COS | Cosmic Origins Spectrograph |
| CP, CfP | Call for Proposals |
| CR | Cosmic ray |
| CR-SPLIT | Division of a CCD exposure into shorter exposures to be used for cosmic ray rejection |
| CTE | Charge Transfer Efficiency |
| CTI | Charge Transfer Inefficiency, $\text{CTI} = 1 - \text{CTE}$ |
| CVZ | Continuous Viewing Zone. A range of target declinations for which full-orbit observations may be obtained (without Earth occultation). |
| DQ | Data Quality. DQ flags in the data files indicate various potential or actual problems with the data. |
| DHB | Data Handbook: https://hst-docs.stsci.edu/stisdhb |
| DN | Data Number |
| ETC | Exposure Time Calculator. ETCs are Web based tools, which can be accessed at https://etc.stsci.edu . |
| ERO | Early Release Observations |
| FGS | Fine Guidance Sensors |

| | |
|-------------------------|---|
| <i>FITS</i> | Flexible Image Transport System. A generic IEEE and NASA defined standard file format used for storing image data. |
| <i>FOC</i> | Faint Object Camera |
| <i>FOS</i> | Faint Object Spectrograph |
| <i>FOV</i> | Field of View |
| <i>FSW</i> | Flight Software |
| <i>FTP</i> | File Transfer Protocol. Basic tool used to retrieve files from a remote system. Ask your system manager for information about using FTP. |
| <i>FUV</i> | Far ultraviolet (~912–2000 Å) |
| <i>FWHM</i> | Full Width at Half Maximum |
| <i>GALEX</i> | Galaxy Evolution Explorer |
| <i>GHRS</i> | Goddard High-Resolution Spectrograph |
| <i>GO</i> | General Observer |
| <i>GSC</i> | Guide Star Catalog |
| <i>GTO</i> | Guaranteed Time Observer |
| <i>Help Desk</i> | Facility for getting help on <i>HST</i> related topics: http://hsthhelp.stsci.edu or help@stsci.edu |
| <i>HITM</i> | Hole in the Mirror. Part of the optical path for some calibration lamps. |
| <i>HSP</i> | High-Speed Photometer |
| <i>HST</i> | Hubble Space Telescope |
| <i>HUT</i> | Hopkins Ultraviolet Telescope |
| <i>ICD</i> | Interface control document. Defines data structures used between software or systems to ensure compatibility. |
| <i>IDT</i> | Instrument Definition Team |
| <i>IHB</i> | Instrument Handbook |
| <i>IR</i> | Infrared |
| <i>IRAF</i> | Image Reduction and Analysis Facility. The environment in which -STSDAS operates (no longer supported). |
| <i>IS</i> | Instrument Scientist |
| <i>ISR</i> | Instrument Science Report |
| <i>IUE</i> | International Ultraviolet Explorer |

| | |
|------------------------------|---|
| <i>K</i> | Degree Kelvin |
| <i>LMC</i> | Large Magellanic Cloud |
| <i>LSF</i> | Line spread function |
| <i>MAMA</i> | Multi-Anode Microchannel Array. STIS uses MAMA detectors for FUV and NUV observations. |
| <i>MAST</i> | Barbara A. Mikulski Archive for Space Telescopes. A repository for data from HST, JWST, and other missions: https://mast.stsci.edu/ |
| <i>MCP</i> | Microchannel Plate |
| <i>MSM</i> | Mode-Selection Mechanism |
| <i>ND</i> | Neutral density |
| <i>NIR</i> | Near infrared |
| <i>NICMOS</i> | Near-Infrared Camera and Multi-Object Spectrograph |
| <i>NUV</i> | Near ultraviolet (~2000–4000 Å) |
| <i>OSS</i> | Observation Support System |
| <i>OTA</i> | Optical Telescope Assembly |
| <i>OTFR</i> | On-the-Fly Re-processing. Re-processing of data, using the most recent/appropriate reference files and software, when the data are requested from the archive. |
| <i>PC</i> | Program Coordinator |
| <i>Peakdown</i> | Movement of a target along a slit to center it under an occulting bar. |
| <i>Peakup</i> | Movement of a target in one or both directions to center it in a slit. |
| <i>Phase I</i> | A proposal for observing time on <i>HST</i> |
| <i>Phase II</i> | An approved <i>HST</i> proposal; includes detailed instructions for how a program is to be executed |
| <i>PI</i> | Principal investigator |
| <i>PSF</i> | Point-spread function |
| <i>QE</i> | Quantum efficiency |
| <i>QEH</i> | Quantum efficiency hysteresis |
| <i>QSO</i> | Quasi-stellar object |
| <i>RA</i> | Right ascension |
| <i>reference file</i> | Data file containing STIS parameters or calibration information which is used by the pipeline |

| | |
|------------------------|---|
| <i>rms</i> | Root mean square |
| <i>SAA</i> | South Atlantic anomaly. A region of enhanced background radiation. STIS is not used when the orbital path of HST passes through the SAA. |
| <i>SIM</i> | Space Interferometry Mission |
| <i>SITe</i> | Scientific Image Technologies; company that designed the STIS CCD |
| <i>SM4</i> | Servicing mission 4. Servicing mission in which STIS operations were restored |
| <i>SMOV</i> | Servicing Mission Observatory Verification |
| <i>S/N, SNR</i> | Signal-to-noise ratio |
| <i>ST-ECF</i> | Space Telescope European Coordinating Facility |
| <i>STAN</i> | Space Telescope Analysis Newsletter |
| <i>stenv</i> | Environment for HST and JWST pipelines and (most) packages formerly available through astroconda: https://stenv.readthedocs.io/en/latest/ |
| <i>STIS</i> | Space Telescope Imaging Spectrograph |
| stistools | A suite of software tools for STIS data calibration and analysis: https://stistools.readthedocs.io/en/latest/ |
| <i>stis_cti</i> | Pixel-based CTI correction software for the STIS CCD: https://www.stsci.edu/hst/instrumentation/stis/data-analysis-and-software-tools/pixel-based-cti |
| <i>STMAG</i> | STScI magnitude system; $-2.5 \log (F_{\lambda}) - 21.10$ where F_{λ} is the flux from the source in $\text{erg}/\text{cm}^2/\text{s}/\text{\AA}$ |
| <i>STScI</i> | Space Telescope Science Institute |
| <i>STSDAS</i> | Space Telescope Science Data Analysis System. The complete suite of IRAF data analysis and calibration routines used to process <i>HST</i> data (no longer supported). |
| <i>SV</i> | Science verification. Process of taking observations that can be used for <i>HST</i> instrument calibration. |
| <i>synphot</i> | Synthetic Photometry software package: https://synphot.readthedocs.io/en/latest/ |
| <i>TAC</i> | Telescope Allocation Committee |
| <i>TAS</i> | Target Acquisitions Simulator: https://stistarg.readthedocs.io/en/latest/ |
| <i>TDS</i> | Time-dependent Sensitivity |
| <i>TIR</i> | Technical Instrument Report |
| <i>URL</i> | Uniform resource locator. Address for websites. |
| <i>UV</i> | Ultraviolet |

| | |
|---------------------|---|
| <i>WF/PC</i> | Wide Field/Planetary Camera |
| <i>WFPC2</i> | Wide Field Planetary Camera-2. Replacement for WF/PC installed during first servicing mission of December 1993. |
| <i>WFC3</i> | Wide Field Camera 3 |